# Preface

The theme of the Geophysical Fluid Dynamics Program for summer 2025 was *Instabilities and Bifurcations in GFD*. The first week of principal lectures were delivered by Joseph Pedlosky (WHOI), focusing on the baroclinic instability and other linear and nonlinear instabilities in a geophysical context. The second week of principal lectures were delivered by Laurette Tuckerman (ESPCI Paris), who taught the mathematical underpinnings needed to understand instabilities and bifurcations in fluid systems. These proceedings contain notes on the ten principal lectures, produced by student fellows together with the lecturers. They also contain reports by the student fellows on their summer research projects. Detailed notes are not included for the summer's many other stimulating activities, which included near-daily research seminars, a tutorial on geophysical models by Glenn Flierl, a tutorial on the Dedalus code by Keaton Burns, a presentation by the summer's co-directors on how to give good talks, and an example of a very good talk: the Sears Public Lecture by Jennifer MacKinnon (UC San Diego) entitled "Fresh, Salty or Spicy: How Layering of Different Types of Water Controls Heat, Hurricanes and Habitats in the Gulf of Mexico."

The co-directors this year were Pascale Garaud (UC Santa Cruz) and David Goluskin (University of Victoria). The program fully supported twelve student fellow – two more than usual:

- Edoardo Bellincioni, University of Twente
- Emma Bouckley, University of Cambridge
- Marion Cocusse, École Polytechnique
- Isabela Conde, University of New South Wales
- David Darrow, MIT
- Theo Lewy, University of Cambridge
- Kyle McKee, MIT
- Andrés Posada, Queen's University
- Heng Quan, Princeton University
- Farid Rajkotia-Zaheer, University of Victoria
- Alexandre Tlili, CEA Saclay
- Lin Yao, University of Chicago

Nearly all long-term visitors advised or co-advised the fellows' projects, and all fellows presented their projects beautifully in the program's final week. Laboratory projects were facilitated by able support from Anders Jensen, and the large administrative side of the summer was run smoothly as usual by Julie Hildebrandt and Janet Fields. Lastly, this year's Distinguished Scholar Award was presented to Keaton Burns, for his academic excellence, service to the GFD community supporting use of the Dedalus code, and dedication to mentoring the next generation of fellows.

# Table of Contents



## Principal Lectures



## Fellows Reports

# 2025 Participants

## FELLOWS

| | |
|---|---|
| Edoardo Bellincioni | University of Twente |
| Emma Bouckley | University of Cambridge |
| Marion Cocusse | École Polytechnique |
| Isabela Conde | University of New South Wales |
| David Darrow | Massachusetts Institute of Technology |
| Theo Lewy | University of Cambridge |
| Kyle McKee | Massachusetts Institute of Technology |
| Andrés Posada | Queen's University |
| Heng Quan | Princeton University |
| Farid Rajkotia-Zaheer | University of Victoria |
| Alexandre Tlili | Université Paris-Saclay |
| Lin Yao | University of Chicago |

## STAFF AND VISITORS

| | |
|---|---|
| Dwight Barkley | University of Warwick |
| Emma Boland | British Antarctic Survey |
| Oliver Brown | University of Victoria |
| Dante Buhl | University of California, Santa Cruz |
| Keaton Burns | Massachusetts Institute of Technology |
| Elizabeth Carlson | California Institute of Technology |
| Colm-cille Caulfield | University of Cambridge |
| Claudia Cenedese | Woods Hole Oceanographic Institution |
| Gregory Chini | University of New Hampshire |
| Paul Curtis | Yale University |
| Florentin Daniel | Northwestern University |
| Megan Davies Wykes | University of Cambridge |
| Giovanni Dematteis | University of Torino |
| Raffaele Ferrari | Massachusetts Institute of Technology |
| Glenn Flierl | Massachusetts Institute of Technology |
| Adrian Fraser | University of Colorado |
| Mara Freilich | Brown University |
| Basile Gallet | CEA, Saclay |
| Pascale Garaud | University of California, Santa Cruz |
| Arefe Ghazi Nezami | University of Texas Austin |
| David Goluskin | University of Victoria |
| Xuanting Hao | Scripps Institution of Oceanography |
| Karl Helfrich | Woods Hole Oceanographic Institution |
| Jamie Hilditch | Stanford University |

| | |
|---|---|
| Edward Johnson | University College London |
| Wanying Kang | Massachusetts Institute of Technology |
| Zhiming Kuang | Harvard University |
| Adrien Lefauve | Imperial College London |
| Samuel Lewin | University of California, Berkeley |
| Chang Liu | University of Connecticut |
| Stefan Llewellyn Smith | University of California, San Diego |
| Jennifer MacKinnon | University of California, San Diego |
| Nathan Magnan | Observatoire de la Cote d'Azur |
| Yifeng Mao | Scripps Institution of Oceanography |
| Loren Matilsky | University of California, Santa Cruz |
| Matthew McCormack | University of Edinburgh |
| James McElwaine | Woods Hole Oceanographic Institution |
| Colin Meyer | Dartmouth College |
| Camille Moisset | CEA Paris-Saclay |
| M. Nicholas Moore | Colgate University |
| Philip Morrison | University of Texas Austin |
| Theresa Oehmke | University of New Hampshire |
| Joseph Pedlosky | Woods Hole Oceanographic Institution |
| Shirui Peng | Massachusetts Institute of Technology |
| Nicolaos Petropoulos | Stanford University |
| Bartosz Protas | McMaster University |
| Kasturi Shah | University of Cambridge |
| Nicole Shibley | University of Cambridge |
| Valentin Skoutnev | Columbia University |
| Bruce Sutherland | University of Alberta |
| Shuwen Tan | Columbia University |
| Laurette Tuckerman | Sorbonne University |
| Arstanbek Tulekeyev | University of California Santa Cruz |
| Claire Valva | New York University |
| Adrian van Kan | University of California, Berkeley |
| Baole Wen | York Institute of Technology |
| Jacob Wenegrat | University of Maryland |
| John Whitehead | Woods Hole Oceanographic Institution |
| Carl Wunsch | Harvard University |
| Hojung You | Woods Hole Oceanographic Institution |
| Yaoxuan Zeng | University of Chicago |

# 2025 Principal Lecturers

**Joseph Pedlosky and Laurette Tuckerman**

# 2025 Geophysical Fluid Dynamics Summer School Participants

***First Row (L-R):*** *(Sitting)* Edoardo Bellincioni, David Darrow, Andrés Posada, Emma Bouckley, Kyle McKee, Isabela Conde, Marion Cocusse, Alexandre Tlili, Farid Rajkotia-Zaheer, Lin Yao, Heng Quan, Theo Lewy, Adrian van Kan (standing)

***Second Row (L-R):*** *(Sitting)* Baole Wen, David Goluskin, Edward Johnson, Philip Morrison

***Third Row:*** Jacob Wenegrat (standing), Gregory Chini, Paul Curtis, Camille Moisset, Nicolaos Petropoulos, Matthew McCormack, Colm-cille Caulfield, Shirui Peng, Loren Matilsky (kneeling), Adrian Fraser, Glenn Flierl, Joseph Pedlosky, Valentin Skoutnev, Claudia Cenedese, James McElwaine, Pascale Garaud, Shuwen Tan, Claire Valva, Oliver Brown, Elizabeth Carlson, Chang Liu, Laurette Tuckerman

***Not in photo:*** Ali Arslan, Dwight Barkley, Emma Boland, Dante Buhl, Keaton Burns, Florentin Daniel, Megan Davies Wykes, Raffaele Ferrari, Mara Freilich, Basile Gallet, Arefe Ghaze Nezami, Xuanting Hao, Jamie Hilditch, Wanying Kang, Adrien Lefauve, Samuel Lewin, Stefan Llewellyn Smith, Nathan Magnan, Colin Meyer, Nick Moore, Theresa Oehmke, Bartosz Protas, Kasturi Shah, Nicole Shibley, Bruce Sutherland, Arstanbek Tulekeyev, Jack Whitehead, Yaoxuan Zeng

# Lecture Schedule

## PRINCIPAL LECTURES

Monday, June 16

*Discussion of Quasi Geostrophy, Quasi Geostrophic Potential Vorticity, Conditions for Instability and Physical Interpretation*
Joseph Pedlosky

Tuesday, June 17

*Weakly Nonlinear Theory: The 2-layer Model, Critical Shears for Instability, Multiple Time Scales for Supercritical Flows, Chaos*
Joseph Pedlosky

Wednesday, June 18

*The Role of Topography and Radiation, an Example of Radiation-induced Instability*
Joseph Pedlosky

Friday, June 20

*Instabilities Evolving in Space and Time: The Role of Chaos and Chaotic Shocks*
Joseph Pedlosky

*Giants: A History. Eady and Charney, Their Contributions and the History of the Charney/Burger Problem*
Joseph Pedlosky

Monday, June 23

*Dynamical Systems and Bifurcations*
Laurette Tuckerman

Tuesday, June 24

*Symmetry via Taylor-Couette Flow and Rayleigh-Benard Convection*
Laurette Tuckerman

Wednesday, June 25

*Applications to the Eckhaus Instability, D4 Scenario, and Others*
Laurette Tuckerman

Thursday, June 26

*Transition to Turbulence and the Self-sustaining Process*
Laurette Tuckerman

Friday, June 27

*Codimension-two Birfucations*
Laurette Tuckerman

## SEMINARS

Monday, June 30

*Transition to Turbulence in Stratified Kolmogorov Flows with Horizontal Shear*
Pascale Garaud, U. California Santa Cruz

Tuesday, July 1

*Thin Jet Instabilities*
Glenn Flierl, MIT

Wednesday, July 2

*Asymptotic Transport of Exact Coherent States in Two-Dimensional Rayleigh–Bénard Convection*
Baole Wen, New York Institute of Technology

Thursday, July 3

*Reversals of the Large-scale Circulation in Thermal Convection*
Nick Moore, Colgate University

Monday, July 7

*Ultrasound for Estuaries: Imaging the Hidden Life of Stratified Turbulence*
Adrien Lefauve, Imperial College London

Tuesday, July 8

*Two Openings Are Better Than One: The Fluid Mechanics of Natural Ventilation*
Megan Davies Wykes, University of Cambridge

Wednesday, July 9

*Transport by 2d Turbulence: A Surprising Failure of the Standard Inverse Cascade Theory*
Basile Gallet, CEA Saclay

Thursday, July 10

*Systematic Search for Singularities and Instabilities in Euler Flows*
Bartosz Protas, McMaster University

Friday, July 11

*Angular Momentum Transport I Stellar Stably Stratified Layers: Impact of Dynamo Action (and Waves)*
Florentin Daniel, Northwestern University

Monday, July 14

*A Dynamo Confinement Scenario for the Solar Tachocline in the Appropriate Parameter Regime*
Loren Matilsky, U. California Santa Cruz

Tuesday, July 15

*Interaction Between Tides, Convection and Baroclinic Eddies on Icy Satellites*
Wanying Kang, MIT

Wednesday, July 16

*Cross Scale Energy and Tracer Fluxes from Observations and Theory*
Mara Freilich, Brown University

Thursday, July 17

*From Surface Tension in a Two-layer Model to Breaking Wave-induced Bioluminescence: GFD at Scales < O(1 m)*
Xuanting Hao, Scripps Institution of Oceanography

Friday, July 18

*Spontaneous Generation of Helical Flows by Salt Fingers*
Adrian Fraser, U. Colorado Boulder

Monday, July 21

*Internal Waves Created and Absorbed by Turbulence*
Bruce Sutherland, University of Alberta

Tuesday, July 22

*Fluid Dynamics of Aerosol-filled Vortices in the Stratosphere*
Kasturi Shah, University of Cambridge

Wednesday, July 23

*Parametric Instabilities and Mixing Along the Ocean Seafloor*
Raffaele Ferrari, MIT

Thursday, July 24

*Consistent Spectral Approximations of Koopman Operators and an Application to the Quasi-biennial Oscillation*
Claire Valva, New York University

Friday, July 25

*Assimilation as a Tool for Understanding Large-Time Behavior of Dynamical Systems*
Elizabeth Carlson, California Institute of Technology

Monday, July 28

*Ocean Dynamics of Rapidly Rotating Ice-covered Satellites Due to Heterogeneous Seafloor Heating*
Arefe Ghazi Nezami, University of Texas Institute for Geophysics

Tuesday, July 29

*A Discussion about Ice*
Nicole Shibley, University of Cambridge

Wednesday, July 30

*Coupled Effects of Vortex Dynamics and Shape Change on Ice Cylinders in a Cross-flow*
Sarah Morris, Montana State University

Thursday, July 31

*Topics in Instability and Transition*
Dwight Barkley, University of Warwick

Friday, August 1

*Internal Wave-breaking in a Horizontally Sheared Mean Flow*
Samuel Lewin, University of California Berkeley

Monday, August 4

*Thinking Outside of the Non-dimensional Box*
Jennifer MacKinnon, University of California San Diego

Tuesday, August 5

**Sears Public Lecture**
*Fresh, Salty or Spicy: How Layering of Different Types of Water Controls Heat, Hurricanes and Habitats in the Gulf of Mexico*
Jennifer MacKinnon, University of California, San Diego

Wednesday, August 6

*Exact Solutions to Euler's Equations*
Nick Pizzo, University of Rhode Island

Thursday, August 7

*An Experimental Exploration of Mass Flux with Applications to Particles and Turbulence*
Theresa Oehmke, University of New Hampshire

Friday, August 8

*Resonant Drag Instabilities, or What Happens When You Sprinkle Dust on a Wave?*
Nathan Magnan, Côte d'Azur University

## FELLOWS' PRESENTATIONS

Tuesday, August 19

*Secondary Shear Instabilities on Kelvin-Helmholtz Braids*
Emma Bouckley, University of Cambridge

*Optimal Heat Transport in Steady Rayleigh-Bénard Convection*
Theo Lewy, University of Cambridge

*Ray Theory for Rotating Hyperbolic "Instabilities"*
Farid Rajkotia-Zaheer, University of Victoria

*Weakly Nonlinear Dynamics of Vorticity Patches from Hamiltonian Contour Theory*
Alexandre Tlili, CEA

*Linear Waves vs. Nonlinear Potential Vorticity Mixing—Which Determines the Equatorial Jet Direction in Planetary Atmospheres?*
Heng Quan, Princeton University

Wednesday, August 20

*Pattern Transitions in Faraday Waves: From Hexagons to Beaded Stripes*
Kyle McKee, MIT

*Upslope and Downslope Flow Along Ocean Bottom*
Isabela Conde, University of New South Wales

*The Interaction of a Gravity Wave with an Unstable Horizontal Shear at Low Froude Number*
Marion Cocusse, École Polytechnique

*Effect of Burger Number on Two Rotating Currents*
Edoardo Bellincioni, University of Twente

*Submarine Waterfalls: Dynamics of Gravity Currents over Stepped Slopes*
Andrés Posada, Queen's University

Thursday, August 21

*Global Stability Beyond the Energy Method*
David Darrow, MIT

*Baroclinic Instability as a Driver of Polar Vortices on Giant Planets*
Lin Yao, University of Chicago

# GFD 2025 Lecture 1: Introduction to Quasi-Geostrophic Theory

Joseph Pedlosky; notes by Edoardo Bellincioni and Emma Bouckley

June 16, 2025

*This lecture summarizes Chapters 6 and 7 of the Geophysical Fluid Dynamics book by J. Pedlosky [2]*

## 1 Basics of QG Theory

This lecture series focuses on quasigeostrophic motion of fluids in geophysical systems. First and foremost, let us review some of the basic theory. We consider a system with a horizontal length scale $L$, a vertical length scale $D$, a velocity scale $U$, which is defined on a sphere that rotates with a frequency of $\Omega$. The Coriolis parameter is $f_0 = 2\Omega\sin\vartheta$ at a latitude $\vartheta$. The Rossby number Ro nondimensionalises the rotation effect as

$$\mathrm{Ro} = \frac{U}{f_0 L} \ . \tag{1}$$

Ro compares the inertial timescale $U/L$ with the rotation timescale $1/f_0$, hence for rotation to be the dominant effect, we require $\mathrm{Ro} \ll 1$. This is referred to as Quasi-Geostrophy (QG).

In systems where the effect of rotation is non-negligible, we can anticipate the magnitude of the horizontal pressure gradients to be of the same order as the Coriolis acceleration. At the same time, for a fluid with a vertical background density profile $\rho_s = \rho_s(z)$, the vertical pressure gradients will be of the same order as buoyancy effects. Hence, an expression for the density can be found that accounts for the rotation effects.

$$\rho = \rho_s(z)(1 + \mathrm{Ro} F \rho') \ , \tag{2}$$

with $F = \frac{f_0^2 L^2}{gD}$ being a parameter that compares the horizontal Coriolis effects $f_0 L$ with the vertical buoyancy effects $gD$ (in general is $F \ll 1$), and $\rho'$ a $\mathcal{O}(1)$ dimensionless buoyancy perturbation with an $\mathcal{O}(1)$ variation over $\mathcal{O}(L)$ length scales.

We can now consider the simple case of a fluid parcel that is displaced vertically, and receives a restoring force by buoyancy (gravity). It is easy to derive that the motion has an intrinsic oscillatory frequency, which takes the form

$$N^2 = -\frac{g}{\rho_s}\frac{\partial \rho_s}{\partial z} \ . \tag{3}$$

This frequency takes the name of Brunt–Väisälä frequency.

Having introduced $N$, we can define a "deformation radius" (so-called *internal Rossby radius of deformation*) which will turn out to be the characteristic scale of instabilities of interest:

$$L_D = \frac{ND}{f} \ , \tag{4}$$

and restrain our interest to the motions whose horizontal length scale is of the same order as the deformation radius. As a reference, the deformation radius is in the order of 100 km in the ocean,

and 1000 km in the atmosphere, and this corresponds to the typical eddy size (oceanic eddies and atmospheric cyclones).

Finally, we can compare the vertical (buoyancy) stratification, that acts with a frequency $N$ on a length scale $D$, with the horizontal (Coriolis) stratification, that acts with a frequency $f_0$ on a length scale $L$, using the parameter

$$S = \frac{N^2}{f_0^2}\frac{D^2}{L^2} \ . \tag{5}$$

For our problems of interest, where we have assumed $L$ is order $L_D$, this quantity is of order 1.

In what follows, we use $L$ to scale all horizontal length scales, and $D$ to scale the vertical length scale, $U$ to scale the horizontal velocities, $\mathrm{Ro}UD/L$ for the vertical velocity, $L/U$ to scale time, and $\mathrm{Ro}f_0UL$ to scale pressure (the density has already implicitly been rescaled in equation 2).

For small Rossby number, it can be shown that the governing balances in the momentum equation reduce to hydrostatic and geostrophic balances, expressed in the following dimensionless equations:

$$v_0 = \frac{\partial p_0}{\partial x}, \tag{6}$$

$$u_0 = -\frac{\partial p_0}{\partial y}, \tag{7}$$

$$\rho_0 = -\frac{\partial p_0}{\partial z}. \tag{8}$$

Note that the index 0 on the flow quantities represents the first term in a series expansion in Rossby number, see [2]. Notably, it follows that the horizontal flow is non-divergent, which allows us to introduce a stream function for the horizontal velocity $\psi = p_0$.

## 2 Conservation of Vorticity

In a rotating system, potential vorticity is conserved, and there are three major contributors to that potential vorticity. First, is the relative vorticity of the flow

$$\zeta_0 = \frac{\partial v_0}{\partial x} - \frac{\partial u_0}{\partial y} \ . \tag{9}$$

Secondly, variations of the Coriolis parameter, which can be expanded in first order as

$$f = f_0 + \beta y, \tag{10}$$

when expressed dimensionally, can cause dimensional planetary vorticity variations $\beta y$. And lastly vertical gradients of $\rho_0$ (the first term in the expansion in Rossby number of the variable density field) divided by the stratification parameter $S$ (which measures the background stratification, and can also vary with $z$).

From the original system of equations one can derive the following governing equation for conservation of potential vorticity (Quasi-geostrophic Potential Vorticity equation, QGPV) where hereafter, $\beta$ and $y$ are both dimensionless

$$\frac{\mathrm{d}Q}{\mathrm{d}t} = \frac{\mathrm{d}}{\mathrm{d}t}\left[\zeta_0 + \beta y - \frac{\partial}{\partial z}\left(\frac{\rho_0}{S}\right)\right] = 0 \tag{11}$$

where the notation $\mathrm{d}/\mathrm{d}t$ denotes the derivative following horizontal fluid motions (the vertical velocity only coming in at the next order). The above equation is a conservation equation for

the total vorticity of the flow, $Q$, and accounts for: the intrinsic vorticity of the flow; for changes in vorticity due to latitudinal motion in the $\beta$-plane; and for vertical stretching in a stratified environment.

# 3 The Perturbed Zonal Flow

For our system, which is on the $\beta$-plane and whose stratification is measured by the parameter $S$, the evolution of the stream function is governed by

$$\left[\frac{\partial}{\partial t}+\frac{\partial\psi}{\partial x}\frac{\partial}{\partial y}-\frac{\partial\psi}{\partial y}\frac{\partial}{\partial x}\right]\left[\frac{\partial^2\psi}{\partial x^2}+\frac{\partial^2\psi}{\partial y^2}+\frac{\partial}{\partial z}\left(\frac{1}{S}\frac{\partial\psi}{\partial z}\right)+\beta y\right]=0\ , \tag{12}$$

that holds under the assumption of vertical hydrostatics and $D \ll L$, with the boundary conditions of having a non-slip, solid boundary below (the Earth's surface) and a free-slip fluid above (a higher layer of air or water).

We are now going to consider perturbations to a background zonal flow whose stream function is only a function of the vertical and latitudinal coordinates $\Psi(y,z)$, with a corresponding zonal velocity $U_0=-\partial_y\Psi(y,z)$. Under these assumptions,the background potential vorticity is

$$\bar{Q}=\underbrace{\beta y}_{\substack{\text{beta}\\ \text{effect}}}+\underbrace{\frac{\partial^2\Psi}{\partial y^2}}_{\substack{\text{horizontal}\\ \text{shear}}}+\underbrace{\frac{\partial}{\partial z}\left(\frac{1}{S}\frac{\partial\Psi}{\partial z}\right)}_{\substack{\text{vertical}\\ \text{shear}}}\ , \tag{13}$$

whose $y$-derivative reads

$$\frac{\partial\bar{Q}}{\partial y}=\beta-\frac{\partial^2U_0}{\partial y^2}-\frac{\partial}{\partial z}\left(\frac{1}{S}\frac{\partial U_0}{\partial z}\right)\ . \tag{14}$$

If we now add a perturbation to the stream function, such that

$$\psi(x,y,z,t)=\Psi(y,z)+\varphi(x,y,z,t)\ , \tag{15}$$

this corresponds to a perturbation $q=q(x,y,z,t)$ to the background vorticity $\bar{Q}$. The equation for $q$ will read

$$q=\frac{\partial^2\varphi}{\partial x^2}+\frac{\partial^2\varphi}{\partial y^2}+\frac{\partial}{\partial z}\left(\frac{1}{S}\frac{\partial\varphi}{\partial z}\right)\ . \tag{16}$$

Hence its evolution is given by

$$\left(\frac{\partial}{\partial t}+U_0\frac{\partial}{\partial x}\right)q+\frac{\partial\varphi}{\partial x}\frac{\partial\bar{Q}}{\partial y}+\left(\frac{\partial\varphi}{\partial x}\frac{\partial q}{\partial y}-\frac{\partial\varphi}{\partial y}\frac{\partial q}{\partial x}\right)=0\ . \tag{17}$$

## 3.1 Necessary conditions for instability

The non-linearity of eq. (17) renders it difficult to consider in full. Instead, we shall specify that the initial stream function perturbation $\varphi$ is small and as such can neglect terms of order $\varphi^2$ and higher,

$$\left(\frac{\partial}{\partial t}+U_0\frac{\partial}{\partial x}\right)q+\frac{\partial\varphi}{\partial x}\frac{\partial\bar{Q}}{\partial y}=0. \tag{18}$$

An energy equation may be found by multiplying eq. (18) by $\varphi$ and integrating over the volume of the fluid. The resultant equation relates the rate of change of the sum of kinetic and available

potential energies of the disturbance to the respective growth or decay of perturbation energy. It can be shown from consideration of this energy equation that, in the absence of dissipation, the effect of the fluctuations on the mean flow is merely to redistribute the $x$-averaged zonal momentum. From this, we may specify the following necessary condition for instability:

$$0 = \int_0^{z_T} \int_{-1}^{1} \frac{\partial \bar{Q}}{\partial y} \left( \frac{\partial}{\partial t} \overline{\eta^2} \right) \, \mathrm{d}y \, \mathrm{d}z + \int_{-1}^{1} \left[ \frac{1}{S} \frac{\partial U_0}{\partial z} \frac{\partial}{\partial t} \overline{\eta^2} \right]_{z=z_T} \mathrm{d}y - \int_{-1}^{1} \left[ \left( \frac{1}{S} \frac{\partial U_0}{\partial z} - \frac{\partial \eta_B}{\partial y} \right) \frac{\partial}{\partial t} \overline{\eta^2} \right]_{z=0} \mathrm{d}y, \tag{19}$$

where $\eta$ is the meridional displacement of a fluid element, defined via

$$\frac{\mathrm{d}\eta}{\mathrm{d}t} = v_0, \tag{20}$$

and $\eta_B$ is the variation of the lower boundary and the overbar illustrates an average in the $x$-direction. The boundary terms are evaluated at the lower boundary $z = 0$ and the upper boundary $z = z_T$. In the absence of boundary contributions, this necessary condition for instability may be simplified to

$$0 = \int_0^{z_T} \int_{-1}^{1} \frac{\partial \bar{Q}}{\partial y} \left( \frac{\partial}{\partial t} \overline{\eta^2} \right) \, \mathrm{d}y \, \mathrm{d}z. \tag{21}$$

If the base state is unstable to perturbations to the flow, then obviously the energy of perturbations must grow with time, equally, the displacement in the $y$-direction of any line of fluid elements $\eta$ must grow. Since unstable growth requires $\partial \overline{\eta^2}/\partial t > 0$, we may conclude from eq. (21) that the potential vorticity gradient of the base state $\partial \bar{Q}/\partial y$ must be positive in some domain of $y$ and negative in some others for instability to occur. Note however that in the case of a horizontal temperature gradient on the boundaries, which manifests as a vertical shear $\partial U_0/\partial z$ on the boundary through thermal wind balance (combining hydrostatic balance and geostrophic balance), instability is allowed even if the potential vorticity gradient in the base state does not change sign.

Let us propose an example that is explanatory of the effect of a $y$-gradient of the potential vorticity $Q$, sketched in the following figure

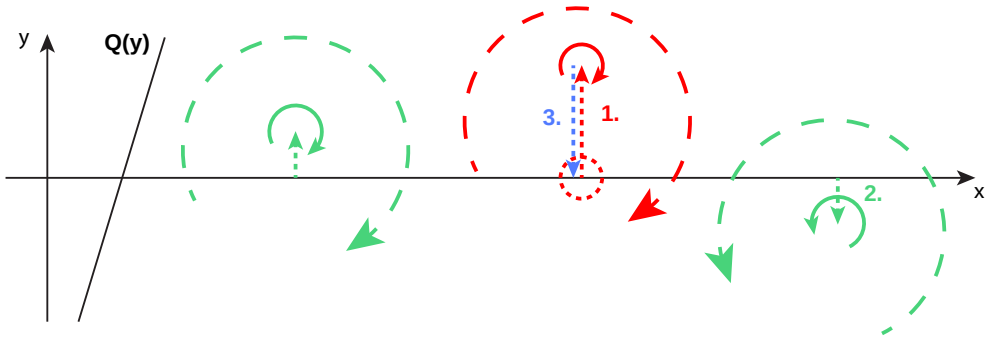


Figure 1: Sketch of an example where the effect of the $y$-gradient of $\bar{Q}$ is stabilizing.

We are in a situation where there is a positive gradient of $\bar{Q}(y)$, as sketched on the left side of the figure. We first consider a fluid parcel that gets displaced towards the North (higher $y$), indicated

by the red dashed circle. Given the background gradient of $\bar{Q}$, it will start rotating clockwise to counteract the increase of $f$. This will induce a motion in the neighbouring parcels, which will then be shifted north on the left and south on the right, as sketched in green. Similarly as for the red parcel, the green parcels will start rotating, in opposite directions. The effect of the neighbouring parcels on the red parcel is to push it southwards. Hence, the effect of a positive $y$-gradient of $\bar{Q}$ is stabilizing.

A second condition for stability is found if,

$$U_0 \frac{\partial \bar{Q}}{\partial y} \leqslant 0, \qquad \text{for all } y,\ z, \tag{22}$$

$$U_0 \left( \frac{1}{S} \frac{\partial U_0}{\partial z} - \frac{\partial \eta_B}{\partial y} \right) \geqslant 0 \qquad z = 0, \tag{23}$$

$$\frac{U_0}{S} \frac{\partial U_0}{\partial z} \leqslant 0 \qquad z = z_T. \tag{24}$$

This is a sufficient condition for stability, and the violation of it is a necessary condition for instability. This condition is related to the uniqueness of the solution if potential vorticity is conserved along streamlines.

Let us further suppose that the base velocity field $U_0$ is related to a potential vorticity $\bar{Q} = \bar{Q}(\Psi)$, which is a function of the stream function alone. The condition in eq. (22) is now equivalent to $d\bar{Q}/d\Psi \leqslant 0$. Whether the solution is unique also depends on the sign of $d\bar{Q}/d\Psi$.

Consider, for example, $\bar{Q}(\Psi) = a^2\Psi$ and suppose, for simplicity, that the potential vorticity is just the relative vorticity $\nabla^2\Psi$. If $a^2 < 0$ such that $d\bar{Q}/d\Psi < 0$ and $\Psi = 0$ on the boundaries, then the solution can always be added to a forced solution and the solution is non-unique. By eq. (22), this non-unique solution is unstable to small perturbations and conversely $a^2 > 0$, a unique solution, implies stability.

### 3.2 Normal mode solutions

In order to determine the instability of these zonal flows, we look for a normal mode solution of the form

$$\varphi(x, y, z, t) = Re\left[\Phi(y, z) e^{ik(x-ct)}\right], \tag{25}$$

where $c = c_r + ic_i$ and $c_i > 0$ corresponds to exponential growth. Upon substitution into eq. (18), we obtain an equation for $\Phi$

$$(U_0 - c)\left[\frac{\partial}{\partial z}\frac{1}{S}\frac{\partial \Phi}{\partial z} + \frac{\partial^2 \Phi}{\partial y^2} - k^2\Phi\right] + \Phi \frac{\partial \bar{Q}}{\partial y} = 0. \tag{26}$$

The boundary conditions may be expressed as

$$(U_0 - c)\frac{\partial \Phi}{\partial z} + \left[S\frac{\partial \eta_B}{\partial y} - \frac{\partial U_0}{\partial z}\right]\Phi = 0 \qquad \text{at the lower boundary,} \tag{27}$$

$$(U_0 - c)\frac{\partial \Phi}{\partial z} - \frac{\partial U_0}{\partial z}\Phi = 0 \qquad \text{at the upper boundary.} \tag{28}$$

It is helpful to consider what we may know *a priori* about the phase speed $c_r$ and growth speed $kc_i$. It was first shown by Howard [1] that the complex eigenvalue $c$, in the absence of the $\beta$ effect,

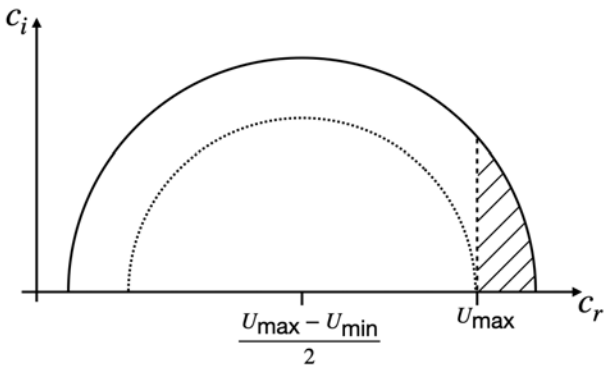


Figure 2: The semicircle in the complex plane in which complex phase speed $c$ must lie. The dotted semicircle illustrates the domain in the absence of the $\beta$ effect, and the solid semicircle illustrates the expansion of this upon the inclusion of the $\beta$ effect. The shaded region is not a possible domain for $c$.

must lie in a semicircle centred at $(U_{\max} + U_{\min})/2$ with radius $(U_{\max} - U_{\min})/2$. Upon including the $\beta$ effect, this semicircle is extended as follows:

$$\left(\frac{U_{\max} - U_{\min}}{2}\right)^2 + \frac{\beta}{k^2 + \pi^2/4}\left(\frac{U_{\max} - U_{\min}}{2}\right) \geqslant \left(c_r - \frac{U_{\max} - U_{\min}}{2}\right)^2 + c_i^2. \tag{29}$$

Note that $c_r < U_{\max}$ and as such a portion of the semicircle is excluded, which is expressed graphically in fig. 2. It is also true that bottom topography sloping in the north-south $y$ direction may add a $\beta$-like effect which allows for unstable modes with $c_r > U_{\max}$.

## 4 The 2-Layer Model

The potential vorticity equation (12) is a non-linear partial differential equation with four independent variables $x$, $y$, $z$ and $t$. We may consider simplifying this system by replacing the continuous density stratification considered previously with a multi-layer system of homogeneous fluid layers of uniform but distinct densities; the simplest such system is a two-layer model. Consider, as illustrated in fig. 3, an upper fluid of density $\rho_1$ and a lower fluid of density $\rho_2$ with $\rho_1 < \rho_2$ bounded between rigid walls at $y = \pm 1$. We introduce stream functions for each layer of fluid $\psi_n$, where the subscript $n = 1,\ 2$ refers to the upper and lower layers respectively. We will consider a base flow with stream function $\Psi_n(y)$ which is purely zonal, such that $U_n(y) = -d\Psi_n/dy$. When there is shear between the layers ($U_1 \neq U_2$), the interface tilts at a fixed slope corresponding to this shear.

In the absence of friction and bottom topography and in parallel with eq. (12), the stream functions satisfy

$$\left(\frac{\partial}{\partial t} + \frac{\partial \psi_n}{\partial x}\frac{\partial}{\partial y} - \frac{\partial \psi_n}{\partial y}\frac{\partial}{\partial x}\right)\left(\nabla_H^2 \psi_n - F_n(-1)^n(\psi_2 - \psi_1) + \beta y\right) = 0,\ n = 1,\ 2, \tag{30}$$

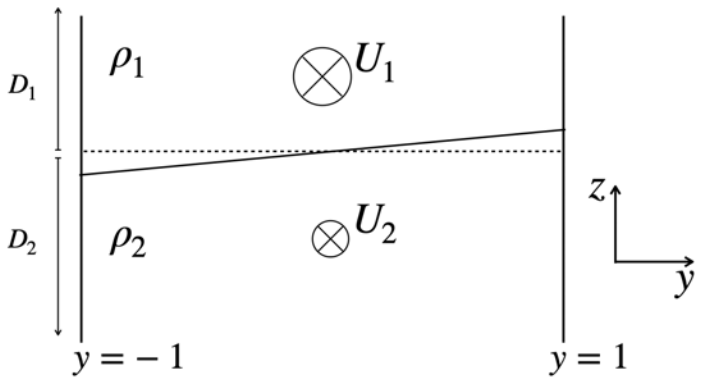


Figure 3: Model set-up for 2-layer system.

where $\nabla_H^2 = \partial^2/\partial x^2 + \partial^2/\partial y^2$ is the horizontal Laplacian and $F_n$ is the stratification parameter defined by

$$F_n = \frac{f_0^2 L^2}{g((\rho_2 - \rho_1)/\rho_0) D_n}, \tag{31}$$

where $\rho_0$ is now the background mean density and $D_n$ is the undisturbed depths of the two layers. The base flow potential vorticity in each layer is given by

$$\bar{Q}_n = \beta y + \frac{d^2\Psi_n}{dy^2} - F_n(-1)^n(\Psi_2 - \Psi_1). \tag{32}$$

Let $\varphi_n$ be the disturbance stream function, so that

$$\psi_n = \Psi_n(y) + \varphi_n(x, y, t). \tag{33}$$

There is a corresponding disturbance potential vorticity $q_n = \nabla_H^2 \varphi_n - F_n(-1)^n(\varphi_2 - \varphi_1)$. When substituted into eq. (30) this gives

$$\left(\frac{\partial}{\partial t} + U_n \frac{\partial}{\partial x}\right) q_n + \frac{\partial \varphi_n}{\partial x} \frac{d\bar{Q}_n}{dy} + \left(\frac{\partial \varphi_n}{\partial x}\frac{\partial q_n}{\partial y} - \frac{\partial \varphi_n}{\partial y}\frac{\partial q_n}{\partial x}\right) = 0. \tag{34}$$

We are considering a small perturbation $\varphi_n$ and as such, for linear analysis, we neglect terms of $O(\varphi_n^2)$ in eq. (34) which simplifies to

$$\left(\frac{\partial}{\partial t} + U_n \frac{\partial}{\partial x}\right) q_n + \frac{\partial \varphi_n}{\partial x} \frac{d\bar{Q}_n}{dy} = 0. \tag{35}$$

As in the continuously stratified case, the boundary conditions are given by

$$\frac{\partial \varphi_n}{\partial y} = 0, \qquad y = \pm 1. \tag{36}$$

We then seek normal mode solutions in the form

$$\varphi_n = Re\left[\Phi_n(y) e^{ik(x-ct)}\right], \tag{37}$$

with $c = c_r + ic_i$. Upon substitution into eq. (35), we obtain the ordinary differential equation for $\Phi_n$:

$$(U_n - c)\left[\frac{d^2\Phi_n}{dy^2} - k^2\Phi_n - F_n(-1)^n(\Phi_2 - \Phi_1)\right] + \Phi_n\frac{d\bar{Q}_n}{dy} = 0, \tag{38}$$

with boundary conditions

$$\Phi_n = 0, \qquad \text{at } y = \pm 1, \qquad \text{for } n = 1,\ 2. \tag{39}$$

Growing solutions exist for eigensolutions $\Phi_n$ whose corresponding eigenvalue $c$ has a positive imaginary component $c_i > 0$. In addition, since the coefficients of eq. (35) are real, the complex conjugate solution similarly exists $\Phi_n^*$ with eigenvalue $c^*$. As such, unstable modes correspond to $c_i \neq 0$.

Through manipulation of the derivative of potential vorticities eq. (32) we arrive at the condition

$$c_i \sum_{n=1}^{2} D_n \int_{-1}^{1} \frac{|\Phi_n|^2}{|U_n - c|^2}\frac{d\bar{Q}_n}{dy}\,\mathrm{d}y = 0. \tag{40}$$

Therefore, for $c_i$ to be non-zero and thus the system unstable, the base state potential vorticity gradient $d\bar{Q}_n/dy$ must be somewhere positive and somewhere negative. It is not necessary for $d\bar{Q}_n/dy$ to vanish anywhere in the domain. For example, the potential vorticity gradient may be positive in one layer and negative in another.

## References


[1] Louis N. Howard. "Note on a paper of John W. Miles". en. In: *Journal of Fluid Mechanics* 10.4 (June 1961), pp. 509–512. ISSN: 1469-7645, 0022-1120. DOI: 10.1017/S0022112061000317.

[2] J. Pedlosky. *Geophysical fluid dynamics*. 1982.

# GFD 2025 Lecture 2: Weakly Nonlinear Theory: The 2-layer Model, Critical Shears for Instability, Multiple Time Scales for Supercritical Flows, Chaos

Joseph Pedlosky; notes by Marion Cocusse and Isabela Conde

June 17, 2025

*This lecture summarizes three papers: 'Finite Amplitude Baroclinic Waves', by J. Pedlosky, in J. Atm. Sci, 1970 [2], 'Finite Amplitude Baroclinic Waves with small dissipation', by J. Pedlosky, in J. Atm. Sci, 1971 [3] and 'Chaotic and periodic behavior of finite-amplitude baroclinic waves' by J. Pedlosky and C. Frenzen, in J. Atm. Sci, 1980 [6].*

## 1 Introduction

In the first lecture, we discussed how to formulate theories to find whether a given current structure was unstable and, if so, the form of the growing perturbation and its growth rate. In this section, we will explore what happens next: does it grow forever? Or, more likely, what happens when the initial exponential growth has passed?

To do this, we need to understand the cause of the instability. There are various types of instabilities and consequently, different barriers to growth. In some cases, the initial perturbation must overcome dissipative effects that prevent growth. For example, for thermal convection, the thermal dissipation and viscous dissipation need to be overcome. In non-rotating shear flows, viscosity damps out instability, so the Reynolds number of the flow needs to exceed a certain value for instability to occur. In those cases, the development of the amplitude of the instability usually follows a simple form: initial exponential growth followed by a smooth transition to a steady state as nonlinear effects come into play [8], [9]. Figure 1 shows such time evolution of the amplitude of the instability for a non-rotating viscous shear flow.

However, in our case, the barriers for instability are not due to viscous or dissipative effects. They are rather due to non-dissipative stabilizing effects like the $\beta$ effect. For the 2-layer model where the flows are independent of $y$ but different in each layer (Phillips' model, [7]) presented here, the criterion for instability requires the potential vorticity to have a different sign in each layer. For other cases, the threshold for instability may depend on the Rossby radius of deformation.

## 2 Overcoming Stability Induced by $\beta$ Effect

### 2.1 Linear Problem

We look at a two layer model with two main hypotheses on the undisturbed flow :

- We consider a basic state of uniform velocities in each layer $U_1$ and $U_2$ in the same direction but of different magnitudes.

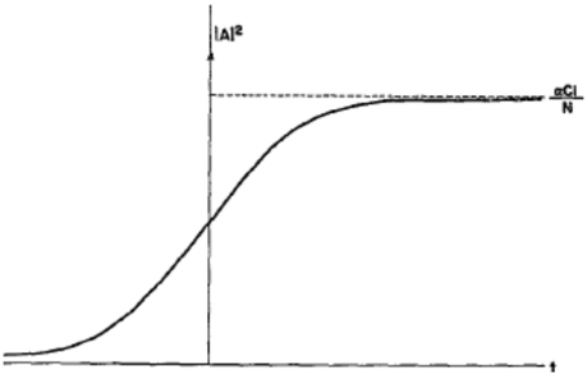


Figure 1: Illustration of the time evolution of the square of the amplitude of the perturbation for a non-rotating viscous shear flow. From [2].

- The undisturbed layer thicknesses are equal (each layer has the same mass) so $D_1 = D_2 = D/2$.

Within this framework, the governing equations for the upper and lower layer are as follows (see Lecture 1):

$$\left(\frac{\partial}{\partial t} + \frac{\partial \psi_1}{\partial x}\frac{\partial}{\partial y} - \frac{\partial \psi_1}{\partial y}\frac{\partial}{\partial x}\right)\left(\nabla^2\psi_1 + F(\psi_2 - \psi_1) + \beta y\right) = -r\nabla^2\psi_1, \tag{1}$$

$$\left(\frac{\partial}{\partial t} + \frac{\partial \psi_2}{\partial x}\frac{\partial}{\partial y} - \frac{\partial \psi_2}{\partial y}\frac{\partial}{\partial x}\right)\left(\nabla^2\psi_2 + F(\psi_1 - \psi_2) + \beta y\right) = -r\nabla^2\psi_2, \tag{2}$$

where $F = F_1 = F_2$ (see previous lecture), namely

$$F = \frac{2f_0^2 L^2}{g((\rho_2 - \rho_1)/\rho_0)D}. \tag{3}$$

The terms in $-r\nabla^2\psi_n$ represent a small amount of dissipation. At first, we will focus on the case where friction is small enough to be ignored: $r = 0$. We can now wonder if an instability can equilibrate without friction, and if so; how?

The interface between the two layers forms a linear slope in $y$ and proportional to the shear, allowing for potential energy to build up. The equation for the thickness of the lower layer $h_2$ is:

$$h_2(y) = \varepsilon F(U_1 - U_2)y + \frac{1}{2}, \tag{4}$$

where the factor $1/2$ corresponds to the ratio of the thickness of individual layers to the total thickness, and $\varepsilon$ is the Rossby number. In terms of stream functions, the basic state can be written as :

$$\psi_1^{(0)} = -U_1 y, \tag{5}$$

$$\psi_2^{(0)} = -U_2 y. \tag{6}$$

Let us consider a linear disturbance of the form

$$\psi_n = \psi_n^{(0)} + \varphi_n(x, y, t), \quad \text{with } n = 1, 2. \tag{7}$$

Linearizing equations (1)-(2) and neglecting friction ($r = 0$) leads to the lowest order:

$$\left(\frac{\partial}{\partial t} + U_1\frac{\partial}{\partial x}\right)\left(\nabla^2\varphi_1 + F(\varphi_2 - \varphi_1)\right) + \frac{\partial\varphi_1}{\partial x}\left(\beta + F(U_1 - U_2)\right) = 0, \tag{8}$$

$$\left(\frac{\partial}{\partial t} + U_2\frac{\partial}{\partial x}\right)\left(\nabla^2\varphi_2 + F(\varphi_1 - \varphi_2)\right) + \frac{\partial\varphi_2}{\partial x}\left(\beta - F(U_1 - U_2)\right) = 0, \tag{9}$$

with the following boundary conditions:

$$\frac{\partial\varphi_1}{\partial x} = \frac{\partial\varphi_2}{\partial x} = 0, \quad \text{at } y = 0, 1. \tag{10}$$

This leads to solutions in the form:

$$\varphi_1 = Re\left(Ae^{i\alpha(x-ct)}\sin(m\pi y)\right), \tag{11}$$

$$\varphi_2 = Re\left(\gamma Ae^{i\alpha(x-ct)}\sin(m\pi y)\right), \tag{12}$$

where the sine function ensures the vanishing of the flow at the boundaries, $A$ is the constant amplitude of the wave in the first layer, and $\gamma$ the constant ratio of the amplitude of the wave in the second layer to the one in the first layer, $\alpha$ the longitudinal wave number, $m$ an integer and $c$ a phase speed that is complex. If the imaginary part of $c$ is greater than zero, the perturbation can grow exponentially.

Substituting this solution into equations (8)-(9) leads to the following set of equations:

$$(c - U_1)(k_m^2 + F) + \beta + FU_s - \gamma F(c - U_1) = 0, \tag{13}$$

$$\gamma\left[(c - U_2)(k_m^2 + F) + \beta - FU_s\right] - F(c - U_2) = 0, \tag{14}$$

where $k_m$ is the total wave number, such that $k_m^2 = \alpha^2 + m^2\pi^2$, and $U_s = U_1 - U_2$ is the shear. This can be viewed, for example, as two equations for the unknown amplitude ratio $\gamma$, and solutions are possible only if

$$c = \frac{U_1 + U_2}{2} - \frac{\beta(k_m^2 + F)}{k_m^2(k_m^2 + 2F)} \pm \frac{(4\beta^2F^2 - k_m^4U_s^2(4F^2 - k_m^4))^{1/2}}{2k_m^2(k_m^2 + 2F)}. \tag{15}$$

The quantity $c$ has a non-zero imaginary part if and only if the radicand of (15) is negative, i.e., if and only if

$$U_s^2 > U_c^2 = \frac{4\beta^2F^2}{k_m^4(4F^2 - k_m^4)} \quad \text{and} \quad k_m^2 < 2F, \tag{16}$$

with $U_c$ the critical shear above which we get growing waves. Figure 2 shows $U_c$ as a function of $k_m^2$ (both quantities are normalized), and only the positive branch $U_c > 0$ is shown for clarity. The case $U_s < 0$ can be obtained by reflection around the $k_m^2$ axis.

## 2.2 Non-linear Problem

### 2.2.1 First order problem

We will suppose that for a given wave number we exceed the critical shear by a small amount $\Delta$:

$$U_s = U_c(k_m) + \Delta, \qquad \Delta \ll U_c. \tag{17}$$

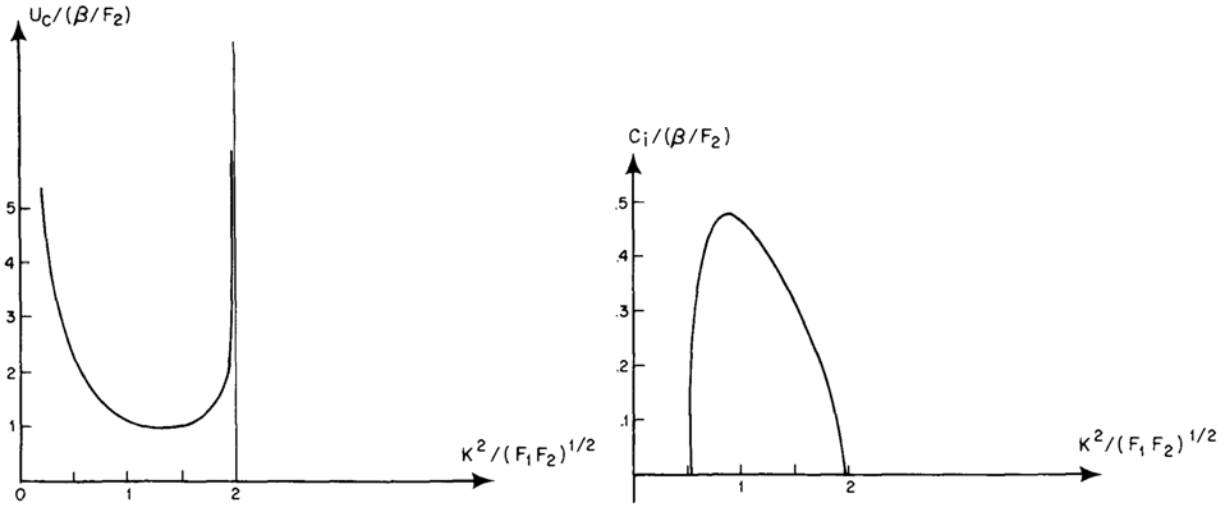


Figure 2: (a) Critical shear $U_c$ as a function of wave number in the case where the undisturbed layer thickness is the same in both layers. (b) The imaginary part of $c$ as a function of the wave number for $U_s = 2\beta/F$, i.e., for a shear which is twice the minimum critical shear. From [5].

From (15), we can get the imaginary part of $c$:

$$c_i = \pm \left( \frac{\sqrt{2}\beta F}{k_m^2(k_m^2 + 2F)} \right) \left( \frac{\Delta}{U_c} \right)^{1/2} + O(\Delta). \tag{18}$$

We see that the growth rate is of order $\Delta^{1/2}$ rather than of order $\Delta$. Since the real part of the phase speed will be order 1, the growth rate will be significantly smaller. This suggests that the problem has two time scales. The first one is the advective time scale which will be the scale of the real part of the wave's phase speed (the wave is getting advected as it is growing), the second time scale is slower and of the order of the growth rate. This slow time is therefore defined by:

$$T = |\Delta|^{1/2} t. \tag{19}$$

This is in contrast with the usual slow time scale of viscous shear flow, of order $|\Delta|$.

We will consider the solution to be a function of these two time scales, so the time derivative becomes:

$$\frac{\partial}{\partial t} + |\Delta|^{1/2} \frac{\partial}{\partial T}. \tag{20}$$

All dependent variables, such as the stream functions, now depend on both the fast and the slow time scales. Introducing this gives the chance for weakly nonlinear effects to balance the growth of the instability.

By writing the equations for the upper and lower layer explicitly as a function of $t$ and $T$, and letting $U_1 = U_2 + U_s = U_2 + U_c + \Delta$, as well as $\psi = \psi_n^{(0)} + \varphi_n$, we obtain (this time, keeping all of

the nonlinear terms):

$$\left(\frac{\partial}{\partial t}+|\Delta|^{1/2}\frac{\partial}{\partial T}+(U_2+U_c+\Delta)\frac{\partial}{\partial x}\right)\left(\nabla^2\varphi_1+F(\varphi_2-\varphi_1)\right)+\frac{\partial\varphi_1}{\partial x}(\beta+FU_c+F\Delta)$$
$$+J\left(\varphi_1,\nabla^2\varphi_1+F(\varphi_2-\varphi_1)\right)=0,$$
$$\left(\frac{\partial}{\partial t}+|\Delta|^{1/2}\frac{\partial}{\partial T}+U_2\frac{\partial}{\partial x}\right)\left(\nabla^2\varphi_2+F(\varphi_1-\varphi_2)\right)+\frac{\partial\varphi_2}{\partial x}(\beta-FU_c-F\Delta)$$
$$+J\left(\varphi_2,\nabla^2\varphi_2+F(\varphi_1-\varphi_2)\right)=0,$$

where $J$ denotes the usual Jacobian.

The solution $\varphi_n$ is also expanded as an asymptotic series in $|\Delta|^{1/2}$:

$$\varphi_n=|\Delta|^{1/2}\varphi_n^{(1)}+|\Delta|\varphi_n^{(2)}+...$$

We can now expand the equations in a series in powers of $|\Delta|^{1/2}$. Keeping the lowest order only to begin with, we have:

$$\left(\frac{\partial}{\partial t}+(U_2+U_c)\frac{\partial}{\partial x}\right)\left(\nabla^2\varphi_1^{(1)}+F(\varphi_2^{(1)}-\varphi_1^{(1)})\right)+\frac{\partial\varphi_1^{(1)}}{\partial x}(\beta+FU_c)=0, \tag{21}$$

$$\left(\frac{\partial}{\partial t}+U_2\frac{\partial}{\partial x}\right)\left(\nabla^2\varphi_2^{(1)}+F(\varphi_1^{(1)}-\varphi_2^{(1)})\right)+\frac{\partial\varphi_2^{(1)}}{\partial x}(\beta-FU_c)=0. \tag{22}$$

Note how this recovers the linear problem with $U_s=U_c$. Similarly expanding the boundary conditions we have:

$$\frac{\partial\varphi_1^{(1)}}{\partial x}=\frac{\partial\varphi_2^{(1)}}{\partial x}=0,\quad \text{for } y=0,1. \tag{23}$$

As in the previous section, solutions can be sought in the form of a wave, whose amplitude now varies on the slow timescale $T$:

$$\varphi_1^{(1)}=Re\left(A(T)e^{i\alpha(x-ct)}\sin(m\pi y)\right), \tag{24}$$

$$\varphi_2^{(1)}=Re\left(\gamma A(T)e^{i\alpha(x-ct)}\sin(m\pi y)\right), \tag{25}$$

where the sine appears to satisfy the boundary conditions that $\varphi_1^{(1)}$ and $\varphi_2^{(1)}$ vanish at $y=0,1$, and

$$c=U_2+\frac{U_c}{2}-\frac{\beta(k_m^2+F)}{k_m^2(k_m^2+2F)}\quad\text{and}\quad\gamma=\frac{k_m^2+F}{F}-\frac{(\beta+FU_c)}{F(U_2+U_c-c)}. \tag{26}$$

To this order, $\gamma$ is real so there is no phase difference between the solutions in the two layers. To get a phase difference, which is crucial to have baroclinic release of potential energy, we need to compute the solution to the next order.

### 2.2.2 Second order problem

At the next order, the nonlinear problem is given by:

$$\left[\tfrac{\partial}{\partial t}+(U_2+U_c)\tfrac{\partial}{\partial x}\right]\left[\nabla^2\varphi_1^{(2)}+F(\varphi_2^{(2)}-\varphi_1^{(2)})\right]+\tfrac{\partial\varphi_1^{(2)}}{\partial x}(\beta+FU_c)$$
$$=-J\left[\varphi_1^{(1)},\nabla^2\varphi_1^{(1)}+F(\varphi_2^{(1)}-\varphi_1^{(1)})\right]-\tfrac{\partial}{\partial T}\left[\nabla^2\varphi_1^{(1)}+F(\varphi_2^{(1)}-\varphi_1^{(1)})\right], \tag{27}$$

$$\left[\tfrac{\partial}{\partial t}+U_2\tfrac{\partial}{\partial x}\right]\left[\nabla^2\varphi_2^{(2)}+F(\varphi_1^{(2)}-\varphi_2^{(2)})\right]+\tfrac{\partial\varphi_2^{(2)}}{\partial x}(\beta-FU_c)$$
$$=-J\left[\varphi_2^{(1)},\nabla^2\varphi_2^{(1)}+F(\varphi_1^{(1)}-\varphi_2^{(1)})\right]-\tfrac{\partial}{\partial T}\left[\nabla^2\varphi_2^{(1)}+F(\varphi_1^{(1)}-\varphi_2^{(1)})\right]. \tag{28}$$

The nonlinear Jacobian terms are all zero as there is no phase difference for the waves. We look for a solution of the above equations of the form:

$$\varphi_n^{(2)} = Re\left[A_n^{(2)}(T)e^{i\alpha(x-ct)}\sin\left(m\pi y\right)\right]. \tag{29}$$

Substituting this solution into the governing equation, we have

$$\gamma A_1^{(2)} - A_2^{(2)} = -\left(\frac{1}{iaF}\right)\frac{dA}{dT}\left[\frac{\beta + FU_c}{(U_2+U_c-c)^2}\right], \tag{30}$$

$$-A_1^{(2)} + \gamma^{-1}A_2^{(2)} = -\left(\frac{\gamma}{iaF}\right)\frac{dA}{dT}\left[\frac{\beta - FU_c}{(U_2-c)^2}\right]. \tag{31}$$

The two left-hand sides being proportional to one another, solutions only exist provided:

$$\underbrace{\frac{dA}{dT}\left(\frac{(\beta+FU_c)}{(U_2+U_c-c)^2} + \gamma^2\frac{(\beta-FU_c)}{(U_2-c)^2}\right)}_{(*)} = 0. \tag{32}$$

For instability to occur we must have ${}^{dA}/_{dT} \neq 0$, so a necessary condition for instability is that $(*)$ must go to zero. It can be shown using the expression for $\gamma$ obtained earlier that this is indeed true. Then, solving for $A_2^{(2)}/A_1^{(2)}$, we can get the solutions up to $O(\Delta)$:

$$\varphi_1 = |\Delta|^{1/2}\, Re\left\{Ae^{i\alpha(x-ct)}\sin(m\pi y)\right\} \tag{33}$$

$$\varphi_2 = |\Delta|^{1/2}\, Re\left\{Ae^{i\alpha(x-ct)}\sin(m\pi y) \times \underbrace{\left[\gamma + \frac{|\Delta|^{1/2}}{i\alpha F}\frac{\beta+FU_c}{(U_2+U_c-c)^2}\frac{1}{A}\frac{dA}{dT}\right]}_{(**)}\right\}. \tag{34}$$

Although we don't yet know how the amplitude $A$ will vary on the long timescale (the scale of the amplitude growth) we can infer important features of the solution in terms of $A$. By understanding what the amplitude depends on, we can draw conclusions about solutions and necessary conditions for instability. This is due to the amplitude's effect on the interface slope and therefore the change in available potential energy and associated phase speed.

For example, we see that $(**)$ is a proportionality constant indicating a phase shift between $\varphi_1$ and $\varphi_2$, where there is a dependence of zonal mean flow of the layers and the amplitude growth rate $A^{-1}dA/dT$. The phase shift is important for transporting energy through waves, taking available potential energy from the tilted interface between the two layers. There will be a phase shift only if $\frac{1}{A}\frac{dA}{dT}$ has a non-zero real part (otherwise, this is just a change in the amplitude).

To find the amplitude equation, it is important to note that another solution can be added at this order, which is independent of $x$ and $t$, and therefore satisfies equations (27) and (28), namely:

$$\varphi_n^{(2)} = \Phi_n^{(2)}(y,T). \tag{35}$$

This represents a correction to the zonal flow $O(|\Delta|)$. Balancing the terms that are independent of $x$ and $t$, and after extensive algebra, we obtain the equation for the correction to the mean flow

driven by the self-interaction of the wave field (see [2] for detail):

$$\frac{\partial}{\partial T}\left[\frac{\partial^2\Phi_1^{(2)}}{\partial y^2}+F(\Phi_2^{(2)}-\Phi_1^{(2)})\right]=\frac{(\beta+FU_c)}{4(U_2+U_c-c)^2}\frac{d|A|^2}{dT}m\pi\sin(2m\pi y), \tag{36}$$

$$\frac{\partial}{\partial T}\left[\frac{\partial^2\Phi_2^{(2)}}{\partial y^2}+F(\Phi_1^{(2)}-\Phi_2^{(2)})\right]=-\frac{(\beta+FU_c)}{4(U_2+U_c-c)^2}\frac{d|A|^2}{dT}m\pi\sin(2m\pi y), \tag{37}$$

where the left-hand side of equations (36–37) represents the change in potential vorticity on the slow timescale while the right-hand side is due to the non-linearity of the wave growth, which is independent of both $x$ and $t$ and only dependent on the slow timescale and unknown amplitude.

Equations (36–37) can now be integrated on the slow timescale $T$ to obtain:

$$\Phi_1^{(2)}=-\Phi_2^{(2)}=-\frac{[|A|^2-|A(0)|^2]}{8(2m^2\pi^2+F)}\frac{(\beta+FU_c)}{(U_2+U_c-c)^2}\times m\pi\left[\sin(2m\pi y)-\frac{\sinh[\sqrt{2F}(y-\frac{1}{2})]}{\cosh\sqrt{F/2}}\left(\frac{m\pi}{\sqrt{F/2}}\right)\right].$$

### 2.2.3 Third order problem: the amplitude equations

Finally, moving on to the next order $O(\Delta^{3/2})$, and requiring that secular terms that would lead to growth of the amplitude on the fast timescale vanish, we obtain the amplitude equation:

$$\frac{d^2A}{dT^2}=\alpha^2c_{0i}^2A-\alpha^2NA[|A(T)|^2-|A(0)|^2], \tag{38}$$

where the constant $N$ is given by:

$$\begin{aligned}N=&(2m^2\pi^2+F)^{-1}\left[\frac{(\beta+FU_c)m^2\pi^2U_c}{8(k_m^2+2F)(U_2+U_c-c)^2}\right]\\&\left[k_m^2(2F-k_m^2)+4m^2\pi^2(k_m^2-F)+(2F-k_m^4)\frac{4\tanh\sqrt{F/2}}{\sqrt{F/2}}\left(\frac{2m^2\pi^2}{2m^2\pi^2+F}\right)\right],\end{aligned}$$

and the complex part of the base state's phase speed satisfies

$$c_{0i}^2=\left(\frac{2\beta^2F^2}{k_m^4(k_m^2+2F)^2}\right)\left(\frac{\Delta}{|\Delta|U_c}\right).$$

We see from the amplitude equation for $A$ that if $\Delta>0$, $c_{0i}^2>0$ so $A$ would grow at the rate of the linear instability, initially when the amplitude is near its initial value, but eventually the growth will be halted when the amplitude grows much larger than its initial value. It is like a mass-spring oscillator whose restoring force increases with the amplitude of the oscillation.

The solution to the amplitude equation for $A$ (equation 38) is aided by writing a general form of $A$ as $A=Re^{i\theta}$. Substituting this ansatz into the equation for $A$ leads to (see [2] for detail):

$$R^2\left(\frac{d\theta}{dT}\right)=L, \tag{39}$$

$$\left(\frac{dR}{dT}\right)^2=\alpha^2[c_{0i}^2+NR^2(0)]R^2-\frac{L^2}{R^2}-\frac{\alpha^2NR^4}{2}+2E, \tag{40}$$

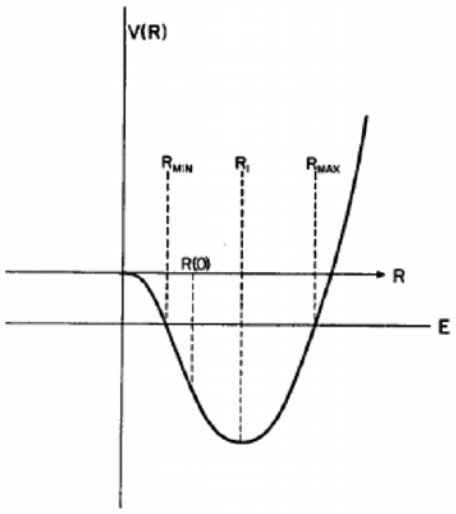


Figure 3: Potential against energy. From [2].

where $E$ is an integral of motion, given by:

$$2E = Q_0^2 - \alpha^2 c_{0i}^2 R^2(0) - \frac{\alpha^2 N R^4(0)}{2} + \frac{L^2}{R^2(0)}, \tag{41}$$

and where,

$$Q_0 = \left(\frac{dR}{dT}\right)_{T=0}. \tag{42}$$

This is identical to the classical equation in particle mechanics where $L$ is the angular momentum of a particle at radius $R$ from the centre and whose energy $E$ is given above in terms of initial conditions.

In the simplest case where $L$ is zero (which will be true if at $T = 0$, $L = 0$ then it will remain so), then:

$$\frac{1}{2}\left(\frac{dR}{dT}\right)^2 + V(R) = E, \text{ where} \tag{43}$$

$$V(R) = -\frac{\alpha^2}{2}[c_{0i} + NR^2(0)]R^2 + \frac{\alpha^2 N R^4}{4}. \tag{44}$$

Figure 3 shows the relation between $V(R)$ and $E$. We see that depending on initial conditions, $E$ could be greater than zero, in which case the solution goes through zero before growing again. This was highly unexpected: instead of the flow amplitude growing monotonically until saturation as in Figure 1, the nonlinearities here produce oscillations!

## 3 Instability, Oscillations and Chaos Due to Friction

In the previous section, we saw that the nonlinear frictionless baroclinic wave can oscillate indefinitely. However, we had ignored friction, so one may ask what is the effect of friction?

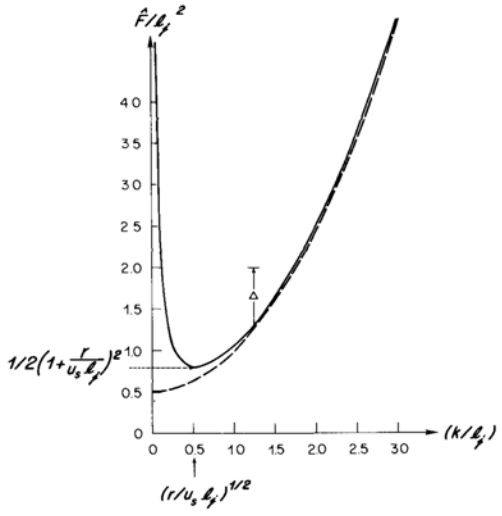


Figure 4: The solid line is the critical condition curve with friction, and the dotted curve is the critical condition in the absence of friction $F_c = k_m^2/2$. From [5].

In this section, we study the effect of friction, and ignore the $\beta$ effect, for simplicity. By setting $\beta = 0$, we will show that oscillations are not only caused by the $\beta$ effect as in the previous section, but can also be caused by friction!

We consider again the two layer model with equal layer heights (when at rest). In the presence of Ekman friction ($r \neq 0$) and absence of $\beta$, the linear stability problem reveals that

$$c = \frac{U_1 + U_2}{2} - \frac{ir(k_m^2 + F)}{k(k_m^2 + 2F)} \pm \frac{\left[k_m^4 U_s^2 (k_m^4 - 4F^2) - 4k_m^2 r^2 F^2/k^2\right]^{1/2}}{2k_m^2(k_m^2 + 2F)}. \tag{45}$$

We see that instability is possible when $F$ exceeds the critical parameter $F_c$:

$$F = \frac{f_0^2 L^2}{g\frac{\Delta\rho}{\rho}\frac{D}{2}} > F_c = \frac{k_m^2}{2} + \underbrace{\frac{2r^2 k_m^2}{k^2 U_s^2}}_{\dagger}. \tag{46}$$

This time, $F_c$ depends on the friction through the term in (†). For low longitudinal wave number $k$ in particular, friction becomes important. In what follows, we assume that

$$F = F_c + \Delta, \tag{47}$$

with $\Delta$ small and $r = O(\Delta^{1/2})$ [6].

Without going into details (the reader is referred to [3] and [6] to see them), the problem can be solved using a multiscale method, which is overall similar but not identical to the one presented in the previous section.

With the same definitions and notations, but with some appropriate rescaling of the amplitude function $A$, of the slow time $T$, and of the stream function $\Phi_1^{(2)} = -\Phi_2^{(2)}$ compared with the previous section, [3] and [6] showed that the amplitude equation in the $\beta = 0$, $r \neq 0$ case is

$$\frac{d^2A}{dT^2} + \frac{3}{2}\gamma\frac{dA}{dT} - A + A\int_0^1 dy \sin(2m\pi y)\frac{\partial^2 \Phi_1^{(2)}}{\partial y^2} = 0, \tag{48}$$

where

$$\gamma = \frac{r}{|\Delta|^{1/2}} \frac{2k_m}{kU_s}, \tag{49}$$

and $\Phi_1^{(2)}$ evolves according to

$$\frac{\partial}{\partial T}\left(\frac{\partial^2 \Phi_1^{(2)}}{\partial y^2} - k_m^2 \Phi_1^{(2)}\right) + \gamma \frac{\partial^2 \Phi_1^{(2)}}{\partial y^2} = \left(\frac{\partial A^2}{\partial T} + 2\gamma A^2\right) \sin(2m\pi y). \tag{50}$$

This problem must usually be solved numerically. By Fourier expanding $\Phi_1^{(2)}$ as

$$-\frac{\partial \Phi_1^{(2)}}{\partial y} = \sum_{j=1,3,5\ldots}^{\infty} U_j(T) \sin(j\pi y), \tag{51}$$

and defining for simplicity

$$B = \frac{dA}{dT} + \gamma A, \tag{52}$$

and

$$U_j(T) = \frac{8jm}{(j^2 - 4m^2)(j^2\pi^2 + k_m^2)}(A^2(T) + V_j(T)), \tag{53}$$

[6] obtains the following system of equations:

$$\frac{dA}{dT} = B - \gamma A \tag{54}$$

$$\frac{dB}{dT} = -\frac{\gamma}{2}B + \frac{\gamma^2}{2}A + A - \frac{2m^2}{\pi^2}A \sum_{k=1} \frac{(k-0.5)^2(A^2 + V_k))}{[(k-0.5)^2 - m^2]^2[(k-0.5)^2 + k_m^2/4\pi^2]} \tag{55}$$

$$\frac{dV_k}{dT} = \frac{\gamma}{[(k-0.5)^2 + k_m^2/4\pi^2]}[A^2((k-0.5)^2 + k_m^2/2\pi^2) - (k-0.5)^2 V_k], \text{ for } k \geq 1. \tag{56}$$

In the numerical solutions presented below, the system of equations was truncated at $k = 12$.

The nature of the solutions with friction, somewhat unexpectedly (at least for Joe!) was often periodic. At a fixed wave number, increasing $\gamma$ leads to a period-doubling cascade (see, e.g., Figures 5 and 6). For even larger values of $\gamma$, the solutions became aperiodic and chaotic (see Figure 7). Finally, for sufficiently large $\gamma$, the solutions reach a steady state (see Figure 8). Figure 9 shows the series of bifurcations in the parameter space $\gamma, k_m$.

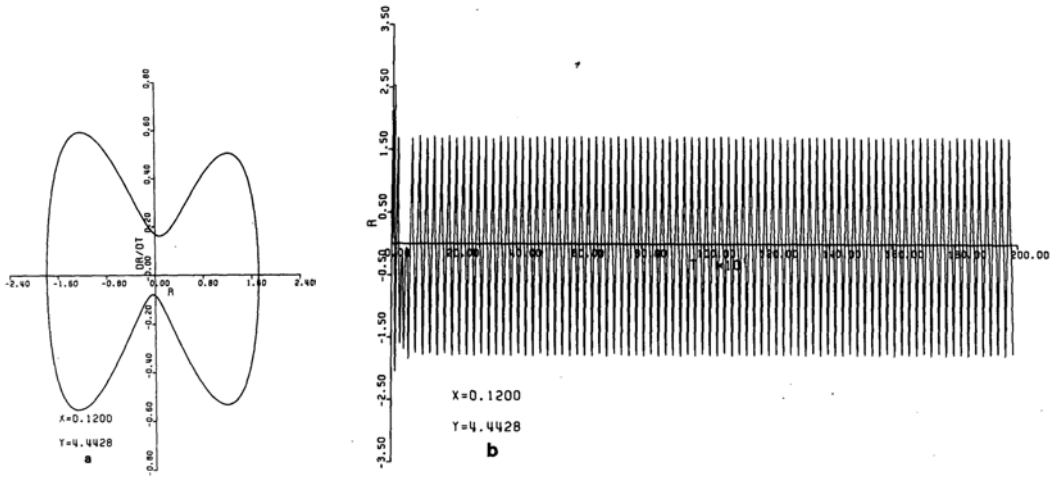


Figure 5: Left: Phase trajectory of asymmetric limit cycle where $\gamma = 0.12$, and $k_m/\pi = \sqrt{2}$. Right: Time history of the solution with the same coefficients as a [6].

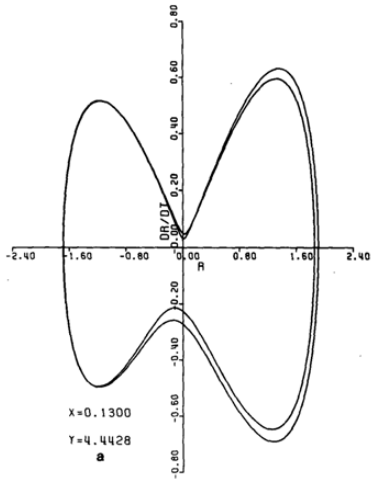


Figure 6: Phase portrait for $\gamma = 0.13$ and $k_m/\pi = \sqrt{2}$. The change in $\gamma$ produces period doubling [6].

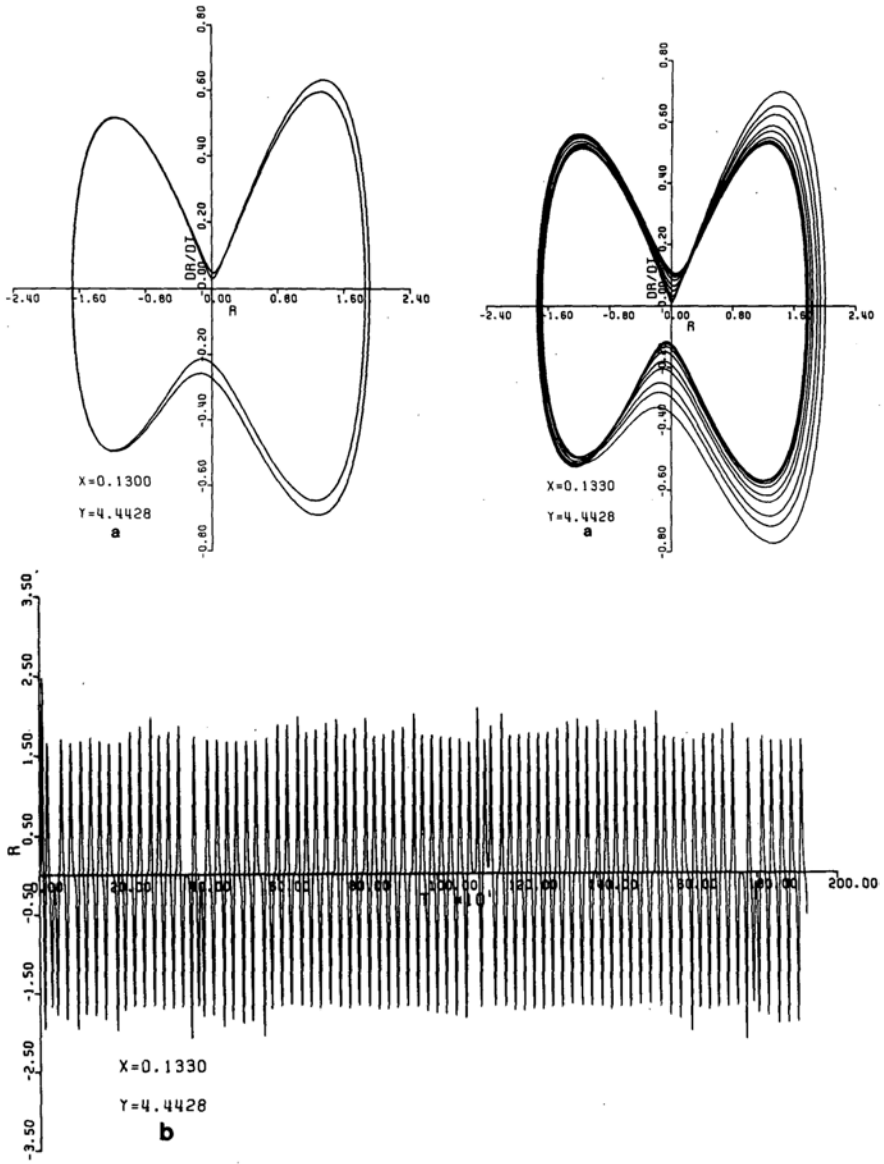


Figure 7: For values of $\gamma$ slightly larger than 1.2 the period doubles until we have an aperiodic cycle. The right panel shows the phase portrait of an aperiodic solution where $\gamma = 0.1330$ and $k_m/\pi = \sqrt{2}$, the bottom shows time series for these values.

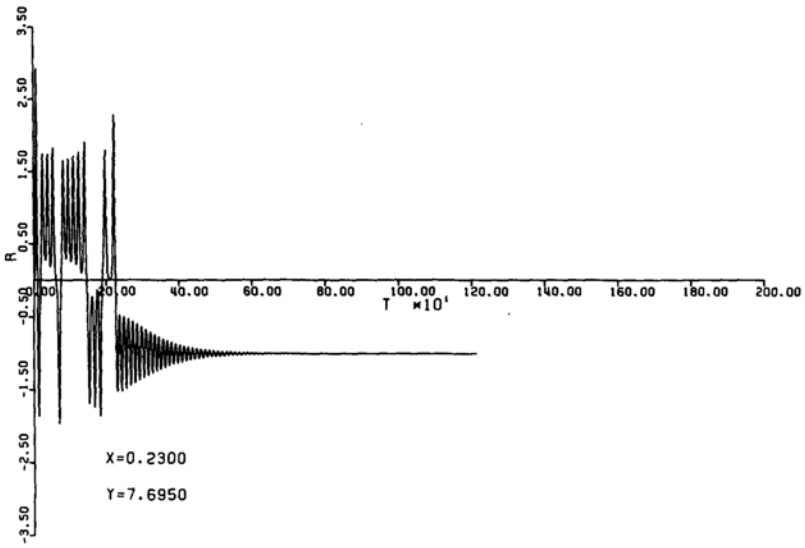


Figure 8: Time series where $\gamma = 0.23$ and $k_m/\pi = \sqrt{6}$. We see that for values of $\gamma$ large enough, the solution reaches a steady state.

**Feigenbaum Constant**

In 1978, Mitchel Feigenbaum discovered a fascinating fact [1]. He examined the simple first order difference equation, which he suggested as a model for population evolution from one generation to the next.

$$x_{n+1} = \gamma f(x_n)$$

Where $f$ was a simple quadratic in $x_n$ as a simple model of population dynamics. Remarkably, he found solutions for $x_n$ that as a function of $n$ were periodic for some values of $\gamma$. As $\gamma$ increased the solutions were periodic in $n$ with the periods doubling as that parameter increased leading eventually to aperiodic or chaotic solutions. The critical values of $\gamma$ for the nth period doubling were found to satisfy the relationship

$$\frac{\gamma_j - \gamma_{j-1}}{\gamma_{j+1} - \gamma_j} = C = 4.669201$$

$C$ is now called the Feigenbaum constant and, remarkably, the critical values of our $\gamma$ satisfy the Feigenbaum ratio. Why, we're not sure.

Finally, in the discussion until now, we have looked only at the case where $\beta$ is zero. Further work including the planetary vorticity gradient $\beta$ can be found in [4], and shows a regularizing effect due to $\beta$ as shown in Figure 11.

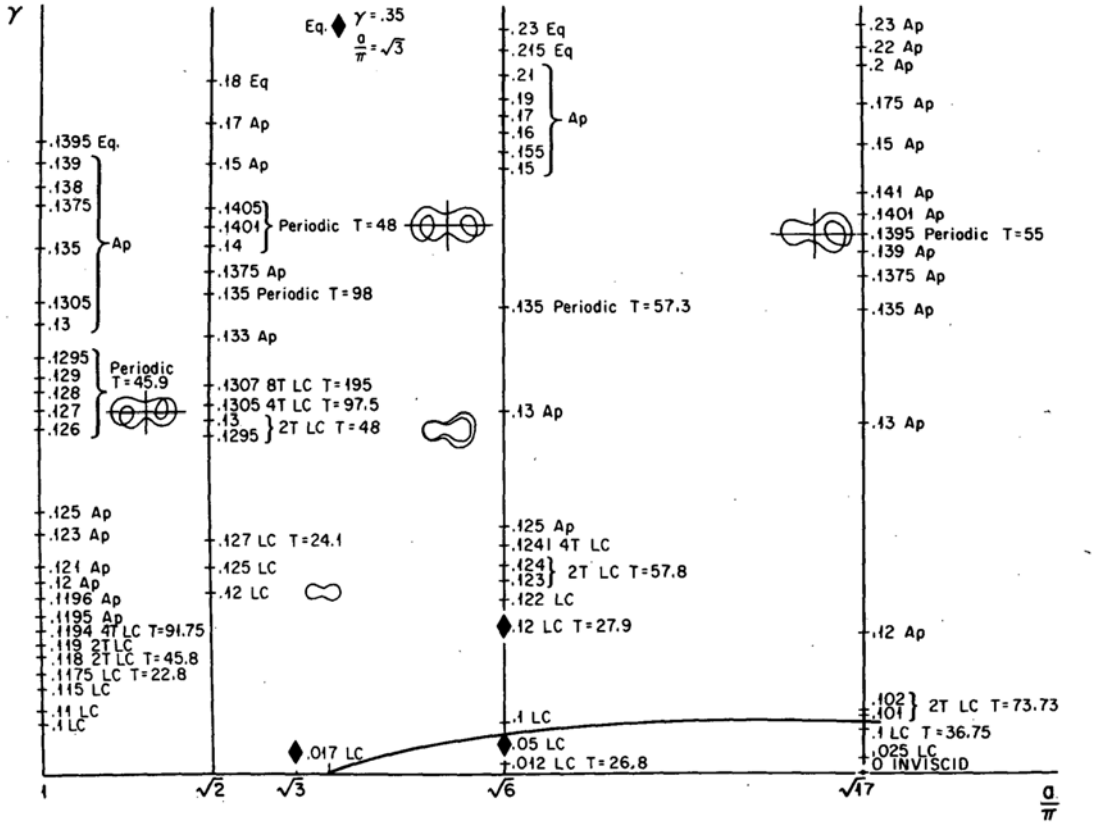


Figure 9: Results from numerical integration completed in [6]. "The entries along each line of constant $a/\pi$ ($a \equiv k_m$ in these notes) are not entered linearly with $\gamma$. The number of each entry refers to the corresponding value of $\gamma$. The entry LC refers to a simple "dog-bone" limit cycle. Entries labelled 2T, 4T, or 8T LC refer to limit cycle solutions with two, four or eight times the fundamental period. Aperiodic solutions are so labelled. Periodic solutions whose phase plane trajectories are not derived by period doubling of the fundamental are also noted with a crude representation of the phase space cycle. [...] Solid line is a rough rendering of their linear stability" [6].

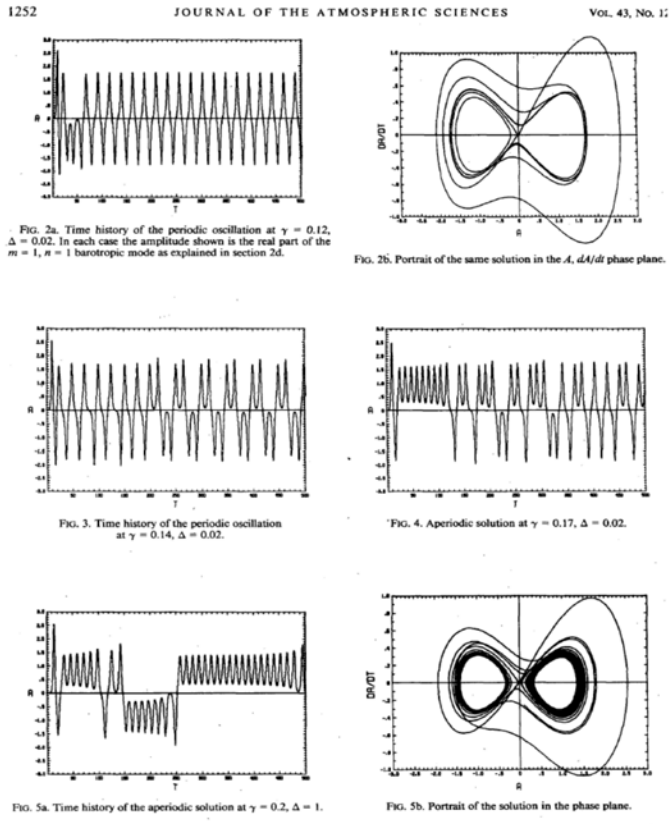


Figure 10: The nature of the instability beyond the asymptotic regime remains similar for $O(\Delta)$

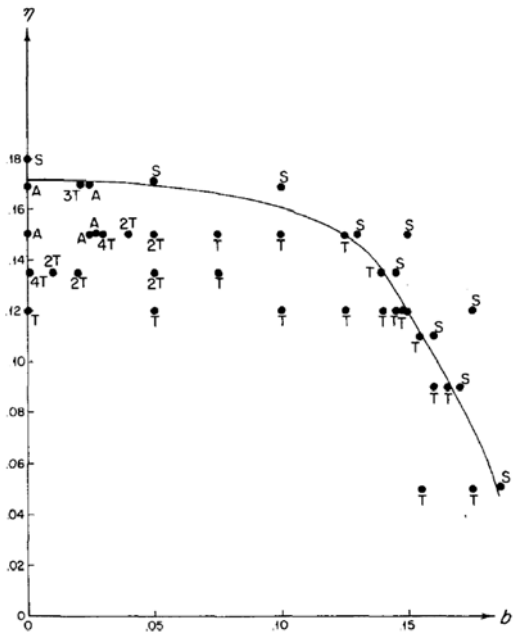


FIG. 3. The regime diagram for finite-amplitude wave behavior for $a^2/\pi^2 = 2$. A point S indicates a steady solution is attained. A point labeled A implies that the solution at that point is aperiodic. Periodic solutions whose periods are multiples of the fundamental are labeled $T$, $2T$, $3T$, $4T$, etc.

Figure 11: Figure from [4]

# References


[1] M. J. Feigenbaum, *Quantitative universality for a class of nonlinear transformations*, Journal of statistical physics, 19 (1978), pp. 25–52.

[2] J. Pedlosky, *Finite-Amplitude Baroclinic Waves.*, Journal of the Atmospheric Sciences, 27 (1970), pp. 15–30.

[3] ——, *Finite-Amplitude Baroclinic Waves with Small Dissipation.*, Journal of the Atmospheric Sciences, 28 (1971), pp. 587–597.

[4] J. Pedlosky, *The effect of $\beta$ on the chaotic behavior of unstable baroclinic waves*, Journal of Atmospheric Sciences, 38 (1981), pp. 717–731.

[5] ——, *Geophysical fluid dynamics*, Springer Science & Business Media, 2013.

[6] J. Pedlosky and C. Frenzen, *Chaotic and periodic behavior of finite-amplitude baroclinic waves*, Journal of Atmospheric Sciences, 37 (1980), pp. 1177–1196.

[7] N. A. Phillips, *Energy transformations and meridional circulations associated with simple baroclinic waves in a two-level, quasi-geostrophic model*, Tellus, 6 (1954), pp. 274–286.

[8] J. T. Stuart, *On the non-linear mechanics of wave disturbances in stable and unstable parallel flows part 1. the basic behaviour in plane poiseuille flow*, Journal of Fluid Mechanics, 9 (1960), pp. 353–370.

[9] J. Watson, *On the non-linear mechanics of wave disturbances in stable and unstable parallel flows part 2. the development of a solution for plane poiseuille flow and for plane couette flow*, Journal of Fluid Mechanics, 9 (1960), pp. 371–389.

# GFD 2025 Lecture 3: Topography-induced Radiative Baroclinic Instability

Joseph Pedlosky, with notes by David Darrow, Theo Lewy and Kyle McKee

June 18, 2025

*This lecture summarizes 'Radiation-induced baroclinic instability' by J. Pedlosky and R.M. Samelson, 1991, GAFD, 58, 243.*

## 1 Problem Motivation

Topography often plays a stabilizing role in shallow water systems – for instance, a constant slope can have a stabilizing effect on the baroclinic instability discussed in Lecture 1. Here, we discuss a system in which this topography can promote instability, as well as excite traveling waves that can propagate through an otherwise stable system. We choose to analyze a layered model (piecewise-homogeneous densities) since it permits a simpler mathematical treatment while still elucidating the key physics of the problem. In particular, our model reveals that the presence of topography may induce a radiative baroclinic instability.

## 2 System Formulation

We consider the two-layer flow depicted in Figure 2. The system comprises two layers of fluid, the top layer having a mean height $H_1$, a density $\rho$, and velocity $U_*\boldsymbol{x}\hat{}$. The bottom fluid layer has mean height $H_2$, a larger density $\rho + \Delta\rho$, and zero velocity. The entire system rotates with a Coriolis parameter $f = f_0 + \beta_0 y$. The system is bounded above by an impermeable rigid lid, and below by topography $h_B(y)$, which is flat except in the small region $-a < y < a$, where the gradient is constant.

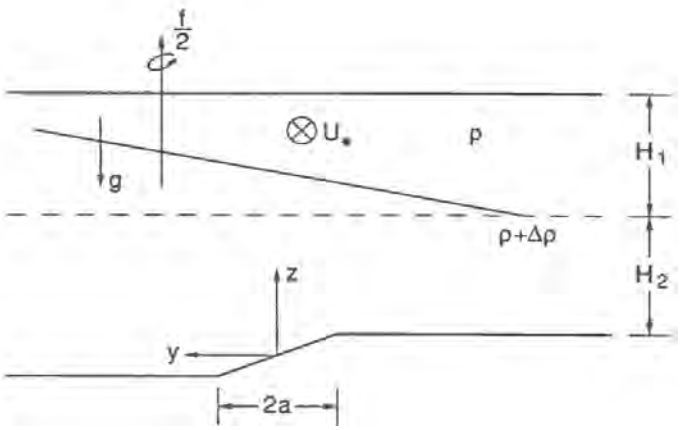


Figure 1: Approximate illustration of the model setup. From [1]

.

We proceed by first outlining the approximations used in analyzing this model, and then we find the base state associated with this flow. The assumptions in our analyses are listed as follows.

1. We assume that the Ekman number based on the vertical scales of interest, $E \equiv \frac{\nu}{f_0 H^2}$, is small. The Ekman number measures the relative importance of friction as compared with the Coriolis acceleration, and $E \ll 1$ allows us to neglect frictional forces in our analyses. In the ocean, this number can be extremely small, outside of a small boundary layer of width $L_{\mathrm{E}}$ within which $E \ll 1$ no longer holds and frictional effects become important. While the Ekman layer is often on the order of tens of meters in the ocean, $H_1$ and $H_2$ might be on the order of kilometers.

2. We assume that the Rossby number is small, $\varepsilon \equiv \frac{U}{f_0 L} \ll 1$, which implies that the dominant balance in the Navier-Stokes equations – as written in the rotating frame – must be between the Coriolis term, pressure gradient, and gravitational force (i.e., inertial terms drop out).

3. We assume the layers to be shallow in the sense that the vertical length scale is much smaller than the horizontal, $\delta \equiv H_k / L_{\mathrm{hor}} \ll 1$. This allows us to make the hydrostatic approximation, wherein the vertical momentum equations dictates that the dominant balance in the vertical is between gravity and a vertical pressure gradient.

4. We assume that the upper surface is rigid and at a fixed pressure, $p_A$. When $\Delta\rho/\rho \ll 1$, and the uppermost boundary is a fluid of much smaller density than $\rho$, this is a good approximation. Heuristically, this is due to the uppermost surface requiring a factor of $\rho/\Delta\rho$ more energy to deform than the interface between the layers, meaning it is much harder to deform.

The equations governing this 2-layer model are the same as in Lecture 1, which after linearization become:

$$\left(\frac{\partial}{\partial t} + U_1 \frac{\partial}{\partial x}\right)\left(\nabla^2\psi_1 + F_1(\psi_2 - \psi_1)\right) + \frac{\partial \bar{Q}_1}{\partial y}\frac{\partial \psi_1}{\partial x} = 0, \tag{1}$$

$$\frac{\partial}{\partial t}\left(\nabla^2\psi_2 - F_2(\psi_2 - \psi_1)\right) + \frac{\partial \bar{Q}_2}{\partial y}\frac{\partial \psi_2}{\partial x} = 0, \tag{2}$$

where

$$F_n = \frac{f_0^2 L^2}{\frac{\Delta\rho}{\rho} g H_n}, \quad \beta = \frac{\beta_0 L^2}{U_*}, \quad U_1 = \frac{U_*}{U_*} = 1, \tag{3}$$

and the background PV gradients are

$$\frac{\partial \bar{Q}_1}{\partial y} = \beta + F_1 U_1 \text{ in the top layer }, \tag{4}$$

$$\frac{\partial \bar{Q}_2}{\partial y} = \beta - F_2 U_1 \text{ in the bottom layer where } |y| > a, \tag{5}$$

$$\frac{\partial \bar{Q}_2}{\partial y} = \beta - F_2 U_1 + \alpha \text{ in the bottom layer where } |y| < a \tag{6}$$

where

$$\alpha = \frac{f_0^2}{U_*} \frac{L}{H_2} \frac{\partial h_B}{\partial y} \tag{7}$$

represents the topography slope.

## 3 Radiative Instability

We now consider the ansatz of $\psi_n = \phi_n(y) e^{ik(x-ct)}$ within layers $n = 1, 2$. Using the linearized potential vorticity equations derived above, we obtain the equations for the eigenmodes $\phi_n(y)$:

$$(U_1 - c)\left[(\frac{d^2}{dy^2} - k^2)\phi_1 + F_1(\phi_2 - \phi_1)\right] + (\beta + F_1 U_1)\phi_1 = 0, \tag{8}$$

$$-c\left[(\frac{d^2}{dy^2} - k^2)\phi_2 - F_2(\phi_2 - \phi_1)\right] + (\beta - F_2 U_1)\phi_2 = 0 \qquad |y| > a, \tag{9}$$

$$-c\left[(\frac{d^2}{dy^2} - k^2)\phi_2 - F_2(\phi_2 - \phi_1)\right] + (\beta - F_2 U_1 + \alpha)\phi_2 = 0 \qquad |y| < a, \tag{10}$$

where the first equation comes from the upper layer, the second from the non-sloping region in the lower layer, and the third from the sloping region in the lower layer. We will solve these subject to continuity conditions on $\phi_n$, $d\phi_n/dy$ at $y = \pm a$ for $n = 1, 2$, as well as that $\phi_n$ remain bounded as $y \to \pm\infty$. It will be useful to consider a supercriticality parameter

$$\Delta = F_2 U_1 - \beta - \alpha.$$

Consistent with Rayleigh's theorem (see lecture 1), we will see than an instability develops in our system when $\Delta > 0$, meaning that the potential vorticity gradient has opposite signs in the different layers. The solution can be deduced straightforwardly in the general case, but it is enlightening to examine the limit $a \ll 1$, corresponding to topography with a length scale much shorter than the deformation radius. With this in mind, we define a local spatial variable

$$\xi = \frac{y}{a}$$

around $y = 0$, which allows us to modify (10) as

$$\frac{d^2\phi_2}{d\xi^2} - a^2\left[(k^2 + F_2)\phi_2 + F_2\phi_1\right] + \frac{\Delta a^2}{c}\phi_2 = 0. \tag{11}$$

Balancing this equation requires the last term to be $O(1)$, meaning that $c = O(a^2)$. For convenience, we define

$$\theta^2 = \frac{\Delta a^2}{c} = O(1).$$

One could now expand (8) and (10) in powers of $a$ to recover a solution in the region $|y| < a$. The most unstable solution is the even one; up to $O(a^2)$, it reads

$$\phi_1 = \frac{F_1 c}{\Delta} C\cos(\theta\xi) + D, \qquad \phi_2 = C\cos(\theta\xi) - D\frac{cF_2}{\Delta}, \tag{12}$$

with $D$ and $C$ undetermined.

We now turn our attention to the region $y > a$ and solve equations (8) and (9) to leading order in $a$. These are constant-coefficient ODEs and hence have exponential solutions, which we write as

$$\phi_1 = Ae^{il(y-a)} - \frac{F_1 cB}{\beta - F_2U_1}e^{-m(y-a)}, \qquad \phi_2 = \frac{AcF_2}{\beta - F_2U_1}e^{il(y-a)} + Be^{-m(y-a)}, \tag{13}$$

with undetermined coefficients $A$ and $B$, as well as wavenumber $l = (\beta/U_1 - k^2)^{1/2}$ and decay rate $m = ((\beta - F_2U_1)/c)^{1/2}$. While the general solution also contains terms with exponents $-il(y-a)$ and $+m(y-a)$, we discount these by assuming no radiation is coming into the system from $y = +\infty$, and that $\phi_1$, $\phi_2$ is bounded there. The first term in both expressions corresponds to a travelling wave radiating in the positive $y$ direction, while the second term is a decaying boundary layer.

Matching the streamfunctions $\phi_i$ and the velocity fields $d\phi_i/dy$ at $y = a$ yields

$$ilA = F_1\left(\frac{c}{\Delta}\right)^{1/2} C\left(\sin\theta + \left(\frac{\Delta}{\beta - F_2U_1}\right)^{1/2}\cos\theta\right),$$

$$D = A,$$

$$B = -AcF_2\left(\frac{1}{\Delta} + \frac{1}{\beta - F_2U_1}\right) + C\cos\theta,$$

and the dispersion relation

$$il\left[\tan\theta - \left(\frac{\beta - F_2U_1}{\Delta}\right)^{1/2}\right] = \frac{F_1F_2c^{3/2}}{\Delta(\beta - F_2U_1)^{1/2}}\left(1 + \frac{\beta - F_2U_1}{\Delta}\right)\left(\tan\theta + \left(\frac{\Delta}{\beta - F_2U_1}\right)^{1/2}\right).$$

To lowest order in $a$, this implies that

$$\tan\left(\frac{\Delta a^2}{c_0}\right)^{1/2} = \tan\theta_0 = \left(\frac{\beta - F_2U_1}{\Delta}\right)^{1/2},$$

and thus

$$c_0 = \frac{\Delta a^2}{[\tan^{-1}[(\beta - F_2U_1)/\Delta]^{1/2}]^2}.$$

To leading order, then, $c$ is real and independent of wavenumber. The next correction allows for an instability:

$$c_1 = c - c_0 = \frac{2iF_1F_2c_0^3}{l(\beta - F_2U_1)\Delta a}\left[1 + \frac{\beta - F_2U_1}{\Delta}\right] = \frac{2iF_1F_2\Delta^2a^5}{l(\beta - F_2U_1)}\left[1 + \frac{\beta - F_2U_1}{\Delta}\right] \Big/ \left[\tan^{-1}\left(\frac{\beta - F_2U_1}{\Delta}\right)^{1/2}\right]^6.$$

The asymptotic approach taken above provides a good approximation to the true solution (see Figure 2), demonstrating the validity of the derived dispersion relation in the small $a$ regime.

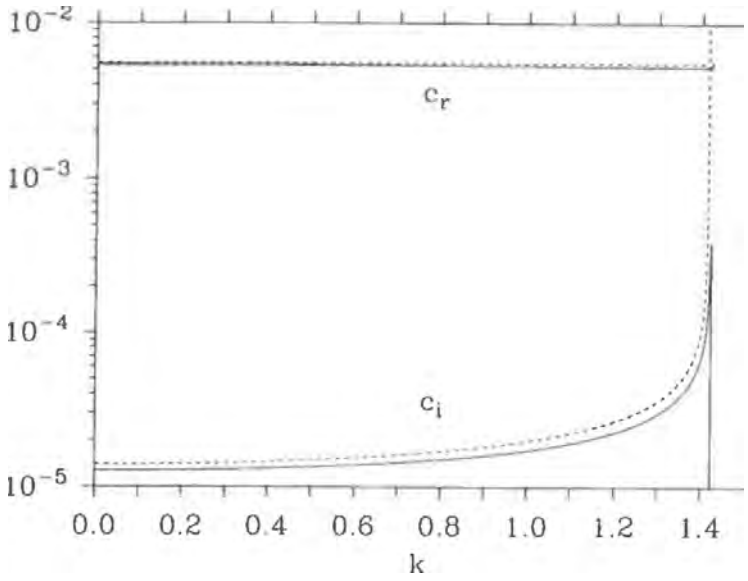


Figure 2: The real and imaginary phase speed for $F_1 = F_2 = U_1 = 1$, $a = 0.1$, $\Delta = 0.5$, $\beta = 2$ calculated using asymptotics (dashed) and numerically (solid). From [1].

The flow is unstable when $\mathrm{Im}(c_1) > 0$, i.e., if $l = (\beta/U_1 - k^2)^{1/2}$ is real. When this occurs, the region outside of the sloping region must support a traveling Rossby wave, suggesting that the presence of radiation is required for instability in this system.

To summarize, we have found a system that would be stable if it had boundaries at $y = \pm a$, and would also be stable without these boundaries if there were no $\beta$-effect to support the radiation of Rossby waves. This means that the radiation is essential in this case to promote the development of the instability by allowing energy to be radiated away from topography.

## References

[1] J. Pedlosky and R. M. Samelson, *Radiation-induced baroclinic instability*, Geophysical and Astrophysical Fluid Dynamics, 58 (1991), pp. 243–262.

# GFD 2025 Lecture 4: Nonlinear Downstream Development of Unstable Baroclinic Waves

Joseph Pedlosky; notes by Andrés Posada-Bedoya, Heng Quan, Farid Rajkotia-Zaheer

June 20, 2025

*This lecture summarizes the papers 'The Nonlinear Downstream Development of Baroclinic Instability' by J. Pedlosky, 2011, Journal of Marine Research, 69, 705, and 'The effect of beta on the downstream development of unstable, chaotic baroclinic waves', by J. Pedlosky, Journal of Physical Oceanography, 2019, 49, 2337. While writing these notes, we noted some typos in the original papers, and have corrected them here to the best of our abilities. Terms that differ from the original papers are marked in red. It is possible that some unidentified typos remain. The general results are robust, however!*

## 1 Introduction

The Gulf Stream and the Kuroshio Extension are among the most energetic and dynamic currents in the ocean. Downstream of the separation points of their respective western boundaries, they become free, inertial, unstable jets characterized by large-amplitude meanders and eddies. The observed time-dependent meandering path eventually leads to turbulence and can be explained in terms of instabilities of the hypothetical flow that, in principle, could exist without such fluctuations.

This lecture presents two simplified models of the spatial and temporal downstream development of linear and nonlinear instabilities sustained by a baroclinic current with no horizontal shear in a channel flow. The models can be considered idealized representations of the response of ocean currents to naturally introduced perturbations at their separation point from the boundary, such as the Gulf Stream and the Kuroshio Extension.

## 2 Setup

We consider a two-layer stratified, rotating channel as shown in Figure 1. Both layers have the same rest thickness $H$ and a constant zonal base flow $U_n$ $(n = 1, 2)$. The flow is semi-infinite $0 \leq x \leq \infty$, where $x$ is the downstream coordinate. The coordinate across the channel is $y$ and the width of the channel is $L$. We will study how a time-dependent boundary condition applied at the origin $x = 0$ affects the downstream unstable current in space and time.

We will study a model without the $\beta$-effect [2] as well as a model with the $\beta$-effect [3].

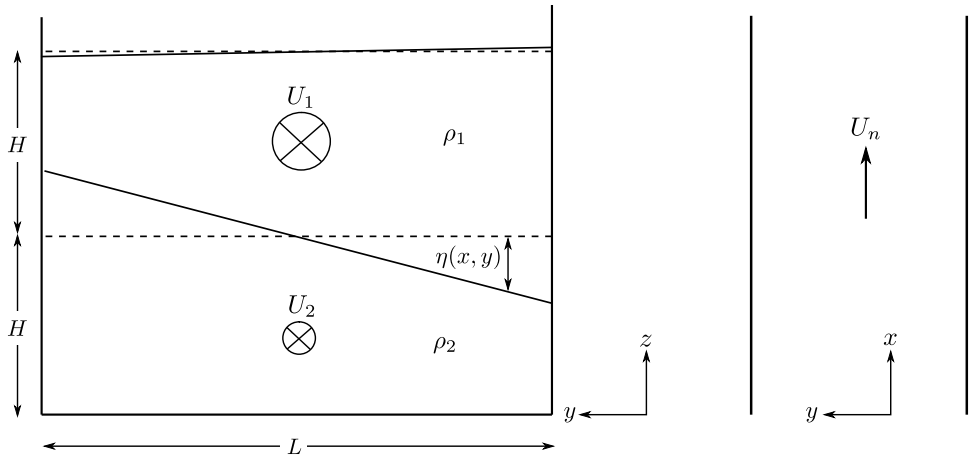


Figure 1: The problem setup. Layers are indicated by the subscript $n$.

### 2.1 Model 1: two layers, friction and $\beta = 0$

We first consider the standard two-layer quasi-geostrophic model without the $\beta$-effect. If we assume the viscous friction has a linear damping term in the momentum equation, then the quasi-geostrophic potential vorticity equation is

$$\left[\frac{\partial}{\partial t} + \frac{\partial \psi_n}{\partial x}\frac{\partial}{\partial y} - \frac{\partial \psi_n}{\partial y}\frac{\partial}{\partial x}\right]\left[\nabla^2\psi_n - F_n(-1)^n\left(\psi_2 - \psi_1\right)\right] = -r\nabla^2\psi_n, \quad n = 1, 2. \tag{1}$$

The quantity $\psi_n$ in this equation is the geostrophic stream function. The parameter $F_n = \frac{f^2L^2}{g'H}$ where $g' = \frac{\rho_2 - \rho_1}{\rho_2}g$, and the right-hand side is the frictional sink of potential vorticity. The parameter $r$ is a nondimensional ratio between the linear friction damping time scale and the advective time scale. The non-dimensional domain is now $x \geq 0$ and $0 \leq y \leq 1$.

The stream function can be written as

$$\psi_n = -U_n y + \varphi_n(x, y, t), \tag{2}$$

where $-U_n y$ is the stream function of the base flow and $\varphi(x, y, t)$ is the perturbation. Given that, the quasi-geostrophic potential vorticity equation becomes

$$\begin{aligned}&\left[\frac{\partial}{\partial t} + \frac{\partial \varphi_n}{\partial x}\frac{\partial}{\partial y} + (U_n - \frac{\partial \varphi_n}{\partial y})\frac{\partial}{\partial x}\right]\left[\nabla^2\varphi_n - F(-1)^n\left(\varphi_2 - U_2 y - \varphi_1 + U_1 y\right)\right] \\ &= -r\nabla^2\varphi_n, \quad n = 1, 2.\end{aligned} \tag{3}$$

The sum of the $n = 1$ equation and the $n = 2$ equation yields the equation for the barotropic stream function perturbation $\varphi_B = \frac{1}{2}(\varphi_1 + \varphi_2)$, namely

$$\left(\frac{\partial}{\partial t} + U_B\frac{\partial}{\partial x}\right)\nabla^2\varphi_B + \frac{U_s}{4}\frac{\partial}{\partial x}\nabla^2\varphi_T + J\left(\varphi_B, \nabla^2\varphi_B\right) + \frac{1}{4}J\left(\varphi_T, \nabla^2\varphi_T\right) = -r\nabla^2\varphi_B. \tag{4}$$

Here, the barotropic base flow is $U_B = \frac{1}{2}(U_1 + U_2)$ and the shear base flow is $U_s = U_1 - U_2$.

The difference of the $n = 1$ equation and the $n = 2$ equation yields the equation for the baroclinic stream function perturbation $\varphi_T = \varphi_1 - \varphi_2$, namely

$$\left(\frac{\partial}{\partial t}+U_B\frac{\partial}{\partial x}\right)\left[\nabla^2\varphi_T-2F\varphi_T\right]+U_s\frac{\partial}{\partial x}\left[\nabla^2\varphi_B+2F\varphi_B\right]+J\left(\varphi_B,\nabla^2\varphi_T-2F\varphi_T\right)$$
$$+J\left(\varphi_T,\nabla^2\varphi_B\right)=-r\nabla^2\varphi_T. \tag{5}$$

The boundary conditions in $y$ are

$$\frac{\partial}{\partial x}\left\{\begin{array}{c}\varphi_B\\ \varphi_T\end{array}\right\}=0,\quad y=0,1. \tag{6}$$

We then perform a linear stability analysis. Normal modes of the stream functions that satisfy these boundary conditions are given by

$$\varphi_n=A_n e^{i(kx-\omega t)}\sin j\pi y, j=1,2,3,... \tag{7}$$

The equations for the normal modes of $\varphi_B=\frac{A_1+A_2}{2}e^{i(kx-\omega t)}\sin j\pi y$ and $\varphi_T=(A_1-A_2)e^{i(kx-\omega t)}\sin j\pi y$ are

$$(-i\omega+ikU_B)(-K^2\varphi_B)+\frac{U_s}{4}ik(-K^2\varphi_T)=rK^2\varphi_B, \tag{8}$$

$$(-i\omega+ikU_B)(-K^2-2F)\varphi_T+U_sik(2F-K^2)\varphi_B=rK^2\varphi_T, \tag{9}$$

where the total wavenumber $K=\sqrt{k^2+l^2}$ where $l=j\pi$. From these two equations, we can derive the following dispersion relation:

$$(i\omega-ikU_B)(K^2+2F)(i\omega-ikU_B-r)-\frac{1}{4}k^2U_s^2(2F-K^2)=rK^2(i\omega-ikU_B-r). \tag{10}$$

Writing the frequency as $\omega=\omega_r+i\omega_r$, the imaginary part of the dispersion relation is trivially solved for $\omega_r=kU_B$, and the real part of the dispersion relation becomes:

$$(K^2+2F)\omega_i^2+2r(K^2+F)\omega_i=\frac{1}{4}k^2U_s^2(2F-K^2)-r^2K^2. \tag{11}$$

For any velocity shear $U_s$ exceeding the critical value

$$U_s>U_c=\frac{2rK}{k\left(2F-K^2\right)^{1/2}}, \tag{12}$$

the right-hand side of equation (11) will be positive, and $\omega_i$ will have a positive root corresponding to exponential growth and instability at any wavenumber. In the following we will consider shears that are greater than the critical shear by an amount $\Delta$. We will discuss two cases. One is the $r=O(1)$ case, i.e., the linear momentum damping timescale is comparable to the advective timescale; the other is the $r=O(\Delta)$ case, i.e., the nearly inviscid case where the linear momentum damping timescale is much smaller than the advective timescale.

### 2.2 Model 2: two layers, friction and $\beta\neq 0$

This model is the same as the model described in section 2.1, now considering $\beta\neq 0$. The quasi-geostrophic potential vorticity equation (1) now becomes :

$$\left[\frac{\partial}{\partial t}+\frac{\partial\psi_n}{\partial x}\frac{\partial}{\partial y}-\frac{\partial\psi_n}{\partial y}\frac{\partial}{\partial x}\right]\left[\nabla^2\psi_n-F_n(-1)^n\left(\psi_2-\psi_1\right)+\beta y\right]=-r\nabla^2\psi_n, \tag{13}$$
$$n=1,2.$$

As a result, the nondimensional equations for the barotropic streamfunction and the baroclinic streamfunction become

$$\left(\frac{\partial}{\partial t}+U_B\frac{\partial}{\partial x}\right)\nabla^2\varphi_B+\frac{U_s}{4}\frac{\partial}{\partial x}\nabla^2\varphi_T+J\left(\varphi_B,\nabla^2\varphi_B\right)+\frac{1}{4}J\left(\varphi_T,\nabla^2\varphi_T\right)+\beta\frac{\partial\varphi_B}{\partial x}=-r\nabla^2\varphi_B. \tag{14}$$

$$\left(\frac{\partial}{\partial t}+U_B\frac{\partial}{\partial x}\right)\left[\nabla^2\varphi_T-2F\varphi_T\right]+U_s\frac{\partial}{\partial x}\left[\nabla^2\varphi_B+2F\varphi_B\right]+J\left(\varphi_B,\nabla^2\varphi_T-2F\varphi_T\right)+J\left(\varphi_T,\nabla^2\varphi_B\right)+\beta\frac{\partial\varphi_T}{\partial x}=-r\nabla^2\varphi_T. \tag{15}$$

In this model, we will only consider a small $\beta$ effect and study the critical curve for instability in terms of $F$, which is at the lowest order independent of $\beta$. By contrast with what we have done in the $\beta=0$ model, here we fix the shear, and write the condition for instability, i.e., $\omega_i>0$ as $F>F_c$ where

$$F_c=\frac{K^2}{2}+\frac{2r^2K^2}{k^2U_s^2}. \tag{16}$$

In this model we will only consider the case $F=F_c+\Delta$ with a small beta effect, i.e., $\beta=O(\Delta^{1/2})$ and a small friction $r=O(\Delta)$, in which case we can approximate $F_c\simeq K^2/2$.

## 3 Nonlinear Instability Theory

We follow the structure of [2] and [3] and develop the nonlinear theory for the two models described above. We begin with the dissipative case, i.e., $r=O(1)$ (case 1) and then move onto the nearly inviscid case $r=O(\Delta)$ (case 2). Both these cases, as in [2], are treated without $\beta$. We close the section by briefly discussing the case when $\beta\neq 0$ and $r=O(\Delta)$ (case 3), by following [3].

### 3.1 Case 1: $\beta=0$, $r=O(1)$

This section presents the linear and non-linear analysis via asymptotic expansion of the model with dissipation i.e., case 1. Assuming $r=O(1)$, the minimum value of $U_c$ (see equation 12) over all wavenumbers $k$ (for given $l>0$) can be computed to be

$$U_{so}=\frac{2r}{(2F)^{1/2}-l}, \tag{17}$$

and is achieved when $K^2=l\sqrt{2F}$. For these parameter values, $\omega_r=kU_B$ and $\omega_i=0$. We introduce slow time and space scales,

$$T=|\Delta|t=\epsilon^2t,\quad X=|\Delta|x=\epsilon^2x,\quad U_s=U_{so}+\Delta.$$

We will expand the barotropic and baroclinic stream functions in terms of the small parameter $\epsilon$. We assume the asymptotic series will have the form

$$\varphi=\epsilon\left[\varphi^{(0)}+\epsilon\varphi^{(1)}+\epsilon^2\varphi^{(2)}+...\right]. \tag{18}$$

Note that $\varphi(x,t,X,T)$. For a well-posed asymptotic expansion we require a relation between the order of $\epsilon$ and $\Delta$. As discussed in [2], the proper relation is $\epsilon=O(\sqrt{\Delta})$.

Substituting the expansions (18) into (4) and (5) and keeping only the lowest order terms recovers the linear equations for $U_s = U_{so}$,

$$\begin{aligned}(\partial_t + U_B\partial_x)\,\nabla^2\varphi_B^{(0)} + \frac{U_{so}}{4}\partial_x\nabla^2\varphi_T^{(0)} &= -r\nabla^2\varphi_B^{(0)},\\ (\partial_t + U_B\partial_x)\left[\nabla^2\varphi_T^{(0)} - 2F\varphi_T^{(0)}\right] + U_{so}\partial_x\left[\nabla^2\varphi_B^{(0)} + 2F\varphi_B^{(0)}\right] &= -r\nabla^2\varphi_T^{(0)}.\end{aligned} \tag{19}$$

Notice the absence of nonlinear terms captured by the Jacobians at this order. It is easy to see these won't enter (19) since they would be of order $\epsilon^2$. As such, (19) are a set of coupled linear PDEs, we assume the ansatz,

$$\begin{aligned}\varphi_B^{(0)} &= \frac{1}{2}A_B(X,T)\exp\left(i\left(kx-\omega t\right)\right)\sin ly + *,\\ \varphi_T^{(0)} &= \frac{1}{2}A_T(X,T)\exp\left(i\left(kx-\omega t\right)\right)\sin ly + *,\end{aligned} \tag{20}$$

where here $k$ and $\omega$ are the wavenumber and frequency of the linear solution for $U_s = U_{so}$. Here $*$ represent the complex conjugates and $A_B$ and $A_T$ are the wave amplitudes that are functions of the slow variables only. We may readily derive a relation between the barotropic and baroclinic amplitudes by employing the properties of the marginally stable solution. Substituting the ansatz (20) into the barotropic equation in (19) and noting that at the marginal stability curve the advecting part of the equation would be zero, yields the relation

$$A_T(X,T) = i\frac{4r}{kU_{so}}A_B(X,T). \tag{21}$$

Going then to the next order, matching terms that are $O(\epsilon^2)$,

$$\begin{aligned}&D_t\nabla^2\varphi_B^{(1)} + \frac{U_{so}}{4}\partial_x\nabla^2\varphi_T^{(1)} + J\left(\varphi_B^{(0)},\nabla^2\varphi_B^{(0)}\right) + \frac{1}{4}J\left(\varphi_T^{(0)},\nabla^2\varphi_T^{(0)}\right) = -r\nabla^2\varphi_B^{(1)},\\ &D_t\left[\nabla^2\varphi_T^{(1)} - 2F\varphi_T^{(1)}\right] + U_{so}\partial_x\left[\nabla^2\varphi_B^{(1)} + 2F\varphi_B^{(1)}\right]\\ &\quad + J\left(\varphi_B^{(0)},\nabla^2\varphi_T^{(0)} - 2F\varphi_T^{(0)}\right) + J\left(\varphi_T^{(0)},\nabla^2\varphi_B^{(0)}\right) = -r\nabla^2\varphi_T^{(1)},\end{aligned} \tag{22}$$

where $D_t = \partial_t + U_B\partial_x$ in the fast variables. Notice the appearance of the non-linear self-interaction terms captured by the Jacobians acting on solutions from the previous order. We may think of them as forcing terms at this order. Furthermore, using the ansatz (20) allows us to make the following simplifications using standard algebraic properties of the Jacobian bracket. Consider the following

$$J\left(\varphi_B^{(0)},\nabla^2\varphi_B^{(0)}\right) = J\left(\varphi_B^{(0)},-K^2\varphi_B^{(0)}\right) = 0, \quad J\left(\varphi_T^{(0)},\nabla^2\varphi_T^{(0)}\right) = J\left(\varphi_T^{(0)},-K^2\varphi_T^{(0)}\right) = 0.$$

Then using the anti-symmetry property of the arguments, the Jacobians in the second equation in (22) are

$$\begin{aligned}&J\left(\varphi_B^{(0)},\nabla^2\varphi_T^{(0)} - 2F\varphi_T^{(0)}\right) + J\left(\varphi_T^{(0)},\nabla^2\varphi_B^{(0)}\right)\\ &= J\left(\varphi_B^{(0)},-K^2\varphi_T^{(0)} - 2F\varphi_T^{(0)}\right) + J\left(\varphi_T^{(0)},-K^2\varphi_B^{(0)}\right)\\ &= 2FJ\left(\varphi_T^{(0)},\varphi_B^{(0)}\right).\end{aligned} \tag{23}$$

We are particularly interested in solutions that provide corrections to the mean flow, i.e., solutions for $\varphi^{(1)}_{B,T}$ that are invariant in $t$ and $x$. These readily satisfy (using equation 21):

$$\frac{\partial^2}{\partial y^2}\varphi^{(1)}_B = 0, \tag{24}$$

and

$$\frac{\partial^2}{\partial y^2}\varphi^{(1)}_T = \frac{4lF}{U_{so}}\sin(2ly)\left|A_B\right|^2, \tag{25}$$

whose solution can be obtained straightforwardly

$$\varphi^{(1)}_T \equiv \Phi_T(X,y,T) = -\frac{F}{lU_{so}}\sin(2ly)\left|A_B\right|^2 + C_T y + D_T. \tag{26}$$

We define $\Phi_T$ to be the correction to the mean flow. The constants of integration $C_T$ and $D_T$ are really functions of the slow variables $X$ and $T$. Furthermore, from the boundary conditions at the origin adapted to the slow spatial scale, we have,

$$\partial_X\varphi^{(1)}_B = 0, \quad \partial_X\varphi^{(1)}_T = 0, \quad \text{at} \quad y = 0,1,$$

and it follows that $C_T = D_T = 0$, and similarly for $\varphi^{(1)}_B = 0$.

At next order i.e., $O(\epsilon^3)$, the expansion begins to include variations on the slow space and time scales and the correction to the mean flow i.e., $\Phi_T$. Furthermore, some of the terms at this order become resonant, so to avoid secular growth of terms, we require a solvability condition. This condition can be expressed in terms of the behaviour of the barotropic amplitude $A_B$. After extensive algebra, that can be found in [2],

$$\left(\frac{\partial}{\partial T} + U_B\frac{\partial}{\partial X}\right)A_B - \sigma A_B + N A_B\left|A_B\right|^2 = 0, \tag{27}$$

where:

$$\begin{aligned}\sigma &= \frac{\Delta}{|\Delta|}\frac{kK}{2}\frac{\left(2F-K^2\right)^{1/2}}{F+K^2},\\ N &= \frac{\epsilon^2}{|\Delta|}\frac{Fk}{8r}\frac{2K^2(2F-K^2)-8l^2(F-K^2)}{2F-K^2}.\end{aligned} \tag{28}$$

Keep in mind (27) also yields information on $A_T$ through the relation (21).

The PDE (27) can be solved via the method of characteristics. Letting $s$ denote the characteristic variable, the characteristic ODEs are

$$\frac{d}{ds}T = 1, \quad \frac{d}{ds}X = U_B, \quad \frac{d}{ds}A_B = \sigma A_B - N A_B|A_B|^2. \tag{29}$$

It is clear from the first ODE that $s = T$ and from the second that $X_0 = X - U_B T$ where $X_0$ is constant on the characteristic. Hence, the characteristic curves are linear. Furthermore, in the $(X,T)$-plane, the line $X = U_B T$ separates characteristic curves that intersect the $X$-axis from those that intersect the $T$-axis. As such, the domain is partitioned into two regions; the first region, for characteristic curves that intersect the $X$-axis, the intersection points prescribe the initial data at $T = 0$. The second region, for characteristic curves that intersect the $T$-axis, the intersection points

prescribe the boundary data influenced by the forcing at $X = 0$. As such, we may find our solution at the wave-front i.e., $X > U_B T$ in region one and behind the wave front, i.e., $X < U_B T$ in region two. The following figure shows the linear characteristic curves and the separation into the two regions.

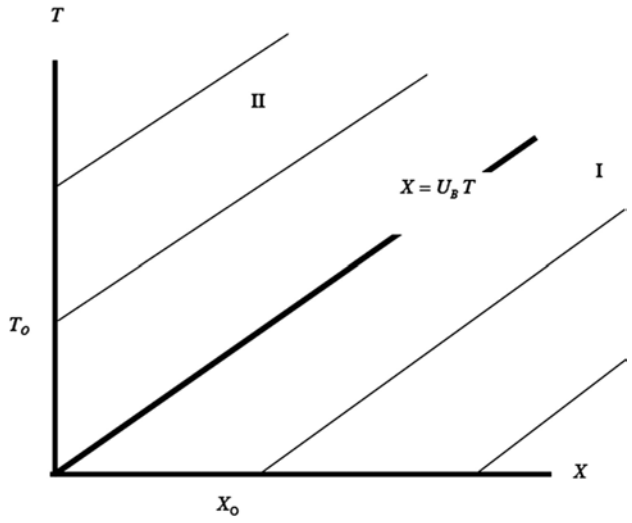


Figure 2: Characteristic curves in the $(X, T)$ plane. From [2].

With this in mind, we first solve the ODE for $A_B$ in (29) in region 2, that is behind the wave front for $X < U_B T$. The ODE is separable and can be solved analytically by direct integration. Following the formulation as in the paper, it is convenient to express the solution as $Z = A_B^2$. Letting $Z_o(T_0)$ denote the square of the amplitude of forcing at the origin, the solution takes the form,

$$Z = \frac{Z_o\left(T - X/U_B\right) e^{2\sigma X/U_B}}{1 + \frac{N}{\sigma} Z_o\left(T - X/U_B\right)\left(e^{2\sigma X/U_B} - 1\right)}. \tag{30}$$

Notice, we have expressed the solution as a function of time and so the solution will propagate as $T_0 = T - X/U_B$.

In similar fashion, perhaps more standard in the characteristic method while solving PDE, solution in region one, i.e. $X > U_B T$, solutions are determined by the initial data $Z_I(X_0)$,

$$Z = \frac{Z_I\left(X - U_B T\right) e^{2\sigma T}}{1 + \frac{N}{\sigma}\left(e^{2\sigma T} - 1\right) Z_I(X - U_B T)}. \tag{31}$$

Note that the solution will be continuous across the front as long as the matching condition $Z_o(0) = Z_I(0)$ is obeyed. The following figures plot the amplitude solution $A_B$ and the correction $\Phi_T$ for some example parameter values.

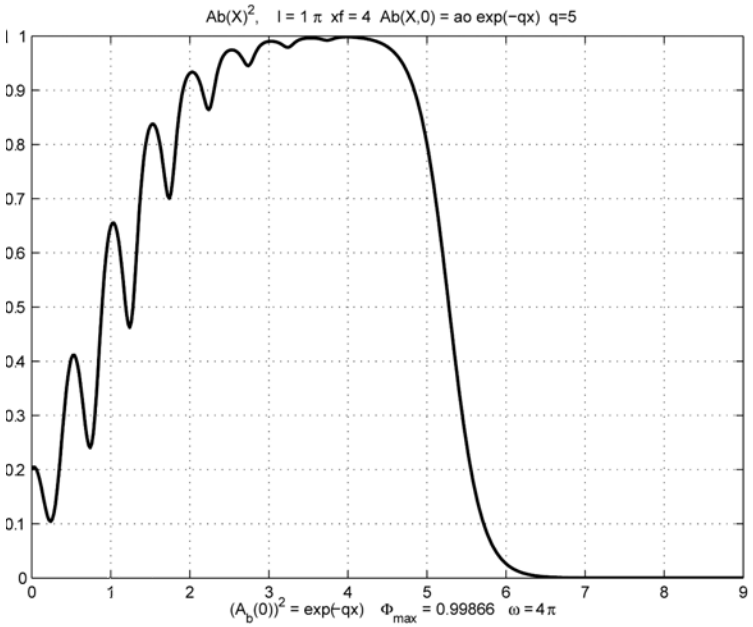


Figure 3: Amplitude of the barotropic mode $A_B$ as a function of $X$. Given the choice of parameters for the plot, the front is located at $X = 4$. From [2].

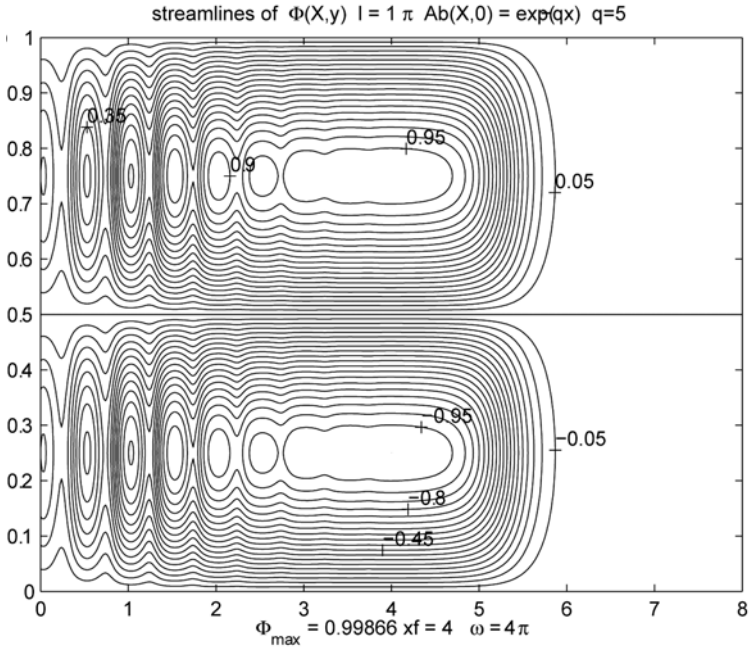


Figure 4: Example plot of the streamlines of the correction to the mean flow $\Phi_T$. The plot looks down onto the $(X, y)$-plane.From [2].

*Note to the reader: beyond this point, we did not fully double-check the algebra from [2] and [3]. Only the obvious typos continue to be marked in red, but it is possible that other typos and algebraic mistakes remain. They do not affect the main results described.*

### 3.2 Case 2: $\beta = 0$, $r = O(\Delta)$

We now consider the problem when the friction is small, i.e. $r = O(\Delta)$, with $\Delta$ representing the supercriticality. In this limit, the right-hand side of (11) reduces to $\simeq k^2 U_s^2 (2F - K^2)/4$, so the condition for instability does not involve the shear and can most simply be written in terms of the parameter $F$ (see Figure 5), as

$$F > F_c = \frac{l^2 + k^2}{2}, \tag{32}$$

which reaches a minimum when $k = 0$.

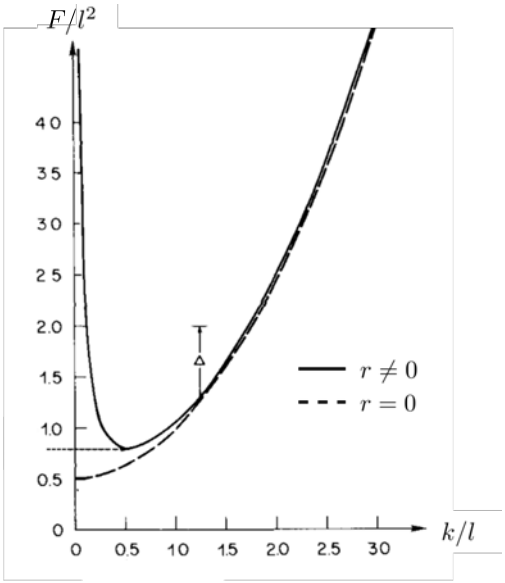


Figure 5: Critical curve for baroclinic instability in the two-layer system with ($r \neq 0$) and without ($r = 0$) friction effects. The supercriticality, $\Delta$, measures the distance above the critical curve, at a fixed $k$. Adapted from [1].

Thus, analogously to the model described in 3.1, here we make the following assumptions:

1. The dissipation is small:
$$r = O(\Delta). \tag{33}$$

2. The basic flow is only slightly supercritical with respect to the rotational Froude number $F$:
$$F = F_c + \Delta = \frac{l^2}{2} + \Delta, \qquad \Delta \ll 1 \tag{34}$$

3. The theory to be developed will be a long wavelength theory for the instability. We will suppose that $k$ is small and to be consistent with (34), expand it as
$$k = \Delta^{1/2} k_0 + \Delta k_1 + ..., \tag{35}$$
while also,
$$\omega = \Delta^{1/2} \omega_0 + \Delta \omega_1 + ..., \tag{36}$$

such that according to linear theory[1],

$$\omega_0 = k_0 U_B, \tag{37}$$

$$\omega_1 - k_1 U_B = i\frac{k_0}{2^{1/2} l}(2 - k_0^2)^{1/2}. \tag{38}$$

In addition, we consider that the solution will be a function of fast and slow space and time variables. We introduce the fast space and time coordinates $\xi$ and $\tau$, and the slow space and time coordinates $X$ and $T$, respectively. From the assumptions above, the instability oscillates in space and time over the fast timescale $\Delta^{1/2}$, while its amplitude evolves in space and time over the slower timescale $\Delta$. Hence, the new space and time scales are related to $x, t$ and $\Delta$ as:

$$\xi = \Delta^{1/2} x, \qquad X = \Delta x, \tag{39}$$

$$\tau = \Delta^{1/2} t, \qquad T = \Delta t. \tag{40}$$

The barotropic and baroclinic stream function perturbations are also functions of $\xi$, $X$, $\tau$ and $T$. For example:

$$\begin{aligned} \frac{\partial \varphi_B}{\partial x} &= \Delta^{1/2}\frac{\partial}{\partial \xi} + \Delta\frac{\partial}{\partial X}, \\ \frac{\partial \varphi_B}{\partial t} &= \Delta^{1/2}\frac{\partial}{\partial \tau} + \Delta\frac{\partial}{\partial T}. \end{aligned} \tag{41}$$

The perturbation stream functions will be expanded in an asymptotic series in the small amplitude $\epsilon = O(\Delta^{1/2})$, as before:

$$\begin{aligned} \varphi_B &= \epsilon(\varphi_B^{(0)} + \epsilon\varphi_B^{(1)} + \epsilon^2\varphi_B^{(2)} + ...), \\ \varphi_T &= \epsilon(\varphi_T^{(0)} + \epsilon\varphi_T^{(1)} + \epsilon^2\varphi_T^{(2)} + ...). \end{aligned} \tag{42}$$

These transformations, along with the assumptions (34), (35), and (36), were inserted into (14) and (15). At the lowest order in $\epsilon$, we recover as usual the linear problem for the critical parameters, whose solution is:

$$\varphi_B^{(0)} = \frac{1}{2} A_B(X,T) e^{i(k_0\xi - \omega_0\tau)} \sin(ly) + *,$$

$$\varphi_T^{(0)} = 0,$$

$$k_0 = \omega_0 / U_B.$$

At the next order in $\epsilon$, we obtain the corrections $\varphi_B^{(1)}$ and $\varphi_T^{(1)}$, which can be added to the lowest-order solutions to get:

$$\varphi_B^{(0)} + \epsilon\varphi_B^{(1)} = \left(\frac{A_B(X,T)}{2} e^{i\theta} + *\right)\sin(ly) + O(\Delta^{1/2}), \tag{43}$$

$$\varphi_T^{(0)} + \epsilon\varphi_T^{(1)} = \Delta^{1/2}\left(\frac{4i}{k_0 U_s}\left[\frac{\partial}{\partial T} + U_B\frac{\partial}{\partial X} + \frac{r}{\Delta}\right]\frac{A_B(X,T)}{2} e^{i\theta} + *\right)\sin(ly) + \Delta^{1/2}\Phi_T(y,X,T), \tag{44}$$

where $\theta = k_0\xi - \omega_0\tau$ and $\Phi_T$ is the baroclinic correction to the mean flow and is a function of only the slow space and time scales $X$, $T$ and $y$, as in the previous section.

[1]Note to the reader: the expression for $\omega_1$, while identical here to that of [2], might be missing terms in $r$ that are formally of the same order.

Assuming solutions of the mean flow correction in the form

$$\Phi_T = P(X,T)\sin(2ly), \tag{45}$$

we obtain at the next order an evolution equation for the correction to the mean flow driven by the time dependence of the instability amplitude and the friction:

$$\left(\frac{\partial}{\partial T} + U_B\frac{\partial}{\partial X}\right)P + \frac{4}{5}\frac{r}{\Delta}P = -\frac{\epsilon}{\Delta^{1/2}}\frac{2}{l}\frac{F_c}{U_s}\left(\frac{\partial}{\partial T} + U_B\frac{\partial}{\partial X} + 2\frac{r}{\Delta}\right)|A_B|^2, \tag{46}$$

which is coupled to the evolution of the instability amplitude,

$$\left(\frac{\partial}{\partial T} + U_B\frac{\partial}{\partial X}\right)^2 A_B + \frac{3}{2}\frac{r}{\Delta}\left(\frac{\partial}{\partial T} + U_B\frac{\partial}{\partial X}\right)A_B - \sigma^2 A_B - \frac{2\epsilon}{\Delta^{1/2}}l^2k_0^2U_sA_BP = 0, \tag{47}$$

where $\sigma^2 A_B$ in (47) is the growth term of the instability amplitude, and the last term on the left is the alteration in the growth rate by its interaction with the base flow, where

$$\sigma^2 = \frac{U_s^2}{2}\left(l^2 - k_0^2\right)\frac{k_0^2}{l^2} - \frac{r^2}{2\Delta^2}.$$

Some parameters in (46) and (47) can be removed by the following rescalings,

$$T' = \sigma T, \qquad X' = \sigma X/U_B, \qquad A_B = A_0A', \qquad P = P_0P', \qquad \gamma = r/\Delta\sigma, \tag{48}$$

where

$$\epsilon = \Delta^{1/2}, \qquad P_0 = \frac{\sigma^2}{k_0^2U_sl}, \qquad A_0 = \frac{\sigma}{k_0l}, \tag{49}$$

so that after dropping the primes, we obtain the final amplitude equations:

$$\left(\frac{\partial}{\partial T} + \frac{\partial}{\partial X}\right)^2 A + \frac{3}{2}\gamma\left(\frac{\partial}{\partial T} + \frac{\partial}{\partial X}\right)A - A - AP = 0, \tag{50}$$

$$\left(\frac{\partial}{\partial T} + \frac{\partial}{\partial X}\right)P + \frac{4}{5}\gamma P = -\left[\left(\frac{\partial}{\partial T} + \frac{\partial}{\partial X}\right)|A|^2 + 2\gamma|A|^2\right]. \tag{51}$$

As in the previous section for the case $r = O(1)$ (see (29) and Figure 2), the characteristics are given by the advection by the barotropic mean flow $U_B$ (now equal to 1 in these rescaled units),

$$\frac{dX}{ds} = 1, \qquad \frac{dT}{ds} = 1, \tag{52}$$

where $s$ is the variable along the characteristic. In terms of this characteristic coordinate $s$, the system (50) and (51) can be written as the set of first-order differential equations:

$$\frac{dA}{ds} = -\gamma A + B, \tag{53}$$

$$\frac{dB}{ds} = -\frac{\gamma}{2}B + \left(1 + \gamma^2/2\right)A - A|A|^2 - RA, \tag{54}$$

$$\frac{dR}{ds} = -\frac{4}{5}\gamma R + \frac{6}{5}\gamma|A|^2, \tag{55}$$

where we have introduced the new function $R$ such that

$$P = -|A|^2 - R. \tag{56}$$

This set of ordinary differential equations is of the form of the well-known Lorenz equations. For a range of moderately small $\gamma$, the solutions have a chaotic behaviour, as can be illustrated by comparing the solution along four characteristics that are closely spaced at $s = 0$ (Figure 6). The chaotic divergence of the solutions with increasing distance along the characteristics implies changes of order one from one characteristic to its neighbour.

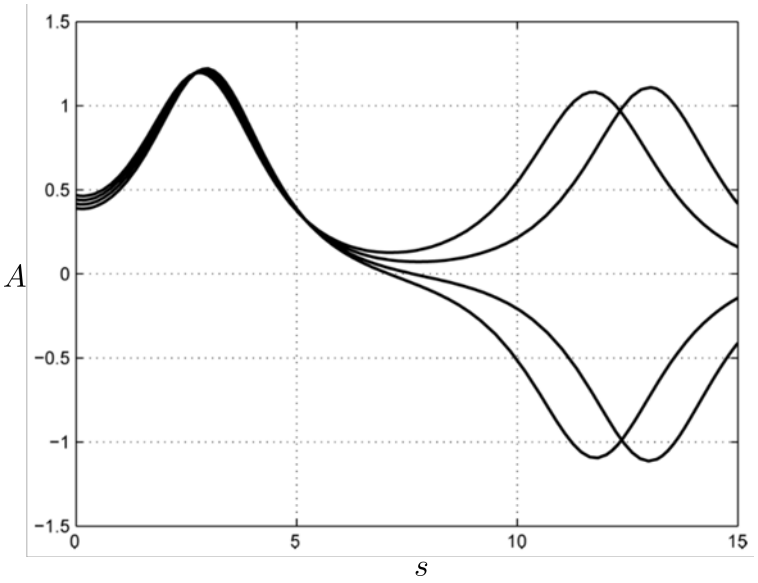


Figure 6: The solution for $A$ along four characteristics closely spaced at $s = 0$. Adapted from [2].

The solution of system (53), (54), (55), (56) can be found by integrating those equations along each characteristic and, to find the solution for fixed time, it is only necessary to label the characteristic by its initial intersection with the $T$ axis as shown in Figure 7.

For a given $X$ and $T$, the solution is found by evaluating the amplitude on each characteristic at the level line $T =$ constant, whose starting value is simply $T_0 = s - T$. Even if the starting values of $T_0$ are close, the chaotic character of the solutions along each characteristic will introduce very rapid changes of the solution at fixed $T$ from one characteristic to its neighbor and hence from one value of $X$ to the next. That is, the sensitivity of the solutions along the characteristics to very small changes in the starting values can lead to very large changes in the solution as a function of $X$ if the solution is carried far enough in $s$, i.e. in $X$, for the chaotic behavior to manifest itself.

As an example, consider a situation with no perturbation ahead of the front, i.e. at $T = 0$ the perturbation is zero everywhere and the solution is forced by the condition at the origin,

$$A(0, T) = 1 - e^{-qT}, \tag{57}$$

where $q$ is a parameter. This forcing has been chosen since it is monotonic, and so the oscillations seen in the solution are internally generated. Figure 8 shows the response in $X$ of the wave amplitude at three times, $T = 3$, 6, and 10 for the region behind the front. For short times ($T = 3$, Fig. 8a), the solution is very smooth but as time goes on the chaotic behavior begins to manifest itself and rapid variations of the solution are clearly seen behind the front, with the emergence of a second

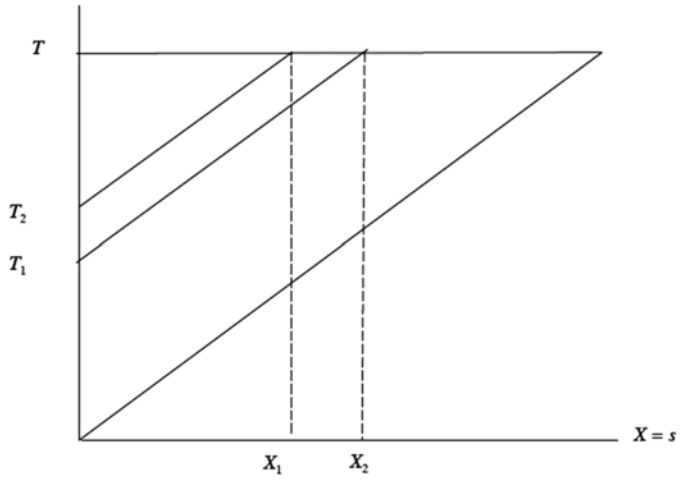


Figure 7: The solution at time $T$ is obtained from the solution along each of the characteristics emanating from $s = X = 0$. Even for small differences $T_2 - T_1$, the variation along the line $T =$ constant can vary rapidly due to the chaotic behavior of the solution along the characteristics, e.g., the sensitivity to the initial conditions at the origin. Adapted from [2].

region of increasing gradient ($T = 10$, Fig. 8c). For a large time, the forcing approaches a constant and the behavior along each characteristic will be nearly identical, which is why the rapid behavior seems to be restricted to the region near the front.

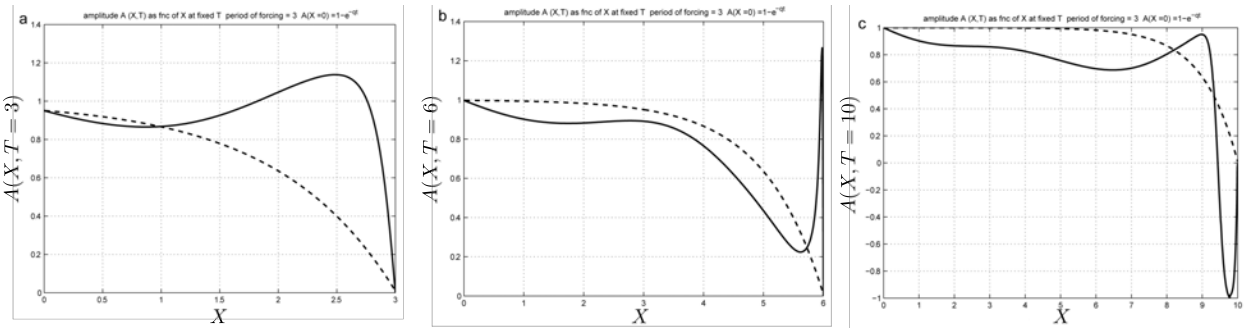


Figure 8: The amplitude of perturbations behind the advancing front at three times (a) $T = 3$, (b) $T = 6$, (c) $T = 10$, when the system is forced at the origin as $A(0, T) = 1 - e^{-qT}$. The rapid variation occurs when the length of the characteristic is large enough to manifest chaotic behavior. Parameters of the problem are $\gamma = 0.12$, $a_0 = 0.5$, $q = 1$, and $ds = 0.01$. Adapted from [2].

If instead of the forcing (57), the system is forced by

$$A(0, T) = a \sin(2\pi T / T_{period}), \tag{58}$$

the solution manifests chaotic behavior in the form of rapid variations of amplitude which occur well behind the front (Figure 9), demonstrating that it is not the front that excites the rapid variation but the sensitivity to slightly varying initial conditions from one characteristic to its neighbor.

These regions of rapid variations in amplitude with $X$ are thus regions that have relatively large meridional (i.e., $y$) velocities and rapid changes in those velocities. Thus, even though the characteristics remain simple, straight parallel lines, the divergence of the solutions on neighboring

characteristics exhibits a behaviour that resembles a "chaotic shock", though not in the traditional sense of gas dynamics or the nonlinear bending and overlap of the characteristic curves in hyperbolic systems [2]. It is the chaotic character of the solutions *along* those characteristics and the divergence of the solutions on neighboring characteristics that provides the shrinking scales in the behavior of the solution.

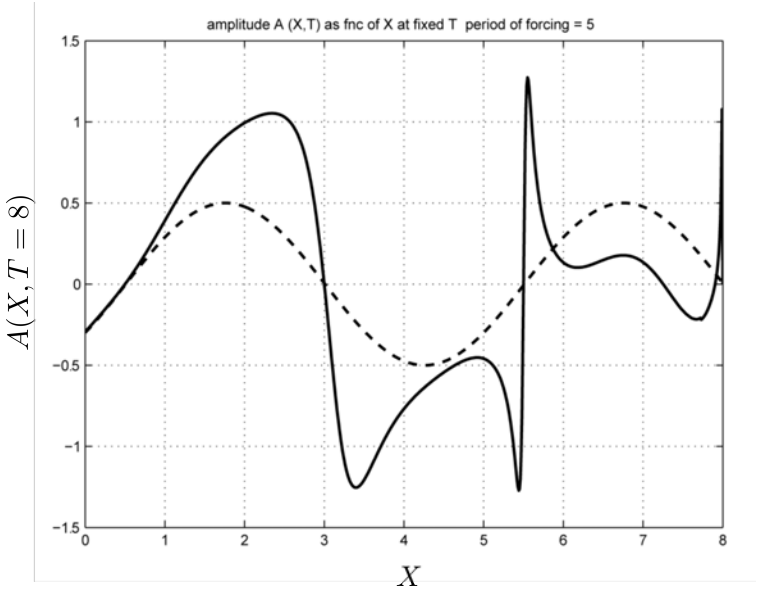


Figure 9: The amplitude of perturbations behind the advancing front at $T = 8$, when the system is forced at the origin as $a \sin(2\pi T/T_{period})$, with $a = 0.5$ and $T_{period} = 5$. Parameters of the problem are $\gamma = 0.12$, and $ds = 0.01$. Adapted from [2].

### 3.3 Case 3: $\beta \neq 0$, $r = O(\Delta)$

As in the previous section, we consider $r = O(\Delta)$, i.e a nearly inviscid situation with weak frictional effects. We now include a small $\beta$ effect, with $\beta = O(\Delta^{1/2})$. Similar to what we have done in the $\beta = 0$ model, we introduce fast space and time coordinates $\xi$ and $\tau$, and the slow space and time coordinates $X$ and $T$ respectively, as :

$$\begin{aligned} \xi &= \Delta^{1/2} x, \quad X = \Delta x, \\ \tau &= \Delta^{1/2} t, \quad T = \Delta t. \end{aligned} \tag{59}$$

Repeating the asymptotic series expansion, we derive at the lowest order in $\epsilon$,

$$\begin{aligned} \varphi_B^{(0)} &= A(X,T) e^{ik_0(\xi - c\tau)} \sin ly + * \\ \varphi_T^{(0)} &= 0, \quad c = U_B, \quad F_c = l^2/2, \end{aligned} \tag{60}$$

where * denotes the complex conjugate of the preceding expression.

In comparison with the previous section, the first order correction now has an additional term involving $\beta$,

$$\begin{aligned} \varphi_T^{(1)} =& \frac{4}{k_0 U_s} \left[ i \left( \frac{\partial}{\partial T} + U_B \frac{\partial}{\partial X} \right) A + \frac{ir}{\Delta} A + \frac{\beta k_0}{\Delta^{1/2} l^2} A \right] \\ & \times e^{i\theta} \sin ly + * + \Phi_T(X, y, T), \end{aligned} \tag{61}$$

where $\Phi_T$ satisfies, at the next order

$$\begin{aligned}\left(\frac{\partial}{\partial T}+U_B\frac{\partial}{\partial X}\right)\left(\frac{\partial^2\Phi_T}{\partial y^2}-2F_c\Phi_T\right)+\frac{r}{\Delta}\frac{\partial^2\Phi_T}{\partial y^2}\\ =-\frac{\epsilon}{\Delta^{1/2}}\frac{4\left(2F_c l\right)}{U_s}\left[\left(\frac{\partial}{\partial T}+U_B\frac{\partial}{\partial X}\right)|A|^2+\frac{2r}{\Delta^{1/2}}|A|^2\right]\sin(2ly).\end{aligned} \tag{62}$$

Assuming a solution of the form $\Phi_T = P(X,T)\sin(2ly)$ leads to

$$\left(\frac{\partial}{\partial T}+U_B\frac{\partial}{\partial X}\right)P+\frac{4}{5}\frac{r}{\Delta}P=-\frac{\epsilon}{\Delta^{1/2}}\frac{4}{5}\left[\left(\frac{\partial}{\partial T}+U_B\frac{\partial}{\partial X}\right)|A|^2+\frac{2r}{\Delta}|A|^2\right]. \tag{63}$$

The evolution equation for the amplitude $A$ is determined at the third order $O(\Delta^{3/2})$,

$$\begin{aligned}&\left(\frac{\partial}{\partial T}+U_B\frac{\partial}{\partial X}\right)^2 A+\frac{3}{2}\left(\frac{r}{\Delta}-i\frac{\beta k_0}{\Delta^{1/2}l^2}\right)\left(\frac{\partial}{\partial T}+U_B\frac{\partial}{\partial X}\right)A\\ &-\sigma^2 A-\frac{\epsilon}{\Delta^{1/2}}\frac{k_0U_s}{8l^2}AP=0,\ \text{where}\\ &\sigma^2=\frac{\left(2-k_0^2\right)k_0^2U_s^2}{8l^2}-\frac{r^2}{2\Delta}+\frac{ir}{\Delta}\frac{\beta k_0}{\Delta^{1/2}l^2}+\frac{\beta^2k_0^2}{2\Delta l^4}.\end{aligned} \tag{64}$$

Rescaling the variables according to

$$T'=\sigma T,\quad X'=\frac{\sigma X}{U_s},\quad A=A_oA',\quad P=P_oP',\quad b=\frac{\beta k_0}{8\sigma\Delta^{1/2}l^2}, \tag{65}$$

where

$$P_o=\frac{\sigma^2\Delta^{1/2}}{\epsilon k_0^2 l U_s},\quad A_o^2=\frac{5}{4}P_o,\quad \gamma=\frac{r}{\Delta\sigma}, \tag{66}$$

we have

$$\begin{aligned}&\left(\frac{\partial}{\partial T}+\frac{\partial}{\partial X}\right)^2 A+\frac{3}{2}(\gamma+ib)\left(\frac{\partial}{\partial T}+\frac{\partial}{\partial X}\right)A-A(1+P)=0\\ &\left(\frac{\partial}{\partial T}+\frac{\partial}{\partial X}\right)P+\frac{4}{5}\gamma P=-\left[\left(\frac{\partial}{\partial T}+\frac{\partial}{\partial X}\right)|A|^2+2\gamma P\right].\end{aligned} \tag{67}$$

Letting as before $P=-|A|^2+R$, we have

$$\begin{aligned}\left(\frac{\partial}{\partial T}+\frac{\partial}{\partial X}\right)^2 A+\frac{3}{2}(\gamma+ib)\left(\frac{\partial}{\partial T}+\frac{\partial}{\partial X}\right)A-A+A\left(|A|^2+R\right)=0,\\ \left(\frac{\partial}{\partial T}+\frac{\partial}{\partial X}\right)P+\frac{4}{5}\gamma P=\frac{6}{5}\gamma|A|^2.\end{aligned} \tag{68}$$

The effect of $\beta$ is explicitly contained in the $b$ term of the $A$ equation, and in $\sigma$ (and therefore $\gamma$). As in the $\beta=0$ model, the characteristics are given by:

$$T-X=T_0. \tag{69}$$

We study an example in which the boundary condition at $X=0$ is given by

$$A\left(0,T=T_o\right)=a\sin 2\pi T/T_{\text{period}}\ . \tag{70}$$

When $\beta$ is small, the system will behave like the $\beta=0$ case. When $\beta$ is large, it can suppress chaos along characteristics, but not before the amplitudes of the real and imaginary parts of the amplitude have had time to grow and differ by $O(1)$ on neighboring characteristics (Figure 10).

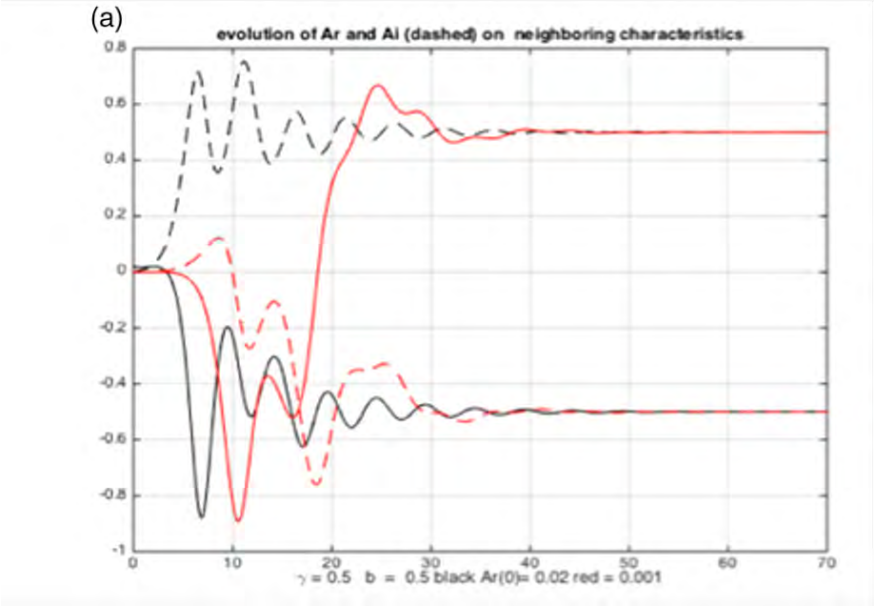


Figure 10: The evolution of the real (solid) and imaginary (dashed) parts of the amplitude along two neighboring characteristics when (nondimensional $\beta$) $b = 0.5$. From [3].

## References

[1] J. Pedlosky, *Geophysical Fluid Dynamics*, Springer US, 1979.

[2] ——, *The nonlinear downstream development of baroclinic instability*, Journal of Marine Research, 69 (2011), pp. 705–722.

[3] ——, *The effect of beta on the downstream development of unstable, chaotic baroclinic waves*, Journal of Physical Oceanography, 49 (2019), pp. 2337–2343.

# GFD 2025 Lecture 5: On the Shoulder of Giants – Eady's and Charney's Models

Joseph Pedlosky; notes by Alexandre Tlili and Lin Yao

June 20, 2025

## 1 Eady

### 1.1 A bit of history

Eric Eady (1915–1966) was a British meteorological researcher who made a significant contribution to the understanding of atmospheric dynamics. While pursuing his Ph.D. at Imperial College London, he developed a simplified model to explain the formation of large-scale weather waves in the troposphere. At that time, the mechanisms behind the generation of such waves were poorly understood. The Norwegian School, led by the meteorologist Vilhelm Bjerknes, emphasized the role of weather fronts in driving these instabilities. Eady's model, along with the subsequent work by Charney (discussed in Section 2), is widely regarded as one of the first mathematical frameworks capable of explaining the generation of large-scale instabilities in stably stratified, rotating, sheared flows. The instability Eady described came to be known as the baroclinic instability.


Figure 1: Eric Eady on Victoria's bridge above the Cam river in Cambridge.

## 1.2 Eady's model of baroclinic instability

### 1.2.1 With a flat bottom

*This section summarizes chapter 7.7 of [6].*

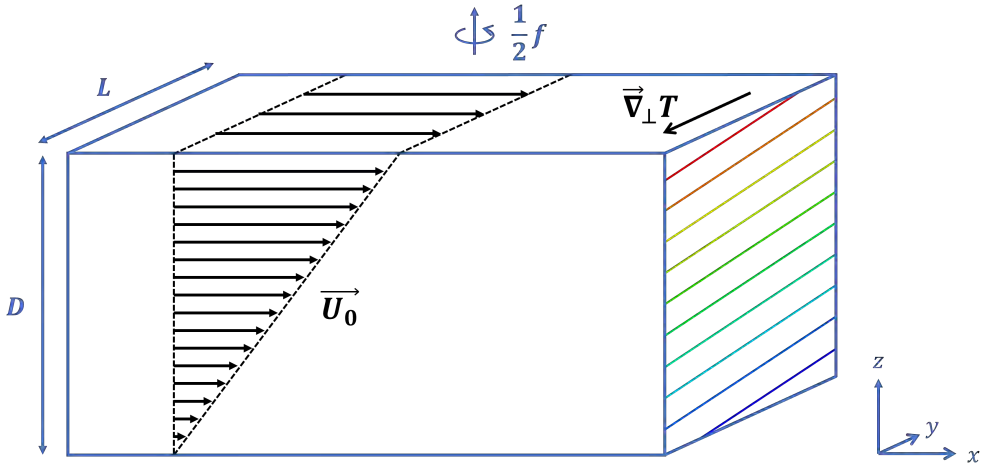


Figure 2: Idealized setup used in Eady's model of baroclinic instability. A constant vertical shear $\partial_z U > 0$ is balanced by a negative horizontal buoyancy gradient $\partial_y B < 0$ in accordance to the thermal wind relation. Top and cross-stream boundaries are stress-free walls and the domain is infinite in the $x$-direction. The colored lines on the right-section show the tilted surfaces of constant buoyancy.

In his seminal 1949 paper [3], Eady introduced an idealized atmospheric model that demonstrated the development of baroclinic instability. He considered a zonal flow $\vec{U} = U(z)\vec{e}_x$ with constant vertical shear $U_z$, geostrophically balanced by a horizontal buoyancy gradient $B_y = -f_0 U_z$ in the $y$-direction. This configuration results in tilted isopycnals (surfaces of constant buoyancy), with a slope of $f_0 U_z N^{-2}$ in the $y$-direction (see Figure 2). The flow is bounded by stress-free, rigid walls both above and below, as well as on the sides, but is infinite in the $x$-direction. The vertical buoyancy gradient, represented by the Brunt-Väisälä frequency $N$, and the planetary vorticity $f_0$ are assumed to be constant, with no consideration of the $\beta$-effect. In geostrophic equilibrium, the divergent-free horizontal velocities and buoyancy field are related through a stream function $\Psi$ as

$$(U, V, B) = (-\Psi_y, \Psi_x, zN^2 + f_0\Psi_z) \tag{1}$$

where the buoyancy $B$ is divided into background stratification $zN^2$ and perturbation $f_0\Psi_z$ induced by the flow due to the thermal wind balance.

Under the anelastic approximation [6], the potential vorticity conservation equation reads

$$(\partial_t + \partial_x\Psi\partial_y - \partial_y\Psi\partial_x)\left(\Psi_{xx} + \Psi_{yy} + \frac{f_0^2}{\tilde{\rho}}\partial_z\left(\frac{\tilde{\rho}}{N^2}\Psi_z\right)\right) = 0 \qquad \text{for} \quad \begin{cases} 0 < z < D \\ 0 < y < L \end{cases}, \tag{2}$$

with $\tilde{\rho}(z)$ the background density at rest. Assuming that the height $D$ of the channel is small in comparison to the vertical length scale of density variations ($N^2 D/g \ll 1$), we recover the

Boussinesq approximation and the potential vorticity equation can be written as

$$(\partial_t + \partial_x\Psi\partial_y - \partial_y\Psi\partial_x)\left(\Psi_{xx} + \Psi_{yy} + \partial_z\left(\frac{f_0^2}{N^2}\Psi_z\right)\right) = 0 \qquad \text{for} \quad \begin{cases} 0 < z < D \\ 0 < y < L \end{cases}. \tag{3}$$

This approximation is well justified for the Ocean, much less for the atmosphere. Nonetheless, we will present the results of Eady's model in this specific case, and will relax this assumption later for Charney's model.

In the absence of friction, the walls impose an impermeability condition on the normal velocity. For the side boundaries, we assume that the stream function vanishes. For the top and bottom boundaries, we apply the buoyancy equation and set the vertical velocity to zero. These two conditions are expressed as follows:

$$\Psi = 0 \qquad \text{at} \quad y = 0,\, L\,, \tag{4}$$

$$(\partial_t + \partial_x\Psi\partial_y - \partial_y\Psi\partial_x)\, f_0\Psi_z = -w|_z N^2 = 0 \qquad \text{at} \quad z = 0,\, D\,. \tag{5}$$

The equations can be non-dimensionalized using

$$(x, y) = L(\tilde{x}, \tilde{y}), \quad t = \frac{L}{DU_z}\tilde{t}, \quad z = D\tilde{z}, \quad \Psi = DLU_z\tilde{\Psi}\,. \tag{6}$$

Dropping the tildes for brevity, equations (3-5) become

$$(\partial_t + \partial_x\Psi\partial_y - \partial_y\Psi\partial_x)\left(\Psi_{xx} + \Psi_{yy} + S^{-1}\Psi_{zz}\right) = 0 \qquad \text{for} \quad \begin{cases} 0 < z < 1 \\ 0 < y < 1 \end{cases} \tag{7}$$

$$\Psi = 0 \qquad \text{at} \quad y = 0,\, 1 \tag{8}$$

$$(\partial_t + \partial_x\Psi\partial_y - \partial_y\Psi\partial_x)\,\Psi_z = 0 \qquad \text{at} \quad z = 0,\, 1, \tag{9}$$

with $S = (N^2D^2)/(f_0^2L^2)$ being the squared ratio of the Rossby deformation radius by the horizontal scale. For the base flow described above, the nondimensional streamfunction can be computed as $\Psi_0(y, z) = -zy$ with uniformly zero potential vorticity, and the velocity reads $U_0(z) = z$.

We are interested in the linear stability of the base flow. Let us consider a perturbation with stream function $\psi$ such that the total stream function is $\Psi(x, y, z, t) = \Psi_0(y, z) + \psi(x, y, z, t)$. Linearizing equations (7-9) for a small perturbation $\psi$ gives

$$(\partial_t + U_0(z)\partial_x)\left(\psi_{xx} + \psi_{yy} + S^{-1}\psi_{zz}\right) = 0 \qquad \text{for} \quad \begin{cases} 0 < z < 1 \\ 0 < y < 1 \end{cases}, \tag{10}$$

with boundary conditions

$$(\partial_t + U_0(z)\partial_x)\,\psi_z - (\partial_z U_0)\psi_x = 0 \qquad \text{at} \quad z = 0,\, 1\,, \tag{11}$$

$$\psi = 0 \qquad \text{at} \quad y = 0,\, 1\,. \tag{12}$$

Equations (10-12) being independent of $x$ and $t$, and since $\psi$ is vanishing at the boundaries $y = 0$ and $y = 1$, we consider the normal mode

$$\psi(x, y, z, t) = Re\left[A(z)e^{ik(x-ct)}\sin(\ell_n y)\right], \tag{13}$$

with $\ell_n = n\pi$ for any positive integer $n$. Note that we do not consider the case $k = 0$ here, for which we can show that the growth rate is zero. Injecting this ansatz into the equations results in the following system

$$\begin{cases} (z-c)\left(A''(z) - S(\ell_n^2 + k^2)A(z)\right) = 0 & \text{for} \quad 0 < z < 1, \\ -cA'(z) - A(z) = 0 & \text{at} \quad z = 0, \\ (1-c)A'(z) - A(z) = 0 & \text{at} \quad z = 1. \end{cases} \tag{14}$$

Introducing the scaled wavenumber $\mu = (S(k^2 + \ell_n^2))^{1/2} > 0$, the continuously differentiable solutions $A(z)$ can be expressed as $A(z) = a\sinh(\mu z) + b\cosh(\mu z)$, with constants $a, b$ chosen to ensure the boundary conditions (14.b/c). Solving for $a$ and $b$ leads to the system

$$\begin{cases} a\mu c + b = 0, \\ a\left[\mu(1-c)\cosh\mu - \sinh\mu\right] + b\left[\mu(1-c)\sinh\mu - \cosh\mu\right] = 0. \end{cases} \tag{15}$$

A nonzero amplitude solution exists provided that the discriminant of the system vanishes, leading to a simple quadratic equation for $c$

$$c^2 - c + \left(\frac{\coth\mu}{\mu} - \frac{1}{\mu^2}\right) = 0\,. \tag{16}$$

The dispersion relation is finally given by the quadratic formula as

$$c = \frac{1}{2} \pm \frac{1}{\mu}\sqrt{\left(\frac{\mu}{2} - \tanh\frac{\mu}{2}\right)\left(\frac{\mu}{2} - \coth\frac{\mu}{2}\right)}\,, \tag{17}$$

where we used the hyperbolic identity $\coth\mu = (\tanh(\mu/2) + \coth(\mu/2))/2$ to factorize the radicand. As $\mu > 0$, we have $\mu/2 > \tanh(\mu/2)$ and the condition for the radicand to be nonnegative is to have $\mu/2 \geq \coth(\mu/2)$, which is true only if $\mu \geq \mu^{(c)} \approx 2.3994$.

Thus, small-wavelength perturbations with $\mu \geq \mu^{(c)}$ generate traveling waves, while perturbations with large enough wavelengths are unstable. Those results are summarized in Figure 3, showing the complex phase speed $c$ of the perturbation (equation 17) as a function of the scaled wavenumber $\mu$.

Eady's model is regarded as one of the simplest models for baroclinic instability, but one has to realize that very little was known about the quasi-geostrophic theory at the time. Indeed, Eady had to derive the QG theory from scratch in his PhD work and 1949 paper. Together with Charney, Eady was able to show that the atmosphere did not need fronts to generate weather waves through the baroclinic instability, by isolating the minimal ingredients for the latter to occur, namely a vertical shear balanced by a horizontal buoyancy gradient. Instead, it was shown later in [4] that weather front formation could be explained within QG theory, feeding from the weather waves generated by the baroclinic instability.

### 1.2.2 With sloping bottom

Following [7], let us now examine the impact of topography on the instability by introducing a sloping bottom $h_B(y) = sy$ in the $y$-direction. We assume a constant negative slope $s < 0$ towards positive $y$, which is shallow enough for the boundary conditions to still be applied at $z = 0$, rather than at $z = h_B(y)$. While the upper boundary condition remains unchanged, the lower

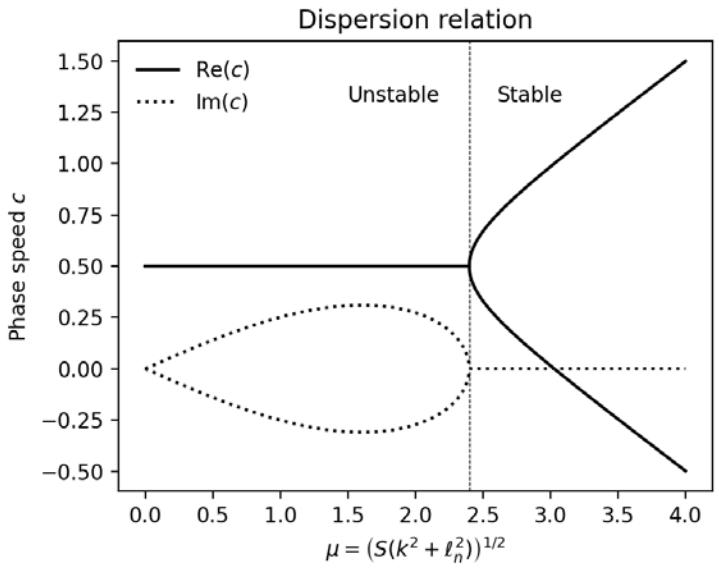


Figure 3: Complex phase-speed of the disturbance as a function of the scaled wavenumber $\mu = \sqrt{S(k^2+\ell_n^2)}$, in Eady's model with a flat bottom. There exists a critical scale wavenumber $\mu^{(c)} \approx 2.3994$ above which the disturbance are traveling waves, but below which an instability occurs.

boundary condition is modified, as the vertical velocity no longer vanishes at the bottom. Instead, (dimensional) vertical velocity at the bottom can be expressed as

$$w(z=0) = v(z=0)h_B'(y) = \partial_x \Psi(z=0)h_B'(y)\,, \tag{18}$$

such that the (dimensional) buoyancy equation evaluated at the bottom boundary becomes

$$(\partial_t + \partial_x\Psi\partial_y - \partial_y\Psi\partial_x)\, f_0\Psi_z = -wN^2 = -N^2 h_B'(y)\Psi_x \qquad \text{at} \quad z=0\,. \tag{19}$$

Using the same non-dimensionalization as in the case with no slope, the dimensionless linearized equations around the base flow $\Psi_0(y,z) = -yz$ become

$$(\partial_t + U_0(z)\partial_x)\left(\psi_{xx} + \psi_{yy} + S^{-1}\psi_{zz}\right) = 0 \qquad \text{for} \begin{cases} 0<z<1 \\ 0<y<1 \end{cases}, \tag{20}$$

$$(\partial_t + U_0(z)\partial_x)\,\psi_z - (\partial_z U_0)\psi_x = 0 \qquad \text{at} \quad z=1\,, \tag{21}$$

$$(\partial_t + U_0(z)\partial_x)\,\psi_z - (\partial_z U_0 + \alpha_T)\psi_x = 0 \qquad \text{at} \quad z=0\,, \tag{22}$$

$$\psi = 0 \qquad \text{at} \quad y=0,\,1\,, \tag{23}$$

with $U_0(z) = z$. The new dimensionless parameter measuring the topographic slope in the equations is

$$\alpha_T = -\frac{sN^2}{f_0 U_z} \tag{24}$$

which can be interpreted as the ratio of the topographic slope to the isopycnals slope. We introduced a minus sign for convenience, so $\alpha_T > 0$ if the two are sloping in the opposite direction. Substituting the normal mode given by equation (13) gives

$$\begin{cases} (z-c)\left(A''(z) - S(\ell_n^2 + k^2)A(z)\right) = 0 & \text{for} \quad 0<z<1, \\ -cA'(z) - (1+\alpha_T)A(z) = 0 & \text{at} \quad z=0, \\ (1-c)A'(z) - A(z) = 0 & \text{at} \quad z=1. \end{cases} \tag{25}$$

Following the exact same steps as in the case of a flat bottom, we can obtain the dispersion relation for the phase speed as

$$c = \frac{1}{2}\left(1 + \alpha_T \frac{\coth\mu}{\mu}\right) \pm \sqrt{\frac{1}{4}\left(1 + \alpha_T \frac{\coth\mu}{\mu}\right)^2 - (1+\alpha_T)\left(\frac{\coth\mu}{\mu} - \frac{1}{\mu^2}\right)}, \tag{26}$$

with the scaled wavenumber defined as $\mu^2 = S(k^2 + \ell_n^2)$ as before. The perturbation is a traveling wave if the radicand is positive, but grows exponentially if the radicand is negative. Solving for the critical values of $\alpha_T$ is straightforward but cumbersome, and gives

$$\alpha_{T,\pm}^{(c)} = \mu\tanh\mu - 2\tanh^2\mu \pm 2\sqrt{(\mu - \tanh\mu)\left(1 - \tanh^2\mu\right)\tanh\mu}\,. \tag{27}$$

For a given value of scaled wavenumber $\mu$, the perturbation is unstable provided that $\alpha_T$ lies between the two critical values $\alpha_{T,\pm}^{(c)}$, and stable otherwise. The stability diagram is given in Figure 4. It shows that large-wavelength perturbations ($\mu < \mu^{(c)}$) that were previously unstable can be stabilized by the topography if the bottom slope is strong enough. On the other hand, small-wavelength perturbations ($\mu > \mu^{(c)}$), which were stable for a flat bottom, can in certain cases become unstable in the presence of topography, when the bottom is sloping in the opposite direction of the isopycnals ($\alpha_T > 0$). However, this instability region becomes exponentially narrower as the scaled wavenumber $\mu$ grows.

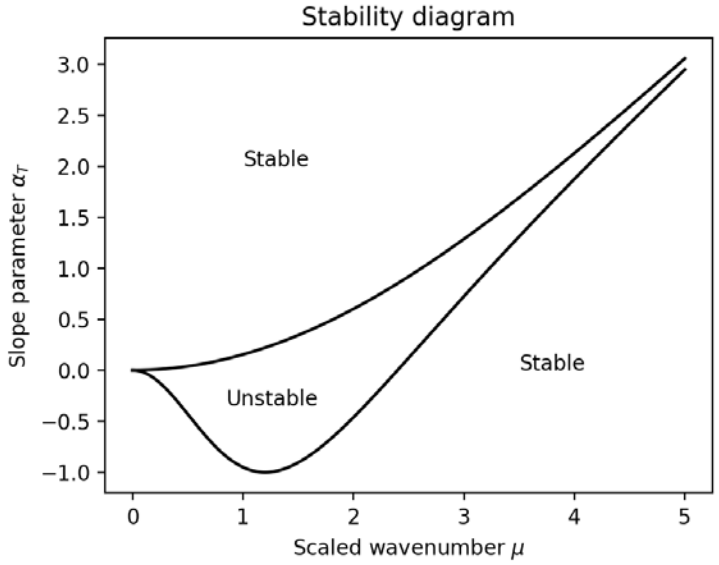


Figure 4: Stability diagram for Eady's model in the case of a sloping bottom. The scaled wavenumber $\mu$ is defined by $\mu^2 = S(k^2 + \ell_n^2)$ and the slope of the boundary is measured by $\alpha_T$ defined in equation (24). Previously unstable long wavelength perturbations can be stabilized by topography, and previously stable short wavelength disturbances can become unstable. Figure from [7].

In both cases — whether or not topography is included — the instability arises from the interaction between two waves located at the upper and lower boundaries. This raises the question of whether the upper boundary is truly relevant for modeling atmospheric dynamics. Moreover, we have neglected both the $\beta$-effect and non-Boussinesq behavior. While these simplifications may be justifiable in a rudimentary ocean model, they omit key features necessary for representing the atmosphere. This gap is addressed by Charney's model, which is introduced in the following section.

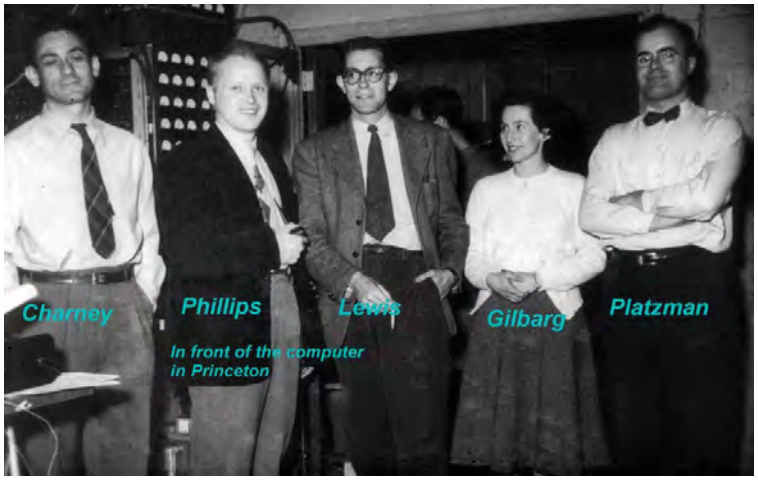


Figure 5: Jule Charney with some of the other members at the Institute for Advanced Studies (IAS) in Princeton.

# 2 Charney

*This lecture summarizes Chapter 7.8 of [6].*

## 2.1 History

Jule Charney (1917-1981) in an American meteorologist, considered as one of the fathers of modern meteorology after World War II. He participated in the development of numerical weather prediction models, and proposed a variety of mathematical models for the circulation of the atmosphere.

Charney was originally interested in aeronautics before starting his PhD, but was advised in particular by von Kármán to consider pursuing a career in meteorology, where a good contribution could be made. He enrolled under the official supervision of Holmboe and was advised by Rossby among others. After his PhD, he pursued a postdoc in Oslo, during which he developed the quasi-geostrophic approximation for atmosphere modeling. In his 1947 paper [2], he was able to suggest a model for the generation of large-scale weather waves in a set-up similar to Eady's model, but without upper boundary and incorporating planetary vorticity gradient.

## 2.2 Charney's model

Charney's assumptions include:

- Constant vertical wind shear $\frac{\partial U_*}{\partial z_*}$,
- Inviscid flow,
- Constant stratification parameter $S = \frac{N^2 D^2}{f_0^2 L^2}$,
- Constant density scale height $H = \left(-\frac{1}{\rho_s}\frac{\partial \rho_s}{\partial z}\right)^{-1}$,
- $\beta \neq 0$.

Note that in the units selected in equation (6), the unit time is $L/D\partial U_*/\partial z_*$, so the dimensionless $\beta$ is $\beta = \beta_* L^2/D\partial U_*/\partial z_*$. The smaller the background shear the larger $\beta$ is.

The overall setup is similar to Eady's model, as illustrated in Figure 2, but with two key differences. First, Charney's model includes the $\beta$-effect. Second, the upper boundary is placed at $z_T \to +\infty$ rather than a finite height.

Charney essentially derived the quasi-geostrophic potential vorticity equation (QGPVE) from first principles. Here, we leverage existing QG theory and present the nondimensionalized QGPV perturbation equation, as given in [6]:

$$\left(\frac{\partial}{\partial t} + U_0\frac{\partial}{\partial x}\right) q + \frac{\partial \phi}{\partial x}\frac{\partial \Pi_0}{\partial y} = 0, \tag{28}$$

where $U_0$ is the basic state zonal flow, with corresponding stream function $\Psi$ such that:

$$U_0 = z = -\frac{\partial \Psi}{\partial y}, \tag{29}$$

$q$ is the perturbation PV,

$$q = \frac{\partial^2 \phi}{\partial x^2} + \frac{\partial^2 \phi}{\partial y^2} + \frac{1}{\rho_s S}\frac{\partial}{\partial z}\left(\rho_s \frac{\partial \phi}{\partial z}\right), \tag{30}$$

where $\phi$ is the stream function perturbation, and $\Pi_0$ is the basic state PV, defined as

$$\Pi_0 = \beta y + \frac{\partial^2 \Psi}{\partial y^2} + \frac{1}{\rho_s S}\frac{\partial}{\partial z}\left(\rho_s \frac{\partial \Psi}{\partial z}\right) = \beta y + \frac{1}{\rho_s S}\frac{\partial}{\partial z}\left(\rho_s \frac{\partial \Psi}{\partial z}\right). \tag{31}$$

Substituting equation (29) into equation (31), we have the PV gradient of the basic state, given by:

$$\frac{\partial \Pi_0}{\partial y} = \beta - \frac{1}{\rho_s S}\frac{\partial}{\partial z}\left(\rho_s \frac{\partial U_0}{\partial z}\right) = \beta - \frac{1}{S\rho_s}\frac{\partial \rho_s}{\partial z} = \beta + \frac{1}{HS}. \tag{32}$$

Thus, the full perturbation QGPV equation (28) becomes:

$$\left(\frac{\partial}{\partial t} + U_0\frac{\partial}{\partial x}\right)\left[\frac{\partial^2 \phi}{\partial x^2} + \frac{\partial^2 \phi}{\partial y^2} + \frac{1}{\rho_s S}\frac{\partial}{\partial z}\left(\rho_s \frac{\partial \phi}{\partial z}\right)\right] + \frac{\partial \phi}{\partial x}\left(\beta + \frac{1}{HS}\right) = 0. \tag{33}$$

The boundary conditions in $y$ are:

$$\frac{\partial \phi}{\partial x} = 0, \quad y = \pm 1.$$

Because the coefficients are independent of $x$ and $t$, the solution can be written in terms of normal modes:

$$\phi = Re[\Phi(y,z)e^{ik(x-ct)}] = Re[\Phi(y,z)e^{ik(x-c_r t)}e^{kc_i t}]. \tag{34}$$

Then equation (33) becomes

$$(U_0 - c)\left[\frac{1}{\rho_s S}\frac{\partial}{\partial z}\left(\rho_s \frac{\partial \Phi}{\partial z}\right) + \frac{\partial^2 \Phi}{\partial y^2} - k^2\Phi\right] + \left(\beta + \frac{1}{HS}\right)\Phi = 0, \tag{35}$$

with boundary conditions in $y$:

$$\Phi = 0, \text{ at } y = \pm 1. \tag{36}$$

The boundary conditions in $z$ are discussed below.

To satisfy the $y-$ boundary conditions, we assume the solutions of the form

$$\Phi = A(z)\sin(\ell_n y),\ \ell_n = n\pi,\ n = 0, 1, 2, \ldots. \tag{37}$$

Then equation (35) reduces to:

$$(z-c)\left(\frac{d^2A}{dz^2} - \frac{1}{H}\frac{dA}{dz} - \mu^2 A\right) + \left(\beta S + \frac{1}{H}\right)A = 0, \tag{38}$$

where as before:

$$\mu^2 = \left(k^2 + \ell_n^2\right)S = \frac{\left(k^2+\ell_n^2\right)}{L^2}L_d^2. \tag{39}$$

Here, $\mu$ is the total horizontal wavenumber measured in units of the Rossby deformation radius $L_d = N_s D/f_0$.

The lower boundary condition is (same as equation 14):

$$c\frac{dA}{dz} + A = 0,\ z = 0. \tag{40}$$

The upper boundary in Charney's model is at $z = +\infty$. In this case, there is no clear definition of fluid depth as in Eady's model, so the vertical scale of the unstable disturbances selects its own vertical scale. This is in contrast with Eady's model, where the vertical scale of the unstable disturbances is the full depth of the fluid layer.

To see why this may be the case, recall from the first lecture that a necessary condition for instability (re-written here in the notations of this lecture and specifically for the Charney model) is that the following holds

$$\int_{-1}^{1} dy \int_0^{z_T} dz \left[\frac{\rho_s|\Phi|^2}{|U_0-c|^2}\frac{\partial \Pi_0}{\partial y}\right] + \int_{-1}^{1} dy \left[\rho_s S^{-1}\frac{|\Phi|^2}{|U_0-c|^2}\right]_{z=z_T} - \int_{-1}^{1} dy \left[\rho_s S^{-1}\frac{|\Phi|^2}{|U_0-c|^2}\right]_{z=0} = 0. \tag{41}$$

In the Eady model, $\partial\Pi_0/\partial y = 0$, so this equation can only be satisfied if the eigenmode interacts with the background shear and stratification near both boundaries. However, when $\partial\Pi_0/\partial y = \beta + 1/HS > 0$, a balance can exist even if $|\Phi| \to 0$ as $z_T \to +\infty$. In that case, the mode can adjust its structure near the lower boundary to compensate the first integral in (41). More specifically, as the background shear becomes smaller, i.e., as $\beta$ increases, the eigenfunction concentrates near the lower boundary so even for weak shear the instability condition can be satisfied.

The vertical scale of perturbations can be estimated noting that:

$$S\frac{\partial \Pi_0}{\partial y} = \beta S + \frac{1}{H} = \frac{\beta_*}{\partial U_*/\partial z_*}\cdot\frac{N^2}{f_0^2}D + \frac{D}{H_*} \equiv D\left(\frac{1}{h_*} + \frac{1}{H_*}\right). \tag{42}$$

where we have identified the new lengthscale

$$h_* = \frac{\frac{f_0^2}{N_s^2}\frac{\partial U_*}{\partial z_*}}{\beta_*} \tag{43}$$

as the vertical length scale over which the advection of PV balances the stretching of planetary vorticity by the vertical velocity field. The dominant term in equation (42) corresponds to the smaller of two vertical scales. This means that the vertical scale of the perturbation is given by

$$D = \min\{h_*, H_*\}. \tag{44}$$

When $D = h_*$, the horizontal length scale is

$$L_d = \frac{N_s D}{f_0} = \frac{\frac{f_0}{N_s}\frac{\partial U_*}{\partial z_*}}{\beta}. \tag{45}$$

Dimensionally, the growth rate is

$$\sigma_* = k_* c_{i*} = O\left(\frac{U}{L_d}\right) = \frac{D}{L_d}\frac{\partial U_*}{\partial z_*}. \tag{46}$$

Equations (44) - (46) thus show that the $\beta$-effect alters the horizontal and vertical scales of the perturbations, but not directly their growth rate.

This dimensional argument can be verified through more formal calculations of the eigenmodes and their growth rates. Equation (38) can be reduced to a standard type by the following transformation:

$$A(z) = (z - c)e^{\nu z}F(z), \tag{47}$$

where

$$\nu = \frac{\delta}{2} - \left(\mu^2 + \frac{\delta^2}{4}\right)^{\frac{1}{2}}, \tag{48}$$

and

$$\delta = \frac{h_*}{H_*}. \tag{49}$$

Equation (38) becomes

$$\xi\frac{d^2F}{d\xi^2} + (2 - \xi)\frac{dF}{d\xi} - (1 - r)F = 0, \tag{50}$$

where $\xi$ is a new variable defined by

$$\xi = (z - c)(\delta^2 + 4\mu^2)^{1/2}, \tag{51}$$

and the parameter $r$ is given by

$$r = \frac{\delta + 1}{(\delta^2 + 4\mu^2)^{1/2}}. \tag{52}$$

Equation (50) is the confluent hypergeometric equation. Charney said that he felt great relief when he realized the equation he had to deal with was a standard mathematical equation. However, the solutions are not tabulated, and it was an immense challenge to use them to discuss the instability of the sheared zonal flow. Charney had no computer to help evaluate the final dispersion relation. He had only a hand-operated mechanical calculator. Colleagues remembered him working late at night and his wife, Eleanor, bringing him supper so he could work without taking a break. The results of his labors produced a curve of zero growth rate in the shear vs. wave length (or zonal wavenumber) parameter space. The curve is shown here in Figure 6.

Using a standard perturbation method, Charney was able to show that slightly above the curve $c$ became complex with a positive imaginary part, i.e., unstable. It was natural to assume that the flow was stable for weaker shears below the curve. This was a widely accepted result.

Charney went on to further work of importance. For years he headed the pioneering project at the Institute for Advance Studies (Princeton) to begin work on using numerical models and computers to forecast the weather i.e., the development of instabilities to finite amplitude as could

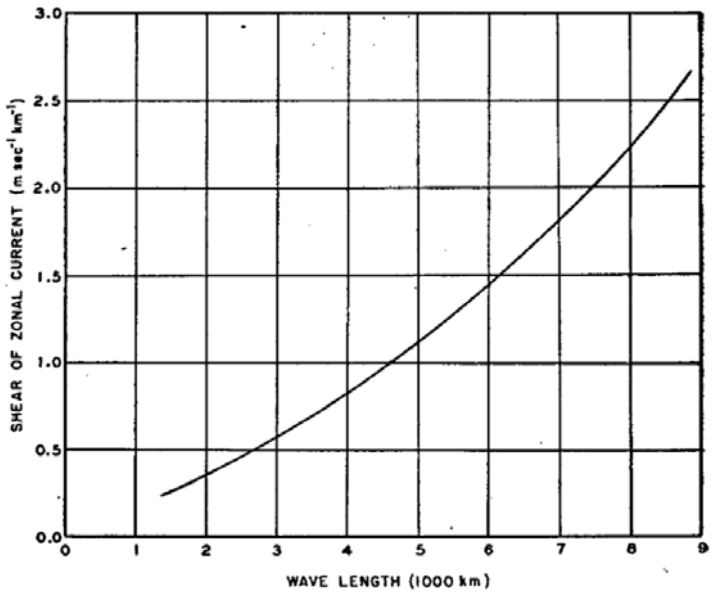


Figure 6: Charney's stability curve for $r = 1$, from [2].

be foreseen by his stability work. He was also the first to provide an inertial model of the western boundary current with no dependence on artificial viscosity coefficients.

Fifteen years later Alewyn Burger submitted a paper to *Tellus*, a Swedish journal founded by Rossby, that claimed that Charney was in error and that his model was unstable for all shears except at a countable (but infinite) number of curves in the $(k, \frac{\partial U_*}{\partial z_*})$ plane ! Those curves correspond to the parameter $r =$ an integer in the confluent hypergeometric equation. Charney's curve corresponds to $r = 1$.

Later calculations by Kuo [5] help clarify the problem by studying the normal mode problem in the limit $\delta \to 0$. In that paper, Kuo showed the frequency and the growth rate as a function of $r$ (Figure 7). It turns out the Charney mode is the mode with the largest growth rate. The higher modes correspond to lower growth rates, and the transition from one unstable domain to another occurs at integer values of $r$.

### 2.3 The scientific legacy of Charney

How did Charney react to Burger's critique? With remarkable grace. Despite Tellus initially rejecting Burger's paper, the U.S. meteorology community invited him to present his results at MIT and WHOI. Charney publicly praised Burger's work and hosted him for dinner at his home, with a young Pedlosky in attendance. Burger's paper was soon published [1].

Charney's impact extended beyond this model. He taught GFD (Figure 8) and, perhaps as importantly, what it really meant to be an honest scientist.

His later contributions were also fundamental. For example, he pioneered numerical weather prediction and developed the first inertial Gulf Stream model. He also derived the QGPVE from the primitive equations and applied it to forecast models (Figure 9).

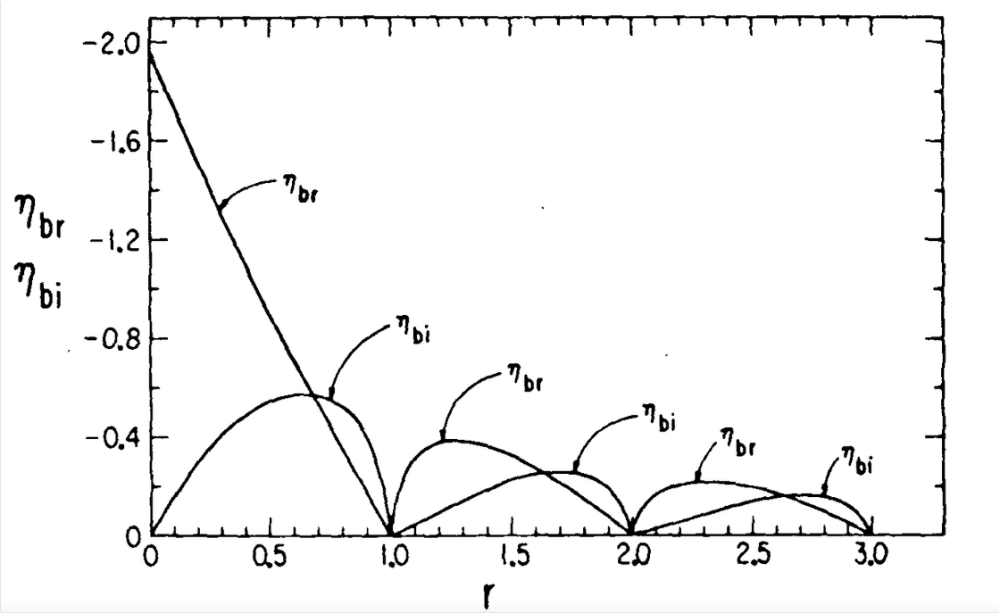


Figure 7: The real and imaginary parts of $c$ as calculated by Kuo for the case $\delta \to 0$. In this figure, the frequency of the wave $c_r$ is proportional to $-\eta_{br}$, and the growth rate $c_i$ is proportional to $-\eta_{bi}$. From [5].

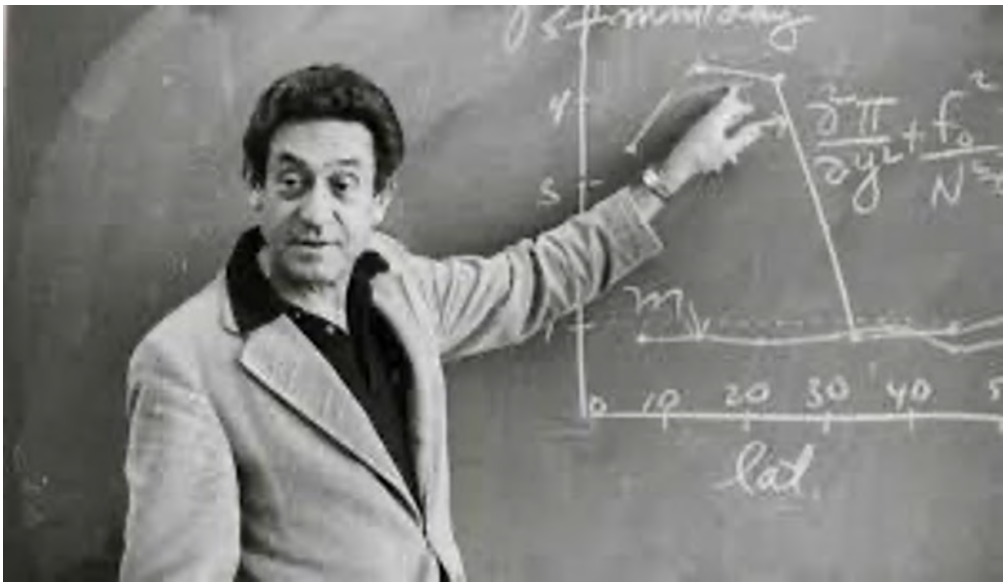

Figure 8: Charney teaching a class.

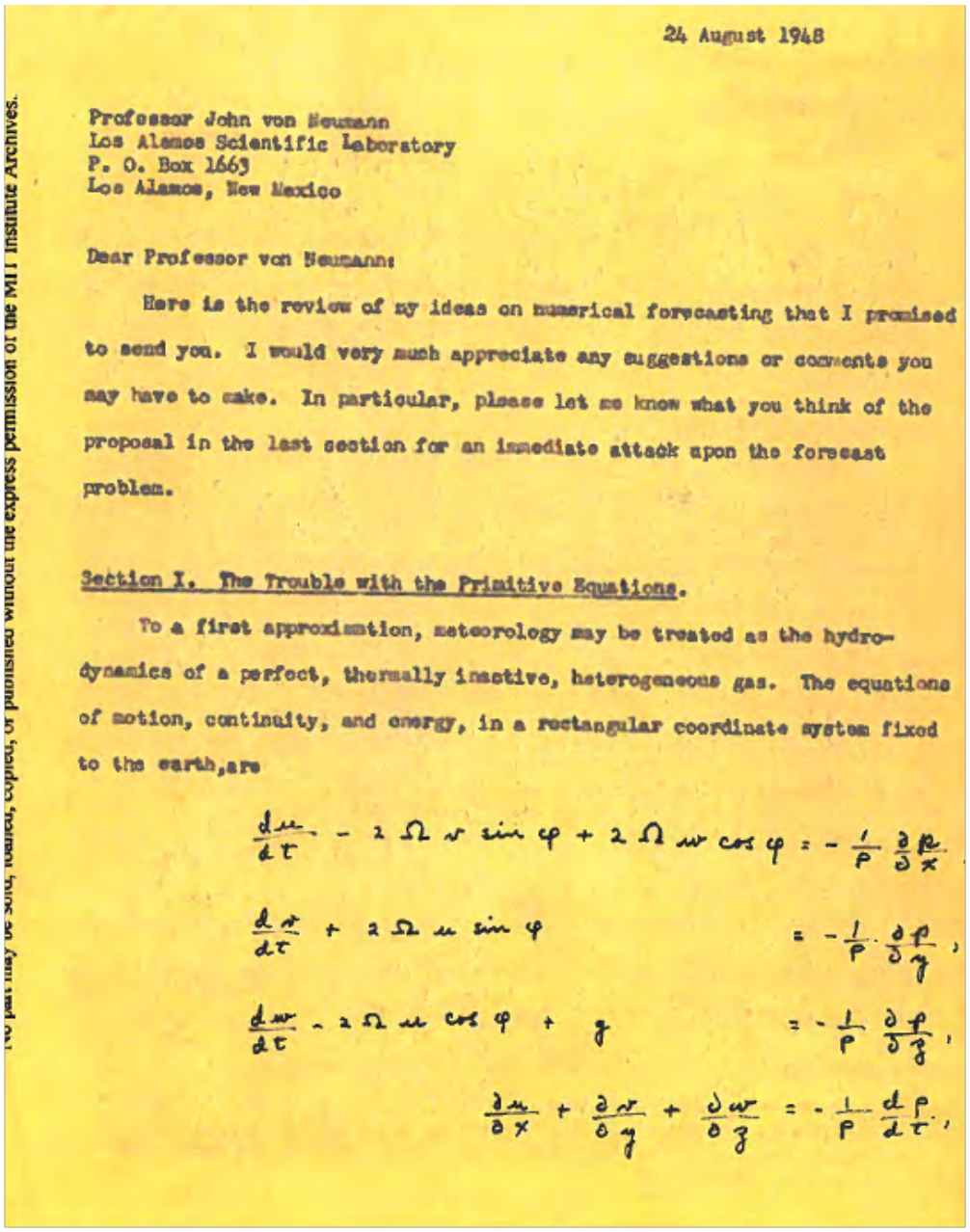

24 August 1948

Professor John von Neumann
Los Alamos Scientific Laboratory
P. O. Box 1663
Los Alamos, New Mexico

Dear Professor von Neumann:

Here is the review of my ideas on numerical forecasting that I promised to send you. I would very much appreciate any suggestions or comments you may have to make. In particular, please let me know what you think of the proposal in the last section for an immediate attack upon the forecast problem.

Section I. The Trouble with the Primitive Equations.

To a first approximation, meteorology may be treated as the hydrodynamics of a perfect, thermally inactive, heterogeneous gas. The equations of motion, continuity, and energy, in a rectangular coordinate system fixed to the earth, are

$$\frac{du}{dt} - 2\Omega v \sin\varphi + 2\Omega w \cos\varphi = -\frac{1}{\rho}\frac{\partial p}{\partial x},$$

$$\frac{dv}{dt} + 2\Omega u \sin\varphi = -\frac{1}{\rho}\cdot\frac{\partial p}{\partial y},$$

$$\frac{dw}{dt} - 2\Omega u \cos\varphi + g = -\frac{1}{\rho}\frac{\partial p}{\partial z},$$

$$\frac{\partial u}{\partial x} + \frac{\partial v}{\partial y} + \frac{\partial w}{\partial z} = -\frac{1}{\rho}\frac{d\rho}{dt},$$



Figure 9: A letter from Charney. He derived and applied the QGPVE to weather prediction.

## References


[1] A. P. Burger, *On the non-existence of critical wavelengths in a continuous baroclinic instability problem*, Journal of Atmospheric Sciences, 19 (1962), pp. 31 – 38.

[2] J. G. Charney, *The dynamics of long waves in a baroclinic westernly current*, Journal of Atmospheric Sciences, 4 (1947), pp. 136 – 162.

[3] E. T. Eady, *Long waves and cyclone waves*, Tellus, 1 (1949), pp. 33–52.

[4] B. J. Hoskins and F. P. Bretherton, *Atmospheric frontogenesis models: Mathematical formulation and solution*, Journal of Atmospheric Sciences, 29 (1972), pp. 11 – 37.

[5] H. Kuo, *Dynamics of quasigeostrophic flows and instability theory*, vol. 13 of Advances in Applied Mechanics, Elsevier, 1973, pp. 247–330.

[6] J. Pedlosky, *Geophysical Fluid Dynamics*, Springer New-York, NY, 2013.

[7] ——, *Baroclinic instability over topography: Unstable at any wave number.*, Journal of Marine Research, 74 (2016), p. 1–19.

# GFD 2025 Lecture 6: Dynamical Systems and Bifurcations

Laurette Tuckerman; notes by David Darrow and Heng Quan

June 23, 2025

## 1 Introduction

A dynamical system can be defined as:

$$\dot{x} = f(x), x, f \text{ vectors in } \mathcal{R}^N \tag{1}$$

Some systems with other forms can be rewritten as dynamical systems. For example:

$$\dot{x} = f(x,t) \Longrightarrow \frac{d}{dt}\begin{pmatrix} x \\ \theta \end{pmatrix} = \begin{pmatrix} f(x,\theta) \\ 1 \end{pmatrix} \text{ with } \theta \equiv t \tag{2}$$

$$\ddot{x} = f(x,\dot{x}) \Longrightarrow \frac{d}{dt}\begin{pmatrix} x \\ y \end{pmatrix} = \begin{pmatrix} y \\ f(x,y) \end{pmatrix} \text{ with } y \equiv \dot{x} \tag{3}$$

## 2 Analysis of One-dimensional Systems

### 2.1 Fixed points and linear stability

A fixed point $\overline{x}$ of the dynamical system $\dot{x} = f(x)$ is a solution to

$$0 = f(\overline{x}). \tag{4}$$

The linear stability of the fixed point $\overline{x}$ can be studied by:

$$\begin{aligned} x(t) &= \bar{x} + \epsilon(t) \\ \frac{d}{dt}(\bar{x} + \epsilon) &= f(\bar{x} + \epsilon) \\ \dot{\epsilon} &= f(\bar{x}) + f'(\bar{x})\epsilon + \frac{1}{2}f''(\bar{x})\epsilon^2 + \cdots \\ &\approx f'(\bar{x})\epsilon \\ \epsilon(t) &= e^{tf'(\bar{x})}\epsilon(0) \end{aligned} \tag{5}$$

If $f'(\bar{x}) > 0$, a perturbation $\epsilon$ will grow exponentially in time so the fixed point $\overline{x}$ is unstable. If $f'(\bar{x}) < 0$, the fixed point $\overline{x}$ is stable.

We assume that $f$ depends on a parameter $\mu$. A steady bifurcation is defined as a change in the number of fixed points (roots of $f$).

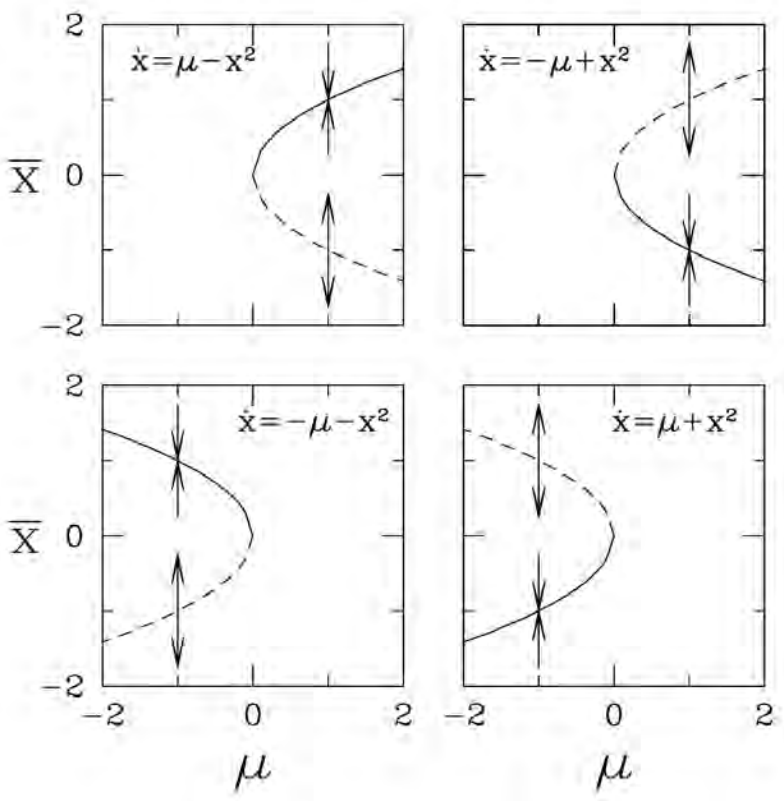


Figure 1: Saddle-node bifurcation diagrams. In each case, there exist two branches of fixed points, one stable and one unstable, on one side of $\mu = 0$, and no fixed points on the other side.

### 2.2 Saddle-node bifurcations

Consider the example

$$f(x, \mu) = \mu - x^2. \tag{6}$$

This is called the normal form of the saddle-node bifurcation. Its fixed points are

$$\overline{x} = \pm\sqrt{\mu} \tag{7}$$

which exist only for $\mu > 0$. Their stability is determined by

$$f'(\bar{x}_\pm) = -2\bar{x}_\pm = -2(\pm\sqrt{\mu}) = \mp 2\sqrt{\mu}. \tag{8}$$

We can see that $\overline{x}_+ = +\sqrt{\mu}$ is stable, whereas $\overline{x}_- = -\sqrt{\mu}$ is unstable.

In addition to (6), there exist three other possible cases:

$$\begin{aligned} f(x, \mu) &= -\mu + x^2 \\ f(x, \mu) &= \mu - x^2 \\ f(x, \mu) &= -\mu - x^2 \end{aligned} \tag{9}$$

We summarize their stability in the bifurcation diagram shown in Fig.1

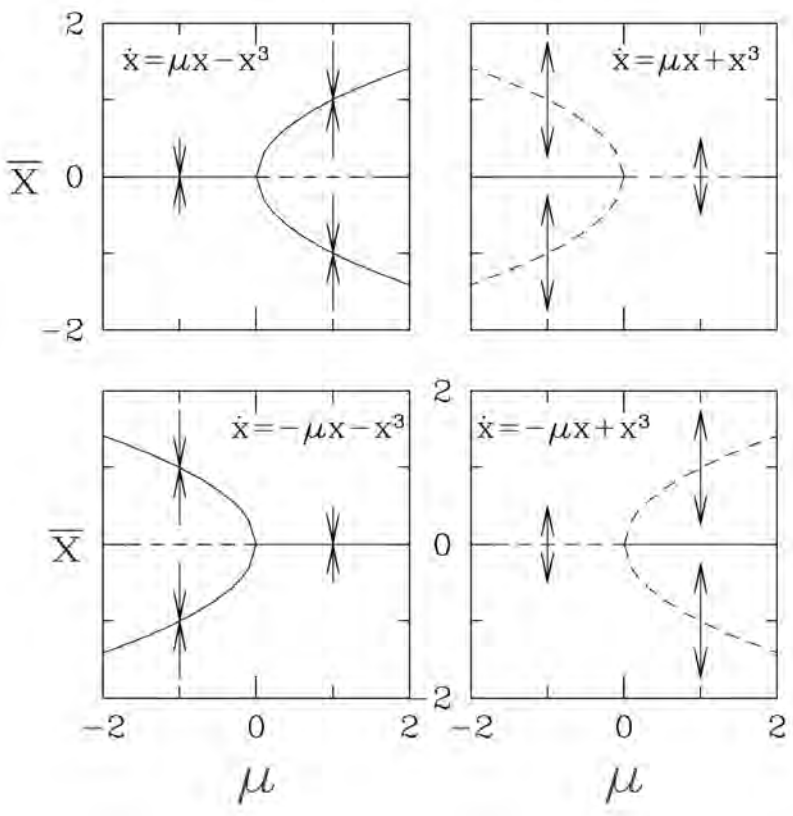


Figure 2: Pitchfork bifurcation diagrams. A branch of fixed points gives rise to two new branches when a critical value of $\mu$ is crossed. The bifurcation is called a supercritical (subcritical) pitchfork if the new branches are stable (unstable). More generally, the bifurcation is supercritical (subcritical) if the two new branches are more stable (less stable) than the branch between them.

### 2.3 Pitchfork bifurcations

The normal forms of the pitchfork bifurcation are:

$$\begin{aligned} f(x,\mu) &= \mu x - x^3 \\ f(x,\mu) &= \mu x + x^3 \\ f(x,\mu) &= -\mu x + x^3 \\ f(x,\mu) &= -\mu x - x^3 \end{aligned} \tag{10}$$

We plot the corresponding bifurcation diagrams in Fig.2. We consider the form $f(x,\mu) = \mu x - x^3$, whose fixed points are

$$0 = \bar{x}\left(\mu - \bar{x}^2\right) \Longrightarrow \begin{cases} \bar{x} = 0 & \text{for all } \mu \\ \bar{x} = \pm\sqrt{\mu} & \text{for } \mu > 0 \end{cases} \tag{11}$$

and whose stability is given by:

$$f'(\bar{x}) = \mu - 3\bar{x}^2 = \begin{cases} \mu & \text{for } \bar{x} = 0 \\ \mu - 3\mu = -2\mu & \text{for } \bar{x} = \pm\sqrt{\mu} \end{cases} \tag{12}$$

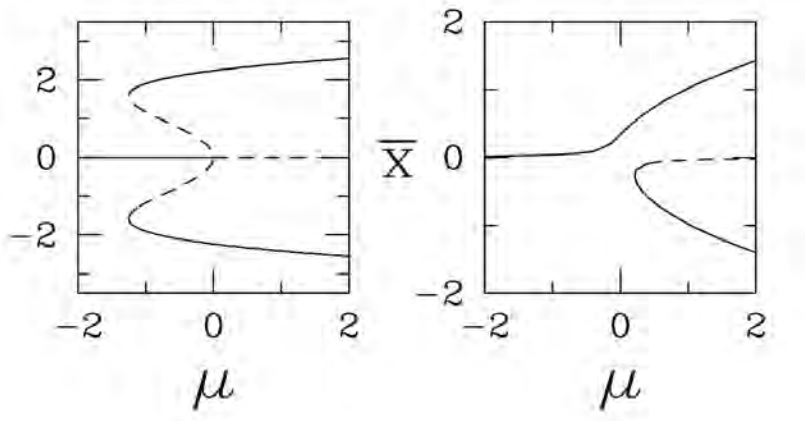


Figure 3: Left: bifurcation diagram for $\dot{x} = \mu x + x^3 - x^5/10$. The fifth-order term stabilizes the trajectories near a subcritical pitchfork bifurcation. This term causes two saddle-node bifurcations. As $\mu$ is increased, there is first one fixed point, then five, then finally three fixed points. Right: diagram for an imperfect pitchfork bifurcation $\dot{x} = 1/27 + \mu x - x^3$. The constant term represents an imperfection that causes the system to prefer one of the two branches. The pitchfork bifurcation has been transformed into a saddle-node bifurcation.

The fixed point $\overline{x} = 0$ is therefore stable for $\mu < 0$ and becomes unstable at $\mu = 0$, where the new branches of fixed points $\overline{x} = \pm\sqrt{\mu}$ are created. These new fixed points are stable. This is called a supercritical pitchfork bifurcation. By contrast, as summarized in Fig.2, the form $f(x, \mu) = \mu x + x^3$ is called a subcritical pitchfork bifurcation.

We can generate variations of the pitchfork bifurcation by adding stablizing higher-order terms or constants, resulting in imperfect pitchfork bifurcations as illustrated in Fig. 3.

### 2.4 Transcritical bifurcations

The normal form of a transcritical bifurcation is:

$$\dot{x} = \mu x - x^2 \tag{13}$$

The stability analysis yields

$$\begin{aligned} 0 = \bar{x}(\mu - \bar{x}) &\Longrightarrow \begin{cases} \bar{x} = 0 \\ \bar{x} = \mu \end{cases} \\ f'(\bar{x}) = \mu - 2\bar{x} &= \begin{cases} \mu \text{ for } \bar{x} = 0 \\ -\mu \text{ for } \bar{x} = \mu \end{cases} \end{aligned} \tag{14}$$

Thus $\overline{x} = 0$ is stable for $\mu < 0$, unstable for $\mu > 0$, whereas $\overline{x} = \mu$ does the opposite. If we add a stablizing higher-order term, the bifurcation diagram will change, as illustrated in Fig.4.

### 2.5 General Conditions

For any function as introduced in (1), the conditions for $(\overline{x}, \overline{\mu})$ to be a bifurcation point of the designated type is summarized in Fig. 5. For a cubic function generalizing a supercritical pitchfork bifurcation:

$$f(x) = \alpha + \mu x + \beta x^2 - x^3 \tag{15}$$

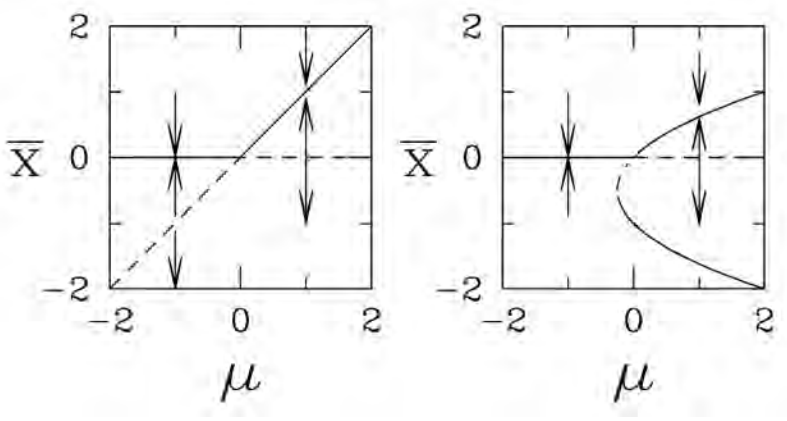


Figure 4: Bifurcation diagrams for a transcritical bifurcation (left) and for a transcritical bifurcation with an added cubic term, leading to an additional stabilizing saddle-node bifurcation (right).

| | $f$ | $f_x$ | $f_\mu$ | $f_{xx}$ | $f_{x\mu}$ | $f_{xxx}$ |
|---|---|---|---|---|---|---|
| steady state | 0 | | | | | |
| bifurcation | 0 | 0 | $\neq 0$ | | | |
| saddle-node | 0 | 0 | $\neq 0$ | $\neq 0$ | | |
| transcritical | 0 | 0 | 0 | $\neq 0$ | $\neq 0$ | |
| pitchfork | 0 | 0 | 0 | 0 | $\neq 0$ | $\neq 0$ |

Figure 5: Summary of conditions on $f(\mu, x)$ for 1D bifurcations.

The possible bifurcation diagrams are summarized in Fig. 6. Equation (15), along with figure 6, is called the *unfolding* of the pitchfork bifurcation.

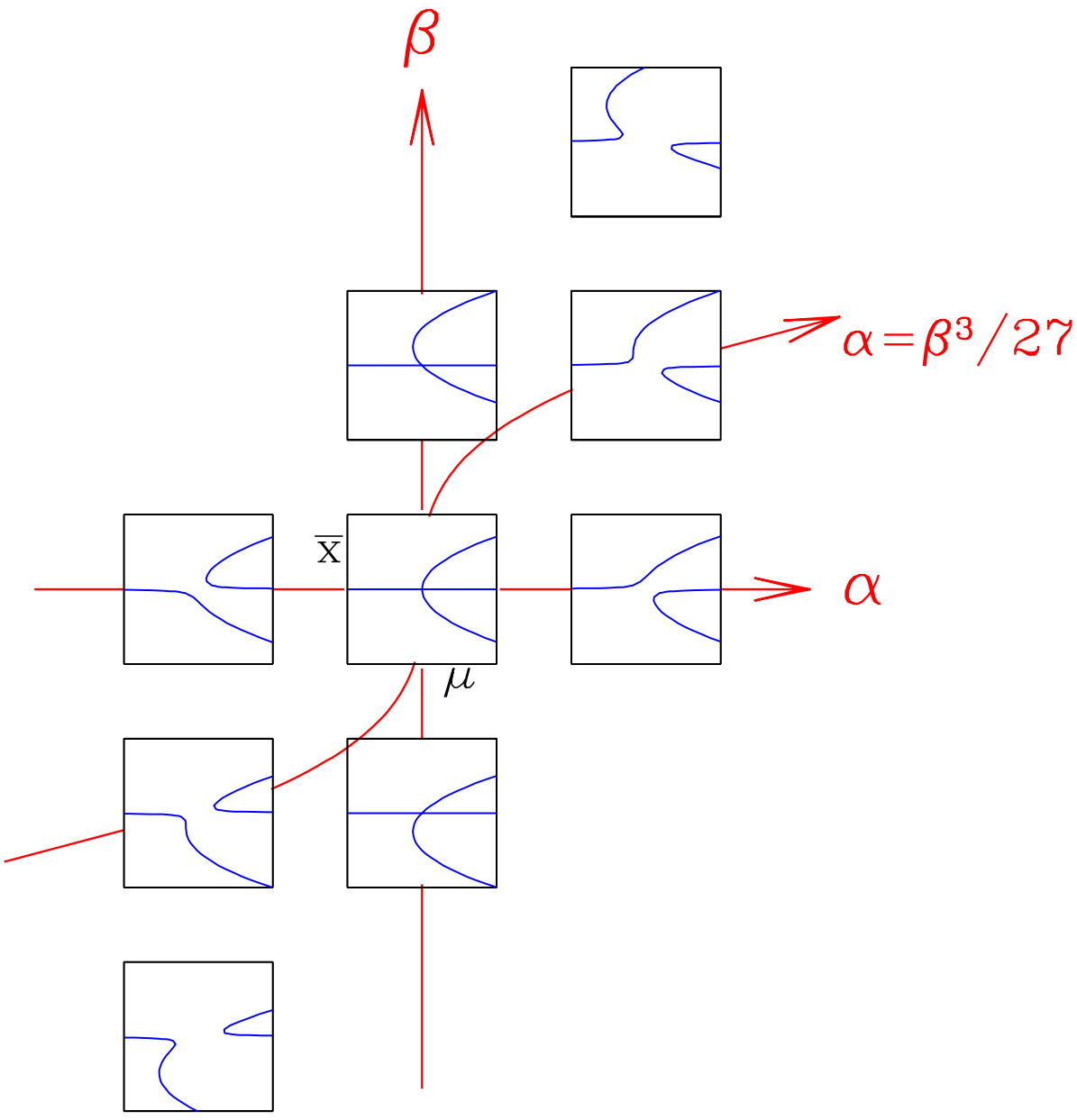


Figure 6: Unfolding of the pitchfork. Bifurcation diagrams $(\mu, \overline{x})$ showing the roots of $0 = \alpha + \mu x + \beta x^2 - x^3$ for nine values of $(\alpha, \beta)$. The pitchfork bifurcation occurs for $\alpha = \beta = 0$ and a transcritical bifurcation for $\alpha = 0$. For $0 < \alpha < \beta^3/27$ and $\beta^3/27 < \alpha < 0$, there are three saddle-node bifurcations; for other non-zero values of $\alpha$ and $\beta$, there is a single saddle-node bifurcation.

# 3 Systems With Two or More Dimensions

## 3.1 From one to many dimensions

Consider a dynamical system

$$\dot{x} = f(x), \qquad x, f \in \mathbb{R}^N, \tag{16}$$

whose fixed points are the zeros of $f$. To study the stability of a given fixed point $\overline{x}$, consider a small perturbation $x(t) = \overline{x} + \varepsilon(t)$. To leading order, we find

$$\dot{\varepsilon} = Df(\overline{x})\,\varepsilon, \tag{17}$$

where $Df$ is the Jacobian matrix of $f$, with components $[Df]_{ij} = \partial f_i/\partial x_j$. The solution to our linearized system is given by

$$\varepsilon(t) = e^{Df(\overline{x})\,t}\varepsilon(0), \tag{18}$$

with the matrix exponential defined via its Taylor series by

$$e^{At} = 1 + At + \frac{1}{2!}(At)^2 + \frac{1}{3!}(At)^3 + \cdots . \tag{19}$$

In particular, a diagonal matrix can be exponentiated element-wise:

$$\exp\begin{pmatrix} \lambda_1 t & & & \\ & \lambda_2 t & & \\ & & \ddots & \\ & & & \lambda_N t \end{pmatrix} = \begin{pmatrix} e^{\lambda_1 t} & & & \\ & e^{\lambda_2 t} & & \\ & & \ddots & \\ & & & e^{\lambda_N t} \end{pmatrix}, \tag{20}$$

and if a matrix $A$ is diagonalized as $A = V\Lambda V^{-1}$, it can be shown that its exponential can be computed in terms of its eigenvalues: $e^{At} = Ve^{\Lambda t}V^{-1}$.

The eigenvalues of $Df$ thus tell us whether a system is stable or unstable to perturbations, and moreover, in which directions perturbations will grow. In particular, the system is stable if and only if the real parts of *all* of the eigenvalues of $Df(\overline{x})$ are negative, and unstable otherwise. If it is unstable, then perturbations will grow along the eigenvectors corresponding to each eigenvalue of positive real part.

In the simplest situation, we have $0 > \lambda_2 > \lambda_3 ...$, and $\operatorname{Re}\lambda_1$ changes sign at a bifurcation. By projecting onto the eigenvector $v_1$ corresponding to $\lambda_1$, we obtain a one-dimensional equation for the bifurcating mode of the system. The first terms in the Taylor series of this equation determine whether we have a saddle-node, pitchfork, or transcritical bifurcation. It is in this way that we obtain bifurcations in physical systems with a large number of degrees of freedom, such as thermal convection.

## 3.2 Systems with complex eigenvalues

Linearizations of real dynamical systems can have complex eigenvalues, which couple the dynamics of two distinct modes. Consider the case

$$A = \begin{pmatrix} & -\omega \\ \omega & \end{pmatrix} \qquad \Longrightarrow \qquad e^{At} = \begin{pmatrix} \cos\omega t & -\sin\omega t \\ \sin\omega t & \cos\omega t \end{pmatrix}. \tag{21}$$

This matrix can be diagonalized over the complex plane, but not over the real line. As a result, if we want to write our system in terms of two real variables, their evolution will necessarily be

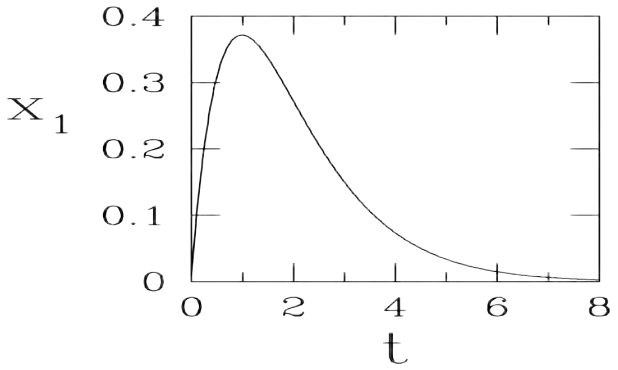


Figure 7: When $(x_1, x_2)$ evolves according to a linear system which is a $2 \times 2$ Jordan block, the coordinate $x_1$ can start to grow, even if the negative eigenvalue of the matrix eventually leads to exponential decay. Here, $\lambda = -1$, $x_1(0) = 0.01$, and $x_2(0) = 1$.

coupled. $2 \times 2$ blocks of this form can arise in larger systems. As an example, we find

$$\Lambda = \begin{pmatrix} \lambda_1 & & & \\ & \mu & -\omega & \\ & \omega & \mu & \\ & & & \lambda_4 \end{pmatrix} \qquad \Longrightarrow \qquad e^{\Lambda t} = \begin{pmatrix} e^{\lambda_1 t} & & & \\ & e^{\mu t}\cos\omega t & -e^{\mu t}\sin\omega t & \\ & e^{\mu t}\sin\omega t & e^{\mu t}\cos\omega t & \\ & & & e^{\lambda_4 t} \end{pmatrix}. \tag{22}$$

### 3.3 Jordan blocks and transient growth

Different dynamics can occur when a matrix is non-diagonalizable. For instance, the *Jordan block*

$$A = \begin{pmatrix} \lambda & 1 \\ & \lambda \end{pmatrix} \tag{23}$$

has only one eigenvector, $v = (1, 0)^T$. It also has *generalized* eigenvectors, which are the solutions $u$ to

$$(A - \lambda)u \propto v. \tag{24}$$

Here, it is easy to verify that $u = (u_1, u_2)^T$ is a generalized eigenvector whenever $u_2 \neq 0$. We typically form an orthonormal basis of eigenvectors and generalized eigenvectors within the $\lambda$-eigenspace: $v = (1, 0)^T$, $u = (0, 1)^T$.

The resulting dynamics can again be found using the matrix exponential:

$$A = \begin{pmatrix} \lambda & 1 \\ & \lambda \end{pmatrix} \qquad \Longrightarrow \qquad e^{At} = e^{\lambda t}\begin{pmatrix} 1 & t \\ & 1 \end{pmatrix}, \tag{25}$$

$$B = \begin{pmatrix} \lambda & 1 & \\ & \lambda & 1 \\ & & \lambda \end{pmatrix} \qquad \Longrightarrow \qquad e^{Bt} = e^{\lambda t}\begin{pmatrix} 1 & t & t^2/2! \\ & 1 & t \\ & & 1 \end{pmatrix}. \tag{26}$$

The $te^{\lambda t}$ terms in these dynamics correspond to transient growth, as depicted in Figure 7.

Two-dimensional linear dynamical systems are straightforward to classify. We classify all of the possible two-dimensional linear systems in Figure 8, and we show the dependence on the trace and determinant of the corresponding matrix in Figure 9.

| Name | Matrix | Behavior | |
|---|---|---|---|
| **Node:**<br>**stable** ($\lambda_2 < \lambda_1 < 0$)<br>**unstable** ($\lambda_2 > \lambda_1 > 0$) | $\begin{pmatrix} \lambda_1 & 0 \\ 0 & \lambda_2 \end{pmatrix}$ | $x_1 = e^{\lambda_1 t} x_1(0)$<br>$x_2 = e^{\lambda_2 t} x_2(0)$ | 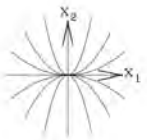 |
| **Star node:**<br>**stable** ($\lambda < 0$)<br>**unstable** ($\lambda > 0$) | $\begin{pmatrix} \lambda & 0 \\ 0 & \lambda \end{pmatrix}$ | $x_1 = e^{\lambda t} x_1(0)$<br>$x_2 = e^{\lambda t} x_2(0)$ | 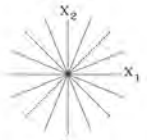 |
| **Degenerate node:**<br>**stable** ($\lambda < 0$)<br>**unstable** ($\lambda > 0$) | $\begin{pmatrix} \lambda & 1 \\ 0 & \lambda \end{pmatrix}$ | $x_1 = e^{\lambda t}(x_1(0) + t x_2(0))$<br>$x_2 = e^{\lambda t} x_2(0)$ | 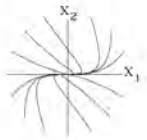 |
| **Non-isolated fixed points:**<br>**stable** ($\lambda < 0$)<br>**unstable** ($\lambda > 0$) | $\begin{pmatrix} 0 & 0 \\ 0 & \lambda \end{pmatrix}$ | $x_1 = x_1(0)$<br>$x_2 = e^{\lambda t} x_2(0)$ | 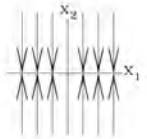 |
| **Saddle:**<br>$\lambda_2 < 0 < \lambda_1$ | $\begin{pmatrix} \lambda_1 & 0 \\ 0 & \lambda_2 \end{pmatrix}$ | $x_1 = e^{\lambda_1 t} x_1(0)$<br>$x_2 = e^{\lambda_2 t} x_2(0)$ | 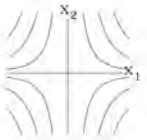 |

| Name | Matrix | Behavior | |
|---|---|---|---|
| **Spiral:**<br>**stable** ($\mu < 0$)<br>**unstable** ($\mu > 0$) | $\begin{pmatrix} \mu & -\omega \\ \omega & \mu \end{pmatrix}$ | $\begin{pmatrix} x_1 \\ x_2 \end{pmatrix} = e^{\mu t} \begin{pmatrix} \cos(\omega t) & -\sin(\omega t) \\ \sin(\omega t) & \cos(\omega t) \end{pmatrix} \begin{pmatrix} x_1(0) \\ x_2(0) \end{pmatrix}$ | 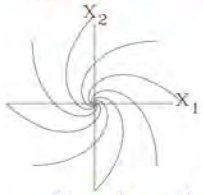 |
| **Center:** | $\begin{pmatrix} 0 & -\omega \\ \omega & 0 \end{pmatrix}$ | $\begin{pmatrix} x_1 \\ x_2 \end{pmatrix} = \begin{pmatrix} \cos(\omega t) & -\sin(\omega t) \\ \sin(\omega t) & \cos(\omega t) \end{pmatrix} \begin{pmatrix} x_1(0) \\ x_2(0) \end{pmatrix}$ | 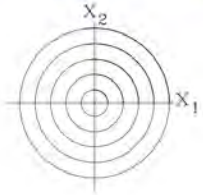 |

Figure 8: All of the possible linear behaviors of a fixed point of a two-dimensional system.

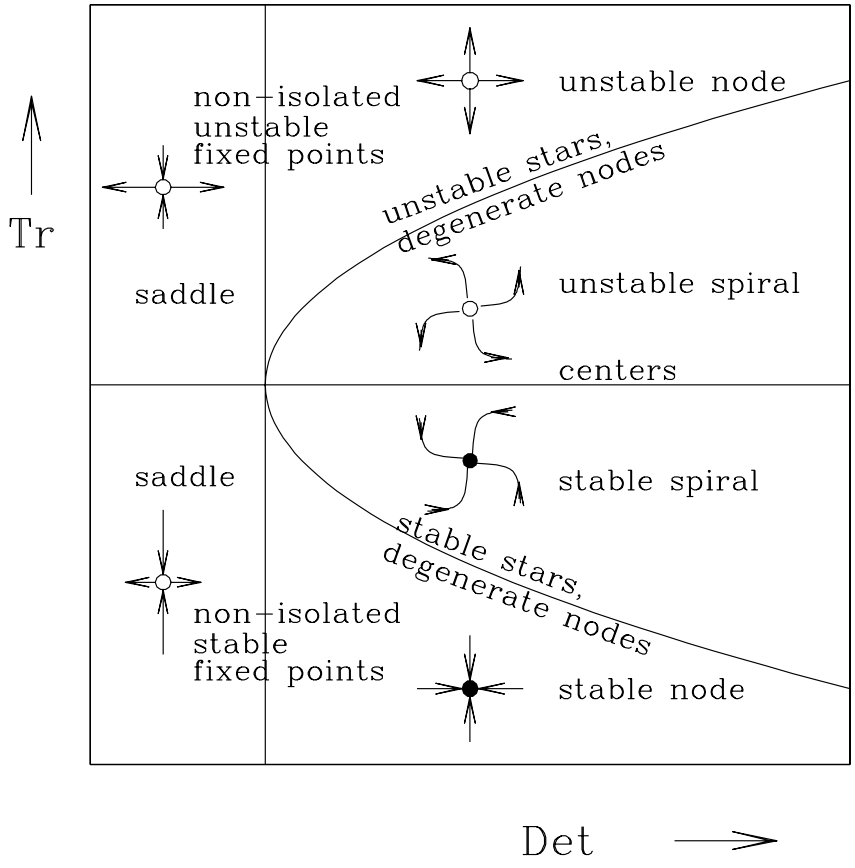


Figure 9: Behavior of two-dimensional linear systems as a function of the trace and determinant of the corresponding $2 \times 2$ matrix.

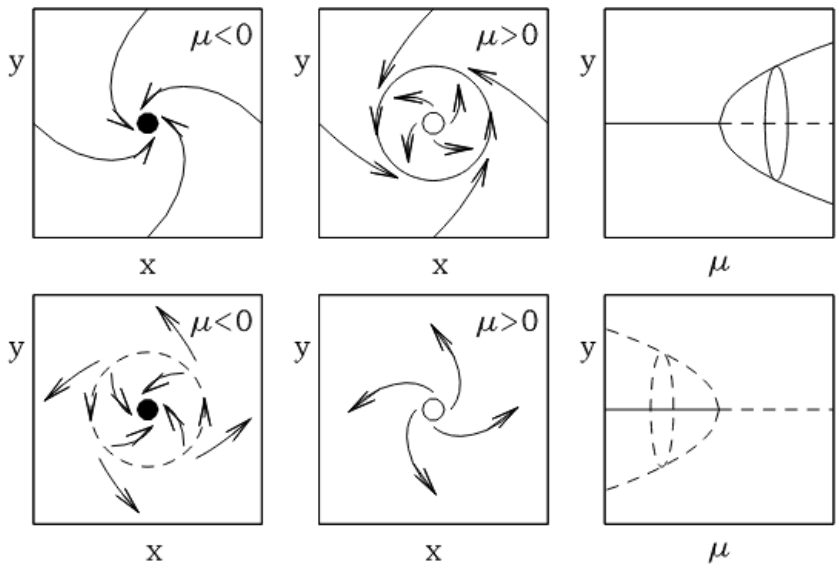


Figure 10: Top: a supercritical Hopf bifurcation ($\alpha > 0$), showing the appearance of a stable limit cycle as $\mu$ crosses zero. Bottom: a subcritical Hopf bifurcation ($\alpha < 0$), showing the appearance of an unstable limit cycle.

### 3.4 Hopf bifurcation

Of particular note is the rightmost portion of Figure 9, where the matrix $A$ of our system has two complex eigenvalues, $\lambda_1$ and $\lambda_2 = \lambda_1^*$. In this scenario, if $\mathrm{Re}(\lambda_1) = \mathrm{Re}(\lambda_2)$ changes sign (and thus the trace of the matrix), then the system undergoes a *Hopf bifurcation*. The simplest nonlinear equation displaying this behavior can be written

$$\dot{z} = (\mu + i\omega)z - (\alpha + i\beta)|z|^2 z \tag{27}$$

for a complex variable $z = re^{i\theta}$. In polar coordinates, we find

$$\dot{r} = \mu r - \alpha r^3, \qquad \dot{\theta} = \omega - \beta r^2. \tag{28}$$

These dynamics correspond to a pitchfork bifurcation in the radial direction and a (potentially-radius-dependent) rotation in the polar angle. The fixed points of $r$ are $r = 0$ and $r = \sqrt{\mu/\alpha}$, and the latter describes a *limit cycle* with constant angular speed $\dot{\theta} = \omega - \beta\mu/\alpha$.

The bifurcation is either supercritical or subcritical depending on the sign of $\alpha$, and it arises at the critical value $\mu = \mu_c = 0$. When $\mu < 0$ and $\alpha > 0$, the only stable point lies at the origin, and all trajectories tend toward it (in a spiral motion). When $\mu > 0$ and $\alpha > 0$, the aforementioned limit cycle appears; interior trajectories spiral outward toward it, and exterior trajectories spiral inward toward it. The subcritical bifurcation, for $\alpha < 0$, is similar, and both are depicted in Figure 10.

### 3.5 Global bifurcations leading to limit cycles

In addition to Hopf bifurcations, *global* bifurcations can create or destroy limit cycles in two dimensions. Two limit cycles can undergo a saddle-node bifurcation in much the same way as two fixed points in the 1-D case. This occurs with the model system

$$\dot{r} = \alpha r(\mu - \mu_c - (r^2 - r_0^2)^2), \qquad \dot{\theta} = \omega. \tag{29}$$

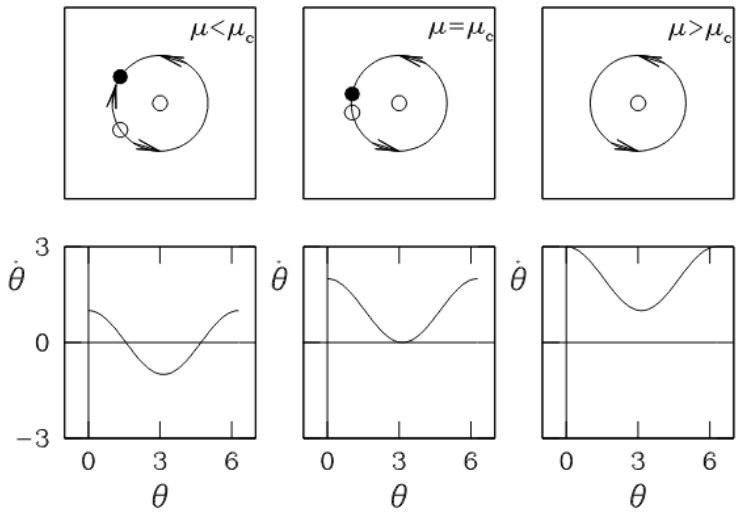


Figure 11: A *SNIPER* (Saddle-Node In a PERiodic Orbit) bifurcation, where two fixed points in an invariant circle give way to a limit cycle.

As $\mu$ crosses $\mu_c$, two limit cycles appear near $r_c$, with stability depending on the sign of $\alpha$.

Furthermore, a saddle-node bifurcation of two fixed points can lead to a limit cycle if the two fixed points lie on a closed trajectory. The following system depicts a *SNIPER* (Saddle-Node In a PERiodic Orbit / Saddle-Node Infinite PERiod), also known as a saddle-node homoclinic bifurcation, an Andronov bifurcation, or a SNIC (Saddle-Node on Invariant Circle):

$$\dot{r} = r(1 - r^2), \qquad \dot{\theta} = \mu + 1 + \cos\theta. \tag{30}$$

This system admits a circle $r = 1$ which is invariant under the dynamics. The circle is only a limit cycle when $\mu > 0$ (or when $\mu < -2$), and otherwise it contains two fixed points, one stable and the other unstable.

A third way of creating or destroying a limit cycle relies on the proximity of two fixed points: one saddle and one spiral. At a homoclinic bifurcation, one of the trajectories leaving the saddle circles the spiral point and returns to the saddle. This trajectory is called a *homoclinic cycle* and takes an infinite time to complete (i.e., to leave or reach the saddle point). An example is provided by the following system:

$$\dot{x} = y, \qquad \dot{y} = -\mu - x + x^2 - xy, \tag{31}$$

whose behavior is depicted in Figure 12. One can distinguish the various kinds of bifurcations involving limit cycles by investigating the amplitude and period of the cycles involved near the bifurcation. A summary is given in Table 1.

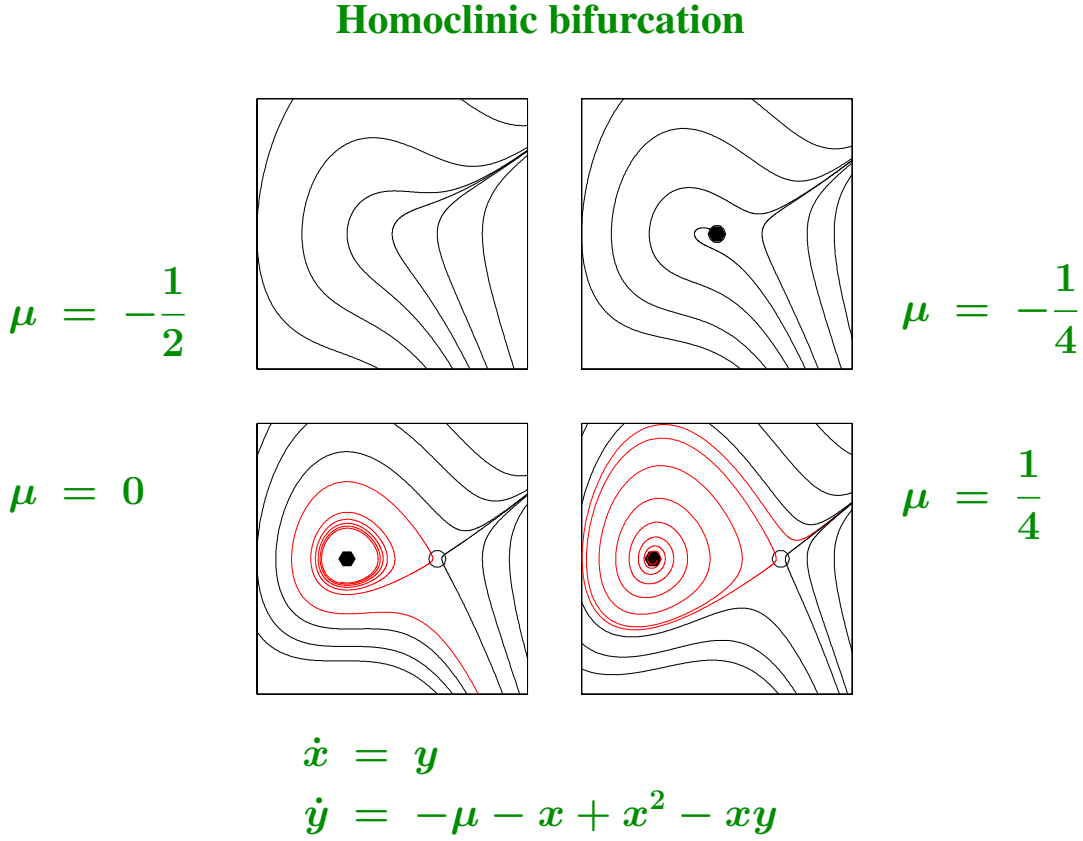


Figure 12: A homoclinic bifurcation. For $\mu < -1/4$, there are no fixed points. At $\mu = -1/4$, a saddle-node bifurcation gives rise to two steady states, a saddle (hollow dot) and another state which becomes a spiral node (solid dot). At $\mu = 0$, the spiral node undergoes a Hopf bifurcation, leading to the creation of a limit cycle, which is reached by all trajectories leaving the spiral node and some trajectories leaving the saddle. By $\mu = 1/4$, the limit cycle has been destroyed by colliding with the saddle.

| | Amplitude | Period |
|---|---|---|
| Supercritical Hopf | $O(\mu^{1/2})$ | $O(1)$ |
| Saddle-node of periodic orbits | $O(1)$ | $O(1)$ |
| Saddle-node in periodic orbit (SNIPER) | $O(1)$ | $O(\mu^{-1/2})$ |
| Homoclinic | $O(1)$ | $O(\log \mu)$ |

Table 1: The amplitudes and periods of limit cycles involved in various kinds of bifurcations as a function of the control parameter $\mu$, where the bifurcation occurs at $\mu = 0$.

# GFD 2025 Lecture 7: Symmetry

Laurette Tuckerman; notes by Emma Bouckley and Theo Lewy

June 24, 2025

## 1 Reflection Symmetry

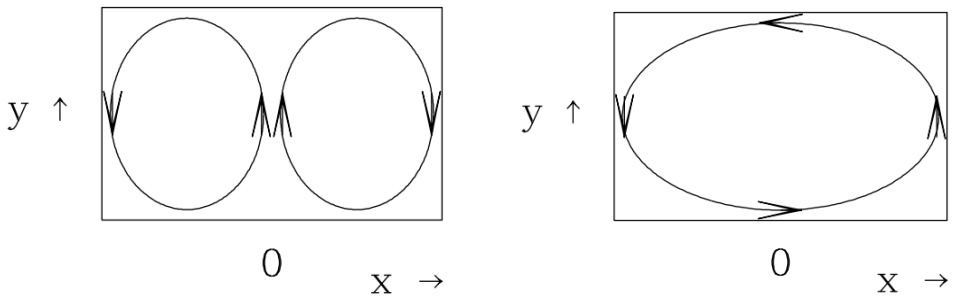


(a) (b)

Figure 1: 2D velocity field that is (a) symmetric and (b) antisymmetric under reflection in $x$.

We begin by considering a rectangular box and formalizing reflection symmetry in $x$ for velocity fields. The velocity fields in figure 1a coincide with our intuitive picture of symmetric and antisymmetric velocity fields. The reflection operator $\kappa$ is defined to act on a 2D velocity field $(u, v)$ via:

$$\kappa \begin{pmatrix} u \\ v \end{pmatrix} (x, y) \equiv \begin{pmatrix} -u \\ v \end{pmatrix} (-x, y) \tag{1}$$

This definition describes reflection of a vector field about the axis $x = 0$. Note that $\kappa$ reverses the sign of $u$ but not that of $v$, just as would a mirror. Definition (1) satisfies the essential property of a reflection operator: $\kappa^2 = I$, where $I$ is the identity. The symmetric velocity field of figure 1a satisfies:

$$\kappa u = u \tag{2a}$$

while the antisymmetric velocity field of figure 1b satisfies:

$$\kappa u = -u \tag{2b}$$

A general velocity field will be neither symmetric nor antisymmetric. It can be decomposed into symmetric and antisymmetric components via:

$$u_s = \frac{1}{2}(I + \kappa)u \tag{3a}$$

$$u_a = \frac{1}{2}(I - \kappa)u \tag{3b}$$

We will return to vector fields shortly, but for the moment, let us now step back and define and study some simpler reflection operators, in order to extract some important mathematical ideas. We will call each of these reflection operators by the same name, $\kappa$, although they will be different operators, acting on different kinds of objects. The operator $\kappa$ and the identity $I$ together form the two-element *group* $Z_2 = \{I, \kappa\}$. A group is defined to be a set and an operation combining two elements of the set to form another element. The operation must be associative, i.e., $a(bc) = (ab)c$, but not necessarily commutative ($ab \neq ba$). The table describing $Z_2$ is given below:

| | I | $\kappa$ |
|---|---|---|
| I | I | $\kappa$ |
| $\kappa$ | $\kappa$ | I |

For a function $f(x)$, we can define a reflection operator via:

$$(\kappa f)(x) \equiv f(-x) \tag{4}$$

This definition corresponds to our intuition. We have $(\kappa \cos)(x) = \cos(x)$, and so $\cos(x)$ is symmetric about $x = 0$ and $(\kappa \sin)(x) = -\sin(x)$, so that $\sin(x)$ is antisymmetric.

Even simpler than a function $f$ is the scalar $a$, and the definition

$$\kappa a \equiv -a \tag{5}$$

Suppose $a$ evolves according to the equation:

$$\frac{d}{dt}a = g(a) \tag{6}$$

We say that a system whose evolution is governed by $g$ has reflection symmetry or is *equivariant* with respect to $\kappa$ if $g\kappa = \kappa g$, i.e., if $g$ and $\kappa$ commute. For $\kappa$ defined by (5), this means that the two quantities

$$\begin{aligned}(g\kappa)(a) &= g(-a)\\ (\kappa g)(a) &= -g(a)\end{aligned} \tag{7}$$

must be equal, i.e., that $g$ must be an odd function of $a$. Now suppose that $g$ is a third-order polynomial, or consider the Taylor expansion of $g$ truncated to cubic order. If $g$ is an odd function of $a$, then

$$\frac{d}{dt}a = g_1 a + g_3 a^3 = (g_1 + g_3 a^2)a \tag{8}$$

Note that this is the normal form for a pitchfork bifurcation.

Let us generalize the definition (5) to act on vectors $(a, s)$ containing two components, one called antisymmetric, $a$, and one called symmetric, $s$.

$$\kappa \begin{pmatrix} a \\ s \end{pmatrix} \equiv \begin{pmatrix} -a \\ s \end{pmatrix} \tag{9}$$

(For the moment, we will use column and row vectors interchangeably.) We see that

$$\kappa \begin{pmatrix} 0 \\ s \end{pmatrix} = \begin{pmatrix} 0 \\ s \end{pmatrix} \text{ and } \kappa \begin{pmatrix} a \\ 0 \end{pmatrix} = -\begin{pmatrix} a \\ 0 \end{pmatrix}, \tag{10}$$

which coincides with definitions (2a) and (2b) of symmetric and antisymmetric vectors. Symmetric solutions are of the form $(0, s)$, antisymmetric solutions of the form $(a, 0)$, and asymmetric solutions (neither symmetric nor antisymmetric) are of the form $(a, s)$.

Now, we need a vector function $G$, which acts on and produces two-dimensional vectors, to govern the evolution of $(a, s)$:

$$\frac{d}{dt}\begin{pmatrix} a \\ s \end{pmatrix} = G(a, s) \equiv \begin{pmatrix} g \\ h \end{pmatrix}(a, s) \tag{11}$$

$G$ is equivariant with respect to $\kappa$ of (9) if

$$\kappa \begin{pmatrix} g \\ h \end{pmatrix}(a, s) = \begin{pmatrix} g \\ h \end{pmatrix}\kappa(a, s) \tag{12}$$

i.e., if

$$\begin{pmatrix} -g \\ h \end{pmatrix}(a, s) = \begin{pmatrix} g \\ h \end{pmatrix}(-a, s) \tag{13}$$

This means that $g$ and $h$ must be antisymmetric and symmetric functions of $a$, respectively. Again specifying $g$ and $h$ to be third-order polynomials, or Taylor series truncated to this order, we obtain

$$\begin{aligned}
g(a, s) &= g_{00} + g_{10}a + g_{01}s + g_{20}a^2 + g_{11}as + g_{02}s^2 + g_{30}a^3 + g_{21}a^2s + g_{12}as^2 + g_{03}s^3 \\
-g(a, s) &= -g_{00} - g_{10}a - g_{01}s - g_{20}a^2 - g_{11}as - g_{02}s^2 - g_{30}a^3 - g_{21}a^2s - g_{12}as^2 - g_{03}s^3 \\
g(-a, s) &= g_{00} - g_{10}a + g_{01}s + g_{20}a^2 - g_{11}as + g_{02}s^2 - g_{30}a^3 + g_{21}a^2s - g_{12}as^2 + g_{03}s^3 \\
h(a, s) &= h_{00} + h_{10}a + h_{01}s + h_{20}a^2 + h_{11}as + h_{02}s^2 + h_{30}a^3 + h_{21}a^2s + h_{12}as^2 + h_{03}s^3 \\
h(-a, s) &= h_{00} - h_{10}a + h_{01}s + h_{20}a^2 - h_{11}as + h_{02}s^2 - h_{30}a^3 + h_{21}a^2s - h_{12}as^2 + h_{03}s^3
\end{aligned}$$

In order to satisfy (13), all terms in $g$ containing even powers of $a$ must vanish, while all terms in $h$ containing odd powers of $a$ must vanish. The result is:

$$\begin{pmatrix} g \\ h \end{pmatrix}(a, s) = \begin{pmatrix} g_{10}a + g_{11}as + g_{30}a^3 + g_{12}as^2 \\ h_{00} + h_{01}s + h_{20}a^2 + h_{02}s^2 + h_{21}a^2s + h_{03}s^3 \end{pmatrix} \tag{14a}$$

$$= \begin{pmatrix} (g_{10} + g_{11}s + g_{12}s^2 + g_{30}a^2)a \\ h_{00} + h_{01}s + h_{02}s^2 + h_{03}s^3 + (h_{20} + h_{21}s)a^2 \end{pmatrix} \tag{14b}$$

$$= \begin{pmatrix} \tilde{g}(a^2, s)a \\ \tilde{h}(a^2, s) \end{pmatrix} \tag{14c}$$

$$= \tilde{g}(a^2, s)\begin{pmatrix} a \\ 0 \end{pmatrix} + \tilde{h}(a^2, s)\begin{pmatrix} 0 \\ 1 \end{pmatrix} \tag{14d}$$

Lines (14c)-(14d) apply to general $g, h$, not merely to cubic polynomials. The functions $\tilde{g}$ and $\tilde{h}$ have as their arguments $s$ and $a^2$, which are said to be *invariants*. An invariant $f$ is a scalar function of $(a, s)$, which satisfies $f\kappa = f$. In contrast, an *equivariant* is a vector function $(g, h)$ of $(a, s)$, as is $\kappa$, which commutes with $\kappa$. This means, in effect, that $(g, h)$ is transformed by $\kappa$ in the same way as $(a, s)$.

$$\begin{array}{ccccc}
\begin{pmatrix} -g(a,s) \\ h(a,s) \end{pmatrix} & \overset{\kappa}{\leftarrow} & \begin{pmatrix} g(a,s) \\ h(a,s) \end{pmatrix} & \overset{G}{\leftarrow} & \begin{pmatrix} a \\ s \end{pmatrix} \\
\begin{pmatrix} g(-a,s) \\ h(-a,s) \end{pmatrix} & \overset{G}{\leftarrow} & \begin{pmatrix} -a \\ s \end{pmatrix} & \overset{\kappa}{\leftarrow} & \begin{pmatrix} a \\ s \end{pmatrix}
\end{array} \tag{15}$$

i.e., $g(-a,s) = -g(a,s)$ and $h(-a,s) = h(a,s)$ as we have seen, meaning that $g$ must be an odd and $h$ an even function of $a$. An invariant is a scalar function of $(a,s)$ which remains the same when its arguments are acted on by $\kappa$.

$$\begin{aligned} f(-a,s) &\xleftarrow{f} \begin{pmatrix} -a \\ s \end{pmatrix} \xleftarrow{\kappa} \begin{pmatrix} a \\ s \end{pmatrix} \\ f(a,s) &\xleftarrow{f} \begin{pmatrix} a \\ s \end{pmatrix} \end{aligned} \tag{16}$$

i.e., $f(-a,s) = f(a,s)$, meaning that $f$ must be an even function of $a$. The functions $f(a,s) = a^2$ and $f(a,s) = s$ both have this property, so they are both invariants. In fact, all invariants can be written as functions of $a^2$ and $s$, and any function of $a^2$ and $s$ is an invariant. Expression (14d) states that the most general equivariant is expressible as a superposition of a few basic equivariants (here, $(a,0)$ and $(0,1)$) with coefficients that are general functions of a few basic invariants (here, $a^2$ and $s$). This remains true in more complicated situations.

We emphasize the difference between a *system* $G$, which is $\kappa$-equivariant and a *solution*, which is $\kappa$-symmetric. It is definitely not true that solutions to a $\kappa$-equivariant system are symmetric. However, there certainly are consequences of $\kappa$-equivariance, of which some are:

*1. If $(a,s)$ is a time-dependent or stationary solution to a $\kappa$-equivariant system, then $\kappa(a,s) = (-a,s)$ is also a solution.*

This follows from applying $\kappa$ to both sides of (14) and commuting $\kappa$ with $d/dt$ and with $G$. This statement means that asymmetric solutions $(a,s), a \neq 0$, occur in pairs $(\pm a, s)$. For example, the existence of the solution in figure 1b in a reflection-symmetric domain implies the existence of another solution, with the arrows reversed. For symmetric solutions $(0,s)$, the statement does not lead to any new solutions. It follows that:

*2. If a $\kappa$-equivariant system has a unique solution, then that solution is symmetric.*

This is the case, for example, if $G$ is a linear system or for the Navier-Stokes equations at sufficiently low Reynolds number.

Let us now discuss the consequences of symmetry on a linear system, where $G$ consists of a matrix acting on $(a,s)$. Selecting only linear terms from (14a), we get

$$\frac{d}{dt}\begin{pmatrix} a \\ s \end{pmatrix} = G\begin{pmatrix} a \\ s \end{pmatrix} = \begin{pmatrix} g_{10} & 0 \\ 0 & h_{01} \end{pmatrix}\begin{pmatrix} a \\ s \end{pmatrix} \tag{17}$$

The matrix $G$ is diagonal, a consequence of its $\kappa$ symmetry. Thus, $a$ and $s$ are not coupled by the linear evolution. Eigenvectors of $G$ are either symmetric or antisymmetric, and not a superposition of the two. This will remain true in more general settings. Consider a general matrix or linear operator $G$, multiplication by which commutes with some reflection operator $\kappa$ on a general vector or function $u$.

*3. If $(\lambda, u)$ is an eigenpair of the linear system $G$, then $\kappa u$ is also an eigenvector of $G$ with the same eigenvalue $\lambda$*

This is easily demonstrated:

$$Gu = \lambda u \implies \kappa G u = \kappa\lambda u \implies G\kappa u = \lambda \kappa u \tag{18}$$

There are two ways for this to happen. One way is for $\kappa u$ to be a multiple of $u$. In this case,

$$\begin{aligned} \kappa u &= cu \\ \kappa^2 u &= \kappa c u \\ u &= c^2 u \\ c &= \pm 1 \end{aligned} \tag{19}$$

Either $c = 1$, in which case $u$ is symmetric, or $c = -1$, in which case $u$ is antisymmetric.

Now suppose that $\kappa u$ is not a multiple of $u$. Then $\lambda$ is an eigenvalue of $G$ with two different linearly independent eigenvectors, i.e., $\lambda$ is a multiple eigenvalue of $G$. This may happen, but is unlikely, unless parameters are especially adjusted to make it so or the system has some other special feature that we have not taken into account. For example, in (17) we would require $g_{10} = h_{01}$. This is unlikely, since symmetric and antisymmetric vectors, such as the velocity fields depicted in figures 1a and 1b, would not be expected to evolve in the same way. However, if $u$ and $\kappa u$ are indeed two linearly independent eigenvectors of $G$, we may define symmetric and antisymmetric eigenvectors as follows:

$$\begin{aligned} \frac{I+\kappa}{2}u, \text{ which is symmetric since } \kappa\frac{I+\kappa}{2}u &= \frac{\kappa+I}{2}u \\ \frac{I-\kappa}{2}u, \text{ which is antisymmetric since } \kappa\frac{I-\kappa}{2}u &= \frac{\kappa-I}{2}u \end{aligned} \tag{20}$$

Let us return to the reflection operator (1) defined for 2D velocity fields and apply it to the Navier-Stokes equations:

$$\partial_t \begin{pmatrix} u \\ v \end{pmatrix} = (NS) \begin{pmatrix} u \\ v \end{pmatrix} \begin{pmatrix} NS_u \\ NS_v \end{pmatrix} \equiv \begin{pmatrix} -(u\partial_x + v\partial_y)u - \partial_x p + \nu(\partial_x^2 + \partial_y^2)u \\ -(u\partial_x + v\partial_y)v - \partial_y p + \nu(\partial_x^2 + \partial_y^2)v \end{pmatrix} \tag{21}$$

subject to $\partial_x u + \partial_y v = 0$. We wish to verify whether this system of equations is equivariant with respect to $\kappa$. The non-trivial part of this calculation is how to treat differentiation. We first establish that the action of differentiation on $(\kappa f)(x) \equiv f(-x)$ is $(\kappa f)'(x) = -f'(-x)$ and $(\kappa f)''(x) = f''(-x)$. This can be seen by considering first principles on $\tilde{f}(x) \equiv (\kappa f)(x) \equiv f(-x)$.

Armed with these results, we calculate the action of the Navier-Stokes evolution operator $NS$ defined in (21) on $\kappa(u, v)](x, y) \equiv (-u, v)(-x, y)$. Operation by $\kappa$ is equivalent to $u, x, \partial_x \to -u, -x, -\partial_x$ and $p, v, y, \partial_y \to p, v, y, \partial_y$.

$$\left[(NS)\kappa \begin{pmatrix} u \\ v \end{pmatrix}\right](x, y) = \begin{pmatrix} -((-u)(-\partial_x) + v\partial_y)(-u) - (-\partial_x)p + \nu(\partial_x^2 + \partial_y^2)(-u) \\ -((-u)(-\partial_x) + v\partial_y)v - \partial_y p + \nu(\partial_x^2 + \partial_y^2)v \end{pmatrix}(-x, y) \tag{22}$$

Acting in the opposite order, we obtain:

$$\begin{aligned} \left[\kappa(NS) \begin{pmatrix} u \\ v \end{pmatrix}\right](x, y) &= \begin{pmatrix} -NSu \\ NSv \end{pmatrix}(-x, y) \\ &= \begin{pmatrix} -[-(u\partial_x + v\partial_y)u - \partial_x p + \nu(\partial_x^2 + \partial_y^2)u] \\ -(u\partial_x + v\partial_y)v - \partial_y p + \nu(\partial_x^2 + \partial_y^2)v \end{pmatrix}(-x, y) \end{aligned} \tag{23}$$

which is identical to the previous result. This is unsurprising: we do not expect any general equations of continuum physics to distinguish between the left and right halves of a domain or between left-going and right-going motion.

It is boundary conditions and body forces that determine whether a system has reflection symmetry. Figures 1a and 1b depict a rectangular box. In a geometry that lacked reflection symmetry in $x$, there would be no possibility of reflection symmetry for the system. Even in a rectangular box, however, only certain boundary conditions will meet the requirement of reflection symmetry. General Dirichlet boundary conditions for a rectangular geometry are:

$$\begin{aligned} u(x=\pm 1, y) &= a_\pm(y) \\ v(x=\pm 1, y) &= b_\pm(y) \\ u(x, y=\pm h) &= c_\pm(x) \\ v(x, y=\pm h) &= d_\pm(x) \end{aligned} \tag{24}$$

Acting with $\kappa$ on these boundary conditions transforms the left-hand-side concerning $(u, v)$, but not the right-hand-side concerning known functions.

$$\begin{aligned} -u(x=\mp 1, y) = a_\pm(y) \quad &\Longrightarrow \quad u(x=\pm 1, y) = -a_\mp(y) \\ v(x=\mp 1, y) = b_\pm(y) \quad &\Longrightarrow \quad v(x=\pm 1, y) = b_\mp(y) r \\ -u(-x, y=\pm h) = c_\pm(x) \quad &\Longrightarrow \quad u(x, y=\pm h) = -c_\pm(-x) \\ v(-x, y=\pm h) = d_\pm(x) \quad &\Longrightarrow \quad v(x, y=\pm h) = d_\pm(-x) \end{aligned} \tag{25}$$

The four transformed boundary conditions in (25) are equivalent to the boundary conditions (24) of the original system if

$$\begin{aligned} a_\pm(y) &= -a_\mp(y) \\ b_\pm(y) &= b_\mp(y) \\ c_\pm(x) &= -c_\pm(-x) \\ d_\pm(x) &= d_\pm(-x) \end{aligned} \tag{26}$$

Other types of boundary conditions, for example, Neumann conditions on the normal derivatives, or a combination of Dirichlet and Neumann conditions, could also be considered. For the system to be reflection-symmetric in $x$, however, the boundary conditions on the left side $x = -1$ and on the right side $x = +1$ must be of the same type.

We return to the types of flows shown in figure 1a and 1b in the beginning of this section. Figure 2a shows an *asymmetric* flow $\boldsymbol{u}_s + \boldsymbol{u}_a$ (neither symmetric nor antisymmetric). Reflection in $x$ transforms $\boldsymbol{u}_s + \boldsymbol{u}_a$ into a different asymmetric flow $\boldsymbol{u}_s - \boldsymbol{u}_a$ shown in Figure 2b. Assuming reflection symmetry in $x$, these two flows are dynamically equivalent: it makes no difference whether fluid descends on the left and rises on the right or vice versa. Transition from a symmetric flow to the asymmetric flows $\boldsymbol{u}_s \pm \boldsymbol{u}_a$ will always occur via a pitchfork bifurcation, shown on the left in figure 3. This reasoning applies in a reflection-symmetric domain whenever the number of cells is odd.

Two symmetric flows $u_s$ and $u_s'$ are illustrated in Figures 2c and e. Both are unchanged under $\kappa$, as shown in Figures 2d and f. Transition to these flows will therefore be associated with transcritical bifurcations, as shown in the figure 3(right). This reasoning applies in reflection-symmetric domains whenever the number of cells is even. In fact, $u_s' = -u_s$, but without any further assumptions, $u_s$ and $u_s'$ are not equivalent: flow rising along the walls and falling in the center is not necessarily equivalent to the opposite. In Boussinesq convection, the further assumption is made that fluid rising and falling are dynamically equivalent, and so a transition to $\pm\boldsymbol{u}_s$ takes place via a pitchfork bifurcation, independent of whether the number of cells is even or odd.

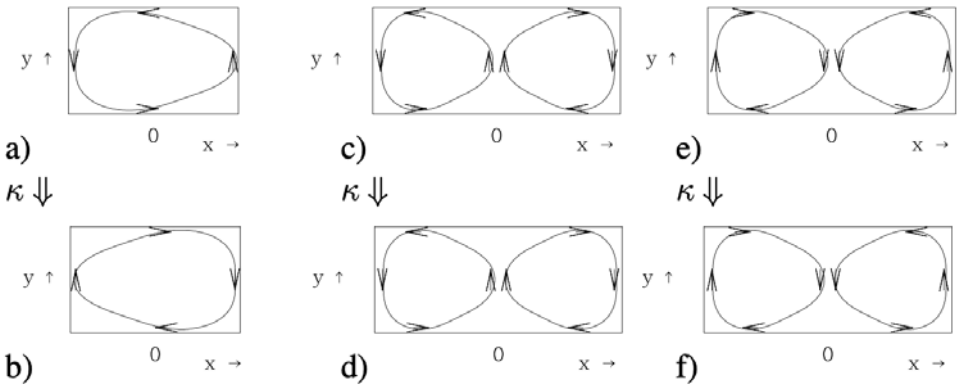


Figure 2: a) asymmetric flow $u_s + u_a$ is mapped into flow below (b) by the $x$-reflection operator $\kappa$. The two flows are therefore dynamically equivalent. (c, e) symmetric flows $u_s$, $u_s'$ are mapped onto themselves (d, f) by $\kappa$.

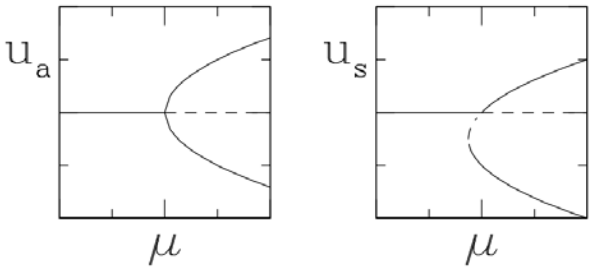


Figure 3: Pitchfork bifurcation (left) associated with bifurcation to asymmetric flow and transcritical bifurcation (right) associated to symmetric flow.

# 2 Rotation

## 2.1 Symmetry groups

The most important symmetry groups of the plane are given by $Z_n$, representing the group of rotations of an $n$-gon, and $D_n$, the same group with the addition of reflections about any of the axes of the $n$-gon. Figure 4 illustrates several of these symmetry groups. The triangle, square, and circle on the second row have symmetries $D_3$, $D_4$, and $O(2)$. In the first row, distinguishing features have been added to each of the shapes in order to break reflection symmetry. As a result, the objects on the first row have symmetries $Z_3$, $Z_4$, and $SO(2)$.

Let us focus on $O(2)$. We begin by studying steady bifurcations. For this purpose, we represent a point $(x, y)$ on the plane by the complex number $z$. We then can represent the action of rotation by $\theta$ and reflection in $y$ by:

$$\begin{aligned} S_\theta z &\equiv e^{i\theta} z \\ \kappa z &\equiv \bar{z} \end{aligned} \tag{27}$$

A crucial fact is that rotation and reflection do not commute:

$$\begin{aligned} \kappa S_\theta z &= \kappa(e^{i\theta} z) = e^{-i\theta} \bar{z} \\ S_\theta \kappa z &= S_\theta \bar{z} = e^{i\theta} \bar{z} \end{aligned} \tag{28}$$

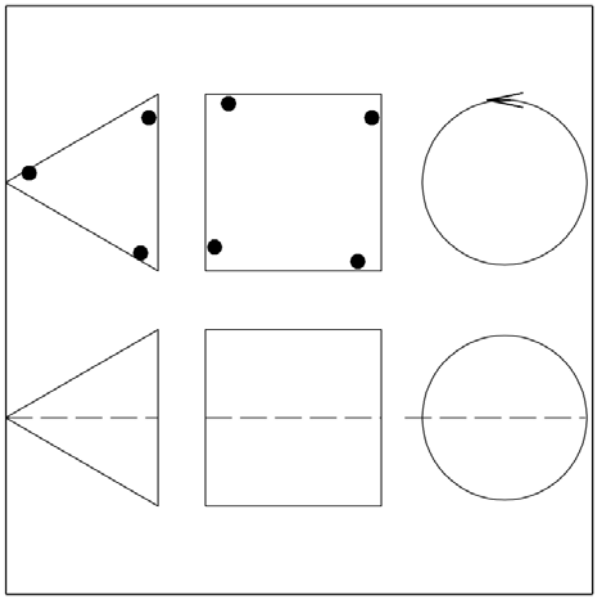

Figure 4: Objects on the first row have symmetries $Z_3$, $Z_4$, and $SO(2)$. Those on the second row have symmetries $D_3$, $D_4$, and $O(2)$.

with the exception of rotation by $\pi$. $S_\theta$ and $\kappa$ are called the *generators* of the group $O(2)$, since any element of $O(2)$ can be formed as combinations of these elements.

Before continuing, let us illustrate how the representation (27) acts on a function $w(\theta, t)$, where $\theta$ is a direction with reflection and rotation symmetry. The function $w$ can be written as:

$$w(\theta, t) = \frac{1}{2}\big(z(t)e^{i\theta} + \bar{z}(t)e^{-i\theta}\big) \tag{29}$$

The real part of $z$ can be seen as the coefficient of $\cos(\theta)$, while the imaginary part of $z$ is the coefficient of $\sin(\theta)$. The operations (27) on $z$ then correspond to the following operations on $w$:

$$\begin{aligned}(S_{\theta_0} w)(\theta) &\equiv w(\theta + \theta_0)\\ (\kappa w)(\theta) &\equiv w(-\theta)\end{aligned} \tag{30}$$

We now discuss transitions that can occur in a dynamical system with symmetry group $O(2)$.

## 2.2 Circle pitchfork bifurcation

Let us now return to the abstract setting and determine which functional forms are equivariant, i.e., which commute with the operations in (27). We consider monomials of $x$ and $y$ or, more conveniently, of $z$ and $\bar{z}$.

$$f(z, \bar{z}) = f_{mn} z^m \bar{z}^n \tag{31}$$

where $f$ is complex. Considering reflection, we have

$$\kappa f(z, \bar{z}) = \overline{f(z, \bar{z})} = \bar{f}_{mn} \bar{z}^m z^n \tag{32a}$$

$$f(\kappa(z, \bar{z})) = f_{mn} \bar{z}^m z^n \tag{32b}$$

Thus, for $f$ to commute with $\kappa$, the coefficient $f_{mn}$ must be real. In order for $f$ to commute with $S_\theta$ for all $\theta$, we calculate

$$S_\theta f(z,\bar{z}) = e^{i\theta} f(z,\bar{z}) = e^{i\theta} f_{mn} z^m \bar{z}^n \tag{33a}$$

$$f(S_\theta(z,\bar{z})) = f_{mn}(e^{i\theta}z)^m \overline{(e^{i\theta}z)}^n = f_{mn} e^{im\theta} z^m e^{-in\theta} \bar{z}^n \tag{33b}$$

Thus, we require that $e^{i\theta(m-n)} = e^{i\theta}$, which can only hold for all $\theta$ if $m - n = 1$. This leads to polynomials of the form:

$$\begin{aligned} f(z,\bar{z}) &= f_{10} z + f_{21} z^2 \bar{z} + f_{32} z^3 \bar{z}^2 + \cdots \\ &= (f_{10} + f_{21}|z|^2 + f_{32}|z|^4 + \cdots) z = \tilde{f}(|z|^2) z \end{aligned} \tag{34}$$

where $\tilde{f}$ is a general real function of $|z|^2$. In the terms introduced in the previous section, the scalar $|z|^2$ is invariant under the group $O(2)$ and the complex number (or two-component vector) $z$ is equivariant. Truncating (34) at cubic order, we derive the evolution equation:

$$\frac{dz}{dt} = (\mu - \alpha|z|^2) z \tag{35}$$

The steady states of (35) are $z = 0$ and $|z| = \sqrt{\mu/\alpha}$, which exist only for $\mu/\alpha > 0$, as illustrated in figure 5. We consider $\mu$ to be the bifurcation parameter, such as a relative Reynolds number $(Re - Re_c)/Re_c$ or Rayleigh number $(Ra - Ra_c)/Ra_c$. The transition occurring at $\mu = 0$ is called a circle pitchfork, because a "circle" of steady states, $z = \sqrt{\mu/\alpha}\, e^{i\theta}$, is created as $\mu$ crosses zero.

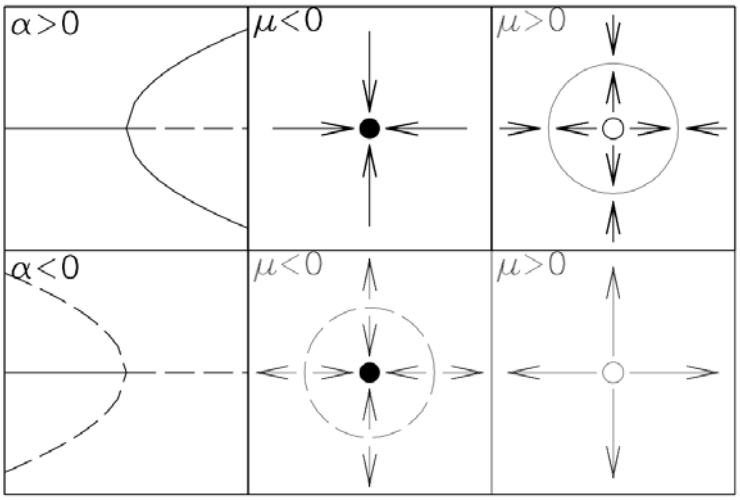


Figure 5: Circle pitchfork bifurcation. The upper diagrams correspond to the supercritical case, the lower diagrams to the subcritical case. Leftmost are the bifurcation diagrams in the $(\mu, r)$ plane, middle and rightmost are phase portraits in the $(x, y)$ plane. Stable steady states are designated by solid dots or solid curves. Unstable steady states are shown as hollow dots or dashed curves.

We may write (35) in Cartesian coordinates $z = x + iy$:

$$\frac{dx}{dt} = (\mu - \alpha(x^2 + y^2)) x \tag{36a}$$

$$\frac{dy}{dt} = (\mu - \alpha(x^2 + y^2)) y \tag{36b}$$

or in polar coordinates $z = re^{i\theta}$:

$$\frac{dr}{dt} = (\mu - \alpha r^2)r \tag{37a}$$

$$\frac{d\theta}{dt} = 0 \tag{37b}$$

Equation (37a) shows that the amplitude $r$ undergoes an ordinary pitchfork bifurcation and (37b) shows that the phase $\theta$ shows no tendency to move. The stability of the trivial state and the bifurcating circle of states can be calculated from either (36a)-(36b) or (37a)-(37b) via the Jacobian matrix:

$$J(x,y) = \begin{bmatrix} \mu - \alpha(3x^2 + y^2) & -2\alpha xy \\ -2\alpha xy & \mu - \alpha(x^2 + 3y^2) \end{bmatrix} \tag{38}$$

or in polar coordinates

$$J(r,\theta) = \begin{bmatrix} \mu - 3\alpha r^2 & 0 \\ 0 & 0 \end{bmatrix} \tag{39}$$

To calculate the stability of the trivial state, we use

$$J(x = 0, y = 0) = \begin{bmatrix} \mu & 0 \\ 0 & \mu \end{bmatrix} \tag{40}$$

which has $\mu$ as a double eigenvalue. The trivial state $(0, 0)$ is stable for $\mu < 0$ and has two unstable directions (corresponding to the two directions of the plane) for $\mu > 0$. Note that the polar form $J(r, \theta)$ of equation (39) would seem to indicate that the two eigenvalues of $(0, 0)$ are $\mu$ and 0. This contradictory result arises from the fact that $\theta$ is not well defined at the origin, so that $J(r, \theta)$ is also not well defined at the origin.

For the bifurcating circle of states, we may write

$$J\left(r = \sqrt{\frac{\mu}{\alpha}}, \theta\right) = \begin{bmatrix} \mu - 3\mu & 0 \\ 0 & 0 \end{bmatrix} = \begin{bmatrix} -2\mu & 0 \\ 0 & 0 \end{bmatrix} \tag{41}$$

whose eigenvalues are $-2\mu$ and 0. The circle pitchfork can be supercritical or subcritical, according to the sign of $\alpha$. If $\alpha > 0$, then the circle of bifurcating states exists for $\mu > 0$ and the eigenvalue $-2\mu$ corresponds to contraction onto the circle $\sqrt{\mu/\alpha}$, i.e., stability. If $\alpha < 0$, then the circle of bifurcating states exists for $\mu < 0$ and the eigenvalue $-2\mu$ corresponds to expansion away from the circle, i.e., instability. The eigenvalue 0 corresponds to the phase invariance, i.e., the fact that the system shows no tendency to move in the direction $\theta$.

## 2.3 O(2) and SO(2)

We now briefly contrast $O(2)$ and $SO(2)$. The group $SO(2)$ omits the reflection $\kappa$. $SO(2)$ symmetry leads to the same equation (34) as in the $O(2)$ case, but, because (32a) and (32b) are not required to be equal, the function $\tilde{f}$ can be complex. Allowing complex coefficients, the normal form (35) becomes

$$\frac{dz}{dt} = (\mu + i\omega - (\alpha + i\beta)|z|^2)z \tag{42}$$

whose polar form is:

$$\frac{d(re^{i\theta})}{dt} = \left(\frac{dr}{dt} + ri\frac{d\theta}{dt}\right)e^{i\theta} = \left[(\mu - \alpha r^2) + i(\omega + \beta r^2)\right]re^{i\theta}$$

$$\frac{dr}{dt} = (\mu - \alpha r^2)r \tag{43a}$$

$$\frac{d\theta}{dt} = \omega + \beta r^2 \tag{43b}$$

According to (43b), there is usually motion along the $\theta$ direction, contrary to the case of $O(2)$,

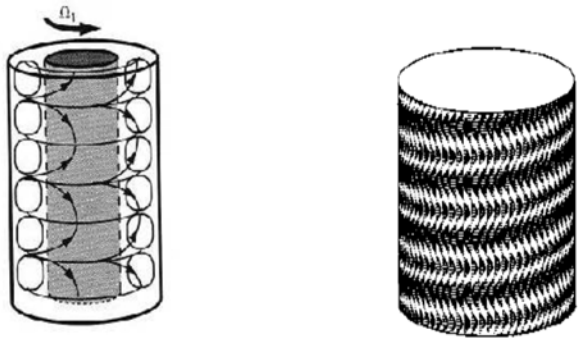


Figure 6: Left: axisymmetric Taylor vortices (reproduced from Tagg [4]). Right: spiral Taylor vortices (reproduced from Antonijoan et al. [1].)

We illustrate the difference between $O(2)$ and $SO(2)$ with the example of Taylor-Couette flow, the flow between differentially rotating concentric cylinders, whose common axis will be assumed to be oriented in the vertical direction; see figure 6. When this flow is modeled with a periodic axial direction, there is translational axial symmetry in the system. In addition, reflections exist in the axial direction, as gravity can be ignored (its contributions can be absorbed into a hydrostatic pressure term). Hence there is $O(2)$ symmetry in the axial direction. In the azimuthal direction, we have rotational symmetry. However, the imposed rotation of the cylinders serves to differentiate clockwise from counter-clockwise rotation, and hence the azimuthal direction has only $SO(2)$ symmetry.

When the two cylinders rotate in the same direction, the first transition to occur breaks the axial ($O(2)$) symmetry and leads to Taylor-vortices, shown on the left in figure 6. These are steady states which resemble tori stacked vertically along the axis of the cylinders. In the infinite-length context, a pair of these vortices define an axially periodic domain and the phase parametrizes a circle of steady states. The azimuthal symmetry is retained.

In contrast, when the ratio between the cylinders' rotation rates is sufficiently negative, the first transition is to spirals, shown on the right in figure 6, which break the azimuthal ($SO(2)$) symmetry as well as the axial symmetry. These spirals have a well-defined rotation rate in the azimuthal direction. However, because of the axial reflection-symmetry, spirals of two varieties exist, of opposite chirality and direction of motion in the axial direction.

## 2.4 Hopf bifurcation and O(2) symmetry

The normal form (35) is inadequate for describing many phenomena that occur in an $O(2)$ symmetric configuration, such as Hopf bifurcation and more complicated spatial structures. This is a consequence of the inadequacy of (27). In particular, the two-dimensional normal form (35) cannot describe a Hopf bifurcation that breaks $O(2)$ symmetry. Such a Hopf bifurcation involves a four-dimensional eigenspace, for the following reason. The coefficients of $\cos(\theta)$ and $\sin(\theta)$ obey identical equations, leading to a block diagonal Jacobian (one block for cos and one for sin). If each block

contained a single component, then the Jacobian would be a diagonal $2 \times 2$ matrix, which cannot have complex eigenvalues. Thus, in order for the Jacobian to have complex eigenvalues, each of the two blocks must contain at least two components, leading to a Jacobian whose minimum size is $4 \times 4$.

Having argued for the need for a four-dimensional normal form, we consider a field $u$ as represented by

$$u(\theta, t) = \left[(z_+(t) + z_-(t))e^{i\theta} + (\bar{z}_+(t) + \bar{z}_-(t))e^{-i\theta}\right] \tag{44}$$

where $z_+$ is the complex amplitude (representing the amplitude and phase) of left-going traveling waves and $z_-$ is that of right-going traveling waves. At linear order, the evolution of $z_\pm(t)$ is described by

$$\frac{d}{dt}\begin{pmatrix} z_+ \\ z_- \end{pmatrix} = \begin{pmatrix} i\omega z_+ \\ -i\omega z_- \end{pmatrix} \tag{45}$$

so that the linear evolution is

$$u(\theta, t) = z_+(0)e^{i(\theta+\omega t)} + z_-(0)e^{i(\theta-\omega t)} + \bar{z}_+(0)e^{-i(\theta+\omega t)} + \bar{z}_-(0)e^{-i(\theta-\omega t)} \tag{46}$$

with $z_\pm(0)$ arbitrary initial amplitudes.

The addition of nonlinear terms compatible with the $O(2)$ symmetry greatly restricts the possible equilibria. We can represent $O(2)$ on four-dimensional vectors $(z_+, z_-)$ via:

$$\begin{aligned} S_{\theta_0}(z_+, z_-) &= (e^{i\theta_0}z_+, e^{i\theta_0}z_-) \\ \kappa(z_+, z_-) &= (\bar{z}_-, \bar{z}_+) \end{aligned} \tag{47}$$

The mathematics of the derivation of the normal form are also more complicated than in the case of a steady bifurcation. Without justification, we give the simplest cubic order equivariant system of evolution equations:

$$\frac{d}{dt}\begin{pmatrix} z_+ \\ z_- \end{pmatrix} = \begin{pmatrix} \left[\mu + i\omega + a|z_-|^2 + b(|z_+|^2 + |z_-|^2)\right]z_+ \\ \left[\mu - i\omega + \bar{a}|z_+|^2 + \bar{b}(|z_+|^2 + |z_-|^2)\right]z_- \end{pmatrix} \tag{48}$$

Note that equations (48) are independent of the phases $\phi_\pm$. Defining $z_\pm = r_\pm e^{i\phi_\pm}$, we derive

$$\frac{dr_\pm}{dt} = \big(\mu + a_r r_\mp^2 + b_r(r_+^2 + r_-^2)\big)r_\pm \tag{49a}$$

$$\frac{d\phi_\pm}{dt} = \pm\big(\omega + a_i r_\mp^2 + b_i(r_+^2 + r_-^2)\big) \tag{49b}$$

The solutions for which $dr_\pm/dt = 0$ are:

$$\begin{aligned} \text{the origin: } & r_+ = 0, r_- = 0 \\ \text{the left traveling waves: } & r_+ = \sqrt{-\frac{\mu}{b_r}}, r_- = 0, \quad \dot{\phi}_+ = \omega - \frac{\mu b_i}{b_r} \\ \text{the right traveling waves: } & r_+ = 0, r_- = \sqrt{-\frac{\mu}{b_r}}, \quad \dot{\phi}_- = -\big(\omega - \frac{\mu b_i}{b_r}\big) \\ \text{the standing waves: } & r_+ = r_- = \sqrt{-\frac{\mu}{a_r + 2b_r}}, \quad \dot{\phi}_\pm = \pm\big(\omega - \frac{\mu(a_i + 2b_i)}{a_r + 2b_r}\big) \end{aligned} \tag{50}$$

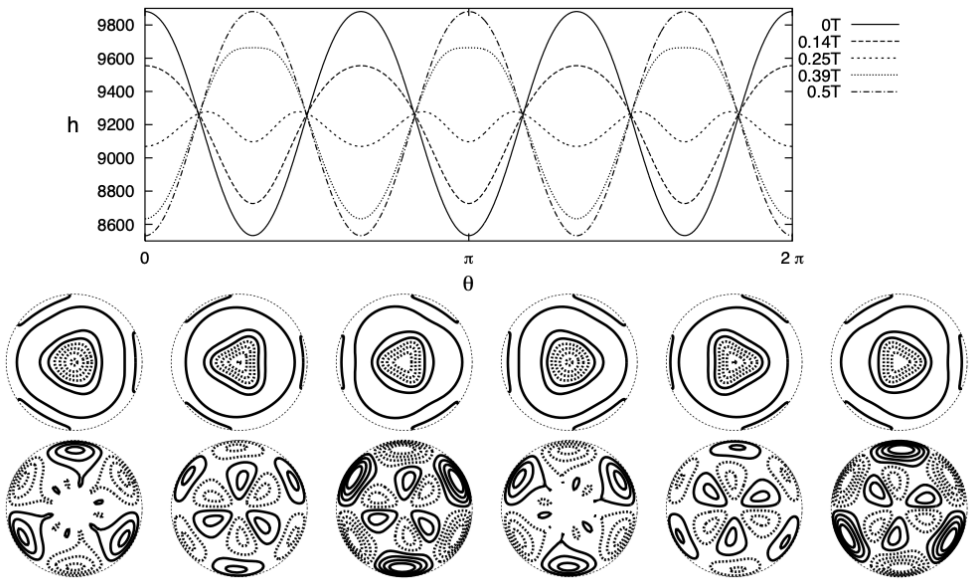


Figure 7: Standing waves in Rayleigh-Bénard convection in a cylinder with $\Gamma$ = R/H = 1.47 and Pr = 1 at at Ra = 26000. Top row: temperature versus $\theta$ at ($r$,$z$) = (0.7,0.3) at five successive times during one oscillation period T. Middle and bottom rows: contours of temperature (middle) and of azimuthal velocity (bottom) on the midplane at t = 0, T/6, 2T/6, 3T/6, 4T/6, 5T/6. From Borońska and Tuckerman [2].

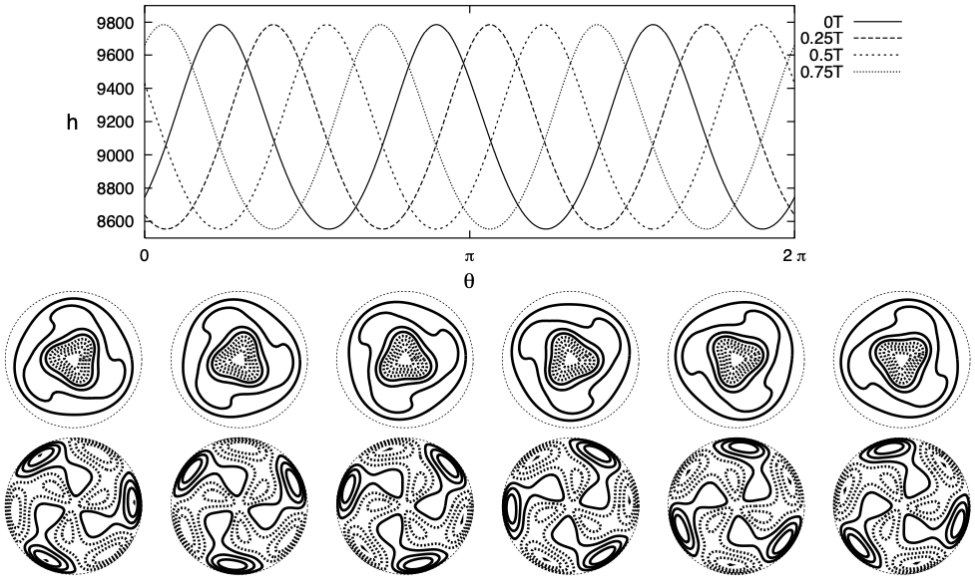


Figure 8: Counter-clockwise traveling wave in Rayleigh-Bernard convection in a cylinder with $\Gamma$ = R/H = 1.47 and Pr = 1 at Ra = 26 000. Top row: temperature versus angle $\theta$ for ($r$,$z$) = (0.7, 0.3), at four different instants during one oscillation period T . Middle and bottom rows: contours of temperature (middle) and of azimuthal velocity (bottom) on the midplane at t = 0, T/6, 2T/6, 3T/6, 4T/6, 5T/6. From Borońska and Tuckerman [2].

Standing and traveling waves are illustrated for a simulation of Rayleigh-Bernard convection in a cylindrical container in figures 7 and 8.

According to the signs and magnitudes of $a$ and $b$, the standing waves and traveling waves branch in the same or the opposite directions in $\mu$. If $b_r < 0$ ($> 0$), then the traveling waves exist for $\mu > 0$ ($< 0$). If $a_r + 2b_r < 0$ ($> 0$), then the standing waves exist for $\mu > 0$ ($< 0$). The lines $b_r = 0$ and $a_r + 2b_r = 0$ thus divide the $(a_r, b_r)$ plane into four sections, as shown in figure 9.

The stability of these states is calculated as follows. At the origin, since angles are not defined, we must write the Jacobian in its Cartesian representation, as we did in (40) concerning the circle pitchfork. We will not do this here and just state that at the origin, the Jacobian is $\mu$ times the identity and hence has four eigenvalues that change sign at $\mu$, along with a four-dimensional eigenspace.

For the non-zero states, we can write the Jacobian in the polar $(r_+, r_-, \phi_+, \phi_-)$ coordinates:

$$\begin{bmatrix} \mu + a_r r_-^2 + b_r(r_+^2 + r_-^2) + 2b_r r_+^2 & 2(a_r + b_r) r_- r_+ & 0 & 0 \\ 2(a_r + b_r) r_- r_+ & \mu + a_r r_+^2 + b_r(r_+^2 + r_-^2) + 2b_r r_-^2 & 0 & 0 \\ 2b_i r_+ & 2(a_i + b_i) r_- & 0 & 0 \\ -2(a_i + b_i) r_+ & -2b_i r_+ & 0 & 0 \end{bmatrix} \tag{51}$$

Since (51) is block lower-triangular, its eigenvalues and eigenvectors are those of its diagonal blocks, as shown by the following reasoning:

$$\begin{bmatrix} A & 0 \\ C & D \end{bmatrix} \begin{bmatrix} X \\ Y \end{bmatrix} = \lambda \begin{bmatrix} X \\ Y \end{bmatrix} \tag{52}$$

$$\begin{cases} AX & = \lambda X \\ CX + DY & = \lambda Y \end{cases} \Rightarrow \begin{cases} (\lambda, X) \text{ is an eigenpair of } A \\ Y = (\lambda I - D)^{-1} CX \end{cases} \text{ or } \begin{cases} X = 0 \\ (\lambda, Y) \text{ is an eigenpair of } D \end{cases} \tag{53}$$

Therefore, the eigenvalues of (51) are those of the lower-right and upper-left blocks. The lower-right block contains only zeros, leading to two zero eigenvalues, whose corresponding eigenvectors are $\phi_\pm$. The eigenvalues of the upper-left block are obtained via the formula for a general $2 \times 2$ matrix:

$$\begin{bmatrix} a & b \\ c & d \end{bmatrix} \tag{54}$$

via

$$\lambda_\pm = \frac{a+d}{2} \pm \sqrt{\left(\frac{a-d}{2}\right)^2 + bc} \tag{55}$$

(In (55), $a, b, c, d$ are unrelated to the notation used for the Hopf-$O(2)$ problem.) Substituting the elements of (51) and the solutions (50) into (55) leads to

$$\begin{aligned} \text{the origin:} \quad & \mu \text{ along } r_+, \quad \mu \text{ along } r_- \\ \text{the left traveling waves:} \quad & -2\mu \text{ along } r_+, \quad -\frac{a_r \mu}{b_r} \text{ along } r_- \\ \text{the right traveling waves:} \quad & -2\mu \text{ along } r_-, \quad -\frac{a_r \mu}{b_r} \text{ along } r_+ \\ \text{the standing waves:} \quad & -2\mu \text{ along } (r_+, r_-), \quad \frac{2a_r \mu}{a_r + 2b_r} \text{ perpendicular to } (r_+, r_-) \end{aligned} \tag{56}$$

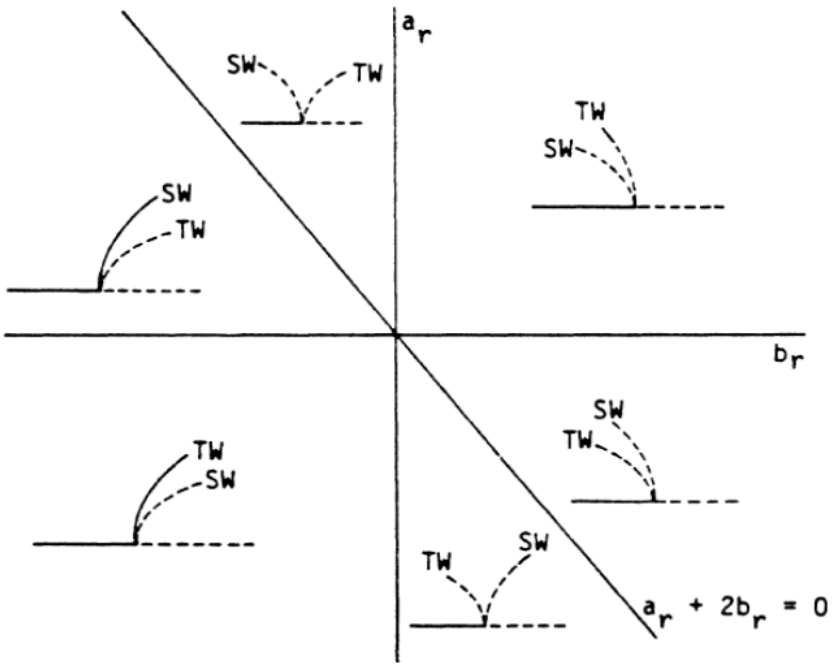


Figure 9: Stability and branching direction of standing waves (SW) and traveling waves (TW) in the parameter plane of the nonlinear coefficients $(a_r, b_r)$. From Knobloch [3].

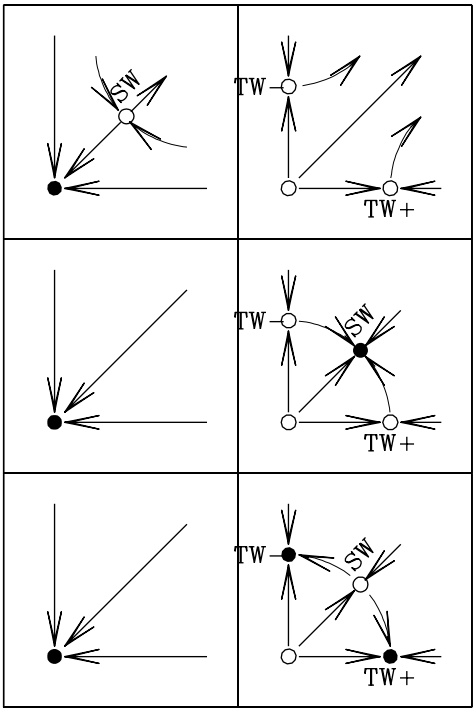


Figure 10: Phase diagrams for Hopf bifurcation with $O(2)$ symmetry when $b_r < 0$. Each diagram shows the $(r_+,r_-)$ plane. Left diagrams: $\mu < 0$. Right diagrams: $\mu > 0$. Top row: $-2b_r < a_r$. Middle row: $0 < a_r < -2b_r$. Bottom row: $a_r < 0$.

If $b_r < 0$, then the traveling waves exist for $\mu > 0$, as shown in (50). Since $-2\mu < 0$, they are stable if and only if $a_r/b_r > 0$, i.e., in the lower left quadrant of the $(a_r, b_r)$ plane, as shown in figure 9. If $b_r > 0$, then the traveling waves exist for $\mu < 0$, so $-2\mu > 0$ and they are not stable. Similarly, if $a_r + 2b_r < 0$, then the standing waves exist for $\mu > 0$ and they are stable if $a_r > 0$, i.e., in the upper-left wedge of the $(a_r, b_r)$ plane. If $a_r + 2b_r > 0$, then the standing waves exist for $\mu < 0$ and so $-2\mu > 0$ and they are not stable.

Some general conclusions are that either the standing waves or the traveling waves are stable, or neither are stable. If one solution is stable, it is that which has the largest amplitude $\sqrt{r_+^2 + r_-^2}$. If neither is stable, then $r_\pm \to \infty$ for some choices of initial conditions or $\mu$-values, unless higher order terms are added to (48) or (49a). This is shown in figures 9 and 10.

To write down the symmetries of the solutions, we must introduce another transformation, namely that of translation in time:

$$T_{t_0} u(t) \equiv u(t + t_0) \tag{57}$$

The group of all the translations in time $S_{t_0}$ is called $S^1$. The original homogeneous stationary state, before bifurcation to waves, has the full space-time symmetry group $O(2) \times S^1$. A traveling wave solution has the space-time symmetry

$$(T_{t_0} S_{\omega t_0} u)(\theta, t) \equiv u(\theta + \omega t_0, t + t_0) = u(\theta, t) \tag{58}$$

for any $t_0$. This set of space-time symmetries, parametrized by $t_0$, forms a group isomorphic to $SO(2)$, which is called $\widetilde{SO}(2)$. The subgroup of transformations leaving a particular solution invariant is called its isotropy subgroup; the isotropy subgroup of a traveling wave solution is $\widetilde{SO}(2)$. Standing waves have an ordinary spatial reflection symmetry in $\theta$:

$$(\kappa u)(\theta, t) \equiv u(-\theta) = u(\theta, t) \tag{59}$$

(For simplicity, we have taken the axis of reflection, which does not move, to be at $\theta = 0$.) Standing waves also have the space-time reflection symmetry:

$$(T_{\pi/\omega} S_\pi u)(\theta, t) \equiv u\left(\theta + \pi, t + \frac{\pi}{\omega}\right) = u(\theta, t) \tag{60}$$

The transformation in (60) is called $Z_2^c$ and is a special case of that in (58). The group of transformations leaving a standing wave solution invariant, i.e., its isotropy subgroup, is called $Z_2 \times Z_2^c$. We can arrange the original symmetry group and the isotropy subgroups in a diagram called the lattice of isotropy subgroups, as shown in figure 11.

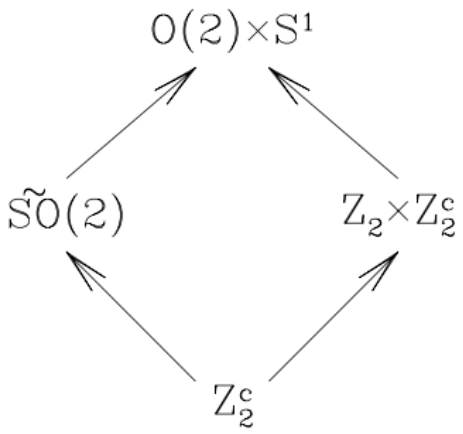


Figure 11: Lattice of isotropy subgroups for $O(2) \times S^1$. Traveling waves have the isotropy subgroup $\widetilde{SO}(2)$, while standing waves have the isotropy subgroup $Z_2 \times Z_2^c$.

## References

[1] J. Antonijoan, F. Marques, and J. Sanchez. Non-linear spirals in the taylor–couette problem. *Physics of Fluids*, 10:829–838, 1998.

[2] K. Borońska and L. S. Tuckerman. Standing and travelling waves in cylindrical rayleigh–bénard convection. *J. Fluid Mech.*, 559:279–298, 2006.

[3] E. Knobloch. Oscillatory convection in binary mixtures. *Phys. Rev. A*, 34:1538–1549, 1986.

[4] R. Tagg. The Couette-Taylor problem. *Nonlinear Science Today*, 4:1–25, 1994.

# GFD 2025 Lecture 8: Applications to the Eckhaus Instability, D4 Scenario, and Others

Laurette Tuckerman; notes by Edoardo Bellincioni, Marion Cocusse and Alexandre Tlili

June 25, 2025

In these lecture notes, we examine how symmetries evolve as fluid systems undergo bifurcations. Using Rayleigh–Bénard convection in a cylindrical cell as a primary example, we trace how solutions emerge from a symmetric base state and progressively break symmetries through successive bifurcations. The mathematical framework of group theory, particularly dihedral groups like $\mathbb{D}_4$, helps us understand which solutions can exist and how they relate to one another. We explore several applications including Couette–Taylor flow and shear-driven cavity flows, showing how symmetry considerations predict the structure of bifurcation diagrams. The notes conclude with the Eckhaus instability, demonstrating how spatially periodic patterns can become unstable through secondary bifurcations.

## 1 An Illustrative Example of $\mathbb{O}(2)$ Symmetry

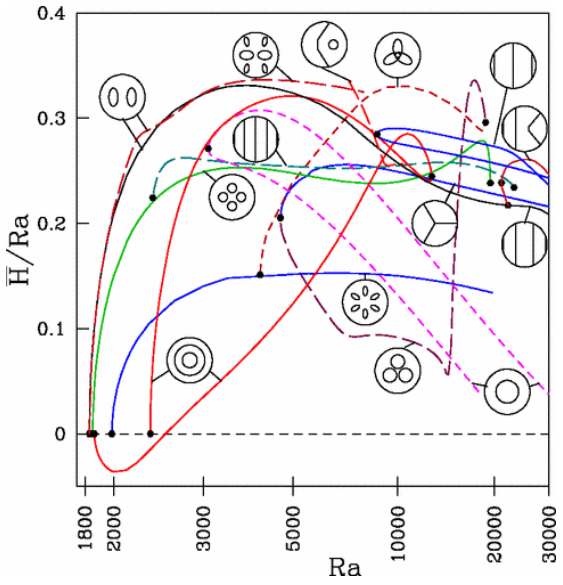


Figure 1: *Borońska and Tuckerman [2], figure 2)* Bifurcation diagram for Rayleigh-Bénard convection in a cylindrical cell, showing Rayleigh number in the horizontal and a response parameter in the vertical. The solid and dashed curves correspond to steady states (without specifying the stability of the states). The bifurcations are indicated by the solid dots. The small sketches are schematic representations of the states on each branch.

Borońska and Tuckerman [2] numerically investigated the stability of Rayleigh–Bénard states, as previously described in an experimental work by Hof et al. [4]. This case is illustrative in the sense that its bifurcation diagram (figure 1) is densely populated with curves in a seemingly random fashion, but qualitative arguments can be extracted by discussing the symmetries of the problem.

A cylindrical Rayleigh–Bénard cell has two classes of symmetries:

- $\mathbb{O}(2)$ symmetry in the angle $\theta$, hence azimuthal rotation and reflection:

  $$[R_{\theta_0}(u_r, u_\theta, u_z, T)](r, \theta, z) \equiv (u_r, u_\theta, u_z, T)(r, \theta - \theta_0, z)$$

  and

  $$[\kappa_{\theta_0}(u_r, u_\theta, u_z, T)](r, \theta, z) \equiv (u_r, -u_\theta, u_z, T)(r, 2\theta_0 - \theta, z)$$

- Boussinesq symmetry $\mathbb{Z}_2$, associated to the transformation $B$ that maps $z \mapsto -z$ and $T \mapsto -T$, which corresponds to flipping the vertical direction *and* the hot/cold plates. (In the $z$-midplane cross-sections in the figures, $B$ corresponds to inverting the colorbars):

  $$[B(u_r, u_\theta, u_z, T)](r, \theta, z) \equiv (u_r, u_\theta, -u_z, -T)(r, \theta, -z)$$

These symmetry operators are *generators* for the group $\mathbb{O}(2) \times \mathbb{Z}_2$, which consist of all products of these operators.

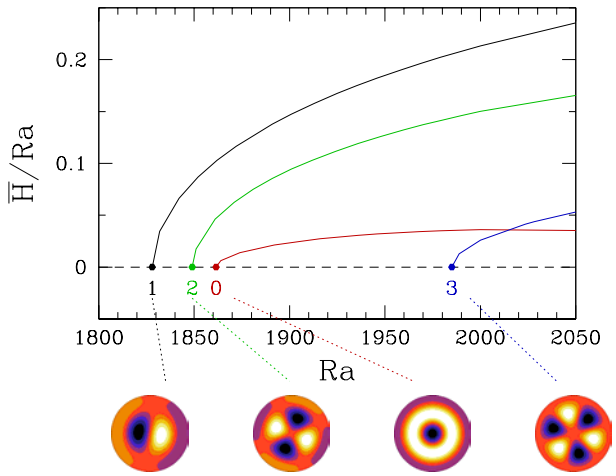


Figure 2: *(from Borońska and Tuckerman [2], figure 3).* Expanded version of the low-Ra range of figure 1. Four of the branches that originate from the conductive state are identified as $m = 1$ (*dipole*), $m = 2$ (*pizza*) $m = 0$ (*two-tori*), and $m = 3$ (marigold).

We first analyze the bifurcation diagram close to the conductive state, which corresponds to $\overline{H}/\mathrm{Ra} = 0$, the dashed horizontal line in figure 1. The quantity $\overline{H}$ is the maximum absolute value over the ring at ($r = 0.3$, $\theta$, $z = 0$) of the deviation of the temperature from that of the conductive state. Because the conductive state is homogeneous in $\theta$, analysis of its linear stability leads to eigenfunctions, which are necessarily trigonometric functions of $\theta$. The branches that bifurcate from the conductive state are not trigonometric, because of the harmonics produced by nonlinear terms, but they are periodic functions of $\theta$ with the same wavelength as the eigenvectors. An expanded portion of the lower left portion of figure is shown in figure 2.

From their horizontal cross-sections, it is clear that all of the branches that bifurcate from the conductive state are periodic in $\theta$ with a wavenumber $m$. The mode (eigenvector) $m = 1$ is referred to as a *dipole* mode, $m = 2$ as *pizza*, $m = 0$ as *two-tori*, and the $m = 3$ as *marigold*. We will analyze the evolution of each branch in the order that they bifurcate from the homogeneous conductive state. In each case, except for $m = 0$, the bifurcation is a circle pitchfork leading from the conductive branch with its $B \times \mathbb{O}(2)$ symmetry to a set ("circle") of branches. Each state along the branch has $\mathbb{D}_{2m}$ symmetry, where the group is generated by reflection $\kappa_{\theta_0}$ for some $\theta_0$ and by the $2m$-fold rotation $B\,R_{\pi/m}$, as we will see below.

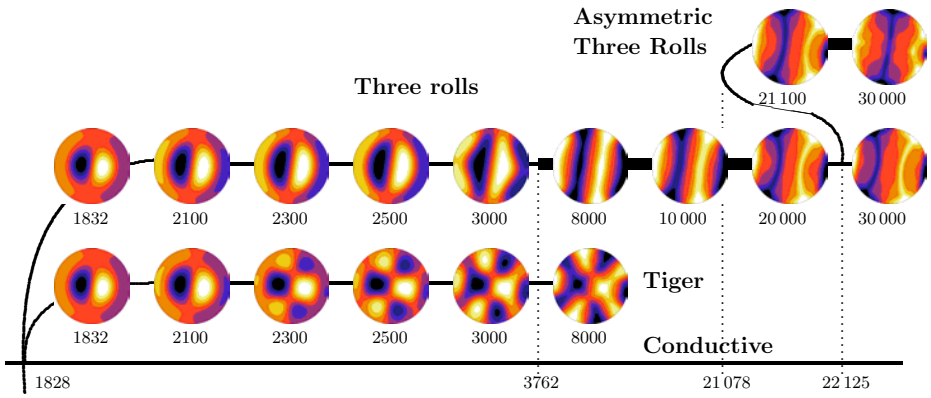


Figure 3: *(from Borońska and Tuckerman [2], figure 14)* Schematic bifurcation diagram following the evolution of the $m = 1$ modes that originate and evolve from the conductive state. The thicker line indicates a stable portion of the branch.

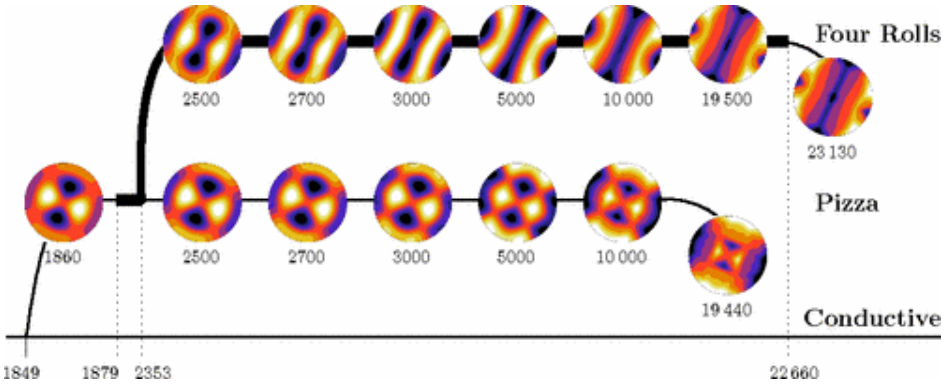


Figure 4: *(from Borońska and Tuckerman [2], figure 5)* Schematic bifurcation diagram for the $m = 2$ modes that originate and evolve from the conductive state. The thicker line indicates a stable portion of the branch.

Starting with $m = 1$, shown in figure 3, we note that this bifurcation leads to two branches that emerge from the same bifurcation point but separate at higher Ra. Following the upper branch, we notice that the dipole evolves into *three rolls*, then becomes stable and later further undergoes a bifurcation leading to *asymmetric three rolls*, where the asymmetry here means broken $\mathbb{D}_2$ symmetry. The lower branch also evolves, creating a patched pattern, which at higher Ra evolves into what the authors call a *tiger* pattern. We note that even though the two branches evolve, they both remain invariant under the transformations generated by $BR_\pi$ and $\kappa_0$, where $\kappa_0$

is azimuthal reflection with respect to an axis, which here is almost horizontal, leading to symmetry group $\mathbb{D}_2 \cong \mathbb{Z}_2 \times \mathbb{Z}_2$. Indeed, symmetries can change only at a bifurcation. A secondary pitchfork bifurcation to the *asymmetric three-roll state* breaks the $\mathbb{Z}_2 \times \mathbb{Z}_2$ symmetry, leaving only the $\mathbb{Z}_2$ symmetry corresponding to $\kappa_0$. Thus, bifurcations lead to successive symmetry breakings of steady solutions. The remaining symmetries form a subgroup of the symmetries prior to the bifurcation and are conserved along each branch until the next bifurcation.

The branch that corresponds to $m = 2$ is shown in figure 4. We note that at Ra $\approx 1879$, the branch transitions from being unstable to stable, and at Ra $\approx 2353$ there is a secondary pitchfork bifurcation. The bottom branch retains the features of the initial *pizza* pattern, which is symmetric under the transformations generated by $BR_{\pi/2}$ and $\kappa_0$ where $\kappa_0$ is either of the two azimuthal reflections preserving the symmetry of the *pizza*; these generate the group $\mathbb{D}_4$. The bifurcation leading to the generation of the *four-roll* pattern breaks the $\mathbb{D}_4$ symmetry and only retains the $\mathbb{D}_2 \cong \mathbb{Z}_2 \times \mathbb{Z}_2$ symmetry, which is a subgroup of $\mathbb{D}_4$.

Figure 2 showed only a single branch with $m = 0$, but a closer look at the Ra $\gtrsim 2050$ region of figure 1 reveals a second branch (in red), also marked as a torus mode. The evolution of all of these branches is shown in figure 5. It is clear that, in these cases, the $\mathbb{O}(2)$ symmetry in $\theta$ is retained.

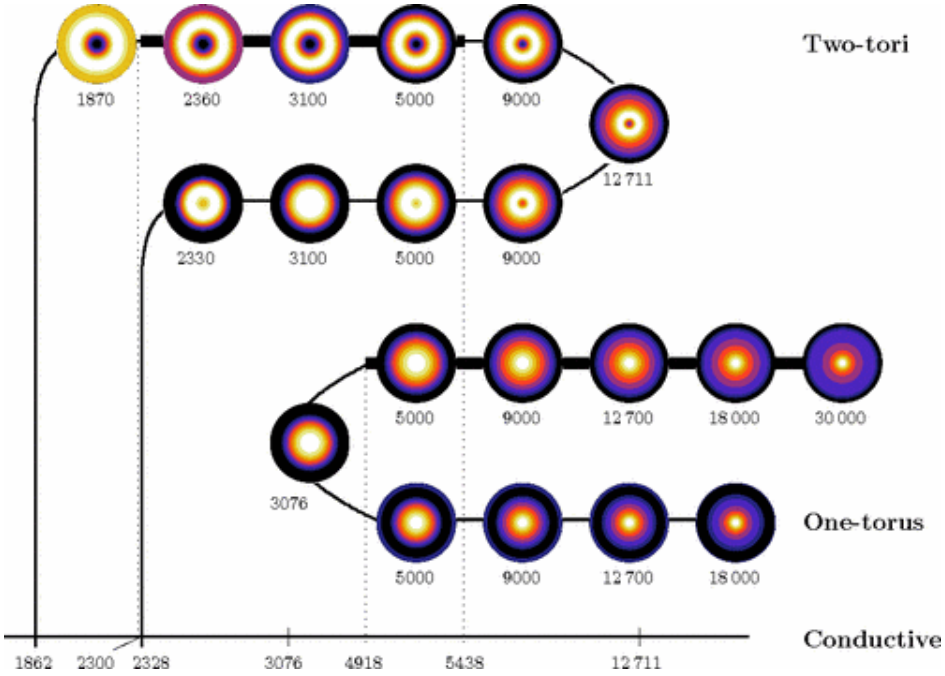


Figure 5: *(from Borońska and Tuckerman [2], figure 8)* Schematic bifurcation diagram for the $m = 0$ modes that originate and evolve from the conductive state, plus the *one-torus* state, which does not originate from the conductive state. The thicker line indicates a stable portion of the branch.

However the Boussinesq symmetry is broken in an ordinary (not circle) pitchfork bifurcation, so that for each branch shown in figure 5, there exists another branch with the yellow and purple colors (hot vs. cold along with upflow vs. downflow) reversed. The two *two-tori* branches are connected via a turning point at Ra $= 12711$, with the top branch being mostly stable and the bottom being unstable. The *one-torus* branch does not bifurcate from the conductive state, but rather appears via a turning point at Ra $= 3076$. Like the *two-tori*, part of the upper branch is stable while the lower branch is unstable.

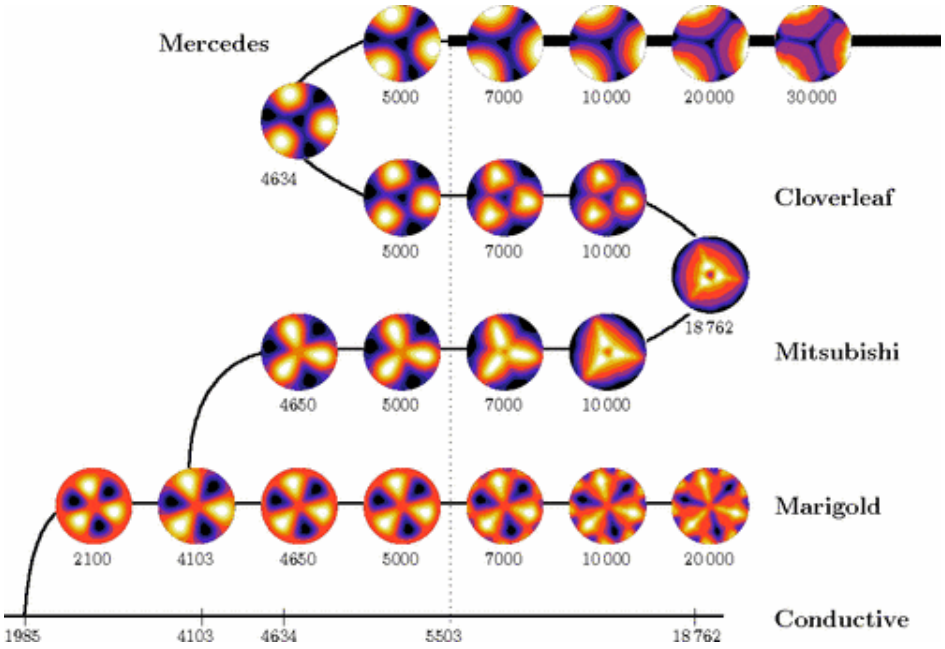


Figure 6: *(from Borońska and Tuckerman [2], figure 12)* Schematic bifurcation diagram for the $m = 3$ modes that originate and evolve from the conductive state. The thicker line indicates stability.

Lastly, we address the evolution of the branch corresponding to $m = 3$. The conductive branch undergoes a circle pitchfork bifurcation at Ra $= 1985$ creating the *marigold* branch, which is always unstable and which has $\mathbb{D}_6 \cong \mathbb{D}_3 \times \mathbb{Z}_2$ symmetry. At Ra $= 4103$, the *marigold* branch gives rise to the (unstable) *Mitsubishi* branch through a pitchfork bifurcation. This pitchfork breaks the $BR_{2\pi/6}$ symmetry, as seen by the fact that in the *Mitsubishi* flows, the purple and yellow portions are qualitatively different. The *Mitsubishi* branch then undergoes a turning point at Ra $= 18762$, evolving into the *cloverleaf* branch, which, through another turning point at Ra $= 4634$, evolves into the *Mercedes* branch. The *Mercedes* branch becomes stable for $Ra \geq 5503$ and is the only stable branch of the set. *Mitsubishi*, *cloverleaf* and *Mercedes* states all have $\mathbb{D}_3$ symmetry.

## 2 A Bit of Theory About the Dihedral $\mathbb{D}_4$ Group

The dihedral group $\mathbb{D}_4$ corresponds to the symmetries of the square. This group is generated by the two following transformations: the rotation $\rho$ of angle $\pi/2$, and the reflection $\kappa$ along the horizontal axis. In complex notation, these two transformations are written as

$$\begin{cases} \rho : z \longmapsto e^{i\pi/2} z = iz \\ \kappa : z \longmapsto \overline{z} \end{cases} \tag{1}$$

where $\overline{z}$ stands for the complex conjugate of $z$. For example, a reflection along the vertical axis is given by $\rho^{-1}\kappa\rho$ (or equivalently by $\rho^2\kappa$). Similarly, a reflection along the diagonal starting from the upper-right corner can written as $\rho\kappa$ (Figure 7). In general, the group $\mathbb{D}_4$ is formed by the eight distinct elements that can be generated as products of $\kappa$ and $\rho$. The multiplication table (called the *Cayley table* or *group table*) of $\mathbb{D}_4$ is given in Table 1.

The ten subgroups of $\mathbb{D}_4$ (i.e. the subsets which are themselves groups) are

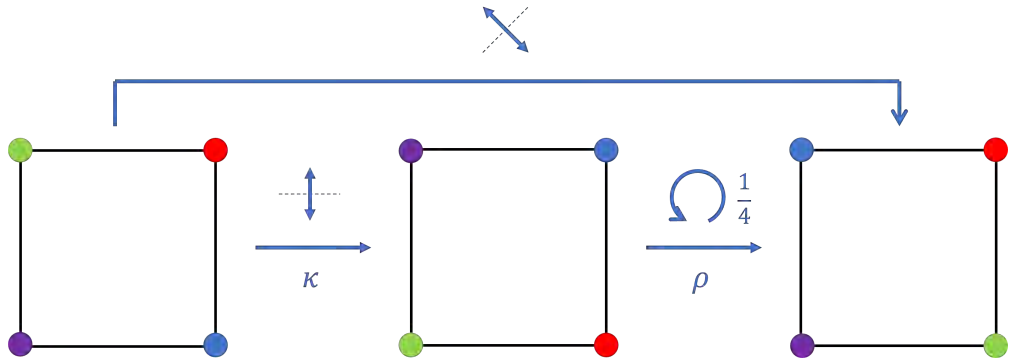


Figure 7: $\mathbb{D}_4$ is the group of symmetries of a square. For instance, the reflection along the diagonal starting from the upper-right corner can be expressed as a combination of a reflection $\kappa$ along the horizontal axis, and a counter-clockwise rotation $\rho$ by $\pi/2$. Colors track the positions of the corners.

| | $e$ | $\rho$ | $\rho^2$ | $\rho^3$ | $\kappa$ | $\kappa\rho$ | $\kappa\rho^2$ | $\kappa\rho^3$ |
|---|---|---|---|---|---|---|---|---|
| $e$ | $e$ | $\rho$ | $\rho^2$ | $\rho^3$ | $\kappa$ | $\kappa\rho$ | $\kappa\rho^2$ | $\kappa\rho^3$ |
| $\rho$ | $\rho$ | $\rho^2$ | $\rho^3$ | $e$ | $\kappa\rho^3$ | $\kappa$ | $\kappa\rho$ | $\kappa\rho^2$ |
| $\rho^2$ | $\rho^2$ | $\rho^3$ | $e$ | $\rho$ | $\kappa\rho^2$ | $\kappa\rho^3$ | $\kappa$ | $\kappa\rho$ |
| $\rho^3$ | $\rho^3$ | $e$ | $\rho$ | $\rho^2$ | $\kappa\rho$ | $\kappa\rho^2$ | $\kappa\rho^3$ | $\kappa$ |
| $\kappa$ | $\kappa$ | $\kappa\rho$ | $\kappa\rho^2$ | $\kappa\rho^3$ | $e$ | $\rho$ | $\rho^2$ | $\rho^3$ |
| $\kappa\rho$ | $\kappa\rho$ | $\kappa\rho^2$ | $\kappa\rho^3$ | $\kappa$ | $\rho^3$ | $e$ | $\rho$ | $\rho^2$ |
| $\kappa\rho^2$ | $\kappa\rho^2$ | $\kappa\rho^3$ | $\kappa$ | $\kappa\rho$ | $\rho^2$ | $\rho^3$ | $e$ | $\rho$ |
| $\kappa\rho^3$ | $\kappa\rho^3$ | $\kappa$ | $\kappa\rho$ | $\kappa\rho^2$ | $\rho$ | $\rho^2$ | $\rho^3$ | $e$ |

Table 1: The multiplication table for the dihedral group $\mathbb{D}_4$ shows all products $ab$, where $a$ is the first column and $b$ in the first row. Note that the group is not commutative, and the commutation rule is given by $\rho\kappa = \kappa\rho^{-1}$.

- With 2 elements : $\{e, \rho^2\}$, $\{e, \kappa\}$, $\{e, \kappa\rho\}$, $\{e, \kappa\rho^2\}$ and $\{e, \kappa\rho^3\}$,
- With 4 elements : $\{e, \rho, \rho^2, \rho^3\}$, $\{e, \rho^2, \kappa, \kappa\rho^2\}$ and $\{e, \rho^2, \kappa\rho, \kappa\rho^3\}$

and the two trivial subgroups $\{e\}$ and $\mathbb{D}_4$ itself. The four subgroups consisting of two elements are all isomorphic to (i.e., have the same structure as) $\mathbb{Z}_2$, but the three subgroups of four elements are of two fundamentally different types. Indeed, we have $\{e, \rho, \rho^2, \rho^3\} \cong \mathbb{Z}_4$ but $\{e, \rho^2, \kappa, \kappa\rho^2\} \cong \{e, \rho^2, \kappa\rho, \kappa\rho^3\} \cong \mathbb{Z}_2 \times \mathbb{Z}_2$, where $\cong$ designates isomorphism.

Finally, one can observe that the multiplication table of $\mathbb{D}_4$ is partitioned into four regions, giving it a large-scale structure (Figure 8). More precisely, we have $(\rho^n)(\rho^m) \in \{\rho^\ell, \ell \in \mathbb{Z}\}$, $(\kappa\rho^n)(\rho^m) \in \{\kappa\rho^\ell, \ell \in \mathbb{Z}\}$, $(\rho^n)(\kappa\rho^m) \in \{\kappa\rho^\ell, \ell \in \mathbb{Z}\}$ and $(\kappa\rho^n)(\kappa\rho^m) \in \{\rho^\ell, \ell \in \mathbb{Z}\}$ for all integers $n$ and $m$. In a sense, we would like to state that

$$\begin{aligned} \overbrace{\{\rho^\ell\}}^{\text{rot.}} \cdot \overbrace{\{\rho^\ell\}}^{\text{rot.}} &= \overbrace{\{\kappa\rho^\ell\}}^{\text{flip}} \cdot \overbrace{\{\kappa\rho^\ell\}}^{\text{flip}} = \overbrace{\{\rho^\ell\}}^{\text{rot.}} \\ \underbrace{\{\kappa\rho^\ell\}}_{\text{flip}} \cdot \underbrace{\{\rho^\ell\}}_{\text{rot.}} &= \underbrace{\{\rho^\ell\}}_{\text{rot.}} \cdot \underbrace{\{\kappa\rho^\ell\}}_{\text{flip}} = \underbrace{\{\kappa\rho^\ell\}}_{\text{flip}} \end{aligned} \tag{2}$$

such that the subsets $\{\rho^\ell\}$ and $\{\kappa\rho^\ell\}$ "behave" as elements of $\mathbb{Z}_2$.

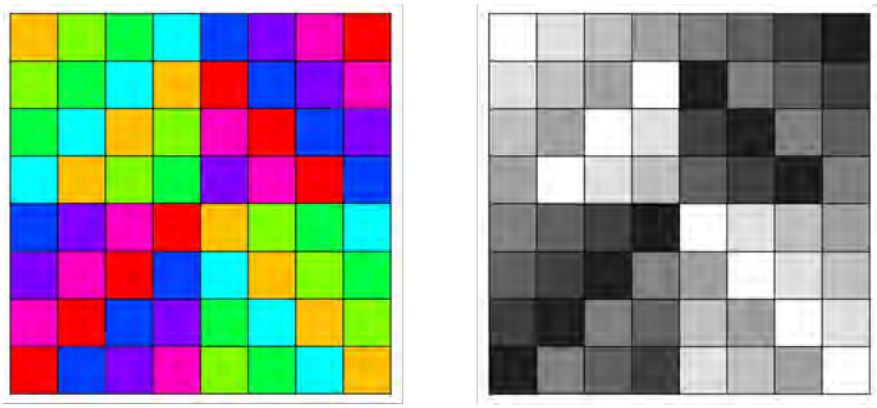

Figure 8: *(adapted from Weisstein [8], figure 2)* Visual multiplication table for the dihedral group $\mathbb{D}_4$. Colors are chosen to highlight the large-scale $2 \times 2$ structure of the multiplication table, which will be discussed using the concept of quotient group.

This idea is formalized using the concept of quotient group. Indeed, given a normal subgroup $N$ of a group $G$ (i.e., $N$ verifies the property that $\forall n \in N, \forall g \in G, g^{-1}ng \in N$), one can define the quotient group $G/N = \{gN, g \in G\}$, where $gN = \{gn, n \in N\}$. In other words, $G/N$ is the set of equivalence classes to the modulo relation $x \sim y \iff yx^{-1} \in N$. Using the property that $N$ is normal, one can show that the set $G/N$ forms a group under the composition law $\cdot$ defined as $(aN)\cdot(bN) = (ab)N$. However, even though it is tempting to say that $G/N \cong G_1 \implies G \cong N \times G_1$, it is not true in general. Instead, the useful relationship between $G/N$, $G$ and $N$ can be expressed with the concept of group extension, but this is beyond the scope of this lecture.

In the case of the dihedral group $\mathbb{D}_4$, the subgroup of rotations $N = \{e, \rho, \rho^2, \rho^3\} \cong \mathbb{Z}_4$ is a normal subgroup and we can thus construct the quotient group $\mathbb{D}_4/N = \{N, \kappa N\}$ formed by the set of rotations $N$ and the set of reflections $\kappa N$. We can easily show that $\mathbb{D}_4/N$ is isomorphic to $\mathbb{Z}_2$, which confirms the intuition presented in (2), but $\mathbb{D}_4$ is not isomorphic to $N \times \mathbb{Z}_2 \cong \mathbb{Z}_4 \times \mathbb{Z}_2$. The other non-trivial normal subgroups of $\mathbb{D}_4$ are $\{e, \rho^2\} \cong \mathbb{Z}_2$, $\{e, \rho^2, \kappa, \kappa\rho^2\} \cong \mathbb{Z}_2 \times \mathbb{Z}_2$ and $\{e, \rho^2, \kappa\rho, \kappa\rho^3\} \cong \mathbb{Z}_2 \times \mathbb{Z}_2$.

## 3 A System with $\mathbb{D}_4$ Symmetry

As discussed previously, the $\mathbb{D}_4$ group describes the symmetries of a square. Figure 9a illustrates the fact that a rotation of 90° of any field – an eigenvector or a nonlinear solution – yields a dynamically equivalent field. Figure 9b illustrates summation: the sum of two eigenvectors with the same eigenvalue is an eigenvector with the same eigenvalue. Summation does *not* create new nonlinear solutions. The situation is as follows. An eigenvector can be rotated by 90° to form another eigenvector with the same eigenvalue. Furthermore, *any* linear combination of these two eigenvectors (and not just the equal superpositions illustrated in Figure 9b) is also an eigenvector, i.e. there exists a doubly infinite set of eigenvectors, all with the same eigenvalue. The inclusion of nonlinear terms, which are consistent with (equivariant with respect to) $\mathbb{D}_4$ symmetry, greatly restricts the number of solutions. We are familiar with the fact that nonlinear terms determine the *amplitude* of nonlinear solutions (unlike eigenvectors, which can have any amplitude). More generally, nonlinear terms also drastically restrict the *form* of possible solutions. In the case of $\mathbb{D}_4$, precisely eight solutions are produced by a pitchfork bifurcation, as we shall now discuss.

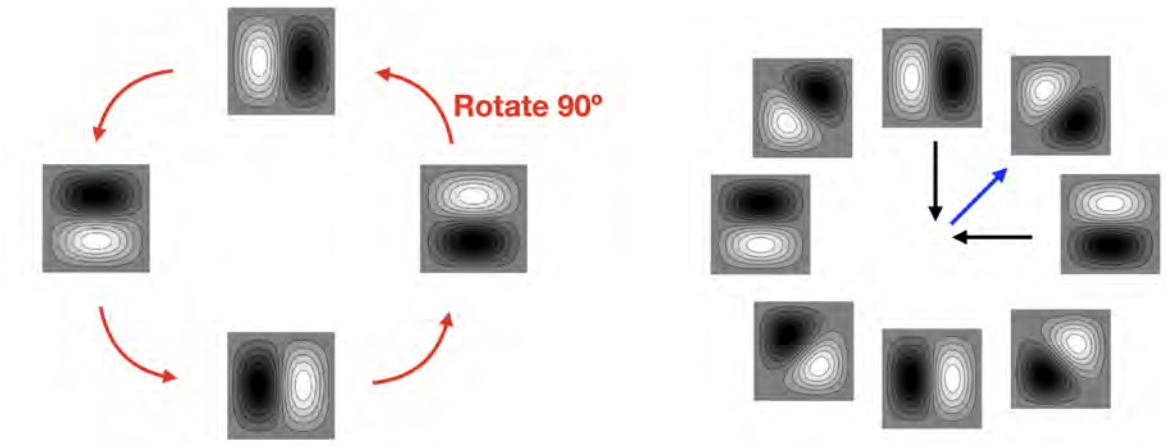


(a) (b)

Figure 9: Illustration of the properties of the $\mathbb{D}_4$ symmetry on convective rolls. (a) 90° rotation of an eigenvector leads to an eigenvector with same eigenvalue, rotation of a nonlinear solution leads to another nonlinear solution. (b) The sum of two eigenvectors with the same eigenvalue is an eigenvector with the same eigenvalue.

The following system captures the essence of a bifurcation breaking $\mathbb{D}_4$ symmetry:

$$\dot{p} = (\mu - ap^2 - bq^2)p, \tag{3a}$$
$$\dot{q} = (\mu - bp^2 - aq^2)q. \tag{3b}$$

This system has eight non trivial equilibrium solutions; we can call four of them rectangular and call the other four diagonal.

$$\text{rectangular solutions} : \begin{cases} p_1 = \pm\sqrt{\mu/a}, & q_1 = 0, \\ p_2 = 0, & q_2 = \pm\sqrt{\mu/a}, \end{cases} \tag{4}$$

$$\text{diagonal solutions} : \begin{cases} p_3 = \pm\sqrt{\mu/(a+b)}, & q_3 = \pm\sqrt{\mu/(a+b)}, \\ p_4 = \mp\sqrt{\mu/(a+b)}, & q_4 = \mp\sqrt{\mu/(a+b)}. \end{cases} \tag{5}$$

They are represented in the $(p, q)$ plane in figure 10. Figure 11 shows the stability and branching directions of the rectangular and diagonal solutions in the parameter plane of the nonlinear coefficients $(a, b)$.

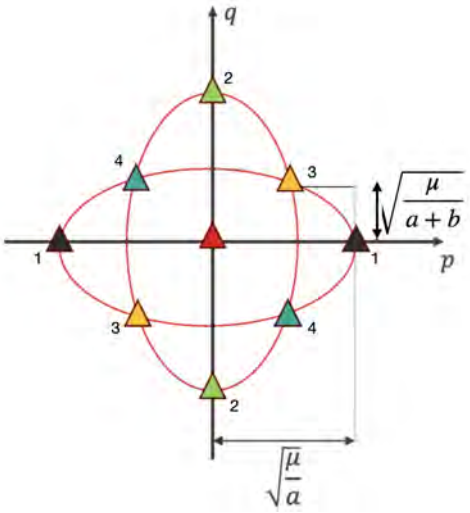


Figure 10: Two-dimensional representation of rectangular and diagonal solutions of a system with $\mathbb{D}_4$ symmetry. The labels next to the triangles correspond to the subscripts of the solutions in (4).

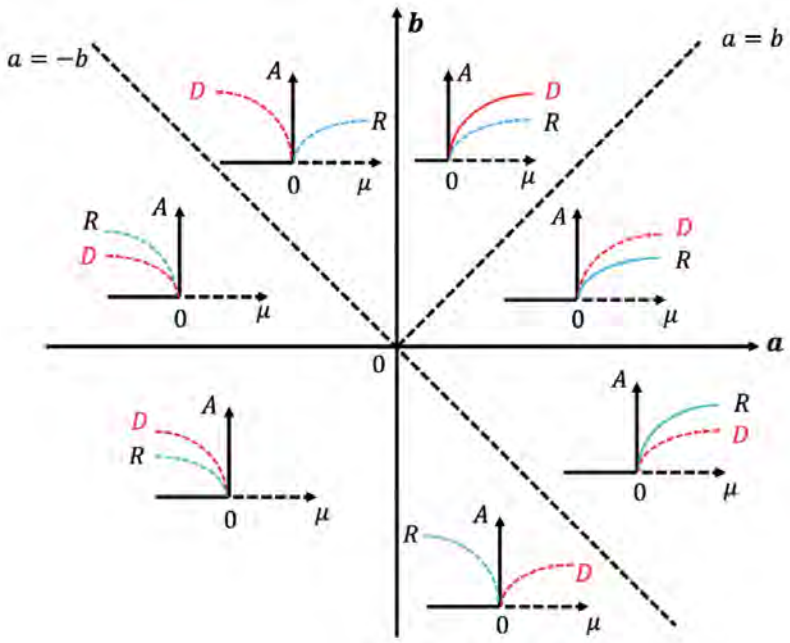


Figure 11: Stability and branching directions of rectangular (R) and diagonal (D) solutions in the parameter plane of the nonlinear coefficients (a,b). Solid (dashed) curves indicate stable (unstable) branches.

This symmetry is found in many systems and contexts. Of these, we can highlight the spirals and ribbons in counter-rotating Couette–Taylor flow. Spirals (analogous to what we have called diagonal solutions) were computed and observed in counter-rotating Couette–Taylor flow for the first time by Taylor in 1923, while ribbons (analogous to what we have called rectangular solutions) were predicted mathematically to exist by Chossat and Iooss [3] and observed experimentally in Tagg et al. [5] much later, in the mid-1980s.

## 4 Steady State Mode Interaction

Let us return to $\mathbb{O}(2)$ symmetry. The instability of a state that is homogeneous (featureless) in $\theta$ is governed by a system of linear partial differential equations, which is also homogeneous in $\theta$. The solutions to such equations are necessarily exponential or trigonometric, more specifically trigonometric in the periodic direction $\theta$.

So far, we have considered one spatial wavenumber at a time. Let us define a function $w$ that has two wavenumbers, $m$ and $n$, for the $\theta$ dependence, in order to describe situations in which these two spatial structures compete and interact. We write:

$$w(\theta) = \frac{1}{2}\left(z_m e^{im\theta} + z_n e^{in\theta} + \bar{z}_m e^{-im\theta} + \bar{z}_n e^{-in\theta}\right). \tag{6}$$

Reflection in $\theta$ and rotation (translation) $\theta$ should have the effect:

$$(S_{\theta_0} w)(\theta) = w(\theta+\theta_0) = \frac{1}{2}\left(z_m e^{im(\theta+\theta_0)} + z_n e^{in(\theta+\theta_0)} + \bar{z}_m e^{-im(\theta+\theta_0)} + \bar{z}_n e^{in(\theta+\theta_0)}\right), \tag{7a}$$

$$(\kappa w)(\theta) = w(-\theta) = \frac{1}{2}\left(z_m e^{-im\theta} + z_n e^{-in\theta} + \bar{z}_m e^{im\theta} + \bar{z}_n e^{in\theta}\right). \tag{7b}$$

This motivates us to prescribe the action of $S_{\theta_0}$ on $(z_m, z_n)$:

$$S_{\theta_0}(z_m, z_n) = (e^{im\theta_0} z_m, e^{in\theta_0} z_n), \tag{8a}$$

$$\kappa(z_m, z_n) = (\bar{z}_m, \bar{z}_n). \tag{8b}$$

We now seek the general form of functions $f(z_m, z_n)$, which are equivalent with respect to (8). We consider monomials:

$$f(z_m, z_n) = \begin{pmatrix} f_m \\ f_n \end{pmatrix}(z_m, z_n) = \begin{pmatrix} f_{mpqrs} z_m^p z_n^q \bar{z}_m^r \bar{z}_n^s \\ f_{npqrs} z_m^p z_n^q \bar{z}_m^r \bar{z}_n^s \end{pmatrix}. \tag{9}$$

As in the single-wavelength case, equivariance with respect to $\kappa$ ($\kappa f = f\kappa$) leads to the requirement that the coefficients in (9) be real. Equivariance with respect to $S_\theta$ ($S_\theta f = f S_\theta$) leads to:

$$S_\theta f(z_m, z_n) = \begin{pmatrix} e^{im\theta} f_{mpqrs} z_m^p z_n^q \bar{z}_m^r \bar{z}_n^s \\ e^{in\theta} f_{npqrs} z_m^p z_n^q \bar{z}_m^r \bar{z}_n^s \end{pmatrix}, \tag{10a}$$

$$f S_\theta(z_m, z_n) = \begin{pmatrix} f_{mpqrs}(e^{im\theta} z_m)^p (e^{in\theta} z_n)^q (e^{-im\theta} \bar{z}_m)^r (e^{-in\theta} \bar{z}_n)^s \\ f_{npqrs}(e^{im\theta} z_m)^p (e^{in\theta} z_n)^q (e^{-im\theta} \bar{z}_m)^r (e^{-in\theta} \bar{z}_n)^s \end{pmatrix}. \tag{10b}$$

This leads to the requirements that:

$$f_{mpqrs} = 0 \text{ or } m = mp + nq - mr - ns, \tag{11a}$$

$$f_{npqrs} = 0 \text{ or } n = mp + nq - mr - ns. \tag{11b}$$

Using this, it is possible to ascertain that a basis for the invariants is:

$$|z_m|^2, |z_n|^2, \text{ and } \Delta \equiv z_m^n \bar{z}_n^m + \bar{z}_m^n z_n^m, \tag{12}$$

i.e. that all invariants are products and sums of these three, and that a basis for the equivariants is:

$$\begin{pmatrix} z_m \\ 0 \end{pmatrix}, \begin{pmatrix} 0 \\ z_n \end{pmatrix}, \begin{pmatrix} \bar{z}_m^{n-1} z_n^m \\ 0 \end{pmatrix}, \begin{pmatrix} 0 \\ z_m^n \bar{z}_n^{m-1} \end{pmatrix}, \tag{13}$$

meaning that all equivariants are sums of these four, with coefficients that are invariants. Thus, the most general equivariant evolution equation is of the form:

$$\frac{d}{dt}\begin{pmatrix} z_m \\ z_n \end{pmatrix} = a\begin{pmatrix} z_m \\ 0 \end{pmatrix} + b\begin{pmatrix} 0 \\ z_n \end{pmatrix} + c\begin{pmatrix} \bar{z}_m^{n-1} z_n^m \\ 0 \end{pmatrix} + d\begin{pmatrix} 0 \\ z_m^n \bar{z}_n^{m-1} \end{pmatrix}, \tag{14}$$

where $a, b, c, d$ are functions of $(|z_m|^2), |z_n|^2, \Delta)$.
Let us now consider (14) truncated to cubic order. Assume $m + n - 1 > 3$. (The two remaining cases (1,2) and (1,3) lead to different analyses.) Then, neither the last invariant nor the last two equivariants contribute at this order, and the most general equivariant is:

$$(a_0 + a_m|z_m|^2 + a_n|z_n|^2)\begin{pmatrix} z_m \\ 0 \end{pmatrix} + (b_0 + b_m|z_m|^2 + b_n|z_n|^2)\begin{pmatrix} 0 \\ z_n \end{pmatrix}. \tag{15}$$

That is, the most general set of evolution equations in the case that $m + n - 1 > 3$ is independent to cubic order of the values of $m$ and $n$ and is:

$$\frac{dz_m}{dt} = (a_0 + a_m|z_m|^2 + a_n|z_n|^2)z_m, \tag{16a}$$

$$\frac{dz_n}{dt} = (b_0 + b_m|z_m|^2 + b_n|z_n|^2)z_n. \tag{16b}$$

Note that (3) for the $\mathbb{D}_4$ case are a special case of (16), in which the coefficients in the two equations are the same, because $p$ and $q$ are related by symmetry whereas $z_m$ and $z_n$ are not.

Since the coefficients $a, b$ are real, the phases play no role and we may replace the complex $z_m, z_n$ by real values $x_m, x_n$. The equations are then just those that apply to the case of rectangular symmetry, $\mathbb{Z}_2 \times \mathbb{Z}_2$. Let us calculate the steady states of (16). We have:

$$x_m = 0 \text{ or } a_0 + a_m x_m^2 + a_n x_n^2 = 0 \quad \text{and} \tag{17a}$$

$$x_n = 0 \text{ or } b_0 + b_m x_m^2 + b_n x_n^2 = 0. \tag{17b}$$

We may plot these conditions in a two-dimensional plane $(x_m, x_n)$. The conditions on the left are the two perpendicular axes, while those on the right are equations for ellipses or hyperbolas, depending on the signs of coefficients $a, b$. The steady states are the intersections of conditions (17a) with conditions (17b), the existence of which depend on the values of coefficients $a, b$. An example of this graphical construction is shown in figure 12, as a function of bifurcation parameter $\mu$ for coefficients $a_0 = \mu, b_0 = \mu - 1, a_m = b_n = -1, a_n = b_m = -2$.

$$\text{the origin}: \quad x_m = 0, \quad x_n = 0, \tag{18a}$$

$$\text{the pure } m \text{ modes}: \quad x_m^2 = -a_0/a_m, \quad x_n = 0, \tag{18b}$$

$$\text{the pure } n \text{ modes}: \quad x_m = 0, \quad x_n^2 = -b_0/b_n, \tag{18c}$$

$$\text{the mixed modes}: \quad x_m^2 = \frac{a_0 b_n - b_0 a_n}{b_m a_n - a_m b_n}, \quad x_n^2 = \frac{a_0 b_m - b_0 a_m}{-(b_m a_n - a_m b_n)}. \tag{18d}$$

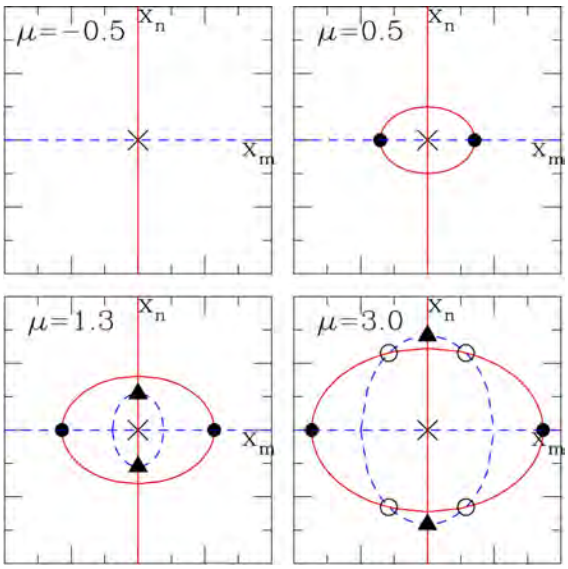


Figure 12: Graphical construction for steady solutions $(x_m, x_n)$. Solid curves are solutions to conditions (17a), dashed curves are solutions to conditions (17b). Steady states are intersections of the two types of curves, where one of conditions (17a) and one of conditions (17b) are simultaneously satisfied. Solid dots are pure $m$ modes, solid triangles are pure $n$ modes, and open circles are mixed modes. For the coefficient values $a_0 = \mu, b_0 = \mu - 1, a_m = b_n = -1, a_n = b_m = -2$ used here,the pure $m$ mode appears at $\mu = 0$, the pure $n$ mode at $\mu = 1$, and the mixed modes at $\mu = 2$.

This mode interaction scenario can be illustrated with the example of a shear-driven cavity flow studied by Bengana et al. [1]. Although [1] describes successive Hopf bifurcations to limit cycles, the same basic scenario holds as for the case of successive pitchfork bifurcations to steady states, since the equations governing the amplitudes of the limit cycles are also given by (16).

Figure 13 shows the deviation of the instantaneous vertical velocity from its temporal mean for each of the two limit cycles, $LC_2$ and $LC_3$. These are analogous to the two pure-mode solutions (18b) and (18c), although here, the fluctuations circulate counter-clockwise around the cavity. The subscripts $2, 3$ labeling the limit cycles refer to the number of maxima of the vertical velocity deviation for each limit cycle.

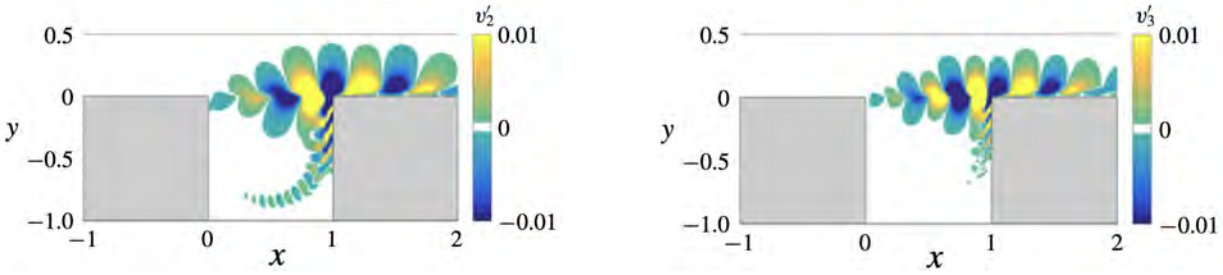


(a) (b)

Figure 13: *(adapted from Bengana et al. [1])* Instantaneous vertical velocity fluctuations for $Re = 4500$. (a) Along the top of the cavity, two maxima (yellow) of the vertical velocity fluctuations can be counted for the $LC_2$ mode. (b) Along the top of the cavity, three maxima of the vertical velocity fluctuations can be counted for the $LC_3$ mode.

The bifurcation diagram is shown in figure 14. For this case, the base flow undergoes a first Hopf bifurcation at $Re_2 = 4126$, leading to $LC_2$ (in blue in figure 14) and a second Hopf bifurcation at $Re_3 = 4348$ leads to $LC_3$ (in red in figure 14). There also exists a quasi-periodic state (QP), analogous to the mixed-mode solution (18d) (in black in figure 14), that connects $LC_2$ and $LC_3$ via subcritical secondary Hopf bifurcations. QP mediates changes in the stability of $\mathrm{LC}_2$ and $\mathrm{LC}_3$. There is a range of bistability between the two subcritical secondary Hopf bifurcations, over which both $\mathrm{LC}_2$ and $\mathrm{LC}_3$ are stable.

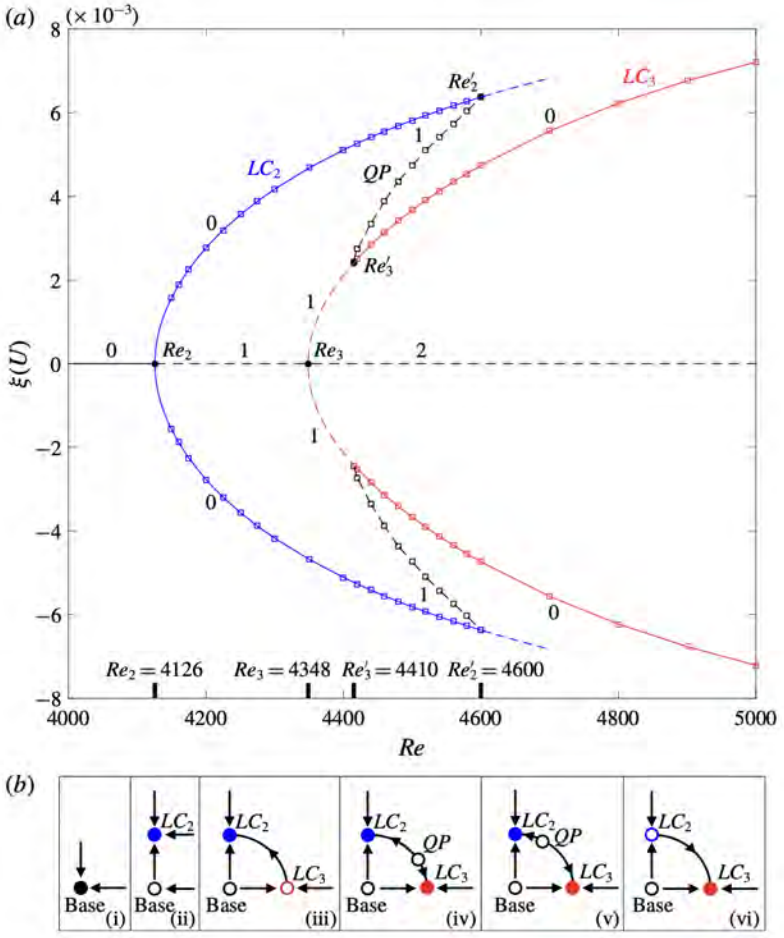


Figure 14: *(from Bengana et al. [1], figure 4)* (a) Bifurcation diagram of the shear-driven cavity flow for $Re \in [4000, 5000]$. The deviation from the mean of the streamwise velocity at one point is plotted against the Reynolds number. The solid dots on the curves and the thick ticks on the abscissa show the critical Reynolds numbers. The integers show the number of unstable directions (counting a complex conjugate pair as a single direction). The first Hopf bifurcation occurs at $\mathrm{Re}_2 \approx 4126$ and the second at $\mathrm{Re}_3 \approx 4348$, giving rise to limit cycles $\mathrm{LC}_2$ and $\mathrm{LC}_3$, respectively. In the range between $\mathrm{Re}_3'$ and $\mathrm{Re}_2'$, there exists a quasi-periodic state QP, which is created and annihilated by subcritical secondary Hopf bifurcations. (b) From left to right, the schematic phase portraits corresponding to the bifurcation diagram. Black dots and hollow circles show the stable and unstable states. (i) Stable base flow. (ii) Stable limit cycle $\mathrm{LC}_2$ is shown as bifurcating in the vertical direction, destabilizing the base flow. (iii) Unstable $\mathrm{LC}_3$ is shown as bifurcating in the horizontal direction. (iv) QP emerges, stabilizing $\mathrm{LC}_3$. (v) QP moves away from $\mathrm{LC}_3$ and towards $\mathrm{LC}_2$. (vi) QP has disappeared, destabilizing $\mathrm{LC}_2$.

## 5 Eckhaus Instability

The Eckhaus instability is a secondary instability in which a one-dimensional, spatially periodic pattern becomes unstable, leading to a transition to another state of a different spatial period. We illustrate this phenomenon through the Ginzburg–Landau (GL) equation:

$$\partial_t A = \mu A + \partial_{xx} A - |A|^2 A, . \tag{19}$$

where we assume a spatially periodic domain of length $L$. In (19), $A$ represents an *envelope* for a pattern with favored wavenumber $q_c$, i.e., the physical quantity is $A(x,t)e^{iq_c x} + c.c.$ so that a wavenumber $Q$ for $A$ is a *deviation* (Figure 15). For any fixed wavenumber $Q$, the GL equation admits the steady periodic solution $A_Q(x) = (\mu - Q^2)^{1/2}\exp(iQx)$, provided that $\mu > \mu_Q \equiv Q^2$. Solution $A_Q$ emerges through a pitchfork bifurcation from the conductive base state $A = 0$ at $\mu = \mu_Q$, and we therefore consider the regime $\mu > \mu_Q$ in what follows.

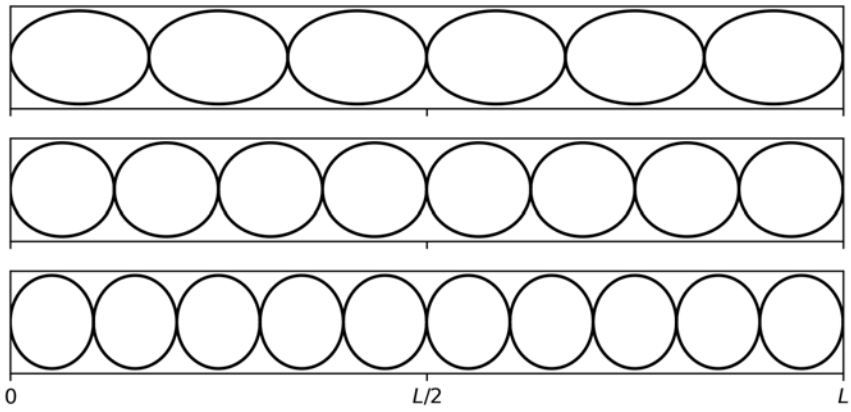


Figure 15: Schematic representations of convection rolls in a Rayleigh-Bénard setup. The physical quantity $A(x,t)e^{iq_c x} + c.c.$ may represent, for example, the vertical velocity in the horizontal mid-plane. For a fixed value of $q_c$, the number of rolls can be varied by changing the envelope $A(x,t)$. From top to bottom, we show cases with $q_c + Q = 3$, $q_c + Q = 4$, and $q_c + Q = 5$, respectively.

To determine whether $A_Q$ is stable, we study the evolution of the modulated field $A(x,t) = (1 + a(x,t))A_Q(x)$ for a small perturbation $a(x,t)$. The linearized dynamics can be written as

$$\partial_t a = 2iQ\partial_x a + \partial_{xx} a - (\mu - Q^2)(a + \overline{a}), \tag{20}$$

where $\overline{\cdot}$ denotes complex conjugation. We separate $a$ into its real and imaginary parts $a = \alpha + i\beta$. We then expand each in a Fourier series and treat each wavenumber $\pm k$ separately, since they are not coupled by (20). Abbreviating their $k^{\text{th}}$ Fourier coefficients as $\hat{\alpha}$ and $\hat{\beta}$, respectively, we obtain

$$\begin{cases} \partial_t \hat{\alpha} = -2iQk\hat{\beta} - k^2\hat{\alpha} - 2(\mu - Q^2)\hat{\alpha}\,, \\ \partial_t \hat{\beta} = +2iQk\hat{\alpha} - k^2\hat{\beta}\,. \end{cases} \tag{21}$$

The eigenvalues of the system (21) are real and given by

$$\lambda_k^{\pm} = -\left(\mu - Q^2 + k^2\right) \pm \sqrt{(2Qk)^2 + (\mu - Q^2)^2}\,. \tag{22}$$

For $k = 0$ (uniform modulation), we find that $\hat{\alpha}$ decays at a rate $-2(\mu - Q^2) < 0$, while $\hat{\beta}$ remains constant, reflecting the phase invariance of the GL equation. These are the eigenvalues

and eigenvectors corresponding to the circle pitchfork that created $A_Q$. (Circle pitchforks are discussed in Lecture 7 and in Section 1 of this Lecture.) Consequently, $A_Q(x)$ is always stable to uniform amplitude modulation.

For $k > 0$, both eigenvalues are negative when $\mu > \mu_Q^k \equiv 3Q^2 - k^2/2$, while at least one eigenvalue is positive if $\mu < \mu_Q^k$, leading to instability of state $A_Q$ to modulating perturbations with wavenumbers $\pm k$. Therefore, we conclude that

$$A_Q \text{ is unstable iff } \mu < \mu_Q^{k_{\min}} \equiv 3Q^2 - k_{\min}^2/2 \tag{23}$$

where $k_{\min}$ denotes the infimum (smallest) of the nonzero wavenumbers admissible in the domain. Thus, $A_Q$ exists as a steady solution for $\mu \geq \mu_Q = Q^2$, but is unstable as long as $\mu < \mu_Q^{k_{min}}$. As $\mu$ increases, $A_Q$ is stabilized through a series of secondary pitchfork bifurcations corresponding to decreasing values of $k$ until $k_{min}$, at which $A_Q$ finally becomes stable. Only the first branch $A_0$ is born stable.

In an infinite domain, $k_{\min} = 0$ and we recover the classical Eckhaus curve $\mu_Q^0 = 3Q^2$. For a periodic domain of finite length $L$, however, we have $k_{\min} = 2\pi/L$, so that $A_Q$ is stabilized for smaller values of $\mu$, since the finite domain size suppresses long-wavelength modulations which would otherwise be unstable.

Although the downward shift of the Eckhaus boundary by $k_{\min}^2/2 \propto (2\pi/L)^2$ in finite domains appears to vanish in the large-domain limit ($L \to \infty$), it was observed by Tuckerman and Barkley [6] that this shift is comparable in size to the spacing of $\mu_Q$ between adjacent wavenumbers and therefore cannot be ignored. As a result, the influence of finite-domain effects on the Eckhaus stability boundary remains significant for all domain sizes. Notably, this finding does not depend on starting from the Ginzburg–Landau equation; it can also be derived from the Swift–Hohenberg equation [7].

We conclude this lecture by a description of the bifurcation diagram of the Eckhaus instability shown in Figure 16 for a finite periodic domain. Rescaling the GL equation, we set $L = 2\pi$, for which the minimal admissible nonzero wavenumber is $k_{\min} = 1$. When $\mu < 0$, the conductive state $A = 0$ is linearly stable to all perturbations. As $\mu$ becomes slightly positive, the conductive state becomes unstable to perturbations with mode number $Q = 0$ and undergoes a supercritical pitchfork bifurcation. The resulting finite-amplitude steady solution $A_0(x) = \sqrt{\mu}$ is stable, since $\mu$ is positive and thus exceeds $\mu_0^1 = 3 \times 0^2 - 1/2 = -1/2$. This is the first branch in Figure 16.

When $\mu$ traverses $\mu_1 \equiv 1$, the conductive state becomes unstable to perturbations with wavenumber $Q = 1$, leading to the creation of the steady finite-amplitude solution $A_1(x) = \sqrt{\mu - 1}\, e^{ix}$. This is the beginning of the second branch from the conductive state. Unlike $A_0$, which is stable at onset, solution $A_1$ is unstable to modulations of the form $(1 + \epsilon \cos x)$ for $\mu < \mu_1^1 \equiv 3 \times 1^2 - 1/2 = 5/2$. Increasing $\mu$ along the branch, $\mu$ eventually exceeds $5/2$ and the state $A_1(x)$ becomes stable. This corresponds to the second part of the second branch, after the secondary pitchfork bifurcation.

Finally, consider the branch corresponding to $A_2(x) = \sqrt{\mu - 4}\, e^{2ix}$. When $\mu > \mu_2 = 4$, the conductive state also becomes unstable to perturbations with wavenumber $Q = 2$ and a steady solution $A_2(x)$ is created. When it is created, $A_2(x)$ is unstable to modulations by both $(1 + \epsilon \cos x)$ and $(1 + \epsilon \cos 2x)$. When $\mu$ traverses $\mu_2^2 = 3 \times 2^2 - 2^2/2 = 12 - 2 = 10$, $A_2(x)$ becomes stable to modulation by $(1 + \epsilon \cos 2x)$ (second part of the third branch), and finally becomes stable when $\mu$ exceeds $\mu_2^1 \equiv 3 \times 2^2 - 1^2/2 = 12 - 1/2 = 23/2$ (third and last part of the third branch).

This pattern continues for all other branches. The conductive state becomes unstable to perturbations with wavenumber $Q$ for $\mu > \mu_Q \equiv Q^2$, leading to the creation of the solution $A_Q(x) = (\mu - Q^2)^{1/2}\, e^{iQx}$. This solution becomes stable for $\mu > \mu_Q^1 = 3Q^2 - 1/2$, after $Q$ secondary pitchfork bifurcations.

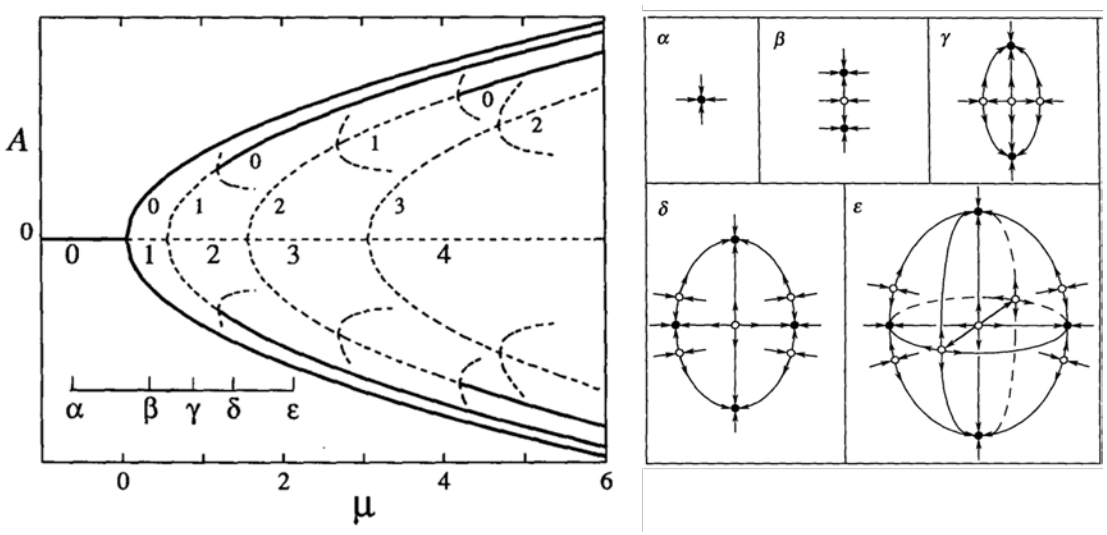


Figure 16: *(from Tuckerman and Barkley [6], figures 2 and 3)* Left: bifurcation diagram for the Eckhaus instability in a periodic domain. Labels on the branches indicate the number of directions to which it is unstable. Stable branches are represented by solid curves, unstable branches by dashed curves. All branches $A = A_Q$ originate from pitchfork bifurcations of the conductive state $A = 0$ Except for the first branch, $A_0$, all are initially unstable and then stabilized after a series of secondary pitchfork bifurcations. Right: schematic phase portraits at various values of $\mu$. The coordinates represent projections of the first two or three unstable directions of the conductive state. Stable steady states are indicated by filled circles, unstable steady states by hollow circles. The values of $\mu$ correspond to the Greek letter labels on the bifurcation diagram at left.

## References


[1] Y. Bengana, J.-C. Loiseau, J.-C. Robinet, and L. Tuckerman. Bifurcation analysis and frequency prediction in shear-driven cavity flow. *J. Fluid Mech.*, 875:725–757, 2019.

[2] K. Borońska and L. S. Tuckerman. Extreme multiplicity in cylindrical Rayleigh-Bénard convection. II. Bifurcation diagram and symmetry classification. *Phys. Rev. E*, 81:036321, 2010.

[3] P. Chossat and G. Iooss. Primary and secondary bifurcations in the Couette-Taylor problem. *Jpn. J. Appl. Math.*, 2:37–68, 1985.

[4] B. Hof, P. Lucas, and T. Mullin. Flow state multiplicity in convection. *Phys. Fluids*, 11: 2815–2817, 1999.

[5] R. Tagg, W. S. Edwards, H. L. Swinney, and P. S. Marcus. Nonlinear standing waves in Couette-Taylor flow. *Phys. Rev. A*, 39:3734, 1989.

[6] L. S. Tuckerman and D. Barkley. Bifurcation analysis of the Eckhaus instability. *Physica D*, 46:57–86, 1990.

[7] L. S. Tuckerman and D. Barkley. Comment on "Bifurcation structure and the Eckhaus instability". *Phys. Rev. Lett.*, 67:1051, 1991.

[8] E. W. Weisstein. Dihedral group D_4. `https://mathworld.wolfram.com/DihedralGroupD4.html`, 2025.

# GFD 2025 Lecture 9: Maps, Period Doubling and Floquet Theory

Laurette Tuckerman; notes by Isabela Conde, Andrés Posada-Bedoya, Lin Yao

June 26, 2025

## 1 Discrete Dynamical Systems or Mappings

We now shift from considering continuous time to a discrete system that is evaluated at each $n$ time step, i.e:

$$x_{n+1} = f(x_n) \qquad\qquad x,\, f \in \mathcal{R}^N \tag{1}$$

### 1.1 Stability of fixed points

To study the stability of this system, we add some perturbation, $\epsilon$ as in continuous systems. In this case we add a discrete $\epsilon_n$ such that $x_n = \bar{x} + \epsilon_n$. Then 1D linear stability is determined via:

$$\begin{aligned} \bar{x} &= f(\bar{x} + \epsilon_n) \\ &= f(\bar{x}) + f'(\bar{x})\epsilon_n + \frac{1}{2}f''(\bar{x})\epsilon_n^2 \dots \\ \therefore \epsilon_{n+1} &\approx f'(\bar{x})\epsilon_n \end{aligned} \tag{2}$$

We see that if $|f'(\bar{x})| < 1$, then $|\epsilon|$ decreases and $\bar{x}$ is stable, conversely if $|f'(\bar{x})| > 1 \iff |\epsilon|$ increases, then the system is unstable. The situation in which $f'(\bar{x}) = 0$ so that $\epsilon_{n+1} \approx \frac{1}{2}f''(\bar{x})\epsilon_n^2$, is called *superstability*.

We extend this to multidimensional systems, for which $f'(\bar{x})$ is replaced by the Jacobian $Df(\bar{x})$ and $\bar{x}$ is a stable fixed point if all of the eigenvalues of $\mu$ of $Df(\bar{x})$ satisfy $|\mu| < 1$, i.e. if all of the eigenvalues lie inside a unit circle.
Figure 1 shows three different cases for eigenvalues $\mu$ of a real system leaving the unit circle:

*(i)* An eigenvalue may exit the unit circle at $(1, 0)$.

*(ii)* A complex conjugate pair of eigenvalues may exit the unit circle at $e^{\pm i\theta}$.

*(iii)* A complex conjugate pair of eigenvalues may exit the unit circle at $(-1, 0)$

Figure 2 gives a graphical reconstruction of cases *(i)* and *(iii)* for a linear map of the form $f(x) = cx$ for different values of $c$. We plot function $f(x)$ in black and a diagonal line $(y = x))$ in red. From some initial point $x_0$, we draw a vertical line until it reaches the function, $f(x)$ then a horizontal line until it hits the diagonal at $x_1$. Repeating this process creates a procedure for iterating $f$. We note that there exists a fixed point at $\bar{x} = 0$, which is stable when $|c| < 1$ and unstable for $|c| > 1$. We can also see from these iterative maps that trajectories proceed monotonically for $c > 0$ and oscillate when $c < 0$.

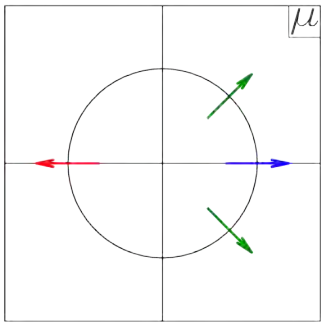


Figure 1: Unit circle showing different possibilities for eigenvalues $\mu$. The blue arrow traverses the unit circle at $(-, 0)$, the green arrows traverse at $e^{\pm i\theta}$, and the red arrow traverses at $(-1, 0)$.

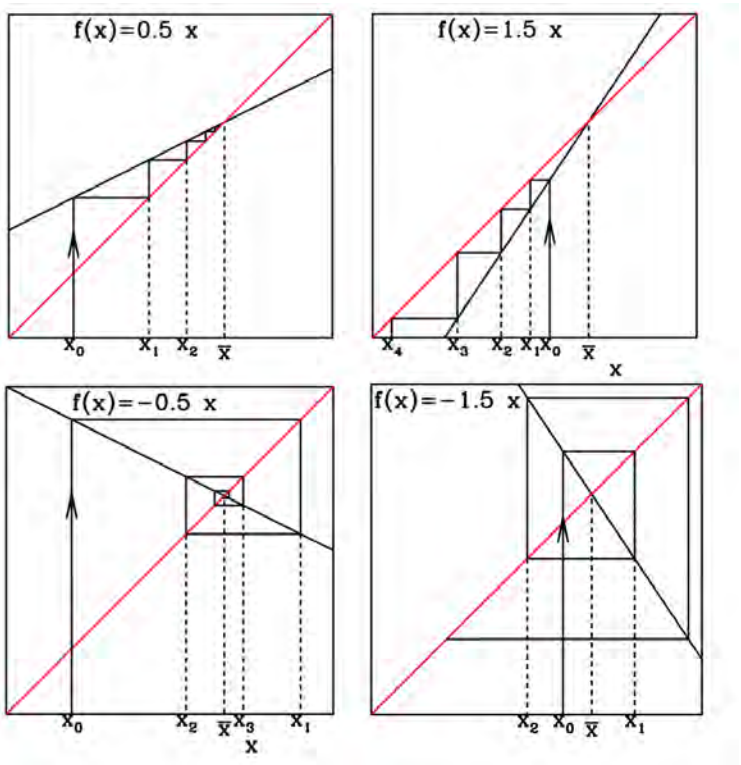


Figure 2: Graphical construction for iterating maps. $f(x) = cx$ with various slopes $c$.

$$(x_0, 0) \to (x_0, x_1 = f(x_0)) \to (x_1, x_1) \to (x_1, x_2 = f(x_1)) \to \cdots \tag{3}$$

As in continuous systems, a loss of stability indicates the occurrence of a bifurcation. Loss of stability is associated with various types of bifurcations. Case *(ii)*, when eigenvalues cross at $\pm e^{i\theta}$, leads to a secondary Hopf, or Neimark–Sacker, bifurcation to a torus. We will not discuss this case here. Case *(i)*, when eigenvalues cross at $+1$, leads to a steady bifurcation, analogous to those seen for continuous dynamical systems.

## 1.2 Steady bifurcations

A steady bifurcation in a discrete-time system may be a saddle-node, a pitchfork, or a transcritical bifurcation. We can write simple equations that display steady bifurcations analogous to those found for flows.

### 1.2.1 Saddle-node bifurcation

$$\dot{x} \to x_{n+1} - x_n = \mu - x_n^2 \quad \Longrightarrow \quad x_{n+1} = f(x_n) = x_n + \mu - x_n^2 \tag{4}$$

Fixed points $\pm\sqrt{\mu}$ satisfying $f(\bar{x}) = \bar{x}$ exist for $\mu > 0$. Their stability is calculated via

$$\begin{aligned} f(x) &= x + \mu - x^2 \\ f'(x) &= 1 - 2xf'(\pm\sqrt{\mu}) = 1 \mp 2\sqrt{\mu} \leq 1 \quad \text{for } \mu > 0 \end{aligned}$$

### 1.2.2 Pitchfork bifurcation

$$\dot{x} \to x_{n+1} - x_n = \mu x_n - x_n^3 \quad \Longrightarrow \quad x_{n+1} = f(x_n) = x_n + \mu x_n - x_n^3 \tag{5}$$

The fixed points $0, \pm\sqrt{\mu}$ satisfy $f(\bar{x}) = \bar{x}$. Their stability is calculated via

$$\begin{aligned} f(x) = x + \mu x - x^3 \Longrightarrow f'(x) &= 1 + \mu - 2x^2 \\ f'(0) &= 1 + \mu \leq 1 \quad \text{for } \mu \leq 0 \\ f'(\pm\sqrt{\mu}) &= 1 - \mu < 1 \quad \text{for } \mu > 0 \end{aligned}$$

Subcritical pitchfork bifurcations and transcritical bifurcations can also occur in discrete-time dynamical systems. Saddle-node and pitchfork (super and subcritical) bifurcations are illustrated in Figure 3.

## 1.3 Period doubling and the logistic map

Case *(iii)* of Figure 1, when an eigenvalue crosses at $-1$, leads to a flip, or a period-doubling bifurcation, a phenomenon that cannot occur for continuous dynamical systems. We now discuss this case in the context of the logistic map, defined as

$$x_{n+1} \;=\; f(x_n) \;\equiv\; a\, x_n\,(1 - x_n), \quad x_n \in [0, 1], \quad 0 < a < 4. \tag{6}$$

$f$ is a quadratic function mapping $[0, 1]$ into itself, with minima at the two endpoints $f(0) = f(1) = 0$ and a maximum at the midpoint $f(1/2) = a/4$.

### 1.3.1 Fixed points and period-doubling

The fixed points of the logistic map (6) satisfy $f(\bar{x}) = \bar{x}$, giving

$$\bar{x} = 0 \quad \text{or} \quad \bar{x} = 1 - \frac{1}{a}. \tag{7}$$

Linear stability follows from

$$f'(x) = a\,(1 - 2x), \quad f'(0) = a, \quad f'\Big(1 - \tfrac{1}{a}\Big) = 2 - a. \tag{8}$$

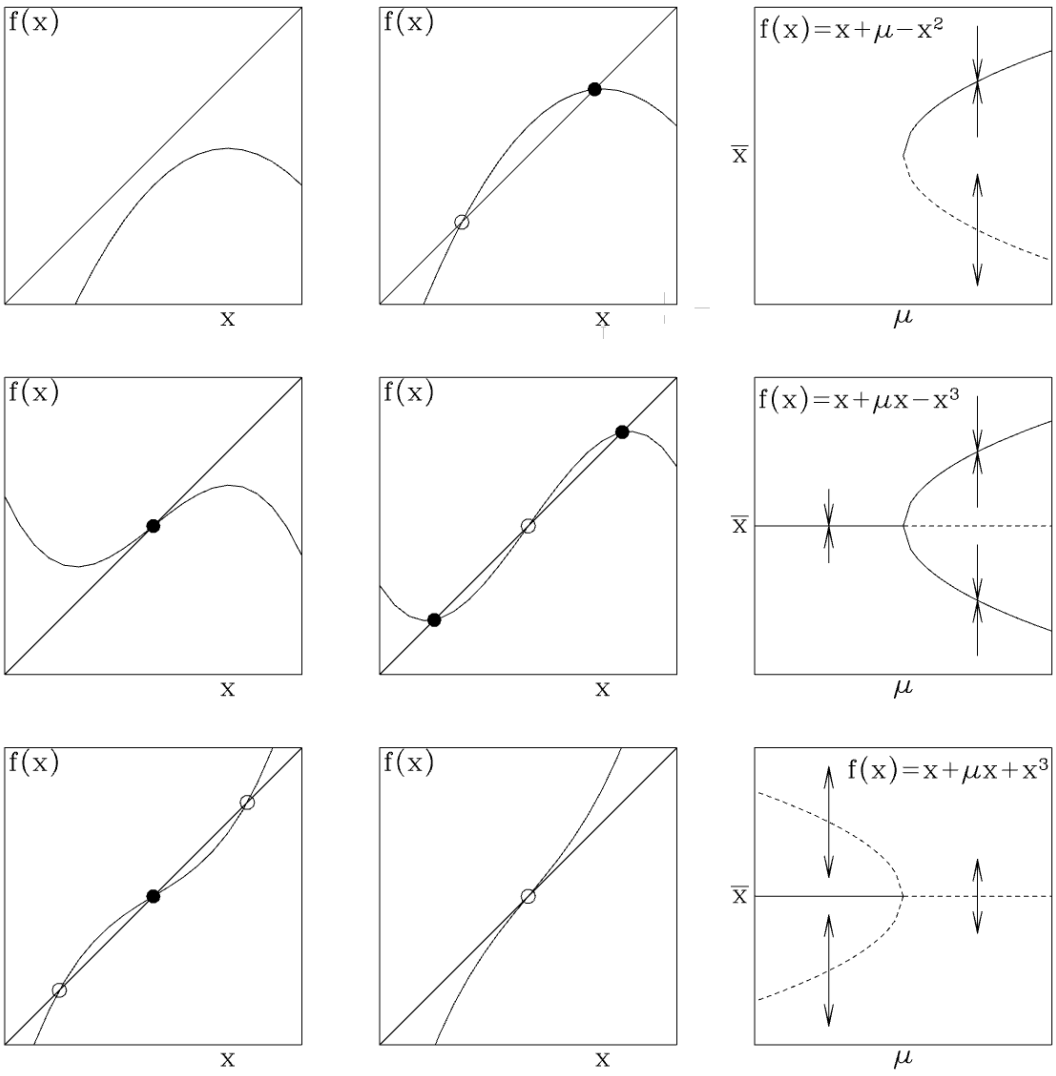


Figure 3: Steady bifurcations for discrete dynamical systems. **Top row:** Saddle-node bifurcation. $f(x) = x + \mu - x^2$ for $\mu = -0.2$ (left) and for $\mu = 0.2$ (middle). **Middle row:** Supercritical pitchfork. $f(x) = x + \mu x - x^3$ for $\mu = -0.2$ (left) and for $\mu = 0.4$ (middle). **Bottom row:** Subcritical pitchfork. $f(x) = x + \mu x + x^3$ for $\mu = -0.4$ (left) and for $\mu = 0.2$ (middle). Right: corresponding bifurcation diagrams.

Hence, $\bar{x} = 0$ is stable for $a < 1$, and $\bar{x} = 1 - 1/a$ is stable for $1 < a < 3$.

At $a = 3$, $f'(1 - 1/a) = -1$ and the fixed point undergoes a *flip* (period-doubling) bifurcation (Figure 4). To find the ensuing two-cycle, define

$$f^2(x) = f\big(f(x)\big), \tag{9}$$

and solve $f^2(x) = x$. One finds two new real roots

$$x_{1,2} = \frac{a + 1 \pm \sqrt{(a-3)(a+1)}}{2a}, \tag{10}$$

which exist for $a > 3$. Their stability is determined by

$$\big(f^2\big)'(x_1)\big(f^2\big)'(x_2) = f'(x_1)\, f'(x_2) = -a^2 + 2a + 4, \tag{11}$$

and the two-cycle loses stability at

$$-a^2 + 2a + 4 = \pm 1 \implies a = 3 \quad \text{or} \quad a = 1 + \sqrt{6} \approx 3.4495. \tag{12}$$

Equation (12) shows that the two-cycle of $f$ is created via a steady-state pitchfork bifurcation at $a = 3$ and that this two-cycle loses stability via a flip bifurcation at $a = 3.4495$, leading to a four-cycle. Examples of $f^2(x)$ and the new fixed points $x_{1,2}$ are shown in the right portion of Figure 4, with $a = 1.6$ and $a = 3.4$. We see that $f^2$ undergoes a pitchfork bifurcation.

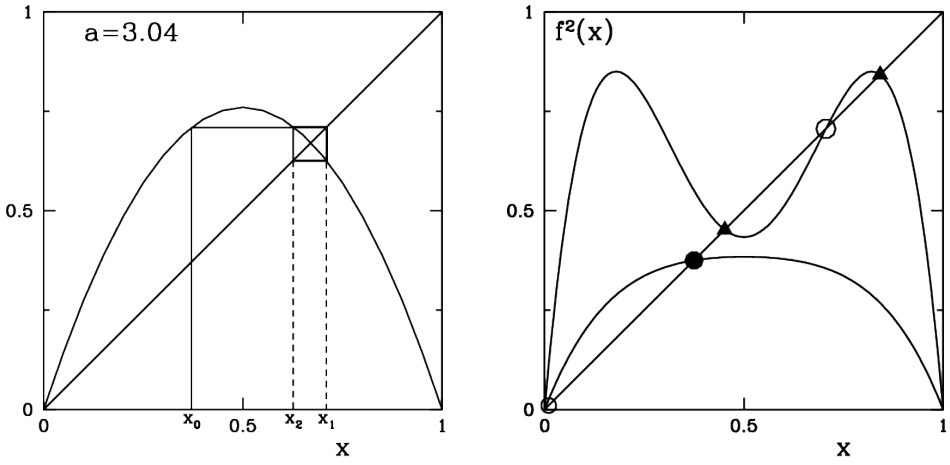


Figure 4: Behavior of logistic map leading to period doubling. Left: For $a = 3.04$, the initial value $x_0$ converges to a two-cycle, given by $x_1$ and $x_2$. Right: Graph of $f^2(x)$. For $a = 1.6$, $f^2$ has the same fixed points as $f$, namely $x = 0$ (unstable, hollow dot) and $x = 1 - 1/a$ (stable, filled dot). For $a = 3.4$, the fixed point $x = 1 - 1/a$ has become unstable, and $f^2$ has two new stable fixed points $x_{1,2}$ (filled triangles), which together comprise a two-cycle for $f$.

Figure 5 shows the $x$ values belonging to the stable regime at each value of $a$: fixed point, two-cycle, etc. Feigembaum [4], simultaneously with Coullet and Tresser [2] discovered that the successive period-doubing bifurcations occur at successively smaller intervals in $r$ and accumulate at the Feigenbaum point $a_\infty \approx 3.5699$ (Table 1). This is called the *period-doubling cascade*.

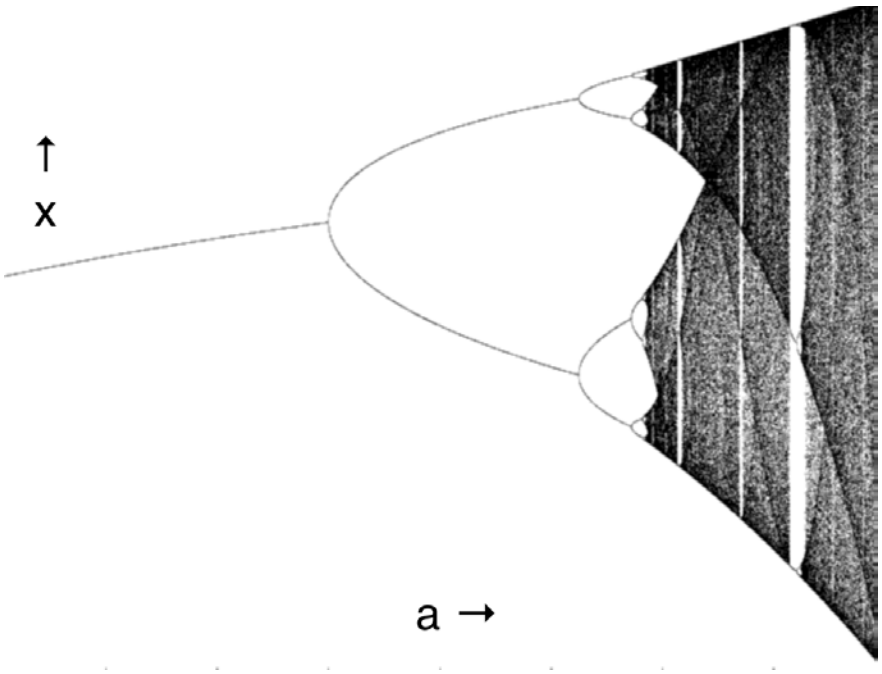


Figure 5: Bifurcation diagram for logistic map, showing period-doubling cascade and periodic windows. For each value of $a$, dots show the $x$ values belonging to the stable fixed point, two-cycle, ...

| $n$ | $2^n$ | $a_n$ | $\Delta_n \equiv a_n - a_{n-1}$ | $\delta_n \equiv \Delta_{n-1}/\Delta_n$ |
|---|---|---|---|---|
| 0 | 1 | 1 | — | — |
| 1 | 2 | 3 | 2 | — |
| 2 | 4 | 3.44948 | 0.449 | 4.45 |
| 3 | 8 | 3.54408 | 0.0948 | 4.747 |
| 4 | 16 | 3.56872 | 0.0244 | 4.640 |
| 5 | 32 | 3.5698912 | 0.00116 | 4.662 |
| ⋮ | ⋮ | ⋮ | ⋮ | ⋮ |
| $\infty$ | $\infty$ | 3.569945672... | 0 | 4.669 |

Table 1: Period-doubling cascade for logistic map.

### 1.3.2 Renormalization

The universality of the period-doubling cascade can be understood via a renormalization operator proposed by Cvitanović [4, footnote 4]:

$$T[f](x) \;=\; -\frac{1}{\alpha}\, f\big(f(-\alpha\, x)\big) \;=\; -\frac{1}{\alpha}\, f^2(-\alpha\, x)\,, \tag{13}$$

where $f^2(x) \equiv f\big(f(x)\big)$. Repeated application yields

$$T^n[f](x) \;=\; -\frac{1}{\alpha}\, T^{n-1}[f]^2(-\alpha\, x) \quad\longrightarrow\quad \phi(x) \quad \text{as } n \to \infty, \tag{14}$$

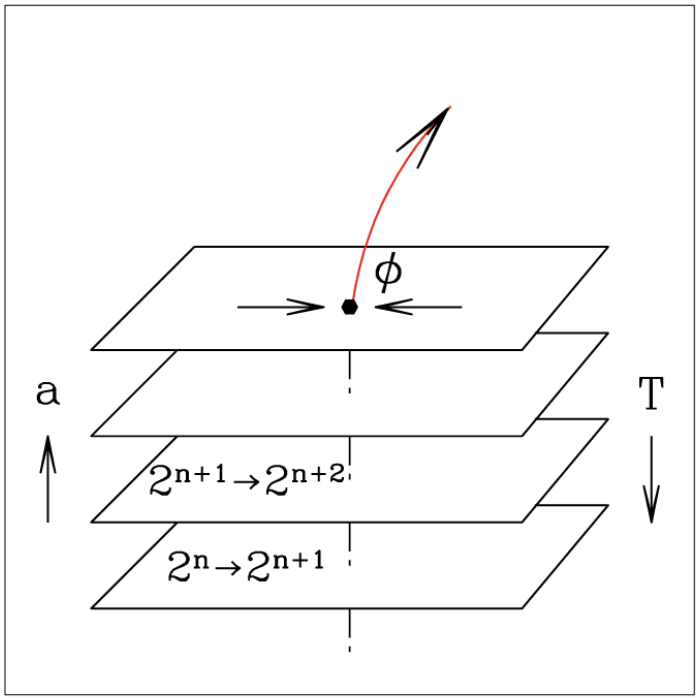


Figure 6: Renormalization cascade for the period-doubling route to chaos.

with the fixed-point function $\phi$ satisfying

$$\phi(x) = T[\phi](x) = -\frac{1}{\alpha}\,\phi^2(-\alpha\,x). \tag{15}$$

Here, we can view $T$ as itself a mapping on mappings, with $\phi$ a fixed point of $T$. In a power-series expansion about $x = 0$,

$$\phi(x) = 1 - \delta\,x^2 + \epsilon\,x^4 + \zeta\,x^6 + \cdots \quad \text{with} \quad \delta \approx 1.528,\ \epsilon \approx 0.105,\ \zeta \approx 0.0267. \tag{16}$$

Each renormalization step effectively doubles the period:

$$f \xrightarrow{T} T[f] = f^2_{\text{rescaled}} \quad , \quad T[f] \xrightarrow{T} T^2[f] = f^4_{\text{rescaled}} \quad , \quad T^n[f] = f^{2^n}_{\text{rescaled}}. \tag{17}$$

Here the subscript "rescaled" indicates the uniform coordinate and amplitude rescaling by $\alpha$ needed to keep the quadratic maximum at $x = 0$ of height 1.

The sequence of bifurcation parameter values $\{a_n\}$ for which an attractive $2^n$-cycle appears can be extracted by tracking where the rescaled map $T^{n-1}[f_{a_n}](x)$ first touches marginal stability (derivative $= -1$ at the fixed point). One finds

$$\frac{a_{n-1} - a_{n-2}}{a_n - a_{n-1}} \longrightarrow 4.6692 \quad (n \to \infty). \tag{18}$$

This value is universal to all map families with quadratic maxima. The process of period-doubling is shown in Figure 6 in the context of renormalization. There are several horizontal "slices," each representing the map at successive bifurcation stages where a stable orbit of period $2^n$ appears as

the control parameter $a$ increases. The downward arrow labeled $T$ indicates the renormalization operator that takes the map with a $2^{n+1}$–cycle, rescales it in both amplitude and horizontal coordinate by the universal factor $\alpha$, and produces a map with a $2^n$–cycle. In the limit $n \to \infty$, after repeated application of $T$, the rescaled map converges to the fixed-point function $\phi(x)$, shown on the top layer; its unstable direction governs the geometry of all period-doubling cascades.

### 1.3.3 Periodic windows

Within the chaotic regime of the logistic map, there exist narrow intervals of the control parameter $a$ where stable periodic orbits reappear. These are known as *periodic windows*. For example, in Figure 5, chaos gives way to a stable period-3 cycle at $a \approx 3.83$. This window includes a full period-doubling cascade:

$$\text{period-3} \;\to\; \text{period-6} \;\to\; \text{period-12} \;\to\; \cdots \tag{19}$$

before returning to chaos. Similar windows exist for other periods (e.g., 5, 6, 7, etc.), embedded within the chaotic sea.

These windows arise due to saddle-node bifurcations, where a stable and an unstable periodic orbit of the same period are simultaneously created. As $a$ increases, the stable orbit undergoes its own period-doubling cascade, eventually becoming chaotic. This local cascade mirrors the global structure of the original bifurcation diagram, exemplifying the *self-similarity* of the system.

According to Sharkovskii's theorem, the existence of a period-3 orbit implies the existence of periodic orbits of all other periods. The period-3 window thus plays a special role in demonstrating the onset of chaos. Periodic windows illustrate how order and chaos can coexist and alternate, even in simple one-dimensional maps like the logistic map.

## 1.4 Example: period-doubling in Rayleigh-Bénard convection

Rayleigh-Bénard convection is the fluid motion that arises when a layer of fluid is heated from below and cooled from above. When the temperature difference exceeds a critical value, the system undergoes a transition from a conductive to a convective state. At higher temperature gradients (i.e., higher Rayleigh numbers), the system can exhibit increasingly complex time-dependent behaviors. One such route to chaos observed in experiments is via a *period-doubling cascade*.

1. As the Rayleigh number Ra increases, the initially steady convection rolls become time-periodic.
2. Further increase in Ra leads to a bifurcation where the oscillation period doubles: the system alternates between two distinct states over each cycle.
3. This period-doubling continues:

$$\text{period-1} \;\to\; \text{period-2} \;\to\; \text{period-4} \;\to\; \text{period-8} \;\to\; \cdots \tag{20}$$

   until the motion becomes chaotic.

Such behavior was observed in laboratory experiments using high-Prandtl-number fluids confined between plates with well-controlled boundary conditions by Libchaber et al. [7]. Time series of temperature fluctuations or velocity at a point within the cell reveal a classic Feigenbaum-type cascade, shown in figure 7. This provides a striking experimental realization of the universal period-doubling route to chaos in a physically extended, fluid-dynamical system.

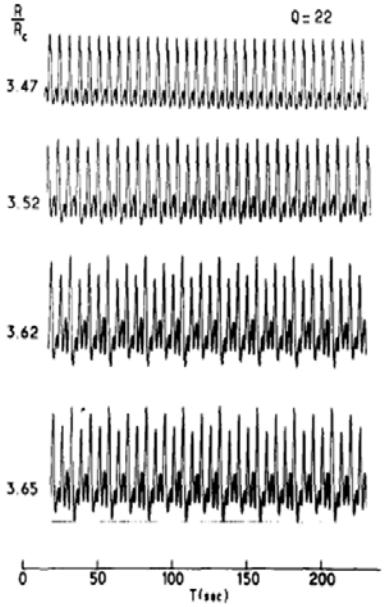


Fig. 3. The period doubling cascade ($\Gamma = 4$, $Q = 22$).

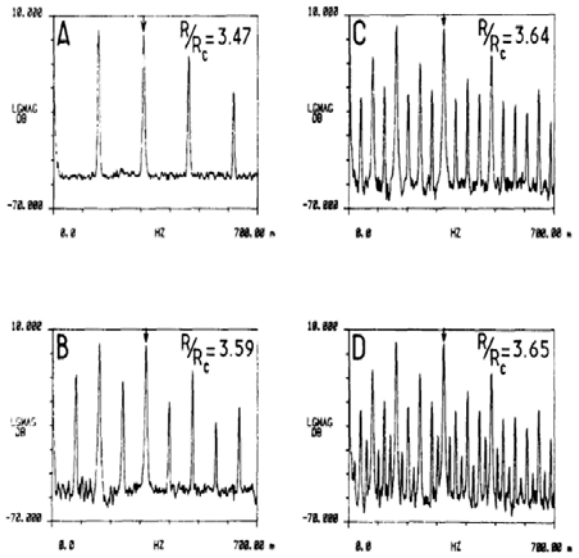


Fig. 4. Fourier spectrum for the period-doubling cascade.

Figure 7: Time series of temperature at a point in a Rayleigh-Bénard cell showing a sequence of period doublings as the Rayleigh number increases. From [7].

### 1.5 Continuous flows to discrete maps

Since physical systems are governed by differential equations, continuous-time dynamical systems would seem a more natural framework than discrete-time systems for physical applications. Where do discrete-time mappings come from? A limit cycle is a closed trajectory of a continuous-time dynamical system. Representing limit cycles as fixed points of discrete systems often make these limit cycles easier to analyze. In three dimensions, this is done by selecting the points at which a limit cycle successively traverses a plane, or, in higher dimensions, a hypersurface. Figure 8 illustrates the correspondence between limit cycles and fixed points of a discrete system, called a Poincaré map.

## 2 Floquet Theory

Once a limit cycle has been created by one of the paths described above, it too can undergo bifurcations and change stability, analogously to fixed points. Floquet theory provides the mathematical framework to describe the linear stability of limit cycles in dynamical systems. Its framework is analogous to the eigenvalue theory for linear systems with constant coefficients, extended to systems with periodic coefficients. In the context of nonlinear systems, Floquet theory is used to study small perturbations around periodic orbits, helping determine whether the system returns to the orbit (stable) or diverges (unstable).

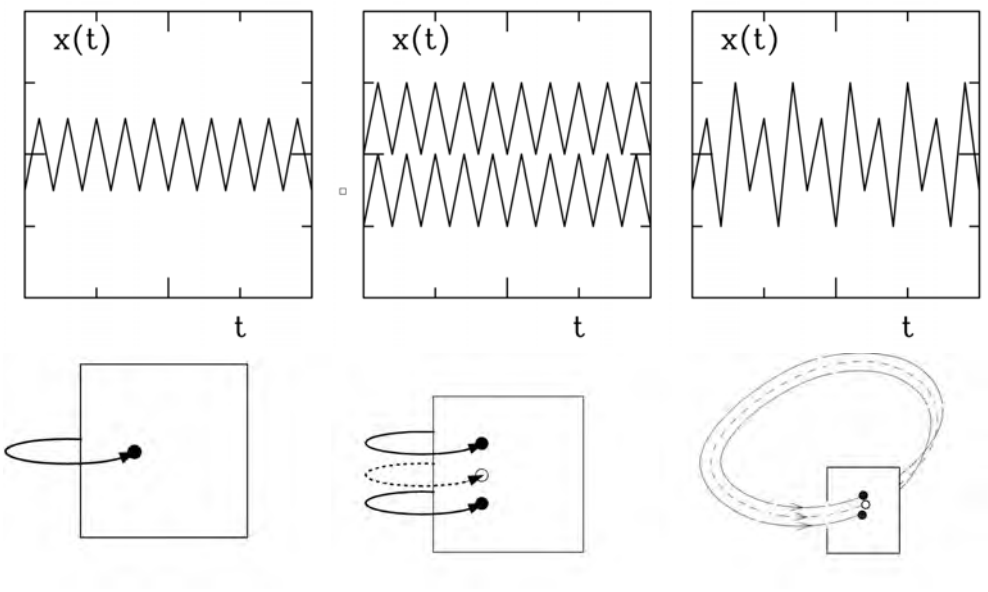


Figure 8: **Top row:** schematic timeseries. Left: Limit cycle before any bifurcation. Middle: After a pitchfork bifurcation, the original limit cycle is unstable and there exist two limit cycles, one on either side of the original limit cycle. Right: After a period-doubling bifurcation, the resulting limit cycle alternates between two versions of the original limit cycle. **Bottom row:** Poincaré map. Left: Limit cycle pierces the plane once. Middle: Unstable limit cycle (dotted curve) surrounded by two new stable limit cycles (solid curves), formed by a pitchfork bifurcation. Each is a fixed point of the Poincaré map. Right: A limit cycle (solid curve) produced by a period-doubling bifurcation pierces the plane twice, at two points surrounding the fixed point of the original limit cycle (dashed curve).

## 2.1 Linear equations with periodic coefficients

A linear differential equation with constant coefficients such as

$$a\ddot{x} + b\dot{x} + cx = 0 \tag{21}$$

has as its general solution

$$x(t) = \alpha_1 e^{\lambda_1 t} + \alpha_2 e^{\lambda_2 t} \tag{22}$$

where $\lambda_{1,2}$ are the two solutions of the quadratic equation,

$$a\lambda^2 + b\lambda + c = 0. \tag{23}$$

This form can be generalized to equations in which the coefficients are not constant, but periodic functions:

$$a(t)\ddot{x} + b(t)\dot{x} + c(t)x = 0 \tag{24}$$

where $a$, $b$ and $c$ are periodic functions with period $T$. The general solution of (24), analogous to the solution (22), is

$$x(t) = \alpha_1(t) e^{\lambda_1 t} + \alpha_2(t) e^{\lambda_2 t} \tag{25}$$

Functions $\alpha_{1,2}(t)$ have the same period as $a(t)$, $b(t)$ and $c(t)$ and are called *Floquet functions*. The exponents $\lambda_1$ and $\lambda_2$ are called *Floquet exponents*. In contrast to the exponents in (22), these are

not the roots of a polynomial and must be calculated numerically or asymptotically. The values $\mu_1 \equiv e^{\lambda_1 T}$, $\mu_2 \equiv e^{\lambda_2 T}$ are called *Floquet multipliers*.

Similarly, for a general first-order and $N^{th}$ order system:

$$\dot{x} = c(t)x \quad \Rightarrow \quad x(t) = e^{\lambda t}\alpha(t) \tag{26}$$

$$\sum_{n=0}^{N} c_n(t)x^{(n)} = 0 \quad \Rightarrow \quad x(t) = \sum_{n=1}^{N} e^{\lambda_n t}\alpha_n(t) \tag{27}$$

where $\alpha_n(t)$'s have period $T$.

## 2.2 Application to limit cycles

Now consider a nonlinear dynamical system:

$$\dot{x} = f(x) \tag{28}$$

with a periodic solution (limit cycle) of period $T$:

$$\bar{x}(t+T) = \bar{x}(t) \tag{29}$$

We perturb around the limit cycle:

$$x(t) = \bar{x}(t) + \epsilon(t) \tag{30}$$

where $\epsilon(t)$ is assumed to remain small. Substituting into the equation gives

$$\dot{\bar{x}} + \dot{\epsilon} = f(\bar{x}(t)) + f'(\bar{x}(t))\epsilon(t) + f''(\bar{x}(t))\epsilon^2(t) + ... \tag{31}$$

which by neglecting high-order terms leads to

$$\dot{\epsilon} = f'(\bar{x}(t))\epsilon(t) \tag{32}$$

which is of the Floquet form (26). Therefore:

$$\epsilon(t) = e^{\lambda t}\alpha(t) \tag{33}$$

with $\alpha(t)$ periodic with period $T$. The limit cycle $\bar{x}(t)$ is stable if the real part of $\lambda$ is negative. If $\lambda$ is complex, this indicates that the period of the perturbation $\epsilon$ is different from that of the limit cycle $\bar{x}(t)$. In order to ensure uniqueness of the imaginary part of $\lambda$, we choose:

$$\mathrm{Im}(\lambda) \in \left(-\frac{\pi}{T}, \frac{\pi}{T}\right] \tag{34}$$

The remainder can be absorbed into the periodic function $\alpha(t)$, as illustrated in Figure 9.

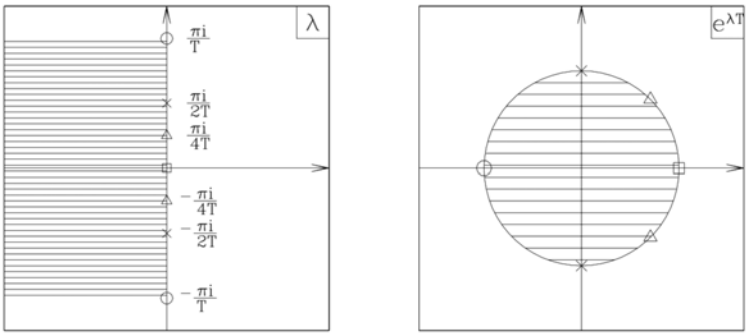


Figure 9: Stability region for Floquet exponents $\lambda$ (left) and for Floquet multipliers $e^{\lambda T}$ (right). The imaginary $\lambda$ axis on the left is mapped into the unit circle on the right.

For a multidimensional system of dimension $N$, the equations above can be generalized to:

$$\dot{\epsilon} = Df(\bar{x}(t))\epsilon \tag{35}$$

$$\epsilon(t) = \sum_{j=1}^{N} e^{\lambda_j t}\alpha_j(t) \tag{36}$$

There are $N$ Floquet exponents and Floquet functions and the limit cycle $\bar{x}$ is stable if all the real parts of the exponents are negative. The Floquet multipliers and Floquet functions are eigenvalues and eigenvectors of the monodromy matrix defined as follows. Let $M(t)$ be an $N \times N$ matrix whose evolution equation and initial condition are:

$$\dot{M} = Df(\bar{x}(t))M, \qquad M(0) = I, \tag{37}$$

where $M(T)$ is called the monodromy matrix. Thus, determining the Floquet exponents requires integrating the evolution equations linearized about $\bar{x}(t)$. The limit cycle $\bar{x}(t)$ is stable if all Floquet exponents have negative real parts or, equivalently, if all Floquet multipliers are within the unit circle; see figure 9.

## 2.3 Examples from fluid dynamics

### 2.3.1 Faraday instability

Faraday discovered in 1831 that vertically vibrating a thin fluid layer produces a pattern of standing waves with lattice patterns of hexagons and squares. More exotic patterns such as quasicrystals and oscillons were later found in the 1990s by imposing a vibration containing two frequencies; see Figure 10.

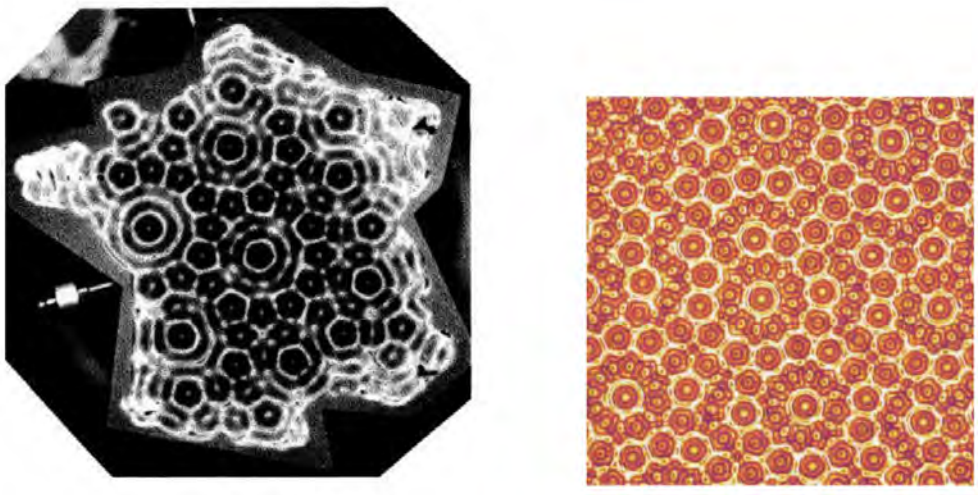

Figure 10: Quasicrystalline patterns of surface waves obtained by vertically oscillating a fluid layer with a two-frequency forcing function. From [3] (left) and [5] (right).

In a frame oscillating with the container, the vibration appears as an oscillatory gravitational force:

$$G(t) = g\,(1 - a\cos(\omega t)) \tag{38a}$$

$$G(t) = g\,(1 - [a\cos(m\omega t) + b\cos(n\omega t + \phi_0)]) \tag{38b}$$

We wish to determine the conditions for the free surface to become linearly unstable. Considering an homogeneous domain in the horizontal, with bounded solutions in the horizontal directions, and the different eigenvectors $k$ decoupled, the perturbation of the surface height is expanded as:

$$\zeta(x, y, t) = \sum_{\mathbf{k}} e^{i\mathbf{k}\cdot\mathbf{x}} \hat{\zeta}_{\mathbf{k}}(t) \tag{39}$$

Because of the time-periodic forcing, this is a Floquet problem:

$$\hat{\zeta}_{\mathbf{k}}(t) = \sum_{j} e^{\lambda^j_{\mathbf{k}} t} f^j_{\mathbf{k}}(t) \tag{40}$$

where $f^j_k(t)$ are $T$-periodic and $\lambda^j_k$ are the Floquet exponents. In the inviscid, sinusoidal forcing case, the problem reduces to the Mathieu equation:

$$\frac{\partial^2 \hat{\zeta}_k}{\partial t^2} + \omega_0^2 [1 - a\cos(\omega t)]\hat{\zeta}_k = 0 \tag{41}$$

where $\omega_0^2$ is a parameter combining the densities of the upper and lower fluids, the surface tension, the wavenumber $k$ and the gravitational acceleration $g$. Instability occurs when one of the Floquet multipliers $\mu = e^{\lambda T}$ satisfies $|\mu| > 1$. A value of $\mu = -1$ indicates a subharmonic response (period doubling), while $\mu = +1$ indicates a harmonic response, as illustrated in Figure 11.

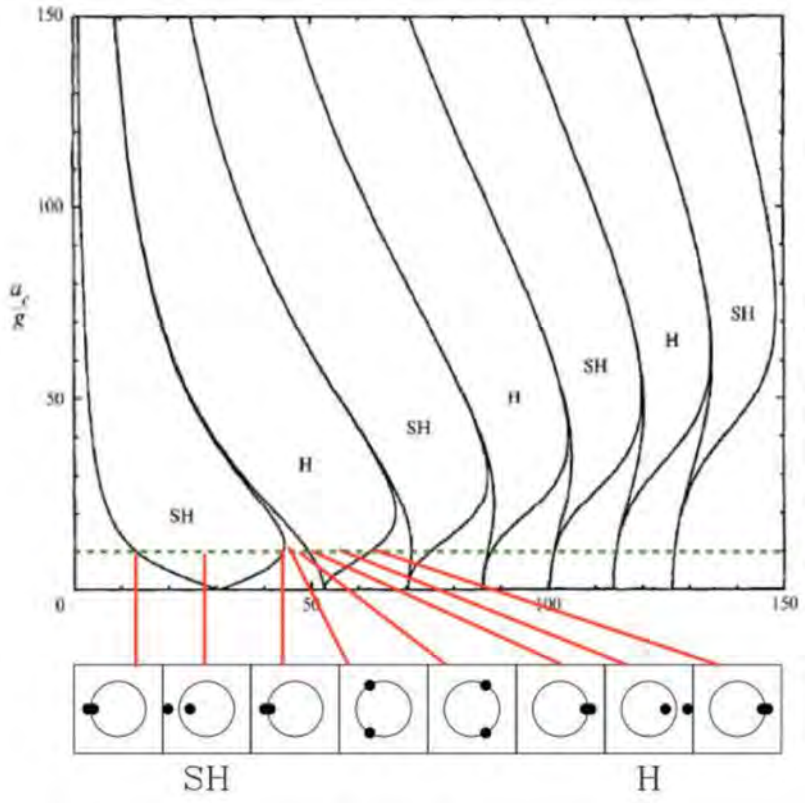


Figure 11: Instability tongues for the Faraday problem in an inviscid fluid. Inside the tongues, one of the Floquet multipliers $\mu$ exceeds one in absolute value. In a harmonic tongue (H), $\mu > 1$ for some $\mu$, while in a subharmonic tongue (SH) $\mu < 1$. Adapted from Kumar and Tuckerman [6].

### 2.3.2 Cylinder wake

Consider the flow past a circular cylinder. At low Reynolds number, the flow is steady. As $Re$ increases, periodic vortex shedding (the von Kármán vortex street) appears (Figure 12), forming a limit cycle.

At higher $Re$, this limit cycle becomes unstable to 3D perturbations. Let $U_{2D}(x, y, t)$ be the 2D time-periodic (i.e., limit cycle) solution:

$$\partial_t U_{2D} = -(U_{2D} \cdot \nabla) U_{2D} - \nabla P_{2D} + \frac{1}{Re} \Delta U_{2D}. \tag{42}$$

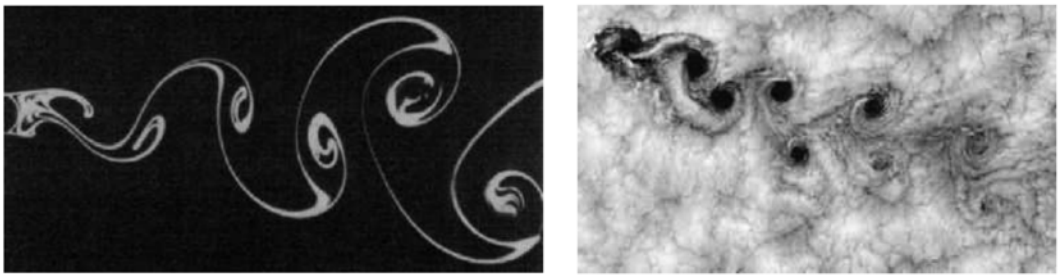

Figure 12: Von Karman vortex street in the lab (left, photograph by S. Taneda; reproduced in [10]) and in nature (right, off the Juan Fernández Islands, Chile, [8]). For the photo on the right, the Taylor-Proudman theorem for a rapidly rotating earth implies that a mountain creates a wake at altitudes far above it.

A perturbation $u_{3D}$ is a solution to the Navier-Stokes equations linearized around $U_{2D}$:

$$\partial_t u_{3D} = -(U_{2D} \cdot \nabla) u_{3D} - (u_{3D} \cdot \nabla) U_{2D} - \nabla p_{3D} + \frac{1}{Re} \Delta u_{3D}, \tag{43}$$

which is a Floquet problem in time via the periodic flow $U_{2D}$. We can therefore decompose $u_{3D}$ as

$$u_{3D} \sim e^{i\beta z} e^{\lambda_\beta t} f_\beta(x, y, t) \tag{44}$$

where $f_\beta$ is $T$-periodic and $\lambda_\beta$ is a Floquet exponent. The corresponding multiplier is $\mu_\beta = e^{\lambda_\beta T}$. For each $\beta$ there is a set of Floquet functions and multipliers.

The Floquet analysis was carried out numerically by Barkley and Henderson [1]. There are actually two bifurcations, to modes with different wavenumbers $\beta$ at different Reynolds numbers $Re$, as shown in Figure 13. It turns out that the limit cycle undergoes a steady bifurcation, i.e., $\mu$ traverses the unit circle at 1, not at $-1$ nor at $e^{\pm i\theta}$. Thus, the temporal behavior of the new 3D solutions is similar to that of the 2D flow. The bifurcation is a circle pitchfork, in that any spatial phase in $z$ is permitted.

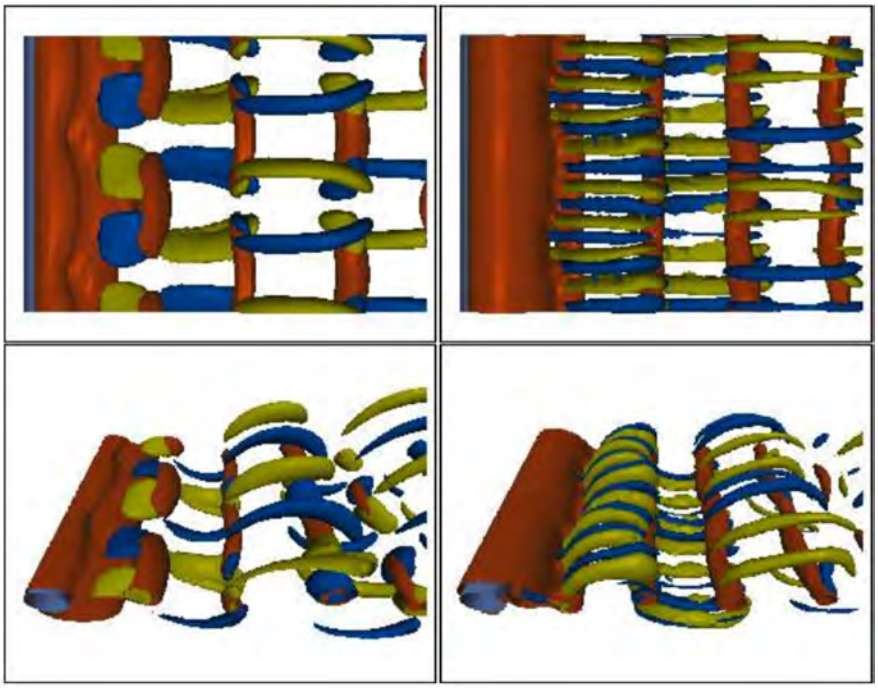

Figure 13: Three-dimensional flow past a cylinder. Left: at Re = 210, mode A with a wavelength near four times the cylinder diameter. Right: at Re = 250, mode B with a wavelength near the cylinder diameter. From Thompson et al. [9].

## References


[1] D. Barkley and R. D. Henderson. Three-dimensional Floquet stability analysis of the wake of a circular cylinder. *J. Fluid Mech.*, 322:215–241, 1996.

[2] P. Coullet and C. Tresser. Iterations of endomorphisms and renormalization group. *C. R. Acad. Sc. Paris A*, 287:577–581, 1978.

[3] W. S. Edwards and S. Fauve. Patterns and quasi-patterns in the Faraday experiment. *J. Fluid Mech.*, 278:123–148, 1994.

[4] M. J. Feigenbaum. Quantitative universality for a class of nonlinear transformations. *J. Stat. Phys.*, 19:25–52, 1978.

[5] A. Kudrolli, B. Pier, and J. P. Gollub. Superlattice patterns in surface waves. *Physica D*, 123: 99–111, 1998.

[6] K. Kumar and L. S. Tuckerman. Parametric instability of the interface between two fluids. *J. Fluid Mech.*, 279:49–68, 1994.

[7] A. Libchaber, C. Laroche, and S. Fauve. Period doubling cascade in mercury, a quantitative measurement. *J. Physique Lett.*, 43:211–216, 1982.

[8] NASA Earth Observatory, Image courtesy of Bob Cahalan. Vortex street off the Juan Fernández islands, 1999. URL `https://earthobservatory.nasa.gov/images/737/`

vortex-street-off-the-juan-fernandez-islands. Landsat 7 ETM+ image, 15 September 1999, NASA GSFC.

[9] M. Thompson, K. Hourigan, and J. Sheridan. Three-dimensional instabilities in the wake of a circular cylinder. *Exp. Therm. Fluid Sci.*, 12:190–196, 1996.

[10] M. Van Dyke. *An Album of Fluid Motion*. Parabolic Press, Stanford, CA, 1982. Plate 44, photograph by S. Taneda.

# GFD 2025 Lecture 10: Patterns of Turbulence

Laurette Tuckerman; notes by Kyle Mckee and Farid Rajkotia-Zaheer

June 27, 2025

## 1 Introduction

The main purpose of this lecture was to introduce the concept of pattern formation in flows transitioning from a laminar state to a turbulent one, with a specific focus on planar *bounded* shear flows. The lecture began with a historical overview of literature describing the transition to turbulence from a laminar base state, an active area of research that dates back over 100 years [29, 34]. The lecture moved on to a discussion of pattern formation within flows (now containing turbulence) that have deviated from the laminar base state. The latter part of the lecture focused on understanding pattern formation in a more broad class of shear flows including Taylor-Couette flow (TCF), cylindrical Poiseuille flow (CPF), and Waleffe flow (WF). A more comprehensive presentation of the latter material may be found in a review paper by the lecturer, "*Patterns in Wall-Bounded Shear-Flows*", Tuckerman et al. [42].

## 2 Previous Approaches to Transition

One seeks to characterize the transition to turbulence from a laminar base state by a critical value of the Reynolds number, measuring the ratio of the advective to viscous forces; Reynolds (1895) [30] originally denoted this dimensionless number by $K$, but 15 years later, Sommerfeld (1909) [34] named it after Reynolds. This section offers a brief overview of historical approaches to describing the transition from laminar to turbulent flow. While many have since been replaced by modern theories, these early efforts remain valuable for understanding how successive hypotheses paved the way for today's understanding.

### 2.1 Linear Stability theory

Mathematical analyses of the linear stability of viscous parallel base states trace back to Sommerfeld, who derived an equation describing the evolution of small perturbations to a steady laminar viscous parallel base flow $U(y)\hat{\boldsymbol{x}}$. The equation – now called the Orr-Sommerfeld (OS) equation – is a fourth-order linear differential equation for a streamfunction of the form $\Psi = \phi(y,t)\exp(\mathrm{i}\alpha x)$

$$\underbrace{-\left(D^2-\alpha^2\right)\phi_t}_{\equiv\mathcal{B}\phi_t} = \underbrace{-\mathrm{i}\alpha\left(\frac{1}{\mathrm{i}\alpha R}\left(D^2-\alpha^2\right)^2 - U\left(D^2-\alpha^2\right)+D^2U\right)\phi}_{\equiv\mathcal{L}\phi}, \tag{1}$$

whose eigenvalues indicate whether perturbations grow or decay. Note that Squire (1933) [35] pointed out that for linear stability, we may restrict our attention to two-dimensional disturbance since the stability of any three-dimensional disturbance corresponds to the stability problem of a two-dimensional disturbance at a lower Reynolds number.

An especially interesting feature of wall-bounded shear flows is that they become unstable for Reynolds numbers much lower than linear theory predicts. By solving the OS equation, Somerfeld's student Heisenberg 1924 [16] obtained a linear stability threshold for plane Poiseuille flow (PPF) of 5610, within a few percent of the exact value of 5772.22 obtained by Orszag 1971 [22] and others [20, 37] However, for PPF, experiments have shown that instability occurs at around $Re \approx 1000$. For planar Couette flow (PCF), linear stability predicts stability at all Reynolds numbers ($R_c \to \infty$) [31], while both experiments [38, 5] and numerical simulations [12, 33] show a transition from the laminar state at Reynolds numbers on the order of 300-400.

Because of the contrast between transition and the linear instability threshold, exploring the route to turbulence is a very active area of research. An overview of candidate theories describing this transition, some of which have been accepted and rejected over the years, are presented in the following sections.

### 2.2 Transient growth and non-normal operators

Although it has been shown for bounded domains that the OS operator admits a complete set of eigenfunctions, these eigenfunctions are not orthogonal because $\mathcal{B}^{-1}\mathcal{L}$ of (1) is non-normal [27, 39]. One consequence of this is the possibility of large transient growth despite linear stability. The notion of transient growth of non-orthogonal eigenfunctions can be demonstrated through a prototypical example in $\mathbb{R}^2$, as follows. Suppose the normalized eigenvectors of some operator are $\boldsymbol{v}_1 = (1,0)^T$ and $\boldsymbol{v}_2 = (1,\epsilon)^T/\sqrt{1+\epsilon^2}$, where $0 < \epsilon \ll 1$ and eigenvalues given by $\lambda_{1,2} = -1, -10$, so that the system is linearly stable (any initial condition decays to $(0,0)^T$ as $t \to \infty$). For an initial condition $\boldsymbol{x}_0 = (1,1)^T$, $\boldsymbol{x}(t) = \left(1 - \frac{1}{\epsilon}\right)\boldsymbol{v}_1 \exp(-t) + \frac{1}{\epsilon}\boldsymbol{v}_2 \exp(-10t)$. At an intermediate time (e.g., $t = 1$), the coefficient of the second eigenvector has almost completely decayed and the norm of the vector $\boldsymbol{x}$ has increased by a factor of $||\boldsymbol{x}(1)||/||\boldsymbol{x}(0)|| \sim O(1/\epsilon)$. The more parallel the eigenvectors and the larger the discrepency between their eigenvalues, the larger the transient growth. The key takeaway is that eigenvalues arising from linear stability are insufficient for describing the evolution when the operator is non-normal. A related concept for analysing stability in systems described by non-normal operators is the pseudospectrum [27].

### 2.3 Other theoretical approaches

Although Squire's theorem tells us that the state that first becomes linearly unstable (at the lowest Reynolds number) corresponds to a two-dimensional disturbance, it fails to describe experiments, indicating that linear stability does not capture all of the physics. Orszag and Patera [24] examined three-dimensional secondary stability superposed on a slightly perturbed two-dimensional planar Poiseuille flow and found that three-dimensional perturbations grew from this state at $Re \approx 1000$. This fully three-dimensional viewpoint was also supported by [23]. At a similar time, a framework for relating turbulence to chaos and strange attractors was investigated [32, 36, 6].

### 2.4 Waleffe's self-sustaining process for shear flows

In the 1990s, focus shifted to determining the smallest periodic boxes that could sustain turbulence in numerical simulations [18, 15]. This ultimately led to the development by Waleffe [43] of the self-sustaining process (SSP) for wall-bounded shear flows, which is now widely accepted as describing transitional turbulence in shear flows.

We demonstrate the SSP by simulating plane Couette flow (PCF) in the minimal flow unit as found by Hamilton et al [15]. We denote the streamwise direction by $\hat{\mathbf{x}}$, the wall-normal direction by $\hat{\mathbf{y}}$, and the spanwise direction by $\hat{\mathbf{z}}$. Lengths are non-dimensionalized by the wall separation.

The flow is driven by the relative motion of impenetrable rigid walls at $y = \pm 1$. The governing equations are the Navier–Stokes equations without body forcing:

$$\partial_t \mathbf{u} + (\mathbf{u} \cdot \nabla)\mathbf{u} + \nabla p = \tfrac{1}{\mathrm{Re}} \nabla^2 \mathbf{u}, \quad \nabla \cdot \mathbf{u} = 0, \quad \mathbf{u}\,(x, \pm 1, z) = \pm \hat{\mathbf{x}}. \tag{2}$$

We enforce periodicity in the streamwise and spanwise directions, using the minimum lengths $L_x = 1.75\pi$ and $L_z = 1.2\pi$ determined by [15] needed to sustain turbulence in PCF at $\mathrm{Re} = 400$. The spatial resolution of $16 \times 16 \times 33$ for the domain was found to suffice [15].

We ran simulations of this configuration using the software package Dedalus [7], with $\mathrm{Re} = 625$ and initial data designed to excite the SSP. Figure 1 illustrates the first step of the SSP [43]: streamwise vortices (left) advect the streamwise velocity contours (right), which would be straight for the laminar flow $\mathbf{U} = y\hat{\mathbf{x}}$. The resulting spanwise dependence of the streamwise velocity constitutes the streaks. These become wavy through a linear instability, shown in Figure 2, which is the second step of the SSP. The third and final feature of the SSP is the generation of the streamwise vortices by the nonlinear self-interaction of the wavy streaks.

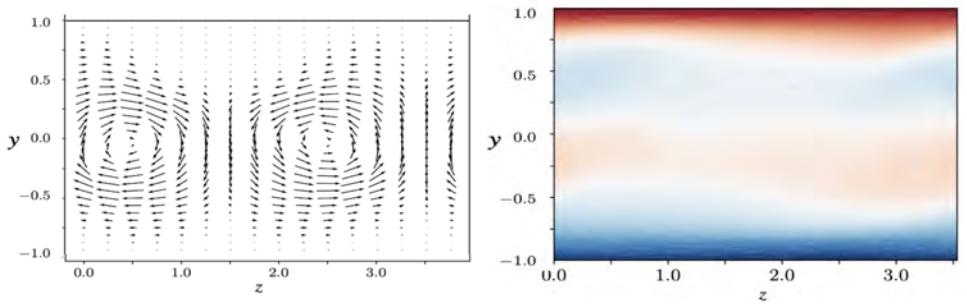


Figure 1: Velocity field in the HKW cell as seen from the $y, z$-plane. Left: velocity vectors for the cross-flow velocities, $v$ and $w$, capture the streamwise vortices. Right: streamwise velocity is advected by the vortices.

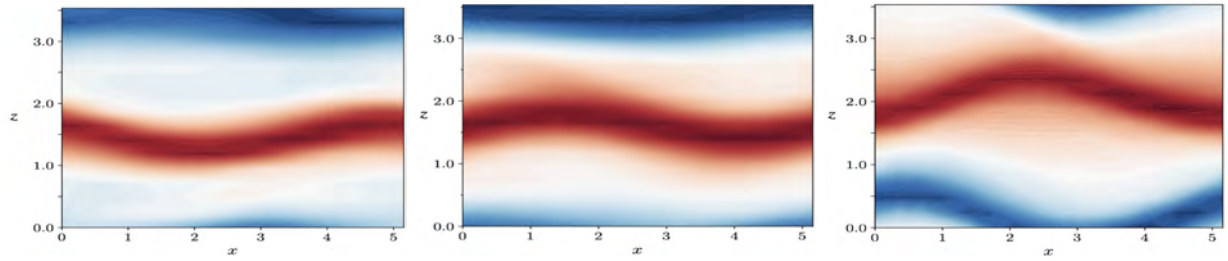


Figure 2: Snapshots of streamwise velocity containing wavy streaks in plane Couette flow in the HKW cell [15]. The snapshots are taken in the $x, z$-plane with $y$ fixed at the mid-plane. Time increases from left to right.

## 3 Turbulent-Laminar Bands in Shear Flows

Experiments by [1, 9, 26] have revealed that transitions to turbulence (between laminar and turbulent flow) in wall-bounded shear flows are characterized by the appearance of long oblique bands. These bands have been observed both numerically and experimentally in plane Couette (PCF) [26, 4, 12], plane Poiseuille [40, 41] and Taylor–Couette (TC) [9, 21, 11] flows, as well as in less

canonical flows, such as annular pipes [17] and rotor-stator flows [10]. Turbulent bands in shear flows appear as regular patterns [26], with a wavelength that is 20 times the length scale of the shear layer. For this reason, they can only be accommodated in domains that have two large and one small dimension. This is not the case in a pipe, whose circumference is comparable to its radius, and so transitional turbulence in pipes does not contain bands, but rather puffs [44, 3], which play a similar role.

A turbulent-laminar pattern in PCF is shown in figure 3, taken from [42]. The turbulent bands are oriented obliquely with respect to the streamwise direction. However, the primary structures within each band are still streamwise aligned. These correspond to the streamwise vortices and streaks shown in the simulation of PCF within the HKW minimal flow unit illustrated in figures 1 and 2.

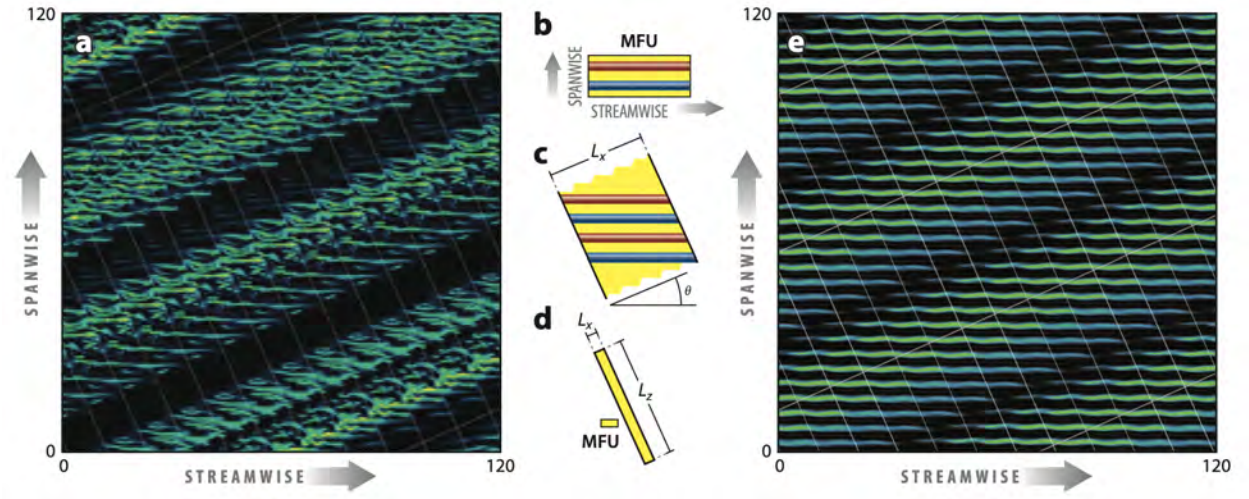


Figure 3: Turbulent-laminar pattern in PCF at Re = 350 calculated within a rectangular box, which is tilted with respect to the streamwise direction at an angle that matches the angle of the bands observed in experiment. Left: result of time-dependent simulation. Middle: Sketch of tilted box used in these simulations, whose dimensions must be such as to accommodate the small-scale streamwise streaks (red and blue bars) as well as the large-scale oblique turbulent bands. Right: steady state calculated by numerical continuation. Left and middle panels from [4], right panel from [28].

We now seek to understand the transition to turbulence in the absence of walls. Waleffe flow (WF) [43], serves as a model that can be studied to understand this transition to turbulence. The boundary conditions are stress-free

$$\partial_z u,\ \partial_z v,\ w = 0, \tag{3}$$

and the flow is driven by a trigonometric body force of the form $\sin(\beta y)$. The resulting flow is visualized in figure4, with the laminar solution represented by the dashed curve.

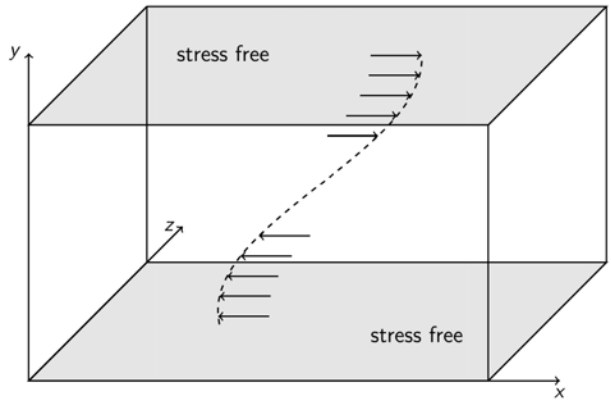


Figure 4: Schematic of the laminar solution of Waleffe flow and domain setup.

Although the boundary conditions and setup of PCF and WF are different, the idea is to use WF to mimic the interior of PCF. That is, we use WF to mimic the bulk flow of PCF excluding boundary layers. Figure 5 shows the construction for this procedure. Figure 5a) compares the linear laminar flow of PCF with the sinusoidal laminar flow of WF (though using different scalings for the height and velocity, for reasons that will soon be made clear). Figure 5b) shows that the mean of turbulent PCF at Re = 500 has boundary layers located at $|y| \gtrsim 0.625$, but that it is almost linear in the interior region $|y| \lesssim 0.625$. Although laminar WF is sinusoidal, its turbulent mean is linear, matching (when scaled as shown) the interior region of the turbulent mean of PCF. We therefore use turbulent WF, a flow without any boundary layers, to mimic turbulent PCF over its interior region. Figure 6 compares simulations of PCF and WF, demonstrating that oblique

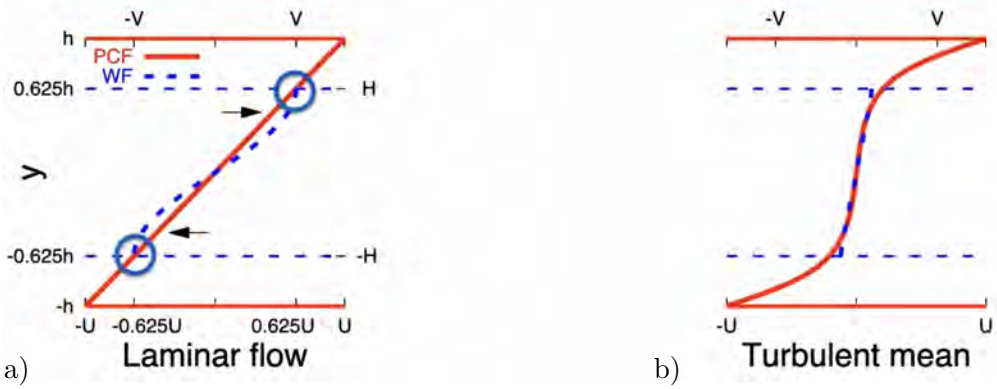


Figure 5: Comparison of PCF (solid red curve) with rigid boundaries and WF (dashed blue curve). a) Laminar PCF is linear, while laminar WF flow is sinusoidal. b) The turbulent mean of PCF for Re = 500 is linear in the interior $|y| \lesssim 0.625$, with boundary layers for $|y| \gtrsim 0.625$. The turbulent mean of WF is linear throughout its domain, with no boundary layers. Thus, a scaled version of WF flow can be used to mimic the interior of PCF.

turbulent bands also appear in the stress-free WF. Moreover, the bands have the same wavelength and angle in the two flows. (The Reynolds number for WF has been redefined to use the reduced height and velocity scales shown in Figure 5.) Notice the surprising feature that walls are not necessary to reproduce the features of transitional turbulence in wall-bounded shear flows. All that is needed is confinement and shear.

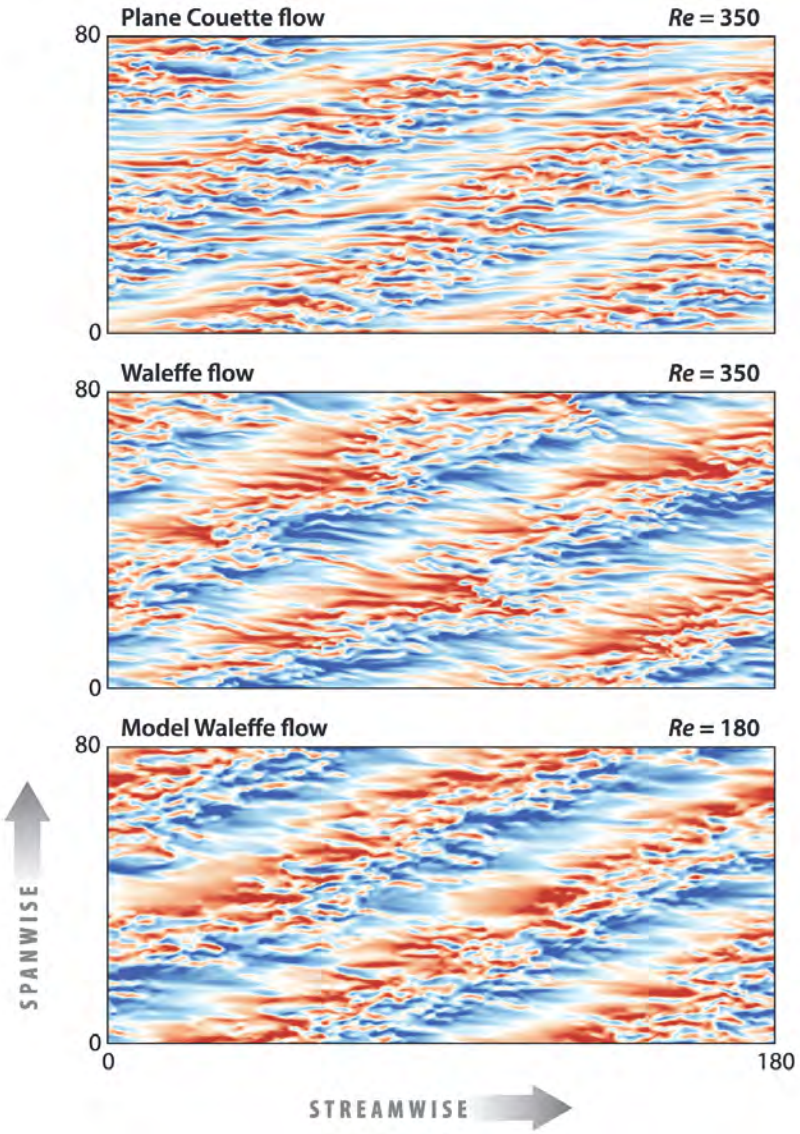


Figure 6: Simulations of PCF, WF and MWF. All three flows display turbulent bands with the same angle and wavelength. The difference in Reynolds numbers is due to the fact that no scaling has been carried out to compensate for the effectively much coarser resolution and consequently reduced viscous dissipation of MWF. Figure taken from [42].

This finding has both theoretical and numerical consequences. To explore this, inspired by Waleffe's model when illustrating the SSP in PCF, the velocity components are expanded in low-order modes in $y$,

$$\begin{aligned} u(x,y,z) &= u_0(x,z) + u_1(x,z)\sin(\beta y) + u_2(x,z)\cos(2\beta y) + u_3(x,z)\sin(3\beta y), \\ v(x,y,z) &= v_1(x,z)\cos(\beta y) + v_2(x,z)\sin(2\beta y) + v_3(x,z)\cos(3\beta y), \\ w(x,y,z) &= w_0(x,z) + w_1(x,z)\sin(\beta y) + w_2(x,z)\cos(2\beta y) + w_3(x,z)\sin(3\beta y). \end{aligned} \tag{4}$$

As before, $x$ and $z$ are periodic directions while $y$ is wall-normal and $\beta = \pi/2H$, with $H$ the wall separation. Incompressibility can be automatically imposed using a poloidal-toroidal decomposition,

which in the horizontally periodic box takes the form

$$\mathbf{u} = f(y)\mathbf{e}_x + g(y)\mathbf{e}_z + \nabla \times \psi(x,y,z)\mathbf{e_y} + \nabla \times \nabla \times \phi(x,y,z)\mathbf{e_y}, \tag{5}$$

where $f(y)\mathbf{e}_x + g(y)\mathbf{e}_z$ is the mean field and purely a function of the wall-normal coordinate, $y$. Furthermore, $\varphi$ and $\psi$ are the poloidal and toroidal potential functions respectively. Substituting (5) into the Navier–Stokes equations, we obtain a system of 7 PDEs in $(x, z, t)$ and 6 ODEs for the non-constant means $f$ and $g$. We note that Waleffe's original model of the SSP used free-slip boundary conditions and is contained within this system. Simulating this model Waleffe flow (MWF), one finds that the flow displays the same transitional behavior as PCF and fully resolved WF, as shown in figure 6.

## 4 Continuous or Discontinuous Transition to Turbulence

A central question regarding the transition to turbulence is whether it is continuous or discontinuous. In the classic transitions to Rayleigh–Bénard convection or Taylor–Couette flow via supercritical bifurcations, rolls appear everywhere, with an intensity that is infinitesimal at onset and increases with the Reynolds or Rayleigh number. In contrast, transitional turbulence is intermittent: the turbulence is of a constant intensity, or nearly so, but it occupies only a small fraction of the domain at onset, called the turbulent fraction $F_t$. The question is whether $F_t$ is a continuous function of the Reynolds number. Pomeau (1986)[25] conjectured that the transition might belong to the universality class of directed percolation. This would imply not only that $F_t$ would depend continuously on Re, but also that power laws with specific exponents would hold near onset. This conjecture has been verified by Chantry et al. 2017 [8] for MWF (see Figure 7a)) and then by Klotz et al. (2022) [19] in a very narrow TCF apparatus used to approximate PCF.

A closely related approach to studying the threshold arises from the dynamical behavior of turbulent bands or puffs, more specifically their tendency to decay (returning to laminar flow) or to split (propagating the turbulence, since the two resulting puffs or bands grow in size). These are both statistical processes, with characteristic lifetimes that depend on the Reynolds number. The threshold is defined as the Reynolds number at which the characteristic lifetimes of these two processes are equal, i.e. the likelihood of splitting overtakes that of decay, marking a critical point for sustained turbulence.

This analysis was first developed and carried out both numerically and experimentally for pipe flow by Avila et al. (2011) [2] who determined that the threshold was $\mathrm{Re}_{\mathrm{pipe}} = 2040$. This was followed by Shi et al. (2013) [33], who determined that the threshold for PCF was $\mathrm{Re}_{\mathrm{PCF}} = 325$ (where we have denoted $\mathrm{Re}_{\mathrm{PCF}}$ merely by Re in other parts of this document), and by Gomé et al. (2020, 2022) [13, 14], who determined that the threshold for sustained turbulence in PPF was $\mathrm{Re}_{\mathrm{PPF}} = 980$ (see Figure 7b)). The difference in these thresholds is due primarily to the different conventions (velocity and length scales) used for defining the Reynolds numbers in these three flows.

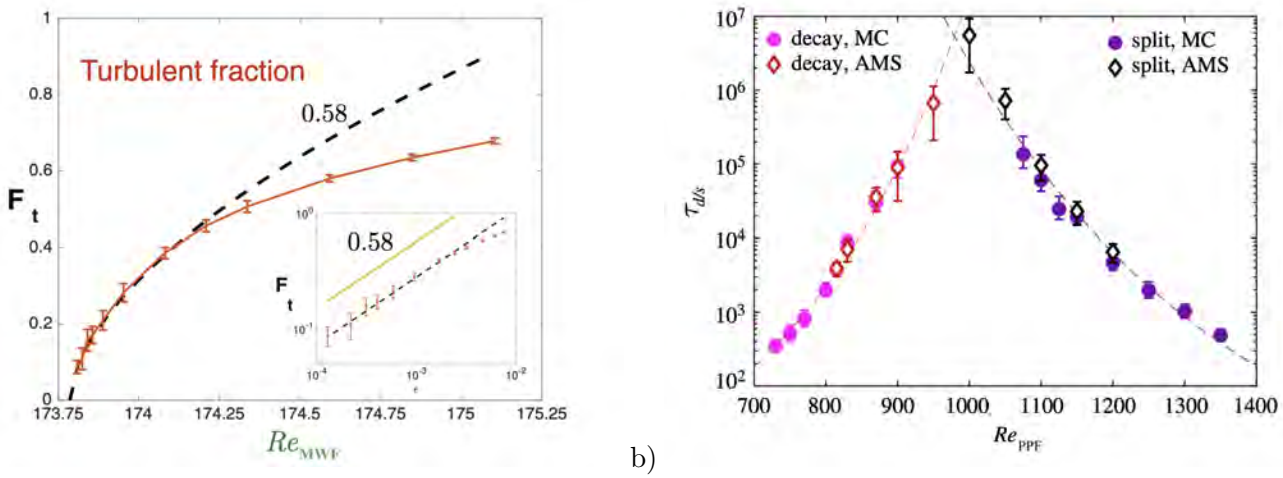


Figure 7: a) Turbulent fraction $F_t$ as a function of Reynolds number $\mathrm{Re}_{\mathrm{MWF}}$ for Model Waleffe Flow. $F_t$ goes continuously to zero at the threshold $\mathrm{Re}^c_{\mathrm{MWF}} \approx 173.75$ with the directed percolation power law $[\mathrm{Re}_{\mathrm{MWF}} - \mathrm{Re}^c_{\mathrm{MWF}}]^{0.58}$. From [8].
b) Timescales for decay (red and magenta, $\tau_d$) and for splitting (black and purple, $\tau_s$) as a function of $\mathrm{Re}_{\mathrm{PPF}}$. The two curves display double exponential behavior and cross at $\mathrm{Re}^c_{\mathrm{PPF}} \approx 980$. Solid symbols are computed using the Monte Carlo method (a large number of simulations) and hollow symbols with the rare-event algorithm of Adaptative Multilevel Splitting. From [13].

## References


[1] C. D. Andereck, S. Liu, and H. L. Swinney. Flow regimes in a circular Couette system with independently rotating cylinders. *J. Fluid Mech.*, 164:155–183, 1986.

[2] K. Avila, D. Moxey, A. De Lozar, M. Avila, D. Barkley, and B. Hof. The onset of turbulence in pipe flow. *Science*, 333:192–196, 2011.

[3] D. Barkley. Theoretical perspective on the route to turbulence in a pipe. *J. Fluid Mech.*, 803: P1, 2016.

[4] D. Barkley and L. S. Tuckerman. Computational study of turbulent laminar patterns in Couette flow. *Phys. Rev. Lett.*, 94:014502, 2005.

[5] S. Bottin, F. Daviaud, P. Manneville, and O. Dauchot. Discontinuous transition to spatiotemporal intermittency in plane Couette flow. 43:171–176, 1998.

[6] A. Brandstäter, J. Swift, H. L. Swinney, A. Wolf, J. D. Farmer, E. Jen, and P. Crutchfield. Low-dimensional chaos in a hydrodynamic system. *Phys. Rev. Lett.*, 51:1442, 1983.

[7] K. J. Burns, G. M. Vasil, J. S. Oishi, D. Lecoanet, and B. P. Brown. Dedalus: A flexible framework for numerical simulations with spectral methods. *Phys. Rev. Research*, 2:023068, 2020.

[8] M. Chantry, L. S. Tuckerman, and D. Barkley. Universal continuous transition to turbulence in a planar shear flow. *J. Fluid Mech.*, 824, 2017.

[9] D. Coles. Transition in circular Couette flow. *J. Fluid Mech.*, 21:385–425, 1965.

[10] A. Cros and P. Le Gal. Spatiotemporal intermittency in the torsional Couette flow between a rotating and a stationary disk. *Phys. Fluids*, 14:3755–3765, 2002.

[11] S. Dong. Evidence for internal structures of spiral turbulence. *Phys. Rev. E*, 80:067301, 2009.

[12] Y. Duguet, P. Schlatter, and D. S. Henningson. Formation of turbulent patterns near the onset of transition in plane Couette flow. *J. Fluid Mech.*, 650:119–129, 2010.

[13] S. Gomé, L. S. Tuckerman, and D. Barkley. Statistical transition to turbulence in plane channel flow. *Phys. Rev. Fluids*, 5:083905, 2020.

[14] S. Gomé, L. S. Tuckerman, and D. Barkley. Extreme events in transitional turbulence. *Phil. Trans. R. Soc. A*, 380:20210036, 2022.

[15] J. M. Hamilton, J. Kim, and F. Waleffe. Regeneration mechanisms of near-wall turbulence structures. *J. Fluid Mech.*, 287:317–348, 1995.

[16] W. Heisenberg. Über stabilität und turbulenz von flüssigkeitsströmen. In *Original Scientific Papers Wissenschaftliche Originalarbeiten*, pages 31–81. Springer, 1924.

[17] T. Ishida, Y. Duguet, and T. Tsukahara. Transitional structures in annular Poiseuille flow depending on radius ratio. *J. Fluid Mech.*, 794, 2016.

[18] J. Jiménez and P. Moin. The minimal flow unit in near-wall turbulence. *J. Fluid Mech.*, 225: 213–240, 1991.

[19] L. Klotz, G. Lemoult, K. Avila, and B. Hof. Phase transition to turbulence in spatially extended shear flows. *Phys. Rev. Lett.*, 128:014502, 2022.

[20] C. C. Lin. On the stability of two-dimensional parallel flows. iii. stability in a viscous fluid. *Q. Appl. Math.*, 3:277–301, 1946.

[21] A. Meseguer, F. Mellibovsky, M. Avila, and F. Marques. Instability mechanisms and transition scenarios of spiral turbulence in Taylor-Couette flow. *Phys. Rev. E*, 80:046315, 2009.

[22] S. A. Orszag. Accurate solution of the Orr–Sommerfeld stability equation. *J. Fluid Mech.*, 50: 689–703, 1971.

[23] S. A. Orszag and L. C. Kells. Transition to turbulence in plane Poiseuille and plane Couette flow. *J. Fluid Mech.*, 96:159–205, 1980.

[24] S. A. Orszag and A. T. Patera. Secondary instability of wall-bounded shear flows. *J. Fluid Mech.*, 128:347–385, 1983.

[25] Y. Pomeau. Front motion, metastability and subcritical bifurcations in hydrodynamics. *Physica D*, 23:3–11, 1986.

[26] A. Prigent, G. Grégoire, H. Chaté, O. Dauchot, and W. van Saarloos. Large-scale finite-wavelength modulation within turbulent shear flows. *Phys. Rev. Lett.*, 89:014501, 2002.

[27] S. C. Reddy, P. J. Schmid, and D. S. Henningson. Pseudospectra of the Orr–Sommerfeld operator. *SIAM J. Appl. Math.*, 53:15–47, 1993.

[28] F. Reetz and T. M. Schneider. Invariant states in inclined layer convection. part 1. temporal transitions along dynamical connections between invariant states. *J. Fluid Mech.*, 898:A22, 2020.

[29] O. Reynolds. Xxix. an experimental investigation of the circumstances which determine whether the motion of water shall be direct or sinuous, and of the law of resistance in parallel channels. *Phil. Trans. R. Soc. A*, (174):935–982, 1883.

[30] O. Reynolds. Iv. on the dynamical theory of incomPhys. Rev. Essible viscous fluids and the determination of the criterion. *Phil. Trans. R. Soc. A*, (186):123–164, 1895.

[31] V. A. Romanov. Stability of plane-parallel Couette flow. *Functional analysis and its applications*, 7:137–146, 1973.

[32] D. Ruelle and F. Takens. On the nature of turbulence. *Commun. Math. Phys.*, 20:167–192, 1971.

[33] L. Shi, M. Avila, and B. Hof. Scale invariance at the onset of turbulence in couette flow. *Phys. Rev. Lett.*, 110:204502, 2013.

[34] A. Sommerfeld. *Ein beitrag zur hydrodynamischen erklaerung der turbulenten fluessigkeitsbewegungen*. Rome: Accademia dei Lincei, Atti del IV Congresso internazionale dei Matematici, 1909.

[35] H. B. Squire. On the stability for three-dimensional disturbances of viscous fluid flow between parallel walls. *Proc. R. Soc. A*, 142:621–628, 1933.

[36] H. L. Swinney. Hydrodynamic instabilities and the transition to turbulence. *Progress of Theoretical Physics Supplement*, 64:164–175, 1978.

[37] L. Thomas. The stability of plane Poiseuille flow. *Phys. Rev.*, 91:780, 1953.

[38] N. Tillmark and P. H. Alfredsson. Experiments on transition in plane Couette flow. *J. Fluid Mech.*, 235:89–102, 1992.

[39] L. N. Trefethen, A. E. Trefethen, S. C. Reddy, and T. A. Driscoll. Hydrodynamic stability without eigenvalues. *Science*, 261:578–584, 1993.

[40] T. Tsukahara, K. Iwamoto, H. Kawamura, and T. Takeda. DNS of heat transfer in a transitional channel flow accompanied by a turbulent puff-like structure. *arXiv:1406.0586 [physics.flu-dyn]*, 2014. Proc. of Turbulence, Heat and Mass Transfer (2006).

[41] L. S. Tuckerman, T. Kreilos, H. Schrobsdorff, T. M. Schneider, and J. F. Gibson. Turbulent-laminar patterns in plane Poiseuille flow. *Phys. Fluids*, 26, 2014.

[42] L. S. Tuckerman, M. Chantry, and D. Barkley. Patterns in Wall-Bounded Shear Flows. *Annu. Rev. Fluid Mech.*, 52:343–367, 2020.

[43] F. Waleffe. On a self-sustaining process in shear flows. *Phys. Fluids*, 9:883–900, 1997.

[44] I. J. Wygnanski and F. H. Champagne. On transition in a pipe. part 1. the origin of puffs and slugs and the flow in a turbulent slug. *J. Fluid Mech.*, 59:281–335, 1973.

# Secondary Shear Instabilities on Kelvin-Helmholtz Braids

Emma Bouckley

August 19, 2025

## 1 Introduction

Stratified shear flows are prevalent in nature, both in the atmosphere and ocean [18]. Owing to this abundance, the instability of these flows has been extensively studied in the literature [13]. In particular, the Kelvin-Helmholtz (KH) instability has been thoroughly investigated as the dominant mode of instability when shear and buoyancy layers are of comparable thickness. The most notable theoretical result from this body of work is the Miles-Howard theorem [6, 11], which states that a sufficient condition for the stability is $Ri > 0.25$, where the Richardson number $Ri$ represents a ratio of stabilising stratification to destabilising shear. The secondary instabilities that subsequently develop on the initial KH instability play a crucial role in the transition to turbulence and the associated mixing [14].

We refer to one wavelength of the KH instability as a 'billow,' consisting of a thick region of overturning —the core— and a long thin region of shear —the braid— connecting adjacent cores. Like the background flow, the braid is a region of stratified shear flow, however, it is more complex; the braid experiences both a straining from the growing cores of the primary billow and an accelerating shear associated with the tilting of the braid. The stability of the braid is therefore complicated. Observations from strongly stratified estuarine shear flow have suggested that most of the mixing occurs along these braid regions rather than within the core as might be expected [5], suggesting the presence of secondary instabilities along the braid. This guides our focus in this report to the occurrence of braid shear instabilities.

Mashayek and Peltier [9, 10] illuminate the 'zoo' of secondary instabilities that may develop on the primary billow, investigating the competition between braid shear instabilities and those in the core. They hypothesise the emergence of braid shear instabilities beyond a critical Reynolds number that depends on the Prandtl and Richardson numbers, and the discussion presented there forms the major motivation of our work. Indeed, secondary shear instabilities on the braid have been considered by many; most approaches develop simple analytical models of braid flow, derived from the Boussinesq equations in a tilted frame of reference, and compare these with the braid flow from simulations [3, 10, 12, 17]. These works often draw an analogy between the stability of the braid and that of a strip of vorticity, drawing on Dritschel et al. [4] to better understand the conditions for braid instability. Owing to the complexity of the braid flow, the problem is also related to the growth of a primary KH billow with an accelerating background flow [7].

In some natural settings, we can expect high Reynolds numbers ($Re \approx 10^6$), high Prandtl numbers ($Pr \approx 10^3$), and strong stratification ($Ri \approx 0.20$) [5], a parameter regime that is

challenging to tackle experimentally and numerically. For this report, we wish to interrogate the high Reynolds number regime, and as such we fix $Pr = 1$ and run 2D simulations to ensure the flow is fully resolved. While 3D secondary instabilities are crucial, dominated by a shear-aligned convective instability, the flow remains 2D until the primary billow saturates [1, 2]. The use of 2D simulations allows us to determine the initial mechanism of secondary instability. However, once significant overturning occurs in either primary or secondary cores, gravitational collapse is expected to induce a 3D transition to turbulence. Our 2D results, therefore, can provide insight as to where we would first expect 3D turbulence.

In this report, we shall explore how the occurrence of secondary shear instabilities changes as we extend current literature values to high Reynolds and Richardson number through 2D direct numerical simulations (DNS). Following previous literature, we similarly develop our own inviscid reduced model in a frame of reference aligned with the tilted braid, however, we opt to include the often-excluded transient evolution of the braid to predict the timescales on which we may expect shear instabilities to develop on the braid. With this aim in mind, we begin by laying out the general analytical model framework in section 2, and describe the corresponding theoretical and numerical braid analysis methods in section 3; this is where we develop our reduced model for the braid. In section 4, we investigate convergence of the simulations and the impact of resolution. We then quantify the primary instability in section 5 before analysing the secondary instabilities in section 6. Finally, a discussion of the results in presented in section 7.

## 2 Theoretical and Numerical Problem Set-up

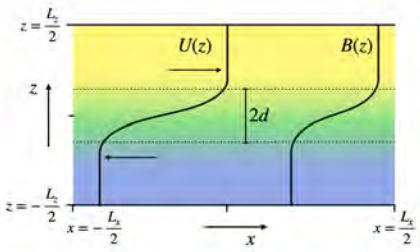


Figure 1: The set-up for stratified shear flow, with sketches of initial velocity $U(z)$ and buoyancy $B(z)$ profiles. The shear layer thickness is $2d$.

Consider a 2-dimensional stably stratified flow with streamwise coordinate $x$ and spanwise coordinate $z$ evolving in time $t$, as illustrated in fig. 1. The flow is assumed to be incompressible with small density variations, valid for the Boussinesq approximation. Thus,

incompressibility, Navier-Stokes and continuity give

$$\nabla \cdot \boldsymbol{u} = 0, \tag{1}$$

$$\frac{D\boldsymbol{u}}{Dt} = -\frac{1}{\rho_0}\nabla p + b\hat{\boldsymbol{z}} + \nu\nabla^2\boldsymbol{u}, \tag{2}$$

$$\frac{Db}{Dt} = \kappa\nabla^2 b, \tag{3}$$

where $\boldsymbol{u}$ is fluid velocity, $p$ is pressure deviation from hydrostatic pressure, $\nu$ kinematic viscosity, $\kappa$ diffusivity of the density field and $b = -\tilde{\rho}g/\rho_0$ is the buoyancy, a measure of the deviation of density $\tilde{\rho}$ from the background density $\rho_0$ multiplied by gravitational acceleration $g$.

The flow is horizontally periodic in the domain $[-L_x/2,\ L_x/2]$ and is subject to free-slip ($\partial u/\partial z = 0$, where $u$ is the horizontal component of velocity) and no-flux conditions ($w = 0$ and $\partial b/\partial z$=0, where $w$ is the vertical component of velocity) at the rigid boundaries at $z = -L_z/2,\ L_z/2$. The flow is initialised with parallel shear flow with the dimensional profiles for velocity and buoyancy are chosen to be of the form

$$U(z)\hat{\boldsymbol{x}} = \Delta U \tanh\left(\frac{z}{d}\right)\hat{\boldsymbol{x}}, \tag{4}$$

$$B(z) = \Delta B \tanh\left(\frac{z}{d}\right), \tag{5}$$

where $\Delta U$ and $\Delta B$ are the dimensional change of velocity and buoyancy across the respective layers of equal thickness $2d$.

This flow is well established to be unstable to the 2D Kelvin-Helmholtz (KH) instability when the Richardson number, defined to be

$$Ri = \frac{d\Delta B}{(\Delta U)^2}, \tag{6}$$

is less than a quarter [6, 11].

To non-dimensionalise the system, lengths are scaled with $d$, velocities with $\Delta U$, buoyancy with $(\Delta U)^2/d$, time with $d/\Delta U$ and pressures with $\rho_0\Delta U^2$. Under this scaling, the governing eqs. (1) to (3) are as follows,

$$\nabla \cdot \boldsymbol{u} = 0, \tag{7}$$

$$\frac{D\boldsymbol{u}}{Dt} = -\nabla p + b\hat{\mathbf{z}} + \frac{1}{Re}\nabla^2\boldsymbol{u}, \tag{8}$$

$$\frac{Db}{Dt} = \frac{1}{PrRe}\nabla^2 b, \tag{9}$$

with initial conditions

$$U(z)\hat{\boldsymbol{x}} = \tanh(z)\hat{\boldsymbol{x}}, \tag{10}$$

$$B(z) = Ri\tanh(z). \tag{11}$$

These equations include 3 dimensionless numbers: the Reynolds number $Re = \Delta U d/\nu$ a ratio of inertial to viscous forces; the Prandtl number $Pr = \nu/\kappa$ a ratio of viscous diffusivity to mass diffusivity and the aforementioned Richardson number a ratio of stratification

to shear. Note here that the non-dimensionalisation is chosen such that the Richardson number is in the initial condition for buoyancy, as this is convenient for the chosen modelling software, Oceananigans. In this report, we shall be concerned with flows within the parameter space $10^3 < Re < 10^6$ and $0.05 < Ri < 0.20$. For brevity, we are not concerned with the influence of the Prandtl number and as such it will be set to unity, although a brief discussion of increasing Prandtl will be presented in section 7. A set of 16 simulations form the basis of our analysis with parameter values $Re = 10^3,\ 10^4,\ 10^5$, and $10^6$ and $Ri = 0.05,\ 0.10,\ 0.15,$ and 0.20. Case names are labelled '$c\_Re\_Ri$' such that $c\_10^3\_0.05$ is a simulation with $Re = 10^3$ and $Ri = 0.05$.

Simulations are run using Oceananigans in Julia, a second-order centred-difference finite volume scheme [19]. The simulation code is adapted from that originally developed by John Taylor and made available on GitHub. The horizontal domain length $L_x$ is chosen to be the wavelength of the fastest growing mode of the linear stability analysis for the KH instability [15], therefore restricting the domain to one billow length and consequently excluding the pairing instability which is the subject of other work but is not our focus here [12]. The vertical domain length $L_z = 20$ is chosen to be sufficiently large to minimise the wall boundary effects on instability growth. The flow is instigated with a perturbation of the fastest growing mode and noise with kinetic energy $10^{-4}$ of the initial parallel flow to kick-start KH instability growth. Due to the large Reynolds number range, we utilise a stretched grid in the $z$ direction to admit an increased resolution in the central region while minimising the increased numerical load. The precise details of this grid and the convergence of solutions under increasing resolution is discussed in detail in section 4.

## 3 Theoretical and Numerical Methods for Braid Analysis

The KH billow has a distinctive shape which can be easily illustrated, as in fig. 2a, composed of two distinctive regions, which we shall refer to as the 'core' and the 'braid'. The core is the region of greatest interface displacement and consists of overturning where denser fluid is lifted over lighter fluid. The braid is an extended sloping region of shear connecting the bottom of one core to the top of the following core; the angle of inclination of the braid is dictated by the core size. There are many secondary instabilities associated with the KH billow, notably the 3D convective instability from the overturning in the core and the 2D shear instability found on the braid, illustrated in fig. 2b, which is the focus of our report. Shear instabilities are not solely restricted to the central braid region and in fact may occur in the overturning layers of the core, however, for practicality we refine our consideration to the central region of the braid that may be considered sufficiently detached from the cores. For simplicity, we shall generically refer to a flow being either braid unstable or core unstable, determined by the location of the initial secondary instability.

An example simulation of the development of the braid shear instability is presented in fig. 3. Initially, solely the primary billow is developing ($t = 50$) before shear billows are triggered on the braid ($t = 75$). These billows are advected into the core before the subsequent collapse of the overturning cores. In order to capture and quantify these braid shear instabilities, we must employ theoretical and numerical methods to analyse the braid, which are presented in the following sections.

(a) (b)

Figure 2: Schematic of the Kelvin-Helmholtz instability, with orange arrows indicating flow velocity. Panel (a) illustrates the primary instability, and panel (b) illustrates secondary shear instabilities on the braid of the primary instability.

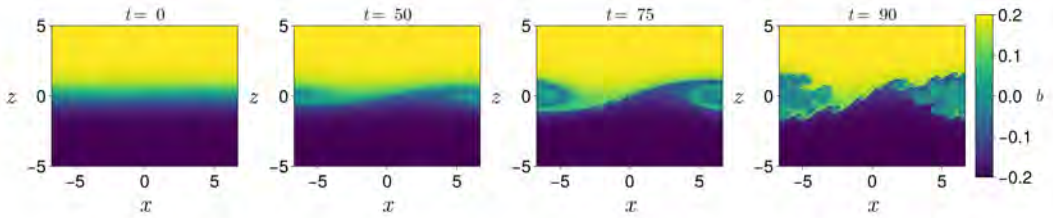


Figure 3: Plots of buoyancy $b$ for $Re = 10^6$ and $Ri = 0.20$ at time snapshots noted in respective panel titles.

### 3.1 Theoretical braid analysis

Following the Corcos and Sherman [3] theory for modelling braid regions, we begin by defining a new braid-aligned coordinate system tilted at an angle $\phi$ to the horizontal. Although in reality the angle of inclination varies slightly along the braid, the variation is insignificant (as we will see) and $\phi$ can be regarded as an average braid inclination over the extended braid region. This frame of reference consists of an along-braid coordinate $x'$ and

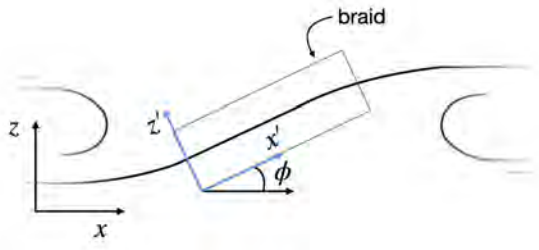


Figure 4: Schematic of the braid-aligned coordinate system.

cross-braid coordinate $z'$ defined by

$$x' = x\cos(\phi) + z\sin(\phi), \tag{12}$$
$$z' = -x\sin(\phi) + z\cos(\phi). \tag{13}$$

where we have assumed that the inflection point of the braid is located at $x = 0,\ z = 0$ and therefore also at $x' = 0.\ z' = 0$. By taking the curl of eq. (8) to find the vertical vorticity $\omega$ equation, and transforming eqs. (7) to (9) to this tilted coordinate system, the governing equations are now,

$$\frac{\partial b}{\partial t} = -u'\frac{\partial b}{\partial x'} - w'\frac{\partial b}{\partial z'} + \frac{1}{RePr}\nabla'^2 b, \tag{14}$$
$$\frac{\partial \omega}{\partial t} = -u'\frac{\partial \omega}{\partial x'} - w'\frac{\partial \omega}{\partial z'} - \cos\phi\frac{\partial b}{\partial x'} + \sin\phi\frac{\partial b}{\partial z'} + \frac{1}{Re}\nabla'^2\omega, \tag{15}$$

where $u'$ and $w'$ refer to the braid-aligned velocities which are parallel and perpendicular to the braid, respectively. Vorticity $\omega$ is invariant under this rotation:

$$u' = u\cos(\phi) + w\sin(\phi) \tag{16}$$
$$w' = -u\sin(\phi) + w\cos(\phi) \tag{17}$$
$$\omega = \frac{\partial u}{\partial z} - \frac{\partial w}{\partial x} = \frac{\partial u'}{\partial z'} - \frac{\partial w'}{\partial x'} \tag{18}$$

Our braid region is a long and thin of flow, and so we assume that gradients in $z'$ are greater than those in $x'$, and as such we may neglect the $\partial/\partial x'$ terms:

$$\frac{\partial b}{\partial t} \approx -w'\frac{\partial b}{\partial z'} + \frac{1}{RePr}\frac{\partial^2 b}{\partial z'^2}, \tag{19}$$
$$\frac{\partial \omega}{\partial t} \approx -w'\frac{\partial \omega}{\partial z'} + \sin\phi\frac{\partial b}{\partial z'} + \frac{1}{Re}\frac{\partial^2 \omega}{\partial z'^2}. \tag{20}$$

In particular, this assumption is adequate as long as the cores are sufficiently far from the braid so as not to disrupt the field. Note that this also implies that vorticity is identical to braid aligned shear $\omega = \partial u'/\partial z'$.

We further assume a uniform strain field $w' = -\gamma z'$ local to the braid to be justified via simulations later; we shall refer to $\gamma$ as the strain. This reduces eqs. (19) and (20) to

$$\frac{\partial b}{\partial t} \approx \gamma z'\frac{\partial b}{\partial z'} + \frac{1}{RePr}\frac{\partial^2 b}{\partial z'^2}. \tag{21}$$
$$\frac{\partial \omega}{\partial t} \approx \gamma z'\frac{\partial \omega}{\partial z'} + \sin\phi\frac{\partial b}{\partial z'} + \frac{1}{Re}\frac{\partial^2 \omega}{\partial z'^2}. \tag{22}$$

From this point, the literature differs in the method in which to make these equations tractable. Corcos and Sherman [3] continue to consider a similarity solution for the full eqs. (21) and (22) at $Pr = 1$. Smyth [12] extends the analysis up to $Pr = 7$ by assuming a steady-state solutions where straining is balanced by viscous dissipation. Mashayek and Peltier [10] considers a frozen background flow, assuming a separation in timescales, to perform a linear stability analysis on the braid.

Much like Corcos and Sherman [3], we are interested in a transient analysis, however, to probe the high-$Re$ limit, we consider an inviscid regime, dropping the viscous diffusion term. The buoyancy equation is now simply,

$$\frac{\partial b}{\partial t} \approx \gamma z' \frac{\partial b}{\partial z'}, \tag{23}$$

which is solved with a self-similar form $b = Ri\ \tanh(z'/\delta(t))$ with an exponential decay of buoyancy thickness $\delta(t)$;

$$\delta(t) = e^{-\int_0^t \gamma\ dt'}. \tag{24}$$

We may further define a braid-aligned buoyancy $b' = b\cos(\phi)$, which evolves as $b' = Ri\cos(\phi)\tanh(z'/\delta(t))$. If the braid is strained for a sufficiently long time without the onset of secondary instabilities, we may expect the braid thickness $\delta$ to reach viscous length scales. This limit would require the viscous diffusion term to be included to balance straining. This is the regime in which the analysis of Smyth [12] is valid.

The inviscid vorticity balance is

$$\frac{\partial \omega}{\partial t} \approx z' \frac{\partial \omega}{\partial z'} + \tan(\phi)\frac{\partial b'}{\partial z'}. \tag{25}$$

While the straining term will similarly thin the vorticity layer, the baroclinic acceleration term is imperative for the expected generation of vorticity along the braid. We focus on modelling the evolution of the strength of vorticity $|\omega|$ or equivalently the magnitude of braid-aligned shear (recall, $\omega \approx \partial u'/\partial z'$) and as such drop the straining term in the following balance:

$$\frac{\partial}{\partial t}\left(\left|\frac{\partial u'}{\partial z'}\right|\right) \approx \tan(\phi)\frac{\partial b'}{\partial z'}. \tag{26}$$

The initial value for shear is simply $\partial u'/\partial z' = 1$, found from the initial background flow. We shall approximate that the evolution of strain is linear in time such that $\gamma \approx (d\gamma_1/dt)t + \gamma_0$ where $d\gamma_1/dt$ is the strain growth rate and $\gamma_0$ is the initial strain, both to be found from simulations. Note, we will also assume a linear rate of increase for the braid angle $\phi \approx (d\phi_1/dt)t + \phi_0$. The initial values for angle $\phi_0$ and strain $\gamma_0$ are both small but non-zero due to initial fastest growing mode perturbation.

We now have a semi-analytical model for shear $\partial u'/\partial z'$ and buoyancy gradient $\partial b'/\partial z'$ evolution on the braid that requires only an input of initial value and linear growth rate of $\phi$ and $\gamma$ from simulation data. Our inviscid model may be summarised as

$$\delta(t) = \exp\left[-\frac{1}{2}\frac{d\gamma_1}{dt}t^2 - \gamma_0 t\right], \tag{27}$$

$$\left|\frac{\partial b'}{\partial z'}\right| = \frac{Ri\cos(\phi)}{\delta(t)}, \tag{28}$$

$$\left|\frac{\partial u'}{\partial z'}\right| = 1 + \int_0^t \tan\left(\frac{d\phi_1}{dt}t + \phi_0\right)\left|\frac{\partial b'}{\partial z'}\right|\ dt. \tag{29}$$

We will explore the efficacy of this model and the constitutive assumptions later in section 6.

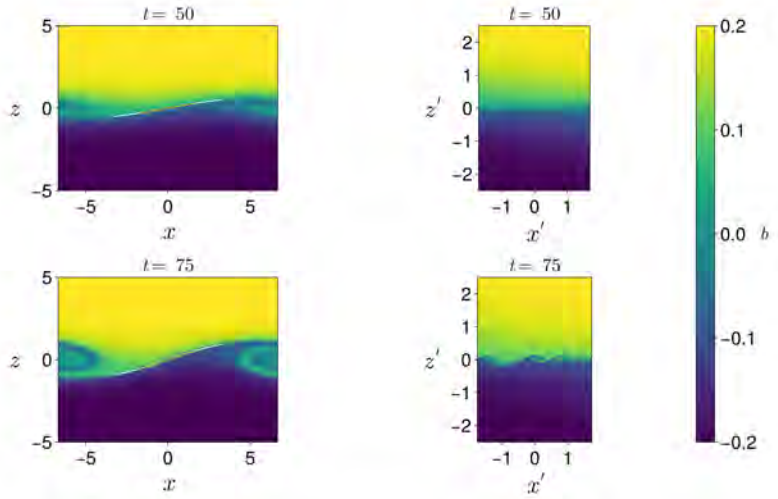


Figure 5: Buoyancy field $b$ for $c\_10^6\_0.20$ at time snapshots noted in respective panel titles. The left column is the original coordinate system, with the braid location marked by a white line. The central region of the braid is highlighted in orange and corresponds to the braid-aligned field illustrated in the right column.

### 3.2 Numerical braid analysis

In this subsection, we describe the numerical braid analysis which allows us to make quantitative justification of the theoretical inviscid model laid out in the previous subsection. We demonstrate this analysis on two snapshots of a simulation to show the possible outputs of this numerical analysis (figs. 5 and 6).

The initial perturbation of the fastest growing mode is positioned so that the braid is located in the centre of the domain, with the cores at the periphery. Therefore, we can reliably locate the braid region in the central half region $[-L_x/4, L_x/4]$. To find the braid, we follow the fitting procedure outlined in Smyth [12].

The braid is defined to be the region of strong shear and as such we find the location of the braid in $z$ for a given $x$ coordinate as the point of greatest shear $\partial u/\partial z$ (or equivalently the strongest buoyancy gradient $\partial b/\partial z$, assuming these are co-located) over the $z$ domain. We use the two neighbouring grid points to interpolate and find the true $z$ value at which the gradient is maximised. By systematically repeating this in the central half region we construct a pointwise function $z_b(x)$ for the braid location. We choose to fit a cubic function $z_c(x)$ to $z_b(x)$; this smooths out the braid and allows us to still locate the original braid as small perturbations grow (see fig. 5).

Given the smoothed braid location $z_c(x)$, we find the $x$-dependent angle of inclination of the braid $\tilde{\phi}$ from the gradient of $z_c(x)$ using $\tan(\tilde{\phi}(x)) = dz_c/dx$. As we shall see, the braid is often flat enough to be considered of constant angle, and so we take the average of $\tilde{\phi}(x)$ along the braid to be representative of generic braid inclination $\phi$ which is directly

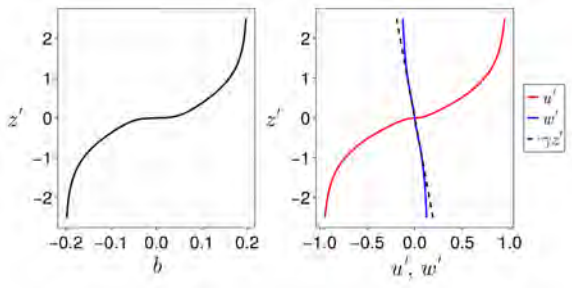


Figure 6: Profiles of averaged buoyancy $b$ and braid-aligned velocities $u'$ and $w'$ for $c\_10^6\_0.10$, the flow in fig. 5, at $t = 50$. The black dashed line illustrates the assumed uniform strain field.

correlated with the amplitude of the primary billow.

We focus again on the central half region of the braid $x \in [-L_x/8, L_x/8]$ to calculate the braid-aligned flow. At each $x$ point, transect are taken centred at and perpendicular to the braid $z_c$ of length $L_z/4$. This allows us to construct a grid of along-braid $x'$ and cross-braid $z'$ points. The spacing of this tilted grid is chosen to reflect the original simulation resolution. At each grid point, we interpolate from the original simulation data to reconstruct a braid -aligned field for buoyancy $b$ and along-braid shearing velocity $u'$ and cross-braid straining velocity $w'$, as is seen in fig. 5 where the braid is fixed at $z' = 0$. This allows for clear visualisation of the secondary instability growth.

Before the growth of secondary instabilities, the flow is assumed to be uniform in $x'$, and so we average along $x'$ to construct profiles of $b$, $u'$ and $w'$ (see fig. 6). Here we can clearly observe the strong shear profile in $u'$ and a straining velocity $w'$ which drives flow into the braid. As previously discussed in section 3.1, we shall assume a uniform straining field $\gamma z'$. To find $\gamma$, we fit a cubic curve to $w'(z')$ and take $\gamma$ to be the gradient of this curve at $z = 0$. Figure 6 shows the comparison of such a linear approximation to $w'$, which has good agreement with $w'$ in $z' \in [-1, 1]$. Since our braid is long and thin, this range can be considered reflective of the braid region and all we need is agreement local to $z' = 0$. Given such profiles for the flow, we can calculate further quantities for our analysis. In particular, we will consider the gradients of these profiles for the buoyancy gradient and shear strength, which can be used to calculate a local 'braid Richardson number' to be discussed later.

# 4 Convergence

Without an analytical solution for the non-linear evolution of the KH instability to compare with, it is necessary to ensure the convergence of solutions when increasing the simulation grid resolution.

We significantly reduced the numerical load by utilising a stretched non-uniform grid in the $z$ direction. This is a grid which is finely resolved in the central region, but coarsely resolved on the boundaries. This method takes advantage of the simple parallel flow near the $z$ boundaries, which does not need to be as highly resolved as the central region where

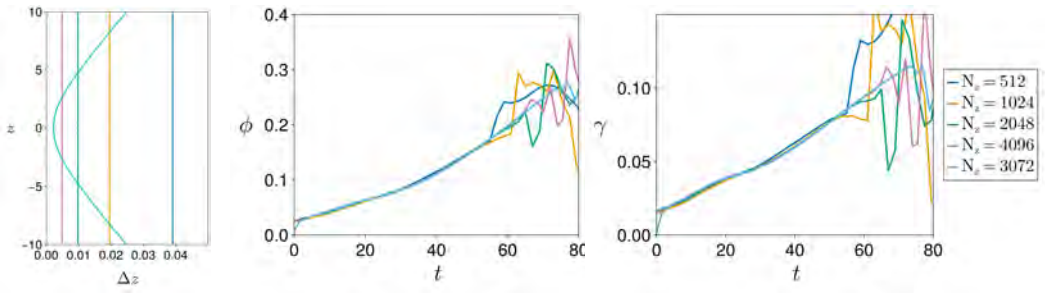


(a) (b) (c)

Figure 7: Results of the convergence test with increasing vertical resolution $N_z$, as noted in the legend for a simulation with $Re = 10^6$ and $Ri = 0.20$. Panel (a) illustrates the profiles of grid spacing $\Delta z(z)$. Panel (b) and (c) illustrate the braid angle $\phi$ and strain $\gamma$ evolution in time $t$, respectively. Vertical resolution $N_z$ given in the legend.

the primary billow grows. To be precise, the grid points are given explicitly by

$$z_k = \frac{7}{10}\frac{L_z}{2\sinh(5)}\sinh\left[5\left(\frac{2k - N_z - 1}{N_z - 1}\right)\right] + \frac{3}{10}\left(\frac{2k - N_z - 1}{N_z - 1}\right), \qquad \text{for } k = 1, ..., N_z, \tag{30}$$

where $N_z$ is the number of vertical grid points and will be referred to as the vertical resolution. Here, the central grid point is 5 times more resolved than that of the boundary. This stretched grid has been adapted from code provided by Amir Atoufi.

Generally, the vertical domain is roughly double the length of the horizontal domain, we expect to have double the number of grid points in the vertical direction $N_z$ versus in the horizontal direction $N_x$ for uniform grids. Note that we are unable to use a stretched grid in the $x$ direction, and so for $N_z = 3072$ we will default to a uniform grid with $N_x = 3072$, $\Delta x \approx 0.005$. The $x$ resolution is particularly important when the braid tilts, as it will impact the cross-braid resolution. For the convergence test, we compare a simulation with this stretched grid to simulations of various uniform spacings, ranging from $N_z = 512$ to 4096 with $N_x = N_z/2$; the vertical grid spacing $\Delta z$ over $z$ is compared in fig. 7a. A high Reynolds number ($Re = 10^6$) is chosen to ensure the limits of our simulation are resolved. Note that we will identify the simulation by the $N_z$ value.

Figures 7b and 7c illustrate the evolution of braid inclination angle $\phi$ and strain $\gamma$ over time with increasing resolution. These figures show negligible difference in the early evolution; clearly the prominent impact of resolution is not on the primary billow growth. The notable difference occurs at late time when there are discontinuous jumps in $\phi$ and $\gamma$. Large jumps or variations in the results are due to the braid diagnostics as described in section 3.2 becoming unreliable due to notable growth of secondary instabilities. For the remainder of the report, numerical braid analytics will stop at the onset of secondary instabilities to exclude this numerical noise but in this plot it serves to illustrate the major impact of resolution — under-resolved simulations will prematurely instigate secondary instabilities on the braid [8]. This is illustrated further in fig. 8, which shows snapshots of the buoyancy field for each resolution at the same time. In the most finely resolved

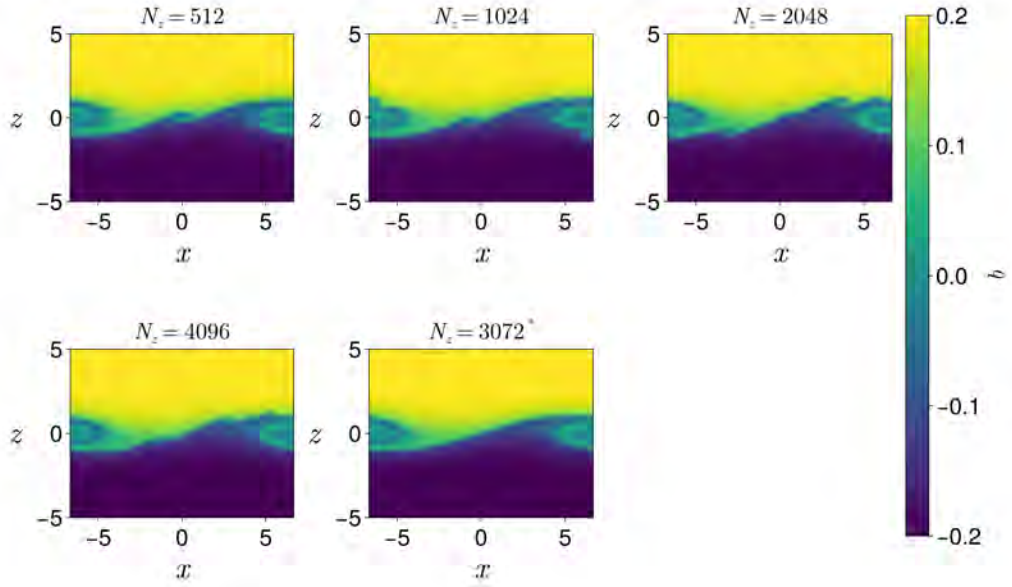


Figure 8: Plots of buoyancy $b$ at $t = 70$ for increasing vertical resolution $N_z$, as noted in respective panel titles (* indicates a stretched grid). Results of the convergence test with increasing vertical resolution $N_z$, as noted in the legend for a simulation with $Re = 10^6$ and $Ri = 0.20$.

case $N_z = 3072$, the secondary instabilities are in early stages of growth and much smaller than in other cases. In contrast, the least resolved case $N_z = 512$, has large instabilities on both the braid and the core. The wavelength of a billow is set by the braid thickness $\delta$, which suggests $\delta$ is limited by the grid resolution, resulting in larger billows at lower resolution. Clearly, grid resolution is important for these small scale effects, which may in fact be triggered by grid noise rather than physical effects.

To further investigate the resolution dependent secondary instabilities, it is natural to consider the convergence of braid-specific quantities. Figure 9 compares the shear profiles $\partial u'/\partial z'$ at three time snapshots to illustrate the resolution dependency. In the first panel, at early time, the braid region is clearly already too thin to be resolved by the $N_z = 512$ simulation as there are only a couple of grid points over $[-0.1,\ 0.1]$. In the second panel, at intermediate time, there is a significant difference with the two lowest resolutions and the remaining cases. Both have insufficient grid points and as a consequence are unable to correctly predict the thickness of the braid (the region of large shear change) which is approximately 0.1; both cases are over-predicting and diffusing the braid. In the third panel, at late time, the two lowest resolution simulations are excluded from the plot as the secondary instabilities have already developed at this time. The braid has further thinned

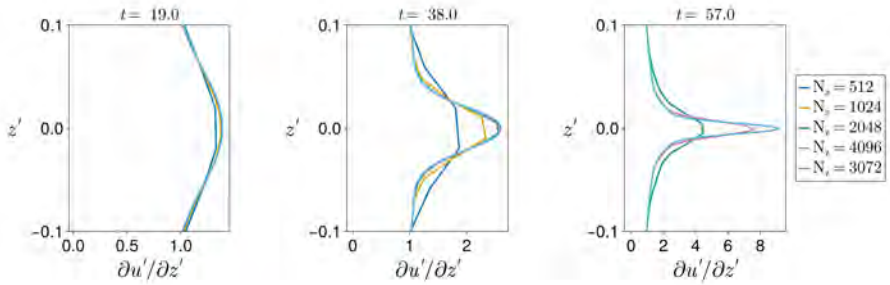


Figure 9: Profiles of braid-aligned shear $\partial u'/\partial z'$ against cross-braid coordinate $z'$ at times $t = 19,\ 38,\ 57$.

and only the most resolved $N_z = 3072$ case is still smooth. The braid thickness is a useful indicator for whether grid spacing is small enough. Predictors for braid thickness will allow us to say a priori the resolution required to accurately capture the braid and onset of secondary instabilities.

We may estimate some minimum braid thickness that the braid can be strained to by considering the limit in which viscosity balances straining, a theoretical limit explored in Smyth [12]. This balance

$$-\gamma z' \frac{\partial b}{\partial z'} \approx \frac{1}{Re\ Pr} \frac{\partial^2 b}{\partial z'^2} \tag{31}$$

is achieved at a buoyancy thickness length scale $\delta \approx (\gamma Re\ Pr)^{-1/2}$. Our inviscid model in eq. (24) shows that $\delta$ has an exponential decay with e-folding timescale $\approx (d\gamma_1/dt)^{-1/2}$ (assuming $\gamma \approx (d\gamma_1/dt)t + \gamma_0$). Therefore, the timescale for $\delta$ decay for linearly increasing strain is approximately the same as for a fixed strain of $\gamma = (d\gamma_1/dt)^{1/2}$. We can use this equivalence to improve the estimation for the viscous length scale:

$$\delta \approx \left( \left[ \frac{d\gamma_1}{dt} \right]^{-\frac{1}{2}} Re\ Pr \right)^{-\frac{1}{2}}. \tag{32}$$

An estimate for strain in fig. 7c gives $d\gamma_1/dt \approx O(10^{-2})$. Therefore, fixing $Re = 10^6$ and $Pr = 1$ we can approximate our viscous length scale as $\delta \approx 10^{-5/2} \approx 0.003$ in this simulation. Recall that this is the steady viscous length scale which we do not expect to reach, and as such acts as a general suggestion rather than a rigorous length scale which must be resolved. From fig. 7a, we note that the stretched grid $N_z = 3072$ approximately reaches this length scale in the centre, although not over the entire braid region. For assurance, it would be beneficial to run a simulation at resolution which reaches this grid spacing over a larger central region to ensure that we are sufficiently converged, however, that falls out of the scope of this report and is discussed as part of future work in section 7. For the remainder of this report, simulation are run with the stretched grid discussed here with $N_z = 3072$ and $N_x = 3072$.

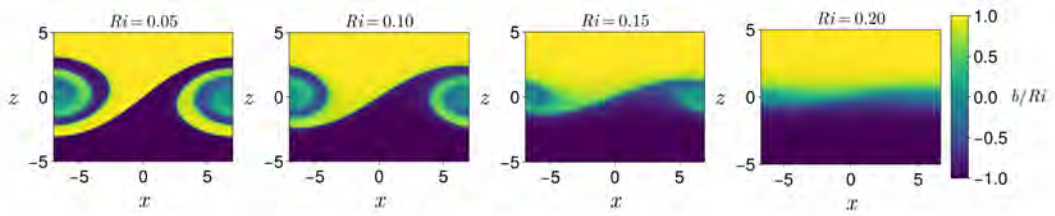


Figure 10: Plots of buoyancy normalised by Richardson number $b/Ri$ for $Re = 10^6$ at $t = 40$ over a range of $Ri$ noted in the panel titles.

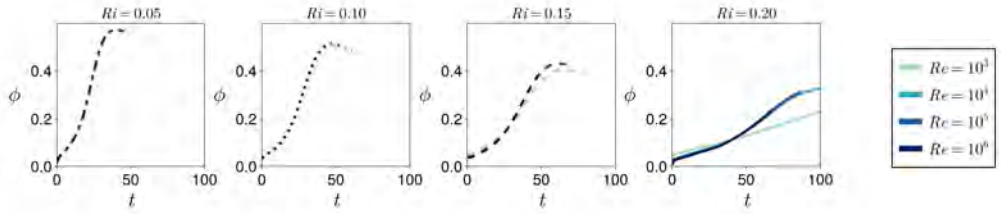


Figure 11: The evolution of braid angle $\phi$ for full simulation range. Light to dark colours represent increasing $Re$ as noted in the legend and line style represent $Ri$: dash dot is $Ri = 0.05$; dot is $Ri = 0.10$; dash is $Ri = 0.15$ and solid is $Ri = 0.20$.

## 5 The Primary Instability

The behaviour of the primary KH billow forms the background flow upon which the secondary instabilities form. As such, it is suitable to begin our analysis by characterising the influence of Reynolds number and Richardson number on primary billow growth; we present here conclusions which are well understood in the literature.

Figure 10 contrasts simulations of fixed $Re = 10^6$ with varying $Ri$. The difference is striking; as $Ri$ increases, the billows are less developed with smaller amplitude and little to no overturning in the cores. This is seen more quantitatively in figs. 11 and 12 where braid angle $\phi$ (a proxy for core amplitude) and strain $\gamma$ (a proxy for core rotation rate) significantly decrease with increasing $Ri$. As the relative importance of stratification increases ($Ri$ increases) greater work is required to raise the denser fluid in the billow, resulting in smaller and weaker cores. Similarly, the growth rate of the billow decreases with increasing $Ri$. Recall that in the inviscid limit, the growth rate is zero when $Ri \geqslant 0.25$.

In contrast, the dependence on $Re$ is less evident. Generally the curves in figs. 11 and 12 collapse on to the same $Ri$-dependent evolution for the $Re$ range considered, and primary billow growth can be considered independent of $Re$ except for $Re = 10^3$. The difference between $Re = 10^3$ simulations and all other simulations is more prominent at higher $Ri$.

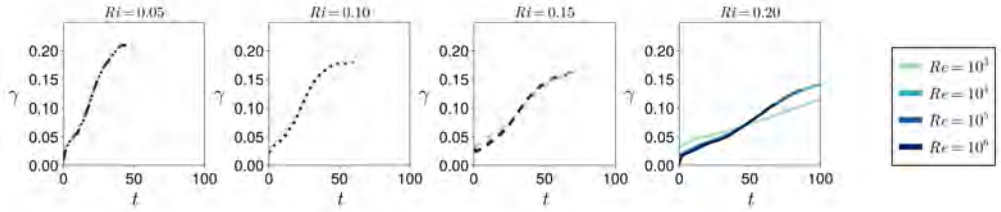


Figure 12: The evolution of strain $\gamma$ for full simulation range. Light to dark colours represent increasing $Re$ as noted in the legend and line style represent $Ri$: dash dot is $Ri = 0.05$; dot is $Ri = 0.10$; dash is $Ri = 0.15$ and solid is $Ri = 0.20$.

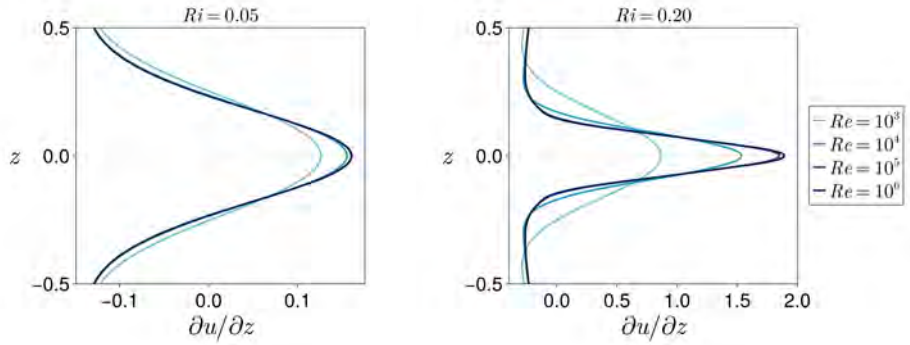


(a) (b)

Figure 13: The initial shear perturbation profiles $\partial u/\partial z$ against $z$ at (a) $Ri = 0.05$ and (b) $Ri = 0.20$ with $Re$ varying from $10^3$ to $10^6$ given by colours light to dark.

That is to say, $Re$ dependence is more sensitive at higher $Ri$. This point can be further elucidated by considering the respective initial perturbations, which, for $c\_10^3\_0.20$, appear to be notably different. This suggests that the subsequent difference in billow growth may be influenced by the initial conditions which, recall, are chosen as the fastest growing mode of the linear stability analysis.

Figure 13 illustrates the starting condition shear $\partial u/\partial z$ against $z$, comparing $Re$ at both a low and high $Ri$. Increasing $Re$ at both $Ri$ values acts to decrease the length scale of the initial perturbation whilst increasing the magnitude of the central peak. In line with the observations from figs. 11 and 12, there is a greater difference in $Re$ at the high $Ri$.

To understand the notable difference in the evolution $c\_10^3\_0.20$, we calculate the viscous length scale from eq. (32). Using $d\gamma_1/dt \approx O(10^{-2})$, taken from fig. 12, the viscous length scale is $\delta \approx O(10^{-1})$, which is of the same order as the initial perturbation; we are not in an inviscid regime, and we expect strong Reynold number effects. At lower $Ri$, the strain growth rate is larger and therefore decreases the viscous length scale and lessens the influence of $Re$ on primary billow growth. Since we wish to explore the inviscid limit using large $Re$, we shall exclude $Re = 10^3$ simulations from further analysis.

# 6 The Secondary Instabilities

Having established the overall growth and behaviour of the primary instability, we are primed to consider the growth of secondary instabilities. Figure 14 presents all simulations at a time when a clear secondary instability is evident. Within this, we identify three notable behaviours: shear instabilities on the braid, our goal behaviour ($c\_10^5\_0.20$); shear instabilities within the core ($c\_10^5\_0.10$); and the core impeding upon the braid ($c\_10^4\_0.05$).

Although these are not distinct behaviours, for the purpose of identifying the onset of shear instabilities on the braid, we classify simulations as either 'braid unstable' (shear instability in the central braid region) or 'core unstable' (all other instabilities, including shear instabilities in the core region), except for $c\_10^5\_0.15$, which we shall consider 'marginally unstable' due to the simultaneous braid and core instabilities. This classification is systematically laid out in table 1. While high Reynolds and high Richardson is generally favourable for the secondary shear instability, this trend alone is insufficient to make a clear distinction; there is evidently more subtlety to the classification, which we shall explore in the rest of this section.

Table 1 also notes a time of instability onset. This time is the $t$ at which the secondary instability can be seen in buoyancy field plots such as the ones in fig. 14, as such it should only be considered an estimate. A more robust metric is required to make this measurement more precise. One such metric could be to consider the power spectrum of kinetic energy of the braid to identify the point at which small wavelengths begin to grow.

| $Ri/Re$ | $10^4$ | $10^5$ | $10^6$ |
|---|---|---|---|
| 0.05 | Core unstable at $t = 49$ | Core unstable at $t = 46$ | Core unstable at $t = 45$ |
| 0.10 | Core unstable at $t = 61$ | Core unstable at $t = 55$ | Braid unstable at $t = 45$ |
| 0.15 | Core unstable at $t = 73$ | Marginally unstable at $t = 65$ | Braid unstable at $t = 49$ |
| 0.20 | Core unstable at $t = 112$ | Braid unstable at $t = 87$ | Braid unstable at $t = 68$ |

Table 1: Type and time of instability onset

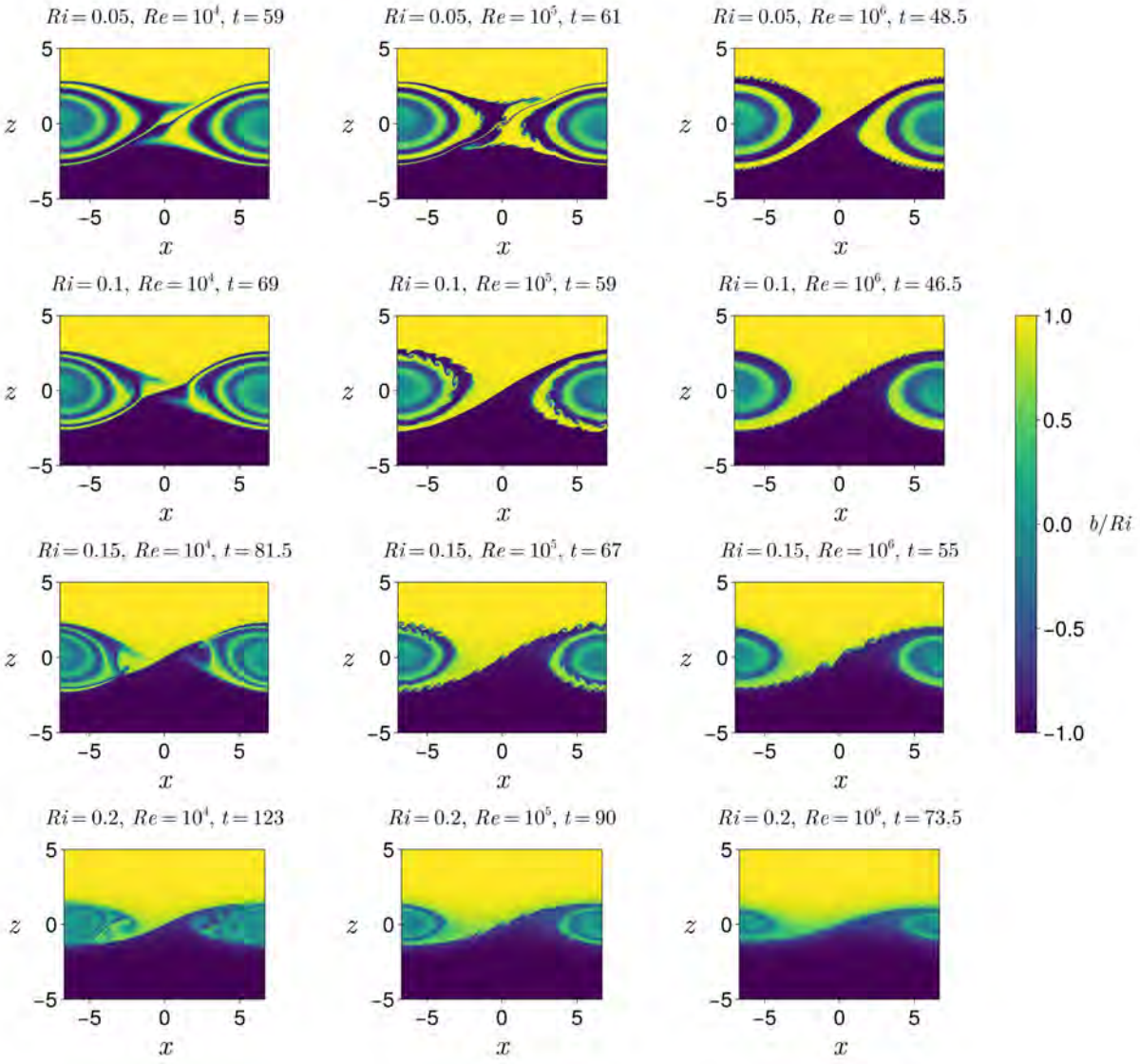


Figure 14: Snapshots of the simulations after the onset of secondary instability over parameter range $Re = 10^4,\ 10^5,\ 10^6$ and $Ri = 0.05,\ 0.10,\ 0.15,\ 0.20$.

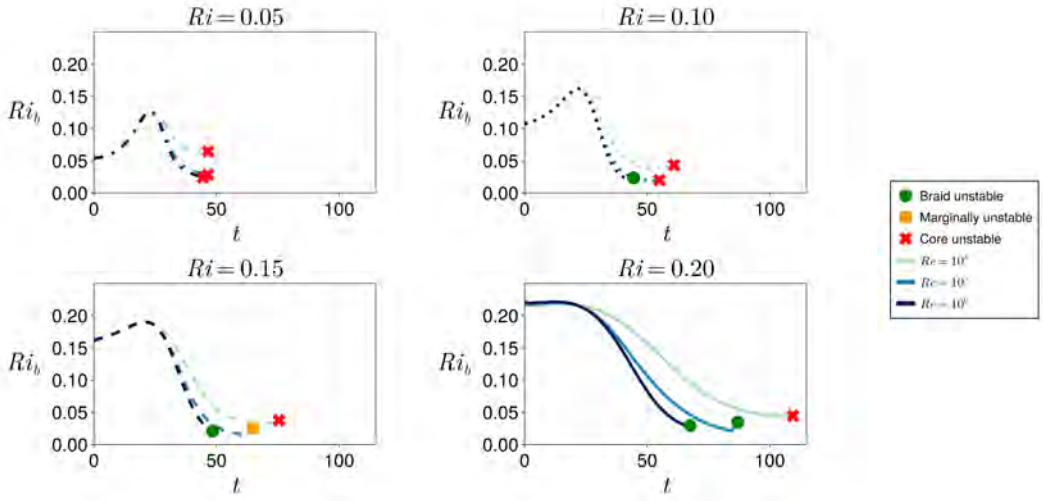


Figure 15: The evolution of braid Richardson number $Ri'$ in time $t$. $Re$ from $10^4$ to $10^6$, as noted in the legend. $Ri$ is given by respective panel titles as well as line style: $Ri = 0.05$ dash dot; 0.10 dot; 0.15 dash; and 0.20 solid. The end points are marked with symbols noted in the legend, representing the type of secondary instability.

### 6.1 Braid Richardson, $Ri'$

We define the braid Richardson number to be

$$Ri' = \frac{\partial b'/\partial z'}{(\partial u'/\partial z')^2}, \tag{33}$$

a local measurement of stratification averaged along the braid. Note that while Miles-Howard theorem does not rigorously apply in this stratified shear flow due to the additional straining and accelerating background flow, it is still common in the literature to consider this quantity as a general indicator of stability. We track the transient evolution of $Ri'$ in fig. 15 and mark the secondary instability as classified in table 1.

Although this analysis focuses on the braid, in the early stages of the flow the braid is not dynamically distinct from the primary billow. Consequently, $Ri'$ is effectively independent of $Re$ for $t \lesssim 25$, reflecting the fact that the growth of the primary billow depends only on $Ri$. Initially, straining increases the stratification and stabilises the flow, directly raising $Ri'$. Once shear begins to intensify, $Ri'$ rapidly decreases and differences in $Re$ become apparent.

While $Ri'$ is informative for understanding the physical mechanisms driving the flow, it is insufficient to distinguish between braid-unstable and core-unstable flow. $Ri'$ remains below 0.25 throughout, and there is no other critical value which signals the onset of braid instability; since strain stabilises the braid, $Ri' < 0.25$ is a necessary but not sufficient condition of instability. Shear intensification becomes the dominant mechanism as $Ri'$ drops

to low values ($Ri' \lesssim 0.05$) corresponding to a weakly stratified flow. The weakly stratified nature of the braid has been noted in literature [3], and an analogy has been drawn between the stability of the braid and that of a strip of vorticity [4]. It has been shown that the strain-to-vorticity ratio $\gamma/\omega$ is a useful metric for the instability of a vorticity strip, and by analogy, the braid. In our reduced model, vorticity is approximately given by shear $S = \partial u'/\partial z'$; we introduce the notation $S$ for simplicity.

### 6.2 Strain to shear, $\gamma/S$

Figure 16 presents the evolution of $\gamma/S$ for all simulations. Much like the $Ri'$ evolution, all simulations exhibit an initially $Re$-independent growth corresponding to primary billow growth. To explore further the $Re$-dependence at later times, when shear dominates, we compare simulation $\gamma/S$ to the prediction from our inviscid model. The inviscid model requires an estimate of the primary billow growth in terms of $\phi$ and $\gamma$. We use a linear fit for both quantities, dependent only on $Ri$, as shown in fig. 17.

Figure 16 shows impressive agreement between the model and the simulation outputs at $Re = 10^6$. As expected, the inviscid model has increasing accuracy with increasing $Re$ with $Re = 10^4$ deviating from the inviscid regime at an earlier time; the baroclinic acceleration is impeded by viscous effects. Our inviscid model effectively captures the initial stabilisation due to straining, and the eventual destabilisation as shear acceleration dominates. These two mechanisms —straining of the buoyancy field and baroclincially-driven shear acceleration— govern the braid evolution. The time at which the relative dominance of these mechanisms changes is surprisingly only weakly dependent on $Ri$, and is also predicted by the inviscid model. The model also accurately predicts the timescale at which $\gamma/S$ becomes small, where 'small' is approximately less than 0.01.

All braid instabilities in fig. 16 occur at a small $\gamma/S$, which suggests that $\gamma/S \approx 0.01$ could be a critical value for braid instability. Other studies have suggested comparably values; Staquet [16] proposes $\gamma/S \approx 0.02$, whereas Smyth [12] proposes $\gamma/S \approx 0.025-0.029$. However, low $\gamma/S$ still is not sufficient to uniquely identify braid instabilities. We note, for example, with $Ri = 0.10$ that both the $Re = 10^5$ and $10^6$ cases reach comparably small $\gamma/S$ but only the latter triggers braid instabilities. Figure 16 suggests that timing plays a role in the prevalence of braid instabilities, as braid instability occurs earlier than other instabilities. In particular, the evolution of $\phi$ in fig. 17 highlights that braid instabilities occur exclusively before the primary billow reaches a maximum amplitude.

To clarify this point, fig. 18 compares primary billow growth to braid instability by plotting $\phi/\phi_{max}$ against $\gamma/S$; the maximum braid angle $\phi_{max}$ to primary billow saturation. This allows us to distinguish secondary shear instabilities on the braid from other secondary instabilities. Braid instabilities occur if a sufficiently small $\gamma/S$ is reached strictly before the saturation of the primary billow. In fact, if the primary billow saturates and reaches the maximum angle ($\phi/\phi_{max} = 1$), secondary core instabilities invariably develop. Coincidentally, the marginally-unstable case $c\_10^5\_0.15$ simultaneously reaches its maximum angle and low $\gamma/S$, explaining the simultaneous occurrence of braid and core instabilities.

The development of secondary instabilities is governed by a race between primary billow growth and baroclinic shear acceleration. In particular, the relative timescales of these mechanisms determine which secondary instability is triggered; if they are comparable,

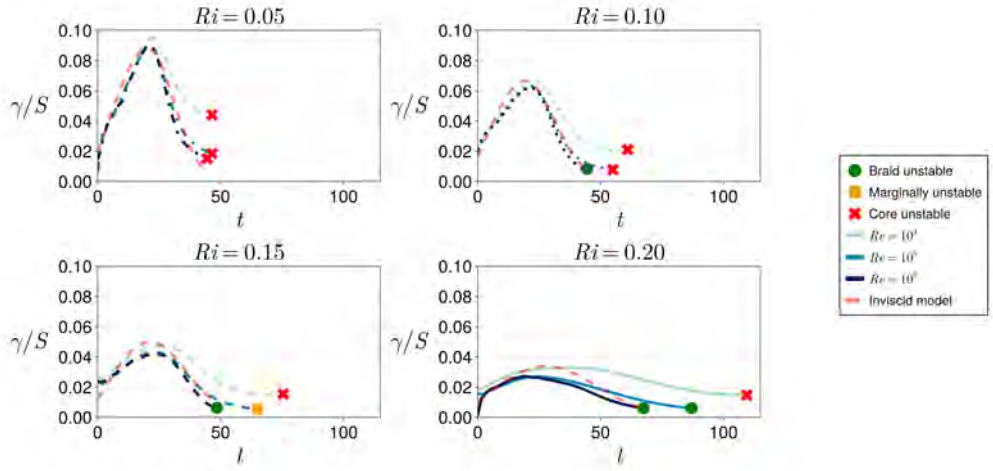


Figure 16: The evolution of $\gamma/S$ in time $t$. $Re$ from $10^4$ to $10^6$, as noted in the legend. $Ri$ is given by respective panel titles as well as line style $Ri = 0.05$ dash dot, 0.10 dot, 0.15 dash and 0.20 solid. The end points are marked with symbols noted in the legend, representing the type of secondary instability. The red dashed line illustrates the inviscid model prediction.

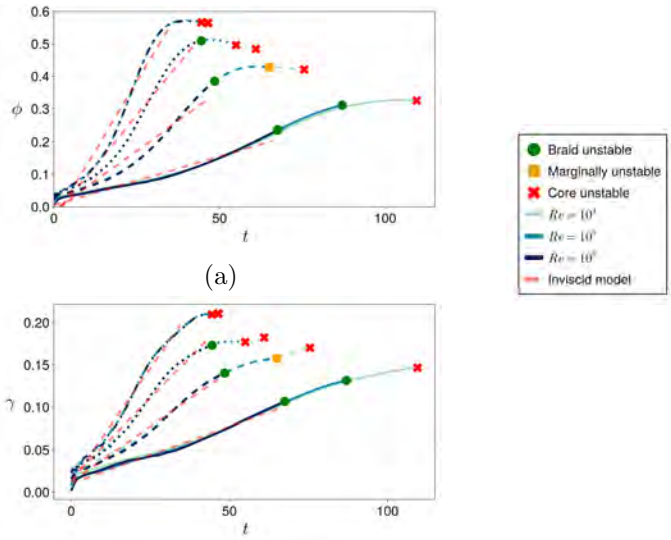


(a)

(b)

Figure 17: The evolution of (a) $\phi$ and (b) $\gamma$ in time $t$. $Re$ from $10^4$ to $10^6$, as noted in the legend. $Ri$ is given by line style $Ri = 0.05$ dash dot, 0.10 dot, 0.15 dash and 0.20 solid. The end points are marked with symbols noted in the legend, representing the type of secondary instability. The red dashed lines represent the linear approximation taken for use in the inviscid model.

marginal behaviour can arise. The timescale for primary billow saturation depends only on $Ri$, whereas the timescale for the braid instability shortens with increasing $Re$. The minimum timescale on which braid instabilities can emerge can be predicted using the inviscid model. If this timescale is shorter than that of billow saturation, braid instabilities are expected to dominate in the inviscid limit.

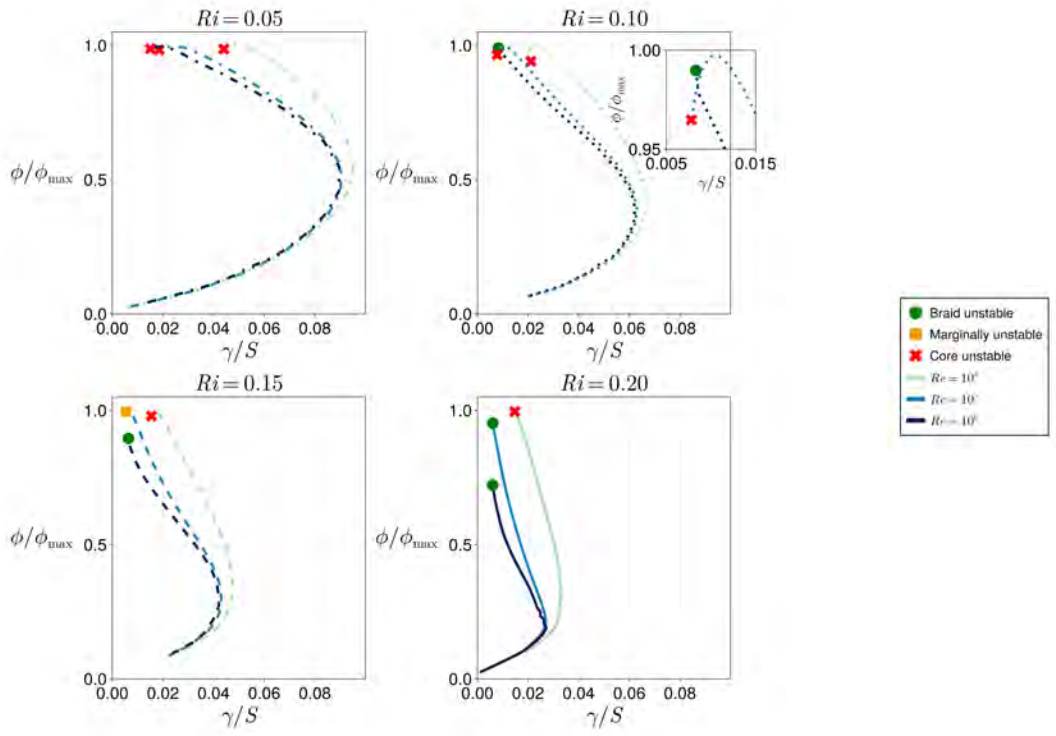


Figure 18: Braid angle $\phi/\phi_{\max}$ against $\gamma/S$. $Re$ from $10^3$ to $10^6$ is represented by colour varying light to dark. $Ri$ is given by line style $Ri = 0.05$ dash dot, 0.10 dot, 0.15 dash and 0.20 solid. The end points are marked with symbols representing core unstable (red cross), braid unstable (green circle) and both braid and core unstable (yellow square).

# 7 Discussion

In this report, we have explored the onset of secondary shear instabilities on the braids of Kelvin-Helmholtz (KH) billows over an extended range of Richardson and Reynolds number to investigate a parameter regime which is more reflective of real-world ocean or estuarine conditions than previous studies. We achieved this through 2D direct numerical simulations in Oceananigans using high resolutions, which allow us to approach the inviscid limit in a way that has been previously inaccessible in the literature.

We differentiated between secondary shear instabilities that develop along the braid, and

other secondary instabilities that arise within the core of the KH billow. To investigate the mechanisms behind shear instabilities on the braid, we developed both numerical methods and an inviscid analytical model to capture the transient evolution of the braid. The stability of the braid is governed by a competition between the stabilising influence of strain and the destabilising influence of baroclinic torque, accelerating the shear flow. This balance is encapsulated in the ratio of strain to shear $\gamma/S$. The inviscid model captures the timescale at which $\gamma/S$ becomes sufficiently small to permit the onset of braid shear instability. Crucially, $\gamma/S$ must decrease sufficiently before the saturation of the primary billow; beyond this point, core instabilities emerge. In fact, 3D instabilities are expected to dominate. Primary billow growth depends only on Richardson number, with more strongly stratified flows growing more slowly, reaching smaller amplitude. Marginal behaviour may occur if the timescales of braid instability and primary growth are comparable.

One particular implication of this report is the increased dependence on Reynolds number at high Richardson number. We are able to reach high Reynolds numbers ($Re = 10^6$) in order to attain an inviscid limit, but for lower values we observe notable differences. Thus, accurate depictions reflective of real-world parameters, require high Reynolds number simulations; a $Re = 10^6$ flow cannot be accurately approximated using $Re = 10^4$ simulations to reduce numerical load. This is numerically challenging and, in particular, remains beyond current realistic capabilities for 3D simulations.

These high Reynolds number flows also require more finely resolved grids. Under-resolved simulations can prematurely trigger secondary instabilities as the grid struggles to resolve the rapidly thinning braid. To reach higher resolutions, we employed a stretched grid which prioritised resolution over the central billow region to minimise the numerical load. At our chosen resolution, we believe that the simulation effectively captures the primary and secondary instability growth, but further higher-resolution simulations will be required to verify the results presented here.

The braid analytics rely on a visual assessment of when secondary instabilities have developed and where they are located. This method is not necessarily quantifiable, and as such an immediate next step will be to develop simple metrics to signify the onset of secondary instabilities, as well as the saturation of the primary billow growth. One such suitable metric for the onset of secondary instabilities could be the identification of peaks in the power spectrum of the braid field. Similarly, primary billow saturation could be represented by a maximum kinetic energy of the primary billow.

We are also interested in extending the Prandtl number to $Pr = O(10^{2-3})$. Increasing the Prandtl number would decrease the buoyancy length scale, and therefore also the viscous length scale, as we showed in eq. (32). This would require increasing the resolution of simulations, rendering the high-$Re$, high-$Pr$ regime difficult to resolve numerically. However, in this regime, we still expect the inviscid model to apply, and therefore for the conclusions of this report to remain applicable. Higher Prandtl numbers lead to distinct buoyancy and shear length scales, with the buoyancy layer becoming much thinner than the shear layer. As a result, increasing Prandtl number can promote the conditions required to instead induce a Holmboe instability [13]. It remains unclear whether this mechanism could be triggered on the braid of a KH billow.

Further considerations may include exploring the influence of viscosity as the braid thins. We noted that lower Reynolds number flows lead to an earlier deviation from the inviscid

model prediction, likely due to the straining of the braid reaching viscous length scales. Can we predict and measure accurately the time and length scales at which viscous effects contribute?

## 8 Acknowledgements

I would like to thank my wonderful advisors, Sam Lewin and Adrien Lefauve, for all their support this summer — both near, through Sam's daily help, and far, through Adrien's insightful comments over Zoom. Thank you also to our directors Pascale Garaud and David Goluskin for their dedication to the program. Most importantly, I'm so grateful to all the other fellows for not only keeping me sane, but also for making this such a memorable summer.

This work used the Delta advanced computing and data resource through allocation PHY250188 from the Advanced Cyberinfrastructure Coordination Ecosystem: Services & Support (ACCESS) program, which is supported by U.S. National Science Foundation grants #2138259, #2138286, #2138307, #2137603, and #2138296. Delta is a joint effort of the University of Illinois Urbana-Champaign and its National Center for Supercomputing Applications, supported by the National Science Foundation (award OAC 2005572) and the State of Illinois.

## References

[1] C. P. Caulfield and W. R. Peltier, *Three dimensionalization of the stratified mixing layer*, Physics of Fluids, 6 (1994), pp. 3803–3805.

[2] ——, *The anatomy of the mixing transition in homogeneous and stratified free shear layers*, Journal of Fluid Mechanics, 413 (2000), pp. 1–47. Publisher: Cambridge University Press (CUP).

[3] G. M. Corcos and F. S. Sherman, *Vorticity concentration and the dynamics of unstable free shear layers*, Journal of Fluid Mechanics, 73 (1976), pp. 241–264.

[4] D. G. Dritschel, P. H. Haynes, M. N. Juckes, and T. G. Shepherd, *The stability of a two-dimensional vorticity filament under uniform strain*, Journal of Fluid Mechanics, 230 (1991), pp. 647–665. Publisher: Cambridge University Press (CUP).

[5] W. R. Geyer, A. C. Lavery, M. E. Scully, and J. H. Trowbridge, *Mixing by shear instability at high Reynolds number*, Geophysical Research Letters, 37 (2010). Wiley Online Library.

[6] L. N. Howard, *Note on a paper of John W. Miles*, Journal of Fluid Mechanics, 10 (1961), pp. 509–512.

[7] C. J. Howland, J. R. Taylor, and C. P. Caulfield, *Testing linear marginal stability in stratified shear layers*, Journal of Fluid Mechanics, 839 (2018). Publisher: Cambridge University Press (CUP).

[8] D. Lecoanet, M. McCourt, E. Quataert, K. J. Burns, G. M. Vasil, J. S. Oishi, B. P. Brown, J. M. Stone, and R. M. O'Leary, *A validated non-linear Kelvin–Helmholtz benchmark for numerical hydrodynamics*, Monthly Notices of the Royal Astronomical Society, 455 (2016), pp. 4274–4288.

[9] A. Mashayek and W. R. Peltier, *The 'zoo' of secondary instabilities precursory to stratified shear flow transition. Part 1 Shear aligned convection, pairing, and braid instabilities*, Journal of Fluid Mechanics, 708 (2012), pp. 5–44.

[10] ——, *The 'zoo' of secondary instabilities precursory to stratified shear flow transition. Part 2 The influence of stratification*, Journal of Fluid Mechanics, 708 (2012), pp. 45–70.

[11] J. W. Miles, *On the stability of heterogeneous shear flows*, Journal of Fluid Mechanics, 10 (1961), pp. 496–508.

[12] W. D. Smyth, *Secondary Kelvin–Helmholtz instability in weakly stratified shear flow*, Journal of Fluid Mechanics, 497 (2003), pp. 67–98.

[13] W. D. Smyth and J. R. Carpenter, *Instability in Geophysical Flows*, Cambridge University Press, 1 ed., Apr. 2019.

[14] W. D. Smyth and J. N. Moum, *Ocean Mixing by Kelvin-Helmholtz Instability*, Oceanography, 25 (2012), pp. 140–149. Publisher: Oceanography Society.

[15] W. D. Smyth, J. N. Moum, and J. D. Nash, *Narrowband Oscillations in the Upper Equatorial Ocean. Part II: Properties of Shear Instabilities*, (2011). Section: Journal of Physical Oceanography.

[16] C. Staquet, *A numerical study of vorticity layers in a two-dimensional stratified shear flow*, Meccanica, 29 (1994), pp. 489–505.

[17] ——, *Two-dimensional secondary instabilities in a strongly stratified shear layer*, Journal of Fluid Mechanics, 296 (1995), pp. 73–126.

[18] S. A. Thorpe, *The near-surface ocean mixing layer in stable heating conditions*, Journal of Geophysical Research: Oceans, 83 (1978), pp. 2875–2885.

[19] G. L. Wagner, S. Silvestri, N. C. Constantinou, A. Ramadhan, J.-M. Campin, C. Hill, T. Chor, J. Strong-Wright, X. K. Lee, F. Poulin, A. Souza, K. J. Burns, J. Marshall, and R. Ferrari, *High-level, high-resolution ocean modeling at all scales with Oceananigans*, Feb. 2025. arXiv:2502.14148 [physics].

# Optimal Heat Transport in Steady Rayleigh-Bénard Convection With No-slip Boundaries

Theo Lewy

August 19, 2025

## 1 Introduction

Thermal convection drives fluid motion and transports energy across a range of natural and industrial contexts. The most well-studied model to capture this effect is no doubt Rayleigh-Bénard convection, where a fluid layer is heated along a lower plate and cooled along an upper plate. The heat can then drive flow due to buoyancy forces, and the resultant convection amplifies the heat transport which would otherwise be due to conduction alone. The amplification factor of heat flux is the Nusselt number $Nu$, corresponding to the ratio of heat flux due to both convection and conduction to the heat flux due to just conduction.

As originally found by Rayleigh, the motionless conductive state becomes unstable when the dimensionless temperature difference, now named the Rayleigh number $Ra$, is above a critical value [8], at which point a convection roll is produced supercritically. These states are steady, can support different numbers of rolls horizontally and vertically in 2D and 3D, and become unstable at large enough $Ra$. For sufficently large $Ra$, instabilities cause the system to transition to fully developed turbulence.

Quantifying how $Nu$ scales for turbulence at asymptotically large $Ra$ is of particular interest, and while a rigorous upper bound of $Nu \leq O(Ra^{1/2})$ has been proven for all states [5], it is not clear whether turbulence can attain this bound. There are 2 scalings commonly discussed: the 'classical' regime $Nu \sim Ra^{1/3}$ where laminar thermal boundary layers restrict heat transport, and the 'ultimate' regime $Nu \sim Ra^{1/2}$ with turbulent boundary layers, and the upper bound is attained. The $Ra$ currently accessible in experiments and in numerics is not sufficiently large to conclusively prove either regime due to the stiffness of the system. In contrast, coherent convection rolls can be studied numerically and theoretically at larger $Ra$, allowing the asymptotic heat transport to be investigated with comparative ease.

For no-slip boundary conditions with fixed $Ra$ ($Ra \gg 1$) and Prandtl number $Pr$, the heat flux of rolls has two maxima as the aspect ratio $\Gamma$ varies [10–12]. These are the global optimum and the local optimum, which globally and locally maximise $Nu$, respectively. Both solutions are associated with an asymptotic $Nu$ and $\Gamma$ dependency on $Ra$. Focusing on global optima, two different asymptotic regimes have been suggested that are in opposition. Scaling arguments in [4] suggest a regime with $\Gamma \sim Ra^{-2/9}$ and $Nu \sim Ra^{1/3}$ in Taylor-Couette flow, which is equivalent in the narrow gap limit to Rayleigh-Bénard with $Pr = 1$. In contrast to this, global optimals computed numerically at $Pr = 1$ instead suggest $\Gamma \sim Ra^{-1/5}$, while agreeing with the $Nu$ scaling [12]. Neither result is clearly asymptotic, and so we turn to matched asymptotics to help identify the asymptotic scalings. This

involves splitting the system into smaller asymptotic regions, identifying the asymptotically valid equations in each region, and matching fields between them. The limiting parameter drops out of the resulting set of reduced equations, allowing the asymptotic structure to be computed.

Matched asymptotics were successful in the stress-free case, where the roll structure and $Nu$ can be computed without needing to converge solutions at high $Ra$, where boundary layers are narrow and hence high resolution is required [3]. There, the asymptotic equations were simple enough to be solved numerically, giving the $Pr$ independent result $Nu = c(\Gamma)Ra^{1/3}$ for rolls with $\Gamma = O(1)$, which is also verified numerically [13]. Even when the asymptotic equations are not numerically simple to solve, scalings are still obtainable using matched asymptotics, as was the case for the no-slip local optimal (*Wen, Takla, Goluskin and Chini*, unpublished at the time of writing).

Mean-zero heating and cooling, where sources and sinks of heat are internal rather than at the boundaries [1, 6, 7], is another system that supports convection rolls. This setup can achieve ultimate turbulence $Nu \sim Ra^{1/2}$ [1, 6] as the heat flux is not limited by laminar boundary layers. The $Nu$ upper bound however is higher than in the Rayleigh-Bénard system, with $Nu \leq O(Ra)$ here, with the bound attained for a stress-free convection roll state [7]. Whether the bound is attained in the no-slip case is not known.

In this report we begin by describing the Rayleigh-Bénard system in section 2. We then use matched asymptotics on a convection roll in section 3 to split the domain into multiple regions, and identify the asymptotic scalings and equations valid in each region in the limit $Ra \to \infty$. To validate our suggested scalings we require converged rolls at large $Ra$, and so in section 4 we describe our implementation of the Newton-GMRES algorithm. While the extreme Rayleigh-Bénard rolls were not converged over the summer that this report covers, we verified the code worked by converging rolls in the no-slip mean-zero heating and cooling system. This system is discussed in section 5, and we lastly conclude in section 6.

## 2 Formulation

We consider the steady 2D Rayleigh-Bénard system with wall-parallel direction $\hat{\boldsymbol{x}}$ and wall-normal direction $\hat{\boldsymbol{z}}$. The equations governing the streamfunction $\psi$, vorticity $\omega$ and temperature $T$ are

$$\partial_z\psi\partial_x\omega - \partial_x\psi\partial_z\omega = \left(\frac{Pr}{Ra}\right)^{1/2}\nabla^2\omega + \partial_x T, \tag{1}$$

$$\nabla^2\psi = -\omega, \tag{2}$$

$$\partial_z\psi\partial_x T - \partial_x\psi\partial_z T = (PrRa)^{-1/2}\nabla^2 T, \tag{3}$$

with $\nabla^2 \coloneqq \partial_x^2 + \partial_z^2$, and velocity $\boldsymbol{u} \coloneqq u\hat{\boldsymbol{x}} + w\hat{\boldsymbol{z}} = \partial_z\psi\hat{\boldsymbol{x}} - \partial_x\psi\hat{\boldsymbol{z}}$. These equations are non-dimensionalised using the domain height $h$, the imposed temperature difference $\Delta$, and the free-fall velocity $\sqrt{g\alpha h\Delta}$, where $\alpha$ is the coefficient of thermal diffusivity, and $g$ is the acceleration due to gravity. Convection rolls are computed in a vertically bounded and horizontally periodic domain of size $[0, \Gamma] \times [0, 1]$, where $\Gamma$ then corresponds to the aspect-ratio. The non-dimensional parameters of the system are the Prandtl number $Pr = \nu/\kappa$ and the Rayleigh number $Ra = g\alpha h^3\Delta/\kappa\nu$, where $\kappa$ is the thermal diffusivity and $\nu$ is the kinematic viscosity. This system is solved subject to no slip and isothermal boundary conditions on the top and bottom boundary

$$\psi|_{z=0,1} = 0, \quad \partial_z\psi|_{z=0,1} = 0, \quad T|_{z=0} = 1, \quad T|_{z=1} = 0. \tag{4}$$

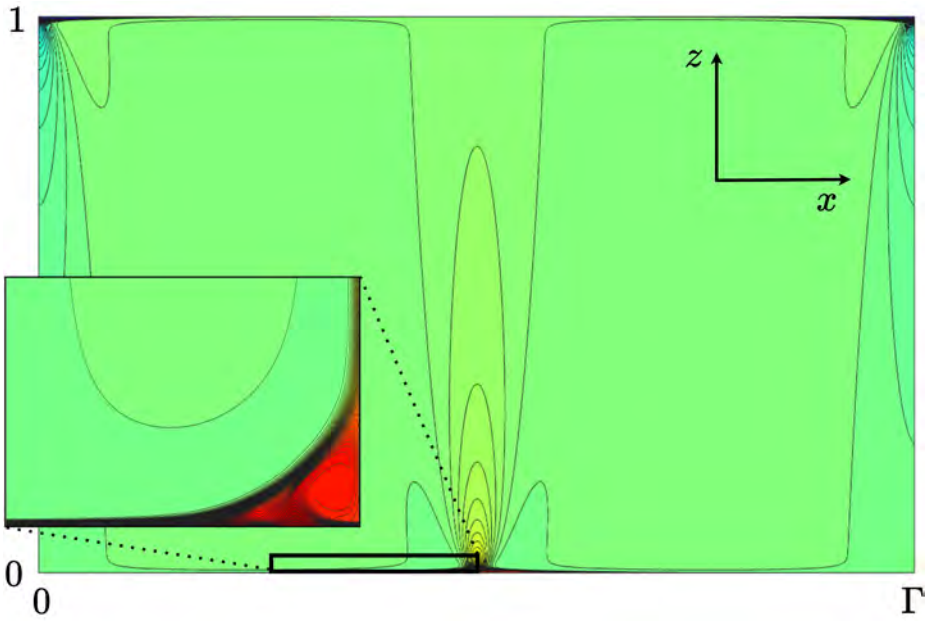


Figure 1: Temperature field of an optimal convection roll at $Ra = 1.8 \times 10^{12}$, $Pr = 0.1$, with $\Gamma^* = 0.0377$. This roll is narrow, but has been plotted in rescaled coordinates to show its structure more clearly. The inset zooms in further on the separation zone structure.

These equations support convection roll structures that have a centro-rotational symmetry $\Omega$ and a reflectional symmetry $\mathcal{R}$ with

$$\Omega(\psi, \omega, T)(x, z) = (\psi, \omega, -T)(\Gamma/2 - x, 1 - z), \tag{5}$$

$$\mathcal{R}(\psi, \omega, T)(x, z) = (-\psi, -\omega, T)(\Gamma - x, z). \tag{6}$$

The latter symmetry implies

$$\psi|_{x=0,\Gamma/2} = 0 \quad \omega|_{x=0,\Gamma/2} = 0 \quad \partial_x T|_{x=0,\Gamma/2} = 0. \tag{7}$$

We show an example convection roll in fig. 1, where the symmetries of the thermal field can be seen. An important conserved quantity of the system is the Nusselt number, $Nu$, which quantifies the total heat transport of the system relative to the heat transport due to conduction alone. This is given by

$$Nu \coloneqq 1 + (PrRa)^{1/2} \langle Tw \rangle = 1 - (PrRa)^{1/2} \langle T \partial_x \psi \rangle \tag{8}$$

where $\langle \cdot \rangle$ denotes a volume average. A useful equivalent form is

$$Nu = \frac{1}{\Gamma} \int_0^\Gamma -\partial_z T - (PrRa)^{1/2} T \partial_x \psi \, dx \tag{9}$$

which can be evaluated at any $z \in [0, 1]$ to give the same value of $Nu$. This $z$-independence can be seen by integrating eq. (3) with respect to $x$, yielding that the derivative of eq. (9) with respect to $z$ vanishes. Equivalence of the two expressions then follows by averaging eq. (9) in the $z$ direction.

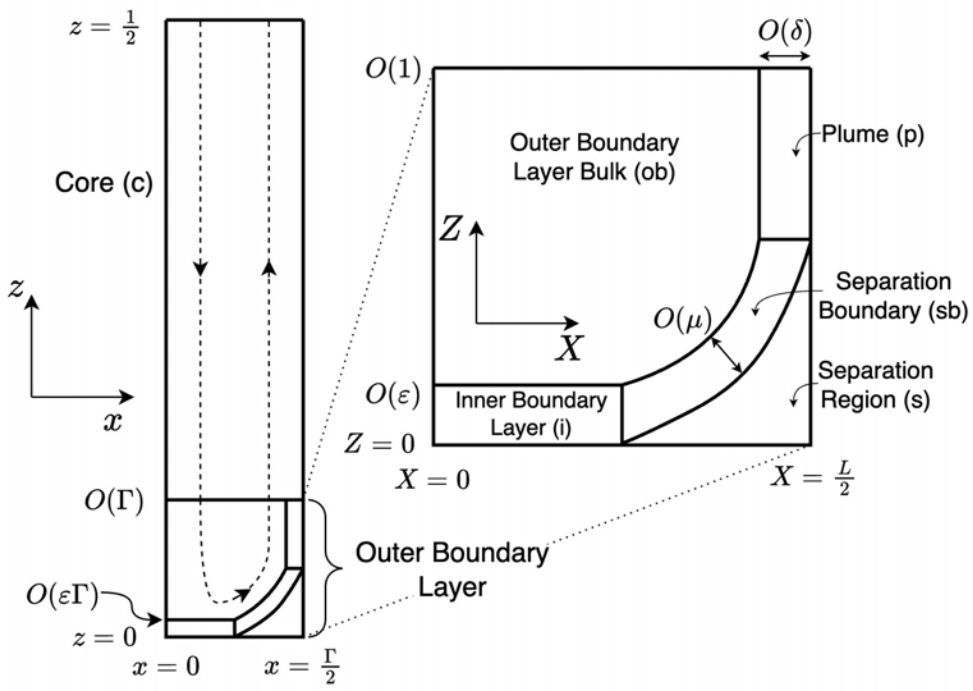


Figure 2: The asymptotic structure of the global optimal convection roll, showing the bottom half of a roll with anticlockwise flow. Right: The structure of the outer boundary layer shown in coordinates $(X, Z) = (Ra^s x, Ra^s z)$.

## 3 Asymptotics

We now aim to identify the asymptotic structure of the global optimal rolls in the asymptotic limit of $Ra \to \infty$. Previous work in [4] identified a regime in which the aspect ratio $\Gamma \sim Ra^{-2/9}$ and the heat flux $Nu \sim Ra^{1/3}$, and described its structure. We believe that this regime was not asymptotic, with a different state achieved at $Ra$ larger than was considered there. To instead verify the aspect ratio scaling found numerically in [12] of $\Gamma \sim Ra^{-1/5}$, we use matched asymptotics. Both regimes find $Nu \sim Ra^{1/3}$.

The regime of [4] finds a core region, an outer boundary layer, an inner boundary layer, and a plume confined within the outer boundary layer. We, in addition, identify a separation region, and a separation boundary that sits between the separation region and the outer boundary layer bulk, and we show this proposed asymptotic structure in fig. 2. Motivated by the conflicting aspect ratio scalings [4, 12], we write $\Gamma = Ra^{-s} L$ with $L = O(Ra^0)$ and $s > 0$ is unknown. The scaling analysis of [4] proposed that $s = 2/9$, while in contrast $s = 1/5$ is suggested by the numerical work of [12]. We do not assume any aspect ratio scaling a priori.

### 3.1 The core

In the core we have that $x \sim \Gamma$ and $z \sim 1$, and we assume that to leading order all fields are independent of $z$. Hence we use an ansatz of

$$\psi = \psi_c^0(X) + \psi_c^1(X,z) \quad \omega = \omega_c^0(X) + \omega_c^1(X,z) \quad T = \frac{1}{2} + T_c^0(X) + T_c^1(X,z), \tag{10}$$

where $X := Ra^s x$, $\psi_c^0 \gg \psi_c^1$, $\omega_c^0 \gg \omega_c^1$ and $T_c^0 \gg T_c^1$. On lengthscales with $X, z = O(1)$, we scale the vorticity advection with horizontal vorticity diffusion and buoyancy in (1) and scale thermal advection with horizontal thermal diffusion in (3). We introduce the unknown $\gamma$ with $\psi_c^0 \sim Ra^\gamma$, and by considering the dominant balance we obtain the scalings

$$\psi_c = Ra^\gamma \tilde{\psi}_c^0(X) + Ra^{s-1/2}\tilde{\psi}_c^1(X,z), \quad \omega_c = Ra^{2s+\gamma}\tilde{\omega}_c^0(X) + Ra^{3s-1/2}\tilde{\omega}_c^1(X,z), \tag{11}$$

$$T_c = \frac{1}{2} + Ra^{3s+\gamma-1/2}\tilde{T}_c^0(X) + Ra^{4s-1}\tilde{T}_c^1(X,z). \tag{12}$$

with all tilded fields $O(1)$. Under these rescalings, (1)-(3) become

$$\begin{aligned} \partial_z\tilde{\psi}_c^1\left(\partial_X\tilde{\omega}_c^0 + Ra^{s-\gamma-1/2}\partial_X\tilde{\omega}_c^1\right) - \left(\partial_X\tilde{\psi}_c^0 + Ra^{s-\gamma-1/2}\partial_X\tilde{\psi}_c^1\right)\partial_z\tilde{\omega}_c^1 = \\ Pr^{1/2}\left(\partial_X^2 + Ra^{-2s}\partial_z^2\right)\left(\tilde{\omega}_c^0 + Ra^{s-\gamma-1/2}\tilde{\omega}_c^1\right) + \left(\partial_X\tilde{T}_c^0 + Ra^{s-\gamma-1/2}\partial_X\tilde{T}_c^1\right), \end{aligned} \tag{13}$$

$$\left(\partial_X^2 + Ra^{-2s}\partial_z^2\right)\left(\tilde{\psi}_c^0 + Ra^{s-\gamma-1/2}\tilde{\psi}_c^1\right) = -\left(\tilde{\omega}_c^0 + Ra^{s-\gamma-1/2}\tilde{\omega}_c^1\right), \tag{14}$$

$$\begin{aligned} \partial_z\tilde{\psi}_c\left(\partial_X\tilde{T}_c^0 + Ra^{s-\gamma-1/2}\partial_X\tilde{T}_c^1\right) - \left(\partial_X\tilde{\psi}_c^0 + Ra^{s-\gamma-1/2}\partial_X\tilde{\psi}_c^1\right)\partial_z\tilde{T}_c = \\ Pr^{-1/2}\left(\partial_X^2 + Ra^{-2s}\partial_z^2\right)\left(\tilde{T}_c^0 + Ra^{s-\gamma-1/2}\tilde{T}_c^1\right). \end{aligned} \tag{15}$$

Asymptotically, we assume $s > 0$ and $s - \gamma - 1/2 < 0$ and so the governing equations in the core are

$$\partial_z\tilde{\psi}_c^1\partial_X\tilde{\omega}_c^0 - \partial_X\tilde{\psi}_c^0\partial_z\tilde{\omega}_c^1 = Pr^{1/2}\partial_X^2\tilde{\omega}_c^0 + \partial_X\tilde{T}_c^0, \tag{16}$$

$$\partial_X^2\tilde{\psi}_c^0 = -\tilde{\omega}_c^0, \tag{17}$$

$$\partial_z\tilde{\psi}_c^1\partial_X\tilde{T}_c^0 - \partial_X\tilde{\psi}_c^0\partial_z\tilde{T}_c^1 = Pr^{-1/2}\partial_X^2\tilde{T}_c^0. \tag{18}$$

These equations are solved subject to the boundary conditions

$$\tilde{\psi}_c^i|_{X=0,L/2} = 0 \quad \tilde{\omega}_c^i|_{X=0,L/2} = 0 \quad \partial_X\tilde{T}_c^i|_{X=0,L/2} = 0, \tag{19}$$

for $i = 0, 1$. The fact that we have treated the leading order fields in this region as $z$ independent sets our asymptotics apart from those of [4], where this was not the case. There, the same dominant balance enforces that $\psi_c \sim Ra^{s-1/2}$, $\omega_c \sim Ra^{3s-1/2}$ and $T_c - \frac{1}{2} \sim Ra^{4s-1}$, while our scalings are $\psi_c \sim Ra^\gamma$, $\omega_c \sim Ra^{2s+\gamma}$ and $T_c - \frac{1}{2} \sim Ra^{3s+\gamma-1/2}$, where $\gamma$ is an extra degree of freedom to be solved for. The scalings of [4] are then recovered if one simply sets $\gamma = s - 1/2$.

### 3.2 Bulk of outer boundary layer

In the bulk of the outer boundary we have that $x \sim \Gamma$ and $z \sim \Gamma$, and so

$$\psi = \psi_{ob}(X, Z), \quad \omega = \omega_{ob}(X, Z), \quad T = \frac{1}{2} + T_{ob}(X, Z), \tag{20}$$

with $Z \coloneqq Ra^s z$. Matching with the core suggests that all variables have the same leading order scaling as in the core, and hence

$$\psi_{ob} = Ra^{\gamma}\tilde{\psi}_{ob}(X, Z), \quad \omega_{ob} = Ra^{2s+\gamma}\tilde{\omega}_{ob}(X, Z), \quad T_{ob} = \frac{1}{2} + Ra^{3s+\gamma-1/2}\tilde{T}_{ob}(X, Z). \tag{21}$$

These rescalings result in exact governing equations of

$$Ra^{\gamma+1/2}\left(\partial_Z\tilde{\psi}_{ob}\partial_X\tilde{\omega}_{ob} - \partial_X\tilde{\psi}_{ob}\partial_Z\tilde{\omega}_{ob}\right) = Pr^{1/2}\left(\partial_X^2 + \partial_Z^2\right)\tilde{\omega}_{ob} + \partial_X\tilde{T}_{ob}, \tag{22}$$

$$\left(\partial_X^2 + \partial_Z^2\right)\tilde{\psi}_{ob} = -\tilde{\omega}_{ob}, \tag{23}$$

$$Ra^{\gamma+1/2}(\partial_Z\tilde{\psi}_{ob}\partial_X\tilde{T}_{ob} - \partial_X\tilde{\psi}_{ob}\partial_Z\tilde{T}_{ob}) = Pr^{-1/2}\left(\partial_X^2 + \partial_Z^2\right)\tilde{T}_{ob}. \tag{24}$$

In the bulk of the outer layer, provided $\gamma + 1/2 > 0$, we therefore asymptotically obtain

$$\partial_Z\tilde{\psi}_{ob}\partial_X\tilde{\omega}_{ob} - \partial_X\tilde{\psi}_{ob}\partial_Z\tilde{\omega}_{ob} = 0, \tag{25}$$

$$\left(\partial_X^2 + \partial_Z^2\right)\tilde{\psi}_{ob} = -\tilde{\omega}_{ob}, \tag{26}$$

$$\partial_Z\tilde{\psi}_{ob}\partial_X\tilde{T}_{ob} - \partial_X\tilde{\psi}_{ob}\partial_Z\tilde{T}_{ob} = 0. \tag{27}$$

meaning vorticity and temperature are advected around the layer. This layer borders the core, the plume, the inner boundary, and the separation boundary. We now briefly introduce the separation boundary, so that we can concretely write down the boundary conditions that are valid for the bulk of the outer boundary layer.

Asymptotically, this separation zone boundary sits within the bulk of the outer boundary, at $Z = C(X)$, where $C$ is unknown but invertible. The curve intersects the bottom boundary at $X = X_0$ (i.e., $C(X_0) = 0$) and the right boundary at $Z = Z_0$ (i.e., $C^{-1}(Z_0) = L/2$). This curved layer will connect the inner boundary layer to the plume of the outer boundary. The boundary conditions in the bulk of the outer boundary are therefore

$$\begin{aligned}\tilde{\psi}_{ob}|_{X=0} = 0, \quad \tilde{\psi}_{ob}|_{Z=0,X<X_0} = 0, \quad \tilde{\psi}_{ob}|_{Z=C(X)} = 0,\\ \tilde{\psi}_{ob}|_{X=L/2,Z>Z_0} = 0, \quad \tilde{\psi}_{ob}|_{Z\to\infty} = \tilde{\psi}_c|_{z\to 0}.\end{aligned} \tag{28}$$

### 3.3 Inner boundary layer

The inner boundary layer sits within the outer boundary layer, with $X \sim 1$ and $Z \sim \varepsilon$, where $\varepsilon$ is unknown, and so

$$\psi = \psi_i(X, \eta), \quad \omega = \omega_i(X, \eta), \quad T = T_i(X, \eta), \tag{29}$$

with $\eta \coloneqq Z/\varepsilon$. We scale advection with vertical diffusion for both vorticity and temperature, and motivated by the fixed thermal boundary condition, consider $O(1)$ temperatures. This yields

$$\psi_i = Ra^{-1/2}\varepsilon^{-1}\tilde{\psi}_i(X,\eta), \quad \omega_i = Ra^{2s-1/2}\varepsilon^{-3}\tilde{\omega}_i(X,\eta), \quad T_i = \tilde{T}_i(X,\eta). \tag{30}$$

Substituting this into (1)-(3) gives

$$\partial_\eta\tilde{\psi}_i\partial_X\tilde{\omega}_i - \partial_X\tilde{\psi}_i\partial_\eta\tilde{\omega}_i = Pr^{1/2}\left(\varepsilon^2\partial_X^2 + \partial_\eta^2\right)\tilde{\omega}_i + \varepsilon^5 Ra^{1-3s}\partial_X\tilde{T}_i, \tag{31}$$

$$\left(\varepsilon^2\partial_X^2 + \partial_\eta^2\right)\tilde{\psi}_i = -\tilde{\omega}_i, \tag{32}$$

$$\partial_\eta\tilde{\psi}_i\partial_X\tilde{T}_i - \partial_X\tilde{\psi}_i\partial_\eta\tilde{T}_i = Pr^{-1/2}\left(\varepsilon^2\partial_X^2 + \partial_\eta^2\right)\tilde{T}_i. \tag{33}$$

Assuming $\varepsilon \ll 1$ and $\varepsilon^5 Ra^{1-3s} \ll 1$, these equations asymptotically become

$$\partial_\eta\tilde{\psi}_i\partial_X\tilde{\omega}_i - \partial_X\tilde{\psi}_i\partial_\eta\tilde{\omega}_i = Pr^{1/2}\partial_\eta^2\tilde{\omega}_i, \tag{34}$$

$$\partial_\eta^2\tilde{\psi}_i = -\tilde{\omega}_i, \tag{35}$$

$$\partial_\eta\tilde{\psi}_i\partial_X\tilde{T}_i - \partial_X\tilde{\psi}_i\partial_\eta\tilde{T}_i = Pr^{-1/2}\partial_\eta^2\tilde{T}_i, \tag{36}$$

which decouples the vorticity from the temperature field, with eq. (34) being the Prandtl boundary layer equation. We now obtain $\varepsilon$ by matching $\psi$ between the inner boundary layer and the outer boundary bulk. We have $\lim_{\eta\to\infty}\psi_i = \lim_{\eta\to\infty} Ra^{-1/2}\varepsilon^{-1}\tilde{\psi}_i(X,\eta) \sim \lim_{Z\to 0} Ra^{\gamma}\tilde{\psi}_{ob}(X,Z) = \lim_{Z\to 0}\psi_{ob}$, and as is the case in a Prandtl boundary layer we assume $\tilde{\psi}_i(X,\eta) \sim \eta$ and $\tilde{\psi}_{ob}(X,Z) \sim Z$. This yields

$$Ra^{\gamma} \sim Ra^{-1/2}\varepsilon^{-2}. \tag{37}$$

In addition, we consider the Nusselt number $Nu$ from (9). As $Nu$ is independent of $z$, it must scale the same when evaluated in the core and at the lower boundary. In the core $Nu \sim Ra^{4s+2\gamma}$, while at the boundary we have $Nu \sim Ra^s\varepsilon^{-1}$, provided the heat transport at $z = 0$ is dominated by the inner boundary layer. Together these yield $Ra^{\gamma} \sim Ra^{-3s/2}\varepsilon^{-1/2}$. This result, along with (37), gives the key scaling

$$Nu \sim Ra^{1/3},$$

as well as

$$\varepsilon = Ra^{s-1/3}, \quad \gamma = -2s + \frac{1}{6}$$

It is worth mentioning that these scales are derived using only knowledge of the core, the bulk of the outer boundary, and the inner boundary layer. The aspect ratio scaling is also not required to derive this. The boundary conditions used with (34)-(36) are

$$\tilde{\psi}_i|_{\eta=0} = 0, \quad \partial_\eta\tilde{\psi}_i|_{\eta=0} = 0, \quad \tilde{T}_i|_{\eta=0} = 1, \quad \tilde{T}_i|_{\eta\to\infty} = 1/2, \tag{38}$$

$$\psi_i|_{\eta\to\infty} \sim \psi_{ob}|_{Z\to 0^+}, \quad \omega_i|_{\eta\to\infty} \sim \omega_{ob}|_{Z\to 0^+} \tag{39}$$

where the final two boundary conditions correspond to exact asymptotic expressions in the limits $\eta \to \infty$ and $Z \to 0$ rather than when $Ra \to \infty$.

### 3.4 The boundary of the separation region

There is a thin boundary layer that surrounds the separation region, and connects the inner boundary layer to the plume of the outer boundary. Asymptotically, this boundary layer sits within the bulk of the outer boundary, and follows the line $Z = C(X)$, where $C$ is unknown and invertible. The curve intersects the bottom boundary at $X = X_0$ (i.e., $C(X_0) = 0$) and the right boundary at $Z = Z_0$ (i.e., $C^{-1}(Z_0) = L/2$). To account for the curvature in this region we introduce 2D Frenet orthonormal coordinates $(s, n)$, with arclength $s$ and perpendicular distance $n$. These coordinates correspond to following the curve $Z = C(X)$ for an arclength of $s$ to reach an 'anchor point' $X_a(s)$, and then traversing a distance $n$ perpendicular to the curve. We use these coordinates as the separation boundary narrows as $Ra \to \infty$, and so the lengthscale on which $n$ varies is asymptotically smaller than that of $s$. We first precisely define our new coordinates. The arclength $s$ is defined by

$$s(X_a) \coloneqq \int_{X_0}^{X_a} \sqrt{1 + C'(\xi)^2}\, d\xi$$

where the prime denotes a derivative. The coordinate $s = s(X_a)$ is monotonic, and hence is invertible with inverse $X_a = X_a(s)$. We then can convert from $(s, n)$ coordinates to $(X, Z)$ via

$$(X, Z) = (X_a(s), C(X_a(s)) + n\hat{\boldsymbol{n}}$$

with curve-normal vector $\hat{\boldsymbol{n}} = (-C'(X_a(s)), 1)/\sqrt{C'(X_a(s))^2 + 1}$. The coordinate scale factors required to change the basis of the governing equations are then

$$h_s \coloneqq \left|\frac{\partial \boldsymbol{X}}{\partial s}\right| = (1 - \kappa n), \quad h_n \coloneqq \left|\frac{\partial \boldsymbol{X}}{\partial n}\right| = 1$$

where $\kappa = C''/(1 + C'^2)^{3/2}$ is the curvature. These expressions allow us to write the governing equations in the new basis, with factors of $h_s$ appearing with derivatives. To simplify our equations, we note that $\kappa = O(1)$ and the layer is asymptotically narrow with $n \ll 1$, and hence $h_s \to 1$. This means that locally the new coordinate system is equivalent to using a Cartesian basis aligned with the curve-tangent and curve-normal (i.e., rotate the basis by $\theta = \tan^{-1}(C'(X_a))$, and so, neglecting curvature, the governing equations are

$$\partial_n\psi\partial_s\omega - \partial_s\psi\partial_n\omega = \left(\frac{Pr}{Ra}\right)^{1/2}\left(\partial_s^2 + \partial_n^2\right)\omega + Ra^{-s}\left(\cos\theta\,\partial_s + \sin\theta\,\partial_n\right)T, \tag{40}$$

$$Ra^{2s}\left(\partial_s^2 + \partial_n^2\right)\psi = -\omega, \tag{41}$$

$$\partial_n\psi\partial_s T - \partial_s\psi\partial_n T = (PrRa)^{-1/2}\left(\partial_s^2 + \partial_n^2\right)T. \tag{42}$$

This region has $s \sim 1$ and is asymptotically narrow with $n \sim \mu$, where $\mu \ll 1$ is to be determined. This motivates the use of the coordinate $\zeta \coloneqq n/\mu$ to be the appropriate across-layer coordinate in this region. We scale advection with diffusion across the layer, and set $T = O(1)$, motivated by matching from the inner boundary layer. Thus,

$$\psi_{sb} = Ra^{-1/2}\mu^{-1}\tilde{\psi}_{sb}(s, \zeta), \quad \omega_{sb} = Ra^{2s-1/2}\mu^{-3}\tilde{\omega}_{sb}(s, \zeta), \quad T_{sb} = \tilde{T}_{sb}(s, \zeta). \tag{43}$$

This rescaling then gives

$$\partial_\zeta \tilde{\psi}_{sb} \partial_s \tilde{\omega}_{sb} - \partial_s \tilde{\psi}_{sb} \partial_\zeta \tilde{\omega}_{sb} = Pr^{1/2} \left( \mu^2 \partial_s^2 + \partial_\zeta^2 \right) \tilde{\omega}_{sb} + \mu^4 Ra^{1-3s} \left( \mu \cos\theta \, \partial_s + \sin\theta \, \partial_\zeta \right) \tilde{T}_{sb}, \quad (44)$$

$$\left( \mu^2 \partial_s^2 + \partial_\zeta^2 \right) \tilde{\psi}_{sb} = -\tilde{\omega}_{sb}, \quad (45)$$

$$\partial_\zeta \tilde{\psi}_{sb} \partial_s \tilde{T}_{sb} - \partial_s \tilde{\psi}_{sb} \partial_\zeta \tilde{T}_{sb} = Pr^{-1/2} \left( \mu^2 \partial_s^2 + \partial_\zeta^2 \right) \tilde{T}_{sb}. \quad (46)$$

Asymptotically, assuming $\mu \ll 1$ and $\mu^4 Ra^{1-3s} \ll 1$, we obtain the reduced equations

$$\partial_\zeta \tilde{\psi}_{sb} \partial_s \tilde{\omega}_{sb} - \partial_s \tilde{\psi}_{sb} \partial_\zeta \tilde{\omega}_{sb} = Pr^{1/2} \partial_\zeta^2 \tilde{\omega}_{sb}, \quad (47)$$

$$\partial_\zeta^2 \tilde{\psi}_{sb} = -\tilde{\omega}_{sb}, \quad (48)$$

$$\partial_\zeta \tilde{\psi}_{sb} \partial_s \tilde{T}_{sb} - \partial_s \tilde{\psi}_{sb} \partial_\zeta \tilde{T}_{sb} = Pr^{-1/2} \partial_\zeta^2 \tilde{T}_{sb}. \quad (49)$$

This region connects to the inner boundary at $(X, Z) = (X_0, 0)$, and to the plume at $(X, Z) = (L/2, Z_0)$. Matching the scales of $\psi$ and $\omega$ with their scales in the inner layer enforces that $\mu = \varepsilon = Ra^{s-1/3}$. The relevant boundary conditions for (47)-(49) are $\tilde{T}_{sb}|_{\zeta \to \infty} = 1/2$, matching conditions on $\psi$ and $\omega$ to their values in the outer boundary as $\zeta \to \infty$, and matching conditions on $\psi$, $\omega$ and $T$ to their values in the separation region as $\zeta \to -\infty$.

### 3.5 Plume

In the plume we have that $X \sim \delta$ and $Z \sim 1$, where $\delta$ is unknown, and so

$$\psi = \psi_p(\chi, Z) \quad \omega = \omega_p(\chi, Z) \quad T = T_p(\chi, Z), \quad (50)$$

with $\chi \coloneqq (X - L/2)/\delta$. On lengthscales with $\chi, Z = O(1)$, we scale vorticity advection with horizontal vorticity diffusion in (1), counterintuitively assuming that buoyancy does not affect the plume to leading order. We also assume $T$ varies on $O(1)$ as it is connected to the separation boundary. We therefore get

$$\psi_p = Ra^{-1/2} \delta^{-1} \tilde{\psi}_p(\chi, Z), \quad \omega_p = Ra^{2s-1/2} \delta^{-3} \tilde{\omega}_p(\chi, Z), \quad T_p = \tilde{T}_p(\chi, Z). \quad (51)$$

where the exponent $s$ is currently unknown. These scalings also imply thermal advection balances horizontal thermal diffusion in (3). Under these rescalings, we obtain

$$\partial_Z \tilde{\psi}_p \partial_\chi \tilde{\omega}_p - \partial_\chi \tilde{\psi}_p \partial_Z \tilde{\omega}_p = Pr^{1/2} \left( \partial_\chi^2 + \delta^2 \partial_Z^2 \right) \tilde{\omega}_p + Ra^{1-3s} \delta^4 \partial_\chi \tilde{T}_p, \quad (52)$$

$$\left( \partial_\chi^2 + \delta^2 \partial_Z^2 \right) \tilde{\psi}_p = -\tilde{\omega}_p, \quad (53)$$

$$\partial_Z \tilde{\psi}_p \partial_\chi \tilde{T}_p - \partial_\chi \tilde{\psi}_p \partial_Z \tilde{T}_p = Pr^{-1/2} \left( \partial_\chi^2 + \delta^2 \partial_Z^2 \right) \tilde{T}_p. \quad (54)$$

Provided $\delta \ll 1$, and $\delta^4 Ra^{1-3s} \ll 1$, which we will eventually verify, we asymptotically obtain

$$\partial_Z \tilde{\psi}_p \partial_\chi \tilde{\omega}_p - \partial_\chi \tilde{\psi}_p \partial_Z \tilde{\omega}_p = Pr^{1/2} \partial_\chi^2 \tilde{\omega}_p, \quad (55)$$

$$\partial_\chi^2 \tilde{\psi}_p = -\tilde{\omega}_p, \tag{56}$$

$$\partial_Z \tilde{\psi}_p \partial_\chi \tilde{T}_p - \partial_\chi \tilde{\psi}_p \partial_Z \tilde{T}_p = Pr^{-1/2} \partial_\chi^2 \tilde{T}_p. \tag{57}$$

This region therefore acts like a jet, advecting and diffusing vorticity and heat from the separation boundary region at $Z = Z_0$. Matching $\psi$ and $\omega$ between these two regions then gives $\delta = \mu = Ra^{s-1/3}$. The boundary conditions used with (55)-(57) are

$$\tilde{\psi}_p|_{\chi=0} = 0, \quad \tilde{\omega}_p|_{\chi=0} = 0, \quad \partial_\chi \tilde{T}_p|_{\chi=0} = 0, \quad \tilde{T}_p|_{\chi\to-\infty} = 1/2, \tag{58}$$

$$\psi_p|_{\chi\to-\infty} \sim \psi_{ob}|_{X\to L/2^-}, \quad \omega_p|_{\chi\to-\infty} \sim \omega_{ob}|_{X\to L/2^-}. \tag{59}$$

The equations that are valid within the plume, separation boundary and the inner boundary all balance the same quantities, with diffusion across the layer balancing advection. In all cases, the layer thickness is the same.

Asymptotically, the heat transport within the outer boundary layer occurs through the plume and hence we should expect that $Nu$ should scale the same in the plume as it did in the core and inner boundary layer. The scalings we have derived are consistent with this, with the convective term in eq. (9) also giving $Nu \sim Ra^{1/3}$.

### 3.6 The separation region

The structure of the separation region is complex, and the asymptotic structure is not clear from the data currently at our disposal. In fig. 3 we show the vorticity of the separation region, and it appears to contain a thin boundary layer that splits it in half. It is unclear whether the asymptotic state has its separation region divided further than this.

Interestingly, the separation region is still evolving at the largest $Ra$ we have access to. In fig. 4 we show the zero streamlines, corresponding to the border of the separation region, for rolls with $1.7 \times 10^{11} \leq Ra \leq 1.7 \times 10^{12}$. We see that the region contains a smaller separation region which is still evolving with $Ra$. At the largest $Ra$ considered, an even smaller tertiary separation region can be seen. The lack of a (simple) clear asymptotic regime here makes it difficult to perform matched asymptotics.

### 3.7 Assumption validity

We made a number of assumptions in our analysis when we considered which terms are asymptotically dominant. These were

- $s > 0$,
- $\gamma + 1/2 > s$,
- $\varepsilon^5 Ra^{1-3s}$, $\mu^4 Ra^{1-3s}$, $\delta^4 Ra^{1-3s} \ll 1$.

As we derived that the inner boundary layer, separation boundary and plume have the same thickness scale $\varepsilon = \mu = \delta = Ra^{s-1/3}$, and that $\gamma = -2s + 1/6$, these assumptions are satisfied so long as $0 < s < 2/9$.

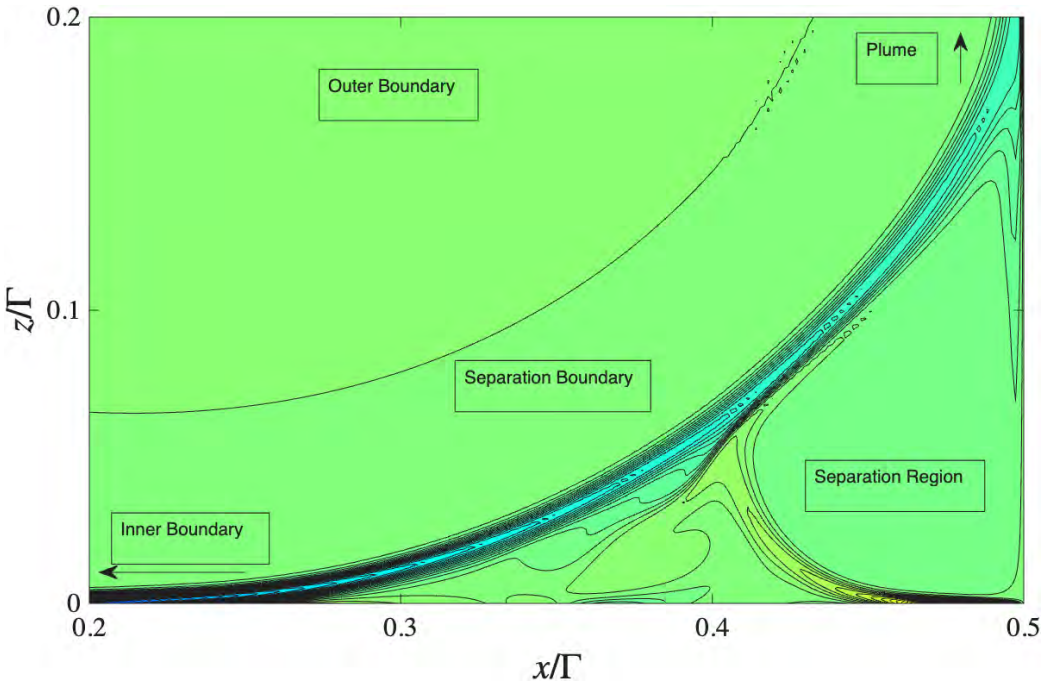


Figure 3: The vorticity in the separation region at $Ra = 1.7\times10^{12}$, $Pr = 0.1$. The curved separation boundary separates the outer boundary from the separation region

### 3.8 Final scalings

The asymptotics described suggest the scalings in each of the regions follow those shown in table 1. These scalings are functions of $s$, which was defined to be the exponent of the aspect ratio $\Gamma \sim Ra^{-s}$. While we have not recovered the value of $s$ explicitly, we can verify whether a given $s$ is reasonable by considering how well the predicted scales in each region are seen in numerically computed rolls. We look over a decade of $Ra$, and look for good collapse of a selection of fields in each region to the scalings predicted. There are two suggestions for $s$ that we check, the $s = 1/5$ suggested numerically in [12], and the $s = 2/9$ from the scaling analysis of [4].

We show the rescaled fields in regions where the scalings are more sensitive to the choice of $s$ in fig. 5 (i.e., the coefficient of $s$ in table 1 has larger absolute value). The region that is most sensitive to the value of $s$ is the streamfunction in the core $\psi_c$, and we see that the collapse to the scalings predicted by $s = 1/5$ is better than that of $s = 2/9$. This trend is visible across each of the shown fields, although it is harder to discern for the other ones where the scaling is less sensitive to the value of $s$.

While our scalings provide further evidence that $s = 1/5$, and hence that the aspect ratio is $\Gamma \sim Ra^{-1/5}$, the rolls are not clearly in an asymptotic regime with all fields collapsing perfectly. The adjustments seen coincide with the separation region evolving significantly as discussed in section 3.6. To demonstrate more conclusively that $s = 1/5$, and that the matched asymptotics presented here are valid, rolls computed at yet higher $Ra$ are required, so that a clean asymptotic structure can be identified. We now aim to find global optimal rolls across another decade of $Ra$.

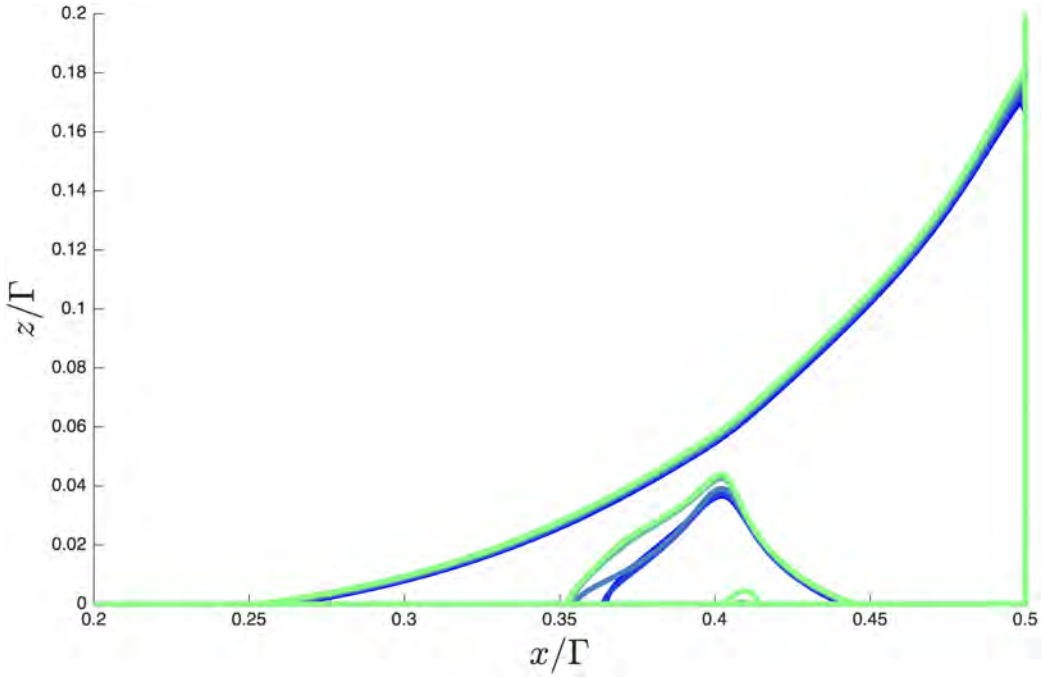


Figure 4: Contours of $\psi = 0$ for the $Ra$ shown in fig. 5, marking separation regions. As $Ra$ increases (shades lighten), a secondary separation region can be seen to grow and change shape. At the largest $Ra$, a tertiary separation region appears at $x/\Gamma \approx 0.4$. This shows that this region is still evolving at $Ra = 1.8 \times 10^{12}$.

| $Ra^{(\cdot)}$ | $\psi$ | $\omega$ | $T - \frac{1}{2}$ | $x$ | $z$ |
|---|---|---|---|---|---|
| c | $-2s + 1/6$ | $1/6$ | $s - 1/3$ | $-s$ | $0$ |
| ob | $-2s + 1/6$ | $1/6$ | $s - 1/3$ | $-s$ | $-s$ |
| p | $-s - 1/6$ | $-s + 1/2$ | $0$ | $-1/3$ | $-s$ |
| i | $-s - 1/6$ | $-s + 1/2$ | $0$ | $-s$ | $-1/3$ |
| $Ra^{(\cdot)}$ | $\psi$ | $\omega$ | $T - \frac{1}{2}$ | $x'$ | $z'$ |
| sb | $-s - 1/6$ | $-s + 1/2$ | $0$ | $-s$ | $-1/3$ |

Table 1: Scalings in each region as a function of $s$, for the global optimal with aspect ratio $\Gamma \sim Ra^{-s}$. The separation boundary (sb) coordinates $(x', z')$ correspond to rotating $(x, z)$ so that they are aligned with the tangent and normal of the layer respectively.

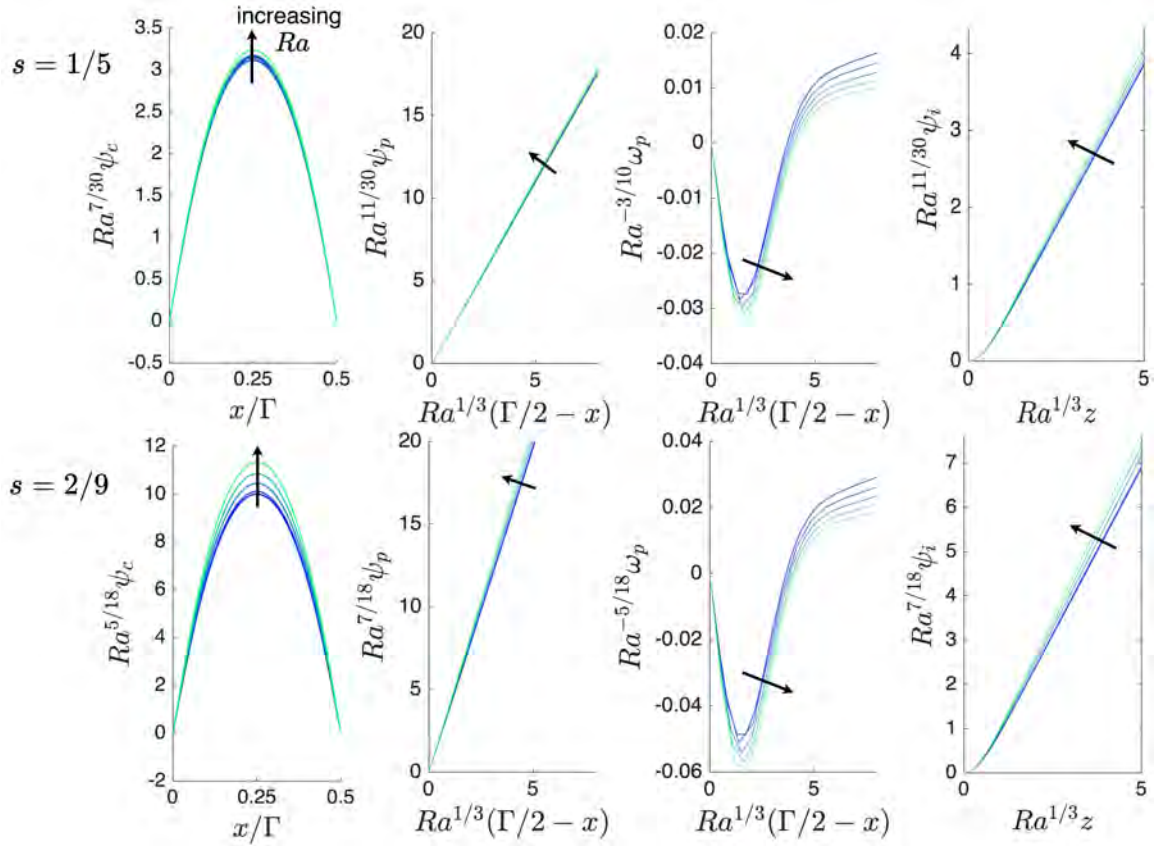


Figure 5: Rescaled fields $\psi_c$ in the core, $\psi_p$ and $\omega_p$ in the plume, and $\psi_i$ in the inner boundary layer for $Ra = 1.7\times10^{11}, 3.2\times10^{11}, 5.6\times10^{11}, 1\times10^{12}, 1.7\times10^{12}$ (dark to light) and $Pr = 0.1$. Arrows denote directions of increasing $Ra$. Top row uses predicted scalings when $s = 1/5$ as suggested by [12], and bottom row when $s = 2/9$ as in [4].

# 4 Converging Solutions

The states converged previously with $Ra < 3 \times 10^{12}$ ($Pr = 0.1$) [12] have not yet reached an asymptotic regime, with the separation zone still evolving with time. To provide further evidence that the suggested aspect ratio scaling is $\Gamma \sim Ra^{1/5}$, we now aim to converge rolls at yet larger $Ra$. To do this we use the Newton-GMRES algorithm, as well as the open source software Dedalus [2]. We use a number of techniques to optimise our code to handle the extreme states with large separation of scales.

We discretise the velocity fields $u$, $v$ and the temperature field $T$ using $N_x$ Fourier modes and $N_z$ ultraspherical modes, and construct the state vector $X$ by concatenating the spectral coefficients of each field. To converge a solution $X$ we use Newton's method to find a zero of the nonlinear function $F(X)$, corresponding to the residual of the primitive governing equations (i.e., equation (2.1) in [12]) and boundary conditions. This residual can be readily accessed in Dedalus. Starting from an initial guess $X_0$, we use Newton's method to produce a vector $\delta X$ that informs an improved state $X_0 + \delta X$. To do this we set

$$0 \approx F(X_0 + \delta X) = F(X_0) + \partial F(X_0)\delta X + O(|\delta X|^2),$$

where $\partial F$ is a Jacobian matrix found using symbolically computed Fréchet derivatives that are accessible in Dedalus. This Taylor expansion then shows that the perturbation $\delta X$ should be chosen to satisfy

$$\partial F(X_0)\delta X = -F(X_0).$$

Ideally, one would invert the Jacobian matrix $\partial F$ to find $\delta X$, however this is not feasible due to the size of the matrix (its size scales linearly with $N_x$ and $N_z$, both of which are large). Due to this, we use the iterative GMRES method instead [9], which is used to solve linear algebra problems of the form $Ax = b$, with matrix $A$ and vectors $x$, $b$. Importantly, the number of GMRES iterations to converge $x$ can be intractably large in cases where the Jacobian $\partial F$ has large condition number and is therefore ill-conditioned. This happens when there is a large separation of scales in the final state, as is the case in the extreme rolls that we seek.

We use a number of techniques to optimise the algorithm. One significant method was preconditioning, which dramatically reduces the number of GMRES iterations needed for convergence. A preconditioner $M$ should have the property that it is a rough inverse of the Jacobian, with $M\partial F \approx \mathbb{I}$, with $\mathbb{I}$ being the identity. If one can be found, then left preconditioning means solving

$$[M\partial F]\,\partial X = -\,[MF(X_0)]$$

using GMRES, where the matrix $M\partial F$ is now better conditioned (i.e., it has a lower condition number) than the original $\partial F$. To construct $M$, we will construct an approximate Jacobian $\partial\tilde{F}$ which we invert. We linearise our equations around the best guess $X_0$ to give $\partial F$, and then we zero terms to produce the approximate Jacobian $\partial\tilde{F}$ so that it is sparse enough to invert using LU factorisation, yielding $M = \partial\tilde{F}^{-1}$. We promote sparsity by 1) zeroing all elements of $X_0$ corresponding to Fourier modes in the $\hat{\boldsymbol{x}}$ direction above a certain wavenumber (typically the first $O(10)$ are kept) and 2) zeroing all elements of $\partial\tilde{F}$ that are below a certain value.

Other techniques were also used. The previous algorithm used to converge rolls [12] used Chebyshev polynomials in the $z$ direction, while we use ultrasphericals. This produces more sparsity in the Jacobian $\partial F$. We also use a matrix-free formulation, in which the matrices $\partial F$

and $M$ are never explicitly constructed, rather only their action on a state vector is known. This removes the need to spend computational time and memory constructing very large matrices making each iteration of the GMRES loop faster. We additionally split our domain into a small number of vertically stacked regions. This allows resolution to be concentrated in the boundary layers that require it. For example, instead of using a grid of $N_z = 512$ collocation points within the full domain, we can use $N_z = 256$ points in $z \in [\delta, 1-\delta]$ and $N_z = 128$ in $z \in [0, \delta]$ and $[1-\delta, 1]$ for some small $\delta$ that lies roughly at the start of the boundary layers.

The resulting Newton-GMRES algorithm is more efficient than the one used to converge the rolls at lower $Ra$ [12]. Converging a single state using the old code took 1 month for the most complex rolls, while we expect that it will take around 3 days using our new code. Importantly, the promoted sparsity means the new code scales better with increasing resolution (which is required to resolve thinner layers as $Ra$ increases). In the coming months we hope to have converged the global optimal rolls across the next decade of $Ra$.

# 5 Mean-Zero Heating and Cooling

To demonstrate that the produced code works, we apply it to a system with mean-zero heating and cooling. Such a system has an internal source and sink of heat, and supports convection rolls. The relevant 2D steady governing equations are

$$\partial_z \psi \partial_x \omega - \partial_x \psi \partial_z \omega = \left(\frac{Pr}{Ra_Q}\right)^{1/2} \nabla^2 \omega + \partial_x T, \tag{60}$$

$$\nabla^2 \psi = -\omega, \tag{61}$$

$$\partial_z \psi \partial_x T - \partial_x \psi \partial_z T = (PrRa_Q)^{-1/2} \left[\nabla^2 T + \sin(2\pi z)\right], \tag{62}$$

which we solve with insulating and no-slip walls

$$\partial_z T|_{z=0,1} = \psi|_{z=0,1} = \partial_z \psi|_{z=0,1} = 0.$$

This differs from the Rayleigh-Bénard case eq. (1)-(3) by containing a mean-zero heating and cooling term in the heat equation, and it uses a heat-flux control parameter $Ra_Q$ rather than the temperature control parameter $Ra$. While in the Rayleigh-Bénard system $Ra$ was set and the Nusselt number was measured, here both are measured, and they are defined in terms of the dimensionless quantities

$$Ra = Ra_Q \sqrt{\langle T^2 \rangle}, \quad Nu = \frac{Ra_Q}{Ra}.$$

This formulation is consistent with [7] which uses a different non-dimensionalisation, and a forcing amplitude which is scaled by $\sqrt{2}$. There, they show that heat transport in the stress-free case is bounded by $Nu \leq O(Ra)$, which is actually attained by convection rolls with $O(1)$ aspect ratios. We now investigate the impact of using no-slip boundaries instead. We numerically compute convection rolls using the flexible Newton-GMRES algorithm described in section 4.

In the Rayleigh-Bénard system, at large fixed $Ra$ there exists a local and a global maxima of $Nu$ as the aspect ratio $\Gamma$ is varied. Here in the internally heated system, only a global optima is seen (see fig. 6a). This narrow optima is plotted in fig. 6b, and seems to have slow stagnant corners in

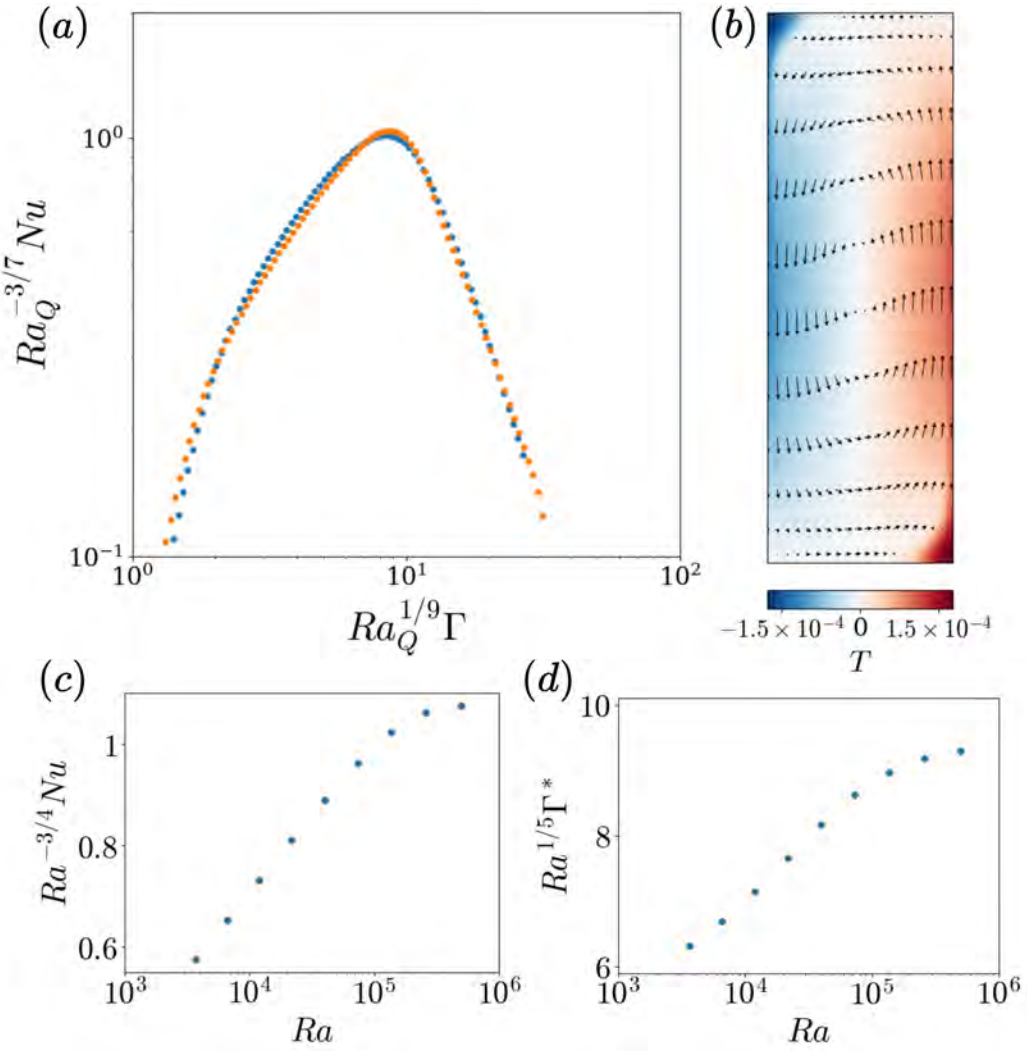


Figure 6: Convection rolls in a mean-zero heated and cooled system. $(a)$ The Nusselt number dependence on the aspect ratio at $Ra_Q = 10^9$ (blue), $10^{10}$ (orange) with $Pr = 1$, $(b)$ the structure of the optimal roll at $Ra_Q = 10^{10}$ with $\Gamma = 0.6743$. Colour denotes temperature while arrows show velocity fields. Optimal roll $(c)$ $Nu$ and $(d)$ aspect ratio $\Gamma^*$ against $Ra$ is shown. Data points correspond to $10^6 \leq Ra_Q \leq 10^{10}$.

the top left and bottom right. We measure $Nu$, $Ra$ and aspect ratio $\Gamma^*$ of the optimal over 4 decades of $Ra_Q$ (yielding over 2 decades of $Ra$), and show compensated plots in fig. 6c,d which roughly suggest that $Nu \sim Ra^{3/4}$ and $\Gamma^* \sim Ra^{-1/5}$, although more rolls will need to be converged to say this conclusively.

These scalings suggest that stress-free convection rolls reach greater heat transport ($Nu \sim Ra$) than no-slip ones ($Nu \sim Ra^{3/4}$). The optimal aspect ratios appear to be the same for both Rayleigh-Bénard and mean-zero heating and cooling, with stress-free rolls having $\Gamma = O(1)$ [3, 7], and no-slip having $\Gamma \sim Ra^{-1/5}$, as found here. We hope to reach optimal rolls at higher $Ra$ in the coming months.

# 6 Discussion

We have identified the structure of the convection rolls that maximise heat flux in no-slip Rayleigh-Bénard using matched asymptotic analysis. Our results suggest that the optimal aspect ratio scales like $\Gamma^* \sim Ra^{1/5}$ in line with the numerics of [12]. The states are still evolving at $Ra \sim 10^{12}$ ($Pr = 0.1$), with a separation zone changing shape and developing more structure, with a secondary and tertiary nested separation zones identifiable. The extreme stiffness in the equations seen for this steady coherent structure means that optimal rolls at even larger $Ra$ are required to conclusively identify the asymptotics.

The rolls discussed here allow the transport of heat via a coherent structure. While heat flux is often discussed in the context of turbulence, it is not immediately obvious whether turbulence or coherent structures are better at transporting heat. In the Rayleigh-Bénard system the optimal heat transport found so far in a coherent structure is $Nu \sim Ra^{1/3}$ [3, 4, 12, 13], which turbulence either asymptotically matches (if the $Nu \sim Ra^{1/3}$ 'classical' regime is asymptotic) or beats (if instead the $Nu \sim Ra^{1/2}$ 'ultimate' regime is). Conversely, in internally heated systems, coherent rolls maximise heat transport, attaining the rigorous upper bound of $Nu \leq O(Ra)$ [7], while turbulence only achieves $Nu \sim Ra^{1/2}$[1, 6]. Whether coherent structures exist in Rayleigh-Bénard that can similarly attain the heat transport upper bound (which there is $Nu \leq O(Ra^{1/2})$ is not known.

Using the Newton-GMRES code we hope to converge rolls both in Rayleigh-Bénard and in the mean-zero heating and cooling systems. In Rayleigh-Bénard, states across another decade or two in $Ra$ should prove sufficient for us to confirm the matched asymptotics presented here. In the mean-zero heating and cooling system, having access to these states would allow us to probe the asymptotic structure using matched asymptotics. Turbulent states often inherit characteristics of the unstable coherent structures that are embedded in their chaotic attractor, and so understanding how these coherent states transport heat may provide us with insight into the turbulence of heated systems.

# 7 Acknowledgements

I'm incredibly grateful to David Goluskin, Greg Chini, Baole Wen and Keaton Burns for all their advice this summer - you were all incredible and I had a wonderful time working with you all. Also to our fearless Directors Pascale Garaud and David Goluskin (again) for running the program, and of course to all the fellows for making this summer unforgettable.

# References


[1] V. Bouillaut, S. Lepot, S. Aumaître, and B. Gallet, *Transition to the ultimate regime in a radiatively driven convection experiment*, Journal of Fluid Mechanics, 861 (2019), p. R5.

[2] K. J. Burns, G. M. Vasil, J. S. Oishi, D. Lecoanet, and B. P. Brown, *Dedalus: A flexible framework for numerical simulations with spectral methods*, Physical Review Research, 2 (2020), p. 023068.

[3] G. P. Chini and S. M. Cox, *Large Rayleigh number thermal convection: Heat flux predictions and strongly nonlinear solutions*, Physics of Fluids, 21 (2009), p. 083603.

[4] K. Deguchi, *On high-Taylor-number Taylor vortices*, Journal of Fluid Mechanics, 967 (2023), p. A11.

[5] C. R. Doering and P. Constantin, *Variational bounds on energy dissipation in incompressible flows. iii. convection*, Phys. Rev. E, 53 (1996), pp. 5957–5981.

[6] S. Lepot, S. Aumaître, and B. Gallet, *Radiative heating achieves the ultimate regime of thermal convection*, Proceedings of the National Academy of Sciences, 115 (2018), pp. 8937–8941.

[7] B. Miquel, S. Lepot, V. Bouillaut, and B. Gallet, *Convection driven by internal heat sources and sinks: Heat transport beyond the mixing-length or "ultimate" scaling regime*, Phys. Rev. Fluids, 4 (2019), p. 121501.

[8] L. Rayleigh, *On the convective currents in a horizontal layer of fluid when the higher temperature is on the under side*, Philosophical Magazine, 32 (1916), pp. 529–546.

[9] Y. Saad and M. H. Schultz, *GMRES: A generalized minimal residual algorithm for solving nonsymmetric linear systems*, SIAM Journal on Scientific and Statistical Computing, 7 (1986), pp. 856–869.

[10] D. Sondak, L. M. Smith, and F. Waleffe, *Optimal heat transport solutions for Rayleigh–Bénard convection*, Journal of Fluid Mechanics, 784 (2015), p. 565–595.

[11] F. Waleffe, A. Boonkasame, and L. M. Smith, *Heat transport by coherent Rayleigh-Bénard convection*, Physics of Fluids, 27 (2015), p. 051702.

[12] B. Wen, D. Goluskin, and C. R. Doering, *Steady Rayleigh–Bénard convection between no-slip boundaries*, Journal of Fluid Mechanics, 933 (2022), p. R4.

[13] B. Wen, D. Goluskin, M. LeDuc, G. P. Chini, and C. R. Doering, *Steady Rayleigh–Bénard convection between stress-free boundaries*, Journal of Fluid Mechanics, 905 (2020), p. R4.

# Ray Theory for Rotating Hyperbolic Instabilities

Farid Rajkotia-Zaheer

August 19, 2025

## 1 Introduction

We study three-dimensional perturbations around generic two-dimensional hyperbolic stagnation points in fluid flows undergoing global rotation. Inspired by the work of Caulfield and Kerswell [5], who laid the groundwork for understanding hyperbolic stagnation points as a model for braid regions in mixing layers in non-rotating fluid systems, our work here extends the analysis to the globally rotating setting. Although, the rotating case has seen recent interest in the literature through the work of Hattori and Hirota [6] and Leblanc and Cambon [8, 9], currently the rotating and non-rotating case are seemingly disparate. One of the outcomes of this work is to show that the work in [5], [6], [8] and [9] form special solutions within a more general theory for hyperbolic stagnation points within a generic rotating fluid flows.

We make use of a local multi-scale analysis around a globally rotating two-dimensional hyperbolic stagnation point. We then employ a ray theoretic approach to study energetics of three-dimensional perturbations around the stagnation point. Dividing the analysis into a weakly and strongly rotating case, through the weakly rotating case we are able to recover the equations presented in [6]. Furthermore, taking the distinguished zero rotation limit, we recover the equations presented in [5] for the non-rotating case. In the strongly rotating case, we show the existence of an instability i.e unbounded perturbation energy growth. We also discover other rich dynamics, including transient and bounded growth of the perturbation energy around the stagnation point.

This work is organized as follows. Section 2 introduces the governing equations and the mathematical machinery used throughout the work. Section 3 shows the multiscale analysis in the context of weak rotation and recovers the results of [5] and [6]. Section 4 shows the multiscale analysis for the strongly rotating case and shows the existence of hyperbolic instabilities within a strongly rotating medium. Section 5 offers conclusions and avenues for future research followed by appendices with mathematical details regarding various results used throughout the work.

## 2 Mathematical Setup

Consider the incompressible Euler equations with Coriolis force

$$\partial_t \mathbf{u} + \mathbf{u} \cdot \nabla \mathbf{u} + f\, \mathbf{e}_z \times \mathbf{u} + \nabla p = \mathbf{0}, \tag{2.1a}$$

$$\nabla \cdot \mathbf{u} = 0, \tag{2.1b}$$

where $\mathbf{u} = (u, v, w)$ and $\mathbf{e}_z$ is the unit vector in the $z$-direction. Let the base flow to be a 2D flow restricted to the $x, y$-plane, $\mathbf{U}(x, y)$. Linearizing about $\mathbf{U}$, the perturbations $\mathbf{u}'$ obey,

$$\partial_t \mathbf{u}' + \mathbf{U} \cdot \nabla \mathbf{u}' + \mathbf{u}' \cdot \nabla \mathbf{U} + f\, \mathbf{e}_z \times \mathbf{u}' + \nabla p' = \mathbf{0}, \tag{2.2a}$$

$$\nabla \cdot \mathbf{u}' = 0, \tag{2.2b}$$

where $p'$ is the perturbation pressure. We further consider $\mathbf{U}$ to be a hyperbolic background flow defined as

$$\mathbf{U}(x, y) = \underbrace{\begin{pmatrix} \varepsilon & -\gamma & 0 \\ \gamma & -\varepsilon & 0 \\ 0 & 0 & 0 \end{pmatrix}}_{=:\mathbf{A}} \begin{pmatrix} x \\ y \\ z \end{pmatrix}, \tag{2.3}$$

where $\varepsilon$ and $\gamma$ are the strain and rotation rates, respectively, with the hyperbolicity assumption $|\varepsilon| > |\gamma|$ implicit throughout this work. Figure 1 is an example of the hyperbolic background flow. The analysis to follow makes use of the quantity,

$$\Delta := \sqrt{\varepsilon^2 - \gamma^2}, \tag{2.4}$$

the eigenvalue of the non-zero 2 by 2 sub-matrix of $\mathbf{A}$.

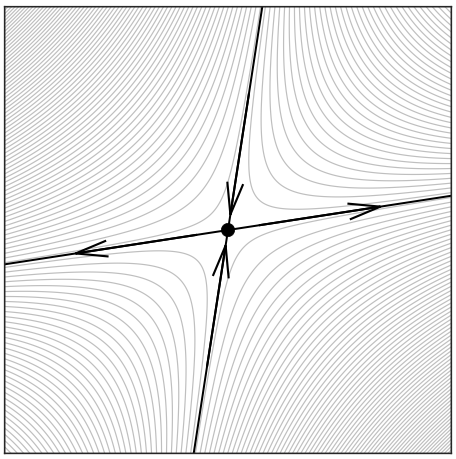

Figure 1: Streamlines of the two-dimensional hyperbolic background flow $\mathbf{U}$ with principle directions of compression and extension in bold arrows. The stagnation point is marked in the centre. The strain and rotation rates are set to $\varepsilon = 1$ and $\gamma = 0.3$ and hence $\Delta \approx 0.95$.

In preparation for the multi-scale and ray theoretic analysis, we assume variations in the background flow are far slower than variations in the wavelength and amplitudes of the perturbations. As such, it is natural to take solutions of (2.2) in terms of a WKB ansatz [2],

$$\left[\mathbf{u}', p'\right] = \left[\hat{\mathbf{u}}, \hat{p}\right](\mathbf{X}, T) \exp\left(i\Theta(\mathbf{x}, t)\right), \tag{2.5}$$

where variations in phase are assumed to be rapid and variations in the amplitude are assumed slow. As such, we assume that $\mathbf{X} = \delta\mathbf{x}$ and $T = \delta t$ where $\delta \ll 1$ is a small parameter. It is then standard to define the wavevector and frequency, respectively,

$$\mathbf{k} = \nabla_{\mathbf{X}}\Theta, \tag{2.6a}$$

$$\omega = -\partial_T\Theta, \tag{2.6b}$$

where $\nabla_{\mathbf{X}}$ denotes the gradient with respect to slow spatial variables, $\partial_T$ denotes the partial derivative with respect to the slow time variable and $\mathbf{k} = (k, \ell, m)$, cf. [4, 10, 11] for an introduction to ray theory in slowly varying media. From (2.6) it is easy to see,

$$\partial_T\mathbf{k} + \nabla_{\mathbf{X}}\omega = 0. \tag{2.7}$$

The local dispersion relation then has the form,

$$\omega(\mathbf{X}) = \Omega\left(\mathbf{k}(\mathbf{X}, T), \mathbf{X}\right), \tag{2.8}$$

with no explicit slow time dependence since $\mathbf{U}$ is assumed constant in time. Applying the chain rule, using (2.7) and re-arranging, the evolution of $\mathbf{k}$ is given through the transport PDE,

$$\partial_T\mathbf{k} + \mathbf{c}_g \cdot \nabla_{\mathbf{X}}\mathbf{k} = -\nabla_{\mathbf{X}}\Omega, \tag{2.9}$$

where the group velocity is defined as $\mathbf{c}_g := \nabla_{\mathbf{k}}\Omega$. Solving (2.9) via the method of characteristics, defines the ray tracing equations,

$$\frac{\mathrm{d}}{\mathrm{d}T}\mathbf{X} = \mathbf{c}_g, \tag{2.10a}$$

$$\frac{\mathrm{d}}{\mathrm{d}T}\mathbf{k} = -\nabla_{\mathbf{X}}\Omega. \tag{2.10b}$$

Note, the system will have Hamiltonian structure in general [4]. We also expand the amplitudes in (2.5) in an asymptotic series with respect to the small parameter $\delta$,

$$\hat{\mathbf{u}} = \hat{\mathbf{u}}_0 + \delta\hat{\mathbf{u}}_1 + \delta^2\hat{\mathbf{u}}_2 + ..., \tag{2.11}$$

and similarly for $\hat{p}$.

# 3 Weak Rotation

We begin by carrying out the multi-scale analysis assuming weak rotation, i.e., $f \sim \mathcal{O}(\delta)$. Substituting (2.5) into (2.2), the leading order momentum and incompressibility conditions are

$$\left(-\omega + \mathbf{k} \cdot \mathbf{U}\right)\hat{\mathbf{u}}_0 = -i\mathbf{k}\hat{p}_0, \tag{3.1a}$$

$$\mathbf{k} \cdot \hat{\mathbf{u}}_0 = 0. \tag{3.1b}$$

Clearly, since $f \sim \mathcal{O}(\delta)$, the Coriolis term does not appear at leading order. The system is linear and taking $\mathbf{k}\times$(3.1a), yields the relation,

$$\omega = \mathbf{k} \cdot \mathbf{U}. \tag{3.2}$$

which, in turn, forces $\hat{p}_0 = 0$. Notice, (3.2) is the dispersion relation which in this case does not support an intrinsic frequency, i.e., is non-dispersive. The group velocity $\mathbf{c}_g$ is defined as

$$\mathbf{c}_g = \nabla_{\mathbf{k}} \left(\mathbf{k} \cdot \mathbf{U}\right) = \mathbf{A}\mathbf{X}. \tag{3.3}$$

That is, under the assumption of weak rotation, the ray paths coincide with the streamlines of the hyperbolic background flow as in fig. 1. The ray system (2.10) in this case takes the from,

$$\frac{\mathrm{d}}{\mathrm{d}T}\mathbf{X} = \mathbf{A}\mathbf{X}, \tag{3.4a}$$

$$\frac{\mathrm{d}}{\mathrm{d}T}\mathbf{k} = -\mathbf{A}^{\mathrm{T}}\mathbf{k}, \tag{3.4b}$$

where $\mathbf{A}^{\mathrm{T}}$ denotes the transpose of $\mathbf{A}$. This follows by negating the spatial derivative of the dispersion relation $\Omega$. To gain equations for the amplitudes along these ray paths we must move to the next order in $\delta$. The momentum equation at this order is

$$\left(\partial_T + \mathbf{U} \cdot \nabla_{\mathbf{X}}\right) \hat{\mathbf{u}}_0 = -f\mathbf{e}_z \times \hat{\mathbf{u}}_0 - i\mathbf{k}\hat{p}_1 - \hat{\mathbf{u}}_0 \cdot \nabla_{\mathbf{X}}\mathbf{U}. \tag{3.5}$$

There is no appearance of $\hat{\mathbf{u}}_1$ since the relation (3.2) will ensure all terms with $\hat{\mathbf{u}}_1$ vanish at this order. Interpreting the PDE to evolve along ray paths and noting that $\hat{\mathbf{u}}_0 \cdot \nabla_{\mathbf{X}}\mathbf{U} = \mathbf{A}\hat{\mathbf{u}}_0$, the system of ODEs is

$$\frac{\mathrm{d}}{\mathrm{d}T}\hat{\mathbf{u}}_0 = -\mathbf{A}\hat{\mathbf{u}}_0 - f\mathbf{e}_z \times \hat{\mathbf{u}}_0 - i\mathbf{k}\hat{p}_1. \tag{3.6}$$

That is, (3.6) governs the evolution of amplitude of perturbations along ray paths. Using the leading order incompressibility condition (3.1b), $\hat{p}_1$ may be eliminated in (3.6) by computing $\frac{\mathrm{d}}{\mathrm{d}T}\left(\mathbf{k} \cdot \hat{\mathbf{u}}_0\right)$. Expressing $\hat{p}_1$ in terms of the other variables,

$$\hat{p}_1 = -\frac{2i}{\mathbf{k}^2}\left[\left(\left(\gamma + f\right)k + \varepsilon\ell\right)\hat{v}_0 - \left(\left(\gamma + f\right)\ell + \varepsilon k\right)\hat{u}_0\right], \tag{3.7}$$

where $\hat{\mathbf{u}}_0 = (\hat{u}_0, \hat{v}_0, \hat{w}_0)$. Substituting (3.7) into (3.6), the resulting ODE system written component wise is

$$\begin{aligned}\frac{\mathrm{d}}{\mathrm{d}T}\hat{u}_0 = \frac{1}{|\mathbf{k}|^2}\Big[ &\left(k^2 - \ell^2 - m^2\right)\left(\varepsilon\hat{u}_0 - \gamma\hat{v}_0\right) + 2k\ell\left((\gamma + f)\hat{u}_0 - \varepsilon\hat{v}_0\right) \\ &+ 2f\left(\ell^2 + m^2\right)\hat{v}_0\Big],\end{aligned} \tag{3.8a}$$

$$\begin{aligned}\frac{\mathrm{d}}{\mathrm{d}T}\hat{v}_0 = \frac{1}{|\mathbf{k}|^2}\Big[ &\left(\ell^2 - k^2 - m^2\right)\left(\gamma\hat{u}_0 - \varepsilon\hat{v}_0\right) + 2k\ell\left(\varepsilon\hat{u}_0 - (\gamma + f)\hat{v}_0\right) \\ &- 2f\left(k^2 + m^2\right)\hat{u}_0\Big],\end{aligned} \tag{3.8b}$$

$$\frac{\mathrm{d}}{\mathrm{d}T}\hat{w}_0 = \frac{2m}{|\mathbf{k}|^2}\Big[k\left(\varepsilon\hat{u}_0 - (\gamma + f)\hat{v}_0\right) + \ell\left((\gamma + f)\hat{u}_0 - \varepsilon\hat{v}_0\right)\Big]. \tag{3.8c}$$

We see that the Coriolis term $f$ acts to increase the background rotation $\gamma$ felt by the system. Furthermore, taking the limit $f \to 0$ recovers the amplitude equations presented in [5].

It will be useful to measure the strength of disturbances through the energy norm at leading order,

$$E := \frac{1}{2}|\hat{\mathbf{u}}_0|^2. \tag{3.9}$$

Then,

$$\frac{\mathrm{d}E}{\mathrm{d}T} = \varepsilon\left(\hat{v}_0^2 - \hat{u}_0^2\right). \tag{3.10}$$

Notice pressure and the Coriolis term do not enter the energy balance as they are inviscid invariants. We define the growth rate of disturbances as

$$\sigma := \frac{1}{E}\frac{\mathrm{d}E}{\mathrm{d}T} = \frac{2\varepsilon\left(\hat{v}_0^2 - \hat{u}_0^2\right)}{|\hat{\mathbf{u}}_0|^2}. \tag{3.11}$$

An immediate consequence of this expression is that perturbations can grow at most at the rate $2\varepsilon$. This coincides with the non-rotating case as seen in [5].

### 3.1 Non-rotating case

We begin our analysis by first considering the non-rotating case. As mentioned before, the equations for this case can be recovered by taking the distinguished limit $f \to 0$. In this case, (3.8) reduce to

$$\frac{\mathrm{d}}{\mathrm{d}T}\hat{u}_0 = \frac{1}{|\mathbf{k}|^2}\left[\left(k^2 - \ell^2 - m^2\right)(\varepsilon\hat{u}_0 - \gamma\hat{v}_0) + 2k\ell\,(\gamma\hat{u}_0 - \varepsilon\hat{v}_0)\right], \tag{3.12a}$$

$$\frac{\mathrm{d}}{\mathrm{d}T}\hat{v}_0 = \frac{1}{|\mathbf{k}|^2}\left[\left(\ell^2 - k^2 - m^2\right)(\gamma\hat{u}_0 - \varepsilon\hat{v}_0) + 2k\ell\,(\varepsilon\hat{u}_0 - \gamma\hat{v}_0)\right], \tag{3.12b}$$

$$\frac{\mathrm{d}}{\mathrm{d}T}\hat{w}_0 = \frac{2m}{|\mathbf{k}|^2}[k\,(\varepsilon\hat{u}_0 - \gamma\hat{v}_0) + \ell\,(\gamma\hat{u}_0 - \varepsilon\hat{v}_0)]. \tag{3.12c}$$

These are exactly the amplitude equations studied in [5]. In that work, these equations were derived by way of a Kelvin plane-wave ansatz. However, as we have shown here, they may be recovered through a more general multiscale and ray theoretic approach.

To solve (3.12), we use one of the initial conditions from [5] leading to bounded energy

growth of perturbations. These initial conditions have the form

$$k(0) = -\sqrt{\frac{(\epsilon - \Delta)}{2\epsilon}}\,\beta, \tag{3.13a}$$

$$\ell(0) = \sqrt{\frac{(\epsilon + \Delta)}{2\epsilon}}\,\beta, \tag{3.13b}$$

$$m(0) = \sqrt{1 - \beta^2}, \tag{3.13c}$$

$$\hat{u}_0(0) = -\sqrt{\frac{(\epsilon - \Delta)(1 - \beta^2)}{2\epsilon}}, \tag{3.13d}$$

$$\hat{v}_0(0) = \sqrt{\frac{(\epsilon + \Delta)(1 - \beta^2)}{2\epsilon}}, \tag{3.13e}$$

$$\hat{w}_0(0) = -\beta. \tag{3.13f}$$

Here $0 < \beta < 1$ is a parameter that measures the relative distance of these set of intial conditions to those that show optimal growth rate in the non-rotating case. We show plots of the solutions of (3.8) in fig. 2 with $\beta = 0.01$. Comparison to the weakly rotating case also initialized from (3.13) is made in fig. 3. Integrating (3.12) initialized from (3.13), we recreate part of figure 2 in [5].

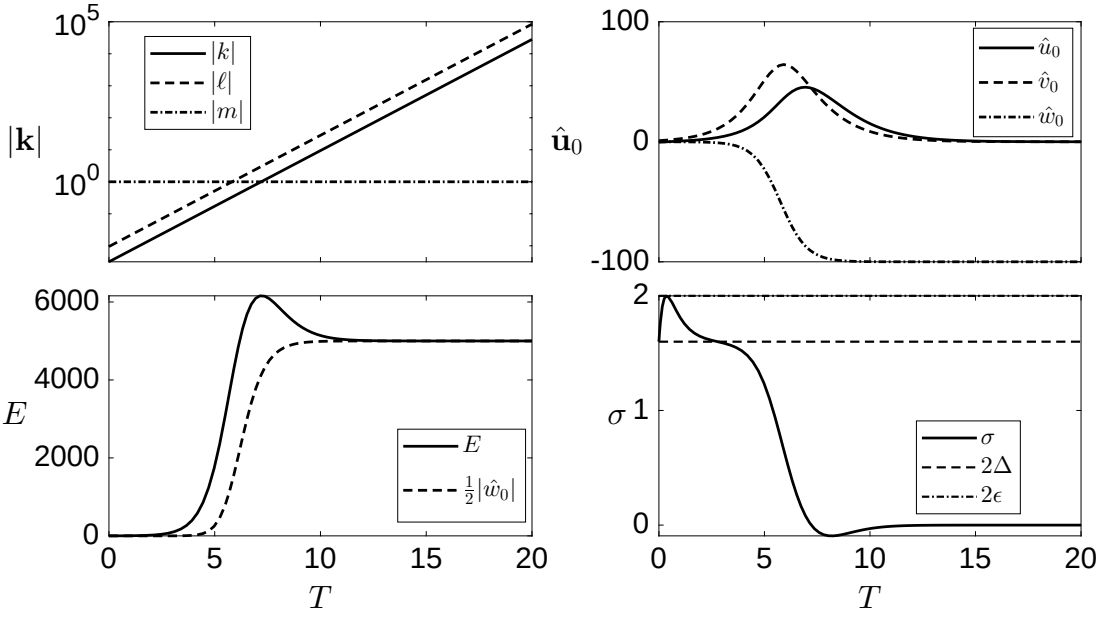


Figure 2: Solution to the amplitude equations in the non-rotating case (3.12) with initial data as in (3.13) and $\beta = 0.01$. **Top left:** Evolution of wavevector components. **Top right:** Evolution of first order velocity field components. These are identical to fig. 3 as the wavevector components are agnostic to the presence of global rotation. **Bottom left:** Perturbation energy evolution compared with perturbation energy in the third component $\hat{w}_0$. **Bottom right:** Perturbation growth rate.

The perturbation growth rate attains its maximal value of $2\varepsilon$ momentarily before decaying to zero in the long time limit. For more details on the dynamics and instabilities in the non-rotating case see [5].

### 3.2 Solutions of the weakly rotating system

We now integrate the amplitudes ODEs in the weakly rotating case (3.6) and compare them to the non-rotating case. We initialize the system with (3.13) as well.

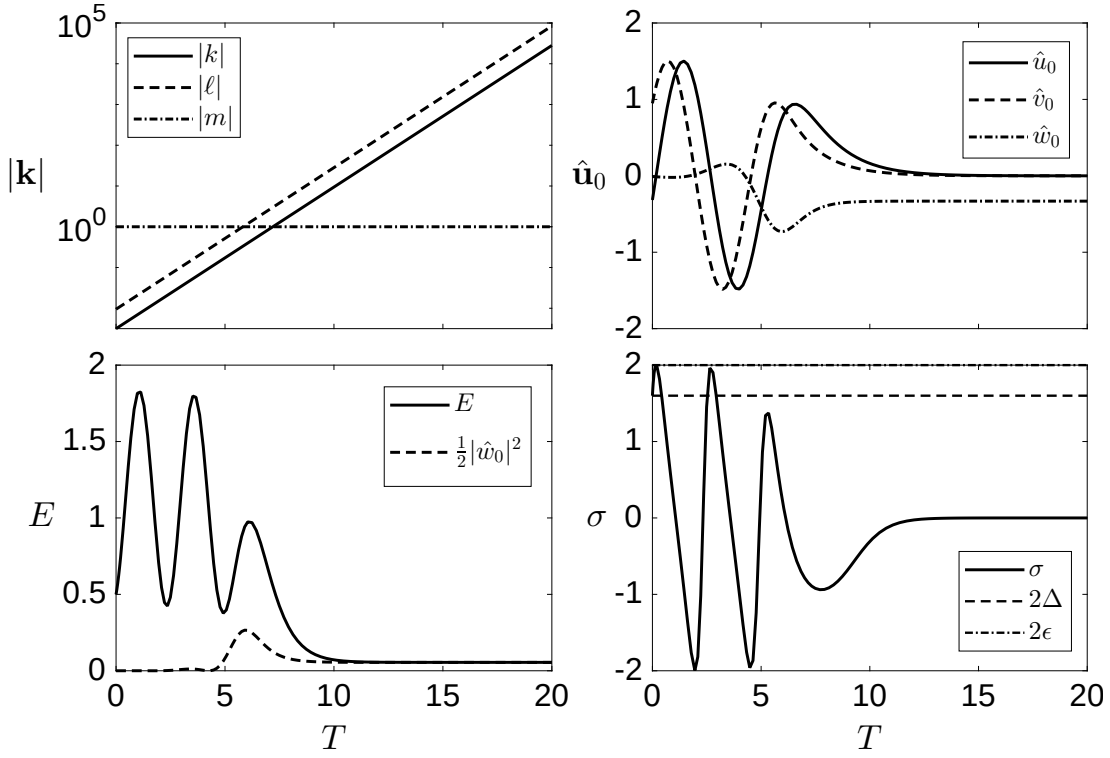


Figure 3: Solution to the amplitude equations (3.8) with initial data as in (3.13) and $\beta = 0.01$. The strain, rotation and Coriolis parameter are set to $\varepsilon = 1$, $\gamma = 0.6$, $f = 0.5$ and $\Delta = 0.8$. **Top left:** Evolution of wavevector components. **Top right:** Evolution of first order velocity field components. **Bottom left:** Perturbation energy evolution compared with perturbation energy in the third component $\hat{w}_0$. **Bottom right:** Perturbation growth rate. The optimal growth rate is $2\varepsilon$.

For the chosen parameter values in fig. 3 and initial data (3.13), the evolution of the wavevector components is exponential in time. The evolution of the velocity components, energy $E$ and energy growth rate $\sigma$ are initially oscillatory before settling down. From the energy plot, we see the energy settles to a non-zero value contained entirely in the third component $\hat{w}_0$ as $T \to \infty$. Correspondingly, the growth rate goes to zero as $T \to \infty$. Comparing the non-rotating case as in fig. 2 to the weakly rotating case in fig. 3, the presence of the Coriolis term induces initial oscillations in the energy of perturbations. As long as the hyperbolicity assumption is observed, the long term behaviour from the same

initial data lead to bounded energy as seen in the bottom left hand plot in fig. 3.

By using multiscale and ray theory tools to understand the dynamics of perturbations around hyperbolic stagnation points in fluid flows undergoing global rotation, we have united the seemingly disparate work presented in [5] and [6] and by extension [8, 9]. Upon performing a formal multiscale expansion of the governing equations and assuming that the rotation is of the order $\delta$, the resulting amplitude PDE (3.5) can be solved via the method of characteristics. We show that these equations (3.8) are the same ones considered by the authors in [6]. By then taking the limit of vanishing Coriolis parameter, we recovered exactly the amplitude equations considered by the authors of [5]. A similar procedure was also performed by the authors of [6], however, their analysis was agnostic, as our multi-scale analysis shows, to the fact that this limit is valid only when $f \sim \mathcal{O}(\delta)$. As such we must consider the case of strong rotation separately.

# 4 Strong Rotation

We now construct a new class of solutions by considering strong rotation, i.e., $f \sim \mathcal{O}(1)$. Carrying out the multiscale expansion, the equations at leading orde,r i.e., $\mathcal{O}(1)$ are

$$(-\omega + \mathbf{k}\cdot\mathbf{U})\,\hat{\mathbf{u}}_0 - if\,\mathbf{e}_z \times \hat{\mathbf{u}}_0 + \mathbf{k}\,\hat{p}_0 = \mathbf{0}, \tag{4.1a}$$

$$\mathbf{k}\cdot\hat{\mathbf{u}}_0 = 0. \tag{4.1b}$$

As opposed to the weakly rotating case, now $f$ explicitly appears in the leading order momentum equation. We must first derive an expression for the dispersion relation, which now due to the presence of rotation, will yield a non-zero intrinsic frequency. Since the rotation does not act on the third component, $\hat{p}_0$ can be expressed as

$$\hat{p}_0 = \frac{1}{m^2}\left(-\omega + \mathbf{k}\cdot\mathbf{U}\right)\left(k\hat{u}_0 + \ell\hat{v}_0\right), \tag{4.2}$$

where leading order incompressibility (4.1b) has been used to eliminate $\hat{w}_0$. Substituting back in (4.1) and expressing the linear system in terms of $\hat{u}_0$ and $\hat{v}_0$ only,

$$\begin{bmatrix} (-\omega + \mathbf{k}\cdot\mathbf{U})\left(1 + \frac{k^2}{m^2}\right) & (-\omega + \mathbf{k}\cdot\mathbf{U})\,\frac{k\ell}{m^2} + if \\ (-\omega + \mathbf{k}\cdot\mathbf{U})\,\frac{k\ell}{m^2} - if & (-\omega + \mathbf{k}\cdot\mathbf{U})\left(1 + \frac{\ell^2}{m^2}\right) \end{bmatrix} \begin{bmatrix} \hat{u}_0 \\ \hat{v}_0 \end{bmatrix} = \mathbf{0}. \tag{4.3}$$

The system will have non-trivial solutions if and only if the determinant of the matrix vanishes. Implementing this condition, the dispersion relation is

$$\omega = \underbrace{\mathbf{k}\cdot\mathbf{U} \pm \underbrace{\frac{fm}{|\mathbf{k}|}}_{=:\omega_{\mathrm{rot}}}}_{=:\Omega(\mathbf{k}(\mathbf{X},T);\mathbf{X},T)}. \tag{4.4}$$

The familiar reader will recognize these as the dispersion relation for inertial waves. Furthermore, $\omega_{\mathrm{rot}}$ is the intrinsic frequency and $\mathbf{k}\cdot\mathbf{U}$ is the Doppler shift. Recalling that

$\mathbf{U} = \mathbf{A}\mathbf{X}$, the group velocity $\mathbf{c}_g = \nabla_{\mathbf{k}}\Omega$ is

$$\mathbf{c}_g = \begin{bmatrix} \varepsilon X - \gamma Y \\ \gamma X - \varepsilon Y \\ 0 \end{bmatrix} \underbrace{\pm \frac{f}{|\mathbf{k}|^3} \begin{bmatrix} -mk \\ -m\ell \\ k^2 + \ell^2 \end{bmatrix}}_{=:\mathbf{c}_{\text{rot}}}. \tag{4.5}$$

We denote $\mathbf{c}_{\text{rot}}$ as the intrinsic group velocity. With this in mind, the advection of the wavevector obeys (2.9), with $\Omega$ as in (4.4). The ray tracing equations can then be derived via the method of characteristics. The characteristic curves are governed by the following system of coupled ODEs

$$\frac{\mathrm{d}X}{\mathrm{d}T} = \varepsilon X - \gamma Y \pm \frac{f}{|\mathbf{k}|^3}(-mk), \tag{4.6a}$$

$$\frac{\mathrm{d}Y}{\mathrm{d}T} = \gamma X - \varepsilon Y \pm \frac{f}{|\mathbf{k}|^3}(-m\ell), \tag{4.6b}$$

$$\frac{\mathrm{d}Z}{\mathrm{d}T} = \pm \frac{f}{|\mathbf{k}|^3}\left(k^2 + \ell^2\right), \tag{4.6c}$$

$$\frac{\mathrm{d}\mathbf{k}}{\mathrm{d}T} = -\mathbf{A}^T\mathbf{k}. \tag{4.6d}$$

As opposed to the weakly rotating case, the presence of strong rotation modifies the ray paths. Namely, this skews them from the streamlines of the hyperbolic background flow. Moreover, strong rotation induces evolution of the $Z$ component in (4.6c) making the ray paths three dimensional. In the non-rotating case, since $f$ does not appear, $Z$ would be invariant in time and hence the ray paths would remain inherently two dimensional and agree with the streamlines of the background flow. As a convention for the rest of this work, we choose the sign of the rotation to be positive, i.e., $f > 0$. Integrating the set of ODEs we may plot the ray paths. The ray paths governed by (4.6) are plotted in fig. 4.

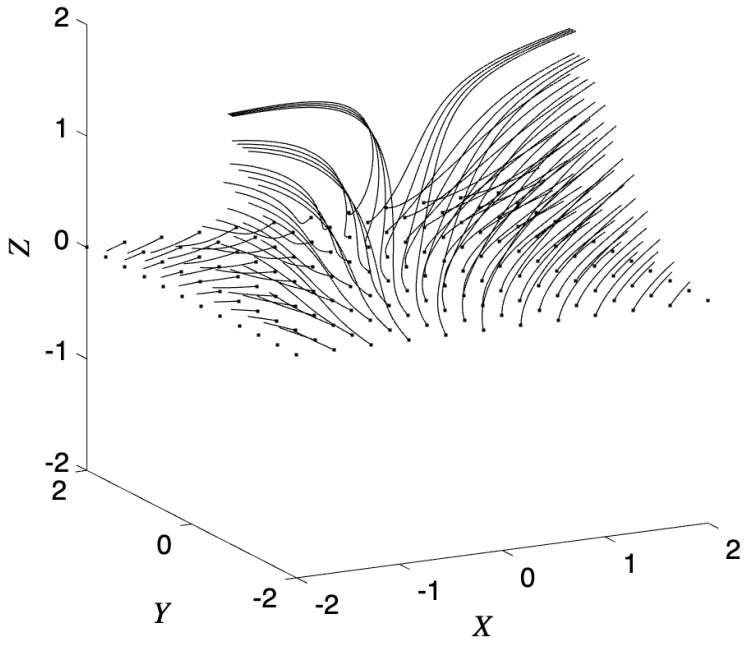


Figure 4: Ray paths governed by (4.6a), (4.6b) (4.6c) plotted from a $12 \times 12$ array of initial positions in the $X, Y$-plane in the square $[-2, 2] \times [-2, 2]$ with $z = 0$, with initial wavevector $\mathbf{k}(0) = (1, 1, 2)$ and rotation $f = 2$. The underlying background field has the hyperbolic stagnation point at the origin.

As seen in fig. 4, in the presence of strong rotation the ray paths for these selected initial positions have rapid growth in the $Z$-direction before tending to a constant value. This can be explained by the ray path equation for $Z$ (4.6c). The asymptote can be computed straightforwardly by integrating

$$\lim_{\tau\to\infty} [Z(\tau) - Z(0)] = \lim_{\tau\to\infty} f \int_0^\tau \frac{k^2 + \ell^2}{|\mathbf{k}|^3} \, \mathrm{d}T. \tag{4.7}$$

Upon substituting the relevant expressions for the solutions of $k, \ell$ and $m$, the integral can be evaluated. Unfortunately, the resulting integrand cannot be evaluated in closed form, it will require expressions in terms of hypergeometric functions. Nonetheless, evaluating numerically and comparing to the ODE integration using the same initial data as in fig. 4,

$$\begin{gathered}\text{ODE integration}: 0.966582, \\ \text{Numerical evaluation of } (4.7): 0.966680,\end{gathered}$$

the asymptote can be approximated with high confidence.

## 4.1 Energy and wave action

We continue with the multiscale analysis by moving to the next order, i.e., $\mathcal{O}(\delta)$ to derive an amplitude or energy equation along ray paths. Equating terms in powers of $\delta$, the

momentum and incompressibility equations at this order are

$$i\left(-\frac{fm}{|\mathbf{k}|}\right)\hat{\mathbf{u}}_1 + f\,\mathbf{e}_z\times\hat{\mathbf{u}}_1 + i\,\mathbf{k}\,\hat{p}_1 = -(\partial_T + \mathbf{U}\cdot\nabla_{\mathbf{X}})\,\hat{\mathbf{u}}_0 - \nabla_{\mathbf{X}}\hat{p}_0 - (\hat{\mathbf{u}}_0\cdot\nabla_{\mathbf{X}})\,\mathbf{U} \tag{4.8a}$$

$$i\,\mathbf{k}\cdot\hat{\mathbf{u}}_1 = -\nabla_{\mathbf{X}}\cdot\hat{\mathbf{u}}_0. \tag{4.8b}$$

Since the dispersion relation yields a non-zero intrinsic frequency due to strong rotation, there is an appearance of $\hat{\mathbf{u}}_1$ on the left hand sides. In order to gain an energy equation, we make use of the Fredholm alternative to derive a solvability condition on (4.8a). From our multiscale analysis, the leading order operator in (4.1) written as a block matrix is

$$\mathcal{L}\begin{bmatrix}\hat{\mathbf{u}}_0\\ \hat{p}_0\end{bmatrix} = \begin{bmatrix}(-\omega+\mathbf{k}\cdot\mathbf{U}) - if\mathbf{e}_z\times & \mathbf{k}\\ \mathbf{k} & 0\end{bmatrix}\begin{bmatrix}\hat{\mathbf{u}}_0\\ \hat{p}_0\end{bmatrix} = \begin{bmatrix}\mathbf{0}\\ 0\end{bmatrix}. \tag{4.9}$$

It is straightforward to establish that the operator is Hermitian. As such, applying the Fredholm alternative, the solvability condition is equivalent to enforcing the orthogonality of $[\hat{\mathbf{u}}_0^*, \hat{p}_0^*]$ with the right hand side of (4.8), where $[\hat{\mathbf{u}}_0^*, \hat{p}_0^*]$ is a member of the kernel of the adjoint of $\mathcal{L}$,

$$\begin{bmatrix}\hat{\mathbf{u}}_0^*\\ \hat{p}_0^*\end{bmatrix}\cdot\begin{bmatrix}-(\partial_T + \mathbf{U}\cdot\nabla_{\mathbf{X}})\,\hat{\mathbf{u}}_0 - \nabla_{\mathbf{X}}\hat{p}_0 - (\hat{\mathbf{u}}_0\cdot\nabla_{\mathbf{X}})\,\mathbf{U}\\ -\nabla_{\mathbf{X}}\cdot\hat{\mathbf{u}}_0\end{bmatrix} = 0. \tag{4.10}$$

The resulting equation is,

$$\frac{1}{2}(\partial_T + \mathbf{U}\cdot\nabla_{\mathbf{X}})\,|\hat{\mathbf{u}}_0|^2 + \nabla_{\mathbf{X}}\cdot(\hat{p}_0\hat{\mathbf{u}}_0) = -\hat{\mathbf{u}}_0^{\mathrm{T}}\,(\nabla_{\mathbf{X}}\mathbf{U})\,\hat{\mathbf{u}}_0. \tag{4.11}$$

Expressing background velocity field as $\mathbf{U} = \mathbf{c}_g - \mathbf{c}_{\mathrm{rot}}$, (4.11) can be re-expressed

$$\begin{aligned}&\frac{1}{2}(\partial_T + \mathbf{c}_g\cdot\nabla_{\mathbf{X}})|\hat{\mathbf{u}}_0|^2\\ &\qquad = -\hat{\mathbf{u}}_0^{\mathrm{T}}\,(\nabla_{\mathbf{X}}\mathbf{U})\,\hat{\mathbf{u}}_0 - \nabla_{\mathbf{X}}\cdot(\hat{p}_0\hat{\mathbf{u}}_0) + \frac{1}{2}\left(\nabla_{\mathbf{X}}\cdot\left(\mathbf{c}_{\mathrm{rot}}|\hat{\mathbf{u}}_0|^2\right) - |\hat{\mathbf{u}}_0|^2\nabla_{\mathbf{X}}\cdot\mathbf{c}_{\mathrm{rot}}\right)\end{aligned} \tag{4.12}$$

The eq. (4.12) is the solvability condition, which may be interpreted as the evolution of perturbation energy along ray paths. Expressing (4.12) in terms of $E$ as defined in (3.9), it is also possible to eliminate the divergence term $\nabla_{\mathbf{X}}\cdot\hat{p}_0\hat{\mathbf{u}}_0$ since it can be shown that

$$\nabla_{\mathbf{X}}\cdot\hat{p}_0\hat{\mathbf{u}}_0 = \nabla_{\mathbf{X}}\cdot\mathbf{c}_{\mathrm{rot}}E. \tag{4.13}$$

With this in mind, (4.12) simplifies to

$$(\partial_T + \mathbf{c}_g\cdot\nabla_{\mathbf{X}})\,E = -\hat{\mathbf{u}}_0\cdot(\hat{\mathbf{u}}_0\cdot\nabla_{\mathbf{X}}\mathbf{U}) - E\,(\nabla_{\mathbf{X}}\cdot\mathbf{c}_{\mathrm{rot}})\,. \tag{4.14}$$

It is well known, the quantity that is conserved in general along ray paths is the wave action, cf. [4, 10, 11]. Let $\mathcal{A}$ denote the wave action, which is defined as

$$\mathcal{A} := \frac{E}{\omega_{\mathrm{rot}}}. \tag{4.15}$$

Since the quantity is invariant in general, it satisfies the conservation law

$$\partial_T \mathcal{A} + \nabla_{\mathbf{X}} \cdot \mathcal{A}\mathbf{c}_g = 0. \tag{4.16}$$

For a proof of this fact within the current context see section A. To use this result to compute an amplitude along rays, we can re-write (4.16) to gain an expression for $\mathcal{A}$ evolving along rays,

$$\left(\partial_T + \mathbf{c}_g \cdot \nabla_{\mathbf{X}}\right) \mathcal{A} = -\mathcal{A} \left(\nabla_{\mathbf{X}} \cdot \mathbf{c}_g\right). \tag{4.17}$$

Therefore, the left hand side is the rate of change of $\mathcal{A}$ along a ray, and we reduce to an ODE with a solution of the form

$$\mathcal{A} = \mathcal{A}_0 \exp\left(-\int_0^T \nabla_{\mathbf{X}} \cdot \mathbf{c}_g \, \mathrm{d}\tau\right), \tag{4.18}$$

where $\mathcal{A}_0$ is the initial wave amplitude. The initial value of the wave action can be deduced via the polarization relations and can thereby be expressed in terms of the initial value of the wavevector components, see section A for details. Equation (4.18) encapsulates the dynamics of wave action and a bundle of ray paths. In particular, if the divergence of the group velocity is negative, i.e., ray paths converge, (4.18) implies $\mathcal{A}$ increases. Conversely, if the divergence of the group velocity is positive, i.e., ray paths diverge, (4.18) implies $\mathcal{A}$ decreases. To quantify this behaviour we must compute the divergence of the group velocity along ray paths. The seeming difficulty is that the current ray tracing equations (4.6) do not capture the evolution of $\nabla_{\mathbf{X}}\mathbf{k}$ along rays. As such, we must extend the ray tracing system to include equations for how spatial derivatives of the wavevector components evolve. A general procedure by which the ray system can be extended in this manner is outlined in [4].

## 4.2 Extended ray system

The ray system (4.6) consists of six equations. We must add equations for $\nabla_{\mathbf{X}} k$ and $\nabla_{\mathbf{X}} \ell$. There is no need to add equations for spatial derivatives of $m$ since $m$ is invariant along rays. Furthermore, since the system is invariant in $Z$, the gradient is restricted to $X$ and $Y$ only. Another simplification can be made by noting, $\nabla_{\mathbf{X}} \times \mathbf{k} = \mathbf{0}$, as such $\partial_Y k = \partial_X \ell$. Therefore, we will need three new equations to extend the ray system in the variables

$$\frac{\mathrm{d}}{\mathrm{d}T}\left(k_X\right), \quad \frac{\mathrm{d}}{\mathrm{d}T}\left(\ell_Y\right), \quad \frac{\mathrm{d}}{\mathrm{d}T}\left(k_Y\right),$$

where subscripts denote the partial derivative with respect to the spatial coordinate $X$ or $Y$. The procedure for extending the ray system to capture amplitude information is described in general in [4], for the details of the calculation applied to the present case see section B. Upon performing the calculation, the extended ray system written explicitly

component-wise is

$$\frac{\mathrm{d}X}{\mathrm{d}T} = \varepsilon X - \gamma Y \pm \frac{f}{|\mathbf{k}|^3}\left(-mk\right), \tag{4.19a}$$

$$\frac{\mathrm{d}Y}{\mathrm{d}T} = \gamma X - \varepsilon Y \pm \frac{f}{|\mathbf{k}|^3}\left(-m\ell\right), \tag{4.19b}$$

$$\frac{\mathrm{d}Z}{\mathrm{d}T} = \pm\frac{f}{|\mathbf{k}|^3}\left(k^2+\ell^2\right), \tag{4.19c}$$

$$\frac{\mathrm{d}k}{\mathrm{d}T} = -\varepsilon k - \gamma\ell, \tag{4.19d}$$

$$\frac{\mathrm{d}\ell}{\mathrm{d}T} = \gamma k + \varepsilon\ell, \tag{4.19e}$$

$$\frac{\mathrm{d}m}{\mathrm{d}T} = 0, \tag{4.19f}$$

$$\begin{aligned}\frac{\mathrm{d}k_X}{\mathrm{d}T} &= -2\left(\varepsilon k_X + \gamma k_Y\right)\\ &\quad\pm\frac{fm}{|\mathbf{k}|^5}\left[\left(-2k^2+\ell^2+m^2\right)k_X^2 + \left(k^2-2\ell^2+m^2\right)k_Y^2 - 6(k\ell)k_Y k_X\right],\end{aligned} \tag{4.19g}$$

$$\begin{aligned}\frac{\mathrm{d}\ell_Y}{\mathrm{d}T} &= 2\left(\varepsilon\ell_Y + \gamma k_Y\right)\\ &\quad\pm\frac{fm}{|\mathbf{k}|^5}\left[\left(k^2-2\ell^2+m^2\right)\ell_Y^2 + \left(-2k^2+\ell^2+m^2\right)k_Y^2 - 6(k\ell)k_Y\ell_Y\right],\end{aligned} \tag{4.19h}$$

$$\begin{aligned}\frac{\mathrm{d}k_Y}{\mathrm{d}T} &= \gamma\left(k_X - \ell_Y\right)\\ &\quad\pm\frac{fm}{|\mathbf{k}|^5}\left[\left(-2k^2+\ell^2+m^2\right)k_Y k_X + \left(k^2-2\ell^2+m^2\right)k_Y\ell_Y - 3k\ell\left(k_Y^2 + k_X\ell_Y\right)\right].\end{aligned} \tag{4.19i}$$

This constitutes a closed system of nine ODEs in the variables $X, Y, Z$, $k, \ell, m$ and $k_X, \ell_Y, k_Y$. Notice, the evolution of $\mathbf{k}$ in this strongly rotating regime is still only determined by the background flow. As such, the solutions from the previous sections and [5] remain valid. With the addition of the three new equations (4.19g)-(4.19i) for the spatial derivatives in the $X$ and $Y$ directions, we may evaluate the divergence of the group velocity as in (4.18) explicitly. As such, the wave action along ray paths will be given in terms of the new variables $k_X, \ell_Y$ and $k_Y$ as well as the evolution of $\mathbf{k}$. For the sake of clarity in what is to follow, we fix the sign of the Coriolis term to be positive. Then, the ODE for $\mathcal{A}$ along ray paths takes the form

$$\frac{\mathrm{d}\mathcal{A}}{\mathrm{d}T} = \underbrace{\mathcal{A}\,\frac{fm}{|\mathbf{k}|^5}\left(\left(-2k^2+\ell^2+m^2\right)k_X + \left(k^2-2\ell^2+m^2\right)\ell_Y - 6\left(k\ell\right)k_Y\right)}_{=-\nabla_{\mathbf{X}}\cdot\mathbf{c}_g}. \tag{4.20}$$

Hence, (4.20) is an auxiliary equation used to determine wave action and thereby energy along ray paths governed by (4.19).

## 4.3 Strongly rotating hyperbolic instabilities

We now embark on solving the extended ray system (4.19)-(4.20) and finding special initial conditions that yield various outcomes for the energy of the perturbation velocity. We find initial conditions that support transient, bounded and unbounded growth. The unbounded growth case shows the existence of hyperbolic instabilities within a strongly rotating fluid medium.

To design a set of initial conditions that captures the various possible behaviours, it will be important to analyse the interplay between the divergence of the group velocity $\mathbf{c}_g$ and the evolution of $\mathcal{A}$ and by extension $E$. The idea is to pick initial conditions that maximize the growth rate of $\mathcal{A}$ and by extension the energy $E$ via the relation (4.15). For any non-zero growth rate in $\mathcal{A}$ we require non-zero initial conditions for the spatial derivatives of the wavevector components $k_X, \ell_Y$ and $k_Y$. Since the wave action is the primary emergent quantity that encodes information about the evolution along rays of energy and amplitude, by (4.18) we are primarily concerned with our derived expression for the divergence of the group velocity

$$\nabla_{\mathbf{X}} \cdot \mathbf{c}_g = \frac{fm}{|\mathbf{k}|^5} \left( \left(2k^2 - \ell^2 - m^2\right) k_X + \left(2\ell^2 - k^2 - m^2\right) \ell_Y + 6\,(k\ell)\, k_Y \right). \tag{4.21}$$

The sign of the divergence of $\mathbf{c}_g$ controls the growth or decay of $\mathcal{A}$ and in turn the energy. For example, a negative divergence implies ray paths are converging thereby increasing the wave action and energy. On the other hand, a positive divergence implies ray paths are moving apart causing wave action and energy to decrease at a commensurate rate.

### 4.3.1 Initial condition for the extended ray system

We now derive initial conditions that will lead to bounded and unbounded energy growth of the perturbation velocity field. Since there are many possibilities through which we may initialize the extended system (4.19), we look into studying the particular case when the components of the wavevector $\mathbf{k}$ decrease exponentially in time. This will drive the horizontal evolution of $\nabla_{\mathbf{X}}\mathbf{k}$ and therefore on the growth rate of energy and the sign of $\nabla_{\mathbf{X}} \cdot \mathbf{c}_g$, thereby also controlling the curvature of a ray bundle. From (4.14) and the energy polarization relations, see section A, the growth rate (3.11) can be expressed as

$$\begin{aligned} \sigma &= \varepsilon \left( \frac{k^2 - \ell^2}{|\mathbf{k}|^2} \right) - \nabla_{\mathbf{X}} \cdot \mathbf{c}_g, \\ &= \varepsilon \left( \frac{k^2 - \ell^2}{|\mathbf{k}|^2} \right) - \frac{fm}{|\mathbf{k}|^5} \left( \left(2k^2 - \ell^2 - m^2\right) k_X + \left(2\ell^2 - k^2 - m^2\right) \ell_Y + 6\,(k\ell)\, k_Y \right). \end{aligned} \tag{4.22}$$

Choosing initial conditions for $\mathbf{k}$ such that $k$ and $\ell$ decay. The ODEs for the spatial derivatives of the wavevector components (4.19g), (4.19h), (4.19i) reduce to, respectively,

$$\frac{\mathrm{d}k_X}{\mathrm{d}T} = -2(\varepsilon k_X + \gamma k_Y) + \frac{f}{m^2}\left[k_X^2 + k_Y^2\right], \tag{4.23a}$$

$$\frac{\mathrm{d}\ell_Y}{\mathrm{d}T} = 2(\varepsilon \ell_Y + \gamma k_Y) + \frac{f}{m^2}\left[\ell_Y^2 + k_Y^2\right], \tag{4.23b}$$

$$\frac{\mathrm{d}k_Y}{\mathrm{d}T} = \gamma(k_X - \ell_Y) + \frac{f}{m^2}[k_Y(k_X + \ell_Y)]. \tag{4.23c}$$

We refer to (4.23) as the asymptotic curvature equations as they encode information about the curvature of a ray bundle in the long time limit. Furthermore, in this limit, (4.22) takes on the asymptotic value

$$\sigma \to \frac{f}{m^2}\left(k_X + \ell_Y\right), \quad T \to \infty. \tag{4.24}$$

Since the curvature ODEs have been reduced to (4.23) they constitute a self-contained nonlinear system in the variables $k_X, \ell_Y$ and $k_Y$. Computing the non-trivial fixed points of the system yields

$$k_X = \frac{m^2}{f}\left(\pm\Delta + \frac{\Delta^2}{\varepsilon}\right), \tag{4.25a}$$

$$\ell_Y = \frac{m^2}{f}\left(\pm\Delta - \frac{\Delta^2}{\varepsilon}\right), \tag{4.25b}$$

$$k_Y = \mp\frac{\gamma\,\Delta\,m^2}{\varepsilon\,f}. \tag{4.25c}$$

Substituting the expressions in (4.25a) and (4.25b) into (4.24), we obtain

$$\sigma_\infty = \pm 2\Delta, \tag{4.26}$$

where $\sigma_\infty$ denotes the asymptotic value of $\sigma$. Note, this will hold for any choice of initial position, non-zero initial curvature and initial conditions for the wavevector leading to exponential decay. Connecting this to the ray paths, computing the asymptotic value of the divergence of the group velocity, we obtain

$$\nabla_{\mathbf{X}} \cdot \mathbf{c}_g \to -\frac{f}{k_z^2}\left(k_X + \ell_Y\right) = \mp 2\Delta, \quad T \to \infty. \tag{4.27}$$

Therefore, picking any non-zero initial conditions for $k_X, \ell_Y$ and $k_Y$ will inevitably lead to solutions attracted towards the stable fixed point of the asymptotic curvature system (4.25),

$$k_X = \frac{m^2}{f}\left(-\Delta + \frac{\Delta^2}{\varepsilon}\right), \quad \ell_Y = \frac{m^2}{f}\left(-\Delta - \frac{\Delta^2}{\varepsilon}\right), \quad k_Y = \frac{\gamma\,\Delta\,m^2}{\varepsilon\,f}. \tag{4.28}$$

This will lead to the asymptotic growth rate of $\sigma_\infty = -2\Delta$, which is complementary to the asymptotic value of $\nabla_{\mathbf{X}} \cdot \mathbf{c}_g = 2\Delta$, i.e., ray paths diverge reducing wave action and thereby energy.

Conversely, this analysis also suggests that there exists a set of initial conditions for the extended ray system (4.19) such that $\sigma_\infty = 2\Delta$, which simultaneously yields $\nabla_{\mathbf{X}} \cdot \mathbf{c}_g = -2\Delta$, i.e., ray paths converge. To see such asymptotic behaviour of the perturbation energy, the initial conditions for $k_X, \ell_Y$ and $k_Y$ in (4.19) must lie on the unstable fixed point of the asymptotic system (4.23), i.e.,

$$k_X(0) = \frac{m^2}{f}\left(\Delta + \frac{\Delta^2}{\varepsilon}\right), \quad \ell_Y(0) = \frac{m^2}{f}\left(\Delta - \frac{\Delta^2}{\varepsilon}\right), \quad k_Y(0) = -\frac{\gamma\,\Delta\,m^2}{\varepsilon\,f}. \tag{4.29}$$

### 4.3.2 Transient energy growth

Transient amplification of wave action and energy correspond to initial conditions that make (4.21) initially negative. The following initial conditions display such behaviour

$$k(0) = \sqrt{\frac{1-m(0)}{1+\frac{\Delta-\varepsilon}{\gamma}}}, \quad \ell(0) = \frac{\Delta-\varepsilon}{\gamma}k(0), \quad m(0) = \frac{1}{2}. \tag{4.30}$$

$$k_X(0) = \frac{m^2}{f}\left(-\Delta + \frac{\Delta^2}{\varepsilon}\right), \quad \ell_Y(0) = \frac{m^2}{f}\left(-\Delta - \frac{\Delta^2}{\varepsilon}\right), \quad k_Y(0) = \frac{\gamma\,\Delta\,m^2}{\varepsilon\,f}. \tag{4.31}$$

The initial condition (4.30) are taken from [5] and cause exponential decrease of wavevector components. Initializing (4.19) with these initial conditions and integrating, the solutions for various quantities are plotted in fig. 5.

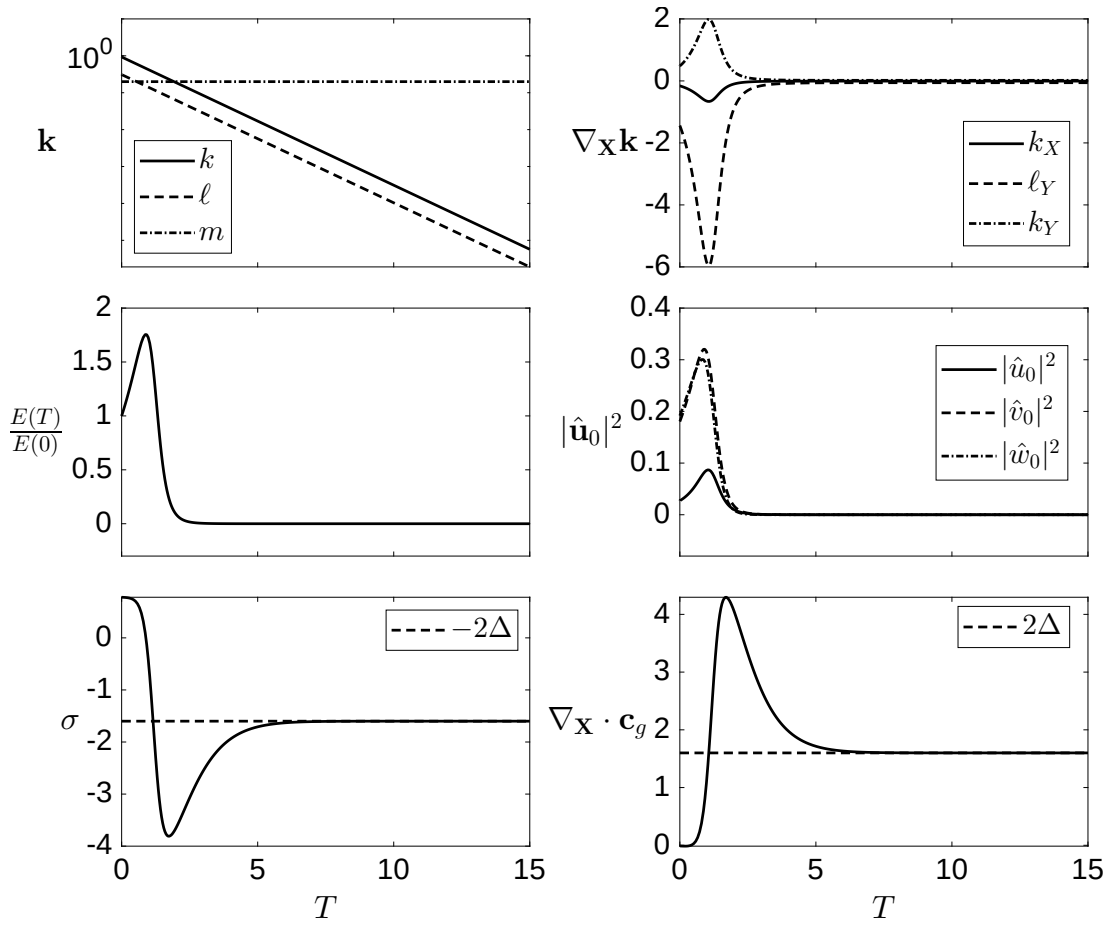


Figure 5: Solution of the extended ray system (4.19) initialized with wavevector initial conditions (4.30), spatial derivative of the wavevector initial condition (4.31) and spatial initial condition $\mathbf{X}(0) = [1, 1, 0]$. The strain and rotation parameters are $\varepsilon = 1$, $\gamma = 0.6$, $\Delta = 0.8$ and $f = 1$. **Top left:** wavevector evolution, exponentially decaying. **Top right:** evolution of spatial derivatives of $\mathbf{k}$. Initialized from the stable fixed point of (4.23). **Middle left:** evolution of energy. Normalized at initial value. **Middle right:** energy stored in velocity components. **Bottom left:** evolution of the energy growth rate. **Bottom right:** evolution of the divergence of group velocity.

Due to (4.30), $\mathbf{k}$ decreases exponentially in time. Initializing $k_X, \ell_Y, k_Y$ with (4.31), makes the divergence of the group velocity, for these chosen parameter values, slightly negative momentarily as seen in the bottom right plot in fig. 5. Since this implies a convergence of a bundle of rays, $E$ increases initially while $\sigma$ remains positive as can be see in the middle left and bottom left panels, respectively. When $\nabla_{\mathbf{X}} \cdot \mathbf{c}_g > 0$, $\sigma$ begins to decrease thereby inducing a transient in $E$. In the limit, $E \to 0$ and $\sigma \to -2\Delta$ and $\nabla_{\mathbf{X}} \cdot \mathbf{c}_g \to 2\Delta$, in agreement with our analysis.

### 4.3.3 Bounded energy growth

In a similar fashion, we may derive initial conditions for (4.19) leading to bounded growth of energy as $T$ increases. Recall, for our current analysis to be valid, the wavevector $\mathbf{k}$ must be initialized in the stable eigen-direction of the system $\frac{\mathrm{d}}{\mathrm{d}T}\mathbf{k} = -\mathbf{A}^{\mathrm{T}}\mathbf{k}$. The initial condition for $m$ that maximized the long time growth rate of kinetic energy was arbitrarily close to unity. To see bounded asymptotic growth of perturbation energy the following initial conditions on $\mathbf{k}$ are considered,

$$k(0) = \sqrt{\frac{1-m^2(0)}{1+\left(\frac{\Delta-\varepsilon}{\gamma}\right)^2}}, \quad \ell(0) = \frac{\Delta-\varepsilon}{\gamma}k(0), \quad m(0) = 1-10^{-n}, \tag{4.32}$$

$$k_X(0) = \frac{m^2}{f}\left(\Delta + \frac{\Delta^2}{\varepsilon}\right), \quad \ell_Y(0) = \frac{m^2}{f}\left(\Delta - \frac{\Delta^2}{\varepsilon}\right), \quad k_Y(0) = -\frac{\gamma\,\Delta\,m^2}{\varepsilon\,f}. \tag{4.33}$$

where $n$ is a non-negative integer. As opposed to (4.31), (4.33) is the unstable fixed point of the asymptotic curvature equations (4.23). By initializing $k_X, \ell_Y$ and $k_Y$ at this point, we expect to see, at least for some period in time, positive growth rate $\sigma = 2\Delta$, which is complementary to a convergence of ray paths quantified by $\nabla_{\mathbf{X}} \cdot \mathbf{c}_g = -2\Delta$. Solving (4.19) with these initial conditions, the solutions are presented in fig. 6.

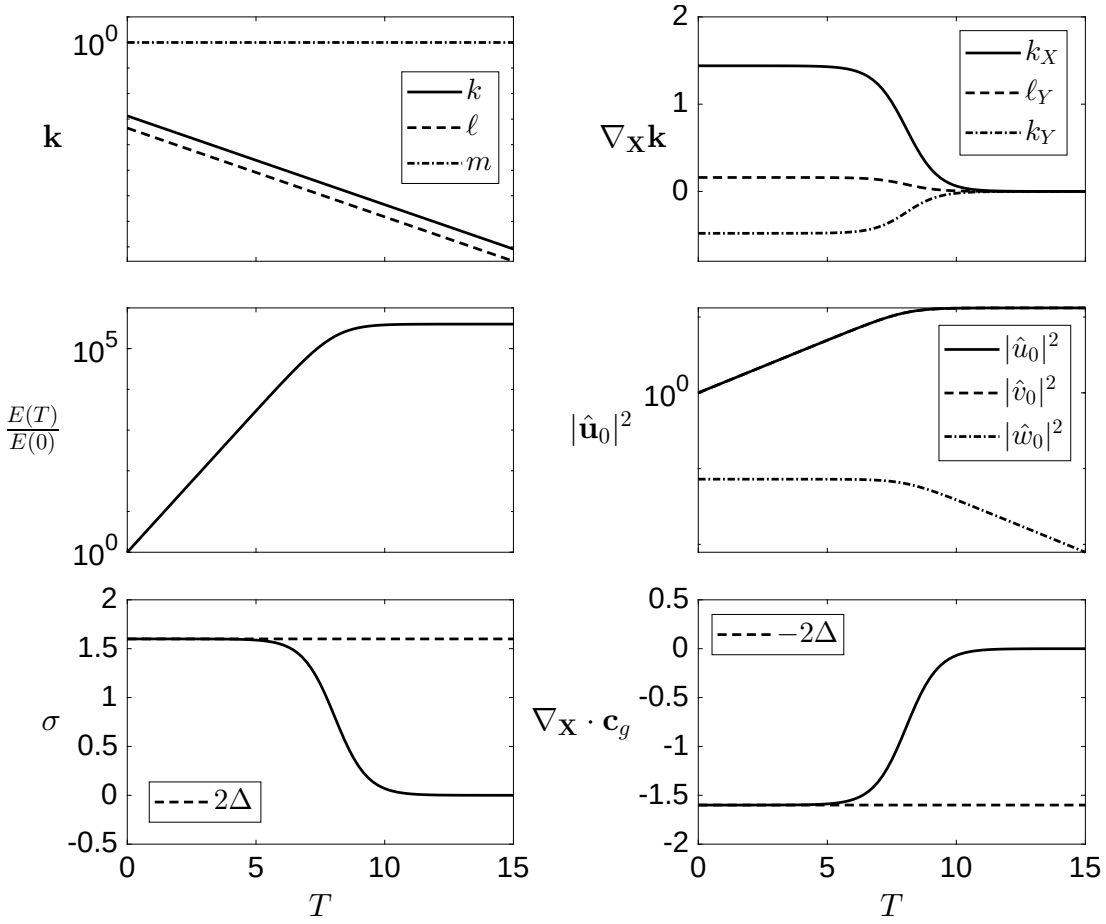


Figure 6: Solution of the extended ray system (4.19) initialized with data (4.32) with $n = 6$ and (4.33) and spatial initial condition $\mathbf{X}(0) = [1, 1, 0]$. The strain and rotation parameters are as in fig. 5. **Top left:** wavevector evolution, exponentially decaying. **Top right:** evolution of spatial derivatives of $\mathbf{k}$. Initialized from the stable fixed point of (4.23). **Middle left:** evolution of energy. Normalized at initial value. **Middle right:** energy stored in velocity components. The $\hat{v}_0$ component agrees with the $\hat{u}_0$ component for all time in this case. **Bottom left:** evolution of the energy growth rate. **Bottom right:** evolution of the divergence of group velocity.

Having initialized $\nabla_{\mathbf{X}}\mathbf{k}$ with (4.32), the solutions in the top right panel remain at this point for a significant period. As our calculations show, during this time, the divergence is negative $\nabla_{\mathbf{X}} \cdot \mathbf{c}_g = -2\Delta < 0$. As ray paths converge, the growth rate remains positive $\sigma = 2\Delta > 0$, commensurate with exponential increase of the perturbation energy as seen in the middle left panel for $\frac{E(T)}{E(0)}$. However, since the wavevector component $m$ was initialized close to the maximizing value leading to maximal growth rate, the instability of the fixed point of (4.23) causes the components of $\nabla_{\mathbf{X}}\mathbf{k}$ to move towards the neutral fixed point at 0. This change induces $\sigma \to 0$ and $\nabla_{\mathbf{X}} \cdot \mathbf{c}_g \to 0$ as $T \to \infty$. Finally, in this limit $E$ approaches a non-zero finite value, thereby showing bounded growth of perturbation energy.

### 4.3.4 Instability: unbounded energy growth

To see unbounded growth of perturbation energy as $T \to \infty$, it is natural to consider the limit of the initial conditions (4.32) and (4.35). Namely, $k, \ell \to 0$ and $m \to 1$ as $n \to \infty$. Therefore, the initial conditions for the system (4.19) leading to unbounded growth of perturbation energy are

$$k(0) = 0, \quad \ell(0) = 0, \quad m(0) = 1, \tag{4.34}$$

$$k_X(0) = \frac{1}{f}\left(\Delta + \frac{\Delta^2}{\varepsilon}\right), \quad \ell_Y(0) = \frac{1}{f}\left(\Delta - \frac{\Delta^2}{\varepsilon}\right), \quad k_Y(0) = -\frac{\gamma\,\Delta}{\varepsilon\, f}. \tag{4.35}$$

The solution of the extended ray system initialized with these conditions are presented in fig. 7.

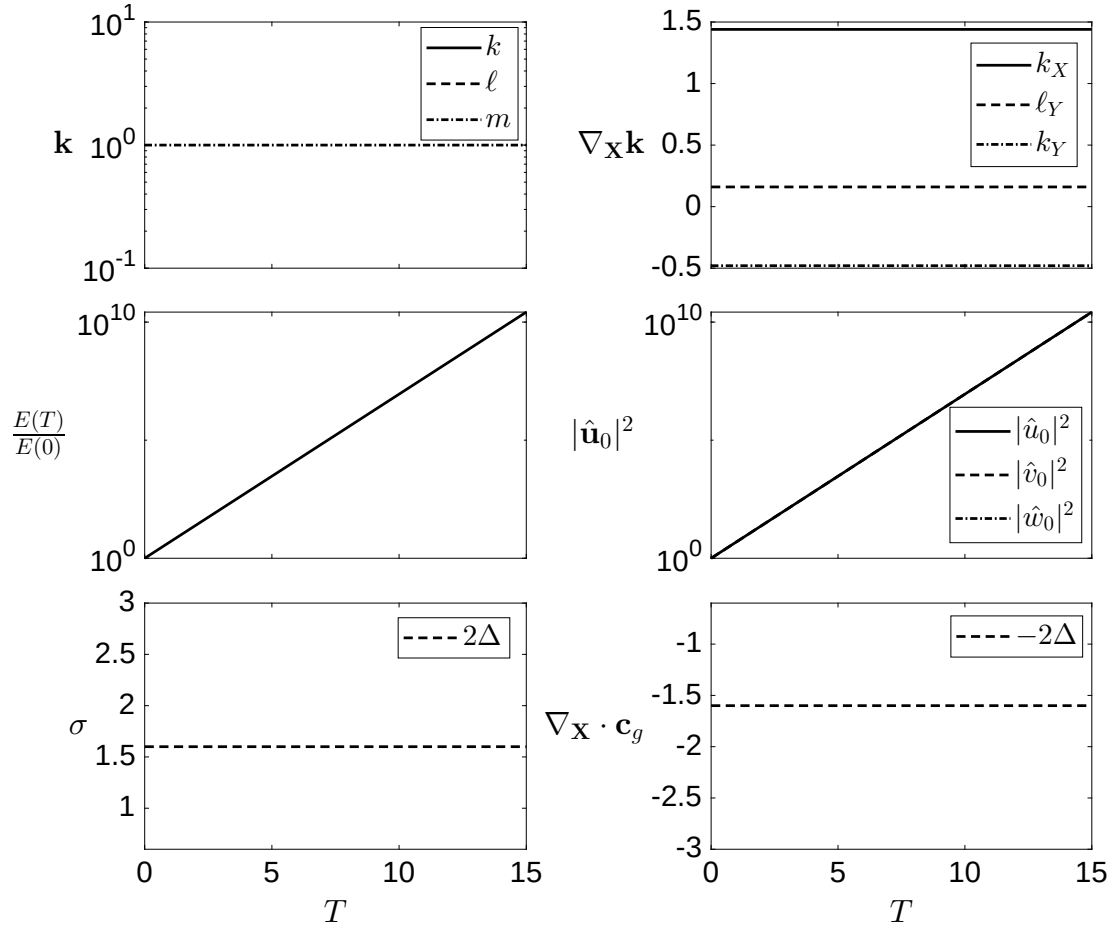


Figure 7: Solution of the extended ray system (4.19) initialized with data (4.34) and (4.35) and spatial initial condition $\mathbf{X}(0) = [1, 1, 0]$. The strain and rotation parameters are as in fig. 5. **Top left:** wavevector evolution, exponentially decaying. **Top right:** evolution of spatial derivatives of $\mathbf{k}$. Initialized from the stable fixed point of (4.23). **Middle left:** evolution of energy. Normalized at initial value. **Middle right:** energy stored in velocity components. **Bottom left:** evolution of the energy growth rate. **Bottom right:** evolution of the divergence of group velocity.

Since the wavevector has been initialized with the streamwise and spanwise components initially zero, they remain zero for all time. Initializing $\nabla_{\mathbf{X}}\mathbf{k}$ at the unstable equilibrium of (4.23), the components also remain constant at the values in (4.35) (dictated by the chosen parameter values as in fig. 5) for all time. Through our calculations for $\sigma$ and the divergence of ray paths, these initial conditions will yield $\sigma = 2\Delta$ and $\nabla_{\mathbf{X}} \cdot \mathbf{c}_g = -2\Delta$ for all time. This is confirmed by the bottom two panels in fig. 7. The constant growth rate implies unbounded exponential growth of perturbation energy as confirmed in the middle panels. These solutions show the existence of a hyperbolic instability within a rapidly rotating fluid system. We should mention, however, that these solutions were derived from a special class of initial conditions that are horizontally invariant, i.e., $k = \ell = 0$ for all time as such they feel no rotation. This then implies that unstable modes in the non-rotating case would be stabilized in the presence of rotation.

# 5 Conclusion

In this work, we have studied the dynamics of perturbations around globally rotating hyperbolic stagnation points in fluid flows. By employing a local analysis around such stagnation points we used a multiscale and ray-tracing methods to study the evolution of energetic quantities transported by the fluid flow. Dividing the analysis into two distinct parts, a weakly and strongly rotating case lead to an assortment of findings. In the weakly rotating case, where the Coriolis parameter was assumed $f \sim \mathcal{O}(\delta)$, we recovered part of the work in [6], who were also studying instabilities around hyperbolic stagnation points in globally rotating systems. Furthermore, by taking the distinguished limit $f \to 0$, we were also able to recover the work of [5], which was the first analysis of generic hyperbolic stagnation points in fluid flows in a non-rotating system. By employing a multiscale approach we have shown the work in [5] and [6] form special solutions of a broader framework of hyperbolic stagnation points within rotating systems.

This work also considers the case of strong rotation, i.e., $f \sim \mathcal{O}(1)$. Performing the multiscale analysis under this assumption made the subsequent task of solving the amplitude/energy PDEs considerably more difficult. Once again using the ray theoretic framework, we used the techniques described in [4], to extend the ray system to include spatial variations of the wavevector $\mathbf{k}$ to encode information along ray paths about the energy of perturbations through the quantity known as the wave action [3, 4, 10, 11]. We then performed a careful analysis to derive initial conditions for the ray system that lead to various dynamics of the perturbation energy along ray paths. We showed the existence of initial conditions leading to transient and bounded growth. Finally, we were also able to show the existence of unbounded growth of energy thereby showing the existence of a strongly rotating hyperbolic instability within a strongly rotating fluid.

The avenues for future work remain rich. In the weakly rotating case, the details of the formalism by which the works presented in [5], [6], [9] are related as being special solutions of a general theory for hyperbolic stagnation points under rotation will be worked out completely. This would unify the existing literature on hyperbolic stagnation points in fluid flows under a general theory. In the strongly rotating case, a comprehensive parameter study and analysis of initial conditions should also be carried out to further explore the possible dynamics of energetics around the stagnation points. In this regard, understanding the sign

of the Coriolis parameter $f$ and its applications to situations of geophysical interest would also be an interesting avenue to pursue. Finally, to further generalize the analysis presented here to problem of physical interest would be to add stratification.

## 6 Acknowledgements

I would like to thank Pascale Garaud, Colm-Cille Caulfield and Greg Chini for their support, patience and expertise throughout this project. It was a joy working and learning under their guidance. I would also like to thank Bruce Sutherland, Sam Lewin, Alexandre Tilli for helpful conversations in preparation of this work.

Thank you to Pascale and David Goluskin for directing a wonderful program as well as all the faculty and staff who attended this year's GFD program. Finally, I would like to thank my fellow fellows for making it a truly special summer.

## Appendix

These appendices provide the details of various calculations used throughout this work.

## A Conservation of Wave Action

We show wave action $\mathcal{A}$ is conserved. To this end, we make use of the polarization relations. These are derived using the leading order equations. We choose to express all variables in terms of the third leading order velocity field component $\hat{w}_0$. Consider (4.3), multiplying the first equation with $k$ and the second by $\ell$ and adding them

$$\frac{|\mathbf{k}|}{m}\left(k\hat{u}_0 + \ell\hat{v}_0\right) = i\left(k\hat{v}_0 - \ell\hat{u}_0\right). \tag{A.1}$$

Notice, this relates the third component leading order velocity to the third component of vorticity,

$$-|\mathbf{k}|\hat{w}_0 = i\zeta, \tag{A.2}$$

by using the leading order incompressibility condition on the left hand side. To gain expressions for the other two components in terms of $\hat{w}_0$, we have the following two relations,

$$i|\mathbf{k}|\hat{w}_0 = k\hat{v}_0 - \ell\hat{u}_0, \tag{A.3a}$$

$$-m\hat{w}_0 = k\hat{u}_0 + \ell\hat{v}_0. \tag{A.3b}$$

Multiplying, the first equation by $k$ and the second by $\ell$ and adding,

$$\hat{v}_0 = \frac{i|\mathbf{k}|k - \ell m}{k^2 + \ell^2}\hat{w}_0. \tag{A.4}$$

Similarly, multiplying the first relation by $-\ell$ and the second by $k$ and adding,

$$\hat{u}_0 = \frac{-\left(i|\mathbf{k}|\ell + km\right)}{k^2 + \ell^2}\hat{w}_0. \tag{A.5}$$

Finally, the pressure can be inferred from (4.2),

$$\hat{p}_0 = \frac{\omega_{\text{rot}}}{m}\hat{w}_0. \tag{A.6}$$

The first order polarization relations are therefore,

$$\hat{u}_0 = \frac{-\big(i|\mathbf{k}|\,\ell + km\big)}{k^2+\ell^2}\,\hat{w}_0, \tag{A.7a}$$

$$\hat{v}_0 = \frac{i|\mathbf{k}|\,k - \ell m}{k^2+\ell^2}\,\hat{w}_0, \tag{A.7b}$$

$$\hat{p}_0 = \frac{f}{|\mathbf{k}|}\,\hat{w}_0. \tag{A.7c}$$

We make implicit use of these relations to show wave action is conserved. Consider the following calculation.

$$\begin{aligned}
\partial_T\mathcal{A} + \nabla_{\mathbf{X}}\cdot\mathbf{c}_g\mathcal{A} &= \frac{|\mathbf{k}|}{fm}\left(\partial_T E + \nabla_{\mathbf{X}}\cdot\mathbf{c}_g E\right) + \frac{E}{fm}\left(\partial_T|\mathbf{k}| + \mathbf{c}_g\cdot\nabla_{\mathbf{X}}|\mathbf{k}|\right),\\
&= \frac{|\mathbf{k}|}{fm}\left(-\hat{\mathbf{u}}_0\cdot\left(\hat{\mathbf{u}}_0\cdot\nabla_{\mathbf{X}}\mathbf{U}\right)\right) + \frac{E}{fm}\left(-\frac{\mathbf{k}}{|\mathbf{k}|}\cdot\left(\mathbf{k}\cdot\nabla_{\mathbf{X}}\mathbf{U}\right)\right),\\
&= -\frac{|\mathbf{k}|}{fm}\left(\hat{\mathbf{u}}_0\cdot\left(\hat{\mathbf{u}}_0\cdot\nabla_{\mathbf{X}}\mathbf{U}\right) + \frac{|\hat{w}_0|}{k^2+\ell^2}\mathbf{k}\cdot\left(\mathbf{k}\cdot\nabla_{\mathbf{X}}\mathbf{U}\right)\right),\\
&= -\frac{|\mathbf{k}|}{fm}\left(\hat{\mathbf{u}}_0^{\mathrm{T}}\nabla_{\mathbf{X}}\mathbf{U}\hat{\mathbf{u}}_0 + \frac{|\hat{w}_0|}{k^2+\ell^2}\mathbf{k}^{\mathrm{T}}\nabla_{\mathbf{X}}\mathbf{U}\mathbf{k}\right),\\
&= -\frac{|\mathbf{k}|}{fm}\left(\hat{\mathbf{u}}_0^{\mathrm{T}}\mathbf{A}\hat{\mathbf{u}}_0 + \frac{|\hat{w}_0|}{k^2+\ell^2}\mathbf{k}^{\mathrm{T}}\mathbf{A}\mathbf{k}\right),\\
&= -\frac{|\mathbf{k}|}{fm}\left(\varepsilon|\hat{u}_0|^2 - \varepsilon|\hat{v}_0|^2 + \frac{|w_0|^2}{k^2+\ell^2}\left(\varepsilon k^2 - \varepsilon\ell^2\right)\right),\\
&= -\frac{|\mathbf{k}|}{fm}\left(\left(\frac{\ell^2(k^2+\ell^2) - k^2(k^2+\ell^2)}{(k^2+\ell^2)^2} + \frac{k^2-\ell^2}{k^2+\ell^2}\right)\varepsilon|\hat{w}_0|^2\right),\\
&= -\frac{|\mathbf{k}|}{fm}\left(\left(\frac{\ell^2 - k^2 + k^2 - \ell^2}{(k^2+\ell^2)}\right)\varepsilon|\hat{w}_0|^2\right),\\
&= 0.
\end{aligned} \tag{A.8}$$

For ease of calculation to our specific case, we have used the definition $\mathbf{U} = \mathbf{A}\mathbf{x}$ midway through. However, keep in mind the following computation will work for a general time independent 2D background flow $\mathbf{U}$. For a general proof and discussion of the conservation of wave action in Hamiltonian systems see [1, 3, 7].

# B Derivation of the Extended Ray System

We present the details of the derivation of (4.19). Recall, the dispersion relation, $\Omega(\mathbf{k}(\mathbf{X},T);\mathbf{X},T)$ and let $c_x$ and $c_y$ to be the $x$ and $y$ components of the group velocity $\mathbf{c}_g$, respectively. It

will be useful to write out the chain-rule for the spatial derivatives with respect to $X$ and $Y$,

$$\frac{\partial}{\partial X} = \left.\frac{\partial}{\partial X}\right|_{\mathbf{k}} + \frac{\partial k}{\partial X}\frac{\partial}{\partial k} + \frac{\partial \ell}{\partial X}\frac{\partial}{\partial \ell}, \tag{B.1a}$$

$$\frac{\partial}{\partial Y} = \left.\frac{\partial}{\partial Y}\right|_{\mathbf{k}} + \frac{\partial k}{\partial Y}\frac{\partial}{\partial k} + \frac{\partial \ell}{\partial Y}\frac{\partial}{\partial \ell}. \tag{B.1b}$$

The transport PDE for $k$ is,

$$\partial_T k + \mathbf{c}_g \cdot \nabla_{\mathbf{X}} k = -\partial_X \Omega. \tag{B.2}$$

Taking the $X$ derivative of both sides, re-arranging and exploiting the chain rule to evaluate,

$$\begin{aligned}
&\partial_T\left(\partial_X k\right) + \mathbf{c}_g \cdot \nabla_{\mathbf{X}}\left(\partial_X k\right) \\
&= -\partial_X\left(\partial_X \Omega\right) - \left(\left(\partial_X c_x\right)\left(\partial_X k\right) + \left(\partial_X c_y\right)\left(\partial_Y k\right)\right) \\
&= -\left[\partial_X^2 \Omega + \frac{\partial^2 \Omega}{\partial X \partial k}\frac{\partial k}{\partial X} + \frac{\partial^2 \Omega}{\partial X \partial \ell}\frac{\partial \ell}{\partial X}\right] - \left(\left(\partial_X c_x\right)\left(\partial_X k\right) + \left(\partial_X c_y\right)\left(\partial_Y k\right)\right) \\
&= -\left[\partial_X^2 \Omega + \frac{\partial^2 \Omega}{\partial X \partial k}\frac{\partial k}{\partial X} + \frac{\partial^2 \Omega}{\partial X \partial \ell}\frac{\partial \ell}{\partial X}\right] - \left[\frac{\partial^2 \Omega}{\partial X \partial k} + \frac{\partial^2 \Omega}{\partial k \partial \ell}\partial_X \ell + \frac{\partial^2 \Omega}{\partial k^2}\partial_X k\right]\left(\partial_X k\right) \\
&\qquad\qquad - \left[\frac{\partial^2 \Omega}{\partial X \partial \ell} + \frac{\partial^2 \Omega}{\partial k \partial \ell}\partial_X k + \frac{\partial^2 \Omega}{\partial \ell^2}\partial_X \ell\right]\left(\partial_Y k\right) \\
&= -\partial_X^2 \Omega - 2\left[\frac{\partial^2 \Omega}{\partial X \partial k}\left(\partial_X k\right) + \frac{\partial^2 \Omega}{\partial X \partial \ell}\left(\partial_Y k\right)\right] - 2\frac{\partial^2 \Omega}{\partial k \partial \ell}\left[\left(\partial_X \ell\right)\left(\partial_X k\right)\right] \\
&\qquad\qquad - \left[\frac{\partial^2 \Omega}{\partial k^2}\left(\partial_X k\right)^2 + \frac{\partial^2 \Omega}{\partial \ell^2}\left(\partial_Y k\right)^2\right]
\end{aligned} \tag{B.3}$$

The penultimate equality follows by recalling that $c_x = \partial_k \Omega$ and $c_y = \partial_\ell \Omega$ and applying the chain rule. The last line follows be re-arranging and recalling the curl free condition, i.e., $\partial_X \ell = \partial_Y k$. Hence, the ODE along ray paths for $\partial_X k$ is

$$\begin{aligned}
\frac{\mathrm{d}}{\mathrm{d}T}\left(\partial_X k\right) = &-\partial_X^2 \Omega - 2\left[\frac{\partial^2 \Omega}{\partial X \partial k}\left(\partial_X k\right) + \frac{\partial^2 \Omega}{\partial X \partial \ell}\left(\partial_Y k\right)\right] - 2\frac{\partial^2 \Omega}{\partial k \partial \ell}\left[\left(\partial_X \ell\right)\left(\partial_X k\right)\right] \\
&- \left[\frac{\partial^2 \Omega}{\partial k^2}\left(\partial_X k\right)^2 + \frac{\partial^2 \Omega}{\partial \ell^2}\left(\partial_Y k\right)^2\right].
\end{aligned} \tag{B.4}$$

The equation for $\partial_Y \ell$ can be obtained identically,

$$\begin{aligned}\frac{\mathrm{d}}{\mathrm{d}T}\left(\partial_Y \ell\right) = &-\partial_Y^2 \Omega - 2\left[\frac{\partial^2 \Omega}{\partial Y \partial \ell}\left(\partial_Y \ell\right) + \frac{\partial^2 \Omega}{\partial Y \partial k}\left(\partial_Y k\right)\right] - 2\frac{\partial^2 \Omega}{\partial \ell \partial k}\left[\left(\partial_Y k\right)\left(\partial_Y \ell\right)\right] \\ &- \left[\frac{\partial^2 \Omega}{\partial \ell^2}\left(\partial_Y \ell\right)^2 + \frac{\partial^2 \Omega}{\partial k^2}\left(\partial_Y k\right)^2\right].\end{aligned} \tag{B.5}$$

To gain the equation for $\partial_Y k$, we take the derivative with respect to $Y$ of (B.2),

$$\begin{aligned}&\partial_T\left(\partial_Y k\right) + \mathbf{c} \cdot \nabla_{\mathbf{X}}\left(\partial_Y k\right) \\ &= -\partial_Y\left(\partial_X \Omega\right) - \left(\left(\partial_Y c_x\right)\left(\partial_X k\right) + \left(\partial_Y c_y\right)\left(\partial_Y k\right)\right) \\ &= -\left[\partial_{XY}^2 \Omega + \frac{\partial^2 \Omega}{\partial X \partial k}\partial_Y k + \frac{\partial^2 \Omega}{\partial X \partial \ell}\partial_Y \ell\right] - \left[\frac{\partial^2 \Omega}{\partial Y \partial k} + \frac{\partial^2 \Omega}{\partial k^2}\partial_Y k + \frac{\partial^2 \Omega}{\partial k \partial \ell}\partial_Y \ell\right]\left(\partial_X k\right) \\ &\qquad - \left[\frac{\partial^2 \Omega}{\partial Y \partial \ell} + \frac{\partial^2 \Omega}{\partial \ell \partial k}\partial_Y k + \frac{\partial^2 \Omega}{\partial \ell^2}\partial_Y \ell\right]\left(\partial_Y k\right) \\ &= -\partial_{XY}^2 \Omega - \left[\frac{\partial^2 \Omega}{\partial X \partial k} + \frac{\partial^2 \Omega}{\partial Y \partial \ell}\right]\left(\partial_Y k\right) - \frac{\partial^2 \Omega}{\partial Y \partial k}\partial_X k - \frac{\partial^2 \Omega}{\partial X \partial \ell}\partial_Y \ell - \frac{\partial^2 \Omega}{\partial k^2}\partial_Y k \partial_X k \\ &\qquad - \frac{\partial^2 \Omega}{\partial k \partial \ell}\left(\partial_Y \ell\right)\left(\partial_X k\right) - \frac{\partial^2 \Omega}{\partial k \partial \ell}\left(\partial_Y k\right)^2 - \frac{\partial^2 \Omega}{\partial \ell^2}\partial_Y \ell \partial_Y k.\end{aligned} \tag{B.6}$$

Therefore, the extended equations in the ray tracing system will be comprised of

$$\begin{aligned}\frac{\mathrm{d}}{\mathrm{d}T}(\partial_X k) &= -\partial_X^2\Omega - 2\left[\frac{\partial^2\Omega}{\partial X\partial k}(\partial_X k) + \frac{\partial^2\Omega}{\partial X\partial \ell}(\partial_Y k)\right] \\ &\quad - 2\frac{\partial^2\Omega}{\partial k\partial \ell}(\partial_X \ell)(\partial_X k) - \left[\frac{\partial^2\Omega}{\partial k^2}(\partial_X k)^2 + \frac{\partial^2\Omega}{\partial \ell^2}(\partial_Y k)^2\right], \qquad \text{(B.7a)}\\ \frac{\mathrm{d}}{\mathrm{d}T}(\partial_Y \ell) &= -\partial_Y^2\Omega - 2\left[\frac{\partial^2\Omega}{\partial Y\partial \ell}(\partial_Y \ell) + \frac{\partial^2\Omega}{\partial Y\partial k}(\partial_Y k)\right] \\ &\quad - 2\frac{\partial^2\Omega}{\partial \ell\partial k}(\partial_Y k)(\partial_Y \ell) - \left[\frac{\partial^2\Omega}{\partial \ell^2}(\partial_Y \ell)^2 + \frac{\partial^2\Omega}{\partial k^2}(\partial_Y k)^2\right], \qquad \text{(B.7b)}\\ \frac{\mathrm{d}}{\mathrm{d}T}(\partial_Y k) &= -\partial_{XY}^2\Omega - \left[\frac{\partial^2\Omega}{\partial X\partial k} + \frac{\partial^2\Omega}{\partial Y\partial \ell}\right](\partial_Y k) \\ &\quad - \frac{\partial^2\Omega}{\partial Y\partial k}(\partial_X k) - \frac{\partial^2\Omega}{\partial X\partial \ell}(\partial_Y \ell) \\ &\quad - \frac{\partial^2\Omega}{\partial k^2}(\partial_Y k)(\partial_X k) - \frac{\partial^2\Omega}{\partial k\partial \ell}(\partial_Y \ell)(\partial_X k) \\ &\quad - \frac{\partial^2\Omega}{\partial k\partial \ell}(\partial_Y k)^2 - \frac{\partial^2\Omega}{\partial \ell^2}(\partial_Y \ell)(\partial_Y k). \qquad \text{(B.7c)}\end{aligned}$$

Turning to our specific case, some immediate simplifications can be made taking the dispersion relation $\Omega$ as in (4.4), since the background $\mathbf{U} = \mathbf{AX}$ is linear in $X$ and $Y$, the second space derivatives on $\Omega$ vanish. Computing out the other derivatives,

$$\frac{\partial^2\Omega}{\partial X\partial k} = \varepsilon, \quad \frac{\partial^2\Omega}{\partial Y\partial \ell} = -\varepsilon, \quad \frac{\partial^2\Omega}{\partial Y\partial k} = -\gamma, \quad \frac{\partial^2\Omega}{\partial X\partial \ell} = \gamma. \qquad \text{(B.8)}$$

$$\frac{\partial^2\Omega}{\partial k^2} = -\frac{fm}{|\mathbf{k}|^5}\left(-2k^2 + \ell^2 + m^2\right), \ \frac{\partial^2\Omega}{\partial \ell^2} = -\frac{fm}{|\mathbf{k}|^5}\left(k^2 - 2\ell^2 + m^2\right), \ \frac{\partial^2\Omega}{\partial k\partial \ell} = \frac{3f}{|\mathbf{k}|^5}k\ell m. \qquad \text{(B.9)}$$

Substituting this into (B.7a), (B.7b), (B.7c) and making the necessary simplifications yields (4.19).

## References


[1] D. G. Andrews and M. McIntyre, *On wave-action and its relatives*, Journal of Fluid Mechanics, 89 (1978), pp. 647–664.

[2] C. M. Bender and S. A. Orszag, *Advanced mathematical methods for scientists and engineers I: Asymptotic methods and perturbation theory*, Springer Science & Business Media, 2013.

[3] F. P. Bretherton and C. J. R. Garrett, *Wavetrains in inhomogeneous moving media*, Proceedings of the Royal Society of London. Series A. Mathematical and Physical Sciences, 302 (1968), pp. 529–554.

[4] O. Bühler, *Waves and mean flows*, Cambridge monographs on mechanics, Cambridge University Press, Cambridge, second edition ed., 2014.

[5] C. P. Caulfield and R. R. Kerswell, *The nonlinear development of three-dimensional disturbances at hyperbolic stagnation points: A model of the braid region in mixing layers*, Physics of Fluids, 12 (2000), pp. 1032–1043.

[6] Y. Hattori and M. Hirota, *Stability of two-dimensional taylor–green vortices in rotating stratified fluids*, Journal of Fluid Mechanics, 967 (2023), p. A32.

[7] W. Hayes, *Conservation of action and modal wave action*, Proceedings of the Royal Society of London. A. Mathematical and Physical Sciences, 320 (1970), pp. 187–208.

[8] S. Leblanc and C. Cambon, *On the three-dimensional instabilities of plane flows subjected to coriolis force*, Physics of Fluids, 9 (1997), pp. 1307–1316.

[9] ——, *Effects of the coriolis force on the stability of stuart vortices*, Journal of Fluid Mechanics, 356 (1998), pp. 353–379.

[10] B. R. Sutherland, *Internal gravity waves*, Cambridge university press, 2010.

[11] G. B. Whitham, *Linear and nonlinear waves*, John Wiley & Sons, 2011.

# Weakly Nonlinear Hamiltonian Dynamics of an Isolated Vortex

Alexandre Tlili

August 19, 2025

## 1 Introduction

Coherent vortical structures are a common feature of two-dimensional and quasi-two-dimensional turbulent flows. In many geophysical systems, such as the atmosphere and oceans, strong rotation and stratification constrain the motion to nearly horizontal planes, allowing long-lived eddies to form and persist. Well-known examples include Jupiter's Great Red Spot [15], which has remained stable for centuries, as well as mesoscale vortices observed in the ocean that can survive up to a few years while transporting heat and nutrients [6, 10, 16]. Laboratory experiments and numerical simulations of two-dimensional turbulence have shown that these coherent vortices can spontaneously form from initially random flow fields [12, 4] or after breakup of larger vortices [5]. Such structures play a crucial role in organizing the flow and influencing large-scale transport properties [13]. Idealized models, from the two-dimensional incompressible Euler equations to layered shallow-water formulations, provide a useful framework for studying their dynamics.

In this report, we focus on the simplest case of vorticity distributions which are barotropic and piecewise-constant. Those distributions were introduced by [17] in the context of contour dynamics as a way to numerically simulate sharp vorticity gradients [7]. More precisely, we revisit the set-up of [8] where a compact axisymmetric base state with inner vorticity $q = 1$ for $r < 1$ and outer vorticity $q_b$ for $1 < r < b$ is perturbed, leading to deformation of the contours separating the different vorticity regions (Figure 1). [8] performed the linearly stability of this set-up and computed that the bifurcation was subcritical (destabilizing nonlinearity). [11] studied the stability of the base-state from energetics arguments similar to Arnold's stability criterion, recovering the same results as the linear stability analysis. Finally, Georges I. Bell proposed in his 1990 GFD report [1] a reduced Hamiltonian model for the nonlinear dynamics of the vortex, by numerically fitting coefficients to match outputs from a contour dynamics code. Indeed, in the absence of viscosity, the system inherits the Hamiltonian properties of the Euler equations [14, 3] and can be described within the non-canonical Hamiltonian formalism. Morrison and Flierl (private communication) derived the Hamiltonians and Poisson brackets associated to different parametrizations of the contours. We heavily build on their work (referred as M&F in the following) in this report.

In Section 2, we use the formalism developed by M&F to derive different low order Hamiltonian approximations of increasing complexity, approximating the full dynamics and derived directly from the equations of motion. We show in Section 3 that it allows to recover

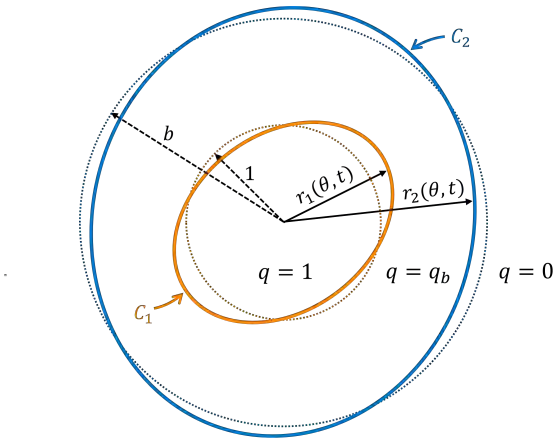


Figure 1: Barotropic piecewise-constant distribution of vorticity with two contours. The dotted curves are the contours of the base state (axisymmetric configuration with dimensionless radii 1 and $b$) and the solid curves correspond to the deformed contours parametrized by $r_i(\theta,t)$. The dimensionless vorticity $q$ is shown in each region.

the stability analysis of [8] and to obtain the amplitude equation close to the bifurcation. In Section 4, we study the steadily rotating solutions, called V-states, of the truncated models, giving possible approximation of the V-states of the full system.

# 2 From the Full Dynamics to Truncated Hamiltonian Models

## 2.1 Contour dynamics

The evolution of piecewise-constant barotropic vorticity distributions can be understood from the dynamics of their contours. In barotropic Euler equations without background strain, the velocity $\boldsymbol{u}(\boldsymbol{x})$ at any point $\boldsymbol{x}$ can be computed from the positions of the contours $C_i$ using the Biot-Savart law [17]. It reads

$$\boldsymbol{u}(\boldsymbol{x}) = \sum_i \frac{\Delta_i}{2\pi} \oint_{C_i} \log|\boldsymbol{x}-\boldsymbol{x}'|\,\mathrm{d}\boldsymbol{\ell}(\boldsymbol{x}') \tag{1}$$

with $\mathrm{d}\boldsymbol{\ell}(\boldsymbol{x}')$ the infinitesimal tangential vector and $(\Delta_i)_i$ the vorticity jumps ($\Delta_1 = 1-q_b$ and $\Delta_2 = q_b$). Then, by material conservation of the vorticity in the barotropic Euler equations, the contours are simply advected by the flow using

$$\frac{\mathrm{d}\boldsymbol{x}}{\mathrm{d}t} = \boldsymbol{u}(\boldsymbol{x})\,. \tag{2}$$

Equations (1) and (2) can be used to numerically solve the evolution of the contours by discretizing them into polygonal shapes. In this report, we used a homemade contour dynamics code following the procedure described in [18] and monitoring the conservation of area and angular momentum to assess the validity of the simulation. In the following, we refer to these simulations as the DNS.

## 2.2 Full Hamiltonian formulation

In this section, we present the Hamiltonian formulation of the contour dynamics problem. Following M&F, we parameterize the position of the perturbed contours $C_i$ in polar coordinates (assuming that no folding has occurred). More precisely, we define

$$\xi_i(\theta,t) = r_i(\theta,t)^2 = b_i + \eta_i(\theta,t)\,, \tag{3}$$

where $\eta_i(\theta, t=0)$ has zero average which respect to $\theta$. From the conservation of the area $\int \frac{1}{2}\xi_i(\theta)\,\mathrm{d}\theta$ enclosed by $C_i$, $\eta_i(\theta,t)$ remains zero-average at all times, which is a strong advantage compared to the parametrization used in [11]. With our nondimensionalization (see Figure 1), we have $b_1 = 1$ and $b_2 = b^2$. Then, M&F showed that the dynamics of the Fourier modes $\eta_{i,m}(t) = (2\pi)^{-1}\int \eta_i(\theta,t)e^{-im\theta}\,\mathrm{d}\theta$ was given by

$$\frac{\mathrm{d}\eta_{i,m}}{\mathrm{d}t} = \frac{2im}{\pi\Delta_i}\frac{\partial H}{\partial \eta^*_{i,m}}\,, \tag{4}$$

with $H$ the Hamiltonian related to the position of the contours by

$$H = -\frac{1}{8}\Delta_i\Delta_j\int_0^{2\pi}\mathrm{d}\theta\int_0^{\xi_i(\theta)}\mathrm{d}\xi\int_0^{2\pi}\mathrm{d}\theta'\int_0^{\xi_j(\theta')}\mathrm{d}\xi'\,G(\rho(\xi,\xi',\theta-\theta'))\,. \tag{5}$$

using Einstein's summation convention for indices $i$ and $j$. The Green function $G$ appearing in the integrals is associated with the inversion of the vorticity/streamfunction relationship in the barotropic Euler equations, and $\rho(\xi,\xi',\theta-\theta')$ is the distance between $\sqrt{\xi}[\cos\theta,\sin\theta]^T$ and $\sqrt{\xi'}[\cos\theta',\sin\theta']^T$. Both read

$$\begin{cases} G(\rho) = (2\pi)^{-1}\log\rho\,, \\ \rho(\xi,\xi',\phi) = \sqrt{\xi+\xi'-2\sqrt{\xi\xi'}\cos\phi}\,. \end{cases} \tag{6}$$

Equations (4-6) express the full dynamics of the contours, as long as no folding occurs ($\eta_i(\theta,t)$ has to remain single-valued) and provided that the origin remains inside the inner contour.

## 2.3 Taylor expansion of the Hamiltonian

This subsection is more technical. Readers who are only interested in the general picture and applications can skip to Section 2.4 and return later to find the explicit coefficients of the truncated models.

We are interested in the dynamics of contours that are weakly perturbed compared to the circular configuration $\xi_i(\theta) = b_i$. As such, we assume $|\eta_i(\theta,t)| \ll b_i$ and perform a Taylor expansion of the Hamiltonian $H$ in increasing powers of the perturbations $(\eta_i)_i$. Following M&F, we expand the integrals as

$$\int_0^{2\pi}\mathrm{d}\theta\int_0^{b_i+\eta_i(\theta)}\mathrm{d}\xi\,f(\xi,\theta;\boldsymbol{p}) = \sum_{n=0}^{N}\frac{1}{n!}\frac{\partial^n}{\partial b_i^n}\left[\int_0^{2\pi}\mathrm{d}\theta\int_0^{b_i}\mathrm{d}\xi\,\eta_i(\theta)^n f(\xi,\theta;\boldsymbol{p})\right] + O\left(\eta_i^{N+1}\right) \tag{7}$$

where $f$ is any smooth function of $\xi$, $\theta$ and possibly other parameters $\boldsymbol{p}$. Then, discarding the logarithmic singularity, the Hamiltonian can be formally expanded as $H = \sum_{p\geq 0} \delta^p H$, where the variation at order $p$ is given according to the Fourier coefficients $(\eta_{i,m})$ by

$$\delta^p H = -\frac{\pi}{4}\Delta_i\Delta_j \sum_{\substack{r+n=p\\ r,n\geq 0}} \frac{1}{n!r!} \sum_{\substack{k_1,\cdots,k_n\in\mathbb{Z}\\ \ell_1,\cdots,\ell_r\in\mathbb{Z}\\ k_1+\cdots+\ell_r=0}} (\eta_{i,k_1}\cdots\eta_{i,k_n})\,(\eta_{j,\ell_1}\cdots\eta_{j,\ell_r})\,\frac{\partial^p I}{\partial A^n \partial B^r}(\ell_1+\cdots+\ell_r|b_i,b_j) \tag{8}$$

where summation over indices $(i,j)$ is implicit and the function $I(M|A,B)$ is related to the Green function by

$$I(M|A,B) = \int_0^A \mathrm{d}\xi \int_0^B \mathrm{d}\xi' \int_0^{2\pi} \mathrm{d}\phi\, \cos(M\phi) G\left(\rho(\xi,\xi',\phi)\right)\,. \tag{9}$$

Using symmetries $I(M|A,B) = I(-M|A,B) = I(M|B,A)$, we can recover the expressions of the first variations of the Hamiltonian. The constant term $\delta^0 H$ corresponding to the base state can be computed, and the linear term $\delta^1 H$ vanishes showing that the reference configuration is indeed an equilibrium point. Both read

$$\delta^0 H = -\frac{\pi}{8(1+\Delta)^2}\left[1+2\Delta+\Delta^2 b^4 + 4\Delta b^2\log b\right] \quad \text{and} \quad \delta^1 H = 0\,. \tag{10}$$

where $\Delta = \Delta_2/\Delta_1$ is the ratio of the vorticity jumps. For the isolated vortex specifically, we have $\Delta = -1/b^2$ and $\delta^0 H = -\frac{\pi}{4}(1+\Delta-2\log b)/(1+\Delta)^2$ which tends to the finite value $\pi/8$ as the outer shell disappears ($b\to 1^+$). Computing the quadratic component of the Hamiltonian (which controls the linear dynamics) gives

$$\delta^2 H = -\frac{\pi}{2}\sum_{m=1}^{\infty} \hat{\eta}_{i,m} A_{ij}^{(m)} \hat{\eta}_{j,m}^* = \sum_{m=1}^{\infty} H_{(m,m)} \tag{11}$$

with the real and symmetric matrices $\boldsymbol{A}^{(m)}$ given by

$$\boldsymbol{A}^{(m)} = \frac{1}{2(1+\Delta)^2}\begin{pmatrix} \left(1-\frac{1}{m}\right)+\Delta & -\frac{\Delta}{mb^m} \\ -\frac{\Delta}{mb^m} & \Delta^2\left(1-\frac{1}{m}\right)+\frac{\Delta}{b^2}\end{pmatrix}\,. \tag{12}$$

We recover the results from M&F, with a prefactor $(1+\Delta)^{-2}$ due to our different non-dimensionalization. Equations (4), (11) and (12) show that Fourier modes are decoupled in the linear dynamics, which was observed by [8] and is a consequence of the axial symmetry $SO_2$ of the problem. The next variations of the Hamiltonian are given by

$$\delta^3 H = -\frac{\pi}{4}\Delta_i\Delta_j \sum_{m,n\in\mathbb{Z}} \left[\frac{1}{3}\eta_{i,m}\eta_{i,n}\eta_{i,-n-m}\frac{\partial^3 I}{\partial A^3}(0|b_i,b_j) + \eta_{i,m}\eta_{i,-n-m}\eta_{j,n}\frac{\partial^3 I}{\partial A^2\partial B}(n|b_i,b_j)\right] \tag{13}$$

at third order (triadic interactions) and we have a fourth order (quartet interactions) that

$$\begin{aligned}\delta^4 H = -\frac{\pi}{4}\Delta_i\Delta_j \sum_{n,m,\ell\in\mathbb{Z}} \Bigg[&\frac{1}{12}\eta_{i,n}\eta_{i,m}\eta_{i,\ell}\eta_{i,-n-m-\ell}\frac{\partial^4 I}{\partial A^4}(0|b_i,b_j) \\ &+\frac{1}{3}\eta_{i,m}\eta_{i,\ell}\eta_{i,-n-m-\ell}\eta_{j,n}\frac{\partial^4 I}{\partial A^3\partial B}(n|b_i,b_j) \\ &+\frac{1}{4}\,\eta_{i,n}\eta_{i,m}\eta_{j,\ell}\eta_{j,-n-m-\ell}\frac{\partial^4 I}{\partial A^2\partial B^2}(n+m|b_i,b_j)\Bigg]\,,\end{aligned} \tag{14}$$

where summation over indices $i$ and $j$ is implied. Variations of the Hamiltonian at order 3 and 4 are much more cumbersome than the previous ones, and providing explicit interaction coefficients for each triad results from a lengthy enumeration of the different permutations appearing in the summation. To simplify the computation, one can focus on a subset of triadic and quartet interactions between different harmonics of a given mode $m > 0$. The different components write

$$H_{(m,m,2m)} = -\frac{\pi}{2} C_{ijk}^{(m,m,2m)} (\eta_{i,m}^* \eta_{j,m}^* \eta_{k,2m} + c.c.)\,, \tag{15}$$

$$H_{(m,2m,3m)} = -\frac{\pi}{2} C_{ijk}^{(m,2m,3m)} (\eta_{i,m}^* \eta_{j,2m}^* \eta_{k,3m} + c.c.)\,, \tag{16}$$

$$H_{(m,m,m,m)} = -\frac{\pi}{2} D_{ijk\ell}^{(m,m,m,m)} \eta_{i,m}^* \eta_{j,m}^* \eta_{k,m} \eta_{\ell,m}\,, \tag{17}$$

$$H_{(2m,m,m,2m)} = -\frac{\pi}{2} D_{ijk\ell}^{(2m,m,m,2m)} \eta_{i,2m}^* \eta_{j,m}^* \eta_{k,m} \eta_{\ell,2m}\,, \tag{18}$$

$$H_{(m,m,m,3m)} = -\frac{\pi}{2} D_{ijk\ell}^{(m,m,m,3m)} (\eta_{i,m}^* \eta_{j,m}^* \eta_{k,m}^* \eta_{\ell,3m} + c.c.)\,, \tag{19}$$

where the tensors $\boldsymbol{C}^{(m,m,2m)}$, $\boldsymbol{C}^{(m,2m,3m)}$, $\boldsymbol{D}^{(m,m,m,m)}$, $\boldsymbol{D}^{(2m,m,m,2m)}$, and $\boldsymbol{D}^{(m,m,m,3m)}$ are functions of $b$ and $\Delta$, or $b$ alone for an isolated vortex. An explicit computation of the tensors can be performed and gives

$$\boldsymbol{C}^{(m,m,2m)} = \frac{1}{(1+\Delta)^2} \left( \begin{array}{cc|cc} -\frac{1}{8} & -\frac{\Delta}{4b^m} & -\frac{\Delta}{8b^{2m}} & \frac{\Delta}{4b^{2+m}} \\ 0 & \frac{\Delta}{8b^{2+2m}} & 0 & -\left(\frac{\Delta}{4b^4} + \frac{\Delta^2}{8b^2}\right) \end{array} \right), \tag{20}$$

$$\boldsymbol{C}^{(m,2m,3m)} = \frac{1}{(1+\Delta)^2} \left( \begin{array}{cc|cc} -\frac{1}{4} & -\frac{\Delta}{4b^{2m}} & -\frac{\Delta}{4b^{3m}} & \frac{\Delta}{4b^{m+2}} \\ -\frac{\Delta}{4b^m} & \frac{\Delta}{4b^{3m+2}} & \frac{\Delta}{4b^{2m+2}} & -\left(\frac{\Delta}{2b^4} + \frac{\Delta^2}{4b^2}\right) \end{array} \right), \tag{21}$$

$$\boldsymbol{D}^{(m,m,m,m)} = \frac{1}{(1+\Delta)^2} \left( \begin{array}{cc|cc} \frac{2-m}{16} & \frac{(2-m)\Delta}{16b^m} & 0 & 0 \\ 0 & \frac{m\Delta}{16b^{2m+2}} & 0 & -\frac{(2+m)\Delta}{16b^{m+4}} \\ \hline \frac{(2-m)\Delta}{16b^m} & 0 & \frac{m\Delta}{16b^{2m+2}} & -\frac{(2+m)\Delta}{16b^{m+4}} \\ 0 & 0 & 0 & \frac{\Delta}{4b^6} + \frac{(2-m)\Delta^2}{16b^4} \end{array} \right), \tag{22}$$

$$\boldsymbol{D}^{(2m,m,m,2m)} = \frac{1}{(1+\Delta)^2} \left( \begin{array}{cc|cc} \frac{2-m}{4} & \frac{(2-m)\Delta}{8b^m} & \frac{(1-m)\Delta}{4b^{2m}} & \frac{m\Delta}{8b^{m+2}} \\ \frac{(1-m)\Delta}{4b^{2m}} & \frac{3m\Delta}{8b^{3m+2}} & 0 & -\frac{(m+2)\Delta}{8b^{m+4}} \\ \hline \frac{(2-m)\Delta}{8b^m} & 0 & \frac{3m\Delta}{8b^{3m+2}} & -\frac{(m+1)\Delta}{4b^{2m+4}} \\ \frac{m\Delta}{8b^{m+2}} & -\frac{(m+1)\Delta}{4b^{2m+4}} & -\frac{(m+2)\Delta}{8b^{m+4}} & \frac{\Delta}{b^6} + \frac{(2-m)\Delta^2}{4b^4} \end{array} \right), \tag{23}$$

$$\boldsymbol{D}^{(m,m,m,3m)} = \frac{1}{(1+\Delta)^2} \left( \begin{array}{cc|cc} \frac{1}{12} & \frac{(2-m)\Delta}{16b^m} & \frac{(2-3m)\Delta}{48b^{3m}} & \frac{m\Delta}{8b^{2m+2}} \\ 0 & \frac{m\Delta}{8b^{2m+2}} & 0 & -\frac{(m+2)\Delta}{16b^{m+4}} \\ \hline 0 & 0 & 0 & 0 \\ 0 & -\frac{(3m+2)\Delta}{48b^{3m+4}} & 0 & \frac{\Delta}{6b^6} + \frac{\Delta^2}{12b^4} \end{array} \right). \tag{24}$$

In Equations (20-24), the indexing conventions for the rank 3 and rank 4 tensors are

$$\boldsymbol{C} = \left( \begin{array}{cc|cc} C_{111} & C_{121} & C_{112} & C_{122} \\ C_{211} & C_{221} & C_{212} & C_{222} \end{array} \right) \qquad \text{and} \qquad \boldsymbol{D} = \left( \begin{array}{cc|cc} D_{1111} & D_{1211} & D_{1112} & D_{1212} \\ D_{2111} & D_{2211} & D_{2112} & D_{2212} \\ \hline D_{1121} & D_{1221} & D_{1122} & D_{1222} \\ D_{2121} & D_{2221} & D_{2122} & D_{2222} \end{array} \right).$$

Finally, the tensors above were given in sparse form, to reduce the redundancy of the coefficients while ensuring that the energy is real-valued. To simplify computations in most applications, it is helpful to use their symmetrized counterparts in accordance with the symmetries of Equations (15-19) with respect to permutations of the indices. The symmetrization rules are given by

$$\begin{aligned}
C_{ijk}^{(m,m,2m)} &\to \frac{1}{2}\left(C_{ijk} + C_{jik}\right) , \\
D_{ijk\ell}^{(m,m,m,m)} &\to \frac{1}{4}\left(D_{ijk\ell} + D_{jik\ell} + D_{ij\ell k} + D_{ji\ell k}\right) , \\
D_{ijk\ell}^{(m,m,m,3m)} &\to \frac{1}{6}\left(D_{ijk\ell} + D_{jik\ell} + D_{ikj\ell} + D_{kji\ell} + D_{jki\ell} + D_{kij\ell}\right) ,
\end{aligned}$$

where the tensor subscripts have been dropped on the RHS for brevity.

### 2.4 Some truncated Hamiltonian models

An important advantage of the Hamiltonian formulation is that it allows us to come up with truncated models that preserve the Hamiltonian structure of the full dynamics. In general, one can choose to keep some terms of the Taylor expansion shown above, either arbitrarily or based on a specified hierarchy of amplitudes for the Fourier modes. If this hierarchy is motivated by physical arguments or observations, one can expect the resulting truncated model to provide a good approximation of the full dynamics. For instance, if one assumes infinitesimal Fourier coefficients, the linear dynamics of all modes are given by the truncated Hamiltonian

$$H_{\text{lin}} = \sum_{m\geq 1} H_{(m,m)} \, . \tag{25}$$

On the other hand, if one is interested in the weakly nonlinear (WNL) dynamics of a mode $m \geq 2$ and assumes that all other modes are initially set to zero, only subharmonic modes $km$ ($k \in \mathbb{Z}^*$) can be excited. If we assume a hierarchy of the form $\boldsymbol{\eta}_m = O(\varepsilon)$, $\boldsymbol{\eta}_{2m} = O(\varepsilon^2)$, $\boldsymbol{\eta}_{3m} = O(\varepsilon^3)$, and so on, we can come up with an approximation of order $O(\varepsilon^4)$ of the Hamiltonian. It reads

$$H_{\text{WNL}} = \underbrace{H_{(m,m)} + H_{(2m,2m)}}_{\text{linear dynamics}} + \underbrace{H_{(m,m,2m)}}_{\text{triad interactions}} + \underbrace{H_{(m,m,m,m)}}_{\text{quartet interactions}} \, . \tag{26}$$

and we have $H = H_{\text{WNL}} + O(\varepsilon^6)$. An extension to the next order, including the interactions with the mode $3m$ gives

$$H_{\text{WNL+}} = H_{\text{WNL}} + \underbrace{H_{(3m,3m)}}_{\text{linear dynamics}} + \underbrace{H_{(m,2m,3m)}}_{\text{triad interactions}} + \underbrace{H_{(2m,m,m,2m)} + H_{(m,m,m,3m)}}_{\text{quartet interactions}}, \tag{27}$$

and compares to the full Hamiltonian as $H = H_{\text{WNL+}} + O(\varepsilon^8)$. The evolution of the system under the truncated Hamiltonians can be solved numerically. Figure 2 shows the evolution of the amplitudes of the Fourier coefficients $\boldsymbol{\eta}_m$ and $\boldsymbol{\eta}_{2m}$, for an isolated vortex with $b = 2.05$, when solving the full dynamics with the DNS (Equations 1-2) or using the truncated Hamiltonians (26) and (27). It shows that both WNL and WNL+ capture well

the nonlinear evolution of the modes $m = 2$ and $2m = 4$, with relative errors less than 1% in the amplitude of the oscillations. However, the oscillations of the mode $2m$ become out of phase after a few turnover times in the WNL model, while they remain in good agreement with the DNS for the WNL+ model. Thus, we expect the truncated models to provide increased accuracy with the number of included terms.

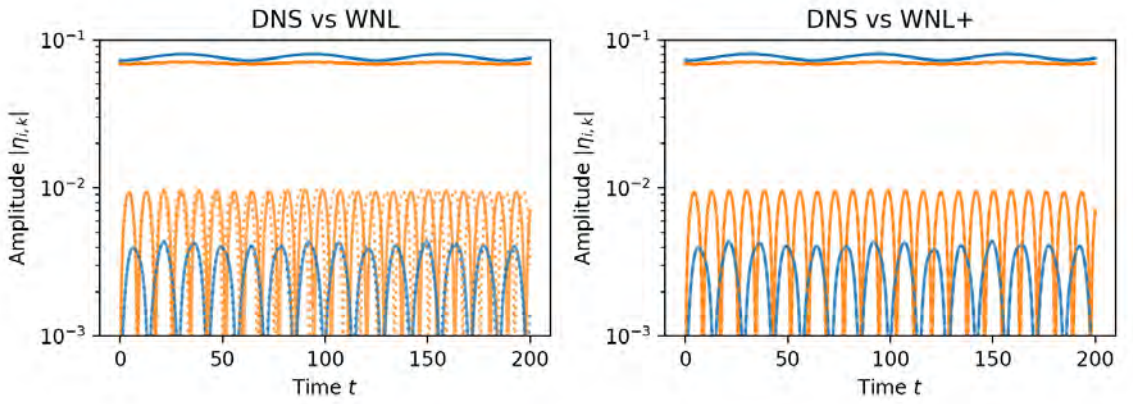


Figure 2: Comparison of Fourier coefficients amplitudes between the DNS and the truncated Hamiltonians $H_{\mathrm{WNL}}$ (left) and $H_{\mathrm{WNL+}}$ (right). Solid lines show the DNS results while dashed and dotted lines correspond to the WNL+ and WNL evolution, respectively. Blue curves correspond to the outer contour $\eta_2$ and orange curves to the inner contour $\eta_1$. The turnover time of the inner vorticity patch is $4\pi\omega_{\mathrm{in}}^{-1}$.

# 3 Linear Bifurcation and Weakly Nonlinear Analysis of an Isolated Vortex

In this section, we use the hierarchy of truncated Hamiltonians derived above to recover the linear stability analysis of [8] and characterize the type of bifurcations for low modes $m$. The derived amplitude equation can be used to predict the position of the separatrix between bounded evolution and vortex splitting, and to find nonlinear solutions close to the bifurcation.

## 3.1 Linear stability analysis

The linear dynamics is given by the second variation of the Hamiltonian, derived in Section (2.3). It reads

$$\delta^2 H = \sum_{m\geq 1} H_{(m,m)} = -\frac{\pi}{2}\sum_{m\geq 1} \eta^*_{i,m} A^{(m)}_{ij} \eta_{j,m} = -\frac{\pi}{2}\sum_{m\geq 1} \boldsymbol{\eta}^*_m \cdot \boldsymbol{A}^{(m)} \cdot \boldsymbol{\eta}_m \tag{28}$$

using Einstein's summation convention on indices $i, j$. From Equation (4), the linear evolution of the Fourier coefficients is given by

$$\forall m, \quad \boldsymbol{L}\cdot\frac{\mathrm{d}\boldsymbol{\eta}_m}{\mathrm{d}t} = -im\,\boldsymbol{A}^{(m)}\cdot\boldsymbol{\eta}_m \quad \longleftrightarrow \quad \frac{\mathrm{d}\boldsymbol{\eta}_m}{\mathrm{d}t} = -im\left(\boldsymbol{L}^{-1}\boldsymbol{A}^{(m)}\right)\cdot\boldsymbol{\eta}_m\,. \tag{29}$$

with $\boldsymbol{L} = \mathrm{diag}(\Delta_1, \Delta_2)$ the $2 \times 2$ diagonal matrix of vorticity jumps. As mentioned in Section 2.3, the Fourier modes are decoupled in the linearized problem, making it a suitable set of normal modes. The linear evolution can then be solved by computing the eigenmode/eigenvalue pairs of the tensors $\boldsymbol{L}^{-1}\boldsymbol{A}^{(m)}$. Indeed, if we focus on a given normal mode $m \geq 1$ and write $\boldsymbol{\eta}_m(t) = e^{-im\Omega_\pm t}\boldsymbol{u}_\pm$, we obtain the generalized eigenvalue problem $\boldsymbol{A}^{(m)} \cdot \boldsymbol{u}_\pm = \Omega_\pm \boldsymbol{L} \cdot \boldsymbol{u}_\pm$ whose solutions are given by the dispersion relation

$$\Omega_\pm = \frac{1}{4}\left(1 - \frac{1}{m}\right) \pm \frac{1}{4mb^{m+1}} \frac{b^2}{b^2-1} \sqrt{\left(b^{m+1}(m-1) - b^{m-1}(m+1)\right)^2 - 4} \tag{30}$$

where we specified that $\Delta = -1/b^2$ for an isolated vortex. Thus, the isolated vortex is linearly stable to a perturbation of the mode $m$ provided the radicand is positive. In this case, the infinitesimal perturbation rotates freely at rates $\Omega_\pm$ without attenuation. On the other hand, if the radicand is negative, $\Omega_+$ (resp. $\Omega_-$) corresponds to an exponentially growing (resp. decaying) perturbation, rotating with rate $\Omega_c = \frac{1}{4}\left(1 - \frac{1}{m}\right)$. The dispersion relation is shown in Figure 3 and recovers the results of [8] (see their Figure 3). [8] also computed analytically for each of the first few modes the critical values $b_c$ of the outer radius below which the isolated vortex becomes linearly unstable for this mode. We recover the same values of $b_c = 2$ for $m = 2$, $b_c = \sqrt{1+\sqrt{2}}$ for $m = 3$ and $b_c = \frac{1}{3}\left(2 + 10^{1/3}\right)$ for $m = 4$. At the critical value $b_c$, the generalized eigenvalue problem is degenerate and admits a unique solution (up to a multiplication of the eigenvector by a complex constant) given by

$$\boldsymbol{A}^{(m)} \cdot \boldsymbol{e}_c = \Omega_c \boldsymbol{L} \cdot \boldsymbol{e}_c \quad \text{at} \quad b = b_c \tag{31}$$

where $\boldsymbol{e}_c$, $\Omega_c$ and $b_c$ are implicit functions of the mode $m$ considered.

### 3.2 Weakly nonlinear analysis at a bifurcation

When the outer radius $b$ is smaller than the critical value $b_c$ associated with a given mode $m \geq 2$, the isolated vortex is linearly unstable to a perturbation of this mode. Using matching of the streamfunction across the boundaries of the isolated vortex, [8] showed that the bifurcation was subcritical in the sense that the nonlinearity is destabilizing. This is also what we observe in numerical simulations. In this section, we adapt the weakly nonlinear analysis performed by M&F in order to compute the influence of the nonlinearities close to the bifurcation.

Let us consider a given mode $m \geq 2$ undergoing a bifurcation at outer radius $b_c$ (linearly unstable if $b < b_c$). Close to the bifurcation, we denote by $\varepsilon = b - b_c \ll 1$ the distance to the bifurcation (signed). The prediction from the linearized dynamics gives the following evolution along the eigenspaces

$$e^{im\Omega_c t}\eta_{j,m}(t) = e^{-im(\Omega_\pm - \Omega_c)t}\eta_{j,m}(0) \tag{32}$$

where the LHS corresponds to the evolution of the perturbation in the frame rotating at rate $\Omega_c$. From a Taylor expansion of the dispersion relation in the vicinity of $b_c$, one can compute

$$m\left(\Omega_\pm - \Omega_c\right) \sim \pm \frac{\varepsilon^{1/2}}{2b_c^{m/2}} \sqrt{\frac{m^2-1}{b_c^2-1}} \quad \text{for} \quad \varepsilon \to 0 \tag{33}$$

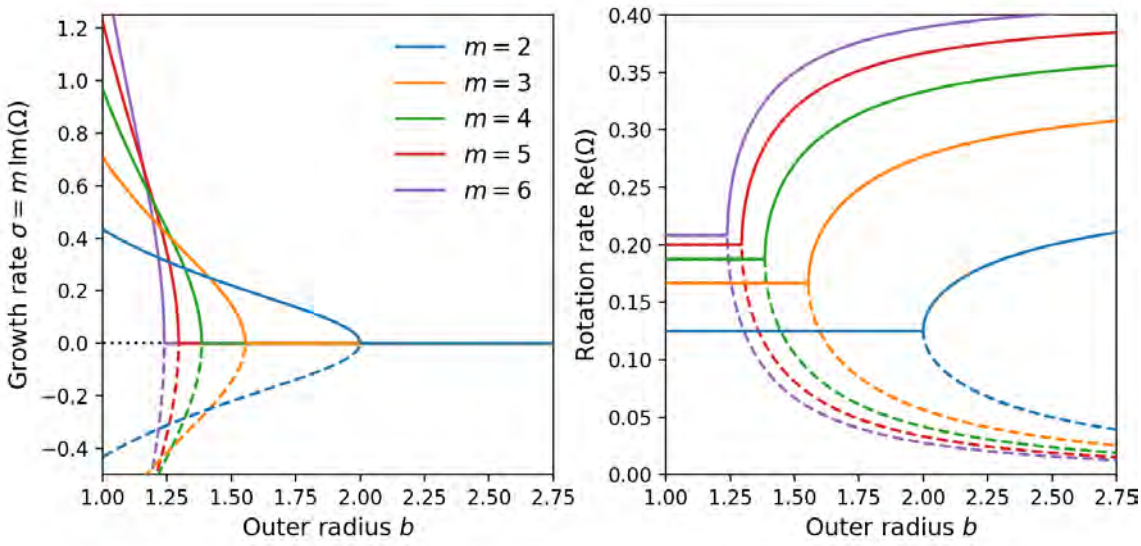


Figure 3: Dispersion relation for the linear dynamics of a perturbation $\boldsymbol{\eta}_m = e^{-im\Omega t}\boldsymbol{u}$. Left: Growth rate $\sigma = m\mathrm{Im}(\Omega)$ of the perturbation. Right: Rotation rate $\mathrm{Re}(\Omega)$ of the perturbation. The left plot recovers the results presented in Figure 3 of [8] up to a factor 2 due to different nondimensionalization (we set the inner vorticity to $q = 1$ instead of setting the azimuthal velocity $v(r = 1) = 1$).

with $\Omega_c = \frac{1}{4}\left(1 - \frac{1}{m}\right)$. Thus, if $b < b_c$ (i.e., $\varepsilon < 0$), the perturbation is purely growing (or decaying) when viewed in the frame rotating at rate $\Omega_c$, with small growth-rate $\sigma \propto \pm|\varepsilon|^{1/2}$. On the other hand, if $b > b_c$ (i.e., $\varepsilon > 0$), the perturbation rotates slowly with frequency $m(\Omega_\pm - \Omega_c) \propto \varepsilon^{1/2}$ with respect to the frame rotating at $\Omega_c$. In both cases, the solution observed in the frame rotating at rate $\Omega_c$ evolves according to a slow timescale $\tau = |\varepsilon|^{1/2}t$. If we assume that in the vicinity of the bifurcation, the weakly nonlinear dynamics is dominated by $\boldsymbol{\eta}_m$ and $\boldsymbol{\eta}_{2m}$ only, with the scalings $\boldsymbol{\eta}_m = O(|\varepsilon|^{1/2})$ and $\boldsymbol{\eta}_{2m} = O(|\varepsilon|)$, we can approximate the truncated Hamiltonian up to order $O(|\varepsilon|^2)$ as

$$\begin{aligned} H = &-\frac{\pi}{2}\left[A_{ij}(b)\eta^*_{m,i}\eta_{m,j} + B_{ij}(b)\eta^*_{2m,i}\eta_{2m,j}\right] \\ &-\frac{\pi}{2}\left[C_{ijk}(b)\left(\eta_{m,i}\eta_{m,j}\eta^*_{2m,k} + c.c.\right) + D_{ijk\ell}(b)\eta_{m,i}\eta_{m,j}\eta^*_{m,k}\eta^*_{m,\ell}\right] \end{aligned} \tag{34}$$

where the tensors $(A_{ij}) = \boldsymbol{A}^{(m)}$ and $(B_{ij}) = \boldsymbol{A}^{(2m)}$ correspond to the linear dynamics of the modes $m$ and $2m$ respectively, and the tensors $(C_{ijk})$ and $(D_{ijk\ell})$ encode the triad $(m, m) \leftrightarrow 2m$ and the quartet $(m, m) \leftrightarrow (m, m)$ interactions, respectively. We enforce $\boldsymbol{C}$ and $\boldsymbol{D}$ to verify the symmetries $C_{ijk} = C_{jik}$ and $D_{ijk\ell} = D_{jik\ell} = D_{k\ell ij}$, respectively, using the symmetrization rules of Section 2.3, which does not modify the Hamiltonian, but alleviate the computations. Using the relation $b = b_c + \varepsilon$, we perform a Taylor expansion of the tensors in the vicinity of the bifurcation as

$$(A_{ij}, B_{ij}, C_{ijk}, D_{ijk\ell})(b) = (A^c_{ij}, B^c_{ij}, C^c_{ijk}, D^c_{ijk\ell}) + \varepsilon(A'_{ij}, B'_{ij}, C'_{ijk}, D'_{ijk\ell}) + O(\varepsilon^2)\,. \tag{35}$$

Finally, we take the following expansions for the perturbations

$$\begin{cases} \boldsymbol{\eta}_m(t) = |\varepsilon|^{1/2} e^{-im\Omega_c t}\boldsymbol{\eta}(t,\tau) \\ \boldsymbol{\eta}_{2m}(t) = |\varepsilon| e^{-2im\Omega_c t}\boldsymbol{\mu}(t,\tau) \end{cases} \quad \text{with} \quad \begin{cases} \boldsymbol{\eta}(t,\tau) = \boldsymbol{\eta}^{(0)}(t,\tau) + |\varepsilon|^{1/2}\boldsymbol{\eta}^{(1)}(t,\tau) + \cdots \\ \boldsymbol{\mu}(t,\tau) = \boldsymbol{\mu}^{(0)}(t,\tau) + |\varepsilon|^{1/2}\boldsymbol{\mu}^{(1)}(t,\tau) + \cdots \end{cases} \tag{36}$$

corresponding to the aforementioned scalings in the reference frame rotating at rate $\Omega_c$. Then, the Hamiltonian equations read

$$\begin{cases} \dfrac{1}{im}L_{ij}(\partial_t\eta_j + |\varepsilon|^{1/2}\partial_\tau\eta_j) + (A^c_{ij} - \Omega_c L_{ij})\eta_j = -\varepsilon A'_{ij}\eta_j - 2|\varepsilon|\left(C^c_{ijk}\eta^*_j\mu_k + D^c_{ijk\ell}\eta^*_j\eta_k\eta_\ell\right), \\ \dfrac{1}{2im}L_{ij}(\partial_t\mu_j + |\varepsilon|^{1/2}\partial_\tau\mu_j) + (B^c_{ij} - \Omega_c L_{ij})\mu_j = -C^c_{jki}\eta_j\eta_k\,. \end{cases} \tag{37}$$

Moreover, we denote by $\boldsymbol{e} = (e_i)$ the real normalized eigenvector in Equation (31) (defined uniquely up to a sign), and define $\boldsymbol{e}^\perp = \hat{\mathbf{z}} \times \boldsymbol{e} = (e_i^\perp)$ its counter-clockwise rotation by $\pi/2$ such that $(\boldsymbol{e}, \boldsymbol{e}^\perp)$ is a direct orthonormal basis of $\mathbb{C}^2$. Then, the evolution equation for $\boldsymbol{\eta}$ at order $O(1)$ writes

$$\frac{1}{im}L_{ij}\partial_t\eta^{(0)}_j + (A^c_{ij} - \Omega_c L_{ij})\eta^{(0)}_j = 0\,. \tag{38}$$

We decompose $\boldsymbol{\eta}^{(0)}(t,\tau) = \alpha_0(t,\tau)\boldsymbol{e} + \beta_0(t,\tau)\boldsymbol{e}^\perp$ and project Equation (38) on the vectors $(\boldsymbol{e}, \boldsymbol{e}^\perp)$. Using the properties $(A^c_{ij} - \Omega_c L_{ij})e_j = e_i(A^c_{ij} - \Omega_c L_{ij}) = 0$ and $e_i L_{ij} e_j = 0$, we obtain

$$\begin{cases} \dfrac{1}{im}\left(e_i L_{ij} e_j^\perp\right)\partial_t\beta_0 = 0\,, \\ \dfrac{1}{im}\left(e_i^\perp L_{ij} e_j\right)\partial_t\alpha_0 + \dfrac{1}{im}\left(e_i^\perp L_{ij} e_j^\perp\right)\partial_t\beta_0 + \left[e_i^\perp(A^c_{ij} - \Omega_c L_{ij})e_j^\perp\right]\beta_0(t,\tau) = 0\,. \end{cases} \tag{39}$$

Since $\boldsymbol{L}$ is invertible and $e_i L_{ij} e_j = 0$, we necessary have $e_i^\perp L_{ij} e_j = e_i L_{ij} e_j^\perp \neq 0$. Similarly, $\boldsymbol{A}^c - \Omega_c\boldsymbol{L}$ is nonzero so $e_i^\perp(A^c_{ij} - \Omega_c L_{ij})e_j^\perp \neq 0$. From these observations, we can deduce step by step that $\partial_t\beta_0 = 0$, then $\partial_t\alpha_0 = 0$ and finally $\beta_0 = 0$. Denoting $\tilde{\mathcal{A}}(\tau) = \alpha_0(\tau)$, we can finally conclude that Equation (38) implies that

$$\boldsymbol{\eta}^{(0)} = \tilde{\mathcal{A}}(\tau)\boldsymbol{e}\,. \tag{40}$$

At order $O(|\varepsilon|^{1/2})$, the evolution equation for $\boldsymbol{\eta}$ writes

$$\frac{1}{im}L_{ij}\partial_t\eta^{(1)}_j + (A^c_{ij} - \Omega_c L_{ij})\eta^{(1)}_j = -\frac{1}{im}(\partial_\tau\tilde{\mathcal{A}})L_{ij}e_j\,. \tag{41}$$

Projecting again on the basis $(\boldsymbol{e}, \boldsymbol{e}^\perp)$ and performing the same manipulations as the previous order, we can show that $\boldsymbol{\eta}^{(1)}$ only varies on the slow timescale $\tau$ as

$$\boldsymbol{\eta}^{(1)}(\tau) = \alpha_1(\tau)\boldsymbol{e} + \frac{1}{im}\left(\partial_\tau\tilde{\mathcal{A}}\right)\boldsymbol{f} \qquad \text{with} \qquad \boldsymbol{f} = \frac{-e_i^\perp L_{ij} e_j}{e_i^\perp\left(A^c_{ij} - \Omega_c L_{ij}\right)e_j^\perp}\boldsymbol{e}^\perp \tag{42}$$

The next order equation for $\boldsymbol{\eta}$ gives

$$\begin{aligned} \frac{1}{im}L_{ij}\partial_t\eta^{(2)}_j + (A^c_{ij} - \Omega_c L_{ij})\eta^{(2)}_j = &-\frac{1}{im}L_{ij}\partial_\tau\eta^{(1)}_j - \mathrm{sgn}(\varepsilon)A'_{ij}\eta^{(0)}_j \\ &- 2\left(C^c_{ijk}\eta^{(0)*}_j\mu^{(0)}_k + D^c_{ijk\ell}\eta^{(0)*}_j\eta^{(0)}_k\eta^{(0)}_\ell\right) \end{aligned} \tag{43}$$

where $\mathrm{sgn}(\varepsilon) = \mathrm{sgn}(b - b_c)$ depends on the position relative to the bifurcation. To solve this equation and obtain the ODE for $\tilde{\mathcal{A}}(\tau)$, we need to solve for the evolution of $\boldsymbol{\mu}^{(0)}(t,\tau)$. It writes

$$\frac{1}{2im} L_{ij} \partial_t \mu_j^{(0)} + (B_{ij}^c - \Omega_c L_{ij}) \mu_j^{(0)} = -\tilde{\mathcal{A}}^2(\tau) C_{jki}^c e_j e_k \,. \tag{44}$$

Since $\boldsymbol{B}^c - \Omega_c \boldsymbol{L}$ is non-singular, we can solve for $\boldsymbol{g}$ such that

$$(B_{ij}^c - \Omega_c L_{ij}) g_j = -C_{jki}^c e_j e_k \qquad \longleftrightarrow \qquad \boldsymbol{g} = -(\boldsymbol{B}^c - \Omega_c \boldsymbol{L})^{-1} \left[ \boldsymbol{e}_c \cdot (\boldsymbol{e}_c \cdot \boldsymbol{C}^c) \right] . \tag{45}$$

Moreover, $\boldsymbol{L^{-1}B}^c - \Omega_c \boldsymbol{I}$ being non-singular with two different eigenvalues, we can compute its spectral decomposition $\boldsymbol{L}^{-1}\boldsymbol{B}^c - \Omega_c \boldsymbol{I} = \boldsymbol{P\Lambda P^{-1}}$ where $\boldsymbol{P}$ is invertible and $\boldsymbol{\Lambda}$ is a real diagonal non-singular matrix. Then, equation (44) writes

$$\partial_t \left( \boldsymbol{\mu}^{(0)} - \tilde{\mathcal{A}}^2(\tau) \boldsymbol{g} \right) = -2im \boldsymbol{P\Lambda P^{-1}} \left( \boldsymbol{\mu}^{(0)} - \tilde{\mathcal{A}}^2(\tau) \boldsymbol{g} \right) \tag{46}$$

and can be solved as

$$\boldsymbol{\mu}^{(0)}(t,\tau) = \tilde{\mathcal{A}}^2(\tau) \boldsymbol{g} + \boldsymbol{P} \exp\left(-2im \boldsymbol{\Lambda} t\right) \boldsymbol{P}^{-1} \cdot \boldsymbol{\nu}(\tau) \,. \tag{47}$$

Thus, the mode $2m$ evolves at dominant order as the superposition of two freely rotating components, corresponding to the linearized dynamics of the mode $2m$, and of a component *locked* to the mode $m$ by nonlinearities, which evolves only on the slow timescale. If we define $\gamma_{kn}(\tau) = P_{kn}[\boldsymbol{P}^{-1} \cdot \boldsymbol{\nu}(\tau)]_n$ (no summation on $n$), we can rewrite Equation (47) in indicial notation as

$$\mu_k^{(0)}(t,\tau) = \tilde{\mathcal{A}}^2(\tau) g_k + e^{-2im\lambda_n t} \gamma_{kn}(\tau) \,, \tag{48}$$

(summation on $n$) where the two eigenvalues $\lambda_n$ are nonzero. Finally, we can inject Equations (40, 42, 48) into Equation (43) for $\boldsymbol{\eta}^{(2)}$ to obtain

$$\begin{aligned} \frac{1}{im} L_{ij} \partial_t \eta_j^{(2)} + (A_{ij}^c - \Omega_c L_{ij}) \eta_j^{(2)} = &- \frac{1}{im} (\partial_\tau \alpha_1) L_{ij} e_j + \frac{1}{m^2} \left( \partial_{\tau\tau}^2 \tilde{\mathcal{A}} \right) L_{ij} f_j - \mathrm{sgn}(\varepsilon) \tilde{\mathcal{A}}\, A'_{ij} e_j \\ &- 2\tilde{\mathcal{A}} |\tilde{\mathcal{A}}|^2 \left( C_{ijk}^c e_j g_k + D_{ijk\ell}^c e_j e_k e_\ell \right) \\ &- 2 e^{-2im\lambda_n t} \tilde{\mathcal{A}}^*(\tau) \gamma_{kn}(\tau) C_{ijk}^c e_j \,. \end{aligned} \tag{49}$$

Projecting the equation of $\boldsymbol{e}_c$ and observing that the periodic forcing is non-resonant ($\lambda_n \neq 0$), we obtain the solvability condition

$$\frac{1}{m^2} \left( e_i L_{ij} f_j \right) \partial_{\tau\tau}^2 \tilde{\mathcal{A}} = \mathrm{sgn}(\varepsilon) \left( e_i A'_{ij} e_j \right) \tilde{\mathcal{A}} + 2\tilde{\mathcal{A}} |\tilde{\mathcal{A}}|^2 \left( C_{ijk}^c e_i e_j g_k + D_{ijk\ell}^c e_i e_j e_k e_\ell \right) . \tag{50}$$

The linearized dynamics of the above equation must be compatible with the linear evolution given by equation (32). This condition provides a quick way of computing the linear coefficient and gives

$$\alpha_m \triangleq -\frac{m^2 \left( e_i A'_{ij} e_j \right)}{e_i L_{ij} f_j} = -\frac{1}{\varepsilon} \left( im \left( \Omega_\pm - \Omega_c \right) \right)^2 = \frac{1}{4 b_c^m} \left( \frac{m^2 - 1}{b_c^2 - 1} \right) > 0 \,. \tag{51}$$

On the other hand, the nonlinear coefficient is given by

$$\mathcal{N}_m \triangleq 2m^2 \frac{C^c_{ijk} e_i e_j g_k + D^c_{ijk\ell} e_i e_j e_k e_\ell}{e_i L_{ij} f_j} \,. \tag{52}$$

We can express equation (50) in terms of the original timescale $t$ by introducing $\mathcal{A}(t) = |\varepsilon|^{1/2}\tilde{\mathcal{A}}(|\varepsilon|^{1/2}t)$ as

$$\partial^2_{tt}\mathcal{A} = -(b-b_c)\alpha_m \mathcal{A} + \mathcal{N}_m \mathcal{A}|\mathcal{A}|^2 \tag{53}$$

(recall that $\varepsilon = b - b_c$) and the evolution of the Fourier mode $\boldsymbol{\eta}_m$ can be approximated as

$$e^{im\Omega_c t}\boldsymbol{\eta}_m(t) = \underbrace{\mathcal{A}(t)\boldsymbol{e}_c}_{O(|\varepsilon|^{1/2})} + \underbrace{\frac{1}{im}(\partial_t \mathcal{A})\boldsymbol{f} + |\varepsilon|\alpha_1(|\varepsilon|^{1/2}t)\boldsymbol{e}_c}_{O(|\varepsilon|)} + O\left(|\varepsilon|^{3/2}\right) \,. \tag{54}$$

Note that we have $-(b-b_c)\alpha_m = \sigma^2$ if $b < b_c$ (linearly unstable) and $-(b-b_c)\alpha_m = -m^2(\Omega_\pm - \Omega_c)^2$ if $b > b_c$ (linearly stable). The evolution for $\alpha_1$ remains unknown (even though it could probably be solved by going to next order, we leave that pleasure to a motivated reader...) but we will not need it in the following.

### 3.3 Classification of the bifurcation

**An anology with the motion of a particle:**
Equation (53) is a one-dimensional steady complex Ginzburg-Landau equation (with time $t$ playing the role of spatial variable). It thus resembles a Stuart-Landau equation but is second order in time. If we decompose $\mathcal{A}(t) = x(t) + iy(t)$ into real and imaginary parts, we can split Equation (53) into a system of two real equations

$$\begin{cases} \ddot{x}(t) = -(b-b_c)\alpha_m x + \mathcal{N}_m R^2 x \,, \\ \ddot{y}(t) = -(b-b_c)\alpha_m y + \mathcal{N}_m R^2 y \,, \end{cases} \tag{55}$$

where we denoted $R(t) = |\mathcal{A}(t)| = \sqrt{x^2(t) + y^2(t)}$ the modulus of the complex amplitude. This system corresponds to the dynamics of a particle with Cartesian coordinates $\mathbf{x}(t) = x(t)\hat{\mathbf{x}} + y(t)\hat{\mathbf{y}}$ in a central force $\mathbf{F} = F(R)\hat{\mathbf{r}}$, where $\hat{\mathbf{r}} = \mathbf{x}/R$ the unitary radial vector. The force is given by $F(R) = -(b-b_c)\alpha_m R + \mathcal{N}_m R^3$ and derives from the radial potential

$$V(R) = \frac{1}{2}(b-b_c)\alpha_m R^2 - \frac{1}{4}\mathcal{N}_m R^4 \,. \tag{56}$$

Equation (55) can thus be recast in the familiar vector form as $\ddot{\mathbf{x}}(t) = -\boldsymbol{\nabla}_{\mathbf{x}} V$.

**Subcritical or supercritical ?**
Since the coefficient $\alpha_m$ is positive (Equation 51), a sketch of the potential $V(R)$ is represented in Figure 4 on each side of the bifurcation. In the linearly unstable regime ($b < b_c$), the linear dynamics is responsible for the growth of the amplitude of the perturbation. The bifurcation is subcritical or supercritical depending on the sign of the nonlinear coefficient $\mathcal{N}_m$. If $\mathcal{N}_m$ is negative, the nonlinearity is stabilizing and the amplitude can have nonlinear oscillations with range set by the two turning points of the potential $V(R)$. If $\mathcal{N}_m$ is

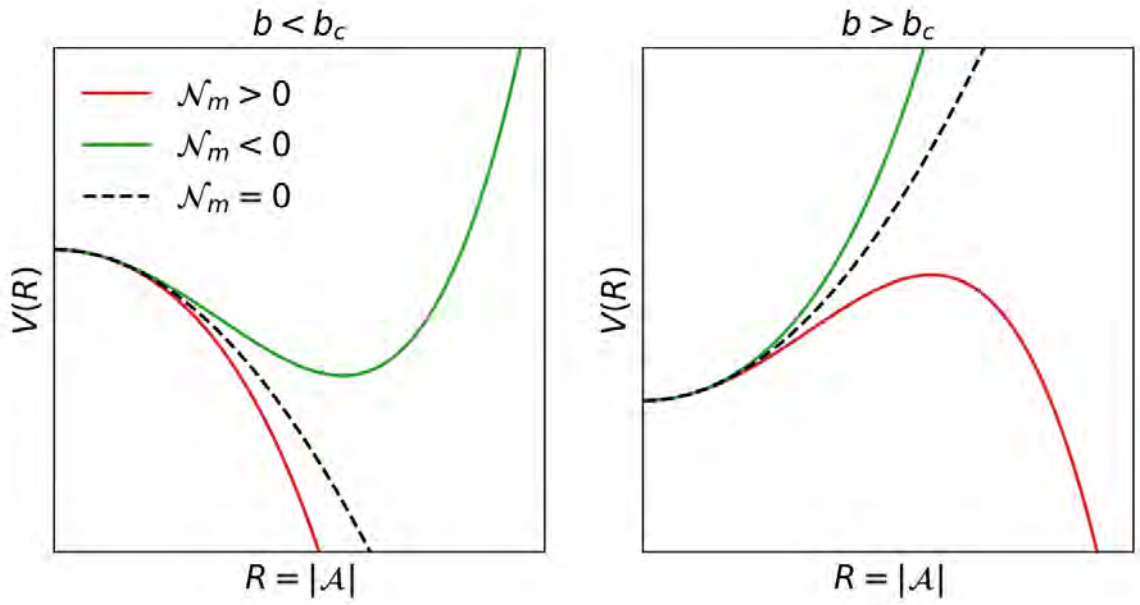


Figure 4: Radial potential $V(R)$ appearing in the weakly-nonlinear evolution of the amplitude of the perturbation. The dashed line corresponds to the linear dynamics, unstable if $b < b_c$ (left) and stable if $b > b_c$ (right). Depending on the sign of the nonlinear coefficient $\mathcal{N}_m$, the bifurcation is sub- or supercritical. The local extrema, when it exists is reached at the amplitude $R_{c,0} = \sqrt{|b - b_c|\alpha_m/\mathcal{N}_m}$.

| $m$ | $b_c$ | $\alpha_m$ | $\mathcal{N}_m$ |
|---|---|---|---|
| 2 | 2 | $1/16$ | $1.95 \times 10^{-2}$ |
| 3 | $\sqrt{1+\sqrt{2}}$ | $\sqrt{10\sqrt{2}-14}$ | $2.37 \times 10^{-1}$ |
| 4 | $\frac{1}{3}(2+10^{1/3})$ | 1.11 | 1.06 |
| 5 | 1.30 | 2.43 | 3.12 |

Table 1: Critical radii and coefficients appearing in the weakly nonlinear amplitude equation (53) for the first few modes $m \geq 2$. Exact results can be obtained up to mode $m = 4$, but numerical approximations are given when the exact expression is cumbersome.

positive, the nonlinearity is destabilizing and the growth of an initially small amplitude is super-exponential. In practice, the nonlinear coefficient $\mathcal{N}_m$ can be computed numerically from Equation (52), using the intermediate vectors $\boldsymbol{f}$ and $\boldsymbol{g}$ given by equations (42.b) and (45), respectively. Table 1 gives the approximate values of the nonlinear coefficient $\mathcal{N}_m$ for the modes $m = 2$ to $m = 5$ and shows that they are all positive, indicating subcritical bifurcations where the nonlinearity is destabilizing. We checked numerically that $\mathcal{N}_m > 0$ up to $m = 50$, with increasing values of $\mathcal{N}_m$, so we assume that the bifurcation is subcritical for all values of $m \geq 2$.

**Hamiltonian associated with the particle's analogy:**
In this paragraph, we derive a simple Hamiltonian which encodes the dynamics at the bifurcation for the mode $m \geq 2$. Let us first start in the frame of reference rotating at rate $\Omega_c$. The evolution equation for $\mathcal{A}(t) = e^{im\Omega_c t}\boldsymbol{\eta}_m(t) \cdot \boldsymbol{e}_c + O(|\varepsilon|)$ writes $\partial_{tt}\mathcal{A} = -V'(|\mathcal{A}|) \times \mathcal{A}/|\mathcal{A}|$ with the potential introduced in Equation (56). Separating $\mathcal{A} = x + iy$ into real and imaginary parts, we recover the two-dimensional motion of a particle in a radial potential as described in a previous paragraph. The corresponding Hamiltonian $H_{p,\mathrm{rot}}$ is given according to the canonical variables $(\boldsymbol{x}, \boldsymbol{p})$ by

$$H_{p,\mathrm{rot}}(\boldsymbol{x}, \boldsymbol{p}) = \frac{1}{2}\boldsymbol{p}^2 + V(|\boldsymbol{x}|)\,. \tag{57}$$

Then, the dynamics in the non-rotating frame of reference can be obtained by back-rotating at rate $m\Omega_c$. This corresponds to the change of variables $X + iY = e^{-im\Omega_c t}(x + iy)$, or equivalently $\boldsymbol{X} = \cos(m\Omega_c t)\boldsymbol{x} - \sin(m\Omega_c t)\hat{\mathbf{z}} \times \boldsymbol{x}$ in vector notation. In the non-rotating frame, the Hamiltonian of the particle writes

$$H_p(\boldsymbol{X}, \boldsymbol{P}) = \frac{1}{2}\boldsymbol{P}^2 + m\Omega_c(P_X Y - P_Y X) + \frac{1}{2}(b - b_c)\alpha_m \boldsymbol{X}^2 - \frac{1}{4}\mathcal{N}_m \boldsymbol{X}^4 \tag{58}$$

where we replaced the potential $V$ by its full expression. The gyroscopic term $P_X Y - P_Y X$ can be written in vector notation as $\hat{\mathbf{z}} \cdot (\boldsymbol{P} \times \boldsymbol{X})$. The flow of the canonical variables $(\boldsymbol{X}, \boldsymbol{P})$ under the Hamiltonian $H_p$ displays the same linear and weakly nonlinear dynamics as $\boldsymbol{\eta}_m$ close to the bifurcation. The variables $\boldsymbol{X} = [X, Y]^T$ and $\boldsymbol{P} = [P_X, P_Y]^T$ are related to $\boldsymbol{\eta}_m$ by $X + iY = \boldsymbol{\eta}_m \cdot \boldsymbol{e}_c$ and $P_X + iP_Y = [\dot{\boldsymbol{\eta}}_m - im\Omega_c \boldsymbol{\eta}_m] \cdot \boldsymbol{e}_c$.

Furthermore, the change of variables $\boldsymbol{X} = (m\Omega_c/\sqrt{\mathcal{N}_m})\tilde{\boldsymbol{X}}$, $\boldsymbol{P} = ((m\Omega_c)^2/\sqrt{\mathcal{N}_m})\tilde{\boldsymbol{P}}$, together with a rescaling of time $\tilde{t} = (m\Omega_c)t$, shows that the pair of canonical variables

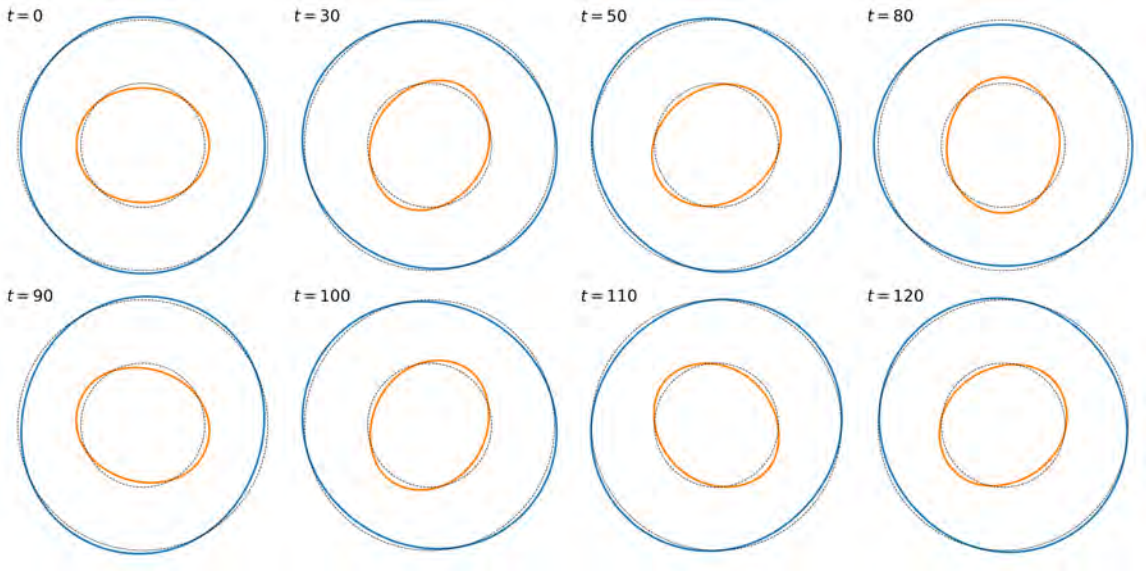


Figure 5: Evolution of a perturbed vortex with $b = 2.02$ according to the DNS. The initial condition is $\boldsymbol{\eta}_2(0) = 0.125\boldsymbol{e}_+$, with other modes set to zero. The dashed circles correspond to the reference axisymmetric base state.

$(\tilde{\boldsymbol{X}}, \tilde{\boldsymbol{P}})$ evolves according to the Hamiltonian flow given by

$$\tilde{H}_p(\tilde{\boldsymbol{X}}, \tilde{\boldsymbol{P}}) = \frac{1}{2}\tilde{\boldsymbol{P}}^2 + (\tilde{P}_X\tilde{Y} - \tilde{P}_Y\tilde{X}) + \frac{1}{2}\mu\tilde{\boldsymbol{X}}^2 - \frac{1}{4}\tilde{\boldsymbol{X}}^4\,, \tag{59}$$

with bifurcation parameter $\mu = \alpha_m(b - b_c)/(m\Omega_c)^2$. This Hamiltonian corresponds to the motion of a particle with charge and mass unity in a uniform magnetic field $\boldsymbol{B} = 2\hat{\boldsymbol{z}}$ and radial electric potential $\frac{1}{2}(\mu - 1)\tilde{\boldsymbol{X}}^2 - \frac{1}{4}\tilde{\boldsymbol{X}}^4$.

### 3.4 Finite-amplitude threshold for destabilization close to the bifurcation

In the linearly stable region $b > b_c$, infinitesimal perturbations of the mode $m$ are expected to rotate without growth nor decay. However, we observe numerically that small finite-size perturbations rotate with oscillating amplitude (Figure 2 and Figure 5) and that large enough perturbations grow monotonically until the vortex splits (Figure 6). The critical amplitude separating these two regimes appears to depend both on the value of $b$ and on the "shape" of the perturbation, given by the normalized initial condition $\boldsymbol{\eta}_m/|\boldsymbol{\eta}_m|$. In this section, we provide a prediction for the critical amplitude close to the bifurcation ($b = b_c + \varepsilon$ with $0 < \varepsilon \ll 1$).

From the amplitude equation derived using weakly nonlinear analysis, we know that the amplitude of a small perturbation evolves nonlinearly according to the potential given in Equation (56). Since we have computed that the nonlinear coefficient $\mathcal{N}_m$ is positive for the first few modes, a critical amplitude $R_{c,0} = \sqrt{(b - b_c)\alpha_m/\mathcal{N}_m}$ exists for $b > b_c$ above which the potential becomes repulsive (Figure 4), leading to unbounded growth of the amplitude. However, this critical amplitude $R_{c,0}$ largely overestimates the amplitude

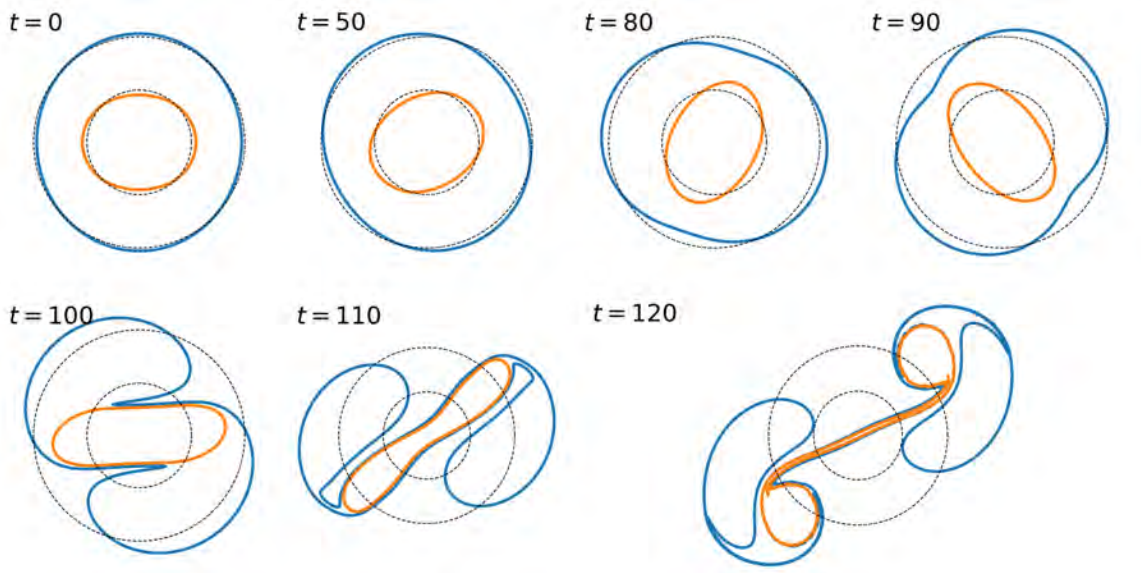


Figure 6: Idem as Figure 5, with initial condition $\boldsymbol{\eta}_2(0) = 0.15\boldsymbol{e}_+$. The last two snapshots are zoomed out to show the splitting into a pair of traveling dipoles.

threshold at which initial conditions lead to unbounded growth. In particular, when the initial condition is in the eigenspace of the linearized dynamics, $R_{c,0}$ appears to provide the correct scaling in $\sqrt{b-b_c}$ but overestimates the observed threshold by a factor close to 2. To explain this discrepancy, one need to introduce the effect of nonzero angular momentum permitted by the two-dimensional motion. If the latter can be safely neglected for infinitesimal perturbations, it significantly modifies the effective potential of the radial motion for finite-sized initial perturbations.

Indeed, if we decompose $\mathcal{A}(t) = R(t)e^{i\Theta(t)}$ in polar form, we can rewrite Equation (53) into a pair of real ODE. It writes

$$\begin{cases} \partial_{tt}R - R(\partial_t\Theta)^2 = -(b-b_c)\alpha_m R + \mathcal{N}_m R^3\,, \\ R\partial_{tt}\Theta + 2(\partial_t R)(\partial_t\Theta) = 0\,. \end{cases} \tag{60}$$

We recover the dynamics of the analogous particle in polar coordinates. Furthermore, by multiplying equation (60.b) by $R$ or by constructing on the analogy with the particle's motion, we find that $C_0 = R^2\partial_t\Theta$ is conserved during the evolution. This quantity is the angular momentum of the analogous particle, and we will call it the areal velocity in the following to prevent any confusion with the angular momentum of the vorticity distribution. From the conservation of $C_0$, the dynamics can be reduced to a one-dimensional radial evolution in an effective potential as $\partial_{tt}R = -V'_{\text{eff}}(R)$, with effective potential given by

$$V_{\text{eff}}(R; C_0) = \frac{C_0^2}{2R^2} + \frac{1}{2}(b-b_c)\alpha_m R^2 - \frac{1}{4}\mathcal{N}_m R^4\,, \tag{61}$$

Figure 7 shows the effective potential for different values of the areal constant $C_0$. It shows that the energy barrier to overcome for unbounded evolution decreases as $|C_0|$ grows

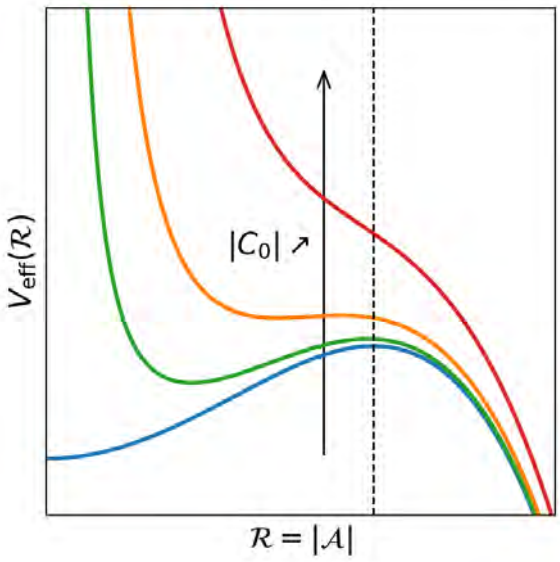


Figure 7: Radial effective potential (Equation 61) for different values of the areal constant $C_0$. When $C_0$ is large enough, the local maxima of $V_{\text{eff}}$ disappears and any initial amplitude leads to unbounded growth.

and even vanishes for values large enough. Knowing whether a given initial condition will lead to a bounded evolution of the perturbation is thus analogous to the Kepler problem in the context of gravitational orbits. We recover that a given initial condition will lead to unbounded growth if $V_{\text{eff}}(\cdot\,; C_0)$ is monotonically decreasing or if the (conserved) effective total energy $\frac{1}{2}(\partial_t R)^2 + V_{\text{eff}}(R; C_0)$ of the analogous particle is larger than the local maximum of $V_{\text{eff}}$.

The existence condition and value of the local maximum of the effective potential for a given value of $C_0$ can be computed using Cardan's formula. We find that the local maximum exists only for $|C_0| < C_c$, where the critical areal constant $C_c$ is given by

$$C_c = \frac{2}{\mathcal{N}_m}\left(\frac{\alpha_m(b-b_c)}{3}\right)^{3/2} . \tag{62}$$

For $|C_0| \geq C_c$, the effective potential $V_{\text{eff}}(\cdot\,; C_0)$ is monotonically decreasing and the initial perturbation will grow unbounded. For $|C_0| < C_c$, the effective potential admits a local maximum whose value is

$$\begin{aligned} &V_{\text{eff},c}(C_0) = \frac{\alpha_m^2(b-b_c)^2}{4\mathcal{N}_m} X(4-3X)\,, \\ &\text{with} \quad X(C_0) = \frac{1}{3}\left\{1 + 2\cos\left[\frac{1}{3}\arccos\left(1 - 2\frac{C_0^2}{C_c^2}\right)\right]\right\}\,, \end{aligned} \tag{63}$$

and the perturbation will remain bounded only if the effective total energy $E_{\text{eff}}$ of the particle verifies $E_{\text{eff}} \leq V_{\text{eff},c}$.

To compute $E_{\text{eff}}$ and $C_0$, we express the initial conditions $\mathcal{A}|_0$ and $\partial_t \mathcal{A}|_0$ in terms of the initial perturbation $\boldsymbol{\eta}_{m,0} = \boldsymbol{\eta}_m(0)$. Using the decomposition $\mathcal{A}(t) = R(t)e^{i\Theta(t)}$ and

assuming $\boldsymbol{\eta}_{2m}(0) = \mathbf{0}$, the initial conditions for the amplitude equation can be computed at dominant order as

$$\begin{cases} R_0 = |\boldsymbol{\eta}_{m,0} \cdot \boldsymbol{e}_c| \\ \dot{R}_0 = m|\boldsymbol{\eta}_{m,0} \cdot \boldsymbol{e}_c| \times \mathrm{Im}\left[\dfrac{\boldsymbol{e}_c \cdot (\boldsymbol{L}^{-1}\boldsymbol{A}^{(m)}) \cdot \boldsymbol{\eta}_{m,0} - \Omega_c(\boldsymbol{e}_c \cdot \boldsymbol{\eta}_{m,0})}{\boldsymbol{e}_c \cdot \boldsymbol{\eta}_{m,0}}\right] \\ \dot{\Theta}_0 = -m \times \mathrm{Re}\left[\dfrac{\boldsymbol{e}_c \cdot (\boldsymbol{L}^{-1}\boldsymbol{A}^{(m)}) \cdot \boldsymbol{\eta}_{m,0} - \Omega_c(\boldsymbol{e}_c \cdot \boldsymbol{\eta}_{m,0})}{\boldsymbol{e}_c \cdot \boldsymbol{\eta}_{m,0}}\right] \end{cases} \tag{64}$$

In particular, if the initial perturbation is aligned with an eigenmode as $\boldsymbol{\eta}_m(0) = \varepsilon^{1/2}\,\eta \boldsymbol{e}_\pm$, the initial conditions for the amplitude equation reduce to

$$\begin{cases} R_0 = \varepsilon^{1/2}|\eta \boldsymbol{e}_\pm \cdot \boldsymbol{e}_c| \approx \varepsilon^{1/2}|\eta|\,, \qquad \dot{R}_0 = 0\,, \\ \dot{\Theta}_0 = -m\,(\Omega_\pm - \Omega_c) \approx \mp \alpha_m^{1/2}\varepsilon^{1/2}\,, \end{cases} \tag{65}$$

such that the areal constant verifies $C_0^2 = \alpha_m \varepsilon^3 |\eta|^4$. The initial radial position and velocity are $R_0 = \varepsilon^{1/2}|\eta|$ and $\partial_t R|_0 = 0$, respectively. We can thus deduce the value of the effective total energy

$$E_{\text{eff}} = \alpha_m (b - b_c)|\eta|^2 - \frac{1}{4}\mathcal{N}_m |\eta|^4\,, \tag{66}$$

which must be compared with the local maxima of the effective potential (using $C_0^2 = \alpha_m (b - b_c)^{3/2}|\eta|^4$), when it exists. We can first show that there is no local maxima in the effective potential if $|\eta|^2 \geq 2\alpha_m/\sqrt{27}\mathcal{N}_m$, i.e., $|\boldsymbol{\eta}_{m,0}| \geq R_{c,1}$. The critical amplitude $R_{c,1}$ is given by

$$R_{c,1} = \sqrt{\frac{2\alpha_m}{\sqrt{27}\mathcal{N}_m}(b - b_c)} = \sqrt{\frac{2}{\sqrt{27}}} R_{c,0}\,. \tag{67}$$

where $R_{c,0} = \sqrt{\alpha_m (b - b_c)/\mathcal{N}_m}$ is the position of the local maxima of $V(R)$. Furthermore, even when $|\boldsymbol{\eta}_{m,0}| < R_{c,1}$, the dynamics can be unbounded if $E_{\text{eff}} > V_{\text{eff},c}$. This condition can be recasted as

$$\mu^2 + X_\mu(4 - 3X_\mu) - 4\mu > 0 \tag{68}$$

with $\mu = (|\boldsymbol{\eta}_{m,0}|/R_{c,0})^2 \leq 2/\sqrt{27}$ and $X_\mu = \frac{1}{3}\left\{1 + 2\cos\left[\frac{1}{3}\arccos\left(1 - \frac{27}{2}\mu^2\right)\right]\right\}$. It can be solved numerically and finally gives $E_{\text{eff}} > V_{\text{eff},c}$ iff $|\boldsymbol{\eta}_{m,0}| > R_{c,2}$, where

$$R_{c,2} \approx 0.5858 \times R_{c,0}\,. \tag{69}$$

Figure 8 shows whether a given initial condition aligned with the eigenmode $\boldsymbol{e}_+$ (which depends on $b$) for $m = 2$ will oscillate nonlinearly or destabilize into a pair of traveling dipoles. It shows that the critical amplitude above which the vortex destabilizes scales as $(b - b_c)^{1/2}$ in the linearly stable region, close to the bifurcation $b_c = 2$. If the naive prediction $R_{c,0}$ gives an upper bound for the critical amplitude, it overestimates it by a factor of almost 2. The refined predictions $R_{c,1}$ and $R_{c,2}$ in the case where the initial condition is aligned with the eigenmode $\boldsymbol{e}_+$ provide much better estimates of the critical amplitude. Close to the bifurcation, for $|b - b_c| < 10^{-2}$, we observe oscillating perturbations

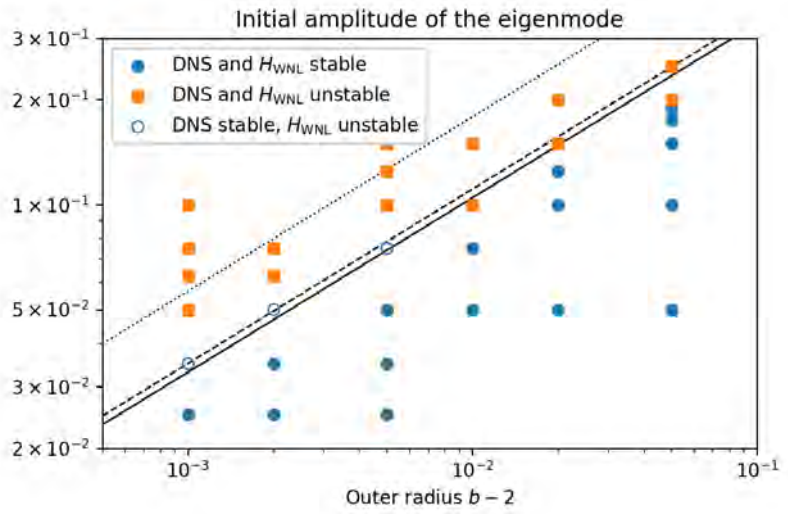


Figure 8: Classification of the evolution of finite-amplitude perturbations initially aligned with the eigenmode $\boldsymbol{e}_+$ for $m = 2$. Blue dots (filled and empty) show initial conditions leading to bounded oscillations and orange squares show initial conditions which destabilize into a pair of propagating dipoles. The three empty blue dots correspond to simulations where the DNS remain bounded but the truncated Hamiltonians $H_{\mathrm{WNL}}$ and $H_{\mathrm{WNL}+}$ lead to folding. The dotted, dashed and solid lines correspond to the quantities $R_{c,0}$ (position of the potential maximum), $R_{c,1}$ (disappearance of the local maximum in $V_{\mathrm{eff}}$) and $R_{c,2}$ (effective energy $E_{\mathrm{eff}}$ larger that the local maximum of $V_{\mathrm{eff}}$), respectively. The latter is the prediction for the critical amplitude.

in the DNS slightly above the predicted threshold for destabilization (blue empty circles in Figure 8). However, numerical simulations of the reduced models with Hamiltonians $H_{\mathrm{WNL}}$ and $H_{\mathrm{WNL}+}$ show destabilizing dynamics, in agreement with the weakly nonlinear prediction. All other performed DNS simulations agree with the truncated models. This discrepancy close to the bifurcation could be due to numerical errors on the conservation of area. Small variations of the area correspond to small modifications of the effective value of $b$, which have the highest impact on the dynamics closest to the bifurcation.

### 3.5 Some finite-amplitude solutions in the linearly stable regime

In this section, we present three families of finite-amplitude solutions of Equation (53) in the linearly stable regime. They take the form of cnoidal waves, solitons and purely rotating motion, respectively. Recalling that the radial dynamics is given by

$$\partial_{tt}R = \frac{C_0^2}{R^3} - \alpha_m(b-b_c)R + \mathcal{N}_m R^3\,, \tag{70}$$

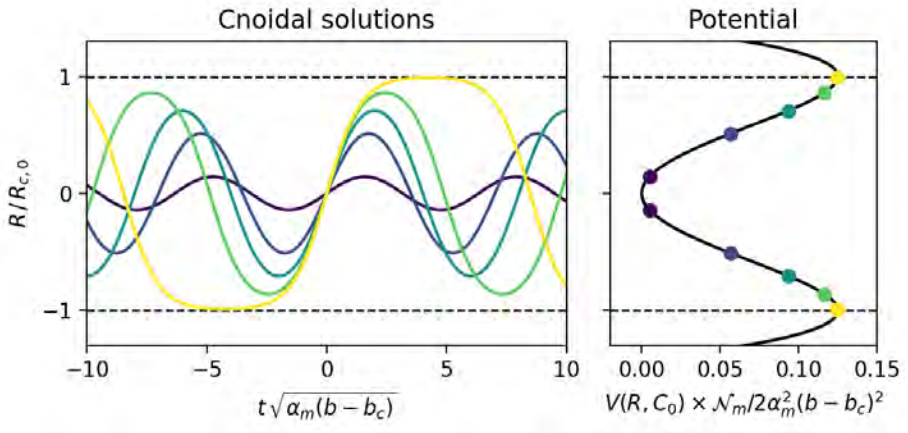


Figure 9: Some exact cnoidal solutions $\mathcal{A}(t) = R(t)e^{i\Theta_0}$ of Equation (53). The turning points are represented together with the potential on the right.

we perform the change of variables $R = \sqrt{2}R_{c,0}\tilde{R}$ and $\tilde{t} = t\sqrt{\alpha_m(b-b_c)}$, with $R_{c,0} = \sqrt{\alpha_m(b-b_c)/\mathcal{N}_m}$. The evolution equation becomes

$$\partial_{\tilde{t}\tilde{t}}\tilde{R} = \frac{\tilde{h}^2}{\tilde{R}^3} - \tilde{R} + 2\tilde{R}^3\,, \tag{71}$$

with $\tilde{h}^2 = C_0^2/(2R_{c,0}^4\alpha_m(b-b_c))$. Equation (71) corresponds to the one-dimensional steady complex Ginzburg-Landau equation (where $\tilde{t}$ plays the role of the spatial variable) and admits periodic cnoidal and "dark solitons" solutions [2]. In particular, a family of periodic nonlinear solutions can be computed exactly in the case of $\tilde{h} = 0$ (a purely radial motion of the particle with $C_0 = 0$). Denoting $\mathrm{sn}(x|m)$ the elliptic sine with parameter $0 \le m \le 1$, we can check that

$$\tilde{R}(\tilde{t}) = \tilde{R}_0\,\mathrm{sn}\left(\tilde{t}\sqrt{1-\tilde{R}_0^2}\middle|\,\frac{\tilde{R}_0^2}{1-\tilde{R}_0^2}\right) \tag{72}$$

is a finite-amplitude solution of Equation (71) with $h = 0$ for any $|\tilde{R}_0| \le 1/\sqrt{2}$. With the original variables, it corresponds to a solution $\mathcal{A}(t) = R(t)e^{i\Theta_0}$ with

$$R(t) = R_0\,\mathrm{sn}\left(t\sqrt{\mathcal{N}_m(R_{c,0}^2 - R_0^2/2)}\middle|\,\frac{R_0^2}{2R_{c,0}^2 - R_0^2}\right) \tag{73}$$

for any amplitude $R_0 \le R_{c,0}$. For small amplitude $R_0 \ll R_{c,0}$, we recover the linear dynamics $R(t) = R_0\sin(t\sqrt{\alpha_m(b-b_c)})$. Those solutions are represented on Figure 9.

Solitons solutions with rotation ($C_0 \neq 0$) can also be found. For any $1/\sqrt{3} \le \tilde{R}_0 \le 1/\sqrt{2}$, we can define $\tilde{a}^2 = 3\tilde{R}_0^2 - 1$ and check that

$$\tilde{R}(\tilde{t}) = \left[\tilde{R}_0^2 - \frac{\tilde{a}^2}{\cosh^2(\tilde{a}\tilde{t})}\right]^{1/2} \tag{74}$$

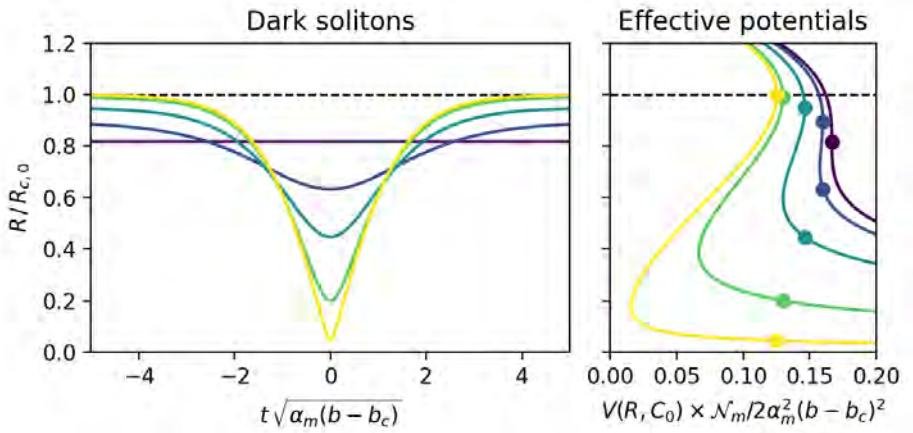


Figure 10: Some exact dark soliton solutions $\mathcal{A}(t) = R(t)e^{i\Theta(t)}$ of Equation (53). The evolution of the magnitude $R(t)$ is shown on the left and the corresponding effective potential in given on the right, together with the maximal amplitude and turning point.

is an exact solution of Equation (71) with $\tilde{h}^2 = \tilde{R}_0^4(1 - 2\tilde{R}_0^2)$. Going back to the original variables, we obtain that for any initial amplitude $R_0$ such that $\sqrt{2/3}R_{c,0} \leq R_0 \leq R_{c,0}$, the dark soliton given by $\mathcal{A}(t) = R(t)e^{i\Theta(t)}$ is a solution of Equation (53) with

$$\begin{cases} R(t) = \left[ R_0^2 - \dfrac{3R_0^2 - 2R_{c,0}^2}{\cosh^2\left(t\sqrt{\mathcal{N}_m(3R_0^2 - 2R_{c,0}^2)/2}\right)} \right]^{1/2}, \\ \dot{\Theta}(t) = \pm\sqrt{\mathcal{N}_m(R_{c,0}^2 - R_0^2)/2} \times \dfrac{R_0^2}{R(t)^2}. \end{cases} \tag{75}$$

In the analogy with the motion of a particle, it corresponds to a particle starting at the local maxima of the effective potential at $t = -\infty$, falling towards the local minima, reaching its turning point at $t = 0$ and going back to its initial position at $t = +\infty$. The radial components of the solutions are represented in Figure 10.

Finally, Equation (53) even admits solutions with constant amplitude $R_0$ of the form

$$\mathcal{A}(t) = R_0 \exp\left(\pm it\sqrt{\mathcal{N}_m(R_{c,0}^2 - R_0^2)}\right) \tag{76}$$

for any $R_0 \leq R_{c,0}$. Those solutions with constant amplitude correspond to vortex states rotating at uniform rate $\omega = \Omega_c \pm \sqrt{\mathcal{N}_m(R_{c,0}^2 - R_0^2)/m^2}$. Those solutions called V-states correspond to circular orbits in the analogy with the Kepler problem. Thus, the weakly nonlinear analysis predicts the existence of V-states with any amplitude $R_0 \leq R_{c,0} = O((b - b_c)^{1/2})$ close to the bifurcation.

## 4 V-states of the Truncated Hamiltonians $H_{\mathbf{WNL}}$ and $H_{\mathbf{WNL+}}$

At the end of Section 3.5, we derived some V-state solutions from the amplitude Equation (53). This equation being only valid close to the bifurcation, we explore in this section

the V-states of the truncated model $H_{\mathrm{WNL}}$, possibly far from the bifurcation. We recall that the Hamiltonian $H_{\mathrm{WNL}}$ reads

$$\begin{aligned} H_{\mathrm{WNL}} &= H_{(m,m)} + H_{(2m,2m)} + H_{(m,m,2m)} + H_{(m,m,m,m)} \\ &= -\frac{\pi}{2}\left(\eta^*_{i,m}A_{ij}\eta_{j,m} + \eta^*_{i,2m}B_{ij}\eta_{j,2m} + C_{ijk}(\eta^*_{i,m}\eta^*_{j,m}\eta_{k,2m} + c.c.)\right. \\ &\qquad \left. + D_{ijk\ell}\eta^*_{i,m}\eta^*_{j,m}\eta_{k,m}\eta_{\ell,m}\right) \end{aligned} \tag{77}$$

where the tensors $\boldsymbol{A}$, $\boldsymbol{B}$, $\boldsymbol{C}$ and $\boldsymbol{D}$ are short for $\boldsymbol{A}^{(m)}$, $\boldsymbol{A}^{(2m)}$, $\boldsymbol{C}^{(m,m,2m)}$ and $\boldsymbol{D}^{(m,m,m,m)}$, respectively,and are defined in Equations (12), (20) and (22) together with their symmetrization rules. We look for V-state solutions rotating at rate $\omega \in \mathbb{R}$. They write $\boldsymbol{\eta}_m(t) = (\eta_j e^{-im\omega t})_{j=1,2}$ and $\boldsymbol{\eta}_{2m}(t) = (\mu_j e^{-2im\omega t})_{j=1,2}$. The evolution equation (4) reduces to

$$\begin{cases} \omega L_{ij}\eta_j = A_{ij}\eta_j + 2C_{ijk}\eta^*_j\mu_k + 2D_{ijk\ell}\eta^*_j\eta_k\eta_\ell\,, \\ \omega L_{ij}\mu_j = B_{ij}\mu_j + C_{jki}\eta_j\eta_k\,, \end{cases} \qquad \text{for} \quad i = 1,2\,. \tag{78}$$

This system involving only real coefficients, we restrict our search to real solutions, corresponding to aligned deformation between the contours (in phase or in phase opposition), and ignore the complex conjugation in the following. Provided that $\omega$ is not an eigenvalue of $\boldsymbol{L}^{-1}\boldsymbol{B}$, the second equation can be inverted using the resolvent $\boldsymbol{R}(\omega) = (\boldsymbol{B} - \omega\boldsymbol{L})^{-1}$, giving $\mu_k = -R_{k\ell}(\omega)C_{nm\ell}\eta_n\eta_m$. Injecting into Equation (78.a) leads to the following pair of nonlinear equations

$$\left(A_{ij} - \omega L_{ij} - 2R_{k\ell}(\omega)C_{nm\ell}C_{ijk}\eta_n\eta_m + 2D_{ijk\ell}\eta_k\eta_\ell\right)\eta_j = 0 \qquad \text{for} \quad i = 1,2\,. \tag{79}$$

This pair of equations is similar to an eigenproblem, except that the matrix depends nonlinearly on the unknown eigenvalue $\omega$ and eigenvector $[\eta_1, \eta_2]^T$. If one considers $\omega$ as a fixed parameter, the problem admits a trivial solution $\eta_1 = \eta_2 = 0$, which we are not interested in. This complicates any numerical search. Instead, we choose to keep $\omega$ unknown and add an equation by imposing a given excess angular momentum $L$ for the solution. This condition writes

$$L = -\frac{\pi}{2}\left(\eta_i L_{ij}\eta_j + \mu_i L_{ij}\mu_j\right) \tag{80}$$

and forbids any trivial solution of the system (79)+(80) for nonzero $L$. This system is solved using Newton's method and numerical continuation on the values of the excess angular momentum $L$, starting from low values of $L$ and eigenmodes of the linearized dynamics. We obtain a continuous family of V-states, with rotation rates $\omega$ spanning the range between the two linear predictions $\Omega_\pm$.

Figure 11 shows the rotation rate $\omega$ of the V-states for $b = 2.005$ as a function of the norm $|\boldsymbol{\eta}_m|$ of the mode $m = 2$. We observe that a V-state of $H_{\mathrm{WNL}}$ can indeed be found for any rotation rate between the linear predictions and that the V-states of the weakly nonlinear analysis (Equation 76 and dashed line in Figure 11) agree reasonably well with the true V-states of $H_{\mathrm{WNL}}$. In particular, the critical amplitude $R_{c,0}$ at which the dashed line turns over provides a very good estimate of the maximal amplitude of V-states of $H_{\mathrm{WNL}}$. However, the weakly nonlinear analysis predicted symmetric solutions on each side of $\Omega_c = (\Omega_+ + \Omega_-)/2$, but this symmetry is slightly broken in the V-states of $H_{\mathrm{WNL}}$.

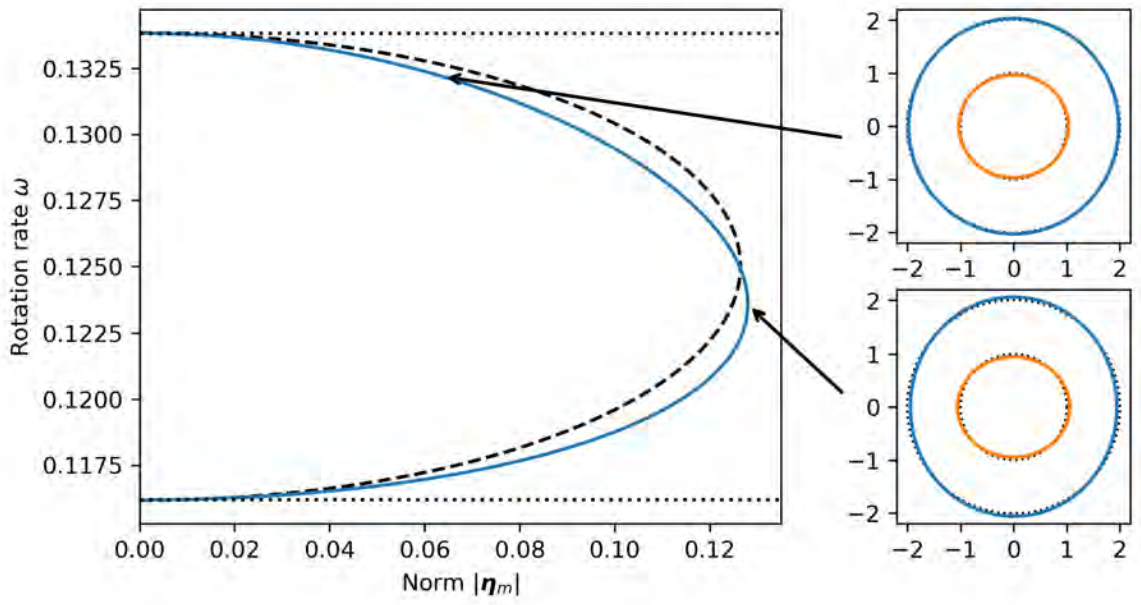


Figure 11: V-states diagram (left) showing the continuous family of V-states of $H_{\mathrm{WNL}}$ (blue solid curve) for $b = 2.005$ and $m = 2$. The rotation rate $\omega$ is plotted against the norm of the Fourier components of the mode $m = 2$. The black dashed curve is the prediction (76) from the amplitude equation close to the bifurcation. The two dotted lines show the rotation rates associated with infinitesimal perturbations (Equation 30). The insets on the right show two V-states of $H_{\mathrm{WNL}}$.

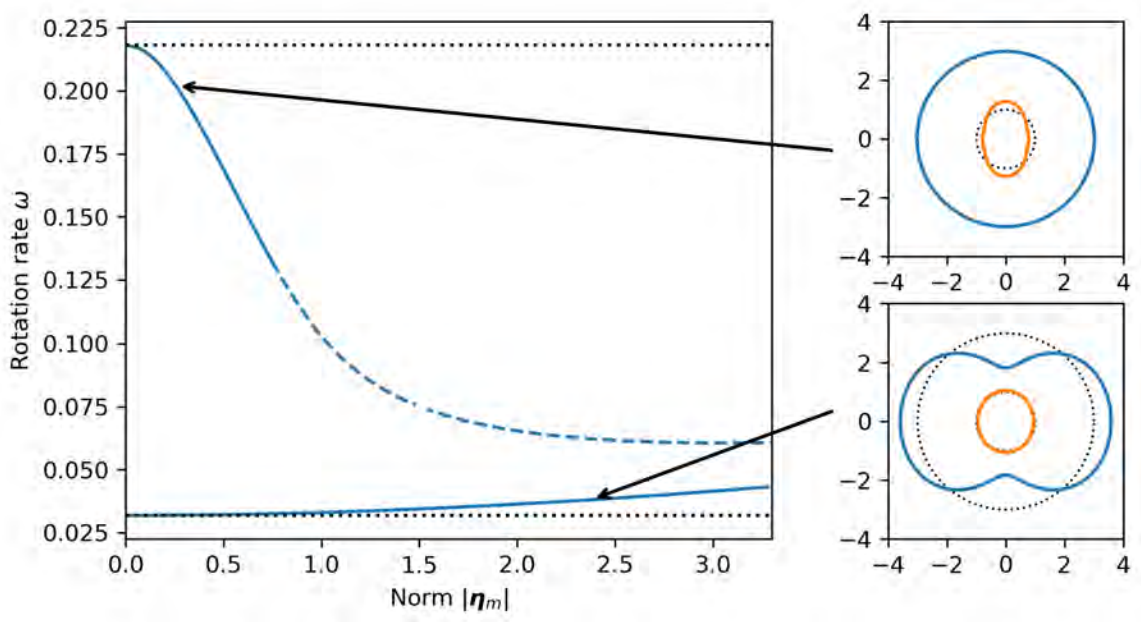


Figure 12: Idem as Figure 11 for $b = 3$ and $m = 2$. The dashed portions corresponds to nonphysical self-intersecting contours.

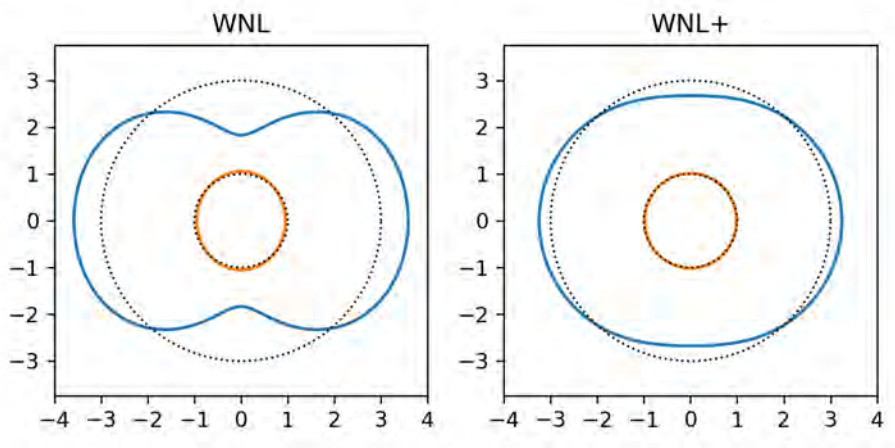


Figure 13: Comparison of two V-states of $H_{\mathrm{WNL}}$ and $H_{\mathrm{WNL+}}$ for $b = 3$ and $m = 2$, both rotating at rate $\omega = 0.038$.

At larger values of $b$, this asymmetry grows stronger as shown in Figure 12 displaying the V-states of $H_{\mathrm{WNL}}$ obtained for $b = 3$ and $m = 2$. In particular, V-states rotating at a rate close to $\Omega_-$ correspond to very large deformations for which the truncation $H_{\mathrm{WNL}}$ cannot provide a good approximation of the full Hamiltonian (5) anymore. For instance, V-states of $H_{\mathrm{WNL}}$ can correspond to self-intersecting contours (dashed curve in Figure 12) when $|\boldsymbol{\eta}_m|$ is too large, which is nonphysical and should be prevented by the full Hamiltonian.

One can consider higher-order terms by numerically solving for the V-states of $H_{\mathrm{WNL+}}$. Looking for solutions of the form $\boldsymbol{\eta}_m(t) = (\eta_j e^{-im\omega t})_j$, $\boldsymbol{\eta}_{2m}(t) = (\mu_j e^{-2im\omega t})_j$ and $\boldsymbol{\eta}_{3m}(t) = (\lambda_j e^{-3im\omega t})_j$, the V-state equations can be written as

$$\begin{cases} \omega L_{ij}\eta_j = A_{ij}\eta_j + 2C_{ijk}\eta_j^*\mu_k + 2D_{ijk\ell}\eta_j^*\eta_k\eta_\ell + \tilde{C}_{ijk}\mu_j^*\lambda_k + \tilde{D}_{jik\ell}\mu_j^*\eta_k\eta_\ell + 3\hat{D}_{ijk\ell}\eta_j^*\eta_k^*\lambda_\ell\,, \\ \omega L_{ij}\mu_j = B_{ij}\mu_j + C_{jki}\eta_j\eta_k + \tilde{C}_{jik}\eta_j^*\lambda_k + \tilde{D}_{ijk\ell}\eta_j^*\eta_k\mu_\ell\,, \\ \omega L_{ij}\lambda_j = \tilde{B}_{ij}\lambda_j + \tilde{C}_{jki}\eta_j\mu_k + \hat{D}_{jk\ell i}\eta_i\eta_k\eta_\ell\,, \end{cases}$$

where the eight tensors $\boldsymbol{A}$, $\boldsymbol{B}$, $\tilde{\boldsymbol{B}}$, $\boldsymbol{C}$, $\tilde{\boldsymbol{C}}$, $\boldsymbol{D}$, $\tilde{\boldsymbol{D}}$ and $\hat{\boldsymbol{D}}$ are short for the symmetrized versions of $\boldsymbol{A}^{(m)}$, $\boldsymbol{A}^{(2m)}$, $\boldsymbol{A}^{(3m)}$, $\boldsymbol{C}^{(m,m,2m)}$, $\boldsymbol{C}^{(m,2m,3m)}$, $\boldsymbol{D}^{(m,m,m,m)}$, $\boldsymbol{D}^{(2m,m,m,2m)}$ and $\boldsymbol{D}^{(m,m,m,3m)}$, respectively. All of them are defined in Equations (12) and (20)-(24). Again, restricting our search to real solutions and assuming one can invert $(B_{ij} - \omega L_{ij})_{ij}$ and $(\tilde{B}_{ij} - \omega L_{ij})_{ij}$, the previous system can be reduced to a pair of two equations by solving for $\boldsymbol{\lambda}(\omega, \boldsymbol{\eta}, \boldsymbol{\mu})$ in the third equation, injecting the results in the second equation and solving for $\boldsymbol{\mu}(\omega, \boldsymbol{\eta})$.

The resulting equation for $\boldsymbol{\eta}$ is lengthy and does not provide much insight, but can be used to numerically solve for V-states of $H_{\mathrm{WNL+}}$. We find that the curve of $\omega$ as a function of $|\boldsymbol{\eta}_m|$ for $m = 2$ (not shown) is only slightly modified compared to $H_{\mathrm{WNL+}}$. However, for a given value of $\omega$, the resulting V-states appear to be less dog-boned shaped and less often self-intersecting, due to the addition of the mode $\boldsymbol{\eta}_{3m}$ (Figure 13).

## 5 Conclusion and Perspectives

We have shown that the dynamics of a close-to-axisymmetric isolated vortex with piecewise constant vorticity distribution could be well approximated by low-order Hamiltonian systems obtained through Taylor expansion of the original Hamiltonian. A comparison of two degrees of truncation, namely $H_{\mathrm{WNL}}$ and $H_{\mathrm{WNL+}}$, suggests that adding more modes and nonlinear interaction terms can improve the quality of the approximation. From $H_{\mathrm{WNL}}$, we derived an amplitude equation at the onset of instability by extending the work of M&F to be valid on each side of the bifurcation. We showed that the bifurcations of the first few modes were subcritical and analogous to the bifurcation of a charged particle in a radial potential superimposed to a uniform perpendicular magnetic field. Those results consolidate the findings of [8] with an Hamiltonian approach. From an analogy with the Kepler problem, we provided a prediction for the separatrix between initial conditions leading to bounded oscillations and those leading to unbounded growth, which was in good agreement with the numerical observations close to the bifurcation. Finally, we showed numerically that the truncated Hamiltonian $H_{\mathrm{WNL}}$ and $H_{\mathrm{WNL+}}$ admit V-states with any rotation rate within the rotation rates of infinitesimal perturbations. Those V-states have good chances to be relevant approximations to true V-states of the full dynamics.

This latter point remains to be verified using a solver for the V-states of the full dynamics, such as the synthetic annealing method of [9], and this is the subject of future work. Furthermore, the linear stability of the V-states of the truncated Hamiltonians $H_{\mathrm{WNL}}$ and $H_{\mathrm{WNL+}}$ (with respect to the dynamics of the truncated system) needs to be studied. This could open a way of estimating the linear stability of close-to-circular V-states of the full dynamics.

Finally, it might be interesting to extend the truncated models to interactions with modes outside the sets of subharmonics of a given mode $m$. From Equation (13), computing all triads of the form $(m, k) \leftrightarrow (m + k)$ is reduced to an enumeration process. Then, the Hamiltonian $\delta^2 H + \delta^3 H$ truncated to a given mode $k_{\max}$ could provide a fun set-up for numerical simulations of wave turbulence.

## 6 Acknowledgments

I owe my sincerest thanks to my supervisors, Glenn Flierl, Phil Morrison, and Ted Johnson, for their constant support and encouragement throughout this project. I am especially grateful to Glenn for his warm presence in Woods Hole and for our daily trailer meetings, where he always offered thoughtful advice and fresh ideas. I also want to thank Phil for inspiring me to take on this topic and for generously sharing his deep knowledge of Hamiltonian systems, and Ted for his help with the numerical simulations. A big thank you to all the fellows and staff who made this summer unforgettable, especially my roommate "Leo Thewy". I can't wait for another round of softball with everyone! Finally, I thank Professor Dritschel for providing his 1988 code, which served as an essential benchmark for my work.

## References


[1] *Whoi-91-03*, tech. rep., Woods Hole Oceanog. Inst. Tech. Rept., 1990.

[2] *Whoi-92-16*, tech. rep., Woods Hole Oceanog. Inst. Tech. Rept., 1992.

[3] *Whoi-94-l2*, tech. rep., Woods Hole Oceanog. Inst. Tech. Rept., 1994.

[4] R. Benzi, S. Patarnello, and P. Santangelo, *Self-similar coherent structures in two-dimensional decaying turbulence*, Journal of Physics A: Mathematical and General, 21 (1988), pp. 1221–1237.

[5] X. J. Carton, G. R. Flierl, and L. M. Polvani, *The generation of tripoles from unstable axisymmetric isolated vortex structures*, Europhysics Letters (EPL), 9 (1989), pp. 339–344.

[6] D. B. Chelton, M. G. Schlax, and R. M. Samelson, *Global observations of nonlinear mesoscale eddies*, Progress in Oceanography, 91 (2011), pp. 167–216.

[7] D. G. Dritschel, *Contour dynamics and contour surgery: Numerical algorithms for extended, high-resolution modelling of vortex dynamics in two-dimensional, inviscid, incompressible flows*, Computer Physics Reports, 10 (1989), pp. 77–146.

[8] G. R. Flierl, *On the instability of geostrophic vortices*, Journal of Fluid Mechanics, 197 (1988), pp. 349–388.

[9] G. R. Flierl, P. J. Morrison, and R. Vilasur Swaminathan, *Jovian vortices and jets*, Fluids, 4 (2019), p. 104.

[10] T. R. Group, *Gulf stream cold-core rings: Their physics, chemistry, and biology*, Science, 212 (1981), pp. 1091–1100.

[11] R. C. Kloosterziel and G. F. Carnevale, *Formal stability of circular vortices*, Journal of Fluid Mechanics, 242 (1992), pp. 249–278.

[12] J. C. Mcwilliams, *The emergence of isolated coherent vortices in turbulent flow*, Journal of Fluid Mechanics, 146 (1984), pp. 21–43.

[13] J. Meunier and B. Gallet, *Effective transport by 2d turbulence: Vortex-gas theory vs scale-invariant inverse cascade*, Physical Review Letters, 134 (2025), p. 074101.

[14] P. J. Morrison, *Hamiltonian description of the ideal fluid*, Reviews of Modern Physics, 70 (1998), pp. 467–521.

[15] A. A. Simon, F. Tabataba-Vakili, R. Cosentino, R. F. Beebe, M. H. Wong, and G. S. Orton, *Historical and contemporary trends in the size, drift, and color of jupiter's great red spot*, The Astronomical Journal, 155 (2018), p. 151.

[16] Y. Wang, F. J. Beron-Vera, and M. J. Olascoaga, *The life cycle of a coherent lagrangian agulhas ring*, Journal of Geophysical Research: Oceans, 121 (2016), pp. 3944–3954.

[17] N. J. Zabusky, M. Hughes, and K. Roberts, *Contour dynamics for the euler equations in two dimensions*, Journal of Computational Physics, 30 (1979), pp. 96–106.

[18] Q. Zou, E. Overman, H.-M. Wu, and N. Zabusky, *Contour dynamics for the euler equations: curvature controlled initial node placement and accuracy*, Journal of Computational Physics, 78 (1988), pp. 350–368.

# Tilted Rossby Waves or Turbulent Potential Vorticity Mixing: What Determines the Equatorial Jet Direction on Jupiter?

Heng Quan

August 19, 2025

## 1 Introduction

The atmospheric circulation on Jupiter features a zonally banded pattern of latitudinally alternating prograde and retrograde zonal jets. Several observational datasets [11, 19, 18] have revealed that there is a single wide and strong prograde equatorial jet in the tropics, whereas there are multiple narrower and weaker jets in the mid-latitudes (Figure 1). The prograde equatorial jet has been the subject of considerable research and will be the focus of this report.

The prograde equatorial jet is not physically intuitive at first glance. For an idealized freely evolving atmosphere, conservation of angular momentum suggests that the zonal mean zonal wind should increase poleward in the tropics, resulting in a minimum zonal velocity near the equator [7]. Because a maximum zonal velocity near the equator is observed instead, the prograde equatorial jet on Jupiter must have a source of angular momentum that drives a net transport of eastward momentum towards the equator.

Two theories are predominantly invoked to explain the emergence of the prograde equatorial jet on Jupiter. The first theory invokes eddy momentum transport towards the equator induced by tilted Rossby waves, including both vertical and transport in the $\sim 3000$ km-thick convective zone [3] or horizontal transport only in the $\sim 50$ km-thick outermost weather layer [17, 13, 22]. The second theory invokes the turbulent potential vorticity (PV) mixing process, where the sign of the meridional gradient of the planetary PV (i.e., the beta effect) determines the direction of momentum transport [23]. These two theories have been studied separately in previous work, but to our best knowledge have not been systematically studied together. As we will show later, tilted Rossby waves and turbulent PV mixing can cause opposite equatorial jet directions in certain cases.

In the present work, we study the simultaneous effects of these two theories by implementing simulations of stochastically forced two-dimensional turbulence in a rotating shallow-water model on the sphere. Using these simulations, we aim to

1. Identify the mechanism dominating momentum transport in different dynamical regimes;
2. Explain the formation of Jupiter's prograde equatorial jet in light of both theories.

This report is organized as follows. In Section 2, we describe the model we use and its numerical setup. In section 3, we introduce the tilted Rossby wave theory and the turbulent

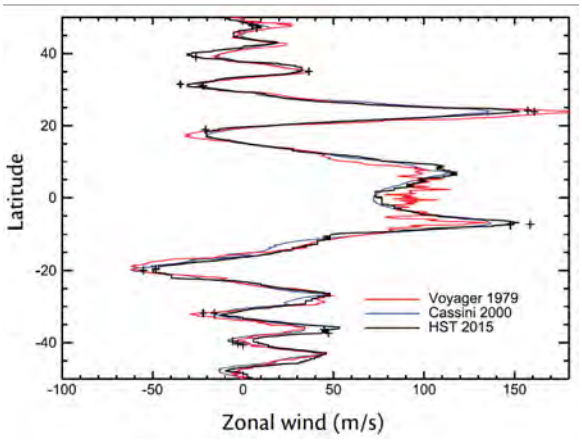


Figure 1: The latitudinal profiles of zonal mean zonal velocity on the outer surface of Jupiter from different observational datasets. This figure is from [18].

PV mixing theory. In Section 4, we show our simulation results, starting from the simplest case and gradually adjusting the model to be more complex and realistic. In Section 5, we summarize our conclusions.

## 2 Methods

Figure 2 shows a schematic of Jupiter's cross section. The innermost layer is primarily composed of metallic hydrogen, which is extremely conductive and generates a strong electromagnetic field. This electromagnetic field efficiently dissipates the kinetic energy through Ohmic dissipation [9, 5], so we consider the gas inside the Ohmic dissipation layer to be stagnant. The middle layer is the convective layer with deep jets, and the outermost layer is the weather layer where the zonal jets are directly observed. On Jupiter-like fast-rotating planets, the atmospheric motions spontaneously organize into Taylor columns parallel to the rotation axis [21]. These Taylor columns extend through the convective layer to the weather layer, and horizontal motions are largely invariant along the Taylor columns.

There are two primary ways to model the jets on Jupiter. The first is to use a deep model for the entire depth of the Taylor columns [3, 14, 23], which can explicitly resolve the convective forcing and the topographic beta effect. The second is to use a shallow model for the weather layer [4, 16, 17, 13, 22]. This report employs the shallow model. We start from the simplest setup: a single-layer spherical shallow-water model of the weather layer. In future work, we will incorporate the topographic beta effect into the shallow model.

We employ the following governing equations of the spherical shallow-water model

$$\frac{\partial \mathbf{u}}{\partial t} + (\mathbf{u}\cdot\nabla)\mathbf{u} + f\hat{r}\times\mathbf{u} = -\nabla\varphi - k_{\text{hyper}}\nabla^4\mathbf{u} - k_{\text{fric}}\mathbf{u} + \mathbf{F}, \tag{1}$$

$$\frac{\partial \varphi}{\partial t} + gH\nabla\cdot\mathbf{u} + \nabla\cdot(\varphi\mathbf{u}) = -k_{\text{rad}}\varphi. \tag{2}$$

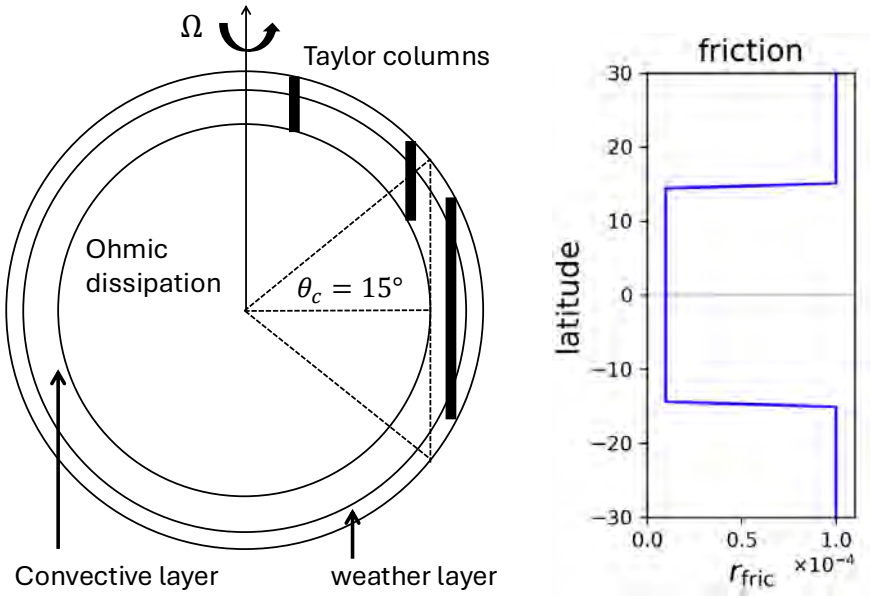


Figure 2: Left: Schematic showing the internal structure of Jupiter. Right: The idealized latitudinal profile of the nondimensional frictional damping coefficient (details in text).

All terms on the left-hand sides of equations 1 and 2 have their standard meanings. The two-dimensional (2-D) velocity field on a spherical shell is denoted by $\mathbf{u} = (u, v)$, and the Coriolis parameter is given by $f = 2\Omega \sin\theta$, where $\Omega$ is the planetary rotation rate and $\theta$ denotes the latitude. The symbol $\phi$ represents the geopotential anomaly. As sketched in Figure 3, we have

$$gh = gH + g\eta = gH + \varphi, \tag{3}$$

where $H$ is the average depth of the weather layer.

On the right-hand side of equations 1 and 2, $\mathbf{F}$ is a stochastic forcing term parameterizing the small-scale energy injection from convection and baroclinic eddies, $-k_{\text{fric}}\mathbf{u}$ is a frictional damping term (meant to capture the effect of the Ohmic dissipation layer, which acts as a bottom drag on the Taylor columns), $-k_{\text{rad}}\varphi$ is a radiative damping term (meant to capture the effect of radiative cooling of the upper weather layer), and $-k_{\text{hyper}}\nabla^4\mathbf{u}$ is a hyper-viscosity term to ensure numerical stability and achieve high-Reynolds-number behavior at large scales.

The stochastic forcing term $\mathbf{F}$ we use is similar to previous work [16, 13]. The energy is injected into a single spherical harmonic meridional wavenumber $l = 64$ and across all zonal wave numbers $-64 \leq m \leq 64$, with a constant energy injection rate $\varepsilon$. The forcing $\mathbf{F}$ at two adjacent time steps is not correlated.

The radiative damping coefficient $k_{\text{rad}}$ and the hyper-viscosity coefficient $k_{\text{hyper}}$ are globally uniform. The frictional damping coefficient $k_{\text{fric}}$ is tropically suppressed, as shown in Figure 2. This reflects the fact that atmospheric Taylor columns are not connected to the Ohmic dissipation layer outside the tangent cylinder, implying a much weaker frictional damping in the tropics (approximately $|\theta| \leq 15°$ for Jupiter). Overall, the governing equa-

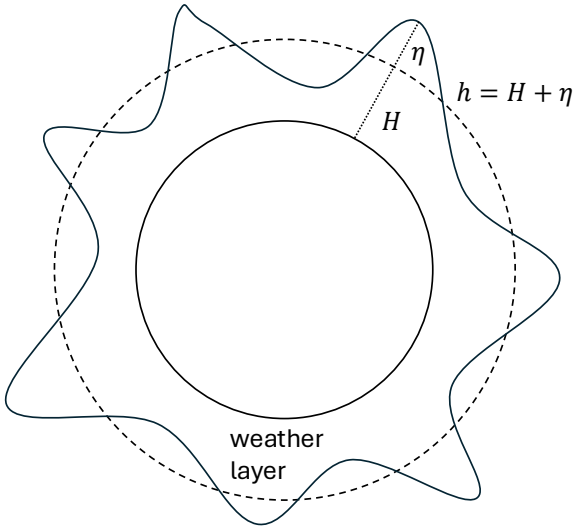


Figure 3: Schematic of the spherical shallow-water model for the weather layer of Jupiter, showing a top surface slightly perturbed from the perfect sphere. This figure is not to scale.

tions 1 and 2 are fairly standard in studies of shallow models [17, 13, 22]. However, our setup is unique in that we explicitly suppress the frictional damping in the tropics and systematically explore the separate and combined effects of both frictional and radiative damping.

To nondimensionalize the shallow-water equations, we use the planetary radius $R$ as the length scale and $T = 1/(2\Omega)$ as the timescale. The nondimensional shallow-water equations are

$$\frac{\partial \mathbf{u}'}{\partial t'} + (\mathbf{u}' \cdot \nabla')\mathbf{u}' + f'\hat{r} \times \mathbf{u}' = -\nabla'\varphi' - \nu\nabla'^4\mathbf{u}' - r_{\text{fric}}\mathbf{u}' + \mathbf{F}'(\varepsilon). \tag{4}$$

$$\frac{\partial \varphi'}{\partial t'} + \lambda_d^2 \nabla' \cdot \mathbf{u}' + \nabla' \cdot (\varphi'\mathbf{u}') = -r_{\text{rad}}\varphi' \tag{5}$$

Note that the nondimensional Coriolis parameter $f' = \sin\theta$. Variables with prime are nondimensional, and below we drop the prime for simplicity. The dimensional coefficients $k_{\text{fric}}, k_{\text{rad}}, k_{\text{hyper}}$ become nondimensional coefficients $r_{\text{fric}}, r_{\text{rad}}, r_{\text{hyper}}$. We use the following Jupiter-relevant values as the default nondimensional numbers to be consistent with [22], and perturb them to explore a wide parameter space.

- Hyper-viscosity coefficient $r_{\text{hyper}} = 2 \times 10^{-11}$;
- Radiative damping coefficient $r_{\text{rad}} = 2 \times 10^{-3}$;
- Frictional damping coefficient $r_{\text{fric}} = 1 \times 10^{-5}$ for $|\theta| \leq 15°$, and $r_{\text{fric}} = 1 \times 10^{-4}$ for $|\theta| > 15°$ (the global mean $r_{\text{fric}}$ is similar to [22] who used uniform frictional damping);
- Energy injection rate $\varepsilon = 1 \times 10^{-10}$;

- $\lambda_d = \frac{L_d}{R} = 0.025$, where the (polar) deformation radius $L_d = \frac{\sqrt{gH}}{2\Omega}$.

We numerically integrate the nondimensional shallow-water equations 4 and 5 using Dedalus [2], which can solve initial-value partial differential equations using a pseudospectral method in terms of spherical harmonic basis functions. We use a T255 triangular truncation with a 3/2 dealiasing factor, such that nonlinear terms are evaluated on a grid with 768 grid points in the zonal direction and 384 grid points in the meridional direction. We run each simulation until the zonal mean zonal velocity reaches a statistically stationary state where the energy injection is balanced by dissipation, and present nondimensional results based on long-time averages over this steady state.

# 3 Theories

## 3.1 The formation of jets

In 2-D turbulence, small-scale eddies tend to spontaneously organize into large-scale structures through a process known as the inverse energy cascade, during which the energy injected at small scales inversely cascades towards larger scales [8, 1, 20]. The inverse energy cascade starts to be influenced by the spatial anisotropy due to the beta effect at the beta scale $L_\beta \propto (\varepsilon\beta^{-3})^{1/5}$, where zonal jets start to form. Beyond that, the energy continues cascading to larger scales and the zonal jets grow wider until reaching the Rhines scale $L_R \propto \sqrt{U/\beta}$ ($U$ is a characteristic velocity) [12], where the inverse energy cascade is arrested by dissipation. Thus, the Rhines scale is the characteristic width of jets in steady state.

The direction of a jet can be explained by the zonal mean momentum budget. By calculating the zonal average of equation 1, we have

$$\frac{\partial \bar{u}}{\partial t} = \overline{v\zeta} + f\bar{v} - k_{\text{fric}}\bar{u} - k_{\text{hyper}}\nabla^4\bar{u} + \overline{F_\phi}, \tag{6}$$

where $\bar{u}$ is the zonal mean zonal velocity, $v$ is the meridional velocity, $\zeta = \hat{r}\cdot(\nabla\times\mathbf{u})$ is the relative vorticity, and $\overline{F_\phi}$ is the zonal mean zonal component of the forcing $\mathbf{F}$. Using the eddy-mean decomposition, we obtain

$$\frac{\partial \bar{u}}{\partial t} = \overline{v'\zeta'} + \bar{v}\bar{\zeta} + f\bar{v} - k_{\text{fric}}\bar{u} - k_{\text{hyper}}\nabla^4\bar{u} + \overline{F_\phi}. \tag{7}$$

For the equatorial jet, $\bar{v} \approx 0$, $f \approx 0$, and $\overline{F_\phi} \approx 0$. The dominant active term in equation 7 is the zonal mean eddy meridional vorticity flux $\overline{v'\zeta'}$, whereas the damping terms are passive terms in that they eventually stop the zonal flow from growing but do not drive a zonal flow themselves. For an incompressible 2-D flow, i.e., $\nabla\cdot\mathbf{u} = 0$, the $\overline{v'\zeta'}$ term can be rewritten as

$$\overline{v'\zeta'} = -\frac{\partial}{\partial y}\overline{u'v'}. \tag{8}$$

The latter term is more familiar, representing the meridional convergence of eddy-induced momentum flux.

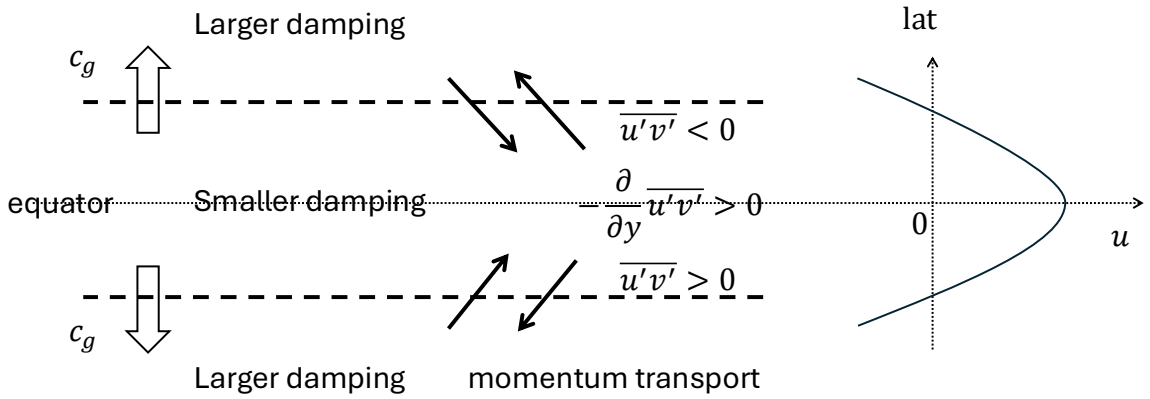


Figure 4: Schematic showing how tilted equatorial Rossby waves affect the equatorial jet direction (details in text).

The equatorial jet direction is largely determined by the sign of $\overline{v'\zeta'}$ in the early jet growth stage. There are two relevant theories: One argues that $\overline{v'\zeta'}$ is determined by tilted equatorially trapped Rossby waves, the other argues that $\overline{v'\zeta'}$ is controlled by a turbulent potential vorticity mixing process. Below we introduce each theory separately.

### 3.2 Tilted Rossby waves

The spatial structure of linear waves on an equatorial beta plane in a freely evolving shallow-water system can be analytically obtained following the standard approaches described in [10, 6]. With a globally-uniform radiative damping or frictional damping, analytical wave solutions featuring tilted equiphase lines and decaying amplitudes can still be obtained [13, 22]. However, here we focus on the physical picture rather than on the mathematics.

The nondimensional shallow-water equations 4 and 5 can be combined into one single global quasi-geostrophic potential vorticity (QGPV) equation if we assume the Rossby number $Ro = U/(2\Omega L) \ll 1$ ($L$ represents the characteristic horizontal length scale of the flow), the surface height perturbation $\eta \ll H$ and $|\partial f/\partial\theta| \ll |\partial u/\partial\theta|, |\partial v/\partial\theta|$ [15]. The nondimensional QGPV equation reads

$$\frac{\partial}{\partial t}\left(\zeta - \frac{\psi}{\lambda_d^2}\sin^2\theta\right) + \mathbf{u}\cdot\nabla\left(\zeta - \frac{\psi}{\lambda_d^2}\sin^2\theta\right) + \beta v = F_\zeta - r_{\text{fric}}\zeta - \nu\nabla^4\zeta + r_{\text{rad}}\frac{\psi}{\lambda_d^2}\sin^2\theta, \quad (9)$$

where $\psi$ is the quasi-geostrophic streamfunction satisfying $\zeta = \nabla^2\psi$ and $\mathbf{u} = \hat{r}\times\nabla\psi$. The nondimensional beta is $\beta = \cos\theta$, and the forcing term is given by $F_\zeta = \hat{r}\cdot(\nabla\times\mathbf{F})$.

The QGPV equation 9 shows that both the radiative damping and the frictional damping are tropically suppressed: the former is proportional to $\sin^2\theta$, and the latter has the imposed staircase profile (Figure 2). The tropically suppressed damping induces a poleward energy transport in the tropics, hence a poleward group velocity $c_g$ of equatorial Rossby waves [13]. As sketched in Figure 4, the poleward group velocity manifests itself as the westward tilt of the equiphase lines with increasing absolute value of latitude for Rossby waves,

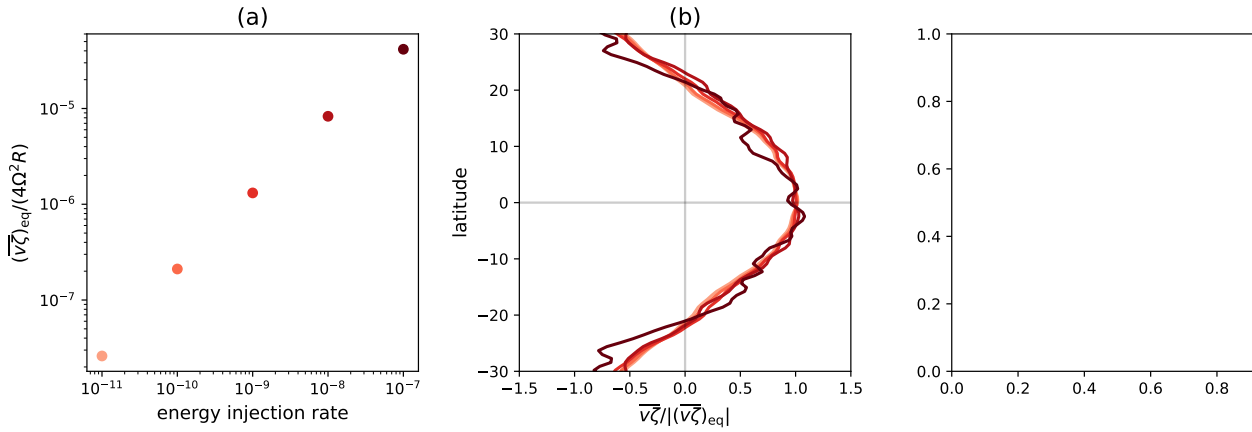


Figure 5: (a) The nondimensional equatorial zonal mean meridional vorticity fluxes, $(\overline{v\zeta})_{\mathrm{eq}}$, for linear shallow-water simulations with radiative damping only and different energy injection rates. (b) The meridional profiles of the zonal mean meridional vorticity flux $\overline{v\zeta}$ normalized by their equatorial values for the same simulations. A darker color represents a larger energy injection rate.

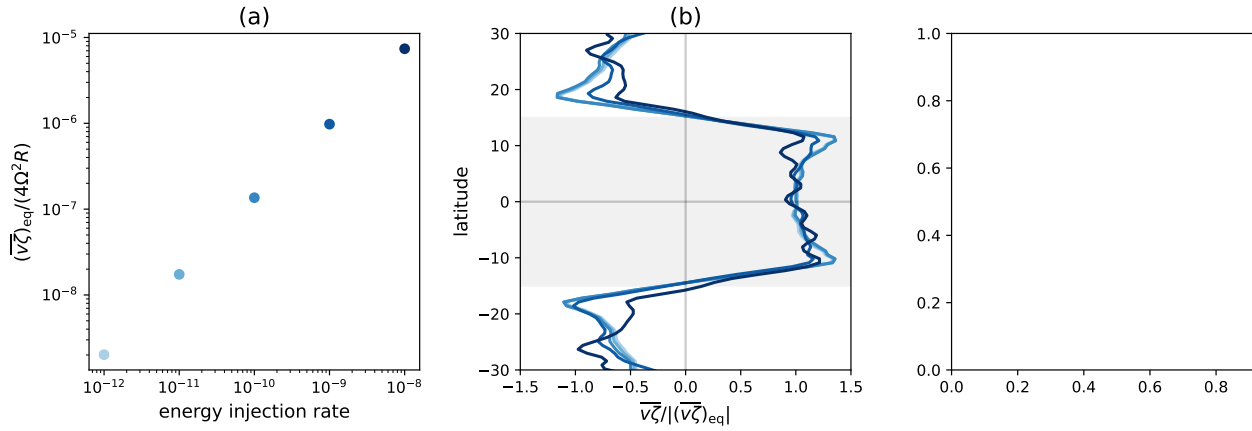


Figure 6: (a) The nondimensional equatorial zonal mean meridional vorticity fluxes, $(\overline{v\zeta})_{\mathrm{eq}}$, for linear shallow-water simulations with frictional damping only and different energy injection rates. (b) The meridional profiles of the zonal mean meridional vorticity flux $\overline{v\zeta}$ normalized by their equatorial values for the same simulations. A darker color represents a larger energy injection rate.

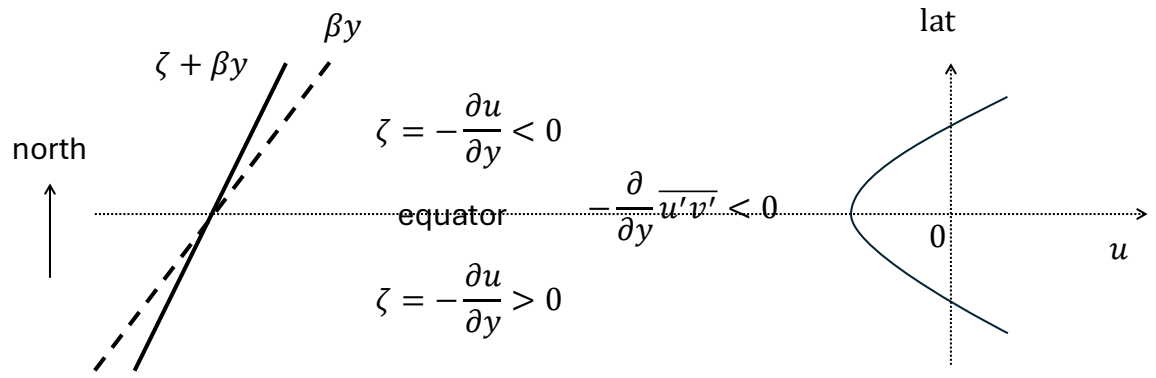


Figure 7: Schematic showing how the potential vorticity mixing process affects the equatorial jet direction (details in text).

resulting in a transport of eastward momentum towards the equator in both hemispheres. Therefore, tilted equatorial Rossby waves in rapidly rotating, Jovian-like planets tend to induce a positive momentum acceleration and a prograde equatorial jet with radiative and/or frictional damping.

To verify the sketch in Figure 4, we numerically integrate the following linear shallow-water equations to a steady state:

$$\frac{\partial \mathbf{u}}{\partial t} + f\hat{r} \times \mathbf{u} = -\nabla\varphi - \nu\nabla^4\mathbf{u} - r_{\text{fric}}\mathbf{u} + \mathbf{F}(\varepsilon). \tag{10}$$

$$\frac{\partial \varphi}{\partial t} + \lambda_d^2 \nabla \cdot \mathbf{u} = -r_{\text{rad}}\varphi. \tag{11}$$

The linear shallow-water equations sustain the equatorial waves in linearized analytical theories [13, 22], and these waves determine the equatorial jet direction in the early growth stage when the nonlinear terms are small. Both radiative damping (Figure 5) and frictional damping (Figure 6) alone result in a positive equatorial $\overline{v\zeta}$ in linear shallow-water simulations, confirming the positive momentum acceleration expected from Figure 4. Therefore, we expect a prograde equatorial jet in nonlinear shallow-water simulations due to tilted equatorial Rossby waves.

### 3.3 Potential vorticity mixing

The potential vorticity (PV) is a materially conserved variable for a freely evolving shallow-water system

$$\frac{\mathrm{D}}{\mathrm{D}t}\left(\frac{\zeta + f}{h}\right) = 0. \tag{12}$$

We consider incompressible (i.e., constant $h$) turbulent flows on an equatorial beta plane, where the background planetary vorticity is $f = \beta y$. The eddies seek to homogenize the potential vorticity across the equator, but cannot do so perfectly because of forcing and damping. As sketched in Figure 7, this homogenization of PV causes the absolute vorticity

$\zeta + f$ to be more well-mixed than $f$. As a result, there is a switch of the sign of $\zeta$ across the equator, which requires a minimum zonal velocity on the equator. In our shallow-water simulations the flow is compressible, so the potential vorticity $H(\zeta + f)/h$ is homogenized instead of the absolute vorticity $\zeta + f$. This difference, however, does not qualitatively affect the sketch in Figure 7 as we will show later. Therefore, we expect that the turbulent potential vorticity mixing process tends to induce a negative momentum acceleration and a retrograde equatorial jet.

# 4 Results

As discussed above, the tilted Rossby waves tend to cause a prograde equatorial jet, while the turbulent PV mixing process tends to cause a retrograde equatorial jet in the single-layer shallow-water model with tropically suppressed damping. We now study which process dominates in different cases.

## 4.1 Case I: radiative damping only

We first consider the case with radiative damping only and zero frictional damping. Figure 8(a)(b) shows the magnitude and meridional structures of the equatorial zonal jet in the steady state of shallow-water simulations with different energy injection rates. Consistent with previous studies [17, 13, 22], all of our simulations result in a prograde equatorial jet, which becomes stronger and wider for a larger energy injection rate (The characteristic jet width $L_R \propto \sqrt{U/\beta}$). This is consistent with the effect of tilted equatorial Rossby waves (Figure 4 and 5). In contrast, a prograde equatorial jet means a larger meridional PV gradient than the planetary PV gradient (see Figure 8(c)), which is contradictory to the effect of mixing turbulent potential vorticity (Figure 7). Therefore, the positive momentum acceleration and the associated prograde equatorial jet appear to be due to tilted equatorial Rossby waves in this case.

## 4.2 Case II: frictional damping only

Next, we consider the case with frictional damping only and zero radiative damping. Figure 9(a)(b) shows the magnitude and meridional structures of the equatorial zonal jet in the steady state of shallow-water simulations with different energy injection rates. Only the simulation with the weakest energy injection results in a prograde equatorial jet, while other simulations result in retrograde equatorial jets. A retrograde jet means a smaller meridional PV gradient than the planetary PV gradient (see Figure 9(c)), which is consistent with the effect of turbulent potential vorticity mixing (Figure 7). By contrast, a retrograde jet is contradictory to the effect of tilted equatorial Rossby waves (Figure 4 and 6). While previous studies predicted that the tropically suppressed frictional damping (Figure 2) would result in a prograde equatorial jet dominated by tilted Rossby waves [13, 22], our results indicate that the effect of PV mixing is stronger, resulting in a negative momentum acceleration and an associated retrograte equatorial jet in this case.

It seems that the prograde equatorial jet under the weakest energy injection in Figure 9(a)(b) is due to positive momentum acceleration from tilted Rossby waves. However, we

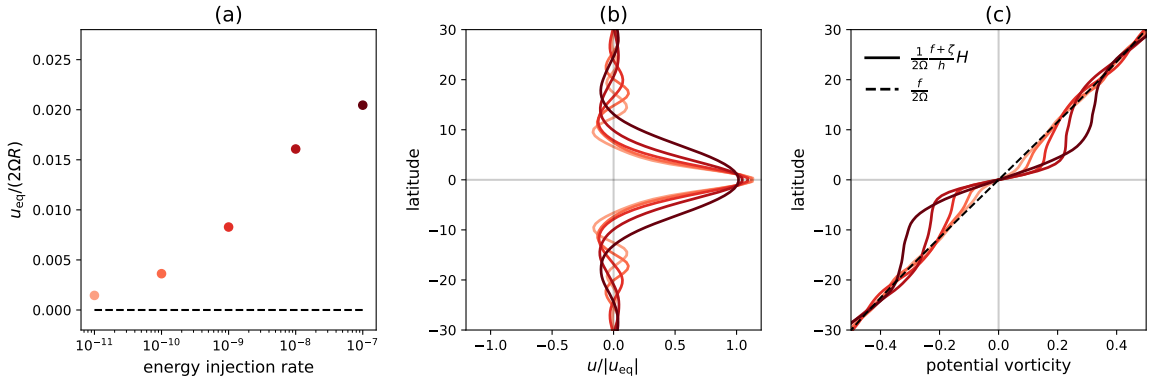


Figure 8: (a) The nondimensional equatorial zonal mean zonal velocity for simulations with radiative damping only and different energy injection rates. (b) The meridional profiles of zonal mean zonal velocity normalized by their equatorial values for the same simulations. (c) The meridional profiles of nondimensional zonal mean potential vorticity for the same simulations (solid) and the nondimensional planetary vorticity (dashed). A darker color represents a larger energy injection rate.

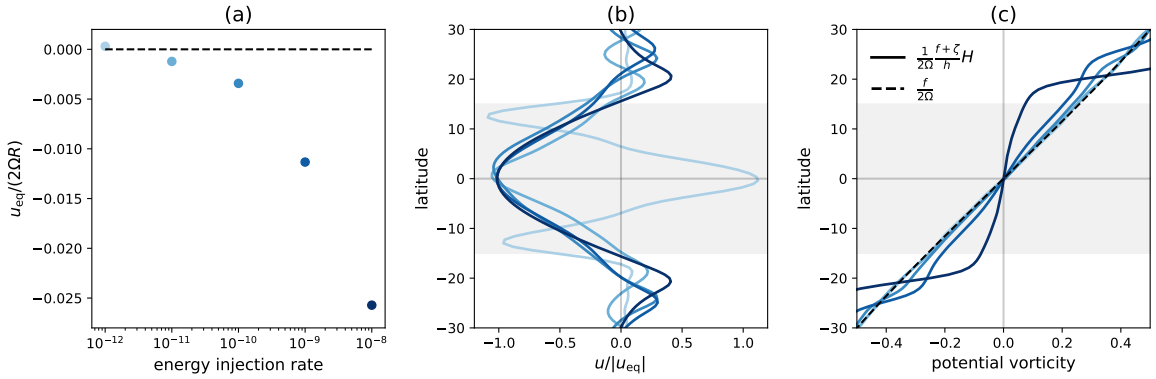


Figure 9: (a) The nondimensional equatorial zonal mean zonal velocity for simulations with frictional damping only and different energy injection rates. (b) The meridional profiles of zonal mean zonal velocity normalized by their equatorial values for the same simulations. (c) The meridional profiles of nondimensional zonal mean potential vorticity for the same simulations (solid) and the nondimensional planetary vorticity (dashed). A darker color represents a larger energy injection rate.

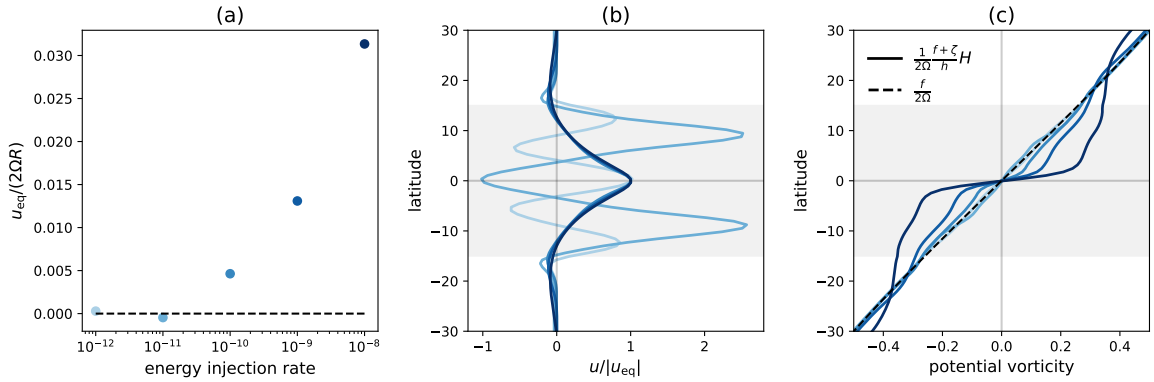


Figure 10: Same as Figure 9 but with the stochastic energy injection only in the tropics, i.e., $|\theta| < 15°$.

argue that it is instead due to insufficient PV mixing. The zonal mean zonal velocity is close to zero at $|\theta| = 15°$ under the influence of frictional damping, and the jet mixes PV in the tropics ($|\theta| < 15°$). The width of the jet $L_R \propto \sqrt{U/\beta}$ is positively correlated with the characteristic velocity and the energy injection rate. A single retrograde jet emerges under strong energy injection, which mixes PV in the entire tropics ($|\theta| < 15°$). However, there are multiple narrower jets in the tropics ($|\theta| < 15°$) under weak energy injection, so that PV is mixed around each retrograde jet. With the energy injection rate of $\varepsilon = 10^{-12}$, there is one prograde equatorial jet surrounded by two retrograde jets in the tropics ($|\theta| < 15°$) (Figure 9(b)), and PV is partially mixed by the two retrograde jets to the north and south of the equator.

We conduct another group of simulations to distinguish between the prograde equatorial jet resulting from insufficient PV mixing and that resulting from tilted Rossby waves. We repeat the simulations in Figure 9, but with the stochastic energy injection only in the tropics ($|\theta| < 15°$). By doing so, we have a tropically amplified energy injection in addition to the tropically suppressed frictional damping, which enhances the energy transport and momentum transport of tilted Rossby waves (Figure 4). As a result, the jet direction in Figure 10 is dominated by tilted Rossby waves. Under strong energy injection, the positive momentum acceleration from tilted Rossby waves causes a single prograde equatorial jet in the tropics ($|\theta| < 15°$) (Figure 10(a)(b)) and a larger meridional PV gradient than the planetary PV gradient (Figure 10(c)). Under weak energy injection, there are multiple jets in the tropics ($|\theta| < 15°$) and PV is partially mixed. Figure 10(b) indicates that the jet closest to $|\theta| = 15°$ in the tropics ($|\theta| < 15°$) is always prograde (for any number of jets) due to the positive momentum acceleration from tilted Rossby waves around $|\theta| = 15°$. These prograde jets near $|\theta| = 15°$ are oppositely directed compared to the profile of mean zonal velocity for the weakest energy injection in Figure 9(b). This contrast further demonstrates that the prograde equatorial jet under the weakest energy injection in Figure 9(b) is due to insufficient PV mixing instead of tilted Rossby waves.

To summarize, the turbulent PV mixing process determines the equatorial jet direction in simulations with tropically suppressed frictional damping. A single retrograde jet emerges under strong energy injection, while multiple narrower jets emerge under weak energy in-

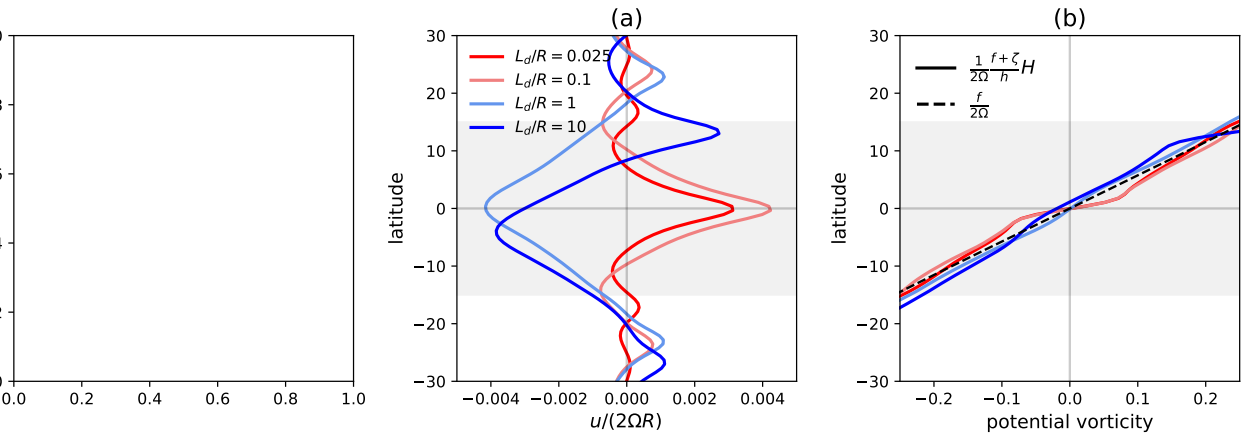


Figure 11: (a) The meridional profiles of nondimensional zonal mean zonal velocity for simulations with both damping terms and different Rossby deformation radii. (b) The meridional profiles of nondimensional zonal mean potential vorticity for the same simulations (solid) and the nondimensional planetary vorticity (dashed). These simulations have a modest nondimensional energy injection rate of $\varepsilon = 10^{-10}$.

jection. In the latter case the equatorial jet may be retrograde or prograde, depending on whether PV mixing occurs across the equator.

### 4.3 Case III: both damping terms

Finally, we consider the more realistic case with both radiative damping and frictional damping. Based on the case studies presented above, we expect that the equatorial jet direction depends on the relative importance of the two damping terms. If the radiative damping dominates, we expect a prograde equatorial jet controlled by tilted Rossby waves; if the frictional damping dominates, we expect a retrograde equatorial jet controlled by turbulent PV mixing, as long as there is enough energy injection to yield a single jet in the tropics ($|\theta| < 15°$).

We conduct shallow-water simulations with both damping terms and varying Rossby deformation radius under a fixed energy injection rate of $\varepsilon = 10^{-10}$. A larger deformation radius means that the flow is more incompressible and that the radiative damping is less important. Consider the $\lambda_d \to \infty$ limit of the shallow-water equations 4 and 5: In this case the shallow-water model becomes the incompressible barotropic model with a constant surface height, so the system does not feel the radiative damping. Figure 11 shows the mean flows and PV profiles in the steady state for simulations with different $\lambda_d$. The results are consistent with our expectations. With a small deformation radius (red curves), the radiative damping dominates, resulting in a prograde equatorial jet controlled by tilted Rossby waves (Figure 11(a)) and a larger meridional PV gradient than the planetary PV gradient (Figure 11(b)). With a large deformation radius (blue curves), the frictional damping dominates, resulting in a retrograde equatorial jet controlled by turbulent PV mixing (Figure 11(a)) and a smaller meridional PV gradient than the planetary PV gradient (Figure 11(b)).

The nondimensional numbers of the $L_d/R = 0.025$ simulation in Figure 11(a) are similar

to the corresponding Jovian-like values [22], and that simulation qualitatively reproduces the prograde equatorial jet on Jupiter. Therefore, we propose a possible explanation for the prograde equatorial jet on Jupiter within the single-layer shallow-water model framework: The effect of tilted Rossby waves dominates over the effect of turbulent PV mixing due to strong radiative damping, resulting in a positive momentum acceleration and a prograde equatorial jet.

# 5 Conclusions

In this study, we use a single-layer shallow-water model to study the prograde equatorial jet on Jupiter. We note that the same approach could also be applied to other planets. We introduce two alternative theories that make predictions about the equatorial jet direction. The momentum transport from tilted Rossby waves causes a prograde equatorial jet when we have a tropically suppressed damping, while the momentum transport from turbulent PV mixing causes a retrograde equatorial jet when we have a positive planetary beta (and the energy injection is strong enough that there is only one tropical jet). We study which mechanism dominates in different cases, and explain the prograde equatorial jet on Jupiter considering both theories. Our findings are:

1. If the radiative damping is the dominant damping, the momentum transport from tilted Rossby waves is likely the dominant process, causing a prograde equatorial jet.

2. If the frictional damping is the dominant damping, the momentum transport from turbulent PV mixing is the dominant process. A single retrograde jet emerges in the tropics (i.e., outside the tangent cylinder) under strong energy injection, while multiple narrower jets emerge under weak energy injection. In the latter case the equatorial jet may be retrograde or prograde, depending on whether PV mixing occurs across the equator.

3. In Jupiter's weather layer, the radiative damping is thought to be the dominant damping [17, 22], so the momentum transport from tilted Rossby waves may dominate over the momentum transport from turbulent PV mixing, resulting in a prograde equatorial jet.

Many important questions remain open. We plan to study the fundamental physical difference between radiative damping and frictional damping to explain why the effect of tilted Rossby waves dominates under radiative damping, while turbulent PV mixing dominates under frictional damping. We also plan to incorporate the topographic beta effect relevant to deep planetary atmospheres [23] into the shallow-water model and explore how it affects the equatorial jet direction.

# 6 Acknowledgements

I sincerely thank my advisors Loren Matilsky, Adrian Van Kan, Geoffrey Vallis, Wanying Kang and Glenn Flierl for their guidance. I thank Yaoxuan Zeng for his suggestions and

Keaton Burns for his help on Dedalus. I also thank Pascale Garaud and David Goluskin for organizing the GFD summer program, and other GFD fellows and visitors for their companionship during the summer.

## References

[1] G. Boffetta and R. E. Ecke, *Two-dimensional turbulence*, Annual Review of Fluid Mechanics, 44 (2012), pp. 427–451.

[2] K. J. Burns, G. M. Vasil, J. S. Oishi, D. Lecoanet, and B. P. Brown, *Dedalus: A flexible framework for numerical simulations with spectral methods*, Physical Review Research, 2 (2020), p. 023068.

[3] F. H. Busse, *Convective flows in rapidly rotating spheres and their dynamo action*, Physics of fluids, 14 (2002), pp. 1301–1314.

[4] J. Y.-K. Cho and L. M. Polvani, *The emergence of jets and vortices in freely evolving, shallow-water turbulence on a sphere*, Physics of Fluids, 8 (1996), pp. 1531–1552.

[5] M. French, A. Becker, W. Lorenzen, N. Nettelmann, M. Bethkenhagen, J. Wicht, and R. Redmer, *Ab initio simulations for material properties along the Jupiter adiabat*, The Astrophysical Journal Supplement Series, 202 (2012), p. 5.

[6] A. E. Gill, *Some simple solutions for heat-induced tropical circulation*, Quarterly Journal of the Royal Meteorological Society, 106 (1980), pp. 447–462.

[7] I. M. Held and A. Y. Hou, *Nonlinear axially symmetric circulations in a nearly inviscid atmosphere*, Journal of the Atmospheric Sciences, 37 (1980), pp. 515–533.

[8] R. H. Kraichnan, *Inertial ranges in two-dimensional turbulence*, The Physics of Fluids, 10 (1967), pp. 1417–1423.

[9] J. Liu, P. M. Goldreich, and D. J. Stevenson, *Constraints on deep-seated zonal winds inside Jupiter and Saturn*, icarus, 196 (2008), pp. 653–664.

[10] T. Matsuno, *Quasi-geostrophic motions in the equatorial area*, Journal of the Meteorological Society of Japan. Ser. II, 44 (1966), pp. 25–43.

[11] C. C. Porco, R. A. West, A. McEwen, A. D. Del Genio, A. P. Ingersoll, P. Thomas, S. Squyres, L. Dones, C. D. Murray, T. V. Johnson, et al., *Cassini imaging of Jupiter's atmosphere, satellites, and rings*, Science, 299 (2003), pp. 1541–1547.

[12] P. B. Rhines, *Waves and turbulence on a beta-plane*, Journal of Fluid Mechanics, 69 (1975), pp. 417–443.

[13] I. Saito and K. Ishioka, *Mechanism for the formation of equatorial superrotation in forced shallow-water turbulence with Newtonian cooling*, Journal of the Atmospheric Sciences, 72 (2015), pp. 1466–1483.

[14] T. Schneider and J. Liu, *Formation of jets and equatorial superrotation on Jupiter*, Journal of the atmospheric sciences, 66 (2009), pp. 579–601.

[15] W. H. Schubert, R. K. Taft, and L. G. Silvers, *Shallow water quasi-geostrophic theory on the sphere*, Journal of Advances in Modeling Earth Systems, 1 (2009).

[16] R. K. Scott and L. M. Polvani, *Forced-dissipative shallow-water turbulence on the sphere and the atmospheric circulation of the giant planets*, Journal of the Atmospheric Sciences, 64 (2007), pp. 3158–3176.

[17] ——, *Equatorial superrotation in shallow atmospheres*, Geophysical Research Letters, 35 (2008).

[18] A. A. Simon, M. H. Wong, and G. S. Orton, *First results from the Hubble OPAL program: Jupiter in 2015*, The Astrophysical Journal, 812 (2015), p. 55.

[19] A. A. Simon-Miller and P. J. Gierasch, *On the long-term variability of Jupiter's winds and brightness as observed from Hubble*, Icarus, 210 (2010), pp. 258–269.

[20] S. Sukoriansky, N. Dikovskaya, and B. Galperin, *On the arrest of inverse energy cascade and the Rhines scale*, Journal of the Atmospheric Sciences, 64 (2007), pp. 3312–3327.

[21] G. K. Vallis, *Essentials of atmospheric and oceanic dynamics*, Cambridge university press, 2019.

[22] E. S. Warneford and P. J. Dellar, *Super-and sub-rotating equatorial jets in shallow water models of Jovian atmospheres: Newtonian cooling versus Rayleigh friction*, Journal of Fluid Mechanics, 822 (2017), pp. 484–511.

[23] Y. Zeng, W. Kang, G. R. Flierl, and G. K. Vallis, *Influence of jet depth on the equatorial jet direction on giant planets*, arXiv preprint arXiv:2503.17828, (2025).

# Pattern Transitions in Faraday Waves: From Hexagons to Beaded Stripes

Kyle McKee

August 20, 2025

## 1 Introduction

### 1.1 Faraday waves

When a container of liquid is shaken harmonically in the vertical direction, the effect on the governing equations is to modulate gravity so that $g$ is replaced by $g(t) = g + A\sin(\Omega t)$ in the moving frame of the container for some forcing frequency $\Omega$ and amplitude $A$. For small shaking amplitudes, the base state comprising a flat fluid-air interface is stable. However, when the acceleration is raised beyond a frequency-dependent threshold, the surface becomes unstable to Faraday waves. This instability was discovered by [5] and has been the focus of many theoretical and experimental studies to this day [9, 2, 10, 3]. The linear stability of a vertically shaken container of (inviscid) fluid was first analyzed mathematically by [1], who showed that the amplitude of a surface disturbance corresponding to a container eigenmode evolves according to a Mathieu equation, such that the stability is characterized by the so-called Mathieu tongue diagram (see [1, Fig. 2]). Depending on the values of two known functions of the system parameters, $p(g, A, \cdots)$ and $q(g, A, \cdots)$, the Mathieu tongue diagram indicates whether the point $(p, q)$ is stable (exterior to a tongue) or unstable (inside a tongue). The stability tongues were computed in the case of a real viscous fluid later by [8].

In settings where the flat base state is linearly unstable, the wave amplitude initially undergoes exponential growth, until nonlinearities cause waves to saturate at finite amplitude. The nature of these nonlinearities dictate which spatial patterns emerge in the finite amplitude waves. An active area of research seeks to understand the emergent wave patterns, and the transitions between different patterned states [14, 2, 4, 13].

### 1.2 Hexagonal patterns

The first fully nonlinear numerical simulations of Faraday waves were presented by [11], which opened the door for detailed numerical studies of why patterns emerge and how patterns dynamically switch either periodically, quasiperiodically, or chaotically. One study that built off of this new numerical capability was that of [12], wherein hexagonal Faraday wave patterns were studied numerically. Hexagonal patterns had been previously observed experimentally [7], which served to motivate this study.

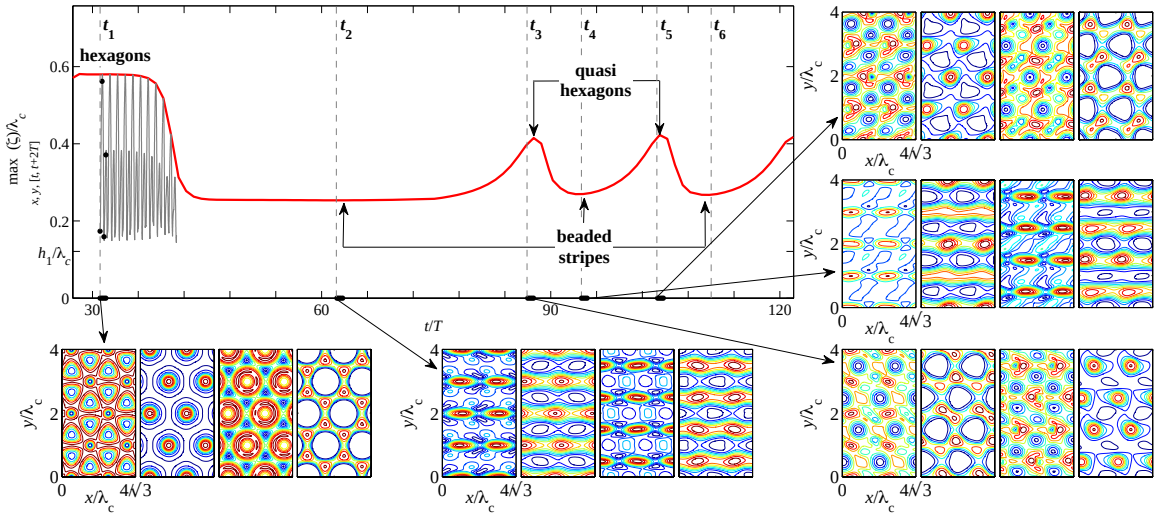


Figure 1: Dynamics observed in [12]. In the top left panel, the red line traces one of the wave vector amplitudes when the system is initialized in the hexagon state. As time progresses, the hexagon state destabilizes in favour of the beaded stripe and quasihexagons.

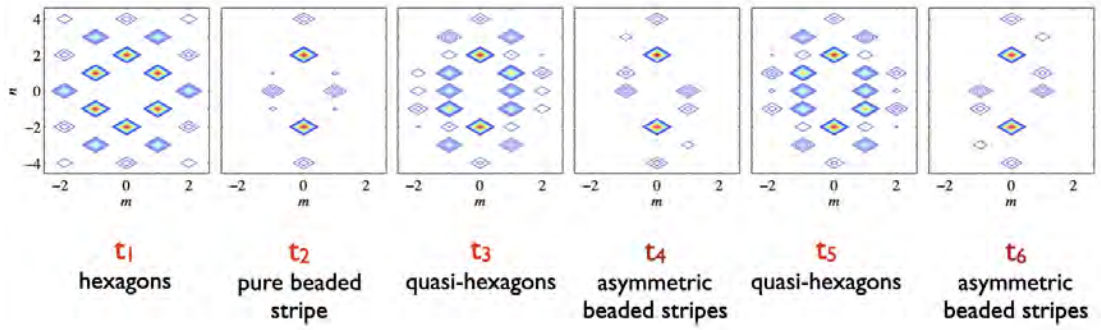


Figure 2: Amplitude of Fourier modes seen in the dynamics of [12]. Beginning in the hexagon state at time $t_1$, the Fourier representation of the wavefield has components mainly on the hexagonal lattice. At a later time, $t_2$, the state has wave components with both on-lattice vectors and the off-lattice vector $\boldsymbol{k}_4$. Quasi-hexagons and asymmetric beaded stripe patterns also contain the same off-lattice vector, $\boldsymbol{k}_4$.

In their work, [12] considered the evolution of Faraday waves on a doubly periodic domain with a rectangular basis cell. The aspect ratio of the rectangle was chosen to be $1/\sqrt{3}$ to ensure that the hexagonal basis vectors were all contained within the working basis. Because the dynamics were solved numerically on a rectangular grid, off-lattice wave vectors are also included in the simulation. The hexagonal lattice wave vectors ($\boldsymbol{k}_1$, $\boldsymbol{k}_2$, and $\boldsymbol{k}_3$) are free to interact with these additional wave vectors, which gives rise to the dynamic pattern switching observed by [12] which are outlined in Fig. 1. In fact, when the amplitudes were initialized in numerical simulations such that the waves began in the hexagonal state (up to some inevitable small perturbation), the state destabilized into a new state involving an off-lattice vector, which we have labeled $\boldsymbol{k}_4$. The transition in the Fourier contributions of the wave patterns can be seen in Fig. 2. Therein, the amplitude of the off-lattice wave vector is seen to grow during the transition and the system tends toward the non-hexagonal stationary state denoted *beaded stripes*. Later, so-called *quasi-hexagons* and *asymmetric beaded stripes* were observed. A key feature of these non-hexagonal states that we will exploit in our analysis, in seeking a minimal model for explaining these transitions, is that the off-lattice vector $\boldsymbol{k}_4$ has the largest off-lattice amplitude in all of these observed states. We will thus derive equations that describe the interactions of the hexagonal lattice vectors with $\boldsymbol{k}_4$. By neglecting other wave vectors in our model, we are implicitly assuming that the the observed dynamical states from [12] are robust enough that they exist even in the absence of the neglected off-lattice modes. The validity of this assumption shall be assessed *a posteriori*.

We proceed by deriving the most general model describing interactions between hexagonal wave vectors and the dominant off-lattice vector, $\boldsymbol{k}_4$, while ignoring the effects of all other wave vectors. We then study the steady states (fixed points) of our model, the stability of these steady states, and the dynamics of transitions between these states. Lastly, we use our model to qualitatively rationalize the dynamics observed in [12] and describe future directions still to be explored.

## 2 Problem Formulation and Amplitude Equations

We now proceed by deriving a set of equations describing the interaction between lattice vectors. The key hexagonal lattice vectors ($\boldsymbol{k}_1$, $\boldsymbol{k}_2$, and $\boldsymbol{k}_3$) along with the most important off-lattice vector $\boldsymbol{k}_4$, which we shall include in our model, are depicted in Fig. 3.

Put mathematically, we seek evolution equations for amplitudes of plane waves, $\{\boldsymbol{z}_1, \boldsymbol{z}_2, \boldsymbol{z}_3, \boldsymbol{z}_4\}$, with corresponding wave vectors $\{\boldsymbol{k}_1, \boldsymbol{k}_2, \boldsymbol{k}_3, \boldsymbol{k}_4\}$. These general evolution equations shall be derived in an abstract fashion, with generic coefficients that should be fixed by the physics being described (i.e., parameters of the Faraday wave system). We note that the amplitude equations involving only the on-lattice vectors have already been derived by [6], and we shall see these equations emerge as a special limit of our general equations when we set $z_4 = 0$.

Our wave ansatz is given by,

$$f(x, y, t) = \sum_{j=1}^{4} z_k(t) e^{\mathrm{i}\boldsymbol{k}_j \cdot \boldsymbol{x}} + \text{c.c.}, \tag{1}$$

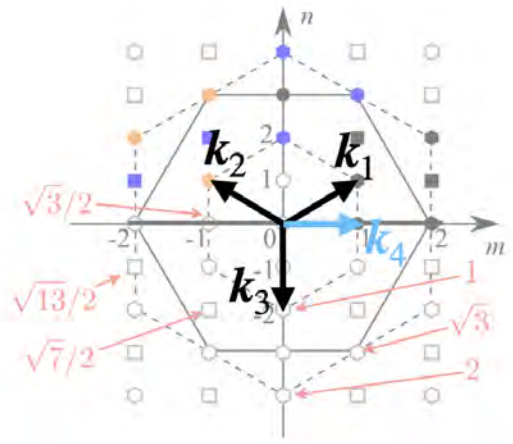


Figure 3: Wave vectors included in our model.

where c.c. denotes complex conjugation, and $\boldsymbol{k}_j$ are three fundamental hexagonal lattice basis vectors along with the off-lattice vector: $\boldsymbol{k}_1 = (1, \sqrt{3})$, $\boldsymbol{k}_2 = (-1, \sqrt{3})$, $\boldsymbol{k}_3 = (0, -2\sqrt{3})$ and $\boldsymbol{k}_4 = (1, 0)$.

## 2.1 Deriving the amplitude equations

In order to derive the evolution equations $\dot{z}_k(t) = f_k(z_1, \cdots, z_4)$, we need to deduce all compatible forms of the right side functions, $f_k$. This is done by matching the possible spatial forms of the waves, and truncating at cubic order. We shall demonstrate this process for the case of $z_1$ and then we suppress the details for the other three terms. The essential idea is that $\dot{z}_p \sim \dot{z}_l \dot{z}_m$ is only possible if $\boldsymbol{k}_p = \boldsymbol{k}_l + \boldsymbol{k}_m$. It is worth noting that $\dot{z}_p \sim \overline{\dot{z}_l \dot{z}_m}$ is possible if $\boldsymbol{k}_p = -\boldsymbol{k}_l - \boldsymbol{k}_m$. Hence the possibility of having conjugate terms means an even larger dictionary of compatible terms.

Considering the evolution of $\dot{z}_1$, we require,

$$(1, 1) = \alpha(0, -2) + \beta(1, 0) + \gamma(-1, 1) + \delta(1, 1), \tag{2}$$

where $\{\alpha, \beta, \gamma, \delta\} \in \mathbb{Z}$ are the amplitude exponents. In general, the equations become,

$$1 = \beta - \gamma + \delta \Rightarrow \boxed{\gamma = \beta + \delta - 1} \tag{3}$$

$$1 = -2\alpha + \gamma + \delta = -2\alpha + \beta + 2\delta - 1 \Rightarrow \boxed{\alpha = \frac{\beta - 2 + 2\delta}{2}}. \tag{4}$$

### 2.1.1 $\delta = 0$

The terms corresponding to $\delta = 0$ satisfy,

$$1 = \beta - \gamma \Rightarrow \boxed{\gamma = \beta - 1} \tag{5}$$

$$1 = -2\alpha + \gamma \Rightarrow \boxed{\alpha = \frac{\beta - 2}{2}}, \tag{6}$$

| | | | |
|---|---|---|---|
| $\beta = -2$ | $\alpha = -2$ | $\gamma = -3$ | $\overline{z_3^2 z_4^2 z_2^3}$ |
| $\beta = 0$ | $\alpha = -1$ | $\gamma = -1$ | $\overline{z_3 z_2}$ |
| $\beta = 2$ | $\alpha = 0$ | $\gamma = 1$ | $z_4^2 z_2$ |
| $\beta = 4$ | $\alpha = 1$ | $\gamma = 3$ | $\overline{z_4^4 z_3 z_2^3}$ |

Table 1: $\dot{z}_1$ terms

from which it follows that $\beta$ is necessarily even to ensure that $\alpha$ is an integer. Note that when $\beta = 0$, we find that $\alpha = \gamma = -1$ corresponding to the term $\overline{z_2 z_3}$. When $\beta = 2$, we find and $\gamma = 1$ and $\alpha = 0$. These and higher order terms are given in Table 1. Terms in blue are both new relative to the equations of [6] and also of at most cubic order (i.e., these terms shall augment those of Hoyle in our model).

### 2.1.2 $\delta = 1$

The terms corresponding to $\delta = 1$ satisfy,

$$\gamma = \beta \tag{7}$$

$$\alpha = \frac{\beta}{2}, \tag{8}$$

which implies that $\beta$ must be even. We will only retain cubic terms. When $\beta = 0$, we find $\gamma = \alpha = 0$ corresponding to the trivial term $z_1$ which we note can have a collection of coefficients that are given in our final equation below. When $\beta = 2$, we find $\alpha = 1$ and immediately see that the corresponding term will be at least of quartic order $\mathcal{O}(z^4)$. The last case to check is $\beta = -2$. In this case, $\alpha = -1$ and again we are left with only terms of an order that is higher than cubic. Hence, there are no terms for $\delta = 1$ other than the trivial ones we've already written down (i.e., none involving $z_4$).

### 2.1.3 $\delta = -1$

The terms corresponding to $\delta = -1$ satisfy,

$$\boxed{\gamma = \beta - 2}, \tag{9}$$

$$\boxed{\alpha = \frac{\beta - 4}{2}}, \tag{10}$$

$$\tag{11}$$

Clearly, we require again that $\beta$ is even. The only cases we need to check are $\beta = -2, 0, 2$. $\beta = -2$ gives $\alpha = -3$, $\beta = 0$ gives $\alpha = -2$ and $\beta = -2$, whereas $\beta = 2$ yields $\alpha = -1$ and $\gamma = 0$. All of the mentioned combinations are at least of quartic powers.

### 2.1.4 $\delta = 2$

The terms corresponding to $\delta = 2$ satisfy,

$$\boxed{\gamma = \beta + 1} \tag{12}$$

$$\boxed{\alpha = \frac{\beta + 2}{2}}, \tag{13}$$

which yields the possible combinations: $\beta = 0, \alpha = 1, \gamma = 1$, $\beta = 2, \alpha = 2, \gamma = 3$,$\beta = -2, \alpha = 0, \gamma = -1$, all of which are of higher order than cubic in $z$.

### 2.1.5 $\delta = -2$

This is the last case to check since, to cubic order we can't have $\delta = -3$ or $\delta = -3$. For $\delta = -2$, the equations read,

$$\boxed{\gamma = \beta - 3} \tag{14}$$

$$\boxed{\alpha = \frac{\beta - 6}{2}}, \tag{15}$$

$$\tag{16}$$

and clearly there are no possible cubic combinations (only need to check $\beta = 0$, in which case $\alpha = -3$ and $\gamma = -3$).

A similar analysis yields all possible equations governing the time-evolution of $\{z_1, z_2, z_3, z_4\}$. The final resulting equations are given as follows,

$$\begin{aligned}
\dot{z}_1 &= \left(\mu - b|z_1|^2 - c\left(|z_2|^2 + |z_3|^2\right) - \beta|z_4|^2\right) z_1 + a\overline{z_2 z_3} + \gamma z_4^2 z_2 \\
\dot{z}_2 &= \left(\mu - b|z_2|^2 - c\left(|z_1|^2 + |z_3|^2\right) - \beta|z_4|^2\right) z_2 + a\overline{z_3 z_1} + \gamma \overline{z_4}^2 z_1 \\
\dot{z}_3 &= \left(\mu - b|z_3|^2 - c\left(|z_1|^2 + |z_2|^2\right) - \tilde{\beta}|z_4|^2\right) z_3 + a\overline{z_1 z_2} \\
\dot{z}_4 &= \left(\tilde{\mu} - g\left(|z_1|^2 + |z_2|^2\right) - h|z_3|^2 - m|z_4|^2\right) z_4 + \zeta z_1 \overline{z_2 z_4},
\end{aligned}$$

where the terms in blue are those that augment the pure hexagon equation of [6]. This set of equations represents our general model of on-lattice wave vector interactions with $\boldsymbol{k}_4$.

## 3 Steady States of the Governing Equations

Clearly, a subset of the steady states of our system are those found by Hoyle [6], wherein $z_4 = 0$. For example, the hexagon state still exists, and it is described by $z_4 = 0$ and

$$z_1 = z_2 = z_3 = r \equiv \frac{a + \sqrt{a^2 + 4\mu(b + 2c)}}{2\,(b + 2c)}. \tag{17}$$

Another state wherein $z_4 = 0$ are the rolls that have $z_1 = z_2 = 0$ and $z_3 = \sqrt{\mu/b}$

However, the stability analysis of theses states as presented in [6], need not carry over to our new equations, since perturbations may now also involve $z_4$. Hence, a new stability

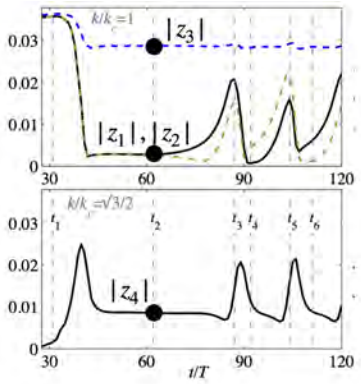


Figure 4: Evolution of the amplitudes of each wave vector in the work of [12]. The circles depict amplitudes in the mixed bead state.

analysis must be carried out to assess the stability of these states in our equations. In fact, if our model is to capture the dynamics observed by [12], we expect that the hexagon state shall go unstable precicely to the growth of $z_4$.

A new state, which we call the pure beaded stripe involves $z_4$ and is given by $z_1 = z_2 = 0$, $z_3 = \sqrt{\mu/b}$, and $z_4 = \sqrt{(\tilde{\mu} - h\mu/b)/m}$. While this state is convenient to write down analytically, it does not quite correspond to the mixed bead state observed by [12] in Fig. 4, which also has non-zero amplitudes of $z_1$ and $z_2$. As we will show later in our bifurcation analysis, a mixed bead state with $z_1 = z_2 \neq 0$ indeed exists and arises out of a bifurcation of the pure beaded stripe; while we do not have a simple analytical expression for the mixed state, it is straightforward to track via Newton iteration after understanding how it arises from a pitchfork bifurcation.

In what follows, we will start with a set of parameters where the basic state when $z_4 = 0$ is well characterized by the analysis of Hoyle. In particular, we start in the regime of the Hoyle diagram given by the value of $\mu$ depicted in Fig. 5, where hexagons and rolls coexist. We then examine the effect of increasing $\tilde{\mu}$ on stability and existence of steady states. A natural limit of the system is $\tilde{\mu} \to -\infty$, which approximates the condition $z_4 = 0$. Note that we have chosen parameters such that the hexagons begin stable when $\tilde{\mu} \to -\infty$. As $\tilde{\mu}$ is increased, the influence of $z_4$ on dynamics becomes more pronounced. In ongoing work, we are investigating the role of $\gamma$ in influencing the dynamics. However, in the present report $\gamma$ has been set to a constant while only $\tilde{\mu}$ is varied. In focusing on this single parameter, we are able to construct a bifurcation diagram of the emergent states.

## 4 Eigenvalues, Linear Stability, and Bifurcations

Beginning with one of our steady solutions to the governing equations, such as the hexagons or pure beaded stripes, we can assess the linear stability of this state by examining the corresponding eigenvalues and eigenvectors of its Jacobian. When the real part of the eigenvalues change sign, there the stability of the state changes. Moreover, when an eigenvalue crosses zero as some parameter (e.g., $\tilde{\mu}$) is varied, there is necessarily a pitchfork bifurcation there

(as long as certain conditions on the Hessian hold). In one direction of adjustment of the bifurcation parameter, new states are born out of this bifurcation. The main branch state also swaps stability at this point.

Thus, by examining the eigenvalues of a steady state, we can both: (1) assess its stability and (2) predict the emergence of new states, which might be stable or unstable. The new states can be found and tracked numerically using a Newton method. This numerical procedure is aided by the fact that we know that these states emerge along the zero eigenvalue eigen-directions of the system at the bifurcation point.

We proceed by assessing the hexagon stability, and show that, indeed, for sufficiently large $\tilde{\mu}$, the hexagon base state destabilizes to the growth of the amplitude $z_4$. We then present results of simulations of our model equations that show, for different values of $\tilde{\mu}$, what the hexagon destabilizes into. We then move on to examine the stability of the pure bead state. By tracking the eigenvalue crossings of this state, we are then able to construct a bifurcation diagram of the steady states of our model as $\tilde{\mu}$ is varied (see Fig. 7).

### 4.1 Stability and dynamics of the hexagon state

The stability of the hexagon base state is found by perturbing the base state, $z_1 = z_2 = z_3 = r$; $z_4 = 0$, with arbitrary complex perturbations $\delta z_1, \delta z_2, \delta z_3$ and $\delta z_4 = x_4 + \mathrm{i}y_4$. In our chosen parameter regime we know the hexagons are stable from the stability analysis of Hoyle. The new mode decouples from the others leading to the following Jacobian,

$$J = \begin{pmatrix} J_{\mathrm{hex},Hoyle} & 0 & 0 \\ 0 & \tilde{\mu} + (\zeta - 2g - h)\, r^2 & 0 \\ 0 & 0 & \tilde{\mu} + (-\zeta - 2g - h)\, r^2 \end{pmatrix}, \tag{18}$$

where $J_{\mathrm{hex},Hoyle}$ corresponds to the 6-by-6 Jacobian of the Hoyle analysis which is independent of $\tilde{\mu}$. Hence the hexagon state becomes unstable if either $\tilde{\mu} > (\zeta - 2g - h)\, r^2$ or $\tilde{\mu} > (-\zeta - 2g - h)\, r^2$. Hence, it is clear that through sufficient increase of $\tilde{\mu}$, it is always possible to destabilize the hexagon to the growth of $z_4$. We now discuss the dynamics corresponding to numerical simulations starting in the hexagon state, subject to small perturbations. Depending on the value of $\tilde{\mu}$, the system can have qualitatively different dynamics. We then construct a bifurcation diagram of the system with varying $\tilde{\mu}$, which puts these dynamics into context.

### 4.2 Dynamics leaving the hexagon state

For three values of $\tilde{\mu}$, our model equations are evolved from the hexagon base state, subject to a random small perturbation. The resulting trajectories (in amplitude coordinates) are plotted in the right panel of Fig. 6. In all cases the hexagon state is unstable and tends toward the pure beaded stripe state. Depending on the value of $\tilde{\mu}$, the eigenvalues of the pure beaded stripe state may be all negative (stable), or some may be positive such that there exists at least one unstable direction (saddle point). In the latter case, a trajectory that leaves the hexagon toward the pure beaded stripe later leaves the pure state either back to the hexagon or into a new orbit. It is thus observed that the dynamics are affected by $\tilde{\mu}$ in two important ways. First, its value can change the stability of a state. Second, it

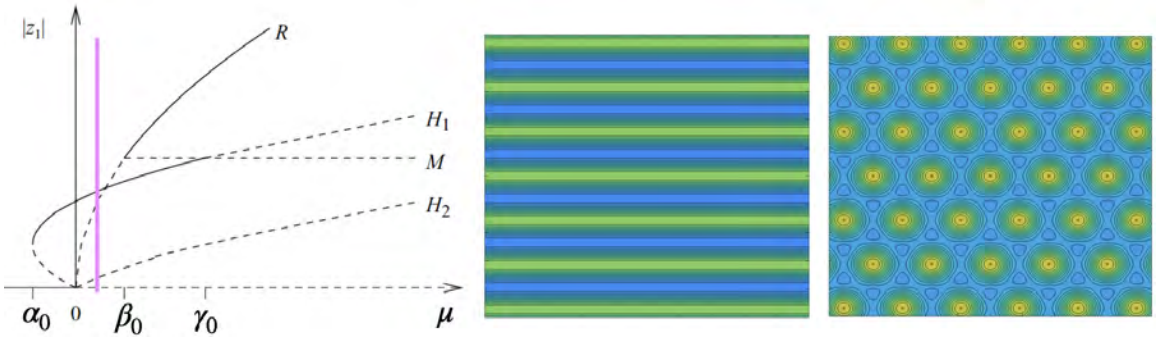


Figure 5: Basic Hoyle state that we begin with. The parameters in the plot are defined by $\alpha_0 = -a^2/(4(b+2c))$, $\beta_0 = a^2 b/(b-c)^2$, and $\gamma_0 = a^2(2b+c)/(b-c)^2$. The roll state and the stable (in the absence of $z_4$) hexagononal state are depicted in the middle and right panels, respectively.

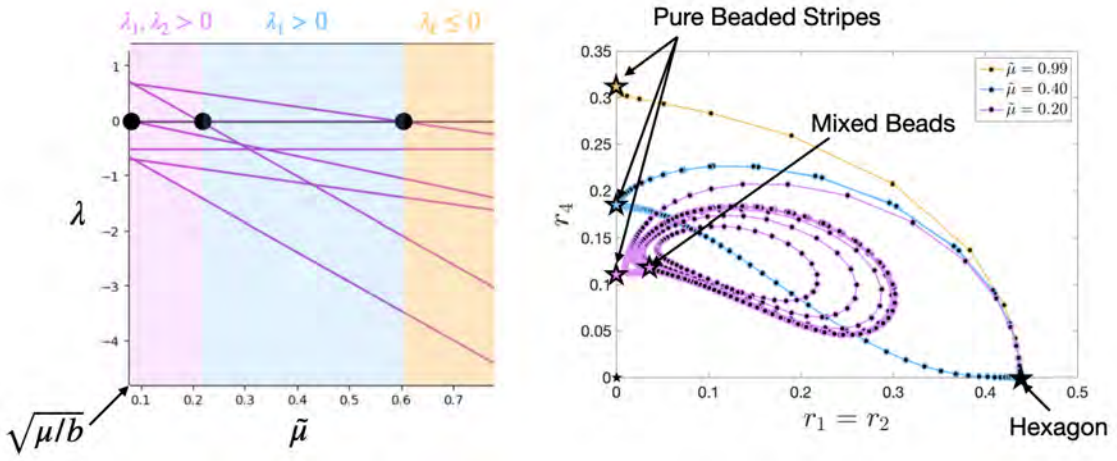


Figure 6: The right panel depicts the dynamics stemming from perturbing the hexagon state, at various values of $\tilde{\mu} \in \{0.2, 0.4, 0.99\}$. The amplitudes of $z_1, z_2, z_4$ are denoted $r_1, r_2, r_4$. When $\tilde{\mu} = 0.99$, the pure mixed bead state is stable and perturbations from the hexagon settle into the pure beaded striped and remain there. As $\tilde{\mu}$ is decreased to 0.4, one eigenvalue of the pure beaded stripe crosses zero and destabilizes. Thus, perturbations from the hexagon approach the pure beaded stripe along a stable direction and then exit along the unstable direction back to the hexagon in a heteroclinic orbit. When $\tilde{\mu}$ is decreased further to 0.2, another eigenvalue crossing gives rise to a new mixed bead state that qualitatively changes the dynamics. A new periodic trajectory emerges. The left panel shows the variation of three eigenvalues of the pure beaded stripe state's Jacobian.

can lead to the emergence of new states, such as the mixed bead, which only exists in the lowest value of $\tilde{\mu}$ plotted.

### 4.3 Bifurcations of the pure beaded stripes

Eigenvalues of the three least stable eigenvectors of the Jacobian of the pure beaded stripe state are plotted in the left panel of Fig. 6. Recalling that the eigenvalue zero-crossing corresponds to a pitchfork bifurcation, we can use the location of the zero-crossing as a starting point for a Newton iteration scheme for finding and following the connected branch of steady states that begin at this bifurcation point. For example, following the branch near the eigenvalue crossing near $\tilde{\mu} \approx 0.6$ yields the unstable branch of steady solutions labeled "Im" in Fig. 7. Eigenvalues and eigenvectors along newly found branches can be computed in MATLAB and the stability of such states may thus be assessed. Eigenvalue crossings events can also be monitored, which may yield new steady states. In what follows, we briefly describe how a complete bifurcation diagram was constructed, which is then presented in Fig. 7.

### 4.4 A complete bifurcation diagram

Repeating this analysis, we can track each new steady state (arising from bifurcations at eigenvalue zero-crossings) using Newton iteration and also compute its eigenvectors and eigenvalues along the way. When there is an eigenvalue zero-crossing event, we then track the new emergent state and repeat this process. Repeating this gives a full bifurcation diagram of states at a given value of $\tilde{\mu}$. In Fig. 7, we plot the bifurcation diagram for the system, only plotting the value of $|z_4|$ in each state for clarity. The stability of each state is indicated in the plot by numeric labels indicating the number of unstable eigen-directions; for example, (0) indicates that there are no unstable directions and hence that the state is stable.

## 5 Comparing Dynamics to [12]

By setting the value of $\tilde{\mu}$ such that our hexagon state and mixed bead amplitudes matched those found in [12], we find the dynamics illustrated in Fig. 8, when the system is initialized in the hexagon state. Qualitative agreement is found between our dynamics and the results of [12]. In particular, the hexagon state is found to destabilize into the mixed bead state and remain there for a considerable amount of time. Eventually the mixed bead state destabilizes in both our model and the numerical simulations of [12]. In our model, the mixed bead destabilizes into a state where $|z_1| = |z_2|$ oscillates out of phase with $|z_4|$, accompanied by small oscillations of $|z_1|$. The numerical simulation of [12] also displays this behaviour. The only qualitatively distinct feature of [12] not captured yet by our simple model is the fact that the condition $|z_1| = |z_2|$ is not exactly satisfied. A small out-of-phase oscillation of these amplitudes exists (cyan and magenta curves) in their simulations. In ongoing work, we are investigating how to capture this symmetry-breaking feature of the dynamics. A hopeful direction is to consider the variation of more parameters than just $\tilde{\mu}$; under some parameter choices, it may be possible to see that an eigenvector of the mixed beaded stripe, possessing

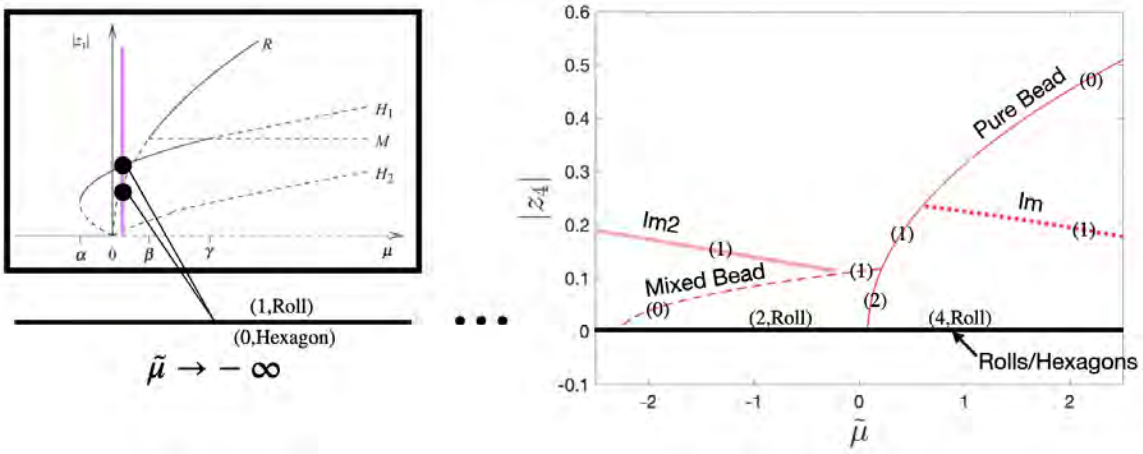


Figure 7: The right panel shows a bifurcation diagram showing the value of $|z_4|$ in various steady states of the governing equations as the parameter $\tilde{\mu}$ is varied. By noting the nature of the pitchfork occuring at each branching point, we are able to label the number of unstable directions associated with each steady state (i.e., (0) indicates stability). The labels "Im" and "Im2" refer to the fact that these states exist as purely imaginary perturbations to the real bast states labeled mixed bead and pure bead. The "Im" and "Im2" states are seemingly unimportant in the dynamics of [12]. When $\tilde{\mu} \to -\infty$, the present states are the stable hexagon and the unstable rolls. Since we only plot $|z_4|$, both of these states correspond to horizontal lines with $|z_4| = 0$. New states emerge as bifurcations from this branch as $\tilde{\mu}$ is increased from $-\infty$.

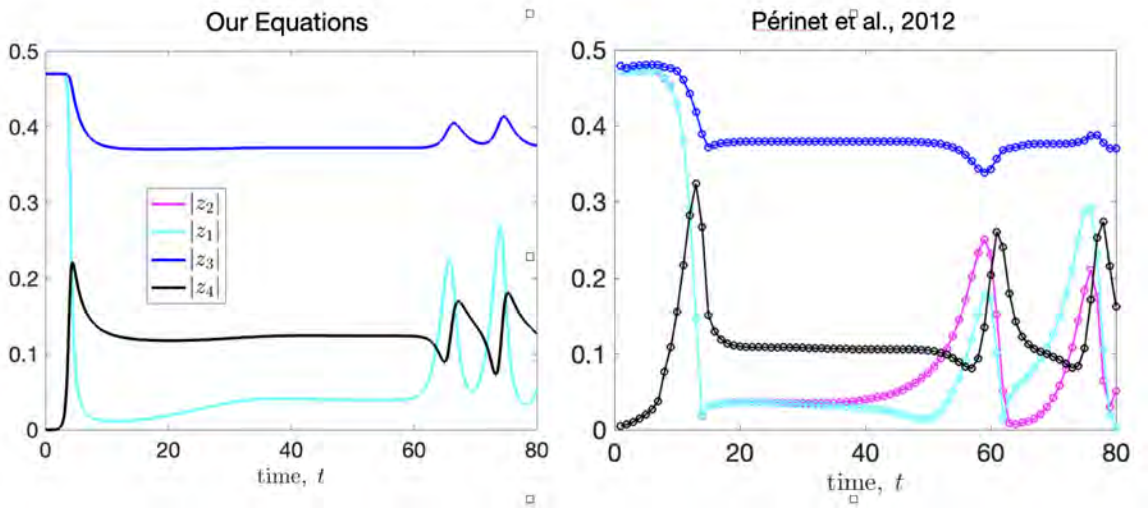


Figure 8: Comparison of simulation of our model equations when $\tilde{\mu}$ is chosen such that the hexagon and mixed bead steady states have amplitudes that approximately match those observed by [12].

equal and opposite components of $z_1$ and $z_2$, becomes unstable. If such a configuration can be found, then the mixed bead should destabilize into a state with $|z_1| \neq |z_2|$ as desired.

## 6 Conclusion and Future Directions

Our model equations, which only retain interactions between the hexagonal lattice and a single off-lattice wave vector, were able to capture key steady states and dynamical transitions observed in the numerical work of [12]. The model also reveals a host of interesting dynamical states and transitions beyond those observed by [12]. It should be possible to observe such states for different values of the Faraday wave simulation parameters. While the model is qualitatively capable of capturing the stability characteristics and transitions seen in [12], one key feature of the dynamics remains to be captured. Particularly, [12] observe a symmetry breaking between the $z_1$ and $z_2$ states that has yet to be seen in our model.

In ongoing work, we are investigating how the coupling constant $\gamma$ may be varied, in addition to $\tilde{\mu}$, in order to attain the symmetry breaking between the $z_1$ and $z_2$ amplitudes that was seen in the numerical simulations of [12]. By examining eigenvectors of the mixed bead state, as a function of system parameters (e.g., $\gamma$), we suspect it should be possible to force the eigenvalue of an eigenvector with $\delta z_1 = -\delta z_2$ to become unstable. If growth occurs along this direction, then the mixed bead should destabilize with $|z_1| \neq |z_2|$.

The analysis presented in this report should be applicable whenever a system with hexagonal symmetry is able to interact with an off-lattice wave vector. Such situations might arise in Faraday waves with certain bottom topographies or in certain condensed matter systems. It is also worth noting that any system with hexagonal symmetry that is being studied numerically on a rectangular lattice might be susceptible to dynamics of the

type described here.

## 7 Acknowledgements

K.M. thanks his mentor Laurette Tuckerman, as well as Nicolas Périnet, for illuminating discussions.

## References

[1] T. B. Benjamin and F. J. Ursell, *The stability of the plane free surface of a liquid in vertical periodic motion*, Proceedings of the Royal Society of London. Series A. Mathematical and Physical Sciences, 225 (1954), pp. 505–515.

[2] P. Chen and J. Vinals, *Pattern selection in faraday waves*, Physical review letters, 79 (1997), p. 2670.

[3] S. Dehe, M. Hartmann, A. Bandopadhyay, and S. Hardt, *The spatial structure of electrostatically forced faraday waves*, Journal of Fluid Mechanics, 939 (2022), p. A6.

[4] W. S. Edwards and S. Fauve, *Patterns and quasi-patterns in the faraday experiment*, Journal of Fluid Mechanics, 278 (1994), pp. 123–148.

[5] M. Faraday, *Xvii. on a peculiar class of acoustical figures; and on certain forms assumed by groups of particles upon vibrating elastic surfaces*, Philosophical transactions of the Royal Society of London, (1831), pp. 299–340.

[6] R. B. Hoyle, *Pattern formation: an introduction to methods*, Cambridge University Press, 2006.

[7] A. Kityk, J. Embs, V. Mekhonoshin, and C. Wagner, *Spatiotemporal characterization of interfacial faraday waves by means of a light absorption technique*, Physical Review E—Statistical, Nonlinear, and Soft Matter Physics, 72 (2005), p. 036209.

[8] K. Kumar and L. S. Tuckerman, *Parametric instability of the interface between two fluids*, Journal of Fluid Mechanics, 279 (1994), pp. 49–68.

[9] J. Miles and D. Henderson, *Parametrically forced surface waves*, Annual Review of Fluid Mechanics, 22 (1990), pp. 143–165.

[10] N. Périnet, P. Gutiérrez, H. Urra, N. Mujica, and L. Gordillo, *Streaming patterns in faraday waves*, Journal of Fluid Mechanics, 819 (2017), pp. 285–310.

[11] N. Périnet, D. Juric, and L. S. Tuckerman, *Numerical simulation of faraday waves*, Journal of Fluid Mechanics, 635 (2009), pp. 1–26.

[12] ——, *Alternating hexagonal and striped patterns in faraday surface waves*, Physical Review Letters, 109 (2012), p. 164501.

[13] A. Skeldon and A. Rucklidge, *Can weakly nonlinear theory explain faraday wave patterns near onset?*, Journal of Fluid Mechanics, 777 (2015), pp. 604–632.

[14] M.-T. Westra, D. J. Binks, and W. Van De Water, *Patterns of faraday waves*, Journal of Fluid Mechanics, 496 (2003), pp. 1–32.

# Upslope and Downslope Flow Along Ocean Bottom Boundaries

Isabela Conde

August 20, 2025

**Abstract**

Vertical circulation is a major redistributor of dissolved gases and heat. As the ocean absorbs 80% of Earth's excess heat, understanding key physical processes of this circulation is vitally important. In the 1960s Walter Munk's *Abyssal Recipes* proposed a theory of global circulation whereby, cold dense water from the poles is rises through the ocean's stratified layers to the surface. Thereafter, theoretical results have put forward that abyssal upwelling occurs mostly along sloping seafloors (Ferrari et al., 2016; Lavergne et al., 2016), largely supported observational studies (Wynne-Cattanach et al., 2024). Recently, Capó et al. (2024) presented results from a regional ocean model and analytical solutions to Boussinesq approximations which show downslope flow when rough topography—or a proxy of this—is introduced. We investigate a similar additions to a hydrostatic Boussinesq approximation and a non-hydrostatic model using Oceananigans. In both, we see an initial downslope flow but, ultimately steady states of upslope flow. We suggest through increased mixing rates at the boundary, the switch between downslope to upslope is prolonged. In a complex model, we might expect that rough topography would result in the system never fully reaching an equilibrated state, ergo displaying a steady downslope flow as seen in Capó et al. (2024).

## 1 Introduction

Vertical circulation is an important factor in understanding global heat transport—the ocean absorbs around 80% of Earth's excess heat, this is circulated from the surface to the Abyssal ocean over many years. Conversely, at high latitudes we have cold dense water forming and sinking to the bottom, to close the abyssal overturning circulation dense polar water must eventually return to the ocean surface, by doing so this water is getting lighter and undergoing a positive watermass transformation through turbulent mixing (Ganachaud and Wunsch, 2000; Lavergne et al., 2016; Munk, 1966). The majority of this vertical movement occurs along sloped sea floor boundaries, where both theory and observations have shown that water moves up along ocean bottom boundaries such as ridges and seamounts (Garrett et al., 1993; Holmes and McDougall, 2020; Montgomery et al., 2000; Wynne-Cattanach et al., 2024). Yet, recent studies using regional ocean models have shown prevalent downslope flow contradictory to this theory (Capó et al., 2024). Our project considers simple theory of flow along these ocean bottom boundaries, with additions that more

closely mimic the more complex case presented in regional ocean models in (Capó et al., 2024).

Munk's *Abyssal Recipes* (1966) was one of the first attempts to connect limited observations to a global theoretical framework. By combining simple scaling arguments with sparse deep-ocean data, Munk estimated the vertical diffusivity required to maintain the large-scale overturning circulation and inferred a global upwelling rate of roughly one centimetre per day. This framework established the idea that diapycnal mixing along rough topography and boundary slopes could close the abyssal circulation.

Seafloor observations of flow and mixing coefficients are complicated to obtain and often expensive, leading to sparse measurements. Even so, the measurements we have supported theoretical theory that upwelling along sloped bottom boundaries is prevalent (Kunze et al., 2012; Montgomery et al., 2000; Wynne-Cattanach et al., 2024). However, there are still observational studies which show downwelling, Simpson and McCandliss (2013) show downwelling off a continental shelf ($<$ 1000m depth) using current doppler profiles, and Xie et al. (2023) show trapped waves over a western Pacific seamount lose energy due to near-inertial waves, resulting in damping and downslope flow.

Recently, Wynne-Cattanach et al. (2024), conducted an extensive oceanographic field campaign which dropped artificial dye along a sloped sea floor of a submarine canyon. They movement of the dye is tracked by measuring the concentration after 3 months. They found the dye moved from denser to lighter water, decreasing it's concentration indicating a positive watermass transformation. They also found the rate at which upwelling was occurring was 10,000 times larger than that calculated by Munk (1966).

Building on these findings, subsequent studies have explored how turbulent mixing and rough topography might underpin such intensified upwelling (Kunze et al., 2012). Kunze et al. (2012) investigate the effect of turbulent mixing on sloping boundaries, they considered microstructure data from two canyons, finding they had relatively thick well stratified and turbulent boundary layers. The thickness of this well-mixed bottom boundary layer was an order of magnitude thinner than the stratified turbulent layer (Kunze et al., 2012). They determined mixing rates should not be reduced along deep-sea sloping boundaries, and if their calculations were extrapolated globally upwelling along canyon slopes may contribute 2–3 times as much diapycnal transport to the world ocean as interior mixing. They also argue that sloping topography affect processes in a fundamentally 2D or 3D manner, and they cannot be accurately described by 1D models.

Another observational study, lead by Montgomery et al. (2000), measured a tracer release in the Brazil basin, the aim was to measure mixing rates along rough topography. Montgomery et al. found diapycnal mixing increases as density surfaces approach the bottom, from measurements they approximated as $2 - 4\,\mathrm{cm^2\,s^{-1}}$, 500m above the sea floor of Mid-Atlantic Ridge and around $10\,\mathrm{cm^2\,s^{-1}}$ close to the bottom. From the same campaign Polzin et al. (1997) investigated spatial variability of mixing rates in the Brazil Basin, finding the over smooth surfaces in the west diapycnal mixing (diffusivity of $0.001\,\mathrm{cm^2\,s^{-1}}$) was reduced compared to rougher bathymetry in the east over the Mid-Atlantic Ridge (diffusivity of $0.5\,\mathrm{cm^2\,s^{-1}}$).

Unlike previous theory, *"Abyssal Slope Currents"* by Capó et al. (2024) show consistent downslope flow. The predominately explain this through the concept of topostrophic currents, where flow along deep-ocean slopes follow the seafloor bathymetry. Using real-

istic simulations of the western Mediterranean, the authors find these flows drive a weak downslope motion, shaping the abyssal buoyancy balance and mixing. They propose a novel one-dimensional model combining topostrophy, bottom drag, and eddy buoyancy transport to explain the observed structure, revising earlier slope-boundary theories by Garrett (1990).

In our study, we make simple additions to further understand the underlying phenomena of the problem. We make two basic additions a simple hydrostatic Boussinesq approximation, the first was originally presented by Garrett (1990) which adds a constant geostrophic interior flow. By doing so we find through slow diffusion of momentum from the boundary to the interior, no steady state solution can be found. To find analytical solutions to this problem we add a buoyancy dampening term, thereby limiting this slow diffusion and allowing the system to reach equilibrium. Our analysis reveals the steady state solution results in upslope flow, and a positive watermass transformation as denser water is converted to lighter water, even if initial states show the converse.

Both of these hydrostatic systems use constant eddy diffusivity and viscosity, yet, it has been shown the mixing rates increase at the seafloor. To investigate the effect of increased mixing at the boundary we use a Richardson number diffusivity constants, first proposed by MacCready and Rhines (1991b) and later used by Benthuysen and Thomas (2012).

Using Oceananigans, we also investigate a 2D non-hydrostatic system with strong geostrophic along-slope flow, motivated in part by evidence that 2D frameworks can better capture dynamics over sloping topography (Kunze et al., 2012). Our analysis finds that an initial downslope flow—whereby, light water sinks below dense water—triggers convective instabilities such that negative stratification quickly disappears. Whereas, in the hydrostatic case, we see for the initial downslope flow there is negative stratification. We propose rather than a steady downslope flow, by way of changing seafloor and rough topography a steady state is never achieved prolonging the downslope flow as seen in Capó et al. (2024).

## 2 Hydrostatic Boussinesq Approximation

The simplest case of flow over a tilted bottom boundary was first presented by Weatherly and Martin (1978) under the Boussinesq and hydrostatic approximations. The momentum and buoyancy equations are

$$\frac{\partial u}{\partial t} - f\,v = b\,\theta + \nu\,\frac{\partial^2 u}{\partial z^2}, \tag{1}$$

$$\frac{\partial v}{\partial t} + f\,u = \nu\,\frac{\partial^2 v}{\partial z^2}, \tag{2}$$

$$\frac{\partial b}{\partial t} + u\,N^2\,\theta = \kappa\,\frac{\partial^2 b}{\partial z^2}. \tag{3}$$

Here, coordinates are rotated where $u$ is cross-slope (at angle $\theta$) and $v$ is along-slope (into/out of the page). We assume small $\theta$.

In equation (1), $b\,\theta$ is the buoyancy term arising from the slope; $\nu\,\partial^2 u/\partial z^2$ and $\nu\,\partial^2 v/\partial z^2$ in equation (1)–(2) represent vertical eddy viscosity; and $\kappa\,\partial^2 b/\partial z^2$ in Eq. (3) is vertical eddy diffusion of buoyancy.

We apply no slip and no flux boundary conditions such that $u = v = 0$ at $z = 0$, and $db/dz + N^2 = 0$ at $z = 0$, and $u, b \to 0$ as $z \to \infty$.

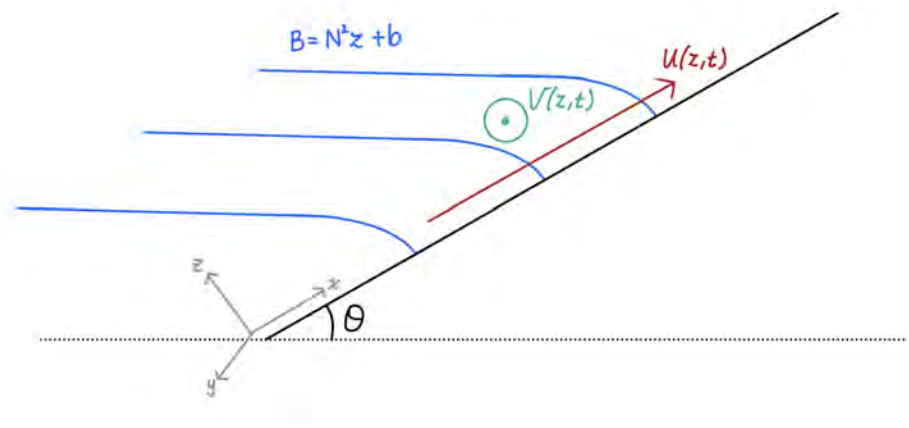


Figure 1: Diagram tilted bottom boundary problem. Blue indicates isopycnals, which tilt at the surface, red is the resulting cross-slope flow, and green is a background along slope flow, which will be further explored in section 2.2. The coordinates are rotated such cross slope flow is in the $x$ direction and $z$ values is normal to slope.

To find numerical solutions to this problem we use code developed by Henry Peterson for *Rapid Spinup and Spindown of Flow along Slopes* (Peterson and Callies, 2022). Figure 2 shows the solution quickly equilibrates and results in a upslope flow in the boundary, and a positive watermass transformation as denser water crosses isopycnals and becomes lighter.

## 2.1 Steady state solution

For $\nu$ and $\kappa$ constant, independent of $z$ then there is a steady solution to the governing Equ. 1–3, for $\partial/\partial t = 0$ we have the following;

$$-fv = b\,\theta + \nu \frac{\partial^2 u}{\partial z^2}, \tag{4}$$

$$fu = \nu \frac{\partial^2 v}{\partial z^2}, \tag{5}$$

$$uN^2\theta = \kappa \frac{\partial^2 b}{\partial z^2}. \tag{6}$$

With the same boundary conditions as above; $u = v = 0$ at $z = 0$, and $db/dz + N^2 = 0$ at $z = 0$, and $u, b \to 0$ as $z \to \infty$.

For a solution of the form $(u, v, b) = (u_0, v_0, b_0)e^{z\delta}$, we can solve for equations 4-6;

$$\begin{pmatrix} \delta^2 & -f/\nu & \theta/\nu \\ f/\nu & \delta^2 & 0 \\ N^2\theta/\kappa & 0 & \delta^2 \end{pmatrix} \begin{pmatrix} u_0 \\ v_0 \\ b_0 \end{pmatrix} = \begin{pmatrix} 0 \\ 0 \\ 0 \end{pmatrix}$$

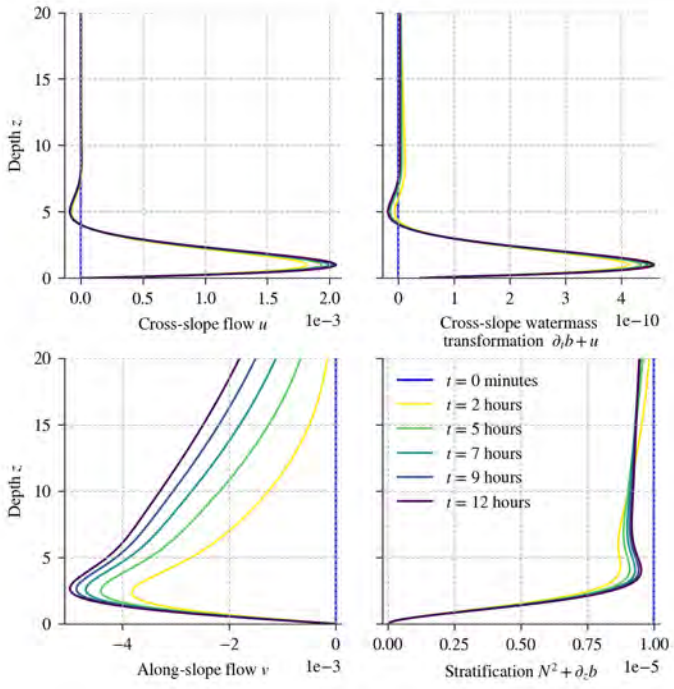


Figure 2: Numerical solutions to equations (1)–(3) for values $f = \nu = \kappa = 1 \times 10^{-4}$, $\theta = 0.022$ and $N^2 = 1 \times 10^{-5}$. Depth indicated as meters above bottom boundary. Solutions found using code produced for (Peterson and Callies, 2022).

Setting the determinant to zero we can solve for $\delta$,

$$\delta^6 - \delta^2 \left( \frac{f^2}{\nu^2} + \frac{N^2\theta^2}{\nu^2\kappa} \right) = 0.$$

To solve let $\lambda = \delta^2$, this gives the following cubic function,

$$\lambda \left[ \lambda^2 - \frac{f^2}{\nu^2} \left( 1 + \frac{N^2\theta^2}{f^2} \frac{\nu}{\kappa} \right) \right] = 0.$$

Where ${}^{N^2\theta^2}/_{f^2}$ is the slope burger number and ${}^{\nu}/_{\kappa}$ is the prandtl number. This gives a non-trivial real solution for $\delta$ as

$$\delta^4 = \frac{f^2}{4\nu^2} \left( 1 + S\mu \right),$$

which is a modified Ekman boundary layer depth, accounting for the boundary slope $\theta$ and stratification $N^2$.

Steady state solutions Can be seen in figure 2, where $f = \nu = \kappa = 1 \times 10^{-4}$, $\theta = 0.022$ and $N^2 = 1 \times 10^{-5}$.

In the absence of interior geostrophic flows, a steady state solution is achieved with an upslope flow driven by diffusion of buoyancy into the boundary layer;

$$uN^2\theta = \kappa \frac{\partial b}{\partial z}$$

Figure 3 shows flow $u$ leaving the upslope end of the box, less dense than when it enters, and so must have lost mass by diffusion while in transit.

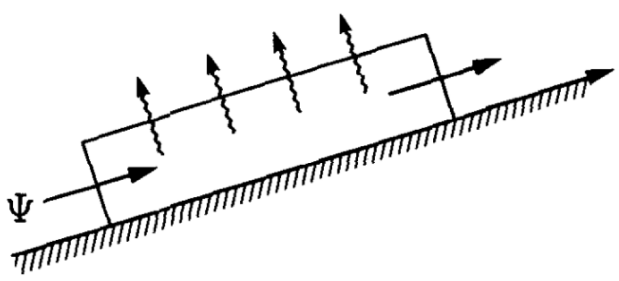


Figure 3: Steady upslope flow and positive watermass transformation requires a diffusive flux through the top of a control volume (Garrett et al., 1993)

We see that without time dependence the steady state solution is driven by buoyancy diffusion resulting in up slope flow and a positive watermass transformation and denser water becomes lighter.

## 2.2 Time dependence

First introduced by Garrett (1990), a time-dependent system whereby a constant along-slope interior geostrophic flow $V$ is added to equations (1)–(3).

$$\frac{\partial u}{\partial t} - f(v - V) = -B\,\theta + \nu\frac{\partial^2 u}{\partial z^2} \tag{7}$$

$$\frac{\partial v}{\partial t} + fu = \nu\frac{\partial^2 v}{\partial z^2} \tag{8}$$

$$\frac{\partial b}{\partial t} + u\,N^2\,\theta = \kappa\frac{\partial^2 b}{\partial z^2} \tag{9}$$

Equation 7 contains the added along-slope geostrophic flow $V$, it can be thought of as an along slope pressure gradient. Initially, an Ekman layer forms on an inertial timescale $t \sim f^{-1}$, here acceleration terms and only briefly significant and after $t >> f^{-1}$, along-slope flow becomes close to geostrophic. Through this addition we impose another boundary condition $v \to V$ as $z \to \infty$. **?** shows how this problem has no steady solutions. The implication of this is that there is slow diffusion within the interior along slope flow and buoyancy perturbations, which doesn't equilibrate. Whereas, a near steady state solution is achieved for the cross slope transport.

Using a background along-slope geostrophic flow of around $1\mathrm{cm\,s^{-1}}$ we obtain the solutions in Figure 4. Figure 4 top right panel indicates that for a strong interior flow, we have an initial downslope flow with negative watermass transformation. Though, our results shows this downslope flow only occurs when there is negative stratification, giving a unrealistic initial flow. Unlike the along-slope flow, cross-slope flow equilibrates fast and reaches a quasi-steady state of upslope flow. Conversely, the along-slope flow doesn't reach an equilibrated state as slow diffusion of momentum from the boundary layer to the interior occurs.

MacCready and Rhines calculated the time it takes for this fast adjustment of the cross-slope flow to the interior, denominated the shutdown time $\tau$.

We firstly consider the buoyancy budget equation of Equation 7, setting the vertical diffusion term to zero as in a steady state no momentum is transferred between interior and boundary layer.

$$\begin{aligned}\frac{\partial b}{\partial t} + uN^2\theta &= 0,\\ \implies fu &= \nu v_{zz},\\ -fv &= \nu u_{zz} + b'\theta,\end{aligned}$$

where $u$, $v$ and $b$ are perturbations from the mean. Set $U = u + iv$, with boundary conditions of no slip and geostrophic interior. Using these values and subbing into the x and y momentum equations gives the following;

$$fU = -i\nu U_{zz} - ib\theta.$$

Solving, $U$ gives the general solution, for $\delta_0 = \sqrt{2\nu/f}$,

$$U(z) = U_p + Ae^{-(1+i)z/\delta_0}.$$

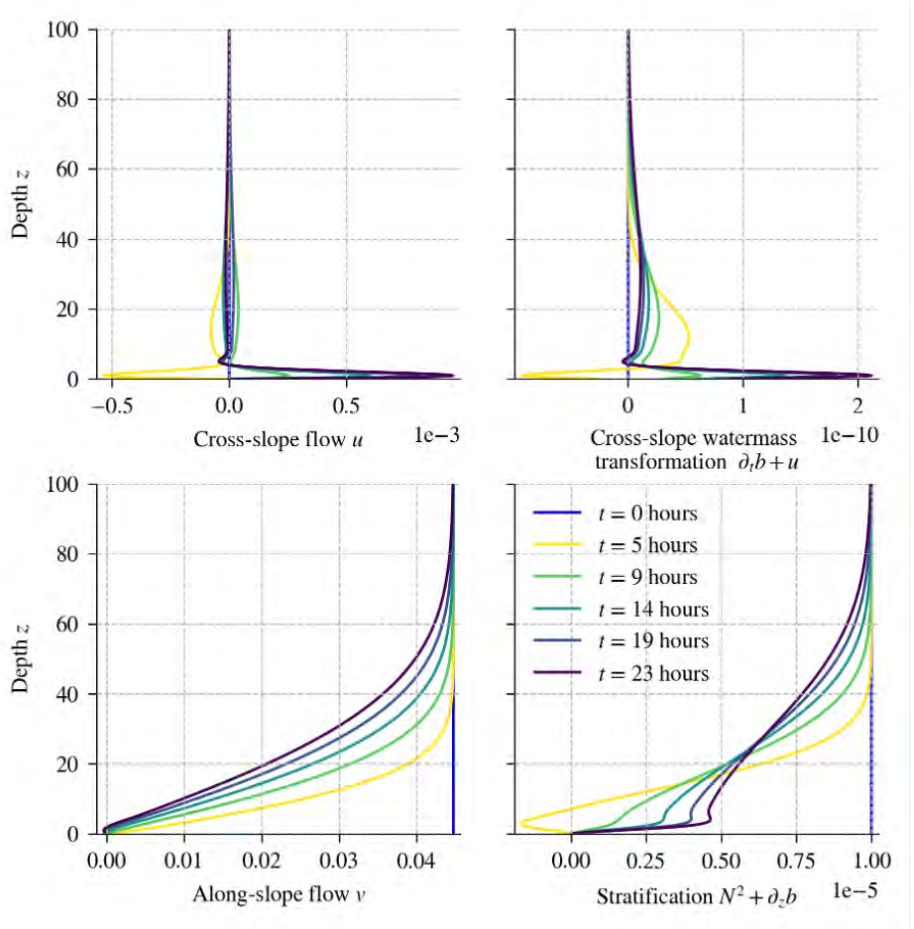


Figure 4: Numerical solutions to equations (7)–(8) for values $f = \nu = \kappa = 1 \times 10^{-4}$, $\theta = 0.022$ and $N^2 = 1 \times 10^{-5}$, and $V \approx 1\,\mathrm{cm\,s^{-1}}$. Depth indicated as meters above bottom boundary. Solutions found using code produced for (Peterson and Callies, 2022).

The particular solution $U_p = {}^{i\theta b}/_{f}$ = Applying boundary gives $U(0) = 0$ implies $A = -{}^{i\theta b}/_{f}$. This gives a solution of the form:

$$U(z) = \frac{i\theta b'}{f}\left[1 - e^{-(1+i)z/\delta_0}\right].$$

Therefore $u = \Re(U)$ and $v' = \Im(U)$.

Next, determine transport ${}^{\partial\mathcal{M}}/_{\partial t}$, integrate with respect to time $\mathcal{M} = \int_0^H u dz$.

$$\frac{\partial \mathcal{M}}{\partial t} = \int_0^H u_t\, dz = \int_0^H \frac{b_t\,\theta}{f}\, e^{-z/\delta_0}\, \sin\left(\frac{z}{\delta_0}\right) dz$$

For $H >> \delta_0$, as the boundary is well mixed $b_z = \text{const}$.

$$\begin{aligned}\frac{\partial \mathcal{M}}{\partial t} &= \int_0^H \frac{b_t\,\theta}{f}\, e^{-z/\delta_0}\, \sin\!\left(\frac{z}{\delta_0}\right) dz \\ &= \frac{\theta}{f}\frac{\delta_0}{2}\frac{\partial b}{\partial t}\end{aligned}$$

This analytical form shows the cross-slope transport responds almost instantly to changes in buoyancy at the boundary—laying the foundation for defining the longer adjustment (shut-down) timescale.

After the initial Ekman layer is formed when $t > f^{-1}$, buoyancy perturbations grow and act against the Ekman flux. Slow diffusion then weakens the cross-slope transport, driving it toward a quasi-steady state. The time taken for this decay is the shut-down timescale $\Delta\tau$.

We can determine a scaling for the shutdown time $\Delta\tau$. First, integrate $\partial_t b + N^2\theta u = \kappa\partial_{zz} b$ over Ekman boundary layer depth from before, as

$$\frac{\delta\Delta b}{\Delta\tau} \sim N^2\theta\, U.$$

Transport in Ekman boundary layer is given as

$$U \sim -\frac{\delta}{2}V.$$

Combining the two relations results in

$$\frac{\delta\Delta b}{\Delta\tau} \sim N^2\theta\frac{\delta}{2}V,$$

$$\Delta\tau \sim \frac{\Delta b}{N^2\theta V},$$

where the Ekman boundary layer reaches equilibrium when forces balance,

$$\Delta b\theta \sim fV.$$

This gives equilibration time

$$\Delta\tau \sim \frac{\Delta b}{N^2\theta V} \sim \frac{fV/\theta}{N^2\theta V} \sim \frac{1}{f}\frac{f^2}{N^2\theta^2} \sim \frac{1}{f\,S}.$$

### 2.2.1 Non-dimensional 1D model

Thus far we have used dimensional models, although, code used to produce Figures 2 and 4–8 have used a non-dimensional model which we then converted back to dimensional coordinates.

To investigate how different parameters From equation 1, we take $^{\partial P}/_{\partial x} = fV$ Peterson and Callies (2022). Then the coefficients of dimensionless parameters will be in terms of the dimensionless parameter $V_0$ the background geostrophic flow.

$$t = \tilde{t}T, \quad z = \tilde{z}\delta, \quad u = \tilde{u}V_0, \quad v = \tilde{v}V_0, \quad b = \tilde{b}\mathcal{B}.$$

$$T = \frac{1}{f}, \quad \delta = \sqrt{\frac{\nu}{f}}, \quad \mathcal{B} = \frac{V_0 N^2 \tan\theta}{f}. \tag{10}$$

First, we nondimensionalise equation (16).

$$\frac{\partial u}{\partial t} - fv = -fV + b\tan\theta + \frac{\partial}{\partial z}\left(\nu\frac{\partial u}{\partial z}\right),$$

Substituting in terms given in equations 20, along with nondimensional parameters,

$$\frac{V_0}{T}\frac{\partial \tilde{u}}{\partial \tilde{t}} - fV_0\tilde{v} = -\frac{V}{V_0} + \mathcal{B}\tan\theta\tilde{b} + \frac{1}{\delta}\frac{\partial}{\partial\tilde{z}}\left(\frac{V_0}{\delta}\nu\frac{\partial\tilde{u}}{\partial\tilde{z}}\right).$$

The term $V_0/T = fV_0$, and $V_0/\delta^2 = V_0 f/\nu$. Making these substitutions gives

$$V_0 f\frac{\partial\tilde{u}}{\partial\tilde{t}} - fV_0\tilde{v} = -fV + \frac{N^2 V_0\tan^2\theta}{f}\tilde{b} + fV_0\frac{\partial^2\tilde{u}}{\partial\tilde{z}}.$$

Divide by $fV_0$,

$$\frac{\partial\tilde{u}}{\partial\tilde{t}} - \tilde{v} = -\frac{V}{V_0} + \frac{N^2\tan^2\theta}{f^2}\tilde{b} + \frac{\partial^2\tilde{u}}{\partial\tilde{z}}.$$

$$\frac{\partial\tilde{u}}{\partial\tilde{t}} - \tilde{v} = -\frac{V\theta}{f\delta} + S\tilde{b} + \frac{\partial^2\tilde{u}}{\partial\tilde{z}^2}. \tag{11}$$

Hence, $\tilde{v} = \frac{V\theta}{f\delta}$.

Next, we nondimensionalise the along slope momentum equation,

$$\frac{\partial v}{\partial t} + fu = \frac{\partial}{\partial z}\left(\nu\frac{\partial v}{\partial z}\right). \tag{12}$$

Making similar substitutions as in the cross-slope momentum equation,

$$\frac{V_0}{T}\frac{\partial\tilde{v}}{\partial\tilde{t}} + fV_0\tilde{u} = fV_0\frac{\partial\tilde{v}}{\partial\tilde{z}}$$

Divide by $fV_0$, where $V/T = fV_0$,

$$\frac{\partial\tilde{v}}{\partial\tilde{t}} + \tilde{u} = \frac{\partial^2\tilde{v}}{\partial\tilde{z}^2} \tag{13}$$

Next we consider the buoyancy tendency term:

$$\frac{\partial b}{\partial t} + uN^2\tan\theta = \frac{\partial}{\partial z}\left[\kappa\left(N^2 + \frac{\partial b}{\partial z}\right)\right],$$

From these nondimensional parameters, the total stratification was given as:

$$\frac{\partial \tilde{B}}{\partial z} = \frac{f\delta \cot\theta}{V} + \frac{\partial \tilde{b}}{\partial z} \tag{14}$$

Where the nondimensional background stratification $\tilde{N}^2$ is then

$$\tilde{N}^2 = \frac{f\delta \cot\theta}{V}$$

Peterson and Callies also give values $\tilde{\tau}_A = 1/S$ and $\tilde{\tau}_S = 1/\sqrt{Ek} = H/\delta$. Then we can expand the numerator as such, with the approximation of $\tan\theta \approx \theta$.

$$\begin{aligned}
\tilde{N}^2 &= \frac{\delta}{H}\frac{f}{N\theta}\frac{NH}{V} \\
&= \frac{\sqrt{\tau_A}}{\tau_S}\frac{NH}{V}. \\
\implies N &= \frac{\tau_S}{\sqrt{\tau_A}}\frac{V}{H}\tilde{N}^2.
\end{aligned}$$

Will also need an expression for $\kappa$ to run the 1d non-dimensional case.

Nondimensionalise buoyancy budget, where $\kappa$ is a function of $z$, and $\kappa = \kappa_0\tilde{\kappa}$. The original is given as:

$$\frac{\partial b}{\partial t} + uN^2\tan\theta = \frac{\partial}{\partial z}\left[\kappa\left(N^2 + \frac{\partial b}{\partial z}\right)\right]$$

From the nondimensional parameter $\mathcal{B}$ and $T$ we can transform $u$'s coefficients as:

$$uN^2\tan\theta = \frac{\mathcal{B}}{T}\tilde{u}$$

Then subbing in the other nondimensional terms:

$$\frac{\mathcal{B}}{T}\frac{\partial \tilde{b}}{\partial \tilde{t}} + \frac{\mathcal{B}}{T}\tilde{u} = \frac{N^2\kappa_0}{\delta}\frac{\partial \tilde{\kappa}}{\partial \tilde{z}} + \frac{\mathcal{B}\kappa_0}{\delta^2}\frac{\partial}{\partial \tilde{z}}\left(\tilde{\kappa}\frac{\partial \tilde{b}}{\partial \tilde{z}}\right)$$

Divide both sides by $\mathcal{B}/T$ gives the following:

$$\frac{\partial \tilde{b}}{\partial \tilde{t}} + \tilde{u} = \frac{\kappa_0 T}{\delta^2}\frac{\partial}{\partial z}\left[\tilde{\kappa}\left(\frac{N^2\delta}{\mathcal{B}} + \frac{\partial \tilde{b}}{\partial \tilde{z}}\right)\right]$$

Then, choose $\kappa_0 = \delta^2/T$, and:

$$\frac{N^2\delta}{\mathcal{B}} = \frac{f\delta\cot\theta}{V}$$

Gives the final solution as

$$\frac{\partial \tilde{b}}{\partial \tilde{t}} + \tilde{u} = \frac{\partial}{\partial z}\left[\tilde{\kappa}\left(\frac{f\delta\cot\theta}{V} + \frac{\partial \tilde{b}}{\partial \tilde{z}}\right)\right]$$

As in Peterson (2022), we have the background stratification as $f\delta\cot\theta/V$.

For $\kappa_0 = \delta^2/T = \nu$, therefore $\kappa = \nu\tilde{\kappa}$.

For $\kappa = \text{const}$, we have the following buoyancy budget.

$$\frac{\partial\tilde{b}}{\partial\tilde{t}} + \tilde{u} = \mu\frac{\partial^2\tilde{b}}{\partial\tilde{z}^2}$$

We still need expressions which help set constants. The prandtl number $\mu = \nu_0/\kappa_0$, $\tau_S = H/\delta$, $\tau_A = f^2/N^2\theta^2$. Then to determine the dimensional units we may pick $H$ and $f$.

Therefore, the non-dimensional parameters can be found from the following relation.

$$\frac{N}{f} \approx \frac{L}{H} \tag{15}$$

Where, now $\frac{N}{f}$ can be chosen Where the RHS is a physical scaling. We choose $f$ and $\nu$, and use the scaling from the nondimensional construction seen previously;

$$\tau_S = \frac{H}{\delta} \tag{16}$$

$$\mu = \frac{\nu}{\kappa} \tag{17}$$

$$\theta = \sqrt{\frac{f^2}{N^2\tau_A}} \tag{18}$$

$$V = \frac{f\delta}{\theta} \tag{19}$$

Where $\delta = \sqrt{\nu/f}$ and we assume $\tilde{v}_0 = 1$.

### 2.3 A steady solution with damping

To find a steady solution we require small damping of the buoyancy perturbation such that it only affects the interior and resulting in the interior not continuously diffusing.

Let's consider the problem with the damping of buoyancy perturbations to achieve a steady state. For simplicity, we will approximate $\tilde{\kappa}$ and $\tilde{\kappa}$ are constant,

$$-\partial_{zz}u = v + Sb, \tag{20}$$

$$-\partial_{zz}v = -u, \tag{21}$$

$$-\mu\partial_{zz}b = -u - \epsilon b, \tag{22}$$

$$\tag{23}$$

where $\mu = Pr^{-1}$ and $\epsilon$ is the weak damping in $f$ units. Assuming exponential solutions of the form $(u, v, b) = (u_0, v_0, b_0)e^{mz}$, we get the system,

$$\begin{pmatrix} \delta^2 & 1 & S \\ -1 & \delta^2 & 0 \\ -1 & 0 & \mu\delta^2 - \epsilon \end{pmatrix} \begin{pmatrix} u_0 \\ v_0 \\ b_0 \end{pmatrix} = \begin{pmatrix} 0 \\ 0 \\ 0 \end{pmatrix}$$

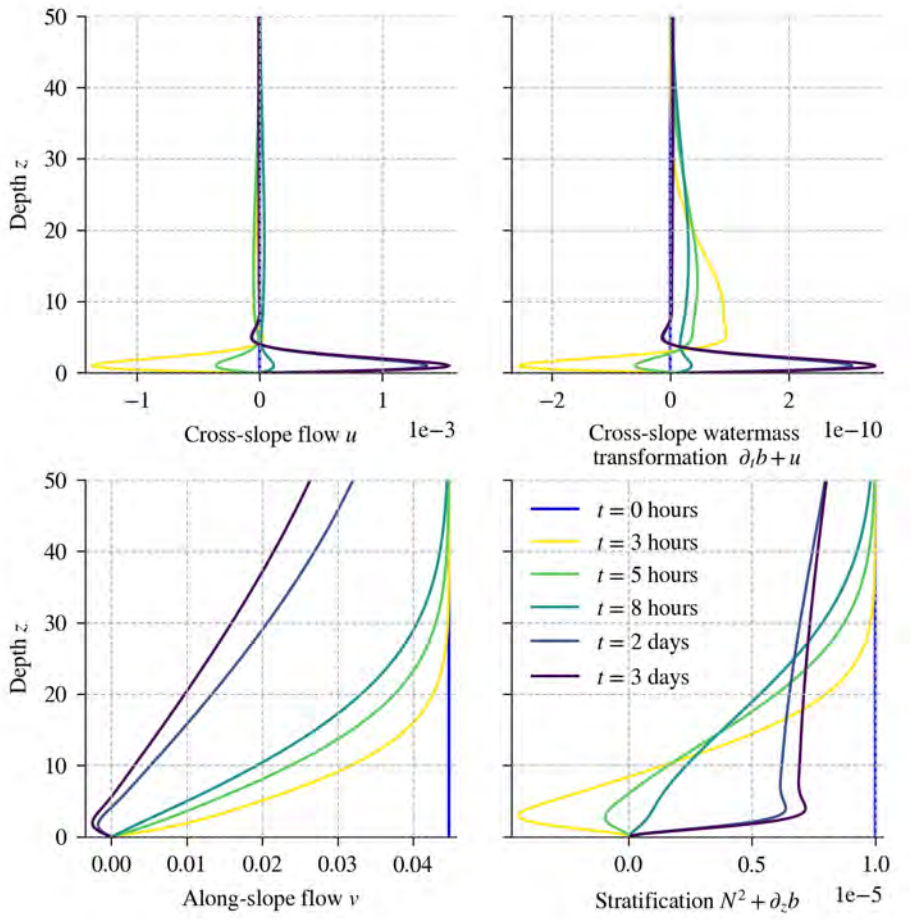


Figure 5: Numerical solutions to equations (7)–(8) for values $f = \nu = \kappa = 1 \times 10^{-4}$, $\theta = 0.022$ and $N^2 = 1 \times 10^{-5}$, and $V \approx 1\,\mathrm{cm\,s^{-1}}$. Depth indicated as meters above bottom boundary, maximum height of simulation $z = 100$m, figure shows the first 50m

We can determine $\delta$ by setting the determinant of the matrix to zero,

$$S\delta^2 + (\mu\delta^2 - \epsilon)(\delta^4 + 1) = 0$$

which is a sixth-order algebraic equation for $m$,

$$\mu\delta^6 - \epsilon\delta^4 + (\mu + S)\delta^2 - \epsilon = 0.$$

Solutions for $\delta^2$ in the limit of small $\epsilon$ are,

$$\delta^2 = \left( \pm i \left( \frac{\mu + S}{\mu} \right)^{1/2} + \frac{S}{2\mu(\mu + S)}\epsilon, \quad -\frac{1}{\mu + S}\epsilon \right)$$

The six roots to order $\epsilon$ are,

$$\delta_{1,2,3,4} = \pm \frac{1 \pm i}{\sqrt{2}} \left( \frac{\mu + S}{\mu} \right)^{1/4} \left( 1 \pm i \sqrt{\frac{S^2}{4\mu(\mu + S)^{3/2}}\epsilon} \right), \qquad \delta_{4,6} = \pm \sqrt{\frac{\epsilon}{\mu + S}}.$$

We can now impose the boundary conditions. Where $z \to \infty$ requires all roots with positive real parts are dropped. The three other boundary conditions at $z = 0$ are:

$$u = 0, \quad b_z = -1, \quad v = -V,$$

which needs to be satisfied using $u(z) = A_1 e^{m_1 z} + A_2 e^{m_2 z} + A_3 e^{m_3 z}$ and thus,

$$u = A_1 + A_2 + A_3 = 0, \tag{24}$$

$$b = \frac{\delta_1}{\mu\delta_1^2 - \epsilon} A_1 + \frac{\delta_2}{\mu\delta_2^2 - \epsilon} A_2 + \frac{\delta_3}{\mu\delta_3^2 - \epsilon} A_3 = -1, \tag{25}$$

$$v = \frac{A_1}{\delta_1^2} + \frac{A_2}{\delta_2^2} + \frac{A_3}{\delta_3^2} = -V \tag{26}$$

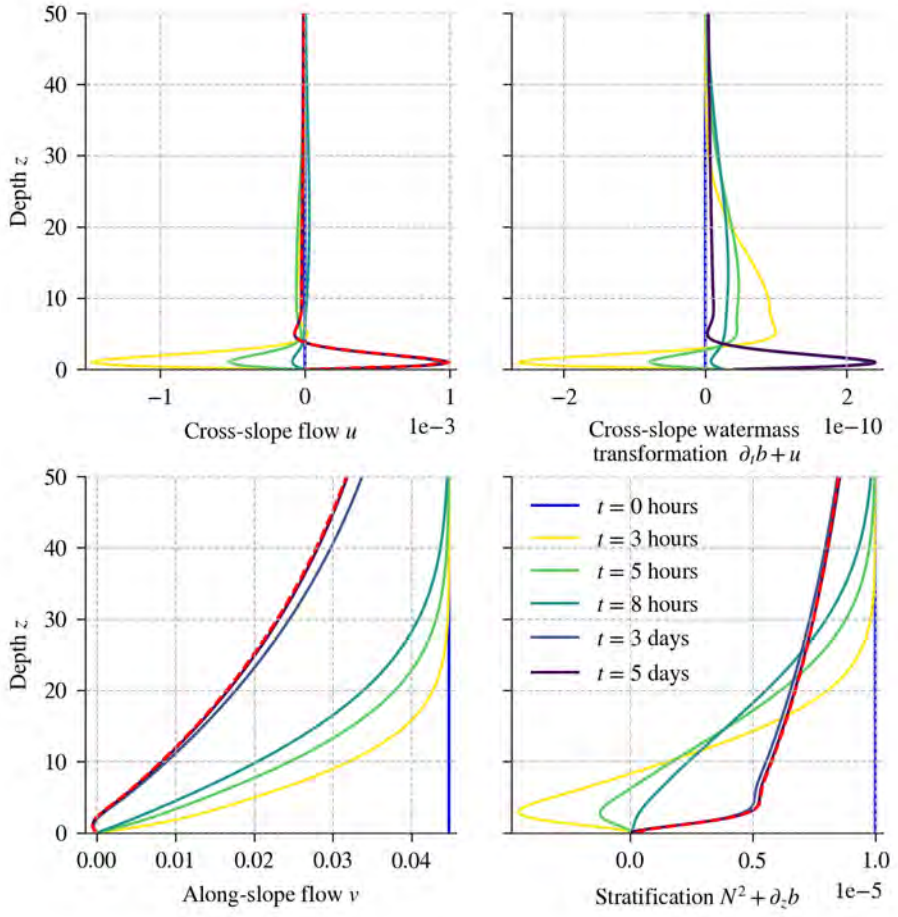


Figure 6: Numerical solutions to equations (20)–(23) for values $f = \nu = \kappa = 1 \times 10^{-4}$, $\theta = 0.022$ and $N^2 = 1 \times 10^{-5}$, $V \approx 1\,\mathrm{cm\,s^{-1}}$, and $\epsilon = 1e^{-3}$. Depth indicated as meters above bottom boundary.

Figure 6 shows numerical solutions to equations (20)–(23) and steady state solution as the red dashed line. As in figure 5, initial solutions show downslope flow, which quickly

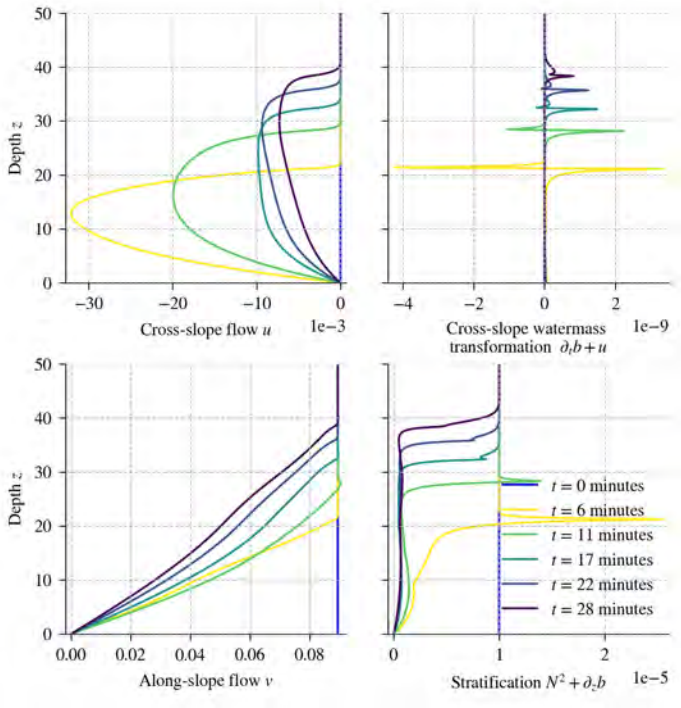


Figure 7: Solutions to equations (7)–(9) with Richardson dependent $\kappa$ and $\nu$. Values of: $f = \nu = \kappa = 1 \times 10^{-4}$, $\theta = 0.022$ and $N^2 = 1 \times 10^{-5}$, $V \approx 1\,\mathrm{cm\,s^{-1}}$, and $\epsilon = 1e^{-3}$. Depth indicated as meters above bottom boundary.

becomes upslope flow. Corresponding to the downslope flow we negative stratification and negative watermass transport.

## 3 Added Richardson Diffusivity

In previous solutions of the tilted bottom boundary, fixed values of diffusivity and viscosity were used, here we introduce a Richardson dependent diffusivity. This scheme was first introduced by MacCready and Rhines (1991b) and later Benthuysen and Thomas (2012). This model is of intermediate complexity with a Richards value (Ri) approximated as;

$$\mathrm{Ri} \equiv \frac{-g}{\rho_0}\frac{\partial \rho}{\partial z}\left[\left(\frac{\partial u}{\partial z}\right)^2 + \left(\frac{\partial v}{\partial z}\right)^2\right]^{-1} \tag{27}$$

Where, diffusivities are large (100 $\mathrm{cm}^2/\mathrm{s}$) when Ri is below 0.2, and small $1\mathrm{cm}^2/\mathrm{s}$ when Ri is greater than 0.3.

The aim of adding this to Peterson and Callies (2022) model is to account for the enhanced mixing along the boundary layer as observed in previous studies (Kunze et al., 2012; Waterhouse et al., 2014). By making it Ri dependent, we set a weak diffusivities in the interior and vice-versa for the boundary layer.

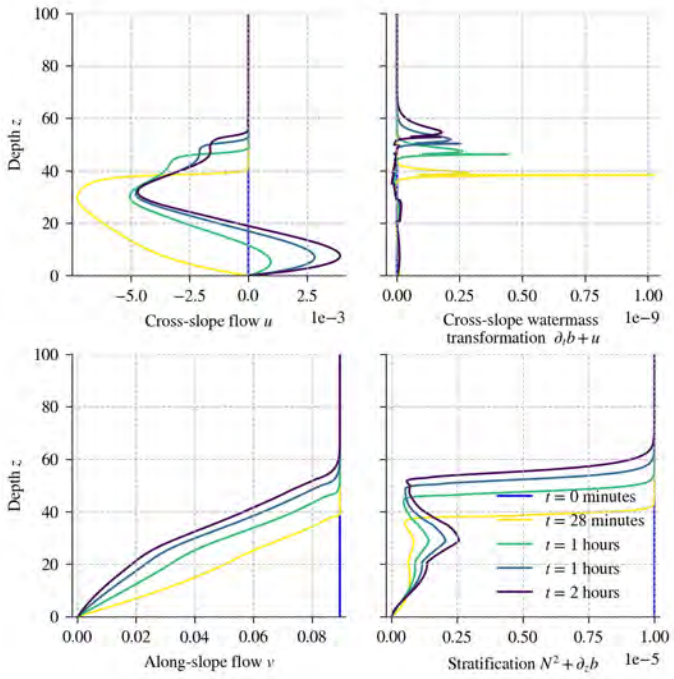


Figure 8: Same as figure 7, run for 4 hours. Solutions to equations (7)–(9) with Richardson dependent $\kappa$ and $\nu$. Values of: $f = \nu = \kappa = 1 \times 10^{-4}$, $\theta = 0.022$ and $N^2 = 1 \times 10^{-5}$, $V \approx 1\,\mathrm{cm\,s^{-1}}$, and $\epsilon = 1e^{-3}$. Depth indicated as meters above bottom boundary.

From a short numerical run, we observe downslope flow; however, unlike in Figures 5 and 6, the mixed layer exhibits positive stratification and watermass transformation, with a brief region of negative watermass transformation just above the boundary layer.

From figure 8 we see that after 30 minutes flow in the boundary layer becomes positive. This is notably quicker transition than in seen in figure 6.

# 4 Nonhydrostatic Case

To understand which representation mixing is more sensible we consider a nonhydrostatic 2D model using oceananigans, a numerical ocean model. We expect the initial negative stratification seen in the hydrostatic model (figure 5) to develop into turbulence.

The equations governing the conservation of momentum in a rotating fluid, including buoyancy via the Boussinesq approximation and including the averaged effects of surface gravity waves at the top of the domain via the Craik–Leibovich approximation are

$$\partial_t \boldsymbol{v} = -(\boldsymbol{v}\cdot\boldsymbol{\nabla})\boldsymbol{v} - (\boldsymbol{V}\cdot\boldsymbol{\nabla})\boldsymbol{v} - (\boldsymbol{v}\cdot\boldsymbol{\nabla})\boldsymbol{V} - \left(f - \boldsymbol{\nabla}\times\boldsymbol{u}^S\right)\times\boldsymbol{v} - \boldsymbol{\nabla}p + b\,\hat{\boldsymbol{g}} - \boldsymbol{\nabla}\cdot\boldsymbol{\tau} + \partial_t\boldsymbol{u}^S + \boldsymbol{F}_{\boldsymbol{v}}\,, \quad (28)$$

where $b\,\hat{\boldsymbol{g}}$ is the buoyancy, $\boldsymbol{\tau}$ is the kinematic stress tensor, $\boldsymbol{F}_{\boldsymbol{v}}$ denotes an internal forcing of the velocity field $\boldsymbol{v}$, $p$ is the kinematic pressure, $\boldsymbol{u}^S$ is the horizontal, two-dimensional

Stokes drift velocity field associated with surface gravity waves, and $f$ is the Coriolis parameter, or the background vorticity associated with the specified rate of rotation of the frame of reference.

As we're considering the Abyssal ocean there are some terms which can be considered negligible, firstly the effective background rotation rate due to surface waves, $-\left(\boldsymbol{\nabla}\times\boldsymbol{u}^S\right)\times\boldsymbol{v}$, $-\left(\boldsymbol{\nabla}\times\boldsymbol{u}^S\right)\times\boldsymbol{v}$ a source of momentum due to forcing or damping of surface waves, and $\boldsymbol{F_v}$ an arbitrary internal source of momentum. This leaves

$$\partial_t\boldsymbol{v} = -(\boldsymbol{v}\cdot\boldsymbol{\nabla})\boldsymbol{v} - (\boldsymbol{V}\cdot\boldsymbol{\nabla})\boldsymbol{v} - (\boldsymbol{v}\cdot\boldsymbol{\nabla})\boldsymbol{V} - \boldsymbol{\nabla}p + b\,\hat{\boldsymbol{g}} - \boldsymbol{\nabla}\cdot\boldsymbol{\tau} + \boldsymbol{F_v}\,, \tag{29}$$

Where, $(\boldsymbol{V}\cdot\boldsymbol{\nabla})\boldsymbol{v}$ is momentum advection, $(\boldsymbol{V}\cdot\boldsymbol{\nabla})\boldsymbol{v}$ advection of resolved momentum by the background velocity field, and $(\boldsymbol{v}\cdot\boldsymbol{\nabla})\boldsymbol{V}$ advection of background momentum by resolved velocity. We also have the Coriols force $\boldsymbol{f}\times\boldsymbol{v}$, kinematic pressure gradient $\boldsymbol{\nabla}p$, buoyant acceleration $b$, and gravity $\hat{\boldsymbol{g}}$. The terms on the right-hand side are:

$$\partial_t\boldsymbol{v} = -(\boldsymbol{v}\cdot\boldsymbol{\nabla})\boldsymbol{v} - (\boldsymbol{V}\cdot\boldsymbol{\nabla})\boldsymbol{v} - (\boldsymbol{v}\cdot\boldsymbol{\nabla})\boldsymbol{V} - \boldsymbol{\nabla}p + b\,\hat{\boldsymbol{g}} - \boldsymbol{\nabla}\cdot\boldsymbol{\tau} + \boldsymbol{F_v}\,, \tag{30}$$

With constant isotropic diffusivity for turbulence closure $\nabla\cdot\tau$. In this case the kinematic stress tensor is defined as

$$\tau_{i,j} = -\nu\sum_{i,j},$$

where $\nu$ is a constant viscosity and $\sigma_{ij} \equiv \frac{1}{2}\left(v_{i,j} + v_{j,i}\right)$ is the strain-rate tensor. The divergence of $\boldsymbol{\tau}$ is then

$$\nabla\cdot\tau = -\nu\nabla^2\boldsymbol{v}.$$

Similar to the hydrostatic case, the confidantes tilted by angle $\theta$, doing so we can compare our results to previous figures. Figure 8 shows solutions to the non-hydrostatic case is turbulent, which was expected for the downwelling favourable case. Yet, unlike with the Richardson dependent diffusivity model, watermass transport is negative in the early boundary layers, this can be seen more clearly in Figure 9.

# 5 Discussion

This report aims to investigate what key physical processes which could drive mean downwelling along tilted seafloors. There remains debate about whether this is primarily upwelling or downwelling; while many observational studies have shown mainly upwelling (Montgomery et al., 2000; Polzin et al., 1997; Wynne-Cattanach et al., 2024), there are still theoretical and observational results which show downwelling (Capó et al., 2024; Xie et al., 2023). Along with observational studies, our understanding of global ocean circulation suggests this is the case, as dense water from the poles eventually rises to the sea surface, becoming lighter in the process.

Our initial results use a Boussinesq hydrostatic approximation of a smooth tilted boundary. We find that by including along-slope geostrophic flow and enhancing mixing in the boundary layer, the time it takes for the cross-slope flow to reach a steady (or quasi-steady) state is increased.

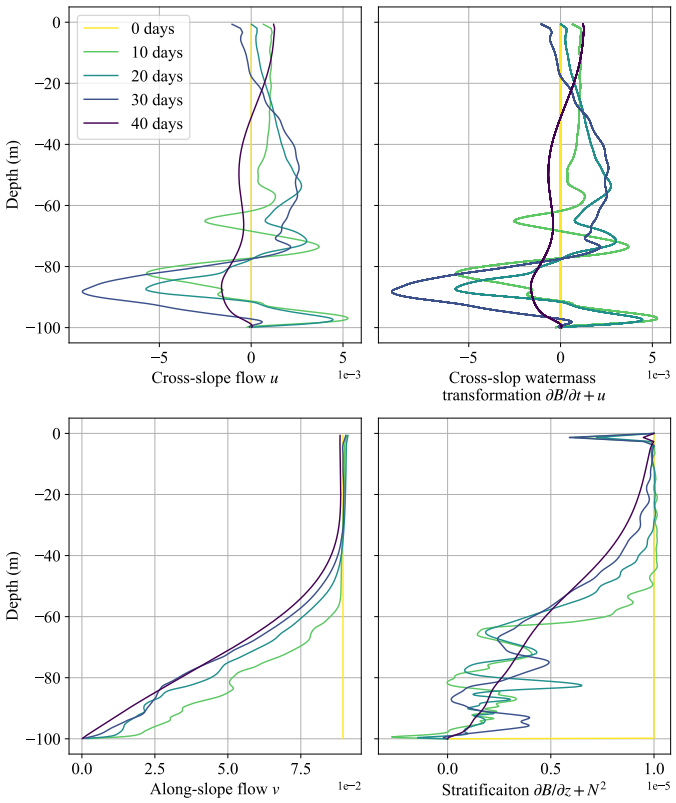


Figure 9: Numerical solutions using Oceananigans non-hydrostatic model, $f = \nu = \kappa = 1 \times 10^{-4}$, $\theta = 0.022$ and $N^2 = 1 \times 10^{-5}$, $V \approx 1\,\mathrm{cm\,s^{-1}}$, and $\epsilon = 1e^{-3}$. Depth indicated as meters above bottom boundary.

Firstly, by adding a constant geostrophic flow as in MacCready and Rhines (1991a), Figure 5 indicates after 8 hours (Figure 5), the cross-slope flow numerical solution returns to upslope. We have found this to be the case for multiple different parameters. A consistent feature of the downwelling is that it coincides with negative stratification and negative water-mass transformation. As lighter water sinks beneath denser water, negative stratification develops. However, in a real scenario, this would trigger a convective instability, as heat would quickly diffuse upward and deepen the boundary layer.

To better understand the steady state solutions of this system, we added a buoyancy damping term such that analytical solutions could be determined. By doing so, we hinder the slow diffusion of along-slope momentum from the boundary into the interior. Our results show it takes around 5 days for the along-slope flow to reach the equilibrated solution, whereas by day 3, the cross-slope flow has reached its steady state. We see slight differences between the numerical solutions in Figures 5 and 6: the solution at hour 8 becomes downslope rather than upslope when the damping term is added. Although this change is small and the water-mass transport in both cases remains positive, with dense water still becoming lighter.

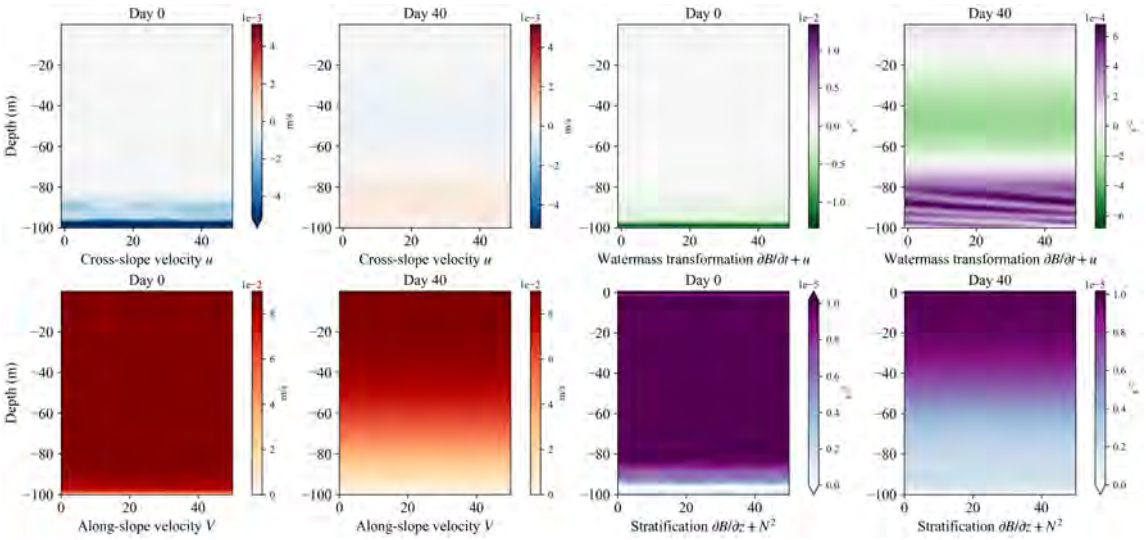


Figure 10: Numerical solutions using Oceananigans non-hydrostatic model, $f = \nu = \kappa = 1 \times 10^{-4}$, $\theta = 0.022$ and $N^2 = 1 \times 10^{-5}$, $V \approx 1\,\mathrm{cm\,s^{-1}}$, and $\epsilon = 1e^{-3}$, panels indicated the time mean over either day 0 or day 40. Depth indicated as meters above bottom boundary.

From observations, we know mixing increases along bottom boundaries, to account for this a Richardson dependent diffusivity was incorporated to the hydrostatic Boussinesq equations for eddy diffusivity $\kappa$, and viscosity $\nu$. By doing so downslope flow in the boundary layer corresponds to positive stratification–increased viscosity allows for mixing of the boundary layer with the interior. As lighter water was pushed under heavier water convective instabilities diffuse momentum upwards and create a thickening mixed layer. Not only this, but within the mixed layer we see a positive watermass transportation, showing that as downslope flow remains, the mixed layer continues to thicken resulting an increase of buoyancy in the bottom layer and hence lighter water doesn't become any denser.

Although, figure 7 shows a significantly shorter downslope flow than figures 5 and 6. This was not expected and previous results (MacCready and Rhines, 1991b), show a longer downslope flow than our numerical results. Further simulations should be run with different parameters.

Next, we used Oceananigans to investigate how a non-hydrostatic system would respond to down slope flow, figure 8 indicates that as lighter water is pushed beneath denser water convective instabilities are triggered. Although, unlike the Richardson dependent system, we see negative watermass transformation in the mixed layer, which was not expected. Further research is needed to understand why this is.

# 6 Conclusion

The motivation of this work was to investigate simple models and understand mechanisms may produce consistent downslope flow. As it stands, while Capó et al. (2024) presents a possible framework, discussion as to how best emulate these complex phenomena will most likely continue.

We've presented known hydrostatic approximations of abyssal sloping boundaries, in mind of delivering a constant and feasible downslope flow (Figure 2 and Figure 6). Yet, our results show that any downslope flow is transitionary, and has negative stratification. When adding buoyancy damping to produce a steady state solution, we find the cross-slope flow always equilibrates to an upwelling case.

Following MacCready and Rhines (1991b), the addition of a Richardson dependent diffusivities mean that the downwelling of light under dense water in the bottom Ekman layer will generate a growing mixed layer as buoyancy of the bottom boundary is increased—yielding downslope flow with a positive stratification and watermass transformation.

These results leads to our general conclusion that through changing topography the cross-slope flow never reaches an equilibrium, protracting the downslope flow while still maintaining a positive watermass transformation.

### Data availability

Code used to produce the hydrostatic models was developed by Peterson and Callies (2022), and is hosted at `https://github.com/hgpeterson/PGModels1Dand2D/tree/main/non_pg_models`. Code used to run Oceananigans model can be found at `https://github.com/Isabela-conde/tilted-boundary-layer`.

### Acknowledgements

I would like to thank Raffaele Ferrari for his wonderful supervision over the summer, his generosity of time and knowledge was above and beyond. I would also like to thank Glenn Flierl who gave many insightful ideas along the way, and took the time to explain those ideas to me multiple times. Henry Peterson was also a great help, we were lucky enough to be able to use his code developed during his PhD, along with this Henry was able to make multiple additions needed for this report, truly, his help was invaluable. I would also like to thank Yuchen Ma, Raffaele's post doc, who helped set up Oceananignas, as well as Pascale Garaud and David Goluskin as 2025's GFD directors. And lastly, a thank you to the rest of the fellows—they were all exceptional.

## References

J. Benthuysen and L. N. Thomas. Friction and diapycnal mixing at a slope: Boundary control of potential vorticity. *Journal of Physical Oceanography*, 42:1509–1523, 9 2012. ISSN 00223670. doi: 10.1175/JPO-D-11-0130.1.

E. Capó, J. C. McWilliams, J. Gula, M. J. Molemaker, P. Damien, and R. Schubert. Abyssal slope currents. *Journal of Physical Oceanography*, 54:2373–2392, 11 2024. ISSN 15200485. doi: 10.1175/JPO-D-24-0028.1.

R. Ferrari, A. Mashayek, T. J. McDougall, M. Nikurashin, and J. M. Campin. Turning ocean mixing upside down. *Journal of Physical Oceanography*, 46:2239–2261, 7 2016. ISSN 15200485. doi: 10.1175/JPO-D-15-0244.1.

A. Ganachaud and C. Wunsch. Improved estimates of global ocean circulation, heat transport and mixing from hydrographic data. *Nature*, 408(6811):453–457, 2000.

C. Garrett. The role of secondary circulation in boundary mixing. *Journal of Geophysical Research: Oceans*, 95(C3):3181–3188, 1990.

C. Garrett, P. MacCready, and P. Rhines. Boundary mixing and arrested ekman layers: Rotating stratified flow near a sloping boundary. *Annual Review of Fluid Mechanics*, 25 (1):291–323, 1993.

R. M. Holmes and T. J. McDougall. Diapycnal transport near a sloping bottom boundary. *Journal of Physical Oceanography*, 50:3253–3266, 11 2020. ISSN 15200485. doi: 10.1175/JPO-D-20-0066.1.

E. Kunze, C. Mackay, E. E. Mcphee-Shaw, K. Morrice, J. B. Girton, and S. R. Terker. Turbulent mixing and exchange with interior waters on sloping boundaries. *Journal of Physical Oceanography*, 42:910–927, 6 2012. ISSN 00223670. doi: 10.1175/JPO-D-11-075.1.

C. D. Lavergne, G. Madec, J. L. Sommer, A. J. Nurser, and A. C. N. Garabato. On the consumption of antarctic bottom water in the abyssal ocean. *Journal of Physical Oceanography*, 46:635–661, 2016. ISSN 15200485. doi: 10.1175/JPO-D-14-0201.1.

P. MacCready and P. B. Rhines. Buoyant inhibition of ekman transport on a slope and its effect on stratified spin-up. *Journal of Fluid Mechanics*, 223:631–661, 1991a.

P. MacCready and P. B. Rhines. Slippery bottom boundary layers on a slope. *Journal of Physical Oceanography*, 23(1):5–22, 1991b.

E. T. Montgomery, K. L. Polzin, L. C. S. Laurent, R. W. Schmitt, J. M. Toole, and J. R. Ledwell. Evidence for enhancedmixing over rough topography in the abyssal ocean. *Nature*, 2000.

W. H. Munk. Abyssal recipes. *Deep-Sea Research and Oceanographic Abstracts*, 13:707–730, 1966. ISSN 00117471. doi: 10.1016/0011-7471(66)90602-4.

H. G. Peterson and J. Callies. Rapid spinup and spindown of flow along slopes. *Journal of Physical Oceanography*, 52:579–596, 4 2022. ISSN 15200485. doi: 10.1175/JPO-D-21-0173.1.

K. Polzin, J. Toole, and R. Ledwell. Spatial variability of turbulent mixing in the abyssal ocean. *Science*, 276:93–96, 4 1997. doi: 10.1126/science.276.5309.93.

J. H. Simpson and R. R. McCandliss. "the ekman drain": a conduit to the deep ocean for shelf material. *Ocean Dynamics*, 63(9):1063–1072, 2013.

A. F. Waterhouse, J. A. MacKinnon, J. D. Nash, M. H. Alford, E. Kunze, H. L. Simmons, K. L. Polzin, L. C. St. Laurent, O. M. Sun, R. Pinkel, et al. Global patterns of diapycnal mixing from measurements of the turbulent dissipation rate. *Journal of Physical Oceanography*, 44(7):1854–1872, 2014.

G. L. Weatherly and P. J. Martin. On the structure and dynamics of the oceanic bottom boundary layer. *Journal of Physical Oceanography*, 8(4):557–570, 1978.

B. L. Wynne-Cattanach, N. Couto, H. F. Drake, R. Ferrari, A. L. Boyer, H. Mercier, M. J. Messias, X. Ruan, C. P. Spingys, H. van Haren, G. Voet, K. Polzin, A. C. N. Garabato, and M. H. Alford. Observations of diapycnal upwelling within a sloping submarine canyon. *Nature*, 630:884–890, 6 2024. ISSN 14764687. doi: 10.1038/s41586-024-07411-2.

X. Xie, Y. Wang, Z. Liu, X. Liu, D. Chen, D. Zhang, and J. Wang. Observation of near-inertial waves in the bottom boundary layer of an abyssal seamount. *Journal of Physical Oceanography*, 53(2):635–645, 2023.

# The Interaction of a Gravity Wave with an Unstable Horizontal Shear at Low Froude Number

Marion Cocusse

August 20, 2025

## 1 Introduction

The stability of stratified shear flows is of major importance for the transport of energy from large scales to dissipative scales in the ocean and atmosphere. Numerous studies have focused on the stability of a vertical shear in a stratified flow [1]. A necessary condition on the Richardson number for the triggering of the shear instability for a vertical flow with an inflection point (Richardson number smaller than 1/4) was established [17], [12]. Theoretical, experimental and numerical studies have since contributed to our knowledge of this flow. By contrast, the stability of its horizontal counterpart still remains relatively less understood, and seems to be almost always unstable. Recent studies at sufficiently high Reynolds number have focused on different horizontal shear profiles and flow set-ups. [8] have studied the stability of a horizontal linear velocity profile for a confined flow, and a number of articles have looked at a hyperbolic tangent profile ([2], [7] or [14]). Several studies have also investigated a sinusoidal velocity profile, also known as the horizontal Kolmogorov flow. In particular, [9] and [6] explored its behavior in astrophysical contexts, while [10] examined two distinct routes through which this flow transitions to turbulence. In the present work, we focus on this flow, namely a horizontal flow with a sinusoidal velocity profile.

Continuing the work of Garaud et al. [10], the goal of this report will be to investigate the stability and the transition to turbulence of a horizontal Kolmogorov flow. Gravity waves also play a crucial role in turbulence and mixing in the ocean [16]. These flows will inevitably interact with shear present in the fluid, impacting both wave breaking and the stability of the shear [13]. We will therefore also study a case of a Kolmogorov flow interacting with a gravity wave.

We will start by presenting in section 2 a linear stability analysis similar to the ones presented in [6] and [10], for a sinusoidal velocity profile as our horizontal shear. We focus on the particular case of low Froude number, and show that the dominant mode of the primary instability ($k_z = 0$) and the vertical modes ($k_z \neq 0$) grow at almost the same rate. An asymptotic analysis to explain this result is performed in section 3, and the scalings for the expansions are checked by comparing them to the full linear stability analysis. Section 4 presents Direct Numerical Simulations (DNS) of the full non-linear evolution of the Kolmogorov flow, we particularly study the primary instability. Two saturation mechanisms are presented depending on the Reynolds number, a viscous saturation in shallow layers

for relatively low Reynolds number and the formation of secondary Kelvin Helmholtz (KH) instabilities at higher Reynolds number. We then move on to a different flow in section 5, to study a slightly less idealized set up. We add a gravity wave propagating at an angle with the horizontal to the horizontal shear and investigate how this affects the primary instability and the saturation mechanisms. We highlight how adding this wave enhances the buoyancy and viscous dissipations of the flow, impacting its mixing properties. Finally, we summarize our results and outline a few unanswered questions that remain after this work in section 6.

# 2 Linear Stability Analysis at Low Froude Number

## 2.1 Governing equations

We consider a generic vertically invariant, horizontal plane-parallel background flow in a Cartesian coordinate system where $\mathbf{e}_x$ points in the streamwise direction, and $\mathbf{e}_z$ points in the upward vertical direction:

$$\overline{\mathbf{u}}_*(y_*) = U_* \overline{U}(k_* y_*)\mathbf{e}_x, \tag{1}$$

where the star subscript denotes the dimensional quantities. $U_*$ and $k_*^{-1}$ are the amplitude and characteristic length for the flow, respectivly, and are used as the unit velocity and length. The corresponding dimensionless background flow is:

$$\overline{\mathbf{u}}(y) = \overline{U}(y)\mathbf{e}_x. \tag{2}$$

The total velocity field $\mathbf{u} = \overline{\mathbf{u}} + \mathbf{u}'$ evolves according to the dimensionless Navier-Stokes equations under the Boussinesq approximation:

$$\frac{\partial \mathbf{u}}{\partial t} + \mathbf{u}.\nabla\mathbf{u} = -\nabla p + \frac{b}{Fr^2}\mathbf{e}_z + \frac{1}{Re}\nabla^2\mathbf{u}, \tag{3a}$$

$$\frac{\partial b}{\partial t} + \mathbf{u}\cdot\nabla b + w = \frac{1}{Pe}\nabla^2 b, \tag{3b}$$

$$\nabla\cdot\mathbf{u} = 0, \tag{3c}$$

with $\mathbf{u} = (u, v, w)$ and $b$ and $p$ are the dimensionless buoyancy and pressure perturbations away from a state of hydrostatic equilibrium, stratified with a constant buoyancy gradient. The unit buoyancy and pressure used are $N_*^2/k_*$ and $\rho_* U_*^2$, respectively, where $N_*$ is the constant buoyancy frequency of the fluid and $\rho_*$ the mean density of the fluid. The dimensionless parameters introduced are the Reynolds number $Re$, the Péclet number $Pe$, and the Froude number $Fr$:

$$Re = \frac{U_*}{k_*\nu_*}, \qquad Pe = \frac{U_*}{k_*\kappa_*}, \qquad Fr = \frac{U_* k_*}{N_*}, \tag{4}$$

where $\nu_*$ and $\kappa_*$ are, respectively, the kinematic viscosity and buoyancy diffusivity of the fluid.

## 2.2 Linear stability analysis

We perform a linear stability analysis of the flow described by equation 2. A similar analysis is presented in [6], the main differences with this study being that we use a different non-dimensionalisation of the equations and a more general base flow. Assuming that $|\mathbf{u}'| \ll |\bar{\mathbf{u}}|$, the linearized perturbation equations are:

$$\frac{\partial u'}{\partial t} + v' \frac{d\overline{U}(y)}{dy} + \overline{U}(y)\frac{\partial u'}{\partial x} = -\frac{\partial p'}{\partial x} + \frac{1}{Re}\nabla^2 u', \tag{5a}$$

$$\frac{\partial v'}{\partial t} + \overline{U}(y)\frac{\partial v'}{\partial x} = -\frac{\partial p'}{\partial y} + \frac{1}{Re}\nabla^2 v', \tag{5b}$$

$$\frac{\partial w'}{\partial t} + \overline{U}(y)\frac{\partial w'}{\partial x} = -\frac{\partial p'}{\partial z} + \frac{b'}{Fr^2} + \frac{1}{Re}\nabla^2 w', \tag{5c}$$

$$\frac{\partial b'}{\partial t} + \overline{U}(y)\frac{\partial b'}{\partial x} + w' = \frac{1}{Pe}\nabla^2 b', \tag{5d}$$

$$\nabla \cdot \mathbf{u}' = 0, \tag{5e}$$

where $p'$ and $b'$ are the pressure and buoyancy perturbations corresponding to the velocity perturbation $\mathbf{u}'$. Note that the viscous term can be neglected for the base flow $\overline{U}$, while it must be kept for the perturbations $\mathbf{u}'$, on the grounds that perturbations might have much smaller scales than the background flow and could be impacted by viscosity.

Exploiting the fact that the coefficients of this set of differential equations are independent of $x$, $z$ and $t$, we use the following normal mode decomposition for $q' \in \{u', v', w', p', b'\}$:

$$q' = \hat{q}(y) e^{ik_x x + ik_z z + \sigma t}, \tag{6}$$

where $k_x$ is the streamwise wavenumber, $k_z$ the vertical wavenumber and $\sigma$ the complex growth rate. The flow is considered linearly unstable whenever the real part of the growth rate $\lambda = \mathcal{R}(\sigma)$ is greater than zero. Substituting this ansatz in equations (5), we get:

$$\sigma\hat{u} + \hat{v}\frac{d\overline{U}}{dy} + ik_x\overline{U}\hat{u} = -ik_x\hat{p} + \frac{1}{Re}\left(\frac{d^2}{dy^2} - k_x^2 - k_z^2\right)\hat{u}, \tag{7a}$$

$$\sigma\hat{v} + ik_x\overline{U}\hat{v} = -\frac{d\hat{p}}{dy} + \frac{1}{Re}\left(\frac{d^2}{dy^2} - k_x^2 - k_z^2\right)\hat{v}, \tag{7b}$$

$$\sigma\hat{w} + ik_x\overline{U}\hat{w} = -ik_z\hat{p} + \frac{\hat{b}}{Fr^2} + \frac{1}{Re}\left(\frac{d^2}{dy^2} - k_x^2 - k_z^2\right)\hat{w}, \tag{7c}$$

$$\sigma\hat{b} + ik_x\overline{U}\hat{b} + \hat{w} = \frac{1}{Pe}\left(\frac{d^2}{dy^2} - k_x^2 - k_z^2\right)\hat{b}, \tag{7d}$$

$$ik_x\hat{u} + \frac{d\hat{v}}{dy} + ik_z\hat{w} = 0. \tag{7e}$$

Garaud et al. [10] studied this eigenproblem for the particular base flow $\overline{U}(y) = \sin(y)$. Figure 1 (extracted from their work) shows the growth rate $\lambda = \mathcal{R}(\sigma)$ as a function of $k_x$

and $k_z$ for two different parameter sets: $Re = Pe = 10000$, $Fr = 0.1$, and $Re = Pe = 10000$, $Fr = 0.01$.

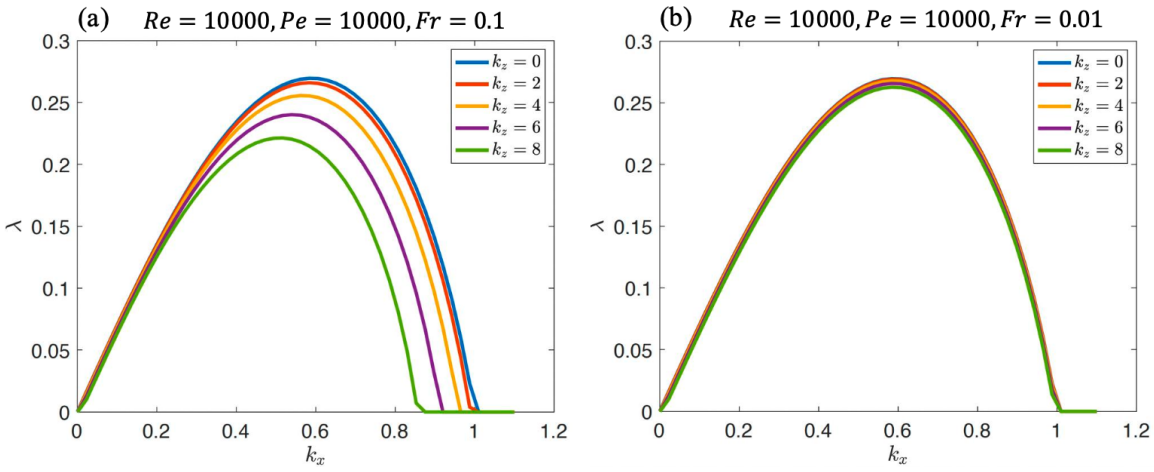


Figure 1: Real part of the growth rate $\lambda = \mathcal{R}(\sigma)$ as a function of $k_x$ for different values of $k_z$. The base flow used here is $U(y) = \sin(y)$, and the parameters are $Re = Pe = 10000$ and $Fr = 0.1$ for panel (a) and $Fr = 0.01$ for panel (b). Extracted from [10].

For both cases, the fastest growing linear mode (i.e., the mode with the largest $\lambda$ over all $k_x$ and $k_y$) is the vertically invariant mode $k_z = 0$. This 2D mode is unaware of the stratification and is therefore not impacted by the Froude number: it remains the same in figures 1a and 1b. Three-dimensional modes are also excited for both parameters, and seem to become more unstable with stronger stratification. Indeed, the modes $k_z = 2$, 4, 6 and 8 have a larger growth rate at $Fr = 0.01$ than at $Fr = 0.1$. For $Fr = 0.01$ (figure 1b), the $k_z \neq 0$ modes grow at almost the same rate as the $k_z = 0$ mode, which is rather surprising given that one would normally expect that increasing the stratification would impede the instability. To better understand why that is the case, we perform an asymptotic analysis of the linear equations in the limit of $Fr \to 0$ in the next section.

# 3 Asymptotic Analysis for Low Froude Number limit

## 3.1 Asymptotic model

We now focus on the low Froude number limit, for which the 3D modes grow almost as fast as the 2D modes. To simplify the analysis, we consider equations 7 in their inviscid and non-diffusive limits (i.e., $Re$, $Pe \to \infty$):

$$\sigma\hat{u} + \hat{v}\frac{d\overline{U}}{dy} + ik_x\overline{U}\hat{u} = -ik_x\hat{p}, \tag{8a}$$

$$\sigma\hat{v} + ik_x\overline{U}\hat{v} = -\frac{d\hat{p}}{dy}, \tag{8b}$$

$$\sigma\hat{w} + ik_x\overline{U}\hat{w} = -ik_z\hat{p} + \frac{\hat{b}}{Fr^2}, \tag{8c}$$

$$\sigma\hat{b} + ik_x\overline{U}\hat{b} + \hat{w} = 0, \tag{8d}$$

$$ik_x\hat{u} + \frac{d\hat{v}}{dy} + ik_z\hat{w} = 0, \tag{8e}$$

where $\hat{u}$, $\hat{v}$, $\hat{w}$, $\hat{p}$ and $\hat{b}$ correspond to the normal modes,and are only a function of the $y$ space variable.

At low Froude number, the $\frac{1}{Fr^2}$ term should dominate the vertical velocity equation. Paradoxically, we see in figure 1 that the effect of stratification seems to decrease as the Froude number decreases. This strongly suggests that the buoyancy field should scale as $Fr^2$. Assuming that the base flow $\overline{U}(y)$, the wavenumbers $k_x$ and $k_z$ and the growth rate $\sigma$ are all of order 1 (which is confirmed by the linear stability analysis above), the scalings for the other variables can be deduced by balancing each other. From the buoyancy equation, we get that the vertical velocity must balance the buoyancy, so $w = O(Fr^2)$ as well. Going back to the vertical velocity equation, the pressure must balance $b/Fr^2$ so $p = O(1)$. Finally, the horizontal velocity equations impose that $u, v = O(1)$. The expansions for the asymptotic analysis are therefore:

$$\begin{pmatrix}\hat{u}\\ \hat{v}\\ \hat{w}\\ \hat{b}\\ \hat{p}\end{pmatrix} = \begin{pmatrix}\hat{u}_0\\ \hat{v}_0\\ 0\\ 0\\ \hat{p}_0\end{pmatrix} + Fr^2\begin{pmatrix}\hat{u}_2\\ \hat{v}_2\\ \hat{w}_2\\ \hat{b}_2\\ \hat{p}_2\end{pmatrix} + Fr^4\begin{pmatrix}\hat{u}_4\\ \hat{v}_4\\ \hat{w}_4\\ \hat{b}_4\\ \hat{p}_4\end{pmatrix} + .... \tag{9}$$

To match these expressions, the growth rate $\sigma$ must also be expanded: $\sigma = \sigma_0 + Fr^2\sigma_1 + ....$

At order $O(1)$, the set of equations (8) reduces to:

$$\sigma_0\hat{u}_0 + \hat{v}_0\frac{d\overline{U}}{dy} + ik_x\overline{U}\hat{u}_0 = -ik_x\hat{p}_0, \tag{10a}$$

$$\sigma_0\hat{v}_0 + ik_x\overline{U}\hat{v}_0 = \frac{d\hat{p}_0}{dy}, \tag{10b}$$

$$0 = -ik_z\hat{p}_0 + \hat{b}_2, \tag{10c}$$

$$\sigma_0\hat{b}_2 + ik_x\overline{U}\hat{b}_2 + \hat{w}_2 = 0, \tag{10d}$$

$$ik_x\hat{u}_0 + \frac{d\hat{v}_0}{dy} = 0, \tag{10e}$$

where we have kept the $O(Fr^2)$ buoyancy equation since it is identically 0 at $O(1)$. Before going any further with this system, a few things can be pointed out. Firstly, no choice has been made for the exact base flow at this stage, this analysis should apply to any horizontal plane-parallel shear flows in the shape $\mathbf{u} = U(y)\overline{\mathbf{e}}_x$ (linear, sinusoidal, hyperbolic tangent...). The counterintuitive observation that modes can continue to grow rapidly at small Froude number is explained by the fact that these vertical motions are slow ($w = O(Fr^2)$), allowing them to "beat" the strong stratification.

We see from this analysis that the horizontal velocity equations and the continuity equation

(equations 10a,b and e) are decoupled from the vertical velocity and the buoyancy, and are the same equations one would obtain for purely 2D perturbations (i.e., $k_z = 0$ mode). They can be solved independently of the other two, and will provide the horizontal velocities and pressure fields $u_0$, $v_0$ and $p_0$, as well as the 0th order growth rate $\sigma_0$. While the horizontal structure and growth rate of the mode is therefore equivalent to that of the $k_z = 0$ mode, these modes have non-trivial vertical structure proportional to $e^{ik_z z}$. The buoyancy field $b_2$ is given by the hydrostatic equilibrium with the pressure in equation (10c). The vertical velocity $w_2$ is finally obtained thanks to the buoyancy field $b_2$ with the buoyancy equation (10d).

Finally, we note that unlike the model presented in [7], this model does not select any $k_z$ mode. In the inviscid limit, we therefore see that all modes with $k_z > 0$ are potentially excited by the horizontal shear instability. In the viscous case, however, we see that the viscous damping rate in the horizontal perturbation equation scales as ${k_z}^2/Re$. For sufficiently large $k_z$, therefore, this term can no longer be neglected compared with $\lambda$, and will ultimately cause the modes to decay instead.

### 3.2 Linear stability analysis of the asymptotic model

To check the validity of the expansions 9, this asymptotic analysis can be compared to the full linear stability analysis carried out in [10] and summarized in section 2.2. In particular, we are interested in comparing the eigenmode structure obtained with the asymptotically reduced equations to that of the full linear equations. To compute the eigenmodes in both cases, we look for periodic solutions for $q\hat{} \in \{u\hat{}_0, v\hat{}_0, w\hat{}_2, p\hat{}_0, \hat{b}_2\}$, with the same $y$ periodicity as $\overline{U}(y)$:

$$\hat{q}(y) = \sum_{n=-N}^{N} q_n e^{iny}. \tag{11}$$

The $k_y$ wavenumber is by construct 1, we therefore omit it from this decomposition. To obtain the eigenmodes in the reduced problem, we substitute this ansatz into equations (10), which leads to an eigenproblem with eigenvectors $\{q_n\}$ and eigenvalues $\sigma$. To compute the eigenmodes in the full linear problem, we follow the steps detailed in [10] (see their Appendix B).

To match the study in [10], a domain size of $4\pi \times 2\pi \times 2\pi$ is chosen. This in turn fixes the wavenumbers of the fastest growing mode that can fit in this domain: $k_x = 0.5$. The different fields ($v, v, w, b$ and $p$) are then reconstructed with the eigenmodes and the ansatzes (6) and (11).

The scaling for the vertical velocity $\hat{w} = O(Fr^2)$ can be checked computing $\frac{b^{full}}{Fr^2} - ik_z p^{full}$, where $b^{full}$ and $p^{full}$ denote the buoyancy and pressure fields reconstructed for the full problem of section 2.2. Equation 8c shows that $\frac{b^{full}}{Fr^2} - ik_z p^{full}$ scales as the vertical velocity, so we expect $\frac{b^{full}}{Fr^2} - ik_z p^{full} \sim \hat{w} = O(Fr^2)$. Figure 2 shows this quantity for two different Froude numbers and confirms the expected scaling for the vertical velocity as, for both cases, the quantity plotted is of order $Fr^2$.

The expansion for the buoyancy can also be checked by comparing the linear stability analysis of the full equations of section 2.2 with the linear stability analysis of the asymptotic model. The quantity $Fr^2 b_2^{asym} - b^{full}$ (where $b_2^{asym}$ is the buoyancy field obtained after the asymptotic analysis) should scale as $Fr^4$. Indeed, we should have $b^{full} = Fr^2 \hat{b}_2 + Fr^4 \hat{b}_4 + o(Fr^4)$, so:

$$\begin{aligned} Fr^2 b_2^{asym} - b^{full} &= Fr^2 \hat{b}_2 - Fr^2 \hat{b}_2 - Fr^4 \hat{b}_4 + o(Fr^4) \\ &= -Fr^4 \hat{b}_4 + o(Fr^4) = O(Fr^4). \end{aligned} \tag{12}$$

Figure 3 shows this quantity for two different Froude numbers. It confirms the expansion for the buoyancy as it does scale as $Fr^4$.

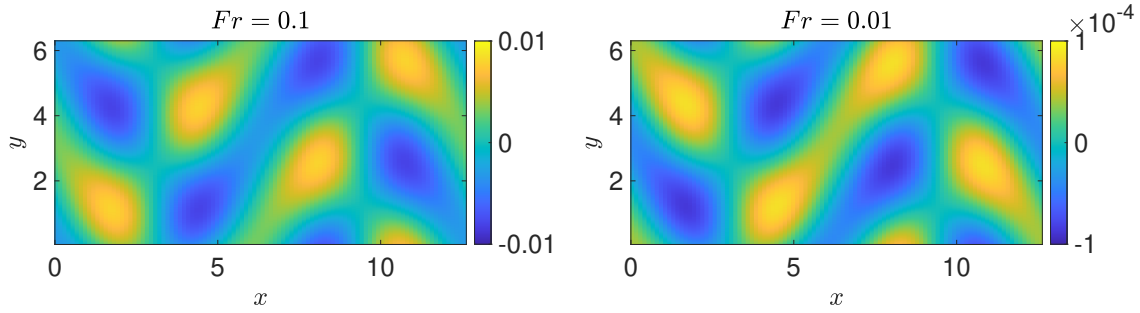


(a) (b)

Figure 2: The quantity $b^{full}/Fr^2 - ik_z p^{full}$ reconstructed from the linear stability analysis of the full problem for wavenumbers $k_x = 0.5$ and $k_z = 1$ is plotted for two different Froude numbers: $Fr = 0.1$ for panel (a) and $Fr = 0.01$ for panel (b), and for the parameters $Re = Pe = 10000$.

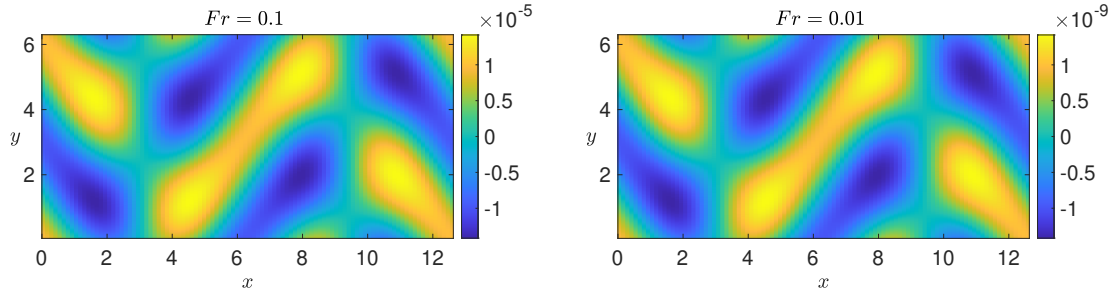


(a) (b)

Figure 3: The quantity $Fr^2 b_2^{asym} - b^{full}$ reconstructed from the linear stability analysis of the asymptotic model and of the full equations for wavenumbers $k_x = 0.5$ and $k_z = 1$ is plotted for two different Froude numbers: $Fr = 0.1$ for panel (a) and $Fr = 0.01$ for panel (b), for the parameters $Re = Pe = 10000$.

In order to compute a correction to the eigenvalue $\sigma_2$, a second order correction to this asymptotic analysis can be written:

$$\sigma_0 \hat{u}_2 + \sigma_2 \hat{u}_0 + \hat{v}_2 \frac{d\overline{U}}{dy} + ik_x \overline{U} \hat{u}_2 = -ik_x \hat{p}_2, \tag{13a}$$

$$\sigma_0 \hat{v}_2 + \sigma_2 \hat{u}_0 + ik_x \overline{U} \hat{v}_2 = \frac{d\hat{p}_2}{dy}, \tag{13b}$$

$$\sigma_0 \hat{w}_2 + ik_x \overline{U} \hat{w}_2 = -ik_z \hat{p}_2 + \hat{b}_4, \tag{13c}$$

$$\sigma_0 \hat{b}_4 + \sigma_2 \hat{b}_2 + ik_x \overline{U} \hat{b}_4 + \hat{w}_4 = 0, \tag{13d}$$

$$ik_x \hat{u}_2 + \frac{d\hat{v}_2}{dy} + ik_z \hat{w}_2 = 0. \tag{13e}$$

This system is coupled to the lower order one through $\sigma_0$, $\hat{u}_0$, $\hat{v}_0$, $\hat{p}_0$, $\hat{w}_2$ and $\hat{b}_2$. Similarly to the lower order problem, the horizontal velocity and continuity equations are decoupled from the vertical and buoyancy equations. Knowing $\hat{u}_2$,$\hat{v}_2$ and $\hat{p}_2$ as well as the lower order solutions, $\hat{b}_4$ and $\hat{w}_4$ can be computed through the vertical velocity and buoyancy equations. This system is however more difficult to solve as it is not quite an eigenproblem. The eigenvalue at this order $\sigma_2$ is multiplied by the eigenvectors at lower order and the eigenvalue at the lower order is multiplied by the eigenvectors at this order. Solving this problem is left to future work.

# 4 Direct Numerical Simulations of the Horizontal Shear Instability at Very Small Froude Number

## 4.1 Initial conditions

Naturally, this linear stability approach only investigates the linear behavior of the system. To study the complete non-linear dynamics of this system, we turn to direct numerical simulations. The pseudo-spectral code PADDI [18] is used to perform DNS. This code solves the dimensionless incompressible Navier-Stokes equations under the Boussinesq approximation (equations (3)). The dimensions of the computational domain are $4\pi \times 2\pi \times \pi/2$, the resolution is $1536 \times 768 \times 192$ equivalent meshpoints, and we impose triply periodic boundary conditions. We focus on the specific case of an initial sinusoidal velocity field, the initial conditions are therefore:

$$\mathbf{u}(x, y, z, 0) = \sin(y)\mathbf{e}_x + n_w(x, y, z)\mathbf{e}_x, \qquad b(x, y, z, 0) = 0, \tag{14}$$

where $n_w$ represents white noise on the grid scale. The background velocity field $\overline{U}(y)$ and the background linear stratification $\overline{b}(z)$ are represented in figure 4.

For this section, we will focus on a single value of the stratification parameter $Fr = 0.1$, and look at two Reynolds and Péclet numbers: $Re = Pe = 5000$ and $Re = Pe = 10000$.

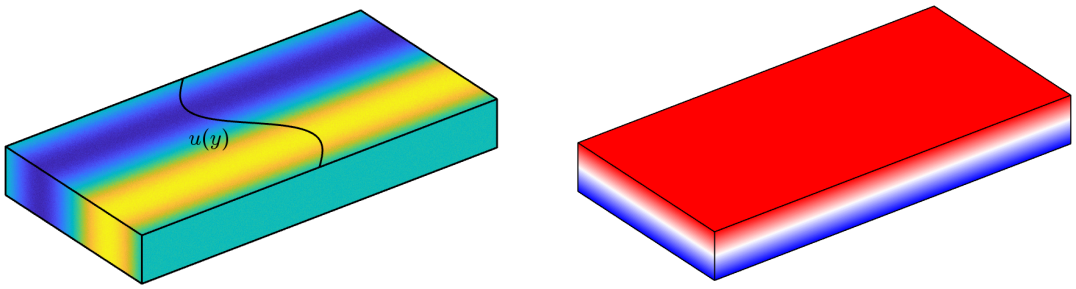


(a) (b)

Figure 4: Initial conditions for (a) the streamwise velocity field and (b) the linear stratification $\overline{b}(z) = z$.

## 4.2 Typical behavior

Figures 5 and 6 show snapshots of the simulations for the parameters $Re = P\,e = 5000$ and $Re = P\,e = 10000$, respectively. More precisely, they show the $u$ velocity field (left panels) and $w$ velocity fields (right panels) on the $x - y$ plane at $z = 0$ (top, larger panels) and on the $x - z$ plane at $y = 0$ (bottom, smaller panels), at three different times. The snapshots were selected to capture the moment the primary instability becomes visible (at $t = 40$), and how it evolves in time (at $t = 50$). The last snapshot (at $t = 62$) is selected to highlight the different saturation behavior depending on the Reynolds number. The primary instability appears as a meander of the mean flow in the horizontal plane for both Reynolds

numbers (top left panels, $t = 40$). A vertical velocity field forms and intensifies as vertical modes of the primary instability develop (right panels). The vertical scales become smaller and smaller as time evolves, forming shallow laminar layers. The saturation mechanism for these scales appears to be different depending on the Reynolds number. For the lower Reynolds number investigated here ($Re = 5000$), viscous saturation occurs between the shallow laminar layers while at the higher Reynolds number ($Re = 10000$), secondary Kelvin Helmholtz (KH) instabilities start to form (see bottom right panel of figure 6). During this

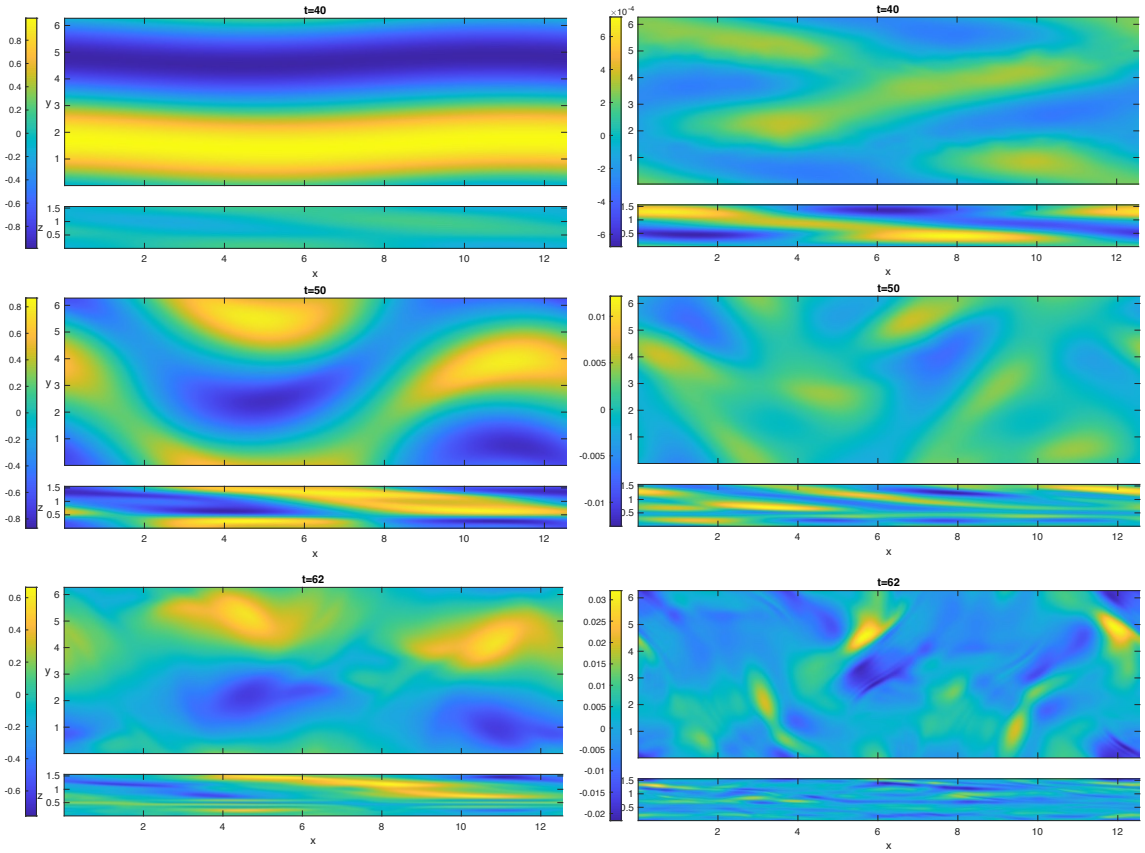


Figure 5: Snapshots at different times of the $x$ velocity $u$ for the panels on the left and the vertical velocity $w$ for the panels on the right. Each panel shows two slices through the computational domain: a horizontal $xy$ slice at $z = 0$ for the top panels and a vertical $xz$ slice at $y = 0$ for the bottom panels, for the simulation with parameters $Re = Pe = 5000$ and $Fr = 0.1$.

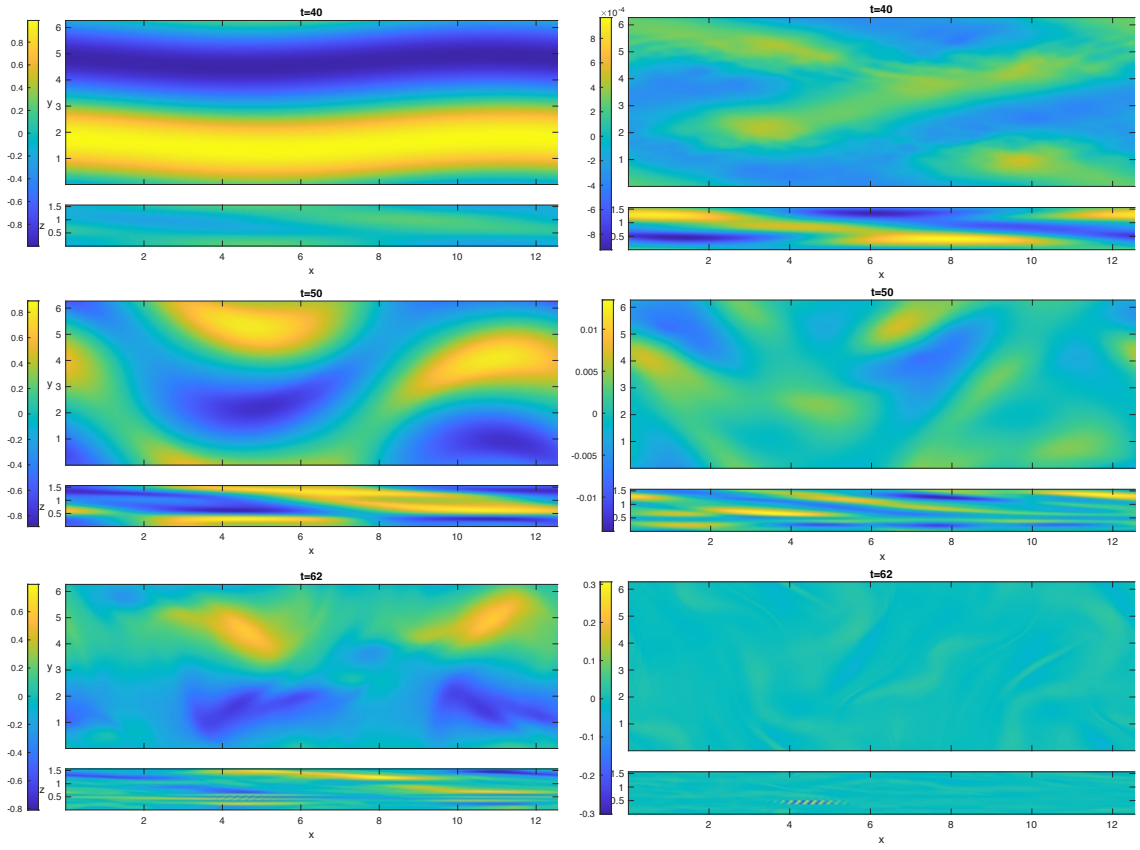


Figure 6: Snapshots at different times of the $x$ velocity $u$ for the panels on the left and the vertical velocity $w$ for the panels on the right. Each panel shows two slices through the computational domain: a horizontal $xy$ slice at $z = 0$ for the top panels and a vertical $xz$ slice at $y = 0$ for the bottom panels, for the simulation with parameters $Re = Pe = 10000$ and $Fr = 0.1$.

### 4.3 Stability of horizontal shear

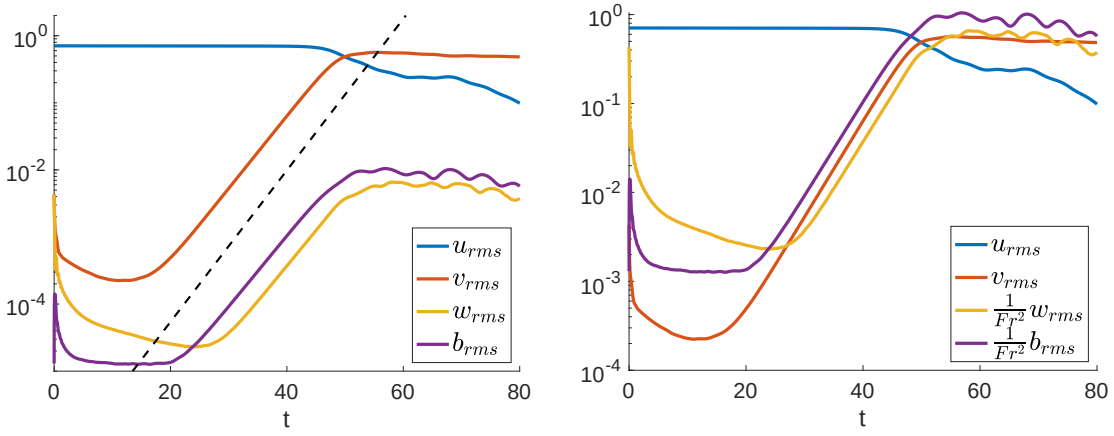


(a) (b)

Figure 7: (a) Root mean squares of the components of the velocity vector and the buoyancy field as a function of time for the parameters $Re = Pe = 5000$ and $Fr = 0.1$. The black dashed line shows an exponential with growth rate $\lambda = 0.26$, corresponding to the growth rate predicted by the linear stability analysis. (b) Same as (a) with $w_{rms}$ and $b_{rms}$ rescaled with $Fr^2$.

To further study the primary instability of this flow, we look at figure 7a showing the root mean square (rms) of the components of the velocity vector and of the buoyancy field: $u_{rms} = <u^2>^{1/2}$, $v_{rms} = <v^2>^{1/2}$, $w_{rms} = <w^2>^{1/2}$ and $b_{rms} = <b^2>^{1/2}$, where $<.>$ denotes the volume average. The mode $k_z = 0$ that grows during the exponentially growing section of $v_{rms}$ (between $t \approx 20$ and $t \approx 50$), grows at the rate predicted by the linear stability analysis (see dashed black line in figure 7a). The plots for $w_{rms}$ and $b_{rms}$ show that modes with a vertical structure ($k_z \neq 0$) also grow. Their growth rate is very close to the one of the $k_z = 0$ mode, in accordance with the linear stability analysis. Figure 7b shows the same root mean squares as figure 7a, except that $w_{rms}$ and $b_{rms}$ are rescaled by $Fr^2$. With this rescaling, they have roughly the same amplitude as the $v_{rms}$ curve, in agreement with the scalings of the asymptotic analysis.

Once the instability reaches non-linear saturation (after $t \approx 50$, or when $u_{rms} \approx v_{rms}$), figure 7b shows that the $Fr^2$ rescaling for $w_{rms}$ and $b_{rms}$ still seems to have roughly the same amplitude as the $v_{rms}$ curve. This is reminiscent of the so-called Lilly regime [15], a non-linear quasi-2D turbulent regime weakly coupled in the vertical direction, and where $w \sim b \sim Fr^2 \mathbf{u}_h$ (where $\mathbf{u}_h$ is the horizontal velocity vector). Another specificity of the Lilly model is that its horizontal divergence is 0 at first order: $\nabla_h \cdot \mathbf{u}_h = 0$. This was also an assumption of the asymptotic model presented in section 3. To check whether the flow at saturation is indeed in the Lilly regime, we compute the divergence of $\mathbf{u}_h$ on a horizontal slice of the DNS. Figure 8 shows the horizontal divergence computed on the slice $z = 0$ at two different times, one during the exponential growth of the primary instability

$t = 40$ (figure 8a) and one after the non-linear saturation is reached, at $t = 60$ (figure 8b). At $t = 40$, the horizontal divergence on the slice is of order $Fr^2$, in agreement with the prediction from the asymptotic analysis. However, in the saturated regime, the horizontal divergence is much greater than $Fr^2$ and is therefore not 0 at first order. The Lilly regime is not appropriate to describe this DNS as it does not support small vertical scales (this model only captures vertical scales much greater than $Fr^2$). The asymptotic analysis showed that the primary instability generates modes with vertical structures with no constraint on their vertical scale $k_z^{-1}$, they can therefore be too small to be encompassed by the Lilly regime, which requires $k_z$ to be of order 1. These small vertical structures can be seen in the vertical snapshots at $t = 50$ and $t = 62$ of figures 5 and 6.

More recent studies have proposed 2D stratified turbulence models that support small vertical scales, namely a study by Brethouwer et al. [3] that allows for a large horizontal scale $l_h$ and a small vertical scale $l_z$ that scale with the Froude number: $l_z \sim Frl_h$ (the continuity equation then imposes that $u_z \sim Fr\mathbf{u}_h$). The DNS with parameters $Re = 5000$ and $Fr = 0.1$ has the characteristics of this regime. However, the DNS for $Re = 10000$ and $Fr = 0.1$ also exhibits small horizontal scales with the apparition of secondary Kelvin-Helmholtz instabilities (figure 6, bottom right panel). A study by Chini et al. [5] developed a more general framework that encompasses the regime described in [3], but that can also support small horizontal scales and specifically KH instabilities, as seen in the simulation for $Re = 10000$.

We have therefore established a pathway to turbulence from a (vertically invariant) horizontal sinusoidal velocity profile. The primary instability arising from this flow creates many vertical scales, including small ones (compared to the horizontal scale). Depending on the Reynolds number, the saturation process is different. For relatively low Reynolds number (around $Re = 5000$), viscous dissipation dominates the process, while for higher Reynolds number (around $Re = 10000$), KH billows form, creating small horizontal scales. Future work will establish whether the same pathways exist at low Péclet number. Furthermore, it will be important to establish the exact value of the critical Reynolds number separating the two possible saturation mechanisms.

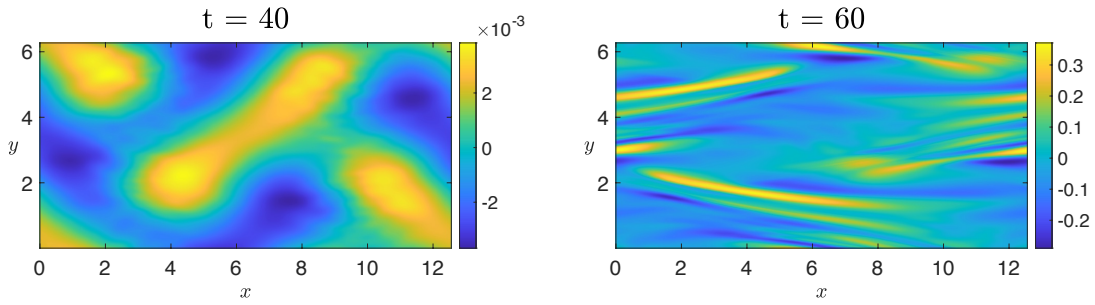


(a) (b)

Figure 8: Horizontal divergence on the slice $z = 0$ at time (a) $t = 40$ and (b) $t = 60$, for the parameters $Fr = 0.1$ and $Re = 5000$.

# 5 Direct Numerical Simulations of the Horizontal Shear and a Gravity Wave

The simple horizontal shear flow studied above is a very idealized model, far from any real life flow. Indeed, naturally occurring shear flows interact with their surroundings, including topography, boundaries with other fluids, or other flows within the same fluid. This section will focus on one such case: the interaction of a horizontal shear with a gravity wave. We will investigate the impact of adding the wave on the primary instability and on the transition to turbulence.

## 5.1 Initial conditions

We choose to add a gravity wave invariant in the $x$ direction but propagating in the $y - z$ plane, with wavenumbers $k_y$ and $k_z$ respectively, and with a $v$ and $w$ velocity component. The amplitude of the $v$ velocity component is chosen to be $A$, and the amplitudes of the $w$ velocity component and the buoyancy field follow through the polarization relation. The initial conditions are given by:

$$u(x, y, z, t = 0) = \sin(y) + n_w(x, y, z), \tag{15a}$$

$$v(x, y, z, t = 0) = A \cos(k_y y + k_z z) \tag{15b}$$

$$w(x, y, z, t = 0) = -\frac{k_y}{k_z} A \cos(k_y y + k_z z), \tag{15c}$$

$$b(x, y, z, t = 0) = \frac{k_y}{k_z \omega} A \sin(k_y y + k_z z), \tag{15d}$$

where the wave frequency $\omega$ is given by the dispersion relation:

$$\omega = \frac{1}{Fr}\frac{k_y}{(k_y^2 + k_z^2)^{1/2}}. \tag{16}$$

White noise on the grid scale $n_w$ is once again added to the $u$ velocity field. The parameters used in this section are: $Re = Pe = 5000$ and $Fr = 0.1$, and the wavenumbers for the wave are $k_y = 2$ and $k_z = 8$. We will vary the amplitude of the $v$ component of the wave $A$ to investigate the impact of the wave. These initial conditions are plotted in figure 9, for the wave amplitude $A = 0.5$.

The horizontal shear flow $u$ imposed at time $t = 0$ is identical to the one used in sections 2-4 of this work. However, it is now modulated by the gravity wave. Before any instability develops, it now has a time dependency and a vertical structure. This new base flow can be computed analytically in the inviscid limit, and the $x$ velocity field becomes:

$$\overline{u}(y, z, t) = \sin\left(y + \frac{A}{\omega}\sin(k_y y + k_z z - \omega t) - \frac{A}{\omega}\sin(k_y y + k_z z)\right). \tag{17}$$

This base flow being much more complex than in the case without the gravity wave, no linear stability analysis is performed here.

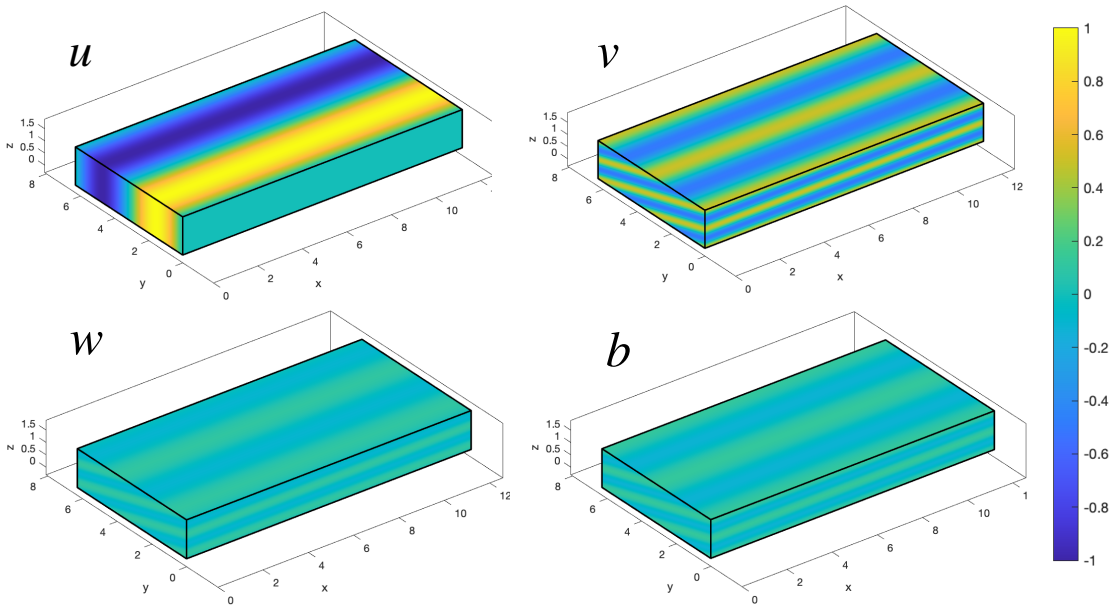


Figure 9: Velocity and buoyancy initial conditions for the DNS with a horizontal shear and a gravity wave with an amplitude $A = 0.5$ for the $v$ component.

Figure 10 shows the typical evolution of the flow for a wave amplitude $A = 0.5$. The first snapshots shown ($t = 2$) can be compared to the initial conditions (see figure 9) and show

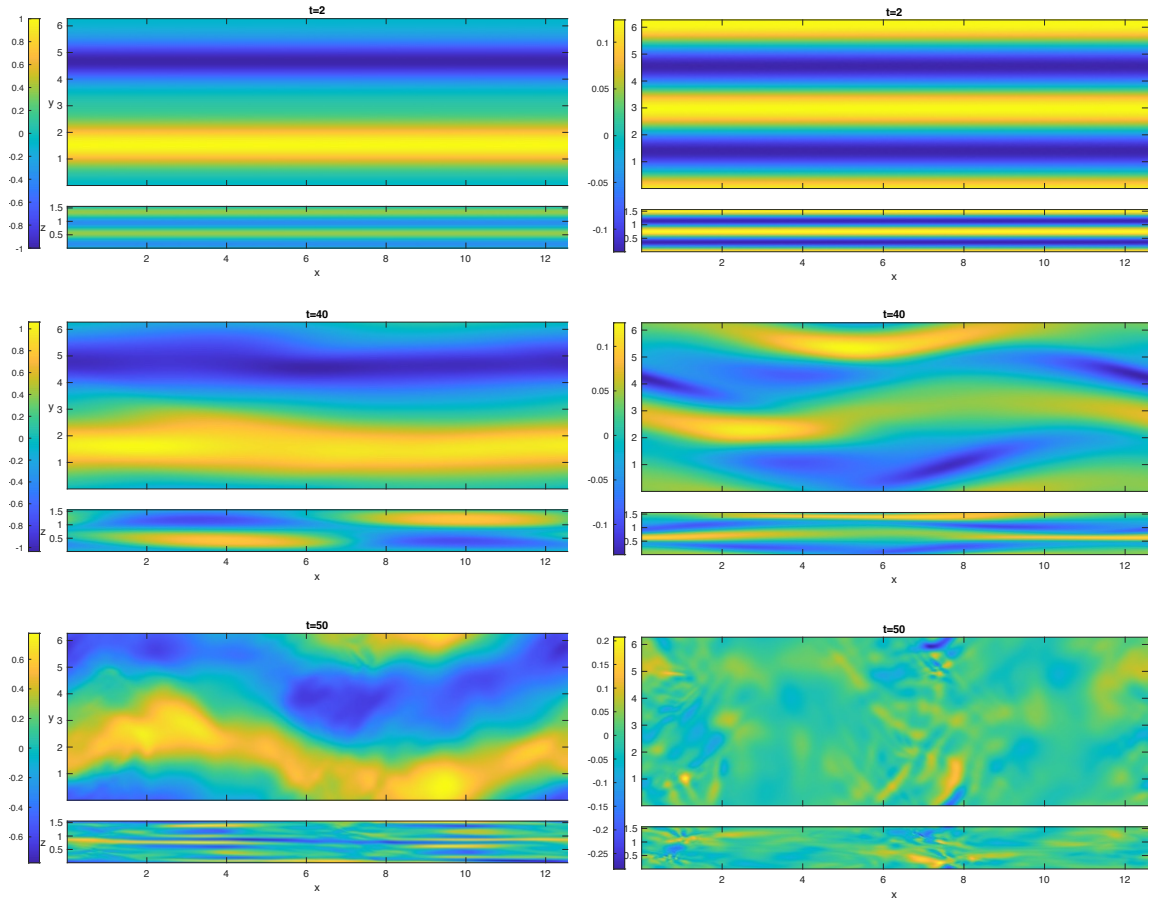


Figure 10: Snapshots at different times of the $x$ velocity $u$ on the left panel and the vertical velocity $w$ on the right. Each panel shows two slices through the computational domain: a horizontal $xy$ slice at $z = 0$ for the top panels and a vertical $xz$ slice at $y = 0$ for the bottom panels, for the simulation with parameters $Re = Pe = 5000$, $Fr = 0.1$ and $A = 0.5$.

the modulation of the shear and the oscillation of the wave. The next snapshots (at $t = 40$) are chosen to show the meandering of the shear and the appearance of the first vertical scales as the primary instability develops. The behavior looks very similar to the one seen in the case without the wave (figures 5 , 6 ). The final snapshots represented (at $t = 50$) correspond to the saturation regime. Crucially, we see that the magnitude of the vertical velocity for this simulation (approximately equal to 0.2) is similar to the case with no wave at $Re = 10000$, even if the Reynolds number is set to $Re = 5000$ here. In what follows, we now study the impact of the wave both on the initial development of the instability and on its saturation.

### 5.2 Impact on the primary instability

The shear in the $x$ direction is impacted by the presence of the wave, which will also impact the primary instability of this flow. The base flow now has three velocity components, so the $v_{rms}$ and $w_{rms}$ cannot be directly linked to the growth of the perturbation, as was done for the shear only case. To extract the growth of the perturbation from the total flow, we can exploit the fact that the base flow is entirely $x$-independent (neither the shear nor the wave have an $x$ dependency). In spectral space, this is equivalent to saying that the base energy contained in the $k_x = 0$ mode is associated to the base flow, while energy contained in any mode with $k_x \neq 0$ is necessarily associated to the perturbations.

The spectral power in the mode $(k_x, k_y)$ can be defined as (in this section, hats denote Fourier transforms):

$$\hat{E}(k_x, k_y, z, t) = \hat{v}(k_x, k_y, z, t)\hat{v}^*(k_x, k_y, z, t), \tag{18}$$

where $\hat{v}(k_x, k_y, z, t)$ is the horizontal Fourier transform of the $y$ velocity component, and $\hat{v}^*(k_x, k_y, z, t)$ is its complex conjugate. The vertically averaged spectral power of the flow perturbation in the $y$ direction is obtained by summing over all the $k_y$ modes and over all the $k_x \neq 0$ modes, and then by performing a vertical average:

$$E'(t) = \frac{1}{L_z} \int \sum_{k_y} \sum_{k_x \neq 0} \hat{E}(k_x, k_y, z, t) dz. \tag{19}$$

By computing this field, we aim at creating a quantity equivalent to ${v_r}^2{}_{ms}$ in terms of growth rate of the primary instability. Figure 11a shows the time evolution of this quantity, for different amplitudes $A$ of the wave. An exponential growth regime can be identified, from which a growth rate can be extracted. This growth rate corresponds to twice the growth rate of the primary instability, so figure 11b shows half of the growth rate extracted from figure 11a as a function of the wave amplitude $A$. The case $A = 0$ corresponds to the case with the shear only studied in the previous section. Adding the gravity wave does not seem to have a drastic impact on the growth rate of the primary instability. For the amplitudes studied, the maximum increase of the growth rate is for the wave amplitude $A = 0.75$ and is about 15% greater than the case with only the shear. Its impact is not monotonic either, going from wave amplitude $A = 0.25$ to $A = 0.75$, the growth rate increases as a function of the amplitude, while going from $A = 0.75$ to $A = 1$, it decreases.

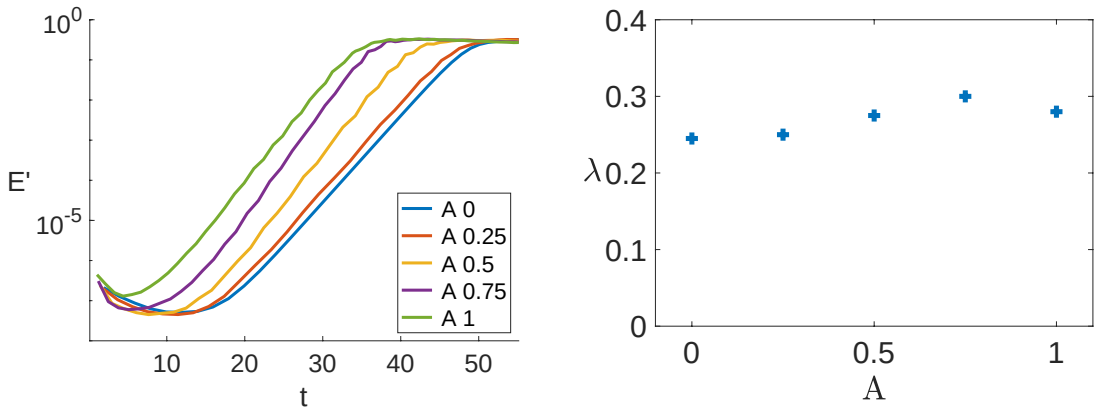


(a) (b)

Figure 11: (a) Logarithm of the evolution of the horizontally averaged kinetic energy in the $y$ direction associated with the perturbation for different wave amplitudes, for the parameters $Re = Pe = 5000$ and $Fr = 0.1$. (b) Growth rate extracted from (a) for the different wave amplitudes.

### 5.3 Impact on the transition to turbulence

The study of the mixing properties of turbulent stratified flows has lately gained a lot of traction. A recent review [4] highlights the importance and implications of measuring the mixing efficiency. Here, we will focus on the two main components of the mixing efficiency, the viscous dissipation and the buoyancy dissipation. The viscous dissipation represents the irreversible dissipation of kinetic energy through viscosity, while the buoyancy dissipation represents the irreversible conversion of available potential energy due to mixing across isopycnals. The mixing properties strongly depend on the initial conditions and on the instabilities arising from them. Although the instability mechanism seems similar with and without the gravity wave, the viscous and buoyancy dissipations are strongly impacted by the presence of the wave.

#### 5.3.1 Viscous dissipation

The viscous dissipation is defined as:

$$\varepsilon = \frac{1}{Re} < |\nabla \mathbf{u}|^2 >, \tag{20}$$

where $< . >$ denotes the volume average.

Figure 12a shows the evolution of the viscous dissipation for different wave amplitudes, going from $A = 0$ (no wave) to $A = 1$ (the amplitude of the $v$ component of the wave is equal to the amplitude of the velocity of the horizontal shear). For the case without a wave, there is very little viscous dissipation until around $t \approx 40$, as the flow is still quite laminar (see snapshots in figure 5, top panels). As the flow becomes turbulent, a peak in viscous dissipation quickly appears and then fades slowly. For the cases with a wave, there is more viscous dissipation initially, and it increases with the wave amplitude. The

oscillations that can be seen until around $t = 35 - 40$ are due to the wave oscillating and modulating the shear. The dissipation peak occurs earlier, is shorter and more intense as the wave amplitude increases. By adding the wave, we add kinetic and potential energy to the system, which means that there is more energy to be dissipated. This might explain the more intense peak in energy dissipation seen when we increase the wave amplitude. Figure 12b shows the same viscous dissipation rescaled by the total initial energy (kinetic and potential) of the system $E_0$, defined as:

$$E_0 = \frac{1}{2}(u^2 + v^2 + w^2 + \frac{1}{F_r^2}b^2). \tag{21}$$

With this rescaling, the maximum instantaneous dissipation is the same for all wave amplitudes. It, however, does not explain the earlier onset of the peak or the fact that it fades faster as the wave amplitude is increased.

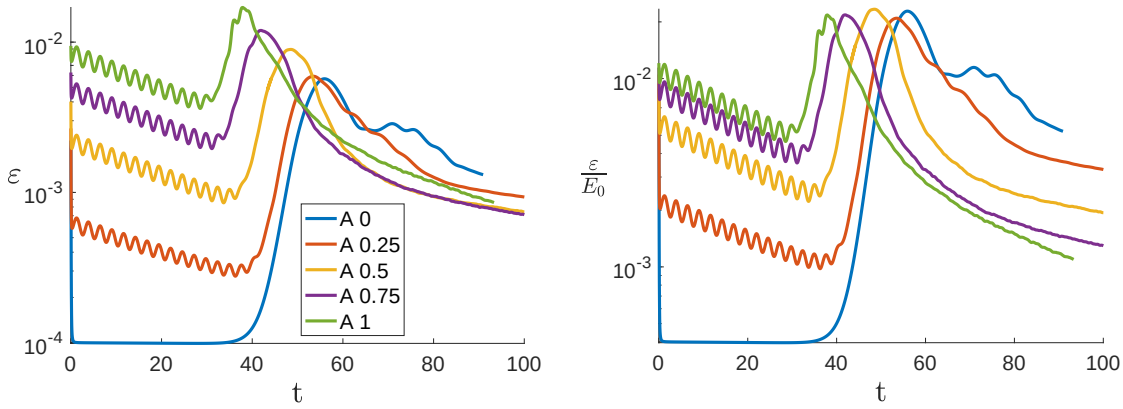


(a) (b)

Figure 12: (a) Evolution of the viscous dissipation for different wave amplitudes, for the parameters $Re = Pe = 5000$, $Fr = 0.1$. (b) Evolution of the same viscous dissipation rescaled with the total initial energy of the system.

For more insight into the viscous dissipation, we can rewrite it in terms of enstrophy $|\boldsymbol{\omega}|^2$, where $\boldsymbol{\omega} = \nabla \times \mathbf{u}$ is the vorticity and $|\boldsymbol{\omega}|^2 = |\nabla \times \mathbf{u}|^2 = |\nabla \mathbf{u}|^2$. The enstrophy can be decomposed into the vertical ($|\boldsymbol{\omega}_z|^2$) and a horizontal ($|\boldsymbol{\omega}_h|^2$) enstrophy, where $\boldsymbol{\omega}_z$ and $\boldsymbol{\omega}_h$ are the vertical and horizontal components of the vorticity.

Figure 13a shows the evolution of the horizontal, vertical and total enstrophy for a wave amplitude of $A = 0.5$. The horizontal enstrophy clearly dominates the total enstrophy, so the viscous dissipation can be rewritten as:

$$\begin{aligned} \varepsilon = \frac{1}{Re} < |\nabla \mathbf{u}|^2 > &= \frac{1}{Re} < |\boldsymbol{\omega}|^2 > \\ &= \frac{1}{Re} < |\boldsymbol{\omega}_h|^2 + |\boldsymbol{\omega}_z|^2 > \\ &\sim \frac{1}{Re} < |\boldsymbol{\omega}_h|^2 > . \end{aligned} \tag{22}$$

Garaud et al. [11] have shown that horizontal enstrophy is strong in the shallow layer-like laminar regions that can be seen on the vertical snapshots with and without the wave (figures 5, 6, 10). These layers have strong vertical shear that dominate the viscous dissipation. Adding the wave enhances the motion of the $k_z \neq 0$ modes of the primary instability, intensifying these layers.

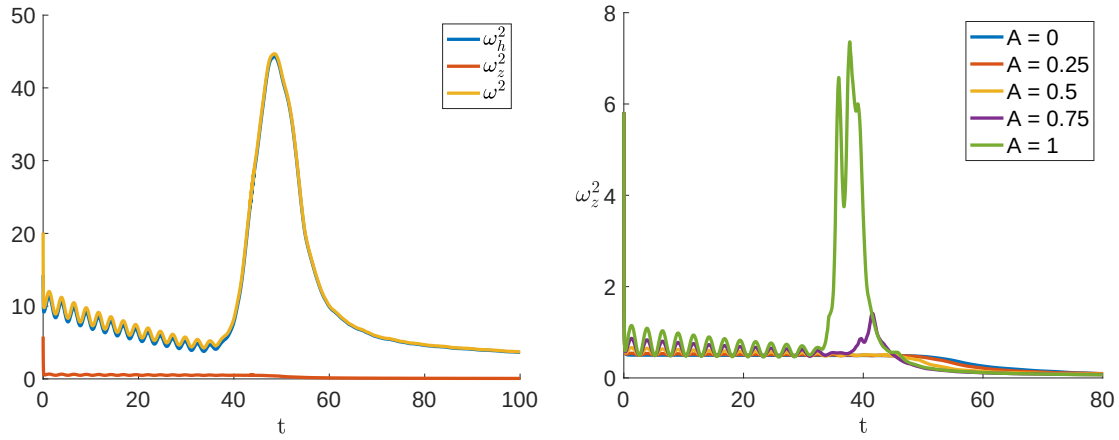


(a) (b)

Figure 13: (a) Evolution of the horizontal, vertical and total enstrophy for a wave amplitude of $A = 0.5$ and the parameters $Re = Pe = 5000$ and $Fr = 0.1$. (b) Evolution of the vertical enstrophy for different wave amplitudes and for the parameters $Re = Pe = 5000$ and $Fr = 0.1$.

### 5.3.2 Buoyancy dissipation

The buoyancy dissipation is defined as:

$$\chi = \frac{1}{Fr^2 Pe} < |\nabla b|^2 > . \tag{23}$$

Similarly to the viscous dissipation, figure 14a shows that the buoyancy dissipation for the case without the wave peaks after the onset of the instability (around $t \approx 60$). It then remains high over about 20 time units (from $t = 60$ to $t = 80$ approximately) before fading. When the wave amplitude is increased, the peak occurs earlier and becomes narrower. However, unlike the viscous dissipation case, the increased initial total energy due to the wave does not fully explain the more intense peak in buoyancy dissipation. Figure 14b shows the buoyancy dissipation rescaled with $E_0$, the peaks are closer to each other but the maximum dissipation reached is still higher for the higher wave amplitudes, particularly for the amplitudes $A = 0.75$ and $A = 1$.

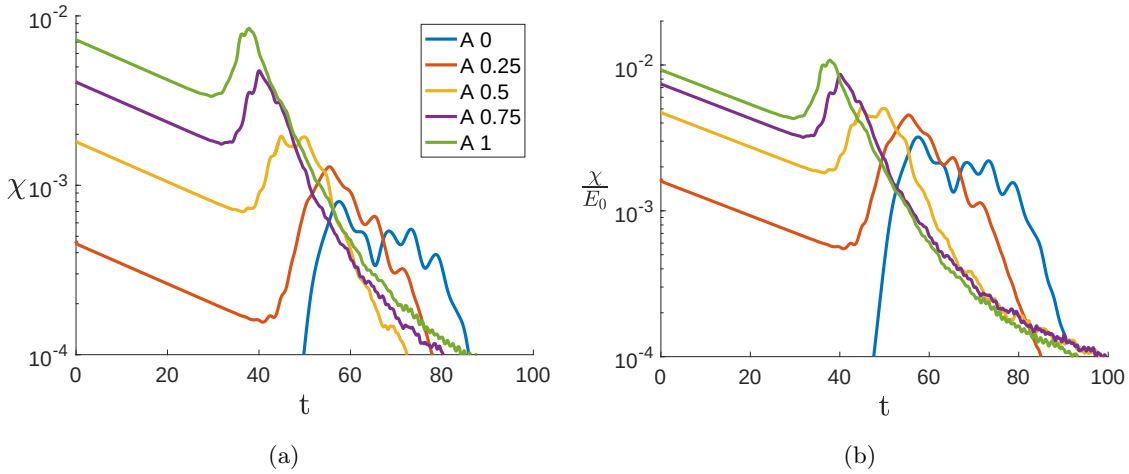


(a) (b)

Figure 14: (a) Evolution of the buoyancy dissipation for different wave amplitudes, for the parameters $Re = Pe = 5000$, $Fr = 0.1$. (b) Evolution of the buoyancy dissipation rescaled with the total initial energy of the system.

The buoyancy dissipation cannot be explained by the shallow laminar layers discussed previously, as horizontal flows do not cause buoyancy transport. The added microscopic diffusion at the interfaces between the shallow layers at different temperatures are probably not enough to explain the increase in buoyancy dissipation either. Instead, we can turn to the vertical enstrophy, shown in figure 13b for different wave amplitudes. For the two highest wave amplitudes tested ($A = 0.75$ and $A = 1$), a peak in vertical enstrophy appears around $t = 40$, or more specifically, it appears around the time the buoyancy dissipation is at its maximum. Garaud et al. [11] have shown that the vertical enstrophy $\omega_z^2$ is a good diagnosis for the turbulent patches in the flow. Here, the snapshots for the highest wave amplitudes seen in figure 15b show small scale secondary Kelvin Helmotlz instabilities that correspond to turbulent patches. To attribute these KH instabilities to the high buoyancy dissipation, we look at spatial joint probability distribution functions (pdf) of the vertical enstrophy and of the buoyancy dissipation, at a fixed time. Figure 16 shows pdfs with the logarithm of the vertical enstrophy on the $x$ axis and the logarithm of the buoyancy dissipation on the $y$ axis. Figure 16a shows these pdfs for the simulation with wave amplitudes $A = 0.25$ (top panel) and $A = 1$ (bottom panel) at an time close to their respective buoyancy dissipation maxima. These wave amplitudes were chosen because of the different characteristics they exhibit: the case for $A = 0.25$ barely has any secondary KH instabilities (see figure 15a), while we see many of them around the peak in buoyancy dissipation for the case $A = 1$ (see figure 15b). To better capture the difference between these two cases, figure 16b shows the difference between the two pdfs (case $A = 1$ minus case $A = 0.25$). It shows that the positive region (yellow patch) where there is a lot of buoyancy dissipation for the case $A = 1$ is obtained for higher vertical enstrophy than the negative region (dark blue patch), that corresponds to the region where more of the buoyancy dissipation occurs for the case $A = 0.25$. We have previously attributed a high vertical enstrophy to secondary KH instabilities thanks to [11], and we have now attributed regions of high vertical enstrophy to enhanced buoyancy dissipation, we can therefore attribute the enhanced buoyancy dissipation to the secondary

KH instabilities.

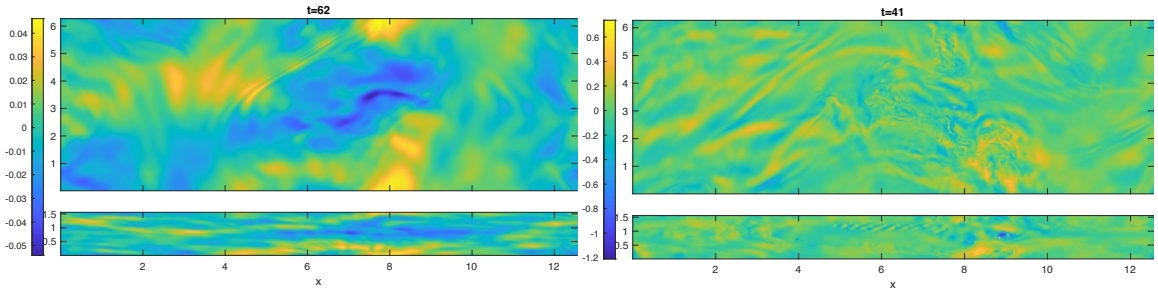


(a) (b)

Figure 15: Snapshots of the vertical velocity $w$ for (a) $A = 0.25$ at time $t = 62$ and (b) $A = 1$ at time $t = 41$ . Each panel shows two slices through the computational domain: an $xy$ slice at $z = 0$ for the top panels and an $xz$ slice at $y = 0$ for the bottom panels, for the simulations with parameters $Re = Pe = 5000$ and $Fr = 0.1$.

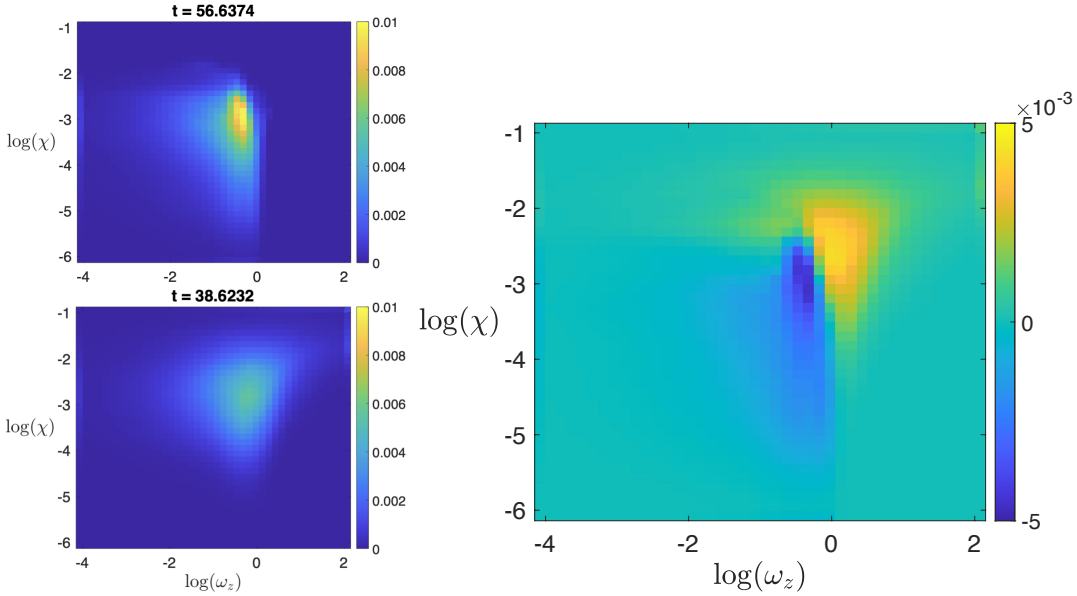


(a) (b)

Figure 16: (a) Joint pdf of the vertical enstrophy ($x$ axis) and the buoyancy dissipation ($y$ axis) for a wave amplitude $A = 0.25$ for the top panel and $A = 1$ for the bottom panel at a time close to their respective maximum instantaneous buoyancy dissipation. (b) Difference between these two pdfs ($A = 1 - A = 0.25$).

# 6 Conclusion and Future Works

The stability of a horizontal Kolmogorov flow at low Froude number has been investigated, continuing the work of Garaud et al. [10]. In particular, an asymptotic analysis in the limit of low Froude number is carried out to explain the generation of small vertical scales from the primary instability. The horizontal equations are the same as the 2D horizontal shear equations, decoupled from the vertical. The mode structure is therefore the 2D mode in the horizontal, and a vertical structure given by $e^{ik_z z}$, with no constraint on $k_z$. The lack of constraint on $k_z$ explains why many $k_z \neq 0$ can grow. At lowest order, the growth rate for the vertical modes is therefore the same as that of the unstratified flow. The saturation mechanism differs depending on the Reynolds number: for lower Reynolds number (around $Re = 5000$), viscosity limits the size of the vertical scales, while at higher Reynolds number (around $Re = 10000$), secondary Kelvin-Helmholtz instabilities appear between the shallow layers.

To study a slightly less idealized problem, a gravity wave propagating in the $y$ and $z$ directions was then added to the horizontal shear. The stability of this new system was investigated and it was shown that the primary instability is not drastically affected by the addition of the wave. However, adding the wave and increasing its amplitude promotes the development of secondary KH instabilities. It also has a significant impact on the viscous and buoyancy dissipations. These dissipation events become shorter and more intense as the wave amplitude is increased. We have established a direct link between the presence of secondary KH instabilities and the significant enhancement of buoyancy dissipation. However, a criterion for the apparition of the secondary KH instabilities is still lacking. The well established criterion on the Richardson number for the vertical shear instability $Ri < 1/4$ ([17], [12]) does not capture the apparition of the instability in this case. Indeed, we have identified zones in the domain where the Richardson number is negative but no KH instabilities appear. These low Richardson zones might be too transient or local to trigger the instability.

The effect of other parameters also remains to be investigated. Preliminary results show that the Froude and Reynolds numbers have an impact on the apparition of KH instabilities and on dissipations. Figure 17 shows the buoyancy dissipation for two different Froude numbers (figure 17a) and for two different Reynolds number (figure 17b). Increasing either of these parameters also seems to increase the intensity of the peak of buoyancy dissipation, although with different dynamics. The direction of propagation of the wave should also be investigated, as the choice made here ($k_y = 2$, $k_z = 8$) could have impacted the general behavior described.

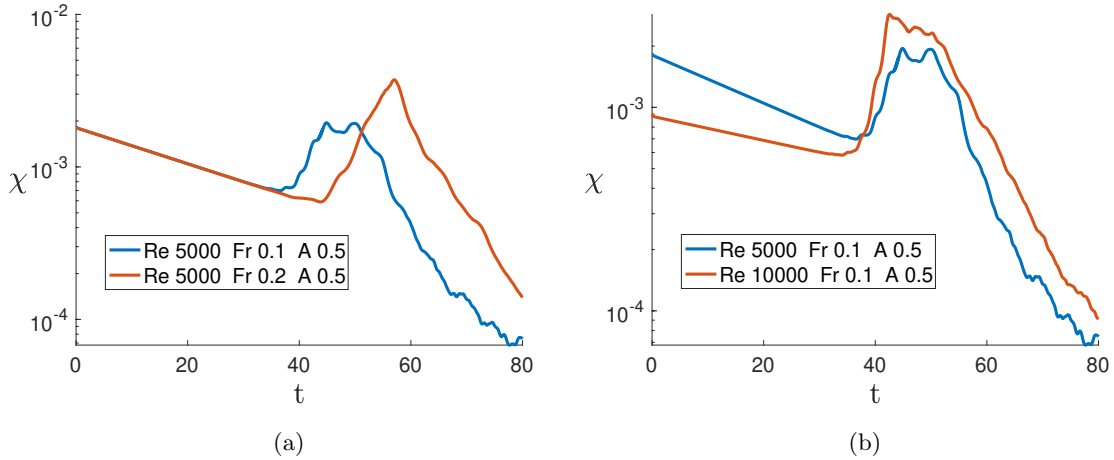


Figure 17: (a) Evolution of the buoyancy dissipation for two different Froude numbers $Fr = 0.1$ and $Fr = 0.2$, and for the parameters $Re = 5000$ and a wave amplitude of $= 0.5$. (b) Evolution of the buoyancy dissipation for two different Reynolds number $Re = 5000$, and $Re = 10000$, and for $Fr = 0.1$ and a wave amplitude of $A = 0.5$.

## 7 Acknowledgements

I would like to thank my supervisors Pascale Garaud and Colm-cille Caulfield for their guidance and enthusiasm throughout this summer. It was a pleasure working with both of you. I also want to thank the directors, Pascale Garaud and David Goluskin, as well as the staff and visitors, for their dedication to this program.

Finally, I would like to thank the fellows for making this summer such a fun and unforgettable experience.

## References

[1] N. J. Balmforth and Y.-N. Young, *Stratified kolmogorov flow*, Journal of Fluid Mechanics, 450 (2002), pp. 131–167.

[2] S. Basak and S. Sarkar, *Dynamics of a stratified shear layer with horizontal shear*, Journal of Fluid Mechanics, 568 (2006), pp. 19–54.

[3] G. Brethouwer, P. Billant, E. Lindborg, and J.-M. Chomaz, *Scaling analysis and simulation of strongly stratified turbulent flows*, Journal of Fluid Mechanics, 585 (2007), pp. 343–368.

[4] C. Caulfield, *Layering, instabilities, and mixing in turbulent stratified flows*, Annual Review of Fluid Mechanics, 53 (2021), pp. 113–145.

[5] G. P. Chini, G. Michel, K. Julien, C. B. Rocha, and C.-c. P. Caulfield, *Exploiting self-organized criticality in strongly stratified turbulence*, Journal of Fluid Mechanics, 933 (2022), p. A22.

[6] L. Cope, P. Garaud, and C.-c. P. Caulfield, *The dynamics of stratified horizontal shear flows at low péclet number*, Journal of Fluid Mechanics, 903 (2020), p. A1.

[7] A. Deloncle, J.-M. Chomaz, and P. Billant, *Three-dimensional stability of a horizontally sheared flow in a stably stratified fluid*, Journal of Fluid Mechanics, 570 (2007), pp. 297–305.

[8] G. Facchini, B. Favier, P. Le Gal, M. Wang, and M. Le Bars, *The linear instability of the stratified plane couette flow*, Journal of Fluid Mechanics, 853 (2018), pp. 205–234.

[9] P. Garaud, *Horizontal shear instabilities at low prandtl number*, The Astrophysical Journal, 901 (2020), p. 146.

[10] P. Garaud, D. Buhl, J. Johnstone, A. Tulekeyev, and N. van Duker, *Transition to turbulence in horizontally-sheared stratified kolmogorov flows*, Manuscript submitted for publication to the Journal of Fluid Mechanics, (2025).

[11] P. Garaud, G. P. Chini, L. Cope, K. Shah, and C.-c. P. Caulfield, *Numerical validation of scaling laws for stratified turbulence*, Journal of Fluid Mechanics, 991 (2024), p. R1.

[12] L. N. Howard, *Note on a paper of john w. miles*, Journal of Fluid Mechanics, 10 (1961), pp. 509–512.

[13] C. J. Howland, J. R. Taylor, and C. Caulfield, *Shear-induced breaking of internal gravity waves*, Journal of fluid mechanics, 921 (2021), p. A24.

[14] S. F. Lewin and P. C. Colm-cille, *Evidence for layered anisotropic stratified turbulence in a freely evolving horizontal shear flow*, Journal of Fluid Mechanics, 983 (2024), p. A20.

[15] D. K. Lilly, *Stratified turbulence and the mesoscale variability of the atmosphere*, Journal of Atmospheric Sciences, 40 (1983), pp. 749–761.

[16] J. A. MacKinnon, Z. Zhao, C. B. Whalen, A. F. Waterhouse, D. S. Trossman, O. M. Sun, L. C. S. Laurent, H. L. Simmons, K. Polzin, R. Pinkel, et al., *Climate process team on internal wave–driven ocean mixing*, Bulletin of the American Meteorological Society, 98 (2017), pp. 2429–2454.

[17] J. W. Miles, *On the stability of heterogeneous shear flows*, Journal of fluid Mechanics, 10 (1961), pp. 496–508.

[18] A. Traxler, S. Stellmach, P. Garaud, T. Radko, and N. Brummell, *Dynamics of fingering convection. part 1 small-scale fluxes and large-scale instabilities*, Journal of fluid mechanics, 677 (2011), pp. 530–553.

# Towards a Stability Analysis of Two Interacting Gravity Currents in a Rotating Environment.

Edoardo Bellincioni

August 20, 2025

***To the reader***

*On top of providing a summary of the research project conducted during the 2025 GFD Program, the intent of this report is to help a student who, like the author at the beginning of the project, is not familiar with the physics of gravity currents and rotating flows, as well as with the mathematical tricks and techniques for cylindrical coordinates and linear stability analysis. To the expert applied mathematician, I apologise for the possible pedantry. To the expert experimentalist, I remark that the main aim of this project was the analytical model and the instabilities, and experiments were only conducted in the last week of the project.*

## 1 Introduction

In the context of the interaction between multiple fluids in a rotating environment, one of the classical, simple, yet powerful models is the one proposed by Normann Phillips in 1951 [7], which was later referred to as the"two-layer model". There, a system of two vertically stacked fluids is considered, with the bottom and lid being rigid. The fluids have two different densities, the top one being lightest. The system is rotating at a fixed angular velocity. Quasi-geostrophy is assumed, and the model allows study of the (interface) perturbations around a stable flow configuration. Due to its simplicity, this model proved extremely powerful in modelling a variety of geophysical flows, both in the atmosphere and in the hydrosphere. In different formulations, the constraints on the bottom and top boundaries are released, allowing for complex interactions with the bottom topography and the presence of free-surface effects (see Vallis [9]).

The versatility of Phillips' model is further corroborated by its application to geophysical systems which are, at first glance, only loosely connected with the original setup. An example is the work of Griffiths and Linden [5], where the authors study the stability of an isolated eddy in a rotating environment, and qualitatively (*sic*) compare their results with the prediction of a later version of the Phillips model [8].

There are, however, many situations in which a two-layer model is not sufficient to capture the complexity of the system. An example is the Antarctic Circumpolar Current (ACC), which is composed of multiple layers of waters with different salinity/temperature/ density, stacked on top of each other, see figure 1. The modelisation of systems of this kind brought the development of a three-layer model, first proposed by Davey [3]. Literature in

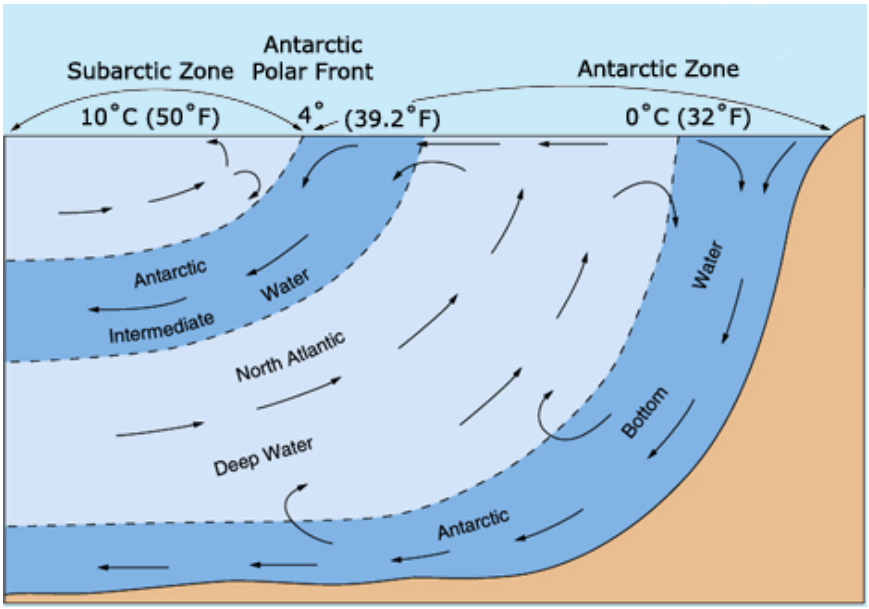


Figure 1: Schematic of a meridional cross-section of the Antarctic Circumpolar Current (North left, South right), showing the different layers of water masses with different densities. The continental mass is sketched on the right in brown. From WHOI - Dive and Discover.

this field is not as abundant as for the two-layer configuration, but a number of contributions studied the setup in different configurations: stratified; with sloping bottom; with varying thickness of the layers; with a linear stability analysis; providing a (predictive) model. The most recent work is that of Lobo et al. [6], which also provides a good overview of the existing literature on the topic.

Another important set of physical situations in which multiple fluids interact is that of river currents (floating) on top of an ocean. An example is the Western Maine Coastal Current (WMCC), where multiple sources of fresh water (from rivers and freshwater bays) flow into the Atlantic Ocean, and, under the effect of the Coriolis force, are deflected to the right, thus forming buoyant currents flowing southwards along the coast of Maine. Churchill et al. [2] report measurements of velocity and CTD (Conductivity, Temperature and Depth) in transects off the coast of Maine, showing the presence of multiple layers of water masses with different densities and velocities, see figure 2.

As for multiple stacked fluids (as the ACC), a qualitative understanding of the fundamental dynamics of this system can be obtained by studying the simplified case of a single current on top of a large rotating reservoir. This behaviour, that of a *single* floating current, has been extensively investigated, in different configurations, for example by Griffiths et al. [4] and Griffiths and Linden [5]. The first considered a current with two free lateral interfaces, while the second considered the current wall-bounded at $y = 0$ (experiments were conducted in a rotating table with the current being bound by the axis of the table). Both of these works elaborate on the baroclinic instabilities in the system.

More recently, Cenedese et al. [1] studied the interactions between *two* floating currents

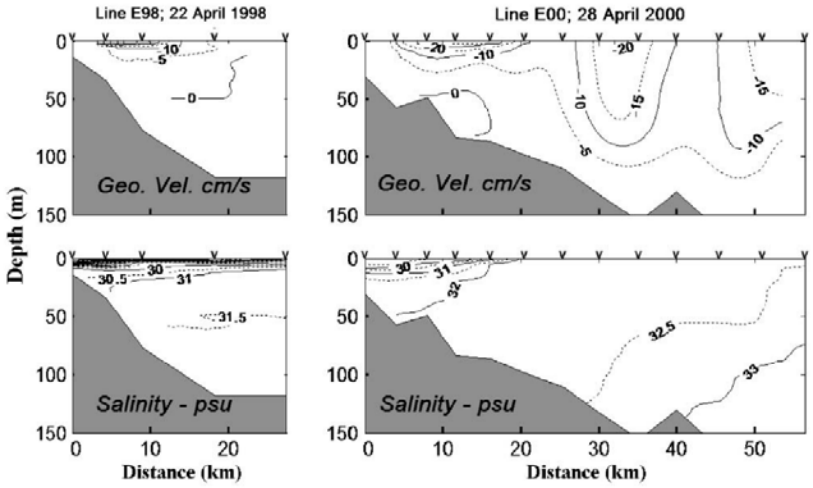


Figure 2: Two zonal transects off the coast of Maine measuring geostrophic velocity (top) and salinity (bottom). Especially in the top right figure, two southwards currents can be clearly identified by the peaking negative values in the contours. (Adapted from figure 6 of Churchill et al. [2])

on top of a rotating reservoir, in a laboratory setting. By means of an analytical model and laboratory experiments, the authors investigated the geostrophic adjustment of two floating currents on top of a denser fluid. They nondimensionalised their findings with the Rossby radius of deformation (ratio between a typical velocity scale and the Coriolis parameter) and Burger number (ratio between the Rossby radius and an intrinsic lengthscale of the system). The authors report that their laboratory experiments indicate that the solutions found with the analytical model are unstable, but for a sufficiently long average in time, the experimental results should align with the model prediction.

The focus of the aforementioned work was on reproducing in a laboratory setting a system that would be similar, at least qualitatively, to the WMCC. The authors, hence, expressed the equations of motion in a cartesian coordinate system, which is the most suited when working with an idealised straight coastline. This choice, however, makes the analytical treatment of the instabilities that occur at the fronts more cumbersome, if not impossible. Hence, it is the focus of this work to express the equations in a cylindrical coordinate system, and work towards the linear stability of the fronts.

This report is structured as follows. In section 2 we propose a model for the cross-sectional profiles of the currents in steady state. In section 3 we report on the experimental results. In section 4, we sketch an analysis of the linear stability of the one-current problem. Lastly, in section 5, we draw conclusions from this work and elaborate on the outlook for future, further developments.

## 2 Cross-sectional Depth Profile in Steady State

In this section we will derive an expression for the velocity and interfacial depth cross-sectional profiles of two fluids rotating gravity currents in steady state. Panel 3a shows our system's configuration at $t = 0$: two concentric regions with rectangular cross section contain two lighter fluids, above a denser fluid, under a rigid lid, rotating in solid body rotation with the fluid beneath it. The densities of the fluids are $\rho_i$ ($i \in 1, 2, 3$) with $\rho_1 < \rho_2 < \rho_3$. The initial cross section of the light fluids is $[0, L_i] \times [0, H_i]$. Being more buoyant than the environment, the two fluids spread radially when the radial constraints are released (panel 3b), until the Coriolis effect balances the gravitational spreading, and the fluids adjust to a depth $h_i = h_i(r)$ and a radial extent of $r = l_2$ and $r = l_3$.

The derivation of the equations of motion will be done under the shallow water approximation of the Navier-Stokes equations (SWE), in a rotating, cylindrical-coordinates frame of reference $(\hat{r}, \hat{\theta}, \hat{z})$. We refer the reader to specialised textbooks (e.g., Vallis [9]) for a detailed derivation of the SWE, but we briefly summarise hereafter the main assumptions:

- the typical horizontal lengthscales are much larger than the vertical ones, $L_{\text{hor}} \gg L_{\text{ver}}$
- consequently, the typical horizontal velocity scales are much larger than the vertical ones, $u_{\text{hor}} \gg u_{\text{ver}}$
- the equations are depth integrated, hence
  - there is no $\hat{z}$ (vertical) dependency in the flow
  - there is no vertical velocity $u_z$ (in agreement with $u_{\text{hor}} \gg u_{\text{ver}}$)
- the radial gradients of the interfaces are small, $\partial_r h_i \ll 1$

As we — for now — intend to model the adjusted, steady, stable state, we assume

- no time evolution, $\partial_t \cdot = 0$
- no azimuthal dependency (no azimuthal structures), $\partial_\theta \cdot = 0$
- no radial motions, $u_r = 0$

Under these conditions, the shallow water equations read

$$\partial_t \mathbf{u} + (\mathbf{u} \cdot \boldsymbol{\nabla})\mathbf{u} + \mathbf{f} \times \mathbf{u} = -\frac{\boldsymbol{\nabla} p}{\rho} \ , \tag{1}$$

where $\mathbf{u}$ is the flow velocity, $\mathbf{f}$ is the Coriolis parameter, and the pressure term on the RHS is the effect of buoyancy (i.e., gravity), which is yet to be determined (with $\rho$ a reference density). To understand how the pressure term in the SWE looks when the two floating currents are considered, we shall start by taking as a reference pressure the pressure at a

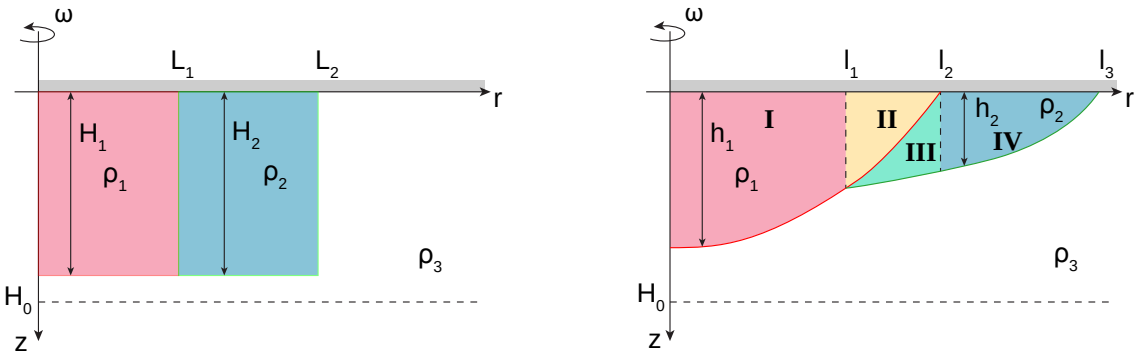


(a) Initial state

(b) Adjusted state

Figure 3: Radial adjustment of two floating currents in a rotating environment. The fluids are initially kept in rectangular cross sections (left panel), and, after the radial constrains are released, they adjust until they reach an equilibrium profile (right panel). The top is considered a rigid lid. $H_0$ indicates the depth of a reference pressure in the fluid. $\rho_i$ are the densities of the fluids. $H_i$ are the initial depths, $h_i(r)$ the adjusted depths. $L_i$ are the initial radial extents, and $l_i$ the adjusted radial extents. In the right panel, four regions are identified, marked I to IV: I and II are in the first fluid, III and IV in the second fluid.

depth $H_0$, as in figure 3. Hence, the pressure will read [1]

$$p = \begin{cases} g\rho_1 z + c_1 & z \in [0, h_1] \\ g\rho_2 z + c_2 & z \in [h_1, h_1 + h_2] \\ g\rho_3 z + c_3 & z \in [h_1 + h_2, +\infty] \end{cases} \tag{2}$$

with "$z \in [\dots]$" we intend "for all the points $(r, \theta, z)$ such that $z \in [\dots]$", and $c_i$ are three constants.

We then impose the pressure at $z = H_0$ as $P_0$

$$p = P_0 = g\rho_3 H_0 + c_3 \implies c_3 = P_0 - \rho_3 g H_0 \ , \tag{3}$$

Then, we apply continuity of pressure at the interface between fluid 2 and 3

$$g\rho_2(h_1 + h_2) + c_2 = g\rho_3(h_1 + h_2) + c_3 \tag{4}$$

$$c_2 = g(h_1 + h_2)(\rho_3 - \rho_2) + c_3 = \tag{5}$$

$$= g(h_1 + h_2)(\rho_3 - \rho_2) + P_0 - \rho_3 g H \ . \tag{6}$$

We do similarly at the 1–3 interface

$$g\rho_1 h_1 + c_1 = g\rho_3 h_1 + c_3 = \tag{7}$$

$$= g\rho_3 h_1 + P_0 - \rho_3 g H_0 \tag{8}$$

$$c_1 = g[h_1(\rho_3 - \rho_1) - \rho_3 H_0] + P_0 \ . \tag{9}$$

[1] Note that throughout this derivation we define the heights $h_i$ as the *thicknesses* of the layers, and not as the depth of the interfaces. The depths of the interfaces can trivially be obtained summing the $h_i$ of the layers.

Thus, we can write the pressure everywhere

$$p = \begin{cases} g[\rho_1(z-h_1)+\rho_2(-h_2)+\rho_3(h_1+h_2-H_0)]+P_0 & z\in[0,h_1] \\ g[\rho_2(z-(h_1+h_2))+\rho_3(h_1+h_2-H_0)]+P_0 & z\in[h_1,h_1+h_2] \\ g[\rho_3(z-H_0)]+P_0 & z\in[h_1+h_2,+\infty] \end{cases} \tag{10}$$

We then calculate the gradient of the pressure, $\boldsymbol{\nabla} p$

$$\boldsymbol{\nabla} p = \begin{cases} g[\rho_1(\hat{z}-\boldsymbol{\nabla} h_1)+\rho_2(-\boldsymbol{\nabla} h_2)+\rho_3\boldsymbol{\nabla}(h_1+h_2)] & z\in[0,h_1] \\ g[\rho_2(\hat{z}-\boldsymbol{\nabla}(h_1+h_2))+\rho_3\boldsymbol{\nabla}(h_1+h_2)] & z\in[h_1,h_1+h_2] \\ g\rho_3\hat{z} & z\in[h_1+h_2,+\infty] \end{cases} \tag{11}$$

If we consider as the reference density the density of the bottom fluid $\rho_3$, we can re-arrange equation 11 in term of the reduced gravity $g_i' = g\frac{\rho_3-\rho_i}{\rho_3}$. We also neglect the $\hat{z}$ direction of the pressure gradient, because it will not drive motions in the horizontal ($\boldsymbol{\nabla} \equiv \boldsymbol{\nabla}_{\text{hor}}$)

$$\frac{\boldsymbol{\nabla} p}{\rho_3} = \begin{cases} g_1'\boldsymbol{\nabla} h_1 + g_2'\boldsymbol{\nabla} h_2 & z\in[0,h_1] \\ g_2'\boldsymbol{\nabla}(h_1+h_2) & z\in[h_1,h_1+h_2] \\ 0 & z\in[h_1+h_2,+\infty] \end{cases} \tag{12}$$

Finally, the momentum equations will read

$$\partial_t\mathbf{u} + (\mathbf{u}\cdot\boldsymbol{\nabla})\mathbf{u} + \mathbf{f}\times\mathbf{u} = \begin{cases} -g_1'\boldsymbol{\nabla} h_1 - g_2'\boldsymbol{\nabla} h_2 & z\in[0,h_1] \\ -g_2'\boldsymbol{\nabla}(h_1+h_2) & z\in[h_1,h_1+h_2] \\ 0 & z\in[h_1+h_2,+\infty] \end{cases} \tag{13}$$

### 2.1 Continuity equation

The continuity equation is trivially the continuity equation in shallow water approximation, defined in each of the two layers

$$\partial_t h_i + \boldsymbol{\nabla}\cdot(h_i\mathbf{u}_i) = 0 \quad \text{for } i\in 1,2\ . \tag{14}$$

### 2.2 Conservation of potential vorticity

For later calculations, we will use the conservation of (Rossby) potential vorticity (PV). It is instructive to prove that our flow conserves PV. For simplicity, we here (only here) assume WLOG that $g_1' = g_2' = 1$. We call the flow's intrinsic vorticity $\boldsymbol{\xi} = \boldsymbol{\nabla}\times\mathbf{u}$. We start by stating this equality

$$(\boldsymbol{\nabla}\times\mathbf{u})\times\mathbf{u} = \boldsymbol{\xi}\times\mathbf{u} = (\mathbf{u}\cdot\boldsymbol{\nabla})\mathbf{u} - \frac{1}{2}\boldsymbol{\nabla}\left(u^2\right)\ , \tag{15}$$

which allows us to re-write the momentum equation

$$\partial_t\mathbf{u} + (\mathbf{u}\cdot\boldsymbol{\nabla})\mathbf{u} + \mathbf{f}\times\mathbf{u} = -\boldsymbol{\nabla}\left(h_1+h_1\right) \tag{16}$$

as

$$\partial_t \mathbf{u} + (\boldsymbol{\xi} + \mathbf{f}) \times \mathbf{u} = -\boldsymbol{\nabla} \left( h_1 + h_1 + \frac{u^2}{2} \right) \ . \tag{17}$$

We take the curl of this equation, to obtain

$$\partial_t \boldsymbol{\xi} + \boldsymbol{\nabla} \times [(\boldsymbol{\xi} + \mathbf{f}) \times \mathbf{u}] = 0 \ , \tag{18}$$

as the curl of a gradient is zero.

We then apply the following nabla identity

$$\boldsymbol{\nabla} \times (\boldsymbol{A} \times \boldsymbol{B}) = \boldsymbol{A} \boldsymbol{\nabla} \cdot \boldsymbol{B} + (\boldsymbol{B} \cdot \boldsymbol{\nabla}) \, \boldsymbol{A} + \boldsymbol{B} \boldsymbol{\nabla} \cdot \boldsymbol{A} - (\boldsymbol{A} \cdot \boldsymbol{\nabla}) \, \boldsymbol{B} \tag{19}$$

to the second term of equation 18, to obtain

$$\boldsymbol{\nabla} \times [(\boldsymbol{\xi} + \mathbf{f}) \times \mathbf{u}] = (\boldsymbol{\xi} + \mathbf{f})(\boldsymbol{\nabla} \cdot \mathbf{u}) + (\mathbf{u} \cdot \boldsymbol{\nabla})(\boldsymbol{\xi} + \mathbf{f}) + \cancel{\mathbf{u} \boldsymbol{\nabla} (\boldsymbol{\xi} + \mathbf{f})} - \cancel{((\boldsymbol{\xi} + \mathbf{f}) \cdot \boldsymbol{\nabla}) \mathbf{u}} \ , \tag{20}$$

where: the last term is zero as the $\boldsymbol{\nabla}$ operator acts on the $(r, \theta)$ plane, while both $\boldsymbol{\xi}$ and $\mathbf{f}$ are oriented along $\hat{z}$; and the second to last term is zero as $\mathbf{u}$ is only in the $(r, \theta)$ plane, while $\boldsymbol{\nabla}(\boldsymbol{\xi} + \mathbf{f})$ is only along $\hat{z}$.

Equation 20 allows us to re-write equation 18 as

$$\partial_t (\boldsymbol{\xi} + \mathbf{f}) + (\mathbf{u} \cdot \boldsymbol{\nabla})(\boldsymbol{\xi} + \mathbf{f}) = -(\boldsymbol{\xi} + \mathbf{f})(\boldsymbol{\nabla} \cdot \mathbf{u}) \ . \tag{21}$$

We recognise the advective derivative in the terms on the LHS, so

$$D_t (\boldsymbol{\xi} + \mathbf{f}) = -(\boldsymbol{\xi} + \mathbf{f})(\boldsymbol{\nabla} \cdot \mathbf{u}) \ . \tag{22}$$

We now expand and rewrite the continuity equation

$$\partial_t h_i + \boldsymbol{\nabla} \cdot (h_i \mathbf{u}) = 0 \tag{23}$$

to

$$\partial_t h_i + \mathbf{u} \cdot \boldsymbol{\nabla} h_i + h_i (\boldsymbol{\nabla} \cdot \mathbf{u}) = 0 \tag{24}$$

$$\boldsymbol{\nabla} \cdot \mathbf{u} = -\frac{\partial_t h - \mathbf{u} \cdot \boldsymbol{\nabla} h}{h} \ , \tag{25}$$

hence

$$D_t (\boldsymbol{\xi} + \mathbf{f}) = +(\boldsymbol{\xi} + \mathbf{f}) \frac{\overbrace{\partial_t h - \mathbf{u} \cdot \boldsymbol{\nabla} h}^{D_t h}}{h} \ . \tag{26}$$

Multiplying by $1/h$, we get

$$\frac{1}{h} D_t (\boldsymbol{\xi} + \mathbf{f}) = \frac{1}{h^2} (\boldsymbol{\xi} + \mathbf{f}) D_t h \ , \tag{27}$$

which leads to

$$D_t \left( \frac{\boldsymbol{\xi} + \mathbf{f}}{h} \right) = 0 \ , \tag{28}$$

which is the conservation of potential vorticity in the shallow water approximation. We will apply this conservation law by saying that the initial PV $\mathbf{f}/H$ equals to the PV at time $t$.

### 2.3 Regions I and IV

To find the steady-state, cross-sectional profiles of the interfaces, we can divide the domain in four parts, I to IV, as in figure 3b. The first fluid is in region I ($r \in [0, l_1]$) and II ($r \in [l_1, l_2]$), while the second fluid is in region III ($r \in [l_1, l_2]$) and IV ($r \in [l_2, l_3]$). We start with the simplest regions, where there is no overlap between the two fluids, so regions I and IV. We note that, in these regions, the governing equations are the same as for the case with a single current.

The two governing equations are conservation of momentum and conservation of potential vorticity. Continuity is identically satisfied for our flows. The centripetal term arising from the rotating frame of reference requires particular attention, which we address in Appendix A. In the following derivations we will neglect this term.

In regions I and IV, under the assumption of steady state, the governing equations 13 read:

$$\text{mom} : (\mathbf{u} \cdot \boldsymbol{\nabla})\mathbf{u} + \mathbf{f} \times \mathbf{u} = -g' \boldsymbol{\nabla} h \tag{29}$$

$$\text{PV} : \frac{f}{H} = \frac{f + \xi}{h} \tag{30}$$

Where we wrote only the $\hat{z}$ component of the PV equation. We note that in these regions (I and IV), there will be no coupling term in the equation for fluid 1 coming from fluid 2, and vice versa.

We will address each term individually. First, let us write out the advective term in cylindrical coordinates under our assumptions

$$(\mathbf{u} \cdot \boldsymbol{\nabla})\mathbf{u} = \left( \cancel{-\frac{u_\theta^2}{r}}, \frac{u_r u_\theta}{r} \right) , \tag{31}$$

where the $\hat{r}$ term of the directional derivative is the centripetal term, which, as we said, we neglect (see Appendix A). For the Coriolis term, we have

$$\mathbf{f} \times \mathbf{u} = \begin{vmatrix} \hat{r} & \hat{\theta} & \hat{z} \\ 0 & 0 & f \\ u_r & u_\theta & 0 \end{vmatrix} = f(-u_\theta \hat{r} + u_r \hat{\theta}) . \tag{32}$$

Hence, in the $\hat{r}$ direction the momentum equation reads

$$f u_\theta = g' \partial_r h . \tag{33}$$

The expression for vorticity is

$$\xi = \frac{1}{r} \partial_r (r u_\theta) . \tag{34}$$

We now write out the PV conservation

$$\frac{f}{H} = \frac{f + \frac{1}{r}\partial_r (r u_\theta)}{h} , \tag{35}$$

which can be expanded to

$$\partial_r \left( r u_\theta \right) = f r \left( \frac{h}{H} - 1 \right) \tag{36}$$

$$\frac{u_\theta}{r} + \partial_r u_\theta = f \left( \frac{h}{H} - 1 \right) \ , \tag{37}$$

and using equation 33, and multiplying by $r^2$, we get

$$\frac{g'}{f} \frac{\partial_r h}{r} + \frac{g'}{f} \partial_r^2 h = f \left( \frac{h}{H} - 1 \right) \ , \tag{38}$$

which can be rewritten as a Bessel equation

$$r^2 \partial_r^2 h + r \partial_r h - r^2 \frac{f^2}{g'} \left( \frac{h}{H} - 1 \right) = 0 \ , \tag{39}$$

with general solution

$$h(r) = H + c_i I_0(\lambda r) + c_k K_0(\lambda r) \ , \tag{40}$$

where $I_0$ and $K_0$ are the zeroth-order modified Bessel function of the first and second kind, respectively, $\lambda = \frac{f}{\sqrt{g' H}} = \frac{1}{L_{\mathrm{Ro}}}$ (with $L_{\mathrm{Ro}}$ the Rossby radius of deformation), and $c_i$ and $c_k$ are two constants to be determined by boundary conditions.

## 2.4 Regions II and III

In regions II and III, the two height profiles will influence each other, and the general solution will be a combination of the two individual solutions.

Following a similar derivation as for regions I and IV, we can write the governing equations

$$\begin{cases} u_{\mathrm{II}} = \frac{g'_1}{f} h'_{\mathrm{II}} + \frac{g'_2}{f} h'_{\mathrm{III}} \\ \frac{u_{\mathrm{II}}}{r} + u'_{\mathrm{II}} = f \left( \frac{h_{\mathrm{II}}}{H_1} - 1 \right) \\ u_{\mathrm{II}} = \frac{g'_2}{f} \left( h'_{\mathrm{II}} + h'_{\mathrm{III}} \right) \\ \frac{u_{\mathrm{III}}}{r} + u'_{\mathrm{III}} = f \left( \frac{h_{\mathrm{III}}}{H_2} - 1 \right) \end{cases} \tag{41}$$

whose general solutions are

$$h_{\mathrm{II}}(r) = H_1 + c_1 I_0(\lambda_2 r) + c_2 K_0(\lambda_2 r) + c_3 I_0(\lambda_3 r) + c_4 K_0(\lambda_3 r) \tag{42}$$

$$h_{\mathrm{III}}(r) = H_2 + r_2 \left( c_1 I_0(\lambda_2 r) + c_2 K_0(\lambda_2 r) \right) + r_3 \left( c_3 I_0(\lambda_3 r) + c_4 K_0(\lambda_3 r) \right) \ . \tag{43}$$

Heuristically, the presence of $\lambda_2$ and $\lambda_3$ can be interpreted as the effect of the interaction between the two fluids, and the factors $r_2$ and $r_3$ as a rotation in the plane of the solutions. The parameters $\lambda_2$ and $\lambda_3$ are determined by the two positive solutions of a quartic equation

$$\lambda^4 - \frac{f^2 (H_2 g'_2 + g'_1 H_1)}{g'_2 H_1 H_2 (g'_1 - g'_2)} \lambda^2 + \frac{f^4}{g'_2 H_1 H_2 (g'_1 - g'_2)} = 0 \ , \tag{44}$$

and $r_2$ and $r_3$ can be obtained from

$$r_{2,3} = \frac{H_2}{H_1} \ - \ \frac{H_2 (g_1 - g_2)}{f^2} \lambda_{2,3}^2 \ . \tag{45}$$

These expressions were obtained with the aid of a symbolic calculus software (Maple).

## 2.5 Boundary conditions

We then have the functions for the fluids' profiles in the four regions,

$$h_{\mathrm{I}}(r) = H_1 + c_1 I_0(\lambda_1 r) + c_2 K_0(\lambda_1 r) \tag{46}$$
$$h_{\mathrm{II}}(r) = H_1 + c_3 I_0(\lambda_2 r) + c_4 K_0(\lambda_2 r) + c_5 I_0(\lambda_3 r) + c_6 K_0(\lambda_3 r) \tag{47}$$
$$h_{\mathrm{III}}(r) = H_2 + r_2 \left(c_3 I_0(\lambda_2 r) + c_4 K_0(\lambda_2 r)\right) + r_3 \left(c_5 I_0(\lambda_3 r) + c_6 K_0(\lambda_3 r)\right) \tag{48}$$
$$h_{\mathrm{IV}}(r) = H_2 + c_7 I_0(\lambda_4 r) + c_8 K_0(\lambda_4 r) \tag{49}$$

We have 8 unknown constants $(c_1, c_2, c_3, c_4, c_5, c_6, c_7, c_8)$ and 3 unknown interface position $(l_1, l_2, l_3)$, hence we seek for 11 boundary conditions. Ten of which are

1. finite velocity at $r = 0$
2. continuity of the velocity in the first fluid at $r = l_1$, $u_{\mathrm{I}}(l_1) = u_{\mathrm{II}}(l_1)$
3. continuity of the height in the first fluid at $r = l_1$, $h_{\mathrm{I}}(l_1) = h_{\mathrm{II}}(l_1)$
4. vanishing of the first fluid profile at $r = l_2$, $h_{\mathrm{II}}(l_2) = 0$,
5. vanishing of the second fluid profile at $r = l_1$, $h_{\mathrm{III}}(l_1) = 0$,
6. continuity of the velocity in the second fluid at $r = l_2$, $u_{\mathrm{III}}(l_2) = u_{\mathrm{IV}}(l_2)$
7. continuity of the height in the second fluid at $r = l_2$, $h_{\mathrm{III}}(l_2) = h_{\mathrm{IV}}(l_2)$
8. vanishing of the second fluid profile at $r = l_3$, $h_{\mathrm{IV}}(l_3) = 0$
9. conservation of volume of the first fluid, $\int_0^{l_1} r h_{\mathrm{I}}(r) dr + \int_{l_1}^{l_2} r h_{\mathrm{II}}(r) dr = \frac{L_1^2 H_1}{2}$,
10. conservation of volume of the second fluid, $\int_{l_1}^{l_2} r h_{\mathrm{III}}(r) dr + \int_{l_2}^{l_3} r h_{\mathrm{IV}}(r) dr = \frac{(L_2^2 - L_1^2) H_2}{2}$,

To obtain the eleventh, we need to consider a characteristic solution that follows the flow during the initial radial adjustment. The details of this derivations are proposed in Appendix B. In short, for an element of fluid that starts at radial position $R_0$ and, after adjustment, reaches position $R$, the adjusted azimuthal velocity reads

$$U = f \frac{R^2 - R_0^2}{2R} \ . \tag{50}$$

We choose to apply it to a point of which we know the initial and adjusted position, namely at the most bottom-left point of the second fluid, which starts at radius $r = L_1$ and zero velocity, and hence gets adjusted at radius $r = l_1$ at a velocity

$$u_{\mathrm{II}}(l_1) = f \frac{l_1^2 - L_1^2}{2 l_1} \ , \tag{51}$$

which constitutes our eleventh boundary condition.

## 2.6 Relevant nondimensional numbers

For the adjusted state to be steady, the system needs to be characterised by the balance between the radial spreading effect of buoyancy and the azimuthal turning effect of rotation. We thus set the typical time scale to $T = 1/f$, and the length scale to the Rossby radius of deformation for the inner fluid (we could equivalently have chosen the second fluid) $L_{\mathrm{Ro}} = \sqrt{g_1' H_1}/f$, hence the velocity scale is simply $U_1 = \sqrt{g_1' H_1}$. We note that this choice corresponds to fixing the Rossby and Froude numbers for the first fluid to

$$\mathrm{Ro}_1 = \tfrac{U_1}{fL_1} = 1 \quad \text{and} \quad \mathrm{Fr}_1 = \tfrac{U_1}{\sqrt{g_1' H_1}} = 1 \ .$$

Hence, the nondimensionalised equations read

$$\partial_t \mathbf{u} + (\mathbf{u}\cdot\boldsymbol{\nabla})\mathbf{u} + \hat{z}\times\mathbf{u} = \begin{cases} -\boldsymbol{\nabla} h_1 - \frac{g_2'}{g_1'}\boldsymbol{\nabla} h_2 & z \in [0, h_1] \\ -\frac{g_2'}{g_1'}\boldsymbol{\nabla}(h_1 + h_2) & z \in [h_1, h_1 + h_2] \end{cases} \tag{52}$$

There is another nondimensional number that plays a more central role in the focus of this work, and it is the Burger number [2]. We define the Burger number as the ratio between the Rossby radius of deformation and a typical horizontal lengthscale

$$\mathrm{Bu}_i = \frac{L_{\mathrm{Ro},i}}{L_{\mathrm{hor},i}} = \frac{\sqrt{g_i' H_i}}{f L_i} \ , \tag{53}$$

which is defined for each fluid, and in general the two Burger numbers will be different. If we now consider that the typical horizontal lengthscale for the adjusted state is the Rossby radius of deformation (balance between buoyancy and Coriolis), and that the intrinsic horizontal lengthscale is the initial radius of the fluids, before adjustment, it is easy to see that the Burger number measures how much the fluid has radially spread compared to its initial width.

The reader might have been puzzled by our choice of working in cylindrical coordinates, as the equations of motions of the two fluids could have been derived in cartesian coordinates, as was done by Cenedese et al. [1], which relieves the calculations of the Bessel functions. However, and this is clearly explained by Cenedese et al. [1], the cartesian approximation is only valid for small Burger numbers, i.e., when the fluid does not spread much compared to its initial width, as for higher Bu the "radial nature" of the horizontal spreading becomes relevant. Figure 4 shows two examples of adjusted states, one for low Bu and one for high Bu, plotting the results of our current model in cylindrical coordinates and that of Cenedese et al. [1] in cartesian coordinates. From these two examples, it is evident that the inaccuracy of the cartesian model increases with increasing Bu.

[2] The Burger number is named after Alewyn P. Burger, not Jan M. Burgers who gave name to the equation.

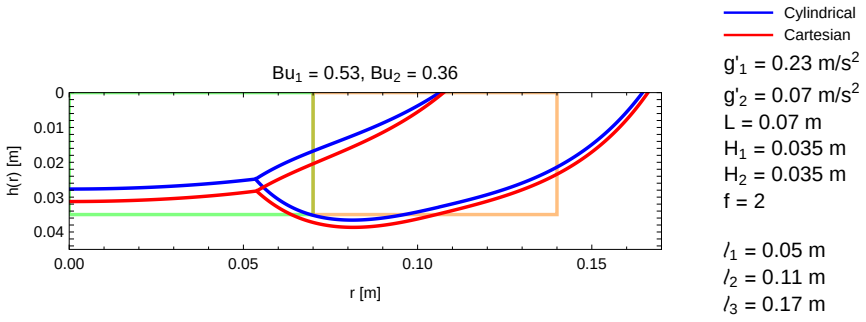


(a) Low Bu

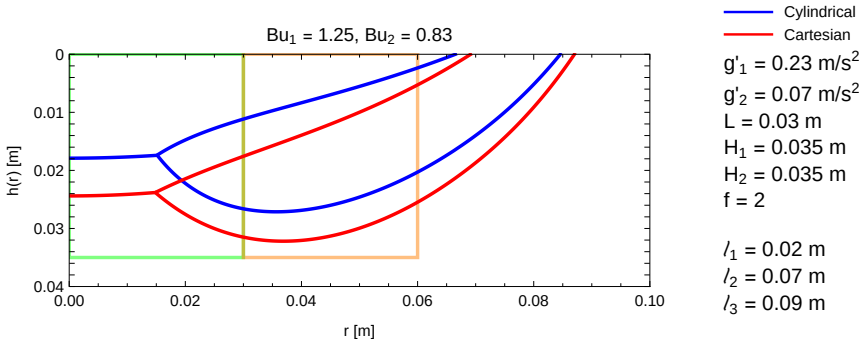


(b) High Bu

Figure 4: Comparison between a low-Bu (panel a) radial adjustment and a high-Bu one (panel b), visualised through the cross-secion of the two fluids. The transparent rectangles indicate the initial boundaries of the two fluids, while the solid lines indicate the adjusted states. The blue lines are the results of the cylindrical model proposed in this work, while the red lines are the results of the cartesian model proposed by Cenedese et al. [1]. The titles have the values of the Burger numbers ($\mathrm{Bu}_i$) for the two fluids. The legend reports: the reduced gravities $g_i'$; the initial width $L$, same for both fluids; the initial thicknesses $H_i$; the Coriolis parameter $f$; the adjusted distances $l_i$.

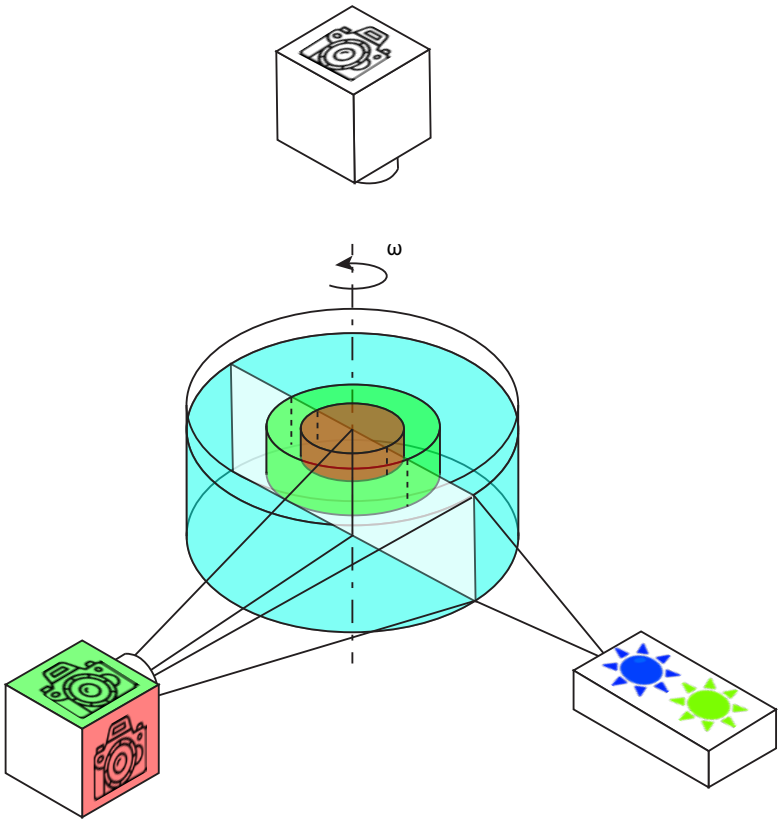


Figure 5: Schematic of the experimental setup. A rotating tank is filled with sea water (shown in cyan) and two concentric cylinders are suspended in the centre of it. The inner cylinder is filled with fresh water (in red) and the outer one with a 50-50 volume mixture of fresh water and sea water (in green). Once the system has reached solid body rotation, the cylinders are lifted, thus releasing the buoyant fluids which generate the two currents. Two LED lights (blue and green) are expanded in a vertical sheet which illuminates a cross-section of the tank. Two cameras fitted with colour filters record the evolution of the currents. A third camera is mounted above the tank to record the free surface deformation.

# 3 Laboratory Experiments

## 3.1 Experimental setup

All the experiments were conducted in a plexiglass cylindrical tank with diameter of one meter. The tank was initially filled with sea water (density $\rho_s = 1021.15\,\mathrm{kg\,m^{-3}}$) to a level of 25 cm from the bottom, for a total volume of approximately 118 L. Two bottom-less, concentric hollow cylinders were suspended with pulleys in the centre of the tank. The smaller hollow cylinder had a radius of 6 cm, while the larger had a radius of 12 cm. Two peristaltic pumps, supplied by two plastic containers, were secured to the rotating table and used to fill the inner cylinders. The tubes coming out of the two pumps were connected to a long bar, which allowed them to be removed after the filling was concluded. The end of each tube was covered by a small sponge, to avoid a monodirectional momentum input by the pumped water. The fluid for the inner cylinder was fresh water (density $\rho_s = 998.48\,\mathrm{kg\,m^{-3}}$), dyed with fluorescein (with a concentration[3] of 0.5 ppm), while the fluid for the region between the two cylinders was a 50-50 volume mixture of fresh water and sea water and dyed with Rhodamine-B (also 0.5 ppm). The tank (and the pulley system) was mounted on a rotating table, set to a rotating speed of 0.5 Hz (Coriolis parameter $f = 2\Omega = 1\,\mathrm{Hz}$). The temperature of the water in the tank as well as in the lab was monitored with a digital thermometer to ensure that no convective motion was present due to possible temperature differences between the water and the environment (the typical difference was fluctuating about $\pm 0.5\,^{\circ}\mathrm{C}$).

In order to capture the time evolution of the two fronts, a fluorescence-based illumination setup was arranged in the tank. Blue (445 nm) and green (520 nm) LED lights were focused on a plane by means of optical fibers, and oriented vertically, and radially towards the center of the tank, as shown in figure 5. The colours of the LEDs were chosen to excite the two dyes in the fluids. Two BASLER a2A4508-20umPRO cameras (18 Mpx, 1″ sensor, pixel size 2.5 µm), with Nikkor AF f/2.8 28 mm lenses, were mounted side by side perpendicularly to the illuminating plane, and controlled by a computer. The cameras were fitted with colour filters so that each would isolate one of the two excited dyes. The cameras are spatially calibrated for images to be meaningfully overlapped, but were *not* synchronised in time: the acquisition rate was set to 5 fps, but a bottleneck in the data transfer rate between the cameras and the computer meant that the time interval between frames is inconsistent and the cameras quickly went out of sync. Additionally, by default, the Basler software (pylon) does not save the timestamp of the frames, not in the filename, nor in the EXIF data.

A third camera (Vision Systems Technology VA-8MC-C16-A0, 8 Mpx, 4/3" sensor, pixel size 5.5 µm) was mounted vertically above the tank, thus visualising the fluids' free surface, with an acquisition rate of 1 frame per second. It should be pointed out here that the illumination setup was not optimised for this camera, as the lighted plane was perpendicular to the camera's field of view. The densities were measured with a DMA5500 Anton-Paar densitometer at a set temperature of 20 °C.

[3]The solution was created adding 0.5 g of dye to 500 mL of water, and then 0.5 mL of such solution was added to 1 L of water.

### 3.2 Experimental observations and quantitative results

The experiments were conducted by starting up the rotating table at a fixed angular velocity, with the full circular tank, and the inner cylinders lowered, but empty. Solid body rotation was checked depositing small speckles of dust (or the like) on the surface of the water, and once the speckles' angular velocities were the same as that of the tank's, the peristaltic pumps were activated to fill up the inner cylinders. The thickness of both layers was set to 8 cm, but could be easily varied in different repetitions of the experiment. Once the filling was concluded, the bar holding the tubes was removed. Then, the experiment was initiated by lifting the hollow cylinders. When lifting the cylinders, care was taken to not introduce any unnecessary disturbances in the water.

Figure 6 reports four views of the surface of the fluids, as seen by the top camera. The best contrast was obtained by converting the RGB image to HSV, and selecting only the saturation channel. In the first frame, figure 6a, the two fluids are still separated by the two cylinders, and in the frame it is possible to see the strings that are holding the cylinders in place. After lifting the cylinders, the two adjusting fluids undergo radial oscillations, with waves that perturb the free surface. Figure 6b, shows an example of a radial peak in the oscillations of the fluids. Due to the camera being black and white, the interfaces of the fluids are not clear in this frame. The origin of the waves that perturb the surface are multiple. First and foremost, there are the gravity waves induced by the response of the bottom fluid to the newly set top surface conditions. Secondly, as the two top fluids are lighter than the bottom one, their free surface initially sits higher than the surrounding (they "float" on top of the bottom fluid), and surface waves are generated by the vertical displacement of the mass of the two fluids that was initially resting above the free surface. Lastly, the lifting of the cylinders is unavoidably a source of perturbations: if done too slowly, the fluids can start leaking out from the bottom of the cylinders, while the top fluid is still contained within; if done too quickly, the shear-induced vertical motion of the fluids can significantly alter the subsequent adjustment. Figure 6c shows a frame of the adjusted state. The two fluids are distinguishable by the different intensities (brighter for the lighter inner fluid, darker for the outer denser one), and this state is approximately maintained for 30 s. After this time, at approximately 80 s from the beginning of the experiment, the central vortex of the inner fluid starts migrating away from the centre, as shown in figure 6d. This migration is probably due to some initial small asymmetry, that grows in time until reaches to an unstable state. We cannot comment on the reproducibility of the migration due to the small number of repetitions of the experiments. It should be noted that, for many reasons (camera's shutter speed and frame rate, lighting setup), these images do not clearly show any azimuthal structure, which were nonetheless observed in the experiments.

Figure 7 shows two frames from the side cameras: one with the cylinders in place, and one representing the adjusted state. We note that the fluids continue to oscillate radially until the end of the experiment (which is considered as when diffusion and mixing smear out the sharp gradients at the interfaces), albeit with decreasing amplitude. When looking at figure 7b, one can comment that the outer interface of the second fluid is well captured by our model, as well as the bottom interface of the first fluid, but the interface between the two fluids is not well represented. Given the single repetition of this experiment, we are unsure on the source of this discrepancy. Additionally, due to the synchronisation problem

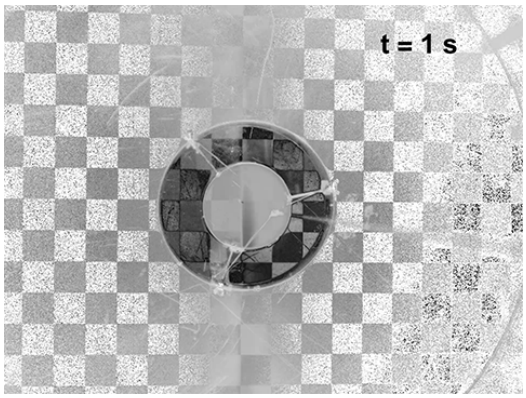


(a) Initial state

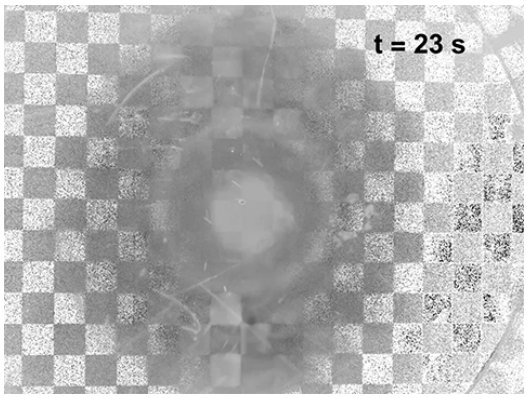


(b) Radial oscillations

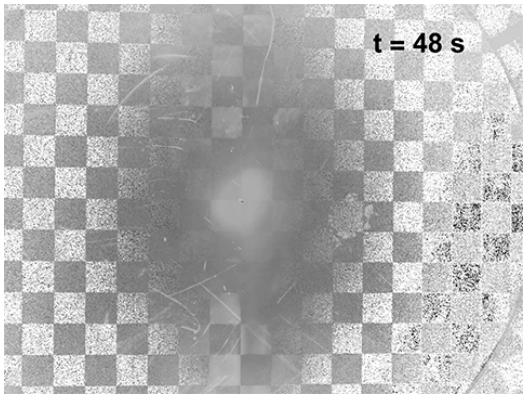


(c) Adjusted state

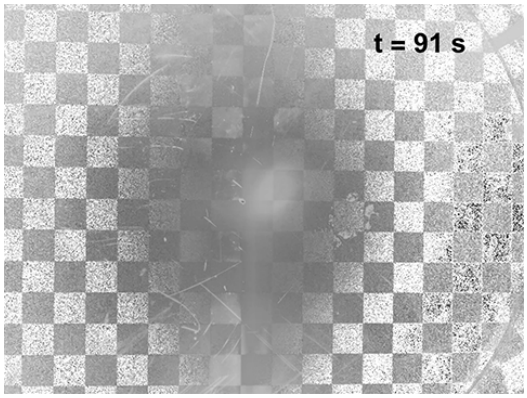


(d) Migration of central vortex

Figure 6: Four frames from the top camera, showing the evolution of the free surface during one experiment. The timestamps are: (a) 0 s, (b) 23 s, (c) 48 s, (d) 91 s. The images have been contrast-enhanced for better visualisation.

between the two cameras, the two overlapping images might not represent the same physical instant. Nonetheless, our model captures the overall depth of the two fluids better than the cartesian model of Cenedese et al. [1], which could be expected, given the relatively high Burger numbers of the two fluids ($\mathrm{Bu}_1 = \mathrm{Bu}_2 = 1.57$, for reference, Cenedese et al. [1] always considered $\mathrm{Bu} < 0.6$).

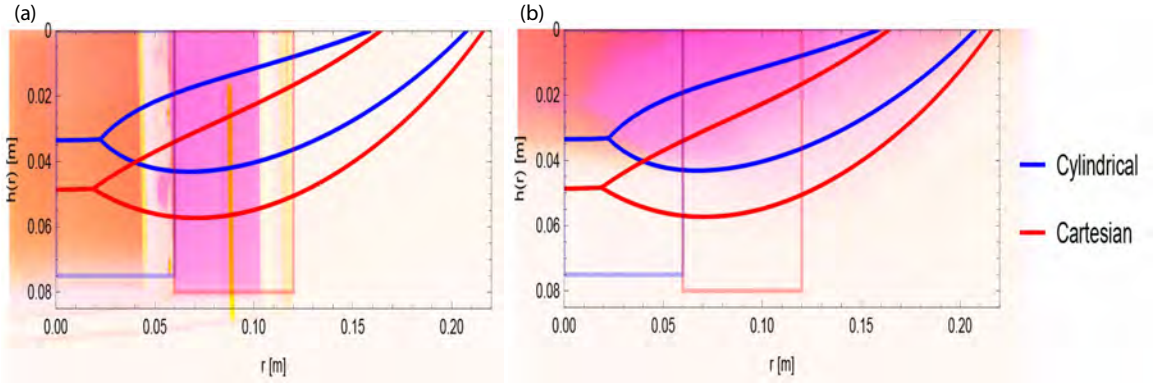


Figure 7: Side view of the initial (panel a) and adjusted (panel b) states of the two fluids, in false colors as seen from the side cameras. Overlapped on the experimental images are: as transparent red and blue lines, the initial profiles of the fluids; as solid lines, the profiles obtained from our model (see section 2), marked as "Cylindrical", in blue, and from the cartesian model of Cenedese et al. [1], marked as "Cartesian", in red. In the left plot, the shadows of the cylinders are visible on the bottom.

A last comment on the experimental results is to be done on the role of diffusion and mixing, which we have neglected in our calculations, but are unavoidably present in the experiments. For example, using the sponge at the end of the filling tubes, we *reduced* the mixing induced by the pump, but did not eliminate it. Additionally, the filling process takes approximately 5-10 minutes, in which the fluids have time to diffuse into each other, at the open bottom of the hollow cylinders. Moreover, the vertical shear induced by the lifting of the cylinders is a source of mixing. Lastly, as the fluids spread and become thinner, the smearing of the interfaces due to mixing and diffusion makes the thickness of the interfaces themselves closer to the total thickness of the fluids.

## 4 Linear Stability Analysis for One Current

Having developed our analytical model in cylindrical coordinates, we can now proceed to study the linear stability of the adjusted state. For simplicity, we will consider only the case of a single current. The case of two currents can be treated in a similar way, but the algebra becomes quickly cumbersome. The case of a single current is sketched in figure 8. For reference, this configuration is the same as the one described in Griffiths and Linden [5].

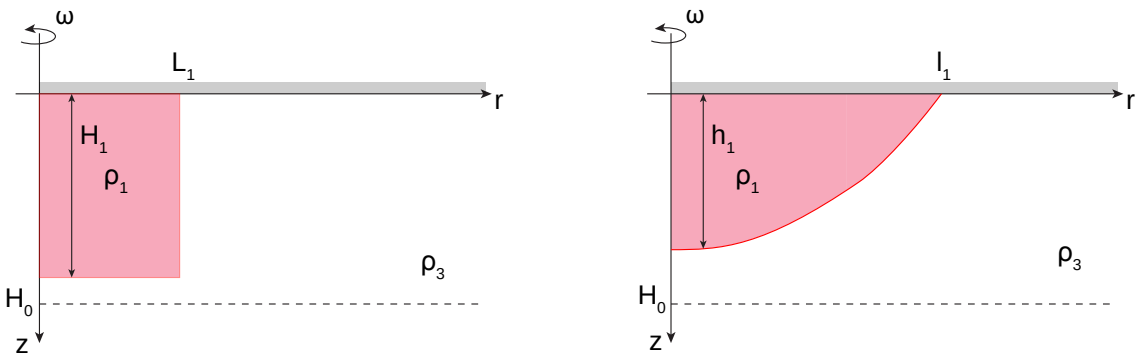


(a) Initial state

(b) Adjusted state

Figure 8: Radial adjustment of a single, floating current in a rotating environment. The fluid is initially kept in a rectangular cross section (left panel), and, after the radial constraint is released, it adjusts until it reaches an equilibrium profile (right panel). $H_0$ indicates a reference pressure in the fluid.

We start from the the equations of motion, here expressed with the physical units set to 1

$$\begin{aligned} \text{mom} &: \partial_t \mathbf{u} + (\mathbf{u}\cdot\boldsymbol{\nabla})\mathbf{u} + \hat{z}\times\mathbf{u} = -\boldsymbol{\nabla} h \\ \text{cty} &: \partial_t h + \boldsymbol{\nabla}\cdot(h\mathbf{u}) = 0 \end{aligned} \tag{54}$$

We perturb each of the fields with a wave-like perturbation

$$(v,u,h) = (0,\bar{u},\bar{h}) + (\hat{v},\hat{u},\hat{h})\exp\left[i(k\theta-\omega t)\right] \tag{55}$$

As for the steady state, we neglect the centripetal term, hence the terms of equations 54 read (the steady state terms are not indicated):

- $\partial_t(v,u) = -i\omega(\hat{v},\hat{u})$
- $(\mathbf{u}\cdot\boldsymbol{\nabla})(v,u) = \left( \underbrace{\cancel{v\partial_r v}}_{\bar{v}=0} + \frac{u}{r}\partial_r v - \underbrace{\cancel{\frac{u^2}{r}}}_{\substack{\text{centripetal}\\ \text{term}}}, v\partial_r u + \frac{u}{r}\partial_\theta u + \frac{uv}{r} \right) =$
  $= \left(\frac{\bar{u}}{r}ik\hat{v}, \hat{v}\partial_r\bar{u} + \frac{ik}{r}\hat{u}\bar{u} + \frac{\bar{u}\hat{v}}{r}\right)$
- $\hat{z}\times\mathbf{u} = (-u,+v) = (-\hat{u},\hat{v})$
- $\boldsymbol{\nabla} h = \left(\partial_r, \frac{\partial_\theta}{r}\right)\left(\hat{h}\exp\right) = \left(\partial_r\hat{h}, \frac{ik}{r}\hat{h}\right)$
- $\partial_t h = -i\omega\hat{h}$
- $\boldsymbol{\nabla}\cdot(h\mathbf{u}) = \boldsymbol{\nabla}\cdot\left[\left(\bar{h}+\hat{h}\exp\right)\left((0,\bar{u})+(\hat{v},\hat{u})\exp\right)\right] = \frac{1}{r}\partial_r(r\bar{h}\hat{v}) + \frac{ik}{r}\hat{h}\bar{u} + \frac{ik}{r}\bar{h}\hat{u}$

Which result in the following equations

$$\hat{r} : \hat{v}\left(\frac{ik}{r}\bar{u} - i\omega\right) + \hat{u}(-1) + \partial_r\hat{h} = 0 \tag{56}$$

$$\hat{\theta} : \hat{v}\left(1 + \frac{\bar{u}}{r} + \partial_r\bar{u}\right) + \hat{u}\left(\frac{ik}{r}\bar{u} - i\omega\right) + \hat{h}\frac{ik}{r} = 0 \tag{57}$$

$$\text{cty} : \hat{v}\left(\frac{\bar{h}}{r} + \bar{h}\partial_r + \partial_r\bar{h}\right) + \hat{u}\frac{ik}{r}\bar{h} + \hat{h}\left(\frac{ik}{r}\bar{u} - i\omega\right) = 0 \tag{58}$$

Which can be written in matrix form as

$$A\begin{pmatrix}\hat{v}\\ \hat{u}\\ \hat{h}\end{pmatrix} = \begin{pmatrix} \frac{ik}{r}\bar{u} - i\omega & -1 & \partial_r \\ \left(1 + \frac{\bar{u}}{r} + \partial_r\bar{u}\right) & \frac{ik}{r}\bar{u} - i\omega & \frac{ik}{r} \\ \left(\frac{\bar{h}}{r} + \bar{h}\partial_r + \partial_r\bar{h}\right) & \frac{ik}{r}\bar{h} & \frac{ik}{r}\bar{u} - i\omega \end{pmatrix}\begin{pmatrix}\hat{v}\\ \hat{u}\\ \hat{h}\end{pmatrix} = 0 \tag{59}$$

Noting the shape of the diagonal terms, we can multiply the matrix by $-i$ to obatin a classical form of the eigenvalue problem $A\mathbf{v} = \omega\mathbf{v}$ (note that we are rotating the eigenvalues by 90 degrees in the complex plane)

$$\begin{pmatrix} \frac{k\bar{u}}{r} & i & -i\partial_r \\ -i\left(1 + \frac{\bar{u}}{r} + \partial_r\bar{u}\right) & \frac{k\bar{u}}{r} & +\frac{k}{r} \\ -i\left(\frac{\bar{h}}{r} + \bar{h}\partial_r + \partial_r\bar{h}\right) & \frac{k}{r}\bar{h} & \frac{k\bar{u}}{r} \end{pmatrix}\begin{pmatrix}\hat{v}\\ \hat{u}\\ \hat{h}\end{pmatrix} = \omega\begin{pmatrix}\hat{v}\\ \hat{u}\\ \hat{h}\end{pmatrix} \tag{60}$$

And look for the eigenvalues of this matrix. Unfortunately, at the current state, we are unable to provide further results on the linear stability analysis.

# 5 Conclusions and Outlook

In this project we addressed the problem of two floating currents on top of a denser fluid in a rotating environment. We set forth an analytical model, expressed in cylindrical coordinates, based on the shallow-water approximation of the Navier–Stokes equations, that allowed us to predict the steady-state, cross-sectional profiles of the currents as a function of the physical parameters. In the development of such model, we dedicated particular care to the role of the centripetal term in the radial momentum equation. Neglecting such term, the solutions for the cross-sectional interfaces profiles are combinations of zeroth-order modified Bessel functions of the first and second kind, scaled horizontally.

We run laboratory experiments in a 1 m-diameter rotating tank, filled with sea water, where two light fluids were initially contained in two axisymmetric cylindrical regions, bounded by hollow bottom-less cylinders. The inner-most fluid was filled with fresh water, while the one in the annular region had a density that was the average of sea and freshwater. Experiments were initiated lifting the radial bounds, thus allowing the fluids to spread, until buoyancy effects were balanced by rotational ones. Our analytical model captures well the overall depth of the two fluids, but, at least in the experiment analysed here, fails to properly represent the interface between the two lighter fluids. Nonetheless, our cylindrical-coordinates formulation is more suited to model currents with high Burger

number, than the cartesian one of Cenedese et al. [1], which represents better currents along straight coasts.

Having expressed the governing equations in cylindrical coordinates, we could investigate the linear stability of our system. In this work, we present the linearised system in the classical form of the eigenvalue problem, but we leave the rest of the investigation for future work. We note, however, that the same care that was dedicated to the centripetal term in the steady state should be applied to the linearised equations, as the flow without the centripetal term in principle does not conserve potential vorticity, and the corresponding equation is one of the governing equations of the problem.

In fact, for this work to be "concluded" — as if one could ever say that of a research project — the results of the linear stability analysis of one current need to be integrated with the (numerical) solutions, and the linearised equations for two currents need to be derived and analysed. Additionally, the outcome of such stability studies needs to be compared with laboratory experiments or numerical simulations with the added complexity that shorter wavelength perturbations are the ones that are most efficiently damped by diffusion and shear, hence the analytical and experimental spectra of unstable frequencies might be shifted due to the absence of any damping in the equations.

With the full linear stability analysis, the results of this work could be connected with natural occurrences of multiple currents interacting at the surface of a large reservoir, like the Western Maine Coastal Current, or with the dynamics of multiple isolated eddies, whose steady state already have been studied extensively and are reported in literature.

## 6 Acknowledgements

I wish to express my heartly gratitude to Claudia Cenedese and Jim McElwaine, who supervised this project. During its twists and turns, from analytical models to experimental work, I have appreciated and valued the expertise of each, and, most of all, the synergy between the different perspectives, as well as the curiosity and interest in learning from everyone's point of view.

My thanks also go to Anders Jensen, who, with his technical support, promptly (very promptly!) made the experiments possible.

This project also benefitted from conversations with other GFD 2025 Fellows, especially the ones who are experts in (shallow water) equations, such as Alexandre Tlili and David Darrow, and the ones who are experts in linear stability analysis, such as Theo Lewy, as well as the ones that listened and helped me with ideas, like Marion Cocusse, Emma Bouckley, Andrés Posada and Kyle McKee.

## References

[1] C. Cenedese, J. A. Lerczak, and G. Bartone, *A Geostrophic Adjustment Model of Two Buoyant Fluids*, Journal of Physical Oceanography, 42 (2012), pp. 1932–1944.

[2] J. H. Churchill, N. R. Pettigrew, and R. P. Signell, *Structure and variability of the Western Maine Coastal Current*, Deep Sea Research Part II: Topical Studies in Oceanography, 52 (2005), pp. 2392–2410.

[3] M. Davey, *Baroclinic instability in a fluid with three layers*, n.a., 34 (1977), pp. 1224–1234.

[4] R. W. Griffiths, P. D. Killworth, and M. E. Stern, *Ageostrophic instability of ocean currents*, J. Fluid Mech., 117 (1982), pp. 343–377.

[5] R. W. Griffiths and P. F. Linden, *The stability of vortices in a rotating, stratified fluid*, J. Fluid Mech., 105 (1981), pp. 283–316.

[6] M. Lobo, S. M. Griffies, and W. Zhang, *Vertical Structure of Baroclinic Instability in a Three-Layer Quasigeostrophic Model over a Sloping Bottom*, Journal of Physical Oceanography, (2025).

[7] N. A. Phillips, *A simple three-dimensional model for the study of large-scale extratropical flow patterns*, Journal of the Atmospheric Sciences, (1951).

[8] ——, *Energy Transformations and Meridional Circulations associated with simple Baroclinic Waves in a two-level, Quasi-geostrophic Model*, Tellus, 6 (1954), pp. 273–286.

[9] G. K. Vallis, *Atmospheric and Oceanic Fluid Dynamics: Fundamentals and Large-Scale Circulation*, Cambridge University Press, Cambridge, 2 ed., 2017.

# A The Centripetal Term

This appendix elaborates on the importance of the centripetal term in the radial momentum equation. We here consider a single current, in steady state. A similar reasoning applies to the case of two currents. The derivation is similar to the one presented in section 2.3, but the centripetal term is maintained, hence, in the $\hat{r}$ direction we have

$$-\frac{u_\theta^2}{r} - u_\theta = -\partial_r h \ . \tag{61}$$

The first term of the LHS corresponds to the centripetal term, and hereafter quantify the error introduced when neglecting the centripetal term.

With the centripetal term, it is more clear (and therefore instructive) to derive the solution for the velocity profile, instead of the height profile. This is due to the fact that for equation 61, the relation between $h$ and $u$ is no longer that of a first derivative (in other words, $u \propto I_1 \implies h \propto I_0$). We will start from the radial momentum equation and the conservation of PV.

$$\begin{cases} \frac{u_\theta^2}{r} + f u_\theta = g' \partial_r h \\ \frac{u_\theta}{r} + \partial_r u_\theta = f\left(1 + \frac{h}{H}\right) \end{cases} \tag{62}$$

which, after few algebraic manipulations, can be written as

$$r^2 \partial_r^2 u_\theta + r \partial_r u_\theta - u_\theta \left(1 + \frac{f^2}{g' H} r^2\right) = \frac{f}{gH} r u_\theta^2 \ , \tag{63}$$

which is not a Bessel equation anymore, due to the term on the RHS, and does not have a simple analytic solution (if it has one), but can be integrated numerically.

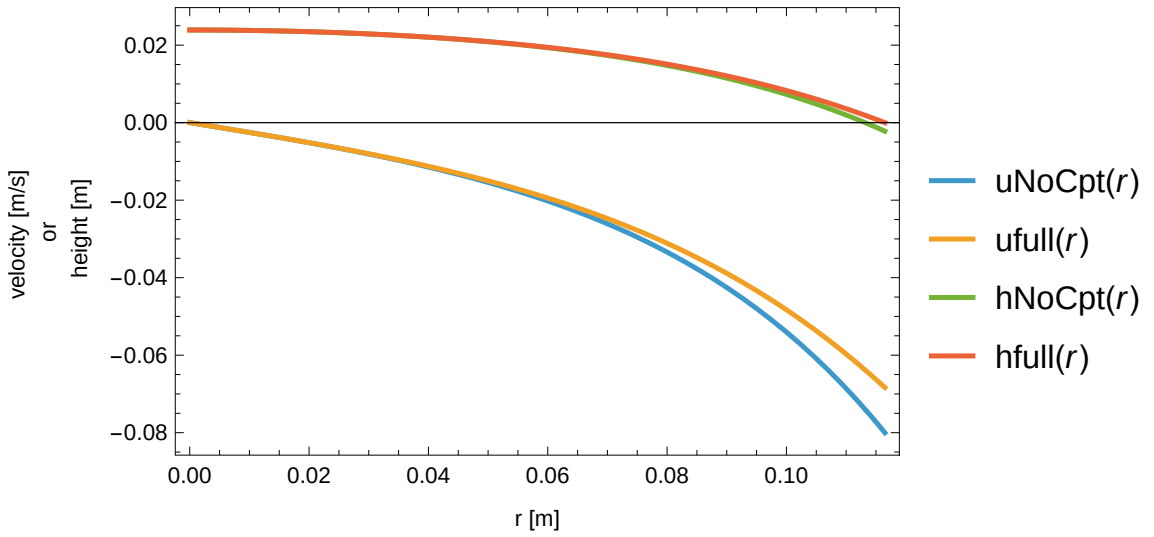


Figure 9: Comparison between the velocity profiles of a single current with (orange line) and without (blue line) the centripetal term. The green line indicates the height profile of the current, calculated with the centripetal term.

If we draw the two solutions numerically integrated, for typical parameter values, we get the profiles shown in figure 9, where the boundary conditions for the solution with the centripetal term were forced to match the value and first derivative of the analytic solution without the centripetal term.

If we now plot the normalized difference between the two solutions for the velocity we note (in figure 10) that the difference is at most 15%, where the radius is the biggest.

# B Derivation of the Characteristic Solution

This appendix presents the calculation performed to derive the eleventh boundary condition. We here consider a single current, in steady state. If we write out the continuity, momentum and potential vorticity conservation equations, we have

$$\partial_t h + u_r \partial_r h + \frac{u_\theta}{r}\partial_\theta h + h\partial_r u_r + \frac{h}{r}\partial_\theta u_\theta + \frac{h u_\theta}{r} = 0, \tag{64}$$

$$\partial_t u_r + u_r \partial_r u_r + \frac{u_\theta}{r}\partial_\theta u_r + \partial_r h - \frac{u_\theta^2}{r} - f u_\theta = 0, \tag{65}$$

$$\partial_t u_\theta + u_r \partial_r u_\theta + \frac{u_\theta}{r}\partial_\theta u_\theta + \frac{1}{r}\partial_\theta h + \frac{u_r u_\theta}{r} + f u_r = 0, \tag{66}$$

$$-\frac{\omega}{f} = \frac{\partial_\theta u_r - \partial_r(r u_\theta)}{rf} = 1 - \frac{h}{h_0}. \tag{67}$$

Now consider the initial radial relaxation that is axisymmetric and look for a character-

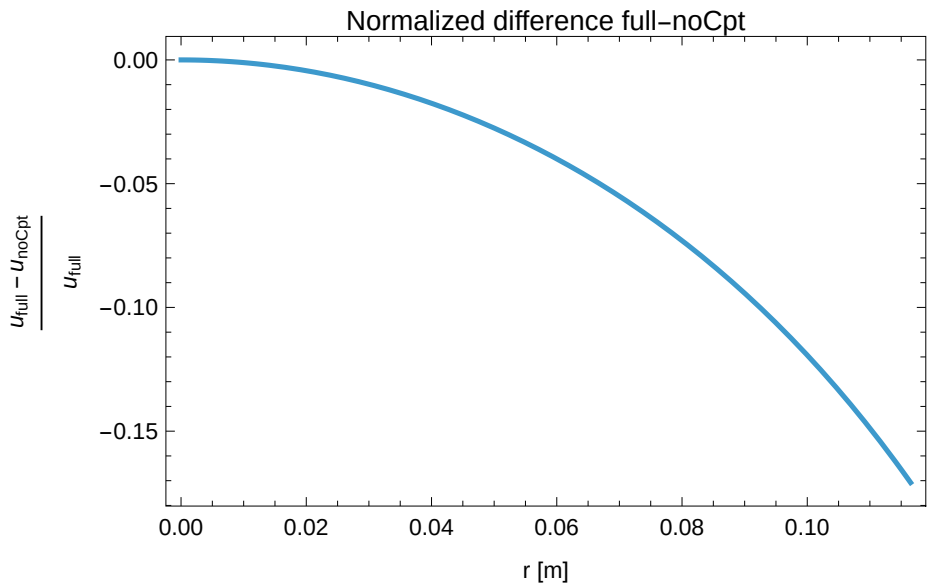


Figure 10: Normalised difference between the two solutions for the velocity, with and without the centripetal term. The difference is normalised with respect to the solution with the centripetal term.

istic solution $\dot{R} = u_r(t, R)$. Let us define

$$H(t) = h(t, R(t)), \tag{68}$$
$$V(t) = u_r(t, R(t)), \tag{69}$$
$$U(t) = u_\theta(t, R(t)). \tag{70}$$

Then, differentiating with respect to $t$ using $\dot{R} = u_r = V$ and simplifying we get

$$\dot{H} = V\partial_R H = \partial_t h + \dot{R}\partial_r h = -H\partial_r u_r|_{r=R} - \frac{HU}{R} \tag{71}$$
$$\dot{V} = V\partial_R V = \partial_t u_r + \dot{R}\partial_r u_r = -\partial_r h|_{r=R} + \frac{U^2}{R} + fU \tag{72}$$
$$\dot{U} = V\partial_R U = \partial_t u_\theta + \dot{R}\partial_r u_\theta = V\left(f - \frac{U}{R}\right) \tag{73}$$
$$-\frac{U}{R} - \partial_r u_\theta|_{r=R} = f\left(1 - \frac{h}{h_0}\right). \tag{74}$$

Now the $\dot{U}$ equation can easily be solved to get

$$U = \frac{R^2 - R_0^2}{2R}, \tag{75}$$

where $R_0 = R(t = 0)$ and the initial condition $U(t = 0) = 0$ has been used.

# Dynamics of Gravity Currents Over Stepped Slopes

Andrés Posada-Bedoya

August 20, 2025

## 1 Introduction

Gravity currents are buoyancy-driven flows in which density differences drive the motion mainly in the horizontal direction. They can be found in a wide variety of geophysical settings, generated both naturally and by human activities. Examples of gravity currents are sea breeze fronts, oceanic overflows, avalanches, sand storms, oil spillages and pollutant discharge in water bodies [27]. Due to their importance in a range of engineered and natural situations, laboratory experiments and numerical simulations have been extensively used to investigate gravity currents travelling along a flat, horizontal surface [25, 26, 3] or flowing over a sloping bottom [9, 18].

Motivated by the presence of complex topography in the natural and built environment, attention has been paid recently to topographic features and how they affect the propagation of dense bottom gravity currents. Several recent studies have investigated the impact of bottom-mounted roughness elements of different geometries and in different arrangements on gravity currents over a horizontal [8, 30, 19] and sloping [24] bottom. Some studies have considered continuous roughness like sinusoidal [22] or parabolic [21] bottom. However, one particular configuration that has received little attention [12, 28] is the stepped-like topography with abrupt changes in water depth, which is the focus of the present work.

At field scales, this configuration is of relevance to turbidity currents over stepped-like bathymetric features, such as cyclic steps and crescent-shaped bedforms, in submarine canyons [14, 10]. The flow conditions required to form these upstream-migrating bed forms remain debated because the interactions between turbidity currents and active bed forms are difficult to measure directly. Recent field observations have revealed energetic turbidity currents driving sediment transport and resuspension in these environments, potentially able to maintain and drive the migration of the bedforms [14]. These interactions generate complex current–sediment dynamics that remain poorly understood [4]. A question motivated by these field observations [14] is: how does stepped topography influence the dynamics of gravity currents?

The study of gravity currents over stepped topography is also relevant from a numerical modelling perspective. Ocean models frequently represent topography as a "staircase" when using z-level (height-based) vertical grids. Sensitivity studies comparing terrain-following and z-level coordinates have shown that z-level models often predict deeper and slower gravity currents under equivalent conditions [1, 11]. Reconciling the two approaches, so that models consistently reproduce gravity current height, speed, and density across diverse terrains, remains an open challenge. Improved understanding of gravity current behaviour

over stepped topography could therefore enhance predictions of mixing rates and intrusion depths in regions characterized by both stepped and smooth slopes.

The present study employs lock-exchange laboratory experiments to investigate the dynamics of gravity currents in the presence of stepped topography. Comparisons are made between flows over uniform slopes and stepped topographies to quantify how step size influences front velocity, dilution, and ambient fluid entrainment.

The paper is structured as follows. Section 2 describes the experimental setup and measurement techniques. Section 3 presents qualitative and quantitative analyses of the flow evolution, including the effects of topography on current speed and bulk entrainment. A parameterization for entrainment over stepped topography is introduced in Section 3.3. A synthesis of the effects of the stepped topography on the gravity currents is discussed along with a shallow-water model incorporating the effects of discrete steps.

# 2 Materials and Methods

## 2.1 Experimental setup

The experiments were conducted in a glass-walled rectangular tank measuring 1.2 m in length, 0.3 m in width, and 0.5 m in height. Dense gravity currents were generated through the classic partial lock-exchange setup [26]. The dense (lock) fluid was initially separated from the ambient fluid by a Perspex gate positioned 20 cm from the left wall (Figure 1). The gate was actuated by a pneumatic piston system to ensure repeatable and consistent releases. Two small holes located at the water surface level allowed the water levels on both sides of the gate to equilibrate during filling.

Fresh water, previously settled at room temperature in a stirring tank, was used as the ambient fluid. The total water depth $H = 0.46$ m was kept constant across all experiments. Both compartments were filled to the same free-surface level. The dense fluid was prepared by diluting a pre-mixed brine solution (Kosher salt in water) to achieve the desired density. The fluid density was measured with an Anton Paar DMA5000 densimeter, with an accuracy of $\pm 0.004$ kg m$^{-3}$. The dense fluid was dyed with black printing ink, chosen for optimal contrast in monochromatic imaging. To minimize mixing, the dense solution was gently pumped at the bottom of the lock compartment through a pipe fitted with a sponge diffuser, producing an initial interface thickness of less than 1 mm.

The variable topography was constructed from PVC slabs matching the tank width and tightly fitted against the sidewalls to minimize leakage. The slabs could be slid relative to one another to form stepped configurations of various geometries. For each configuration, the slabs were screwed to an aluminum frame to fix them in place for each experiment. The uppermost slab remained fixed throughout all tests and supported both the lock region and a 20 cm-long horizontal section downstream of it. The current first propagated along this flat section before descending the sloping or stepped topography. For the reference case, a uniform slope was constructed using a single Perspex sheet connecting the edge of the uppermost fixed slab to the tank bottom at a 2:1 (horizontal:vertical) inclination.

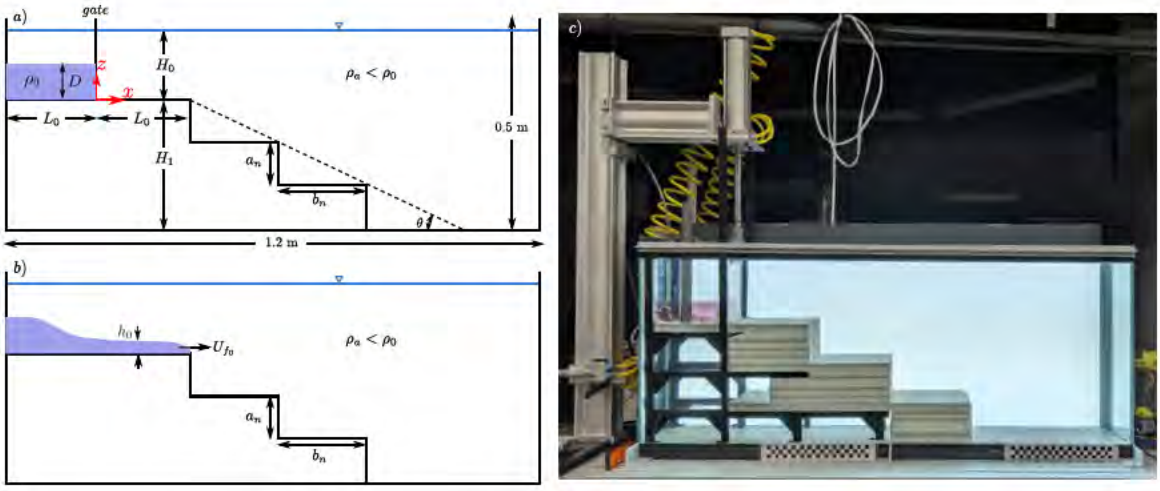


Figure 1: Schematic of the experimental setup (a) before and (b) after gravity current lock release. In all the experiments, $\theta = 26.5°$, $b_n = 2a_n$, $H_0 = 0.16$ m, $H_1 = 0.3$ m, $L_0 = 0.2$ m, and $\rho_a = 998.47$ kg m$^{-3}$. (c) Experimental setup for a case with 3 steps of 10 cm height each.

## 2.2 Density field measurements

Two-dimensional, spanwise-averaged density fields were obtained using a light attenuation technique [7, 8, 19]. Image acquisition was performed with a Basler a2A4508-20umPRO-GMAX2518 scientific camera, which captured monochromatic images at a resolution of 4504 $\times$ 2250 pixels (Mono 12 format, 4096-bit depth) and a frame rate of 15 Hz. To optimize data throughput, images were cropped to the region of interest following the topography and stored as binary files during capture.

The camera was positioned 7.1 m from the front wall of the tank to minimize parallax errors. A zoom lens was adjusted so that the field of view covered the entire fluid depth and approximately 0.94 m in the streamwise direction, including about one-third of the lock region and 10 cm beyond the downstream edge of the variable topography. Both the camera and the tank were fixed in place throughout calibration and all experimental runs to ensure consistent alignment and reproducibility.

Illumination was provided by a uniform LED light sheet mounted along the side of the tank opposite to the camera. A diffusing screen ensured spatially uniform brightness across the entire imaging area. Preliminary tests confirmed that the illumination remained stable over the duration of the experiments.

The light attenuation technique is based on Beer's Law, which relates the measured light intensity to the dye concentration. For each pixel, a calibration curve was fitted between the normalized intensity $I/I_0$ and the dye concentration $c$:

$$\frac{I}{I_0} = Ke^{-Ac} + (1 - K), \tag{1}$$

where $I$ is the pixel intensity corresponding to concentration $c$, $I_0$ is the background intensity in the absence of dye, and $K$ and $A$ are the calibration constants. The local dye

concentration at each pixel was then obtained from

$$c = \frac{1}{A} \log \left( \frac{\frac{I}{I_0} + K - 1}{K} \right). \tag{2}$$

Calibration was performed using 20 known dye concentrations ranging from clear water ($c = 0$) to $c = 4$ ml/l, corresponding to twice the dye concentration used in the lock fluid (2 ml/l). Figure 2 presents the spatial distribution of the calibration parameters $A$ and $K$, together with the coefficient of determination ($R^2$) for each pixel, demonstrating the robustness of the fits. Selected calibration curves are also shown to illustrate the quality of the calibration.

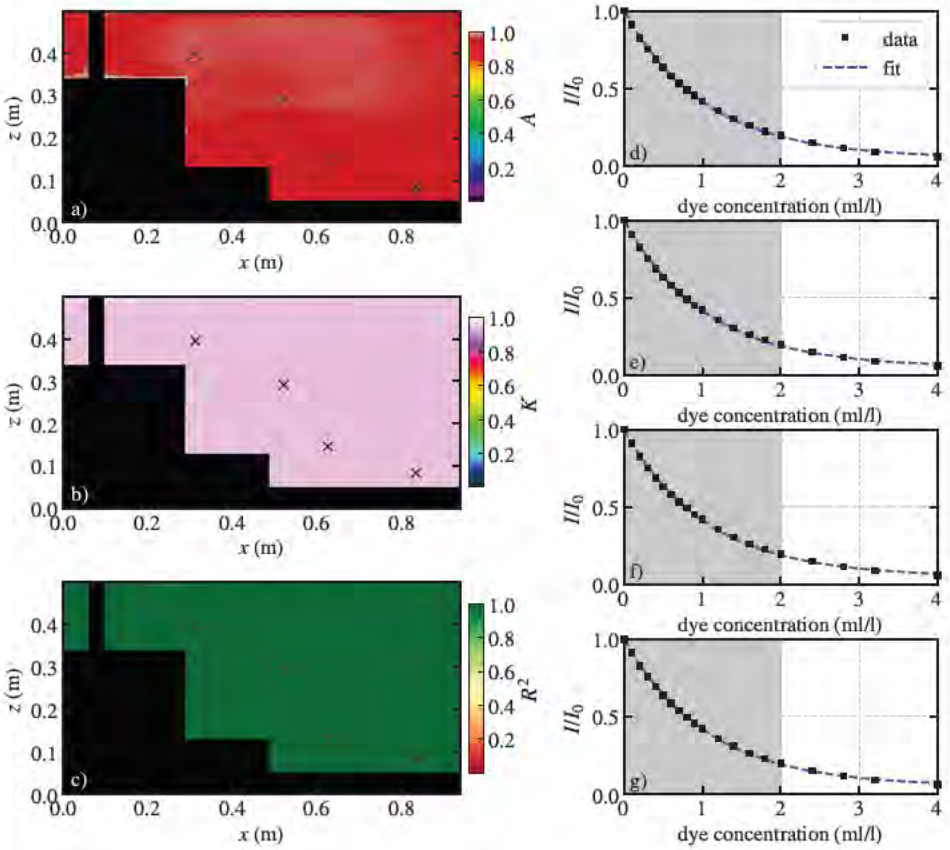


Figure 2: Spatial distribution of the fitted calibration parameters (a) $A$ and (b) $K$ and the (c) $R^2$ coefficient of determination (see equation 1). The black area is a mask of the region beneath the supporting aluminum structure and the lock gate. (d-g) Examples of fitted calibration curves at the four locations indicated by crosses in panels a-c. The grey shaded area indicates concentration values less than 2 ml/l, which was the initial concentration of the dense fluid in the lock.

A linear relationship between dye and salt concentration was assumed throughout the experiments, consistent with previous studies [23, 8, 19]. The resulting output was a nondi-

| Exp. | $D$ (cm) | $D/H$ | $\rho_0$ (kg m$^{-3}$) | $g'$ (m s$^{-2}$) | $a_n$ (cm) |
|---|---|---|---|---|---|
| 1-6 | 4 | 0.250 | 1148.0 | 1.452 | 0/2/4/6/8/10 |
| 7-12 | 6 | 0.375 | 1044.4 | 0.430 | 0/2/4/6/8/10 |
| 13-18 | 8 | 0.500 | 1019.2 | 0.181 | 0/2/4/6/8/10 |
| 19-24 | 10 | 0.625 | 1009.0 | 0.093 | 0/2/4/6/8/10 |
| 25-30 | 12 | 0.750 | 1005.2 | 0.054 | 0/2/4/6/8/10 |

Table 1: Experimental parameters. The measured density across all the experiments was always within 0.2% of the reported here.

mensional, spanwise-averaged, two-dimensional density field, derived from the dye concentration $c(x, z)$ as

$$\rho^*(x, z) = \frac{c(x, z)}{c_0} = \frac{\rho(x, z) - \rho_a}{\rho_0 - \rho_a} \tag{3}$$

where $c_0$ is the dye concentration of the lock fluid, $\rho_0$ and $\rho_a$ are the densities of the lock and ambient fluids, respectively, and $\rho(x, z)$ is the dimensional density field.

### 2.3 Parameter space

Six bottom topographies were investigated: five stepped geometries and one uniform 2:1 sloping case used as a reference. In the stepped configurations, the individual step height ($a_n$) varied from 2 cm to 10 cm, arranged such that the overall mean slope of the topography was approximately 2:1. The cases are denoted $a_0$-$a_5$, where $a_0$ corresponds to the uniform slope and $a_5$ to the largest step height.

For each topography, five experiments were conducted with varying dense-fluid density ($\rho_0$) and initial lock height ($D/H$), resulting in a total of 30 experiments. Several runs were repeated to verify the repeatability and robustness of the setup.

To isolate the influence of topography on the gravity current dynamics, a constant initial Reynolds number was targeted across all experiments. The Reynolds number was defined as

$$Re_0 = \frac{U_{f_0} h_0}{\nu} \sim \frac{h_0^{3/2} g_0'^{1/2}}{\nu}, \tag{4}$$

where $\nu$ is the kinematic viscosity, $h_0$ is the current height, $g_0' = \Delta\rho/\rho_a$ is the reduced gravity. The subscript 0 refers to quantities measured along the initial flat section in front of the gate, before the current interacts with the slope.

Maintaining a constant $Re_0$ required simultaneous variation of $\rho_0$ and $D$. From equation 4, it follows that $g_0'$ (and thus $\rho_0$) must decrease approximately with the cube of the current height to preserve dynamic similarity. To explore a broad range of initial conditions, $D$ was varied between $0.25H_0$ and $0.75H_0$, where $H_0 = 0.16$ m is the water depth above the lock region. The densest current had a density of 1145 kg m$^{-3}$, while the lightest current was adjusted to yield a measurable density difference of approximately 5 kg m$^{-3}$. Table 1 summarizes the parameters of all the experiments.

## 2.4 Gravity current properties

### 2.4.1 Front position and speed

The instantaneous front position of the gravity current, $x_f$, was defined as the foremost point of the current nose. In the experiments, $x_f$ was determined by tracking the evolution of the non-dimensional iso-density contour at $\rho^* = 0.02$, following the procedure of previous studies [23, 16, 31]. The temporal evolution of $x_f(t)$ was used to compute the instantaneous front velocity, $U_f = dx_f/dt$.

### 2.4.2 Nondimensional parameters

The flow dynamics were characterized using three nondimensional parameters: the Froude number ($Fr$), the Reynolds number ($Re$), and the normalized step height ($a_n/(D/2)$). Bulk values of $Fr$ and $Re$ were estimated separately for the flat region ahead of the lock (subscript 0) and for the sloping region (subscript $s$):

$$Fr = \frac{U_f}{\sqrt{g'h\cos\theta}}, \tag{5}$$

$$Re = \frac{U_f h}{\nu}, \tag{6}$$

where $h$ is the current height, $U_f$ is the front speed, $g' = g\Delta\rho/\rho_a$ is the reduced gravity, $\theta$ is the bottom slope and $\nu$ is the kinematic viscosity.

### 2.4.3 Bulk entrainment

As the dense current advances, it entrains ambient fluid, increasing its total volume and height through mixing. Variations in current volume and height are therefore indicative of instantaneous entrainment dynamics [20, 5]. Two complementary methods were used to estimate the bulk entrainment coefficient.

The first method provided a single bulk entrainment coefficient for each experiment, based on the classical definition [9]:

$$E = \frac{1}{\bar{U}_f}\frac{D\langle h_\sigma\rangle}{Dt} = \frac{w_E}{\bar{U}_f}, \tag{7}$$

where $w_E$ is the entrainment velocity, $D/Dt$ is a material derivative, and $\langle h_\sigma\rangle$ is a bulk measure of current height obtained from the vertical dispersion of density. Here, $\langle\rangle$ is used to indicate averaging in the streamwise direction. Because the stepped bottom caused overhanging regions that made the center of mass an unsuitable measure of height, $h_\sigma$ was computed as the vertical standard deviation of the density field:

$$h_\sigma(x,t) = \frac{\int_0^H \rho^*(x,z,t)(z-h_\mu)^2 dz}{\int_0^H \rho^*(x,z,t)dz}, \tag{8}$$

where $h_\mu$ is the center of mass at each streamwise location,

$$h_\mu(x,t) = \frac{\int_0^H \rho^*(x,z,t)z dz}{\int_0^H \rho^*(x,z,t)dz}. \tag{9}$$

The characteristic current height was defined as $h = 3\langle h_\sigma \rangle$, corresponding to the vertical extent delimited by the $\rho^* = 0.02$ contour approximately.

The entrainment analysis was performed within a control volume moving with the current, ensuring that both the nose and head were always included, following the approach of Zhou et al. [30]. The quantities $h_\sigma$ and $h_\mu$ were averaged in this moving reference frame. The bulk entrainment coefficient was evaluated between $x_f = 0.35$ m and $x_f = 0.8$ m along the variable-bottom region, sufficiently far downstream to capture fully developed flow conditions.

To examine the temporal evolution of entrainment, the second method followed the approach of [23, 16, 31], based on the rate of change of the current volume:

$$\mathcal{V}(t) = B \int_{\Omega_f} \alpha(x, z, t) dA, \tag{10}$$

where $B$ is the width of the tank, $dA = dxdz$ is the pixel area, $\Omega_f$ denotes the control volume in the moving frame of reference. The indicator function $\alpha$ identifies the current region as:

$$\begin{cases} \alpha = 1, & \rho^* \geq 0.02 \\ \alpha = 0, & \rho^* < 0.02. \end{cases} \tag{11}$$

The entrainment flow rate was then computed as the temporal derivative of the current volume:

$$Q(t) = \frac{d\mathcal{V}}{dt} = \frac{\mathcal{V}_i - \mathcal{V}_{i-1}}{t_i - t_{i-1}}, \tag{12}$$

where $i$ denotes the time index. The instantaneous entrainment velocity is then computed by dividing the flow rate by the entrainment area $A_E = x_f B$:

$$w_E(t) = \frac{Q(t)}{A_E(t)} = \frac{Q(t)}{x_f(t) B}. \tag{13}$$

Finally, the time-dependent entrainment coefficient was calculated as

$$E(t) = \frac{w_E(t)}{U_f(t)}. \tag{14}$$

A second bulk entrainment coefficient was obtained by time-averaging $E(t)$ between the same two streamwise locations used in Method 1, ensuring direct comparability between the two estimates.

# 3 Results

## 3.1 Overview of the flow dynamics

After the gate was removed, the dense current propagated along the initial flat section, rapidly reaching the slumping regime of constant front velocity that follows the initial acceleration phase [15]. The flow development in this region established the properties of the current prior to its propagation over the variable-bottom section. The initial evolution, front velocity $U_{f_0}$, and gravity current height $h_0$ were consistent across experiments with

the same lock height $D/H$ and initial density $\rho_0$. The initial Reynolds number was of the same order in all the experiments, $Re_0 \sim 2000 - 3000$ (Fig. 3a), while the corresponding Froude number $Fr_0 = U_{f_0}/\sqrt{g_0' h_0} \sim 0.8 - 1.2$ was lower for shallower currents (Fig. 3b).

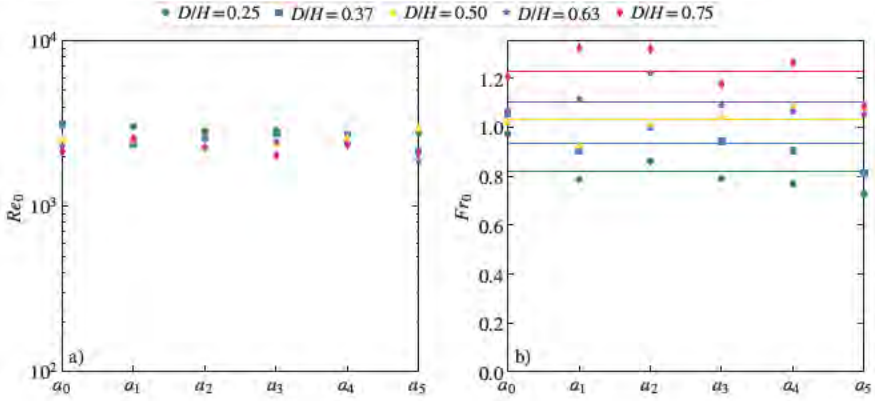


Figure 3: (a) Reynolds number and (b) Froude number during the slumping regime over the initial flat region. Horizontal lines in (b) indicate the average $Fr_0$ across cases with the same $D/H$.

Visual inspection of the experiments shows that step size strongly influenced the current's dynamics, particularly its speed, volume, and dilution. Figure 4 presents representative snapshots of the non-dimensional instantaneous density field for experiments with the same initial $D/H = 0.5$ over four different topographies. Although this case is used illustratively, the same trends were observed across all conditions. The occupied area and height of the gravity current increased with step size, indicating enhanced mixing and entrainment of ambient fluid. The steps also modified the density distribution, trapping dense fluid upstream within the step cavities. Consequently, the mean density within the current head decreased with increasing step height, in contrast to the uniform-slope case, where dense fluid continuously fed the head from the thin layer near the bed.

In the uniform-slope experiments, the current advanced with a distinct nose followed by a growing head region higher than the trailing tail. Early in the downslope phase, a diluted nose propagated ahead while the denser fluid remained in the tail (Fig. 4). Over time, this dense tail fluid drained downslope and fed the head, increasing its buoyancy and causing continuous acceleration. This behavior is evident in the time series of $x_f$ and $U_f$ (Fig. 5a,g) and is consistent with the mechanism described by Maxworthy and Nokes [18], who showed that in small-aspect-ratio locks, only the portion of the fluid closest to the gate will compose the head of the current, and a large portion of the released fluid remains in the tail and later supplies buoyancy to the head, sustaining acceleration. The initial flat-bottom development in the present experiments similarly produces a small aspect ratio that promotes this mechanism. The sequence in Figs. 4a–c illustrates this process.

In contrast, in the presence of steps, dense fluid trapped within the steps could no longer feed the head, reducing the downstream transfer of buoyancy (Fig. 4). As a result, the downslope acceleration phase shortened as step size increased, and the currents reached a quasi-steady velocity earlier. The mean propagation speed decreased with increasing

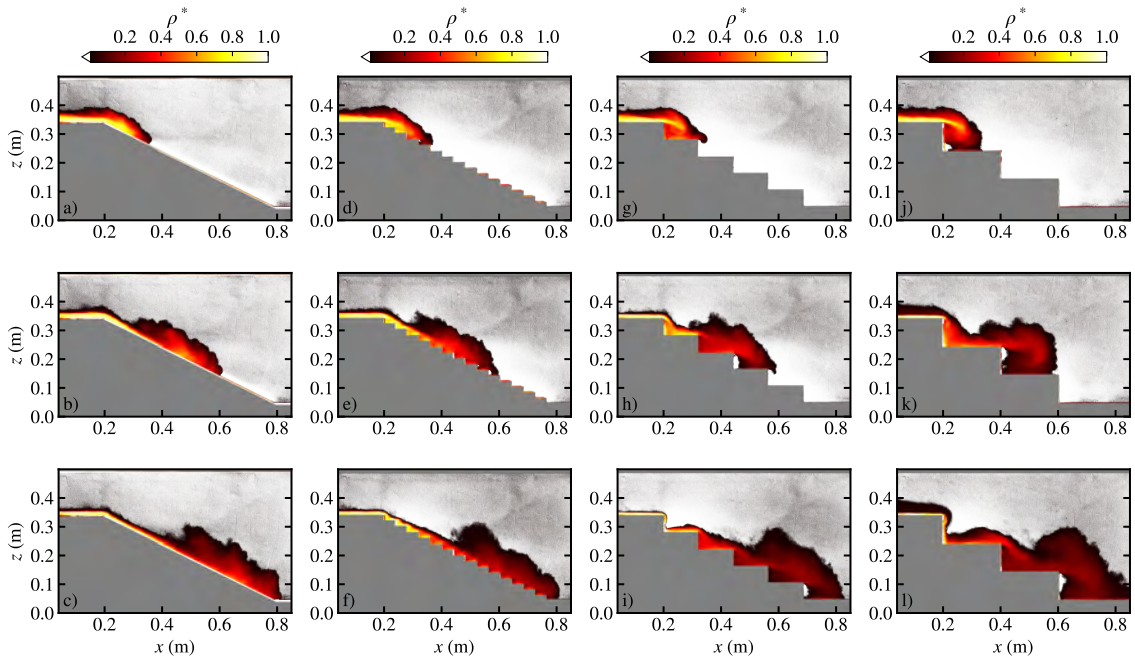


Figure 4: Snapshots of the nondimensional density field $\rho^*$ for experiments with initial $D/H = 0.5$ and $g' = 0.181$ m s$^{-2}$ over four topographies: (a-c) uniform slope, and steps of size (d-f) $a_1 = 2$ cm, (g-i) $a_3 = 6$ cm, and (j-l) $a_5 = 10$ cm. Values lower than 0.01 are masked. Snapshots correspond to $x_f \approx 0.35$, 0.6 and 0.8 m.

step size (cf. middle column of Fig. 5). In all stepped configurations, the current exhibited alternating acceleration and deceleration as the front impinged upon the treads and cascaded down the risers, respectively. This effect was more pronounced for larger steps and shallower currents (i.e., larger $a/(D/2)$), as reflected in the increased variability of $x_f$ and $U_f$ (Fig. 5). With more steps, this variability diminished, approaching the smoother evolution observed on the uniform slope.

For the uniform-slope cases, the bulk Froude number remained in the range $Fr$ ∼1-2, increasing slightly between $x_f = 0.2$ m and $x_f = 0.6$ m, and then decreasing downstream (Fig. 5m). Because of the downstream acceleration, $Fr_s > Fr_0$. In the stepped cases, $Fr_s$ decreased with the step size due to the decrease in $U_f$ (Fig. 5n-r). The flow often alternated between subcritical and supercritical regimes in response to the abrupt changes in depth at each step. Typically, the current decelerated and thickened when passing over a riser (subcritical), and accelerated and thinned after impinging upon the tread (supercritical). However, the precise locations of these transitions varied across experiments due to evolving buoyancy and trajectory differences (for example, sometimes skipping the direct interaction with a step).

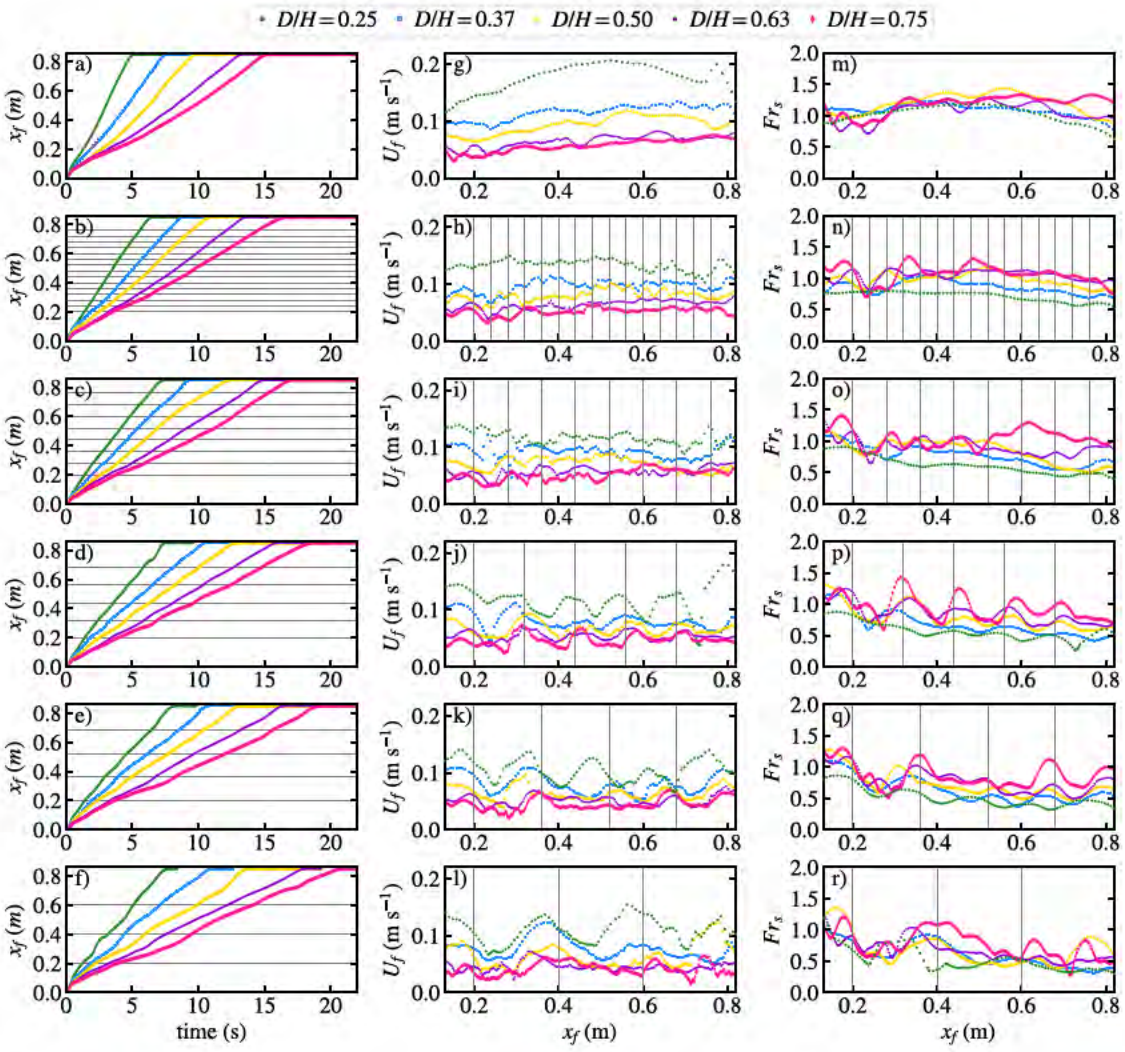


Figure 5: Time series of the gravity current (a-f) front position $x_f$, (g-l) speed $U_f$, and (m-r) bulk Froude number $Fr_s$. Each panel corresponds to a topography: (a,g,m) uniform slope $a_0$, (b,h,n) $a_1 = 2$ cm, (c,i,o) $a_2 = 4$ cm, (d,j,p) $a_3 = 6$ cm, (e,k,q) $a_4 = 8$ cm, and (f,l,r) $a_5 = 10$ cm. Grey lines mark the vertical face of each step; the downslope region begins at $x_f = 0.2$ m.

### 3.2 Unsteady entrainment rate

As the gravity currents propagated downslope, their total height (Fig. 6a-f) and volume (Fig. 6g-l) increased continuously, reflecting ongoing entrainment of ambient fluid. Similar to the front velocity, both quantities exhibited variability around a mean trend, with fluctuations amplifying for larger step sizes and shallower currents. The final height and volume, indicative of cumulative entrainment, also increased with step size for cases sharing the same initial $D/H$ (cf. same colours across panels in Fig. 6).

Entrainment was inherently unsteady in all experiments. In all cases, $E$ decreased on

average downstream, consistent with observations over both flat [23, 31] and rough [17] bottoms. The magnitude of instantaneous $E$ agreed with previously reported values [23, 16, 31]. Entrainment magnitude and variability were smallest on the uniform slope and increased with step size. Nearly periodic entrainment peaks occurred as the current traversed the step treads, with minima over the risers. This pattern was especially pronounced in the larger-step configurations, where the number of entrainment peaks corresponded to the number of steps. For smaller steps, entrainment varied more smoothly, approaching the uniform-slope behavior. Across all topographies, deeper currents exhibited higher entrainment, a result discussed further in Section 4.

Overall, entrainment peaked over the treads and reached minima near the risers. The precise location of each peak varied with $D/H$ and even among steps within the same run. These differences stem from variations in local buoyancy and current trajectory, which affect where the current impacts the tread. Upon impingement, the dense fluid entrains the ambient fluid trapped within the step cavity, generating strong convective mixing that increases the volume of the current. This locally enhanced mixing compensates for the concurrent acceleration that would otherwise reduce $E$. Conversely, right upstream of the riser, the current tends to accelerate, increasing $U_f$ and lowering $E$.

### 3.3 Bulk entrainment model

Both methods for estimating entrainment produced consistent trends of bulk entrainment with the relative step submergence (Fig. 7a). For a given $a/(D/2)$, deeper currents exhibited larger entrainment values, a result discussed further in Section 4.

Increasing the step size exerted two opposing effects on entrainment. On one hand, larger steps reduced front velocity and thus the bulk Froude number $Fr_s$ (Fig. 7b), which would normally decrease $E$. On the other hand, the enhanced turbulence over steps promoted greater mixing and entrainment. The combined influence is captured in the dependence of $E$ on the relative submergence $a/(D/2)$ (Fig. 7a). For $a/(D/2) \lesssim 1$, entrainment was similar to that on the uniform slope ($E/E_{slope} \sim 1$). For $a/(D/2) \gtrsim 1$, $E/E_{slope}$ increased markedly, indicating that when steps protrude above the current depth, turbulence enhancement outweighs the speed reduction. Conversely, when steps are fully submerged, the reduction in flow velocity can offset or exceed the added mixing.

Based on these observations, a modified parameterization for the entrainment coefficient is proposed to account for the effects of stepped topography:

$$\begin{cases} \dfrac{E}{E_{slope}} = 1, & Fr\dfrac{a}{D/2} \le 0.5 \\ \dfrac{E}{E_{slope}} = \dfrac{1}{3} + \dfrac{4}{3} Fr\dfrac{a}{D/2}, & Fr\dfrac{a}{D/2} > 0.5. \end{cases} \tag{15}$$

## 4 Discussion

### 4.1 Synthesis of stepped topography effects

The presence of topographic steps modifies gravity current dynamics in three principal ways: it reduces the current speed, enhances the turbulent mixing that drives ambient-

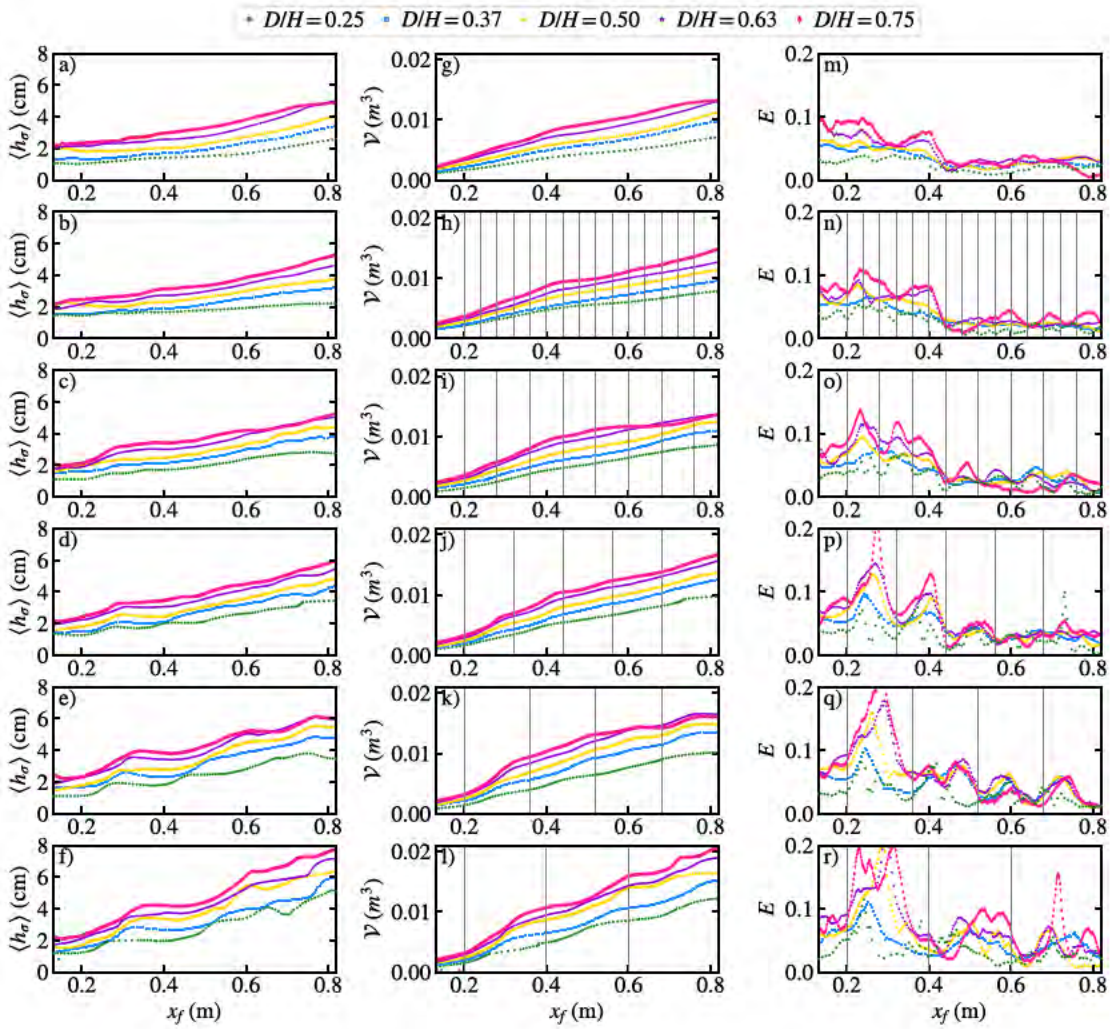


Figure 6: Time series of (a–f) bulk height $\langle h_\sigma \rangle$, (g-l) volume $\mathcal{V}$, and (m-r) entrainment $E$ for all experiments. Each panel corresponds to a topography: (a,g,m) uniform slope $a_0$, (b,h,n) $a_1 = 2$ cm, (c,i,o) $a_2 = 4$ cm, (d,j,p) $a_3 = 6$ cm, (e,k,q) $a_4 = 8$ cm, and (f,l,r) $a_5 = 10$ cm. Grey lines indicate the vertical face of each step; the downslope region begins at $x_f = 0.2$ m.

fluid entrainment, and introduces a new mechanism for buoyancy-flux detrainment from the current head.

The reduction in current speed and the enhanced mixing observed here are consistent with previous numerical sensitivity studies, which found that z-level ocean models tend to predict deeper and slower gravity currents than terrain-following models under comparable conditions [1, 11]. These effects arise from increased vertical mixing and momentum loss over stepped or z-grid discretized bathymetry. However, the buoyancy-flux detrainment identified in this study represents, to our knowledge, a novel mechanism not previously

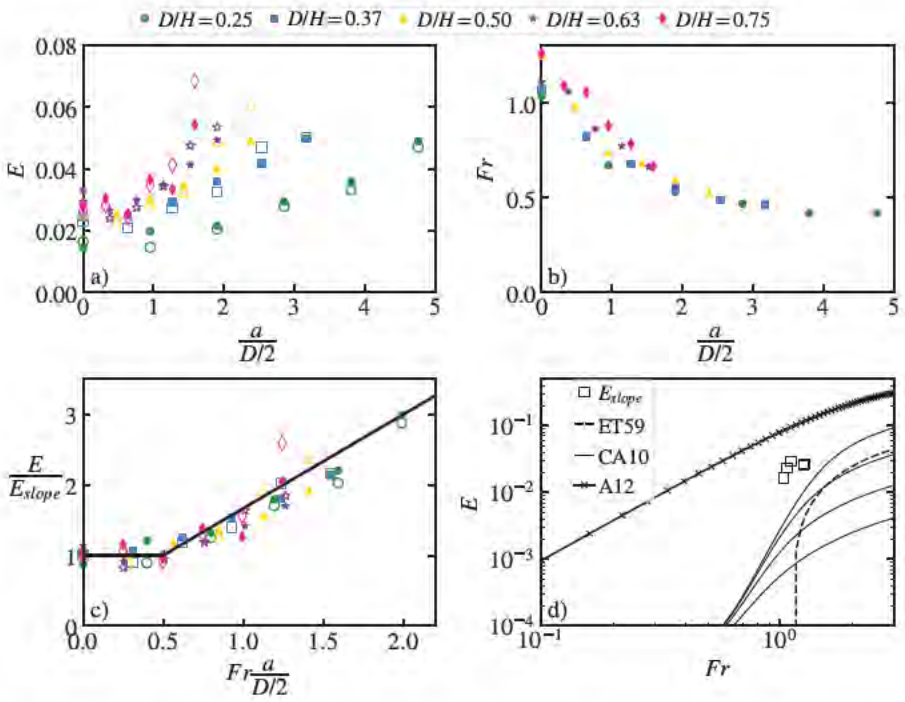


Figure 7: (a) Entrainment $E$ and (b) Froude number $Fr$ versus relative submergence $(a/(D/2))$. (c) Normalized entrainment $(E/E_{slope})$ versus $Fra/(D/2)$. (d) Entrainment over a uniform slope versus $Fr$. Solid and open symbols in (a,c) correspond to estimates from methods 1 and 2, respectively. ET59: Ellison & Turner [9], CA10: Cenedese & Adduce [6] for $Re$ =10, 100, 1000, and 10000, A12: Adduce et al. [2].

described in the literature.

In the presence of steps, as the dense fluid collapses within each step, it induces convective mixing with the underlying ambient water, but a fraction of the dense volume remains behind as the head continues downstream (Fig. 4f,i,l). This process constitutes a localized detrainment of buoyancy from the head into the step cavities. Conceptually, this mechanism is analogous to the "peeling" detrainment described in continuously stratified ambient environments [13], where fluid from the upper boundary of a gravity current continuously detaches and mixes with the surrounding fluid across a range of depths. In contrast, the detrainment observed here occurs intermittently through the lower boundary of the current, peaking at the step treads.

The entrainment analysis indicates that, for the same relative submergence $a/(D/2)$, the entrainment coefficient $E$ tends to be lower in shallower currents (smaller $D/H$) (see Fig. 6a). Part of this dependence can be attributed to the lower bulk Froude number $Fr_s$ for the shallower currents; however, the variation in $Fr_s$ across different $D/H$ values becomes relatively minor for large $a/(D/2)$ (see Fig. 6b). A more substantial contribution likely arises from the detrainment mechanism described above. As the step cavities increase in size, they can retain more dense fluid, effectively removing buoyant volume from the head and competing with the entrainment process.

A simple volume comparison underscores the significance of this effect. For the smallest steps ($a_1$), the total steps cavity volume $\mathcal{V}_{steps} = 0.0018$ m$^3$ represents roughly 75% and 25% of the initially released volume for the shallowest and deepest currents, respectively. For the largest steps ($a_5$), $\mathcal{V}_{steps} = 0.009$ m$^3$, which exceeds the released volume by factors of 3.75 and 1.25, respectively. Thus, the effective storage volume introduced by the steps is dynamically significant. Because shallower currents contain less total volume, their mass balance within the head is more sensitive to losses via detrainment into the step cavities. This explains why, for equivalent submergence $a/(D/2)$, entrainment is consistently lower in shallower cases.

The detrainment can thus be viewed as a buoyancy flux divergence between the head and the underlying steps, with potential implications for the long-term evolution and depositional behavior of gravity currents over complex bathymetry. To capture this exchange process, a modified shallow-water framework is proposed below.

### 4.2 Shallow water model

A one-dimensional shallow-water model is developed to describe the propagation of gravity currents over stepped topography. The effect of the steps is represented by a buoyancy exchange between the downslope current and the fluid retained within the step cavities, idealized as a secondary "box" whose buoyancy evolves in time. By incorporating this exchange, the model accounts for both entrainment from the ambient and detrainment into the step cavities. The governing shallow-water equations [29] for conservation of mass, buoyancy, and momentum are modified as follows:

$$\frac{\partial h}{\partial t} + \frac{\partial}{\partial s}(hu) = E(\mathcal{L}, Fr)u, \tag{16}$$

$$\frac{\partial b}{\partial t} + \frac{\partial}{\partial s}(bu) = \beta\left(\frac{b_s}{\mathcal{L}} - \frac{b}{h}\right)u, \tag{17}$$

$$\frac{\partial b_s}{\partial t} = -\beta\left(\frac{b_s}{\mathcal{L}} - \frac{b}{h}\right)u, \tag{18}$$

$$\frac{\partial}{\partial t}(uh) + \frac{\partial}{\partial s}\left(u^2 h + \frac{1}{2}bh\cos\theta\right) = b\sin\theta - C_D\frac{\mathcal{L}}{h}u^2. \tag{19}$$

Here, $b = g'h$ is the buoyancy, and the subscript $s$ denotes the fluid retained within the fictitious "step box" of effective height

$$\mathcal{L} = \frac{ab}{\sqrt{a^2 + b^2}}, \tag{20}$$

where $a$ and $b$ are the riser and tread dimensions of the step, respectively. The entrainment coefficient $E(\mathcal{L}, Fr)$ follows the parameterization introduced in Section 3.3, and the coefficients $\beta$ (exchange rate) and $C_D$ (drag coefficient) are calibration parameters that can be determined empirically for each configuration.

This formulation explicitly couples entrainment and detrainment processes, enabling the model to predict the evolution of gravity currents interacting with stepped topography.

Future work will focus on validating the model and exploring the parameter space of $\beta$, $E$ and $\mathcal{L}$.

## 5 Conclusions and Future Work

This study investigated the influence of stepped topographies on gravity current dynamics using partial lock-exchange laboratory experiments. The effects of step size and initial current height on propagation speed, entrainment, and dilution were systematically explored.

Three principal impacts of stepped topography on gravity currents were identified:

- A reduction in current speed with increasing step height.
- Enhanced mixing and entrainment of ambient fluid as step size increases.
- Increased detrainment of buoyancy into the step cavities for larger steps.

These mechanisms collectively shape the evolution and fate of gravity currents over complex topography. To capture these effects, a simplified one-dimensional shallow-water model was proposed, incorporating a buoyancy-flux exchange between the current head and the step cavities. Additionally, a new parameterization of the bulk entrainment coefficient was introduced to account for the influence of stepped topography.

Future work should focus on experimental and numerical validation of the proposed shallow-water model and entrainment parameterization, and on exploring their applicability across a broader range of flow conditions and step geometries.

## 6 Acknowledgements

This project was proposed and advised by Claudia Cenedese, Jim McElwaine and Bruce Sutherland. It was a great pleasure to work with them over the summer. I thank Anders Jensen for his valuable help with building the experimental setup. I also want to thank this summer's directors, P. Garaud and D. Goluskin, and the GFD Staff, J. Hildebrandt and J. Fields, for all their support. To the fellows, thank you for all the good times and for making this summer so special.

## References

[1] A. Adcroft, C. Hill, and J. Marshall, *Representation of topography by shaved cells in a height coordinate ocean model*, Monthly Weather Review, (1997), pp. 2293–2315.

[2] C. Adduce, G. Sciortino, and S. Proietti, *Gravity currents produced by lock exchanges: experiments and simulations with a two-layer shallow-water model with entrainment*, Journal of Hydraulic Engineering, 138 (2012), pp. 111–121.

[3] S. L. Bardoel, S. Cheng, L. P. Chamorro, and H. J. Fernando, *Gravity currents past thin two-dimensional obstacles*, Journal of Fluid Mechanics, 1012 (2025), p. A15.

[4] M. J. Cartigny, D. Ventra, G. Postma, and J. H. van Den Berg, *Morphodynamics and sedimentary structures of bedforms under supercritical-flow conditions: new insights from flume experiments*, Sedimentology, 61 (2014), pp. 712–748.

[5] C. Cenedese, *The entrainment hypothesis–80 years old and still going strong*, Journal of Fluid Mechanics, 1000 (2024), p. F2.

[6] C. Cenedese and C. Adduce, *A new parameterization for entrainment in overflows*, Journal of Physical Oceanography, 40 (2010), pp. 1835–1850.

[7] C. Cenedese and S. Dalziel, *Concentration and depth fields determined by the light transmitted through a dyed solution*, in Proceedings of the 8th International Symposium on Flow Visualization, vol. 8, 1998, pp. 1–37.

[8] C. Cenedese, R. Nokes, and J. Hyatt, *Lock-exchange gravity currents over rough bottoms*, Environmental Fluid Mechanics, 18 (2018), pp. 59–73.

[9] T. Ellison and J. Turner, *Turbulent entrainment in stratified flows*, Journal of Fluid Mechanics, 6 (1959), pp. 423–448.

[10] R. G. Englert, A. J. Vellinga, M. J. Cartigny, M. A. Clare, J. T. Eggenhuisen, and S. M. Hubbard, *Controls on upstream-migrating bed forms in sandy submarine channels*, Geology, 51 (2023), pp. 1137–1142.

[11] T. Ezer and G. L. Mellor, *A generalized coordinate ocean model and a comparison of the bottom boundary layer dynamics in terrain-following and in z-level grids*, Ocean Modelling, 6 (2004), pp. 379–403.

[12] A. J. Hogg and E. Skevington, *The motion of gravity currents that simultaneously flow on and drain from a step*, in 7th IAHR Europe Congress, 2022.

[13] C. A. Hogg, S. B. Dalziel, H. E. Huppert, and J. Imberger, *Inclined gravity currents filling basins: the impact of peeling detrainment on transport and vertical structure*, Journal of Fluid Mechanics, 820 (2017), pp. 400–423.

[14] J. E. Hughes Clarke, *First wide-angle view of channelized turbidity currents links migrating cyclic steps to flow characteristics*, Nature communications, 7 (2016), p. 11896.

[15] H. E. Huppert and J. E. Simpson, *The slumping of gravity currents*, Journal of Fluid Mechanics, 99 (1980), pp. 785–799.

[16] M. Maggi, C. Adduce, and G. Lane-Serff, *Gravity currents interacting with slopes and overhangs*, Advances in Water Resources, 171 (2023), p. 104339.

[17] M. Maggi, G. Di Lollo, and C. Adduce, *Dynamics and mixing of gravity currents over an array of cylindrical obstacles*, Physics of Fluids, 37 (2025).

[18] T. Maxworthy and R. Nokes, *Experiments on gravity currents propagating down slopes. part 1. the release of a fixed volume of heavy fluid from an enclosed lock into an open channel*, Journal of Fluid Mechanics, 584 (2007), pp. 433–453.

[19] A. Meredith, C. McConnochie, R. Nokes, and C. Cenedese, *Transient behavior of through-flowing gravity currents interacting with a roughness array*, Physical Review Fluids, 7 (2022), p. 063802.

[20] B. R. Morton, G. I. Taylor, and J. S. Turner, *Turbulent gravitational convection from maintained and instantaneous sources*, Proceedings of the Royal Society of London. Series A. Mathematical and Physical Sciences, 234 (1956), pp. 1–23.

[21] M.-E. Negretti, J.-B. Flor, and E. J. Hopfinger, *Development of gravity currents on rapidly changing slopes*, Journal of Fluid Mechanics, 833 (2017), pp. 70–97.

[22] M. Nicholson and M. R. Flynn, *Gravity current flow over sinusoidal topography in a two-layer ambient*, Physics of Fluids, 27 (2015).

[23] L. Ottolenghi, C. Adduce, R. Inghilesi, V. Armenio, and F. Roman, *Entrainment and mixing in unsteady gravity currents*, Journal of Hydraulic Research, 54 (2016), pp. 541–557.

[24] L. Ottolenghi, C. Cenedese, and C. Adduce, *Entrainment in a dense current flowing down a rough sloping bottom in a rotating fluid*, Journal of Physical Oceanography, 47 (2017), pp. 485–498.

[25] J. W. Rottman and J. E. Simpson, *Gravity currents produced by instantaneous releases of a heavy fluid in a rectangular channel*, Journal of Fluid Mechanics, 135 (1983), pp. 95–110.

[26] J. O. Shin, S. Dalziel, and P. Linden, *Gravity currents produced by lock exchange*, Journal of Fluid Mechanics, 521 (2004), pp. 1–34.

[27] J. E. Simpson, *Gravity currents in the laboratory, atmosphere, and ocean*, Annual review of fluid mechanics, 14 (1982), pp. 213–234.

[28] E. W. Skevington and A. J. Hogg, *Gravity current escape from a topographic depression*, Physical Review Fluids, 9 (2024), p. 014802.

[29] M. Ungarish, *On a similarity solution for lock-release gravity currents affected by slope, drag and entrainment*, Journal of Fluid Mechanics, 990 (2024), p. R3.

[30] J. Zhou and S. K. Venayagamoorthy, *Impact of ambient stable stratification on gravity currents propagating over a submerged canopy*, Journal of Fluid Mechanics, 898 (2020), p. A15.

[31] R. Zhu, Z. He, and E. Meiburg, *Mixing, entrainment and energetics of gravity currents released from two-layer stratified locks*, Journal of Fluid Mechanics, 960 (2023), p. A1.

# Quartic Lyapunov Functionals for 2-D Couette Flow

David Darrow

August 21, 2025

**Abstract**

The classic approach to proving global stability in fluid flows is the *energy method* of Reynolds [24] and Orr [21]: if the fluctuation energy $E$ can be shown to always monotonically decay, it follows that all initial conditions must return to the laminar state $E = 0$. However, the energy method often yields very conservative conditions for global stability to hold, predicting loss of stability much earlier than observed in practice. The recent work of Goulart and Chernyshenko [8], Huang et al. [11], and Fuentes et al. [6] has provided the first approach to prove global stability beyond the limits of the energy method, employing a numerical *sum-of-squares* algorithm to identify Lyapunov functions quartic in the velocity field. Although the sum-of-squares method is an important milestone in global stability analysis, it is a costly black-box solution to the problem, and it offers limited insight into how one might prove global stability more generally.

Inspired by sum-of-squares results, we propose a simpler, quasi-analytical alternative. We focus here on 2-D plane Couette flow, where the energy method guarantees stability only for Reynolds numbers $Re < 177.2$ [21] but numerical evidence suggests global stability for all $Re > 0$. For this system, we identify a family of quartic Lyapunov functions with four total terms and with three free parameters to be chosen according to the system geometry. We use it to verify global stability for $Re = 195.8$ at the box length $L = 1.659$ (which minimizes $Re_E$), and we explain—mathematically and physically—how our Lyapunov function is able to control the transient energy growth that arises when $Re > Re_E$. Our work offers a first step toward a more transparent, flexible approach to global stability beyond the energy method.

## 1 Introduction

Given a dynamical system $\dot{x} = f(x)$ on a manifold $\mathcal{M}$, one says that a stationary state $x_*$ is *(asymptotically) stable* if there is some neighborhood $U \subset \mathcal{M}$ of $x_*$ such that any initial condition $x_0 \in U$ converges to $x_*$ over time. Various mathematical tools exist to investigate asymptotic stability, depending on what one wants to say about the basin of attraction $U$.

One limit of this question is *local stability*: is a given state stable under sufficiently small perturbations, or equivalently, does there exist *any* neighborhood $U$ for which asymptotic stability holds? In many cases, this question can be answered using tools of linear algebra. The state $x_*$ is said to be *linearly stable* (and thus locally stable, for well-behaved systems[1])

[1]Examples include any dynamical systems in finite dimensions with $C^1$ coefficients, and semi-linear parabolic dynamical systems on Banach spaces with Lipschitz coefficients [10].

if the local linear approximation $\delta x \mapsto \nabla f(x_*) \cdot \delta x$ carries eigenvalues of strictly negative real part. Linear stability analysis can provide important insight into the local behavior of a dynamical system, both in fluid mechanics [3] and beyond [1]. However, it yields no information about the global behavior of a fluid flow, and it offers no indication of what perturbations are 'sufficiently small' to be well-approximated by a linearized system. For instance, 3-D plane Couette flow, Pouiseuille flow, and pipe flow all support sustained turbulence at sufficiently large Reynolds numbers $Re \gg 1$, but the laminar states of all three are always linearly stable [3].

The opposite limit is *global stability*, which addresses these concerns: does every initial condition return to a given state, or equivalently, do we have $U = \mathcal{M}$? Unfortunately, unlike the case of local stability, there are limited tools available to prove the global stability of a given system [26]. Until recently, the only approach available (to the authors' knowledge) was the *energy method* of Reynolds [24] and Orr [21], and variants thereof. The energy method is carried out as follows. Consider the following incompressible Navier–Stokes equations in a domain $\Omega \subset \mathbb{R}^d$, $d \in \{2, 3\}$:

$$\mathbf{u}_t + (\mathbf{u} + \mathbf{U}) \cdot \nabla(\mathbf{u} + \mathbf{U}) = -\nabla p + \nu \nabla^2 \mathbf{u}, \qquad \nabla \cdot \mathbf{u} = 0, \tag{1}$$

where $\mathbf{U}$ is a fixed base state and $\nu$ is the dimensionless viscosity of the fluid; we employ $\nu$ in place of the Reynolds number $Re = 1/\nu$ to avoid confusion with the real part $\mathrm{Re}(z)$ of a complex number $z$. We also suppose that the velocity field $\mathbf{u}$ satisfies either no-slip, no-stress, or periodic boundary conditions[2] on any boundaries appearing in the domain, to avoid boundary terms arising in volume integrals.

The (fluctuation) energy of the flow is defined by

$$E = \frac{1}{2}\|\mathbf{u}\|^2 = \frac{1}{2}\int |\mathbf{u}|^2,$$

and—writing $\langle a, b\rangle = \int ab$ for the real inner product—its time derivative reads

$$\dot{E} = \langle \mathbf{u}, \mathbf{u}_t\rangle = \langle \mathbf{u}, -(\mathbf{u} + \mathbf{U}) \cdot \nabla(\mathbf{u} + \mathbf{U}) - \nabla p + \nu \nabla^2 \mathbf{u} + \mathbf{f}\rangle = -\langle \mathbf{u}, \mathbf{u} \cdot \nabla \mathbf{U}\rangle - \nu \|\nabla \mathbf{u}\|^2.$$

Notably, the nonlinear advection and pressure terms vanish in $\dot{E}$; physically, these terms act to move energy about the domain, but not to change its total. Symmetrizing over the first term above, one can write $\dot{E}$ in terms of the *energy stability operator* $\mathcal{E}$:

$$\dot{E} = \langle \mathbf{u}, \mathcal{E}\mathbf{u}\rangle, \qquad \mathcal{E}\mathbf{u} = -\mathbf{T} \cdot \mathbf{u} + \nu \nabla^2 \mathbf{u},$$

where $\mathbf{T} = \frac{1}{2}(\nabla \mathbf{U} + \nabla \mathbf{U}^T)$ is the background stress tensor. So long as $\nabla \mathbf{U}$ is bounded, there exists a (system-dependent) *energy Reynolds number* $Re_E$ such that, for any $\nu > 1/Re_E$, the spectrum of $\mathcal{E}$ is strictly negative. Fix $Re < Re_E$ and let $\lambda_1 = \max \operatorname{spec} \mathcal{E} < 0$. Then

$$\dot{E} \le \lambda_1 \|\mathbf{u}\|^2 = 2\lambda_1 E,$$

and Grönwall's inequality [9] implies global stability. In all, the energy method implies that

$$Re_G \ge Re_E, \tag{2}$$

[2]More rigorously, we suppose that $\Omega$ is a compact domain in $\mathbb{R}^{d-k} \times \mathbb{T}^k$ for some $0 \le k \le d$, where $\mathbb{T}^k$ is the $k$-dimensional torus.

where $Re_G$ is the minimum Reynolds number at which the system loses global stability.

Unfortunately, for many systems, the energy method appears to give a very weak bound on $Re_G$. In 3-D plane Couette flow, for instance, the energy method yields $Re_E = 82.6$, but sustained non-laminar solutions have been observed only for $Re \gtrsim 500$ [18]. The situation for other shear flows is similar [30, 28, 29]; strikingly, in 2-D plane Couette flow, the energy method yields $Re_E = 177.2$, but numerical investigations have failed to find sustained non-laminar solutions at *any* Reynolds number [22, 25, 4].

One might hope to improve upon the energy method by exchanging the energy with a different Lyapunov function of the flow:

**Definition 1.1.** A continuous functional $V : L^2(\Omega;\mathbb{R}) \to \mathbb{R}$ is a (coercive) *Lyapunov function* for the system (1) if it satisfies the following properties:

1. $V[0] = 0$.
2. If $\mathbf{u} \neq 0$, then $V[\mathbf{u}] > 0$ and
$$\dot{V}[\mathbf{u}] = \left\langle \frac{\delta V[\mathbf{u}]}{\delta \mathbf{u}}, \mathbf{u}_t \right\rangle = \left\langle \frac{\delta V[\mathbf{u}]}{\delta \mathbf{u}}, -(\mathbf{u}+\mathbf{U})\cdot\nabla(\mathbf{u}+\mathbf{U}) - \nabla p + \nu\nabla^2\mathbf{u} \right\rangle < 0.$$
3. Given any sequence $\mathbf{u}_i$ with $\|\mathbf{u}_i\| \to \infty$, we have $V[\mathbf{u}_i] \to \infty$.
4. For any $R > 0$, there exists an $\varepsilon > 0$ such that, if $\|\mathbf{u}\| > R$, then $\dot{V}[\mathbf{u}] < -\varepsilon$.

If a Lyapunov function exists for our system at a given Reynolds number, it follows that the system is globally stable [16]; for instance, the energy method amounts to selecting $V = E$, which is a Lyapunov function whenever $Re < Re_E$.

Until recently, however, the energy was often the *only* functional for which one could feasibly prove the conditions of Definition 1.1. The key element that makes the energy method tractable is that both $E[\mathbf{u}]$ and $\dot{E}[\mathbf{u}]$ are quadratic in $\mathbf{u}$, which follows from the fact that $E$ is conserved by nonlinear advection. Extremizing $E$ and $\dot{E}$ thus reduces to a linear eigenproblem, which can be solved numerically (if not analytically) to verify that $E[\mathbf{u}] > 0$ and $\dot{E}[\mathbf{u}] < 0$ for all $\mathbf{u} \neq 0$. In particular problems—namely, if specific components of the energy are individually conserved—one can apply the same analysis to a *reweighted* energy to find stronger bounds on $Re_G$ [13, 7, 27] or to estimate the basin of attraction about the laminar state [14]. Likewise, in 2-D flows under stress-free boundary conditions, vorticity gives rise to a distinct family of Euler invariants (such as the enstrophy) that can be used likewise [12]. Enstrophy and reweighted energy functionals carry similar limitations as the energy, and we count such approaches as examples of the 'energy method' below.

To move beyond the energy method, then, one has to make use of a non-quadratic functional $V[\mathbf{u}]$. Finding global extrema of a non-quadratic functional of $\mathbf{u}$ is not generally tractable, even numerically, so it is difficult to verify that a given non-quadratic functional satisfies $\dot{V}[\mathbf{u}] < 0$. As such, the energy method has generally remained the only feasible route to proving global stability.

Recently, Goulart and Chernyshenko [8] proposed an approach to identify a non-quadratic Lyapunov function by employing a finite-dimensional *sum-of-squares* procedure. In short,

they fix a finite set $(\mathbf{u}_i, \lambda_i)$ of real eigenmodes of $\mathcal{E}$, and they decompose

$$\mathbf{u}(x,t) = \sum_{i=1}^{N} a_i(t)\mathbf{u}_i(x) + \mathbf{v}(x,t).$$

Writing $q = \|\mathbf{v}\|$, they take an ansatz of the form

$$V[\mathbf{u}] = E[\mathbf{u}]^2 + P(a_1, ..., a_N, q), \tag{3}$$

where $P$ is a real, cubic polynomial. Indeed, in any system for which $E[\mathbf{u}]$ is the only quadratic Lyapunov function for $Re < Re_E$, it is clear that $E[\mathbf{u}]^2$ must be the leading term of any quartic Lyapunov function for $Re > Re_E$, up to scaling. Now, the time derivative of $V$ is given by

$$\dot{V}[u] = 2E[\mathbf{u}]\dot{E}[\mathbf{u}] + \frac{\partial P}{\partial a_i}\dot{a}_i + \frac{\partial P}{\partial q}\dot{q},$$

which generally depends on $a_i$ and all (i.e., infinitely many) components of $\mathbf{v}$. Through extensive analysis, one attempts to find a bound of the form

$$\dot{P}(a_1, ..., a_N, \mathbf{v}) \leq Q(a_1, ..., a_N, q) \tag{4}$$

for the system under consideration, where $Q$ is a real, quartic polynomial. At this point, global stability follows if one can solve the finite-dimensional problem

$$\begin{aligned} V[\mathbf{u}] &= \frac{1}{4}\Big(\sum a_i^2 + q^2\Big)^2 + P(a_1, ..., a_N, q) > 0, \\ \dot{V}[\mathbf{u}] &\leq \frac{1}{2}\Big(\sum \lambda_i a_i^2 + \lambda_{N+1} q^2\Big)\Big(\sum a_i^2 + q^2\Big) + Q(a_1, ..., a_N, q) < 0, \end{aligned} \tag{5}$$

for $\mathbf{u} \neq 0$, writing $\lambda_{N+1}$ for the largest eigenvalue of $\mathcal{E}$ not contained in $\{\lambda_1, ..., \lambda_N\}$.

The problem (5) remains quite difficult—in fact, it has been shown that verifying the positivity of a generic quartic polynomial in $N$ variables is NP-hard [17]. For relatively small $N$, however, a practical solution is given by sum-of-squares methods. Such algorithms attempt to find a sum-of-squares decomposition of a given polynomial $p(x_1, ..., x_N)$, as

$$p(x_1, ..., x_N) = \sum_{j=1}^{M} \big(p_j(x_1, ..., x_N)\big)^2,$$

and thus verify that the polynomial is non-negative. This restricted problem can be seen as an example of a *semi-definite program*, for which a variety of practical, polynomial-time algorithms exist [23].

The sum-of-squares approach has yielded promising results thus far. It was successfully applied by Huang et al. [11] to find a Lyapunov function of the form (3) for doubly-periodic rotating Couette flow, a system where a reweighted energy method already gives a sharp bound on $Re_G$. It was also applied by Fuentes et al. [6] to 2-D plane Couette flow, yielding the first proof of global stability for any system beyond $Re_E$.

Although these results represent an important milestone in global stability analysis, there are several obstacles to using the sum-of-squares method as a general-purpose approach to global stability. The sum-of-squares calculation is expensive, for one, and must

be repeated in full for each new domain size and candidate Reynolds number. Consequently, there is currently no way to leverage this approach to verify global stability over a continuous parameter range. Computation time also grows rapidly with the number of degrees of freedom $N$, and the required value of $N$ grows rapidly with the desired bound on $Re_G$—as such, only mild improvements over the energy method have thus far been possible. Perhaps most importantly, the sum-of-squares algorithm is largely a black-box approach to the problem. Although the resulting functional $V[\mathbf{u}]$ is certain to be a workable Lyapunov function, both $V[\mathbf{u}]$ and $Q$ generally contain $O(N^3)$ distinct monomial terms, and it is difficult to interpret either object mathematically or physically. Furthermore, additional sum-of-squares calculations are hidden in the bound (4), so the relation between $Q$ and $\dot{V}[\mathbf{u}]$ is similarly obfuscated.

We here introduce a quasi-analytical proof of global stability for 2-D Couette flow beyond the energy Reynolds number. Taking inspiration from the sum-of-squares approach, we introduce a family of candidate Lyapunov functions of the form

$$V[\mathbf{u}] = E[\mathbf{u}]^2 + 2\gamma_0 E[\mathbf{u}] \int \mathbf{u}\cdot\mathbf{u}_0 + \gamma_1 E[\mathbf{u}] + 2\alpha \,\mathrm{Re}\left[\int \mathbf{u}\cdot\overline{\mathbf{u}_1}\int \mathbf{u}\cdot\mathbf{u}_2\right], \tag{6}$$

denoting by $\mathrm{Re}[z]$ the real part of a complex number $z$; here, $\mathbf{u}_0$, $\mathbf{u}_1$, and $\mathbf{u}_2$ are fixed (complex) energy eigenmodes and $\gamma_0, \gamma_1, \alpha \in \mathbb{R}$ are parameters to be chosen based on the box length $L$ and the Reynolds number $Re$. For instance, at the box length $L = 1.659$ at which Orr [21] showed $Re_E = 177.2$, we show that (6) is a Lyapunov functional for $Re = 195.8$ with

$$\gamma_0 = 0.0456, \qquad \gamma_1 = 0.00606, \qquad \alpha = 0.000469, \tag{7}$$

and where $\mathbf{u}_i$ are fixed eigenmodes of $\mathcal{E}$. Moreover, we offer a simple physical explanation for how the four terms of our Lyapunov function conspire to control the transient energy growth that arises in the system. In short, the added cubic term accounts for the reservoir of energy in the interaction between the background flow $\mathbf{U}$ and the fluctuation $\mathbf{u}$, and the added quadratic term leverages the linear stability of the system to form a reweighted energy that monotonically decays under small perturbations.

Although formulated for 2-D Couette flow at moderate Reynolds numbers, the results presented here offer a first step towards a flexible, analytical route to global stability more broadly. On one hand, we believe that our results will allow for an improved lower bound on $Re_G$ in 2-D Couette flow for a continuum of geometries, and more generally, that the design of our Lyapunov function can be adapted to control transient energy growth in more general systems; for instance, application to 2-D Poiseuille flow requires only minimal changes. On the other hand, our results should lead to substantial computational improvements in the sum-of-squares approach to global stability, by greatly reducing the space of candidate Lyapunov functions and simplifying the polynomial bound (4).

We review the setup of 2-D plane Couette flow in Section 2, and introduce key notation. In Section 3, we prove a simple lemma restricting the space of candidate Lyapunov functions, and we show how (6) arises as a natural ansatz for our solution. In Section 4, we prove an analytical bound of the form (4) for our system, and we use it to prove global stability beyond $Re_E$. In Section 5, we offer a clear, physical interpretation of how our Lyapunov function controls transient energy growth. Finally, in Section A, we introduce a simple toy model to illustrate how quartic Lyapunov functions can outperform the energy method.

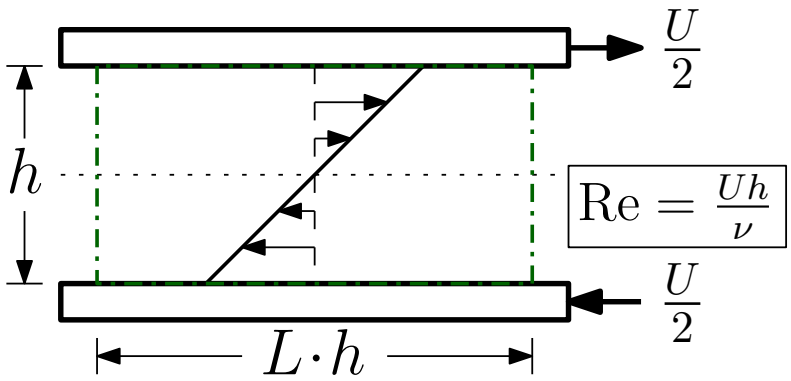


Figure 1: A schematic of 2-D plane Couette flow, reproduced from Fuentes et al. [6] with permission. The flow is bounded between two parallel walls, moving in opposite directions with velocity $U/2$ and thus inducing a background shear profile $\mathbf{U} = (Uy/h)\hat{x}$. We scale coordinates such that $h = U = 1$ and $Re = 1/\nu$.

## 2 Preliminaries

We consider the problem of 2-D (plane) Couette flow, illustrated in Fig. 1. We write coordinates

$$(x, y) \in [-L/2, L/2] \times [-1/2, 1/2],$$

with $x$ the (periodic) streamwise direction and $y$ the wall-normal direction. The base flow is a linear shear profile, $\mathbf{U} = y\hat{x}$, and the fluctuating flow $\mathbf{u}$ evolves according to

$$\mathbf{u}_t + (\mathbf{u} + \mathbf{U}) \cdot \nabla (\mathbf{u} + \mathbf{U}) = -\nabla p + \nu \nabla^2 \mathbf{u}, \qquad \nabla \cdot \mathbf{u} = 0, \qquad \mathbf{u}|_{y=\pm 1} = 0.$$

Here, we write $\nu = 1/Re$ for the dimensionless viscosity of the flow; this notation helps mitigate confusion with the 'real part' $\mathrm{Re}[z]$ of a complex number $z$. It is instructive to write the problem in a streamfunction formulation, with

$$\mathbf{u} = \nabla^\perp \psi = (-\psi_y, \psi_x)$$

for a real function $\psi$. In 2-D Couette flow, the base flow corresponds to a streamfunction $\Psi = -\frac{1}{2}y^2$, and the fluctuation $\psi$ evolves according to the vorticity equations

$$\zeta_t + \{\Psi + \psi, \zeta\} = \nu \nabla^2 \zeta, \qquad \zeta = \nabla^2 \psi, \qquad \psi|_{y=\pm 1} = \psi_y|_{y=\pm 1} = 0. \tag{8}$$

We write $\{a, b\} = a_x b_y - a_y b_x$ for the Poisson bracket of two fields, and

$$\langle a, b, c \rangle \doteq \langle a, \{b, c\} \rangle = \langle \{a, b\}, c \rangle \tag{9}$$

for the corresponding triple product. As above, $\langle a, b \rangle = \int ab$ denotes the real $L^2$ inner product. We maintain the same notation for complex fields, without taking a complex conjugate of either argument; the map $\langle \cdot, \cdot \rangle$ should thus be considered as an indefinite bilinear form. As indicated, we are interested only in the space of streamfunctions with no-slip boundary conditions:

$$\mathcal{H} = \left\{ \phi \in H^1 \;\middle|\; \phi|_{y=\pm 1} = \partial_y \phi|_{y=\pm 1} = 0 \right\},$$

which we decompose along Fourier modes as

$$\mathcal{H} = \bigoplus_k \mathcal{H}_k, \qquad \mathcal{H}_k = \left\{ \phi \in \mathcal{H} \;\middle|\; \phi(x,y) = \hat{\phi}(y) e^{2\pi \mathrm{i} k x/L} \right\}.$$

We further denote the subspaces of positive and negative wavenumber as

$$\mathcal{H}_+ = \bigoplus_{k>0} \mathcal{H}_k, \qquad \mathcal{H}_- = \bigoplus_{k<0} \mathcal{H}_k,$$

so that $\mathcal{H} = \mathcal{H}_0 \oplus \mathcal{H}_+ \oplus \mathcal{H}_-$.

### Energy eigenmodes

In streamfunction notation, the energy associated to a field $\psi$ is defined to be

$$E[\psi] = \frac{1}{2}\|\nabla\psi\|^2 = \frac{1}{2}\langle \nabla\overline{\psi}, \nabla\psi \rangle.$$

Its time derivative along the flow (8) satisfies

$$\dot{E}[\psi] = \langle \psi, \mathcal{E}\psi \rangle, \qquad \mathcal{E} : \psi \mapsto -\psi_{xy} - \nu\nabla^4\psi,$$

superseding our previous notation for the energy stability operator. The operator $\mathcal{E}$ admits a basis of $\mathcal{H}$-orthogonal generalized eigenmodes $(\varphi_i, \lambda_i)$, for which

$$\mathcal{E}\varphi_i = -\lambda_i \nabla^2 \varphi_i.$$

Such a basis is known as an *energy basis* of $\mathcal{H}$, and its elements as *energy eigenmodes*. As before, there is a critical *energy Reynolds number* $Re_E$ such that, for all $Re < Re_E$, we have $\max(\lambda_i) < 0$. In general, if $\lambda_i < 0$, we say that an eigenmode is *energy stable*, and we otherwise say that it is *energy unstable*.

Since $\mathcal{E}$ commutes with the orthogonal projections $\mathcal{H} \to \mathcal{H}_k$, each eigenmode $\varphi_i$ can be chosen to be monochromatic in the streamwise direction, i.e., to lie in a particular subspace $\mathcal{H}_k$. Next, consider the real-linear map $\mathcal{R} : \psi(x,y) \mapsto \overline{\psi(-x,-y)}$, which restricts to

$$\mathcal{R} : \psi(y) e^{2\pi \mathrm{i} k x/L} \mapsto \overline{\psi(-y)} e^{2\pi \mathrm{i} k x/L}$$

on $\mathcal{H}_k$. Since $\mathcal{R}$ commutes with $\mathcal{E}$, we can simultaneously ensure that

$$\varphi_i(x,y) = \overline{\varphi_i(-x,-y)} \tag{10}$$

for any eigenmode $\varphi_i \in \mathcal{H}_\pm$ of $\mathcal{E}$, scaling by i if necessary. When $\varphi_i \in \mathcal{H}_0$, we instead choose it to be real-valued, allowing it to be odd or even (in $y$) as necessary.

### Components of the flow

For any scalar field $\xi$, we denote the component of our flow field $\phi$ along $\xi$ as

$$c_\xi = -\langle \xi, \nabla^2 \psi \rangle,$$

with time derivative

$$\dot{c}_\xi = \langle \xi, \Psi, \zeta \rangle + \langle \xi, \psi, \zeta \rangle - \nu \langle \xi, \nabla^2 \zeta \rangle = \langle \xi, \psi, \zeta \rangle + \langle \mathcal{E}\xi, \psi \rangle + \langle \Psi, \nabla \xi, \nabla \psi \rangle. \tag{11}$$

Choose an $\mathcal{H}$-orthogonal energy eigenbasis $(\varphi_i, \lambda_i)$ for $\mathcal{E}$, as above. For $\varphi_i \in \mathcal{H}_0$, we normalize as $\|\varphi_i\| = 1/\sqrt{2}$; otherwise, we normalize as $\|\varphi_i\| = 1$. Then we find

$$\psi = \sum_{\varphi_i \in \mathcal{H}_0} 2 c_i \overline{\varphi_i} + \sum_{\varphi_i \in \mathcal{H}_- \oplus \mathcal{H}_+} c_i \overline{\varphi_i} = 2 \operatorname{Re} \left[ \sum_{\varphi_i \in \mathcal{H}_0 \oplus \mathcal{H}_+} c_i \overline{\varphi_i} \right],$$

writing $c_i = c_{\varphi_i}$. The energy and its time derivative can then be expressed as follows:

$$E[\psi] = \sum_{\varphi_i \in \mathcal{H}_0 \oplus \mathcal{H}_+} |c_i|^2, \qquad \dot{E}[\psi] = \sum_{\varphi_i \in \mathcal{H}_0 \oplus \mathcal{H}_+} 2 \lambda_i |c_i|^2.$$

## 3 Restricting the Search for Lyapunov Functions

Recall that the sum-of-squares approach to global stability, introduced by Goulart and Chernyshenko [8] and carried out by Fuentes et al. [6] for 2-D Couette flow, attempts to find a cubic polynomial $P$ in $N+1$ flow variables $(a_1, ..., a_N, q)$ such that the ansatz (3) yields a Lyapunov function. A primary difficulty is that the space of candidate polynomials grows with dimension $O(N^3)$, so the resulting sum-of-squares problem is large even for relatively small $N$. The problem size is a substantial obstacle for analysis as well; even if we were to fix a set of $N+1$ flow variables, it is not clear *a priori* which of the possible quartic polynomials provides a workable ansatz for our Lyapunov function.

Here, we leverage the symmetries of 2-D Couette flow to reduce the problem size. The ansatz we arrive at will aid the analysis that follows, but—as we discuss in Section 6—such a reduction may also yield a substantial computational benefit for a sum-of-squares approach to the problem.

Recall the following classical result:

**Lemma 1.** *Suppose the dynamical system (1) is equivariant*[3] *under the continuous, unitary action of a compact group $G$ on $L^2(\Omega; \mathbb{R})$, and suppose a Lyapunov function $V$ exists in the sense of Definition 1.1. Then a Lyapunov function $V_0$ exists such that $V_0 \circ g = V_0$ for any $g \in G$.*

The lemma follows from considering the properties of the averaged functional

$$V_0[\psi] = \int_G V[g \cdot \psi] \, d\mu(g),$$

[3] A dynamical system $\dot{x} = f(x)$ on a Hilbert space $\mathcal{H}$ is *equivariant* under the action of a group $G$ if $g \cdot f(x) = f(g \cdot x)$ for all $g \in G$ and all $x \in \mathcal{H}$.

where $\mu$ is the unique normalized Haar measure on $G$ [5]. It is proved in a finite-dimensional setting, for instance, in the thesis of Oeri [19], but the infinite-dimensional proof is straightforward. In our context, this lemma can be written more explicitly as follows:

**Lemma 2.** *Fix a complete basis $\xi_{k,i} \in \mathcal{H}_k$ for each $k \in \mathbb{Z}$, where $\xi_{-k,i} = \overline{\xi_{k,i}}$ and where the $k = 0$ modes $\xi_{0,i}$ are each chosen to be even or odd. Write $a_{k,i} = a_{\xi_{k,i}}$. If a quartic Lyapunov function exists for 2-D Couette flow with a given domain length and Reynolds number, and it is non-degenerate in the sense that*

$$V[\psi] > r_1\|\nabla\psi\|^4 + r_2\|\nabla\psi\|^2$$

*for some $r_1, r_2 > 0$ and all $\psi \in \mathcal{H}$, then it can be chosen to have the form*

$$V[\psi] = F[\psi] + \sum_{\substack{\ell+m+n=0\\ i,j,k}} B_{ijk}^{\ell,m,n} a_{\ell,i}a_{m,j}a_{n,k} + \sum_{i,j,k} A_{ij}^k \overline{a_{k,i}}a_{k,j},$$

*for appropriate* real *values $B_{ijk}^{\ell,m,n}$ and $A_{ij}^k$, and where $F[\psi]$ is either the squared energy $E[\psi]^2$, the squared enstrophy $Z[\psi]^2 = \|\zeta\|^4$, the product $E[\psi]Z[\psi]$, or the hyper-enstrophy $Z_4[\psi] = \|\zeta^2\|^2$. Moreover, $A_{ij}^k$ is bounded, symmetric, and positive definite for each $k$, and $B_{ijk}^{0,m,-m}$, $A_{ij}^0$, and $B_{ijk}^{0,0,0}$ are nonzero only when the (real) modes $\xi_{0,i}$, $\xi_{0,i}\xi_{0,j}$, and $\xi_{0,i}\xi_{0,j}\xi_{0,k}$ are even in $y$, respectively.*

**Remark.** Here and below, we say that a functional $F[\psi]$ is a 'polynomial' in $\psi$ if it can be decomposed as

$$F[\psi] = F_0 + F_1[\psi] + F_2[\psi,\psi] + \cdots F_N[\psi,...,\psi]$$

for some $N \geq 0$, where $F_j$ is $j$-multilinear in each of its arguments. We say that $F$ is 'quartic' if it is a polynomial with $N = 4$.

*Proof.* There are several claims made by this theorem. First, we claim that the leading term must be given by $E^2$, $Z^2$, $EZ$, or $Z_4$. Indeed, it is clear that, to avoid $\dot{V}[\psi]$ acquiring fifth-order terms in the time derivative, any quartic term in $V[\psi]$ must be invariant under nonlinear advection, i.e., it must be an invariant of the Euler equation

$$\zeta_t + \{\psi,\zeta\} = 0, \qquad \zeta = \nabla^2\psi.$$

By considering the Hamiltonian structure of this equation, it can be shown that the only Euler invariants in our geometry are as follows [20]:

1. The energy $E = \frac{1}{2}\int |\nabla\psi|^2$.
2. The streamwise momentum $P_x = \int \psi_y$.
3. The Casimir invariants $C_f = \int f(\zeta)$, parameterized by differentiable functions $f$ of the vorticity $\zeta = \nabla^2\psi$.

Any leading term proportional to $P_x$ vanishes along a codimension-1 subspace of solutions, violating the hypothesis that $V[\psi] > r_1\|\nabla\psi\|^4$ for some $r_1 > 0$. One can similarly rule out the invariants $C_f$ with $f(\zeta) = \zeta$ or $f(\zeta) = \zeta^3$, leaving only those claimed in the lemma.

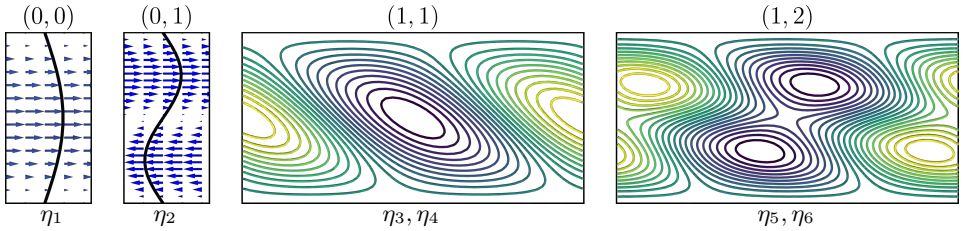


Figure 2: The six modes utilized in the simplest Lyapunov functions identified by Fuentes et al. [6] for 2-D plane Couette flow, counting the $L/2$-translates of the $(1, k)$ modes. Reproduced from Fuentes et al. with permission.

Moving on to lower-order terms, we claim that $A$ and $B$ can only couple together modes that add to zero, that their elements are real, and that $A^0_{ij}$ and $B^{0,0,0}_{ijk}$ can only couple together modes with appropriate parity. The first follows from considering Lemma 1 in light of the $S^1$ action $\phi(x, y) \mapsto \phi(x - x_0, y)$. The second follows likewise from the $\mathbb{Z}_2$ action $\phi(x, y) \mapsto \phi(-x, -y)$, noting that $a_{k,i} \mapsto \overline{a_{k,i}}$ for $k \neq 0$ under the latter action.

Third, we claim that $A^k_{ij}$ is bounded, symmetric, and positive definite for any $k$. Boundedness is a requirement for the Lyapunov function itself to be locally bounded. The Hermitian property (and thus symmetry, since all values are real) can be guaranteed without loss of generality. Positive definiteness is required in order that $V[\psi] > r_2\|\nabla\psi\|^2$ for some $r_2 > 0$. □

To narrow the space of candidate Lyapunov functions further, we proceed by investigating those found by Fuentes et al. [6]. We will use the notation $\eta_i$ for the energy eigenmodes appearing in these candidate functionals, and $a_i = a_{\eta_i}$ for the corresponding coefficients; we reserve the notation $\varphi_i$ and $c_i$ of the preceding section for the objects appearing in our final ansatz.

We parameterize energy eigenmodes by pairs $(k, n)$ of horizontal and vertical wavenumbers. The simplest Lyapunov functions identified by Fuentes et al. involve six real modes, depicted in Fig. 2:

- The $(0, 0)$ mode $\eta_1$, which is odd in the wall-normal coordinate $y$.
- The $(0, 1)$ mode $\eta_2$, which is even in $y$.
- The $(1, 1)$ mode and its $L/2$-translate, $\eta_3$ and $\eta_4$, which are energy unstable.
- The $(1, 2)$ mode and its $L/2$-translate, $\eta_5$ and $\eta_6$, which are energy stable.

In all that follows, we are interested in Reynolds numbers for which only a single mode (along with its $L/2$-translate) is energy unstable. As before, we normalize such that $\|\eta_1\| = \|\eta_2\| = 1/\sqrt{2}$ and $\|\eta_3\| = \|\eta_4\| = \|\eta_5\| = \|\eta_6\| = 1$. We decompose the streamfunction as follows:

$$\psi = \sum_{k=1}^{6} a_k \eta_k + \eta',$$

with $a_k = a_{\eta_k} \in \mathbb{R}$. Following Lemma 2, one can see that any quartic Lyapunov function depending only on $a_k$ and $\|\eta'\|$ can be written as

$$V = E^2 + a_2(w_1 E + w_2 a_1^2 + w_3 a_2^2 + B_{ij}\overline{c_i}c_j) + (w_4 E + w_5 a_1^2 + w_6 a_2^2 + A_{ij}\overline{c_i}c_j), \qquad (12)$$

where $w_k \in \mathbb{R}$ are real weights, $c_1 = a_3 + ia_4$, $c_2 = a_5 + ia_6$, and $A$ and $B$ are $2 \times 2$ Hermitian matrices. To proceed further, we note that, at a minimum, we need one off-diagonal quadratic term to ensure that $\dot{V}$ is not positive in the $\eta_{3,4}$ directions near zero, and one cubic term to ensure the same for large arguments. The simplest such ansatz compatible with (12) is as follows; we write

$$\varphi_0 = \eta_2, \qquad \varphi_1 = \frac{1}{\sqrt{2}}(\eta_3 + \mathrm{i}\eta_4), \qquad \varphi_2 = \frac{1}{\sqrt{2}}(\eta_5 + \mathrm{i}\eta_6),$$

noting that $\varphi_0 \in \mathcal{H}_0$ and $\varphi_1, \varphi_2 \in \mathcal{H}_1$, and we define

$$V[\psi] = E(E + 2\gamma_0 c_0 + \gamma_1) + A_{ij}\overline{c_i}c_j, \qquad A = \begin{pmatrix} & \alpha \\ \overline{\alpha} & \end{pmatrix}, \qquad (13)$$

where $c_i = \langle\overline{\varphi_i}, \psi\rangle$ and where $\gamma_0, \gamma_1, \alpha \in \mathbb{R}$ are free parameters. Of course, this expression is simply a restatement of the functional (6) in our refined notation. Figure 3 confirms numerically that the reduced ansatz (13) yields the same improved estimates of $Re_G$ as the full sum-of-squares algorithm employed by Fuentes et al. [6], in the six mode case.

# 4 Proving Lyapunov's Criteria

Now that we have identified the simple ansatz (13) and confirmed numerically that it yields a substantial improvement over the energy method, we aim to prove quasi-analytically that it is truly a Lyapunov function. Our proof will make use of a sum-of-squares procedure on a single polynomial in the six variables $(c_j, q_k)$, but we are working at present to replace this step with an analytic bound. Below, if $F$ and $G$ are nonlinear functionals with $F[0] = G[0] = 0$, we adopt the notation

$$F[\psi] \succ G[\psi]$$

to mean that $F[\psi] - G[\psi] > 0$ for all nonzero $\psi$. This notion reduces to positive-definiteness when both are quadratic forms.

Let $\varphi_{-1} = \overline{\varphi_1}$ and $\varphi_{-2} = \overline{\varphi_2}$, and let $\mathcal{H}_* \subset \mathcal{H}$ be the complex span of $\varphi_{\pm 1}$ and $\varphi_{\pm 2}$. We decompose the streamfunction as follows:

$$\psi(x, y, t) = 2c_0(t)\varphi_0(y) + \sum_{0<|n|\leq 2} c_n(t)\overline{\varphi_n(x, y)} + \phi_0(y, t) + \phi_1(x, y, t) + \phi_2(x, y, t),$$

where we have split the tail of $\psi$ into real components

$$\phi_0 \in \mathcal{H}_0, \qquad \phi_1 \in (\mathcal{H}_1 + \mathcal{H}_{-1}) \setminus \mathcal{H}_0, \qquad \phi_2 \in \mathcal{H} \setminus (\mathcal{H}_0 + \mathcal{H}_1 + \mathcal{H}_{-1}), \qquad (14)$$

all orthogonal to $\varphi_0 + \mathcal{H}_*$. We write

$$\psi_a = 2c_0\varphi_0 + \sum_{0<|n|\leq 2} c_n\overline{\varphi_n}, \qquad \psi_b = \phi_0 + \phi_1 + \phi_2$$

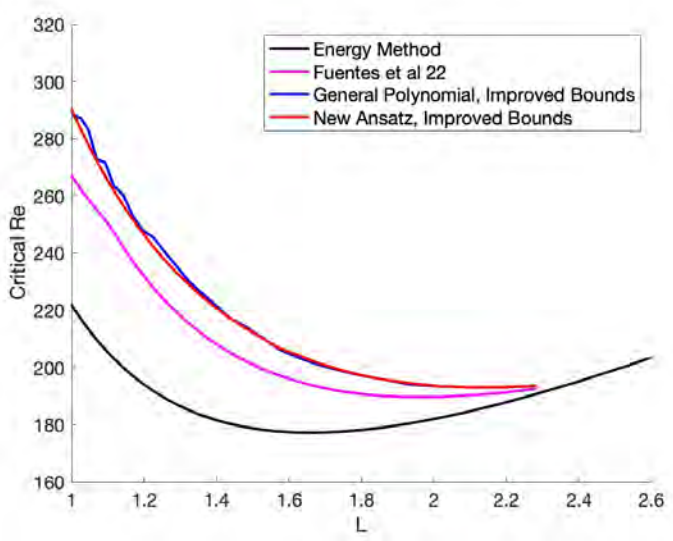


Figure 3: Comparison of improved bounds on $Re_G$ for 2-D plane Couette flow with box length $L$. The pink curve corresponds to the results reported by Fuentes et al. [6] for Lyapunov functions involving six energy modes, and the blue corresponds to the same ansatz but with tighter analytical bounds on $\dot{V}$. The red curve corresponds to the restricted ansatz (13) developed here. We see that the restricted ansatz verifies global stability at (approximately) the same Reynolds numbers as a fully generic Lyapunov function depending on the same six modes, indicating that our choice of ansatz is well justified.

so that $\psi = \psi_a + \psi_b$. With this notation, the energy can be written as

$$E[\psi] = \sum_{n=0}^{2} |c_n|^2 + \sum_{n=0}^{2} q_n^2,$$

writing $q_n = \frac{1}{2}\|\nabla\phi_n\|^2$, and its derivative satisfies

$$\dot{E}[\psi] = \sum_{n=0}^{2} 2\lambda_n |c_n|^2 + \sum_{n=0}^{2} \langle \mathcal{E}\phi_n, \phi_n\rangle \leq \sum_{n=0}^{2} 2\lambda_n |c_n|^2 + \sum_{n=0}^{2} 2\kappa_n q_n^2, \tag{15}$$

with $\kappa_n$ the leading eigenvalues of $\mathcal{E}$ in the subspaces marked out by (14).

### Positivity of the Lyapunov Function

Positivity of the Lyapunov function (13) can be guaranteed by enforcing only a simple condition on $\gamma_0$, $\gamma_1$, and $\alpha$. Indeed, we see that $V[\psi]$ can only be positive for $\psi \propto \varphi_0$ if

$$c_0^2 + 2\gamma_0 c_0 + \gamma_1 > 0$$

for all $c_0 \in \mathbb{R}$, or equivalently, if $\gamma_1 > \gamma_0^2$. In this case, we find

$$V[\psi] > (\gamma_1 - \gamma_0^2)E + A_{ij}\overline{c_i}c_j = (\gamma_1 - \gamma_0^2)\left(c_0^2 + \sum q_i^2\right) + \begin{pmatrix} c_1 \\ c_2 \end{pmatrix}^{\dagger} \begin{pmatrix} \gamma_1 - \gamma_0^2 & \alpha \\ \alpha & \gamma_1 - \gamma_0^2 \end{pmatrix} \begin{pmatrix} c_1 \\ c_2 \end{pmatrix},$$

which is necessarily positive if

$$\gamma_1 - \gamma_0^2 > |\alpha|. \tag{16}$$

Note that the requirements on the asymptotic behavior of $V$ in Definition 1.1 are satisfied automatically, because $V$ is a polynomial in $\psi$.

### Negativity of the Derivative

We differentiate the ansatz (13) as follows,

$$\dot{V}[\psi] = \dot{E}\left(2E + 2\gamma_0 c_0 + \gamma_1\right) + 2\gamma_0 E\dot{c}_0 + 2\,\mathrm{Re}\, A_{ij}\overline{c_i}\dot{c}_j.$$

Expanding and employing (15), we find

$$\begin{aligned} \dot{V}[\psi] \leq\ & 2(\lambda_0|c_0|^2 + \kappa_j q_j^2)(2E + 2\gamma_0 c_0 + \gamma_1) + E(4\lambda_1|c_1|^2 + 4\lambda_2|c_2|^2 + 2\gamma_0\langle\varphi_0, \psi, \zeta\rangle) \\ & + 4\gamma_0 c_0(\lambda_1|c_1|^2 + \lambda_2|c_2|^2) + 2\gamma_0\lambda_0 c_0 E + 2\,\mathrm{Re}\, A_{ij}\overline{c_i}\langle\varphi_j, \psi, \zeta\rangle \\ & + \gamma_1(2\lambda_1|c_1|^2 + 2\lambda_2|c_2|^2) + 2\,\mathrm{Re}\, A_{ij}\overline{c_i}(\lambda_j c_j + \langle y\partial_x\nabla\varphi_j, \nabla\psi\rangle). \end{aligned} \tag{17}$$

With the exception of the first term (which we return to shortly), this expression is organized line-by-line into quartic, cubic, and quadratic components, respectively. In order to demonstrate that $V$ is a Lyapunov functional for our system, we need to show that $V[\psi] > 0$ and $\dot{V}[\psi] < 0$ for all non-zero $\psi$; requirements on the asymptotic behavior of $V$ and $\dot{V}$ are then automatic, since both are polynomial in $\psi$.

We decompose $\dot{V}$ into several components:

$$\dot{V} = \dot{V}_a + \dot{V}_b + \dot{V}_c,$$

$$\begin{aligned}\dot{V}_a \doteq\ & 2(\lambda_0|c_0|^2 + \kappa_j q_j^2)(2E + 2\gamma_0 c_0 + \gamma_1) + E(4\lambda_1|c_1|^2 + 4\lambda_2|c_2|^2 + 2\gamma_0\langle\varphi_0, \psi_a, \nabla^2\psi_a\rangle) \\ & + 4\gamma_0 c_0(\lambda_1|c_1|^2 + \lambda_2|c_2|^2) + 2\gamma_0\lambda_0 c_0 E + 2\,\mathrm{Re}\, A_{ij}\overline{c_i}\langle\varphi_j, \psi_a, \nabla^2\psi_a\rangle \\ & + \gamma_1(2\lambda_1|c_1|^2 + 2\lambda_2|c_2|^2) + 2\,\mathrm{Re}\, A_{ij}\overline{c_i}(\lambda_j c_j + \langle y\partial_x\nabla\varphi_j, \nabla\psi_a\rangle),\end{aligned} \tag{18}$$

$$\dot{V}_b = 2\gamma_0 E\langle\varphi_0, \psi_b, \nabla^2\psi_b\rangle + 2\,\mathrm{Re}\, A_{ij}\overline{c_i}\langle\varphi_j, \psi_b, \nabla^2\psi_b\rangle + 2\,\mathrm{Re}\, A_{ij}\overline{c_i}\langle y\partial_x\nabla\varphi_j, \nabla\psi_b\rangle, \tag{19}$$

$$\begin{aligned}\dot{V}_c = & 2\gamma_0 E(\langle\varphi_0, \psi_a, \nabla^2\psi_b\rangle + \langle\varphi_0, \psi_b, \nabla^2\psi_a\rangle) \\ & + 2\,\mathrm{Re}\, A_{ij}\overline{c_i}(\langle\varphi_j, \psi_a, \nabla^2\psi_b\rangle + \langle\varphi_j, \psi_b, \nabla^2\psi_a\rangle).\end{aligned} \tag{20}$$

The first of these expressions is already a quartic polynomial in the six variables $(c_j, q_k)$; we turn now to the problem of bounding $\dot{V}_b$ and $\dot{V}_c$ by similar expressions, so we can ensure that $\dot{V} \prec 0$ using a sum-of-squares optimization in $\mathbb{C}^6$.

**Bounding Tail Terms**

Here, we bound the terms appearing in (19). First, note that the triple product (9) satisfies

$$\langle a, b, \nabla^2 c\rangle + \langle a, c, \nabla^2 b\rangle = -\langle\nabla a, b, \nabla c\rangle - \langle\nabla a, c, \nabla b\rangle = \langle\nabla b \cdot Q_a \cdot \nabla c\rangle$$

for any scalar fields $a$, $b$, and $c$, where

$$Q_a = \begin{pmatrix} 2a_{xy} & a_{yy} - a_{xx} \\ a_{yy} - a_{xx} & -2a_{xy}\end{pmatrix}.$$

In particular, we find

$$\left|\langle a, b, \nabla^2 c\rangle + \langle a, c, \nabla^2 b\rangle\right| \le \|Q_a\|_{\mathrm{op}}\|\nabla b\|\|\nabla c\|, \tag{21}$$

where $\|\nabla b\| = (\langle\nabla\overline{b}, \nabla b\rangle)^{1/2}$ denotes the $H^1$ norm and

$$\|Q_a\|_{\mathrm{op}} = \max_{(x,y)} \|Q_a(x,y)\|_{\mathrm{op},2\times 2}$$

denotes the operator norm of $Q_a$ on $H^1$. With this in mind, we write

$$\langle\varphi_0, \psi_b, \nabla^2\psi_b\rangle = \langle\nabla\overline{\phi_{1,+}} \cdot Q_{\varphi_0} \cdot \nabla\phi_{1,+}\rangle + \langle\nabla\overline{\phi_{2,+}} \cdot Q_{\varphi_0} \cdot \nabla\phi_{2,+}\rangle,$$

where $\phi_{i,+}$ denotes the component of $\phi_i$ with positive streamwise wavenumber. Of course, we can write $\varphi_0$ explicitly as

$$\varphi_0(y) = \frac{\cos(2\pi y) + 1}{2\pi\sqrt{L}},$$

so we find

$$Q_{\varphi_0} = -\frac{2\pi}{\sqrt{L}}\begin{pmatrix} & \cos(2\pi y) \\ \cos(2\pi y) & \end{pmatrix}.$$

Applying (21) yields the bound

$$|\langle\varphi_0, \psi_b, \nabla^2\psi_b\rangle| \le 2\pi L^{-1/2}(q_1^2 + q_2^2),$$

noting that $q_i^2 = \|\nabla\phi_{i,+}\|^2 = \|\nabla\phi_{i,-}\|^2$ for $i = 1, 2$.

Alternatively, one can improve this bound slightly as follows. Explicitly writing

$$\langle\nabla\overline{\phi_{j,+}} \cdot Q_{\varphi_0} \cdot \nabla\phi_{j,+}\rangle = 2\pi ijkL^{-1/2}\langle\cos(2\pi y)(\overline{\phi_{j,+}}\partial_y\phi_{j,+} - \phi_{j,+}\partial_y\overline{\phi_{j,+}})\rangle,$$

we can maximize this expression over $\mathcal{H}_j$ by solving the appropriate Euler–Lagrange equations:

$$2\pi ijkL^{-1/2}(\cos(2\pi y)\partial_y\phi_{j,+} + \partial_y[\cos(2\pi y)\phi_{j,+}]) = \sigma((jk)^2 - \partial_y^2)\phi_{j,+}.$$

For $L = \pi/2$, for instance, this yields the bound

$$|\langle\varphi_0, \psi_b, \nabla^2\psi_b\rangle| \le 2.774q_1^2 + 4.878q_2^2,$$

which compares favorably to the bound $|\langle\varphi_0, \psi_b, \nabla^2\psi_b\rangle| \le 4.878(q_1^2 + q_2^2)$ we would have found from (21).

To bound the next term in (19), we note that

$$\langle\varphi_j, \psi_b, \nabla^2\psi_b\rangle = \langle\nabla\phi_0 \cdot Q_{\varphi_j} \cdot \nabla\phi_{1,-}\rangle + \langle\nabla\phi_{2,-} \cdot Q_{\varphi_j} \cdot \nabla\phi_{1,+}\rangle + 2\langle\nabla\phi_{2,-} \cdot Q_{\varphi_j} \cdot \nabla\phi_{2,+}\rangle,$$

removing terms for which the streamwise wavenumbers of the integrands do not sum to zero. Using (21) once again yields

$$\left|2\,\mathrm{Re}\, A_{ij}\overline{c_i}\langle\varphi_j, \psi_b, \nabla^2\psi_b\rangle\right| \le 2|\alpha|(|c_1|\|Q_{\varphi_2}\|_{\mathrm{op}} + |c_2|\|Q_{\varphi_1}\|_{\mathrm{op}})(\sqrt{2}q_0q_1 + q_1q_2 + 2q_2^2),$$

noting that $\|\nabla\phi_0\|^2 = 2q_0^2$. Applying Young's inequality, we recover

$$\begin{aligned}&\left|2\,\mathrm{Re} A_{ij}\overline{c_i}\langle\varphi_j, \psi_b, \nabla^2\psi_b\rangle\right| \\ &\qquad \le 2|\alpha|\left(\left(\frac{\varepsilon_1}{2} + \frac{|c_1|^2}{2\varepsilon_1}\right)\|Q_{\varphi_2}\|_{\mathrm{op}} + \left(\frac{\varepsilon_2}{2} + \frac{|c_2|^2}{2\varepsilon_2}\right)\|Q_{\varphi_1}\|_{\mathrm{op}}\right)(\sqrt{2}q_0q_1 + q_1q_2 + 2q_2^2),\end{aligned}$$

for any $\varepsilon_1, \varepsilon_2 > 0$.

Finally, we can bound the final term of (19) as follows:

$$\begin{aligned}|2\,\mathrm{Re}\, A_{ij}\overline{c_i}\langle y\partial_x\nabla\varphi_j, \nabla\psi_b\rangle| &\le 2\,|\langle A_{ij}\overline{c_i}y\partial_x\nabla\varphi_j, \nabla\phi_{1,-}\rangle| \\ &\le 2q_1\|A_{ij}\overline{c_i}y\partial_x\nabla\varphi_j\| \\ &\le \varepsilon_0'q_1^2 + \frac{1}{\varepsilon_0'}A_{ij}A_{k\ell}\langle y\partial_x\nabla\varphi_j, y\partial_x\nabla\overline{\varphi_k}\rangle\overline{c_i}c_\ell \\ &\le \varepsilon_0|\alpha|q_1^2 + \frac{|\alpha|}{\varepsilon_0}\widetilde{A}_{ij}\widetilde{A}_{k\ell}\langle y\partial_x\nabla\varphi_j, y\partial_x\nabla\overline{\varphi_k}\rangle\overline{c_i}c_\ell,\end{aligned}$$

writing $\widetilde{A} = A/|\alpha|$ and $\varepsilon_0 = \varepsilon_0'/|\alpha|$. This change of variables ensures that $|\alpha|$ appears only linearly in our Lyapunov function for each fixed $\varepsilon_0 > 0$, which allows $|\alpha|$ to be an optimization parameter in the sum-of-squares procedure we will use.

**Bounding Mixed Terms**

We now bound the terms appearing in (20). The first of these is found as

$$\begin{aligned}\big|\langle\varphi_0,\psi_a,\nabla^2\psi_b\rangle+\langle\varphi_0,\psi_b,\nabla^2\psi_a\rangle\big| &= |\langle\nabla\psi_a\cdot Q_{\varphi_0}\cdot\nabla\phi_1\rangle|\\ &= |2\,\mathrm{Re}\langle(c_1\nabla\overline{\varphi_1}+c_2\nabla\overline{\varphi_2})\cdot Q_{\varphi_0}\cdot\nabla\phi_{1,+}\rangle|\\ &\le 2\|(c_1\nabla\overline{\varphi_1}+c_2\nabla\overline{\varphi_2})\cdot Q_{\varphi_0}\|q_1\\ &\le \frac{1}{\varepsilon_3}\langle\overline{Q_{\varphi_0}}\cdot\nabla\varphi_j,Q_{\varphi_0}\cdot\nabla\overline{\varphi_k}\rangle\overline{c_j}c_k+\varepsilon_3 q_1^2.\end{aligned}$$

For the second term, we first calculate

$$\langle\nabla\psi_a\cdot Q_{\varphi_j}\cdot\nabla\psi_b\rangle=\overline{c_k}\langle\nabla\varphi_k\cdot Q_{\varphi_j}\cdot\nabla\phi_{2,-}\rangle+c_k\langle\nabla\overline{\varphi_k}\cdot Q_{\varphi_j}\cdot\nabla\phi_0\rangle+2c_0\langle\nabla\varphi_0\cdot Q_{\varphi_j}\cdot\nabla\phi_{1,-}\rangle.$$

Then we find

$$\begin{aligned}&\big|2\,\mathrm{Re}\,A_{ij}\overline{c_i}(\langle\varphi_j,\psi_a,\nabla^2\psi_b\rangle+\langle\varphi_j,\psi_b,\nabla^2\psi_a\rangle)\big|\le 2|A_{ij}\overline{c_i}\langle\nabla\psi_a\cdot Q_{\varphi_j}\cdot\nabla\psi_b\rangle|\\ &\quad\le 2|\alpha||c_1||c_k|(\|Q_{\varphi_2}\cdot\nabla\varphi_k\|q_2+\|Q_{\varphi_2}\cdot\nabla\overline{\varphi_k}\|\sqrt{2}q_0)+4|\alpha||c_1||c_0|\|Q_{\varphi_2}\cdot\nabla\varphi_0\|q_1\\ &\qquad+2|\alpha||c_2||c_k|(\|Q_{\varphi_1}\cdot\nabla\varphi_k\|q_2+\|Q_{\varphi_1}\cdot\nabla\overline{\varphi_k}\|\sqrt{2}q_0)+4|\alpha||c_2||c_0|\|Q_{\varphi_1}\cdot\nabla\varphi_0\|q_1\\ &\quad\le 2|\alpha||c_1|^2(\|Q_{\varphi_2}\cdot\nabla\varphi_1\|q_2+\|Q_{\varphi_2}\cdot\nabla\overline{\varphi_1}\|\sqrt{2}q_0)\\ &\qquad+2|\alpha||c_2|^2(\|Q_{\varphi_1}\cdot\nabla\varphi_2\|q_2+\|Q_{\varphi_1}\cdot\nabla\overline{\varphi_2}\|\sqrt{2}q_0)\\ &\qquad+2|\alpha||c_1||c_2|\big[(\|Q_{\varphi_1}\cdot\nabla\varphi_1\|+\|Q_{\varphi_2}\cdot\nabla\varphi_2\|)q_2\\ &\qquad\qquad+(\|Q_{\varphi_1}\cdot\nabla\overline{\varphi_1}\|+\|Q_{\varphi_2}\cdot\nabla\overline{\varphi_2}\|)\sqrt{2}q_0)\big]\\ &\qquad+4|\alpha||c_1||c_0|\|Q_{\varphi_2}\cdot\nabla\varphi_0\|q_1+4|\alpha||c_2||c_0|\|Q_{\varphi_1}\cdot\nabla\varphi_0\|q_1,\end{aligned}$$

which we pair with the estimates

$$|c_1||c_0|\le\frac{1}{2\varepsilon_5}|c_1|^2+\frac{\varepsilon_5}{2}|c_0|^2,\qquad |c_2||c_0|\le\frac{1}{2\varepsilon_6}|c_2|^2+\frac{\varepsilon_6}{2}|c_0|^2,$$
$$|c_1||c_2|\le\frac{1}{2\varepsilon_4}|c_1|^2+\frac{\varepsilon_4}{2}|c_2|^2,$$

to complete our program.

**Sum of Squares Optimization**

The preceding analysis yields the following polynomial bound on $\dot{V}=\dot{V}[\psi]$:

$$\dot{V}[\psi]\le\dot{V}_a(c_j,q_k)+P_b(c_j,q_k)+P_c(c_j,q_k),$$

where $\dot{V}_a$ is given by (18), $P_b$ collects our bounds on $\dot{V}_b$,

$$\begin{aligned}P_b=\;&2\pi\gamma_0 EL^{-1/2}(q_1^2+q_2^2)+\varepsilon_0|\alpha|q_1^2+\frac{|\alpha|}{\varepsilon_0}\widetilde{A}_{ij}\widetilde{A}_{k\ell}\langle y\partial_x\nabla\varphi_j,y\partial_x\nabla\overline{\varphi_k}\rangle\overline{c_i}c_\ell\\ &+2|\alpha|\left(\left(\frac{\varepsilon_1}{2}+\frac{|c_1|^2}{2\varepsilon_1}\right)\|Q_{\varphi_2}\|_{\mathrm{op}}+\left(\frac{\varepsilon_2}{2}+\frac{|c_2|^2}{2\varepsilon_2}\right)\|Q_{\varphi_1}\|_{\mathrm{op}}\right)(\sqrt{2}q_0q_1+q_1q_2+2q_2^2),\end{aligned}$$

and $P_c$ collects our bounds on $\dot{V}_c$:

$$\begin{aligned}
P_c = 2\gamma_0 E \left( \frac{1}{\varepsilon_3} \langle \overline{Q_{\varphi_0}} \cdot \nabla \varphi_j, Q_{\varphi_0} \cdot \nabla \overline{\varphi_k} \rangle \overline{c_j} c_k + \varepsilon_3 q_1^2 \right) \\
+ 2|\alpha||c_1|^2 (\|Q_{\varphi_2} \cdot \nabla \varphi_1\| q_2 + \|Q_{\varphi_2} \cdot \nabla \overline{\varphi_1}\| \sqrt{2} q_0) \\
+ 2|\alpha||c_2|^2 (\|Q_{\varphi_1} \cdot \nabla \varphi_2\| q_2 + \|Q_{\varphi_1} \cdot \nabla \overline{\varphi_2}\| \sqrt{2} q_0) \\
+ 2|\alpha| \left( \frac{1}{2\varepsilon_4} |c_1|^2 + \frac{\varepsilon_4}{2} |c_2|^2 \right) \big[ (\|Q_{\varphi_1} \cdot \nabla \varphi_1\| + \|Q_{\varphi_2} \cdot \nabla \varphi_2\|) q_2 \\
+ (\|Q_{\varphi_1} \cdot \nabla \overline{\varphi_1}\| + \|Q_{\varphi_2} \cdot \nabla \overline{\varphi_2}\|) \sqrt{2} q_0) \big] \\
+ 4|\alpha| \left( \frac{1}{2\varepsilon_5} |c_1|^2 + \frac{\varepsilon_5}{2} |c_0|^2 \right) \|Q_{\varphi_2} \cdot \nabla \varphi_0\| q_1 \\
+ 4|\alpha| \left( \frac{1}{2\varepsilon_6} |c_2|^2 + \frac{\varepsilon_6}{2} |c_0|^2 \right) \|Q_{\varphi_1} \cdot \nabla \varphi_0\| q_1.
\end{aligned}$$

Though complicated, $P_b$ and $P_c$ are polynomials in the six variables $(c_j, q_k)$, and so a sum-of-squares procedure can ensure that $P_{\text{tot}} = \dot{V}_a + P_b + P_c \prec 0$. We carry this out as follows. First, we fix a box length $L$ and a Reynolds number $Re > Re_E$ that we would like to show corresponds to a globally stable 2-D Couette flow. Second, we fix parameters $\varepsilon_0, ..., \varepsilon_6 > 0$, such that $P_{\text{tot}}$ depends on the remaining parameters $|\alpha|, \gamma_0, \gamma_1 \in \mathbb{R}$ only linearly[4]; linear parameters can be incorporated into the sum-of-squares procedure at minimal cost. We then carry out a nonlinear optimization over eight parameters:

$$\begin{array}{|c|}
\hline
\texttt{Maximize } r \in \mathbb{R} \texttt{ over } (\varepsilon_0, ..., \varepsilon_6) \in \mathbb{R}^8 \texttt{ and } (|\alpha|, \gamma_0, \gamma_1) \in \mathbb{R}^3 \texttt{ such that} \\
|\alpha| \geq 0, \qquad V(c_j, q_k) \geq r E^2, \qquad \dot{V}_a(c_j, q_k) + P_b(c_j, q_k) + P_c(c_j, q_k) \leq -r E^2. \\
\hline
\end{array}$$

If the resulting $r$ is positive, we deduce that $V[\psi]$ is a Lyapunov function and thus that 2-D Couette flow is globally stable at the given box length and Reynolds number. For instance, at the box length $L = 1.659$ at which Orr [21] found $Re_E = 177.2$, we deduce that (6) is a Lyapunov functional for $Re = 195.8$ with parameters given by (7).

## 5 Interpretation of the Lyapunov Function

The goal of the present section is to identify, mathematically and physically, how the four terms of (13) conspire to control the transient energy growth that arises for $Re > Re_E$. There are four distinct terms in our ansatz (13) for $V[\psi]$, which enter into the time derivative

[4]The sign of $\alpha$ can be identified *a priori*; following Section 5, one sees that $\alpha$ must have the same sign as the triple product $\mu = \langle \Psi, \nabla \varphi_2, \nabla \overline{\varphi_1} \rangle \in \mathbb{R}$. Without loss of generality, we fix $\mu > 0$ and thus $\alpha > 0$.

$\dot{V}[\psi]$ as follows:

$$\begin{array}{c} V = E^2 + 2\gamma_0 c_0 E + A_{ij}\overline{c_i}c_j + \gamma_1 E \\ \quad\quad \mathbf{L} \quad\quad \mathbf{N} \quad\quad \mathbf{L} \quad \mathbf{N} \quad \mathbf{L} \quad\quad \mathbf{L} \\ \dot{V} = \underbrace{(2E\dot{E} + \text{quartic})}_{\dot{V}_4} + \underbrace{(\text{cubic})}_{\dot{V}_3} + \underbrace{(\text{quadratic} + \gamma_1 \dot{E})}_{\dot{V}_2} \end{array} \tag{22}$$

Recall that the total energy $E[\psi]$ is unmodified by nonlinear advection, so only linear terms—diffusion and advection by the background flow—appear in $\dot{E}$; these terms are indicated by the black arrows in (22). In our parameter regime, $\dot{E}$ (or equivalently, $\mathcal{E}$) has a single positive eigenvalue along the $\psi_1$ direction, and is otherwise negative definite.

There are only two terms in $\dot{V}$ that can counteract the transient energy growth corresponding to this positive eigenvalue, indicated by the blue arrows in (22): the linear components that arise in differentiating $A_{ij}\overline{c_i}c_j$ and the nonlinear components that arise in differentiating $2\gamma_0 c_0 E$. As we proved in the preceding section, so long as these terms can make both $\dot{V}_4$ and $\dot{V}_2$ 'sufficiently' negative definite, they can also control the (necessarily sign-indefinite) cubic terms of $\dot{V}_3$, indicated by the red arrows in (22). We discuss the mechanics of the quadratic and quartic terms in turn below.

### Quadratic Terms

The quadratic component of $\dot{V}$ accounts only for linear contributions of the time derivative. Consequently, so long as the quadratic form

$$Q = A_{ij}\overline{c_i}c_j + \gamma_1 E \tag{23}$$

is monotonically decreasing under the *linearized* Navier–Stokes equations

$$\zeta_t + \{\Psi, \zeta\} = \nu\nabla^2\zeta,$$

the quadratic component of $\dot{V}$ will be negative definite.

In this direction, we note that, for *any* stable linear system, there exists a reweighted energy functional that always monotonically decreases. The following result is well-known [2]:

**Lemma 3.** *Consider a linear differential equation $\dot{x} = Lx$ on a Hilbert space $\mathcal{H}$, with the domain $\mathrm{dom}(L)$ dense in $\mathcal{H}$, and suppose it admits a $C_0$-semigroup $T(t) : x(0) \mapsto x(t)$. If the system is exponentially stable, i.e., $\|T(t)\| < Ce^{-\alpha t}$ for some $C, \alpha > 0$ and all $t > 0$, then there exists a bounded, quadratic Lyapunov function $Q$.*

*Proof.* Let $\langle \cdot, \cdot \rangle$ be the inner product on $\mathcal{H}$, and consider the map

$$Q[x] = \int_0^\infty \langle T(\tau)x, MT(\tau)x \rangle \, \mathrm{d}\tau$$

for any bounded, self-adjoint $M \succ 0$. The integral in the expression above is well-defined as a consequence of exponential stability, and it is easy to verify that $Q[x] \succ 0$. We find

$$\begin{aligned}\dot{Q}[x] &= \int_0^\infty \left(\langle T(\tau)Lx, MT(\tau)x\rangle + \langle T(\tau)x, MT(\tau)Lx\rangle\right) \mathrm{d}\tau \\ &= \int_0^\infty \left(\langle LT(\tau)x, MT(\tau)x\rangle + \langle T(\tau)x, MLT(\tau)x\rangle\right) \mathrm{d}\tau \\ &= \int_0^\infty \frac{d}{d\tau}\langle T(\tau)x, MT(\tau)x\rangle \,\mathrm{d}\tau = -M\end{aligned}$$

for any $x \in \mathrm{dom}(L)$, so that $\dot{Q}[x] \prec 0$ on $\mathcal{H}$. The result follows. □

In short, the quadratic component of our quartic Lyapunov function can always be constructed, in principle, and one can interpret this fact as expressing the linear stability of the system. Moreover, the construction in Lemma 3 is quite flexible, so it is not surprising that one can form a viable quadratic form $Q[\psi]$ by reweighting only the components of $E[\psi]$ along a finite number of energy modes.

Our own quadratic term works as follows. First, we write

$$\mu = \langle \Psi, \nabla\varphi_2, \nabla\overline{\varphi_1}\rangle,$$

noting that the normalization (10) ensures that $\mu \in \mathbb{R}$. We calculate the quadratic component $\dot{V}_2$ of $\dot{V}$ as follows:

$$\dot{V}_2 = \widetilde{Q}[\psi] + (\text{tail}) = \begin{pmatrix} c_1 \\ c_2 \end{pmatrix}^\dagger \begin{pmatrix} \gamma_1\lambda_1 - 2\alpha\mu & \alpha(\lambda_1+\lambda_2) \\ \alpha(\lambda_1+\lambda_2) & \gamma_1\lambda_2 + 2\alpha\mu \end{pmatrix} \begin{pmatrix} c_1 \\ c_2 \end{pmatrix} + (\text{tail}), \tag{24}$$

where 'tail' terms are those that are linear or quadratic in $\psi_b \in \mathcal{H} \setminus \mathcal{H}_*$. Tail terms are controlled by ensuring that $\widetilde{Q}[\psi]$ is sufficiently negative definite, so we ignore them here.

Immediately, we see that the trace of $\widetilde{Q}[\psi]$ is negative if and only if $\lambda_1 < -\lambda_2$. At the box length $L = 1.659$ that minimizes $Re_E$, we have $\lambda_1 < -\lambda_2$ for all $Re \leq 402.8$, so this restriction is not a problem at present. So long as this is satisfied and

$$-\lambda_1\lambda_2 < \mu^2,$$

which (roughly) verifies that $\varphi_1$ and $\varphi_2$ interact sufficiently strongly (and appears to be satisfied for all parameters), one can ensure $\widetilde{Q}[\psi] \prec 0$ by selecting

$$\alpha = \frac{\gamma_1}{\mu}\,\frac{\lambda_2 - \lambda_1}{4 + (\lambda_1+\lambda_2)^2/\mu^2}.$$

**Quartic Terms**

The quartic component $\dot{V}_4$ of $\dot{V}$ takes the following form:

$$\begin{aligned}\dot{V}_4 &= 2E\dot{E} + 2\gamma_0 E\langle\varphi_0, \psi, \zeta\rangle \\ &= 2E(\langle\psi, \Psi, \zeta\rangle - \nu\|\zeta\|^2 + \gamma_0\langle\varphi_0, \psi, \zeta\rangle) \\ &= 2E\langle\psi, \Psi - \gamma_0\varphi_0, \zeta\rangle - 2\nu E\|\zeta\|^2.\end{aligned} \tag{25}$$

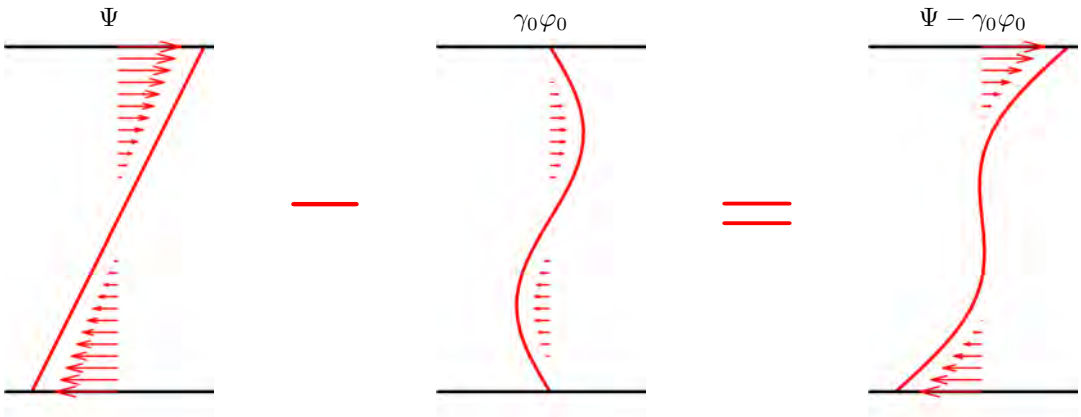


Figure 4: Introducing a cubic term into $V[\psi]$ allows us to counteract the effect of energy instability in the quartic term $\dot{V}_4$ of $\dot{V}[\psi]$, as in (25).

Already, one can see how our ansatz (13) allows us to counteract the effect of energy instability in $\dot{V}_4$. Namely, if $\gamma_0\varphi_0$ is close to $\Psi$, the first term of (25) is small, and the full expression is close to $-2\nu E\|\zeta\|^2 \prec 0$. We depict this effect in Fig. 4 with $\gamma_0 = 1/4$. Moreover, we see that the remaining field $\Psi - \gamma_0\varphi_0$ is large only near the edges of the domain, where the velocity itself is small; consequently, the full integral $\langle\psi, \Psi - \gamma_0\varphi_0, \zeta\rangle$ is reduced greatly.

Physically, one can understand this effect as follows. Up to a constant, the expression

$$E_{\text{tot}}[\psi] = E[\psi] + c_\Psi = E[\psi] - \langle\Psi, \nabla^2\psi\rangle$$

represents the *total* kinetic energy of the fluid, including the background flow $\Psi$. Of course, advection can move energy between the two terms by tilting the flow toward or away from the background shear profile, but it cannot modify the total. As such,

$$\dot{E}_{\text{tot}}[\psi] = -\nu\langle\Psi + \psi, \nabla^4\psi\rangle$$

carries only viscous terms: a negative-definite quadratic term corresponding to viscous damping, and a linear term corresponding to vorticity generation at the boundary.

By choosing $\gamma_0 c_0$ close to $\Psi$, we offset the increase of fluctuation energy by explicitly subtracting off the energy removed from the interaction between $\Psi$ and $\psi$. This procedure introduces positive terms corresponding to viscous generation of vorticity, but *not* at the leading order in $\psi$.

### A General Schematic for Quartic Lyapunov Functions

We have now seen how the quadratic and quartic components of our Lyapunov function are controlled by the physics of the flow: the quadratic component reweights the energy to leverage the flow's linear stability, and the quartic component balances transient growth of the fluctuation energy by incorporating the associated decay of other energy reservoirs. With these principles in mind, a natural generalization of the functional (6) is

$$V[\mathbf{u}] = E[\mathbf{u}]^2 + 2E[\mathbf{u}]\langle\mathbf{V}, \mathbf{u}\rangle + Q[\mathbf{u}], \tag{26}$$

where $\mathbf{V}$ is a vector field close to the background flow $\mathbf{U}$, with the same symmetries, and $Q[\mathbf{u}]$ is a Lyapunov function for the linearized Navier–Stokes equations at $\mathbf{u} = 0$. In our case, $\mathbf{U} = y\hat{x}$ and $\mathbf{V} = (\gamma_0/\sqrt{2})\sin(y)\hat{x}$, and $Q[\mathbf{u}] = \gamma_1 E[\mathbf{u}] + A_{ij}\bar{c}_i c_j$ is an energy functional perturbed along the directions of two energy modes $\mathbf{u}_1$ and $\mathbf{u}_2$. We note that an alternate family of admissible functionals $Q$ is constructed in Lemma 3. For flows with non-uniform internal energy, the cubic term of (26) would have to be modified to account for other reservoirs of energy.

# 6 Discussion and Perspectives

We have here proposed an interpretable, quasi-analytical approach to prove the global stability of 2-D plane Couette flow beyond the energy Reynolds number $Re_E = 177.2$. To this end, we have introduced a family (13) of candidate Lyapunov functions, quartic in the velocity field, with four total terms and three free parameters to be chosen dependent on the Reynolds number and box length. We used such a Lyapunov function to show, for instance, that 2-D plane Couette flow is stable at $Re = 195.8$ at the box length $L = 1.659$ that minimizes $Re_E$. Moreover, we illustrated how the four terms of our Lyapunov function conspire to control the transient energy growth that arises beyond $Re_E$, and we proposed a more general schematic for quartic Lyapunov functions in (26).

The present work offers a first step toward a transparent, flexible approach to improving global stability bounds in more general systems. Moreover, we believe that it should offer a tangible computational benefit for the sum-of-squares approach of Goulart and Chernyshenko [8]. For one, a costly (and complicated) algorithmic element in the work of Fuentes et al. [6] was reducing the space of admissible polynomials (the *state space*) to account for system symmetries. This translational symmetry was implemented as a four-point symmetry (sending $\eta_3 \mapsto \eta_4 \mapsto -\eta_3 \mapsto -\eta_4$, in the notation of Section 3) in the `YALMIP` SDP solver [15], which pre-processes the polynomial coefficient matrix to ensure that only symmetric terms arise in the final result. The 180° rotational symmetry of Couette flow was not implemented, leaving the state space twice as large as necessary. By contrast, as we saw in Section 3, both symmetries are folded into our revised notation, yielding a smaller, complex sum-of-squares problem and eliminating the need for pre-processing. Finally, if the ansatz (26) is generally sufficient, as indicated by our numerical experiments in Fig. 3 and our physical arguments in Section 5, one can eliminate all but a small number of dimensions of the state space.

We are currently working on adapting the present results in a few directions. First, we aim to achieve a fully-analytical proof of global stability for 2-D plane Couette flow beyond the energy threshold, replacing the remaining sum-of-squares procedure with an analytical bound on $\dot{V}$. Second, we are working on leveraging the insights introduced in the present work to greatly simplify and improve the numerical sum-of-squares calculation, in line with our comments above. Finally, we are working on connecting the present stability results with appropriate continuity results to yield a computer-assisted proof of global stability over a continuous range of Reynolds numbers and box lengths.

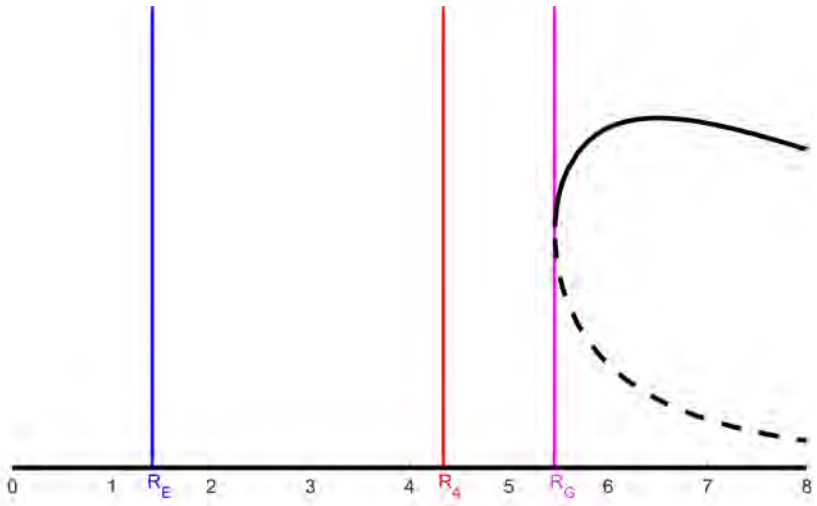


Figure 5: The bifurcation diagram associated to the toy model (27), with three values of the parameter $R$ highlighted: $R_E = \sqrt{2}$ is the largest value at which the (analogue) energy method proves global stability, $R_4 = 4.34$ is the largest value at which a quartic Lyapunov function exists, and $R_G = 5.46$ is the value at which a nonzero stationary solution appears.

### Acknowledgments

I would like to thank my advisors, Elizabeth Carlson (Oregon State University) and David Goluskin (University of Victoria), for suggesting this research direction and collaborating with me throughout the research process.

# Appendix

## A Toy Model for Quartic Lyapunov Function

We introduce a simple toy model to illustrate how a quartic Lyapunov function can yield an improved bound on $Re_G$. Consider the following 3-D ODE:

$$\begin{aligned} \dot{x} &= -\frac{1}{R}x + y - z(x+y) \\ \dot{y} &= -\frac{1}{R}y \qquad - z(x+y) \\ \dot{z} &= -\frac{1}{R}z + y + (x+y)^2, \end{aligned} \tag{27}$$

where $R > 0$. Comparing with the shear flow we focus on above, $z$ might represent a $k = 0$ (i.e., streamwise-constant) wave mode, $x$ and $y$ might represent distinct $k = 1$ modes, and $R$ might represent the Reynolds number of the system. Defining the energy accordingly as $E = \frac{1}{2}(x^2 + y^2 + z^2)$, we have

$$\dot{E} = -\frac{2}{R}E + y(x+z),$$

which remains quadratic in the 'flow' variables $(x, y, z)$. Young's inequality demonstrates that

$$\dot{E} \leq -\frac{2}{R}E + \frac{1}{2\varepsilon_1}x^2 + \frac{\varepsilon_1 + \varepsilon_2}{2}y^2 + \frac{1}{2\varepsilon_2}z^2$$

for any $\varepsilon_1, \varepsilon_2 > 0$. Setting $\varepsilon_1 = \varepsilon_2 = 1/\sqrt{2}$, one finds

$$\dot{E} \leq -\left(\frac{2}{R} - \sqrt{2}\right)E,$$

so we see that the (analogue) energy method proves global stability for $R < R_E = \sqrt{2}$.

On the other hand, one can verify numerically that the following quartic Lyapunov function yields global stability up to $R_4 = 4.34 > R_E$:

$$\begin{aligned} V = E^2 &+ 0.025x^2 + 0.53y^2 + 0.093z^2 - 0.048xz - 0.057yz - 0.11xy \\ &+ 0.059x^3 + 0.042x^2y + 0.76xy^2 + 0.21y^3 - 0.19x^2z \\ &+ 0.16xyz - 0.44y^2z + 0.088xz^2 + 0.31yz^2 - 0.26z^3. \end{aligned}$$

This result can likely be proven with analytic methods, but we do not do so here. By comparison, the first nonzero stationary solution to (27) appears at $R_G = 5.46$. We depict the full bifurcation diagram in Fig. 5.

## References


[1] R. Cooke and V. Arnold, *Ordinary Differential Equations*, Springer Textbook, Springer Berlin Heidelberg, 1992.

[2] R. Curtain and H. Zwart, *An Introduction to Infinite-Dimensional Linear Systems Theory*, Texts in Applied Mathematics, Springer New York, 1995.

[3] P. G. Drazin and W. H. Reid, *Hydrodynamic Stability*, Cambridge Mathematical Library, Cambridge University Press, 2 ed., 2004.

[4] U. Ehrenstein, M. Nagata, and F. Rincon, *Two-dimensional nonlinear plane Poiseuille–Couette flow homotopy revisited*, Physics of Fluids, 20 (2008), p. 064103.

[5] G. Folland, *A Course in Abstract Harmonic Analysis*, Studies in Advanced Mathematics, Taylor & Francis, 1994.

[6] F. Fuentes, D. Goluskin, and S. Chernyshenko, *Global Stability of Fluid Flows Despite Transient Growth of Energy*, Phys. Rev. Lett., 128 (2022), p. 204502. Publisher: American Physical Society.

[7] G. P. Galdi and M. Padula, *A new approach to energy theory in the stability of fluid motion*, Archive for Rational Mechanics and Analysis, 110 (1990), pp. 187–286.

[8] P. J. Goulart and S. Chernyshenko, *Global stability analysis of fluid flows using sum-of-squares*, Physica D: Nonlinear Phenomena, 241 (2012), pp. 692–704. Publisher: Elsevier BV.

[9] T. H. Gronwall, *Note on the Derivatives with Respect to a Parameter of the Solutions of a System of Differential Equations*, Annals of Mathematics, 20 (1919), pp. 292–296.

[10] D. Henry, *Geometric Theory of Semilinear Parabolic Equations*, Lecture notes in mathematics, Springer-Verlag, 1981.

[11] D. Huang, S. Chernyshenko, P. Goulart, D. Lasagna, O. Tutty, and F. Fuentes, *Sum-of-squares of polynomials approach to nonlinear stability of fluid flows: an example of application*, Proceedings: Mathematical, Physical and Engineering Sciences, 471 (2015), pp. 1–18. Publisher: Royal Society.

[12] V. Iudovich, *Example of the generation of a secondary stationary or periodic flow when there is loss of stability of the laminar flow of a viscous incompressible fluid*, Journal of Applied Mathematics and Mechanics, 29 (1965), pp. 527–544.

[13] D. D. Joseph, *Stability of Fluid Motions, Vol. I*, vol. 59 of Springer Tracts in Natural Philosophy, Springer Berlin, Heidelberg, 1 ed., 1976.

[14] R. Kaiser, A. Tilgner, and W. von Wahl, *A Generalized Energy Functional for Plane Couette Flow*, SIAM Journal on Mathematical Analysis, 37 (2005), pp. 438–454.

[15] J. Löfberg, *YALMIP : A Toolbox for Modeling and Optimization in MATLAB*, in Proceedings of the CACSD Conference, Taipei, Taiwan, 2004.

[16] A. Mironchenko and F. Wirth, *Non-coercive Lyapunov functions for infinite-dimensional systems*, Journal of Differential Equations, 266 (2019), pp. 7038–7072.

[17] K. G. Murty and S. N. Kabadi, *Some NP-complete problems in quadratic and nonlinear programming*, Mathematical Programming, 39 (1987), pp. 117–129.

[18] M. Nagata, *Three-dimensional finite-amplitude solutions in plane Couette flow: bifurcation from infinity*, Journal of Fluid Mechanics, 217 (1990), pp. 519–527.

[19] H. E. Oeri, *Convex Optimization Methods for Bounding Lyapunov Exponents*, PhD dissertation, University of Victoria, Victoria, Canada, 2023.

[20] P. J. Olver, *Applications of Lie Groups to Differential Equations*, vol. 107 of Graduate Texts in Mathematics, Springer-Verlag, New York, 2nd ed., 1993.

[21] W. M. Orr, *The Stability or Instability of the Steady Motions of a Perfect Liquid and of a Viscous Liquid. Part II: A Viscous Liquid*, Proceedings of the Royal Irish Academy. Section A: Mathematical and Physical Sciences, 27 (1907), pp. 69–138.

[22] S. A. Orszag and L. C. Kells, *Transition to turbulence in plane Poiseuille and plane Couette flow*, Journal of Fluid Mechanics, 96 (1980), pp. 159–205.

[23] P. Parrilo, *Semidefinite Programming Relaxations for Semialgebraic Problems*, Mathematical Programming, Series B, 96 (2003).

[24] O. Reynolds, *IV. On the dynamical theory of incompressible viscous fluids and the determination of the criterion*, Philosophical Transactions of the Royal Society of London. (A.), 186 (1895), pp. 123–164.

[25] F. Rincon, *On the existence of two-dimensional nonlinear steady states in plane Couette flow*, Physics of Fluids, 19 (2007), p. 074105.

[26] J. Serrin, *On the stability of viscous fluid motions*, Archive for Rational Mechanics and Analysis, 3 (1959), pp. 1–13.

[27] B. Straughan, *The Energy Method, Stability, and Nonlinear Convection*, Applied Mathematical Sciences, Springer New York, 2003.

[28] F. Waleffe, *Homotopy of exact coherent structures in plane shear flows*, Physics of Fluids, 15 (2003), pp. 1517–1534.

[29] A. P. Willis, J. Peixinho, R. R. Kerswell, and T. Mullin, *Experimental and Theoretical Progress in Pipe Flow Transition*, Philosophical Transactions: Mathematical, Physical and Engineering Sciences, 366 (2008), pp. 2671–2684.

[30] J.-P. Zahn, J. Toomre, E. A. Spiegel, and D. O. Gough, *Nonlinear cellular motions in Poiseuille channel flow*, Journal of Fluid Mechanics, 64 (1974), pp. 319–346.

# Baroclinic Instability as a Driver of Polar Vortices on Giant Planets

Lin Yao

August 21, 2025

## 1 Introduction

The polar regions of Jupiter and Saturn exhibit strikingly distinct dynamic features. NASA's Juno mission [22] revealed that Jupiter's poles host stable clusters of cyclones: a central cyclone encircled by eight circumpolar cyclones in the north and five in the south, forming persistent polygonal patterns often termed "vortex crystals" [1]. In contrast, observations from NASA's Cassini mission [21] show that Saturn features a single, massive vortex at each pole, with the northern vortex notably enclosed by a hexagonal jet stream [4] (Fig. 1). This dichotomy poses a fundamental question: what physical mechanisms are responsible for the formation and persistence of these distinct, highly organized vortex structures?

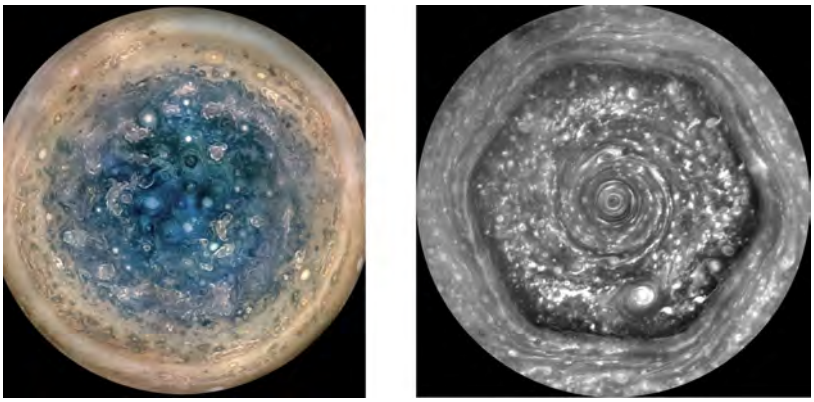

Figure 1: The distinct polar vortex structures of Jupiter and Saturn. (Left) Jupiter's south pole, as observed by the Juno mission [22], displaying a central cyclone surrounded by five circumpolar cyclones arranged in a stable pentagonal pattern. (Right) Saturn's north pole, featuring the prominent hexagonal jet stream enclosing a massive polar vortex. This composite image from the Cassini mission [21] combines data from ultraviolet to infrared wavelengths. *Image Credits: (Left) NASA/JPL-Caltech/SwRI/MSSS/Betsy Asher Hall/Gervasio Robles; (Right) NASA/JPL-Caltech/SSI/Hampton University.*

The energy required to drive the atmospheric dynamics on giant planets originates from two primary sources, as illustrated by Jupiter's energy budget (Fig. 2). Firstly, the planet radiates significantly more energy than it receives from the sun, indicating the existence

of an internal heat flux that can drive convection from the deep interior [19]. The second source is differential solar heating, where the equator-to-pole temperature gradient drives large-scale circulation and generates available potential energy that can be released through baroclinic instability to form eddies and jets [11, 15, 20]. These two energy sources have similar magnitudes based on observations from the Juno mission.

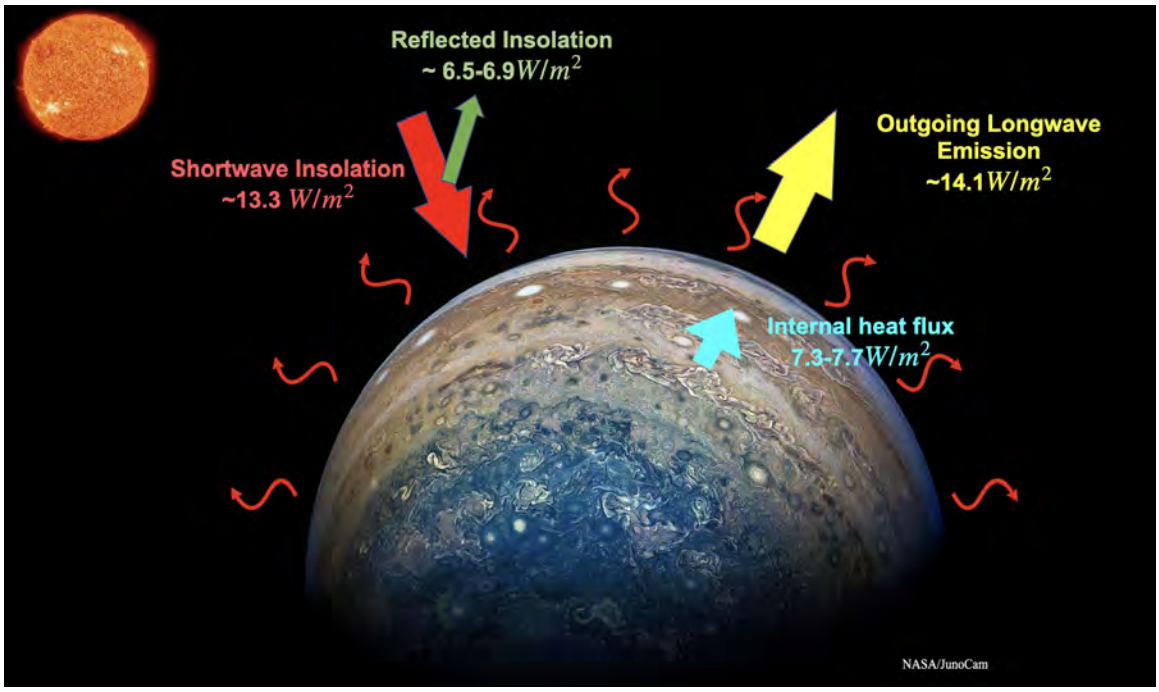


Figure 2: Schematic of Jupiter's planetary energy budget. The planet emits about two times more thermal energy ($14.098 \pm 0.031\,\mathrm{W/m^2}$) than what is absorbed from solar radiation ($6.613 \pm 0.160\,\mathrm{W/m^2}$), indicating the presence of an internal heat source [18, 19]. This budget highlights the two primary drivers of atmospheric dynamics: 1) internal heat flux, which powers deep moist convection, and 2) differential solar heating, which generates available potential energy for baroclinic eddies. *Image credit: NASA/JunoCam.*

To date, it remains unclear whether the polar vortices on Saturn and Jupiter are generated locally (e.g., [28, 29]) or form at lower latitudes and subsequently migrate to the poles [9, 17, 26]. The migration hypothesis is supported by findings that vortices can obtain an anticyclonic shielding layer during their journey [9, 14, 17], which could keep them separated upon reaching the poles [17]. If, however, the vortices are generated locally, it is an open question whether they are driven by convection or by baroclinic instability. The local formation mechanism driven by convection has been investigated extensively using highly idealized configurations, such as shallow water and quasi-geostrophic (QG) systems [5, 10, 23, 24, 27–29]. In these models, convective processes are usually unresolved. They are represented by small-scale randomized perturbations in the initial condition or during the integration of the model, mimicking convection (e.g., [28, 29]). The subsequent development of the randomized perturbations is similar to the inverse energy cascade of two-dimensional (2D) turbulence, where small vortices merge and grow [3, 16]. This growth

continues until the vortex size is halted by processes related to dissipation, planetary rotation, or the constraints of polar geometry. As summarized by [28], the final fluid pattern can vary from turbulent chaos, to a disorganized "vortex soup," to a single polar vortex with a surrounding jet, and to stable organized vortex crystals, depending on the specific model parameters [5, 10, 23, 24, 27–29]. Beyond idealized models, in recent years, full 3D large eddy simulations have shown that Jupiter-like vortices can be realized in a 3D model with resolved convection [7, 8].

However, the role of the other major energy source, i.e., differential solar heating and the resulting baroclinic instability, has yet to be investigated. One may argue that the baroclinic eddies are fundamental to the energy cycle of planetary atmospheres [12, 25, 30], yet their potential to organize into the specific, stable configurations seen on Jupiter and Saturn has not been systematically explored.

This study aims to fill that gap. We investigate whether baroclinic instability, acting alone, is a sufficient mechanism to generate the diverse range of polar vortex regimes observed on the giant planets. Using an idealized two-layer model (Section 2), we explore a wide nondimensional parameter space governed by the strength of the baroclinic shear and atmospheric drag. We first analyze the system's linear instability (Section 3). Then, by simulating the nonlinear evolution of baroclinic eddies (Section 4), we seek to determine whether different regimes, analogous to the vortex crystals of Jupiter and the stable polygonal jet of Saturn, emerge naturally from these fundamental fluid dynamics.

# 2 A Two-Layer QG Model for the Polar Atmosphere on Giant Planets

We employ a two-layer quasi-geostrophic potential vorticity (QGPV) model on a disk coordinate system to simulate the polar atmosphere of a giant planet (Fig. 3). The model is confined to a circular domain of radius $R$ and consists of two immiscible, constant-density layers. The buoyant upper layer (layer 1) has a mean thickness of $H_1$, and the denser lower layer (layer 2) has a mean thickness of $H_2$.

## 2.1 Background state

The model is formulated on a $\gamma$-plane, which approximates the variation of the Coriolis parameter, $f$, near the pole with a parabolic profile:

$$f = 2\Omega_p \sin\theta = 2\Omega_p \cos\left(\frac{\pi}{2} - \theta\right) = 2\Omega_p \cos\left(\frac{r}{a}\right) \approx f_0 - \frac{1}{2}\gamma r^2, \tag{1}$$

where $\Omega_p$ is the planetary rotation rate, $\theta$ is the latitude, $r$ is the radial distance from the pole, $a$ is the planetary radius, $f_0 = 2\Omega_p$ is the Coriolis parameter at the pole, and $\gamma = -f_{rr}|_{r=0} = 2\Omega_p/a^2$ represents the planetary vorticity curvature at the pole.

The background atmospheric flow is modeled as a solid-body rotation in each layer, described by the background streamfunction $\Psi_i$:

$$\Psi_i = \frac{1}{2}\Omega_i r^2, \tag{2}$$

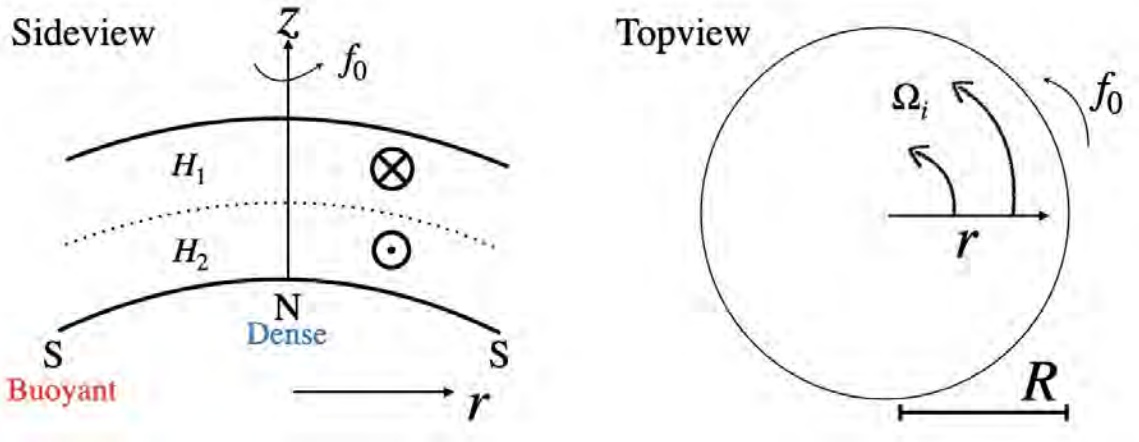


Figure 3: A schematic of the two-layer QGPV model. The side view (left) shows the vertical structure with layers of thickness $H_1$ and $H_2$. The symbols $\otimes$ and $\odot$ represent opposing azimuthal winds, directed inward (into the page) and outward (out of the page), respectively. The top view (right) shows the disk of radius $R$ with a planetary rotation $f_0$ and a background fluid angular velocity $\Omega_i$, $i = 1, 2$.

where the angular velocity $\Omega_i$ for each layer $i \in \{1, 2\}$ is given by:

$$\Omega_i = (-1)^{i+1} 2\alpha_{3-i}\Omega. \tag{3}$$

Here, $\Omega$ represents the magnitude of the vertical shear, which drives the baroclinic instability. The parameter $\alpha_i$ is the fractional thickness of layer $i$:

$$\alpha_i = \frac{H_i}{H_1 + H_2}. \tag{4}$$

This setup establishes a background potential vorticity (PV), $Q_i$, in each layer:

$$Q_i = \nabla^2\Psi_i + \frac{\Psi_{3-i} - \Psi_i}{L_d^2\alpha_i} = (-1)^{i+1} 4\alpha_{3-i}\Omega + \frac{(-1)^i \Omega r^2}{L_d^2\alpha_i},\ i \in \{1, 2\}, \tag{5}$$

where $L_d = \sqrt{g'(H_1 + H_2)}/f_0$ is the Rossby radius of deformation, with $g' = g(\rho_2 - \rho_1)/\rho_1$.

## 2.2 Governing equations

The evolution of the PV anomaly, $q_i$, in each layer is governed by:

$$\frac{\partial q_i}{\partial t} + J(\Psi_i + \psi_i, q_i + Q_i + f) = F_s - \mu(q_i + Q_i) + \nu\nabla^4 q_i, \tag{6}$$

where $J(A, B) := \frac{1}{r}(\frac{\partial A}{\partial r}\frac{\partial B}{\partial \varphi} - \frac{\partial A}{\partial \varphi}\frac{\partial B}{\partial r})$ is the Jacobian operator in polar coordinates. The terms on the right-hand side represent sources and sinks: $F_s$ is a forcing term related to solar radiation, $-\mu(q_i + Q_i)$ is a linear (Rayleigh) drag that damps the total PV, and $\nu\nabla^4 q_i$ is a lateral hyperviscosity included for numerical stability.

The PV anomaly, $q_i$, is related to the streamfunction anomaly, $\psi_i$, through the inversion equation:

$$q_i = \nabla^2 \psi_i + \frac{\psi_{3-i} - \psi_i}{L_d^2 \alpha_i}. \tag{7}$$

To maintain the background state against dissipation, the system is forced by relaxing the PV field toward the background state, $Q_i$. We define the forcing term as:

$$F_s = \mu Q_i. \tag{8}$$

This specific form of forcing simplifies the governing equation by canceling the drag on the background state, which is advantageous for linear stability analysis. The governing equation becomes:

$$\frac{\partial q_i}{\partial t} + J(\Psi_i + \psi_i, q_i + Q_i + f) = -\mu q_i + \nu \nabla^4 q_i. \tag{9}$$

### 2.2.1 Boundary conditions and domain size

The model is solved with the no-penetration boundary condition, where the streamfunction anomaly at the wall is equal to a constant, which we set to zero:

$$\psi_i(r = R) = 0. \tag{10}$$

To ensure mass conservation between the layers, we enforce the global constraint:

$$\int_A (\psi_1 - \psi_2)\, dA = 0, \tag{11}$$

where the integral is taken over the entire area $A$ of the disk.

The domain radius $R$ is scaled by the Rhines scale, $L_{Rh}$, the characteristic length at which turbulence self-organizes into zonal jets under the influence of the planetary vorticity gradient. We set the radius as:

$$R = \eta L_{Rh} = \eta \frac{\Omega}{L_d \gamma}, \tag{12}$$

In our simulations, we set $\eta = 18.6$. This value is selected based on trial experiments and represents a trade-off between two requirements: the domain must be large enough to contain at least one jet, aiming to isolate interior dynamics from boundary effects, while remaining computationally tractable. The formulation for $L_{Rh}$ follows that of [13] and will be rederived in Section 4.3.

## 2.3 Nondimensionalization and key parameters

To distill the fundamental dynamics, we nondimensionalize the governing equations. This procedure reduces the number of free parameters and highlights the key dimensionless numbers that control the flow regime. We choose the characteristic length to be $L_d/\sqrt{2}$, where $L_d$ denotes the Rossby deformation radius and the factor of $\sqrt{2}$ is introduced for convenience in the equal-depth case. We choose the characteristic time scale to be $T_{\text{rot}} = 2(\gamma L_d^2)^{-1}$, representing the timescale associated with planetary rotation.

Scaling the variables in Eq. (9) with these characteristic scales reveals two primary nondimensional parameters that govern the system's physics:

**Nondimensional relaxation ($\hat{\mu}^{-1}$)** This parameter is the ratio of the physical relaxation timescale to the planetary rotation timescale:

$$\hat{\mu}^{-1} = \frac{\mu^{-1}}{2(\gamma L_d^2)^{-1}} = \frac{\text{Relaxation Time}}{\text{Rotation Time}}. \tag{13}$$

It quantifies the efficiency of both the drag and the restoring force. A large value of $\hat{\mu}^{-1}$ (corresponding to weak $\mu$) implies weak damping, allowing instabilities to grow to large amplitudes, and weak restoration toward the background state, which permits the induced jets to partially cancel the background zonal flows and reduce baroclinicity. Conversely, a small value corresponds to strong damping and strong restoration. The effect of $\hat{\mu}^{-1}$ on the final vortex strength is non-monotonic.

**Nondimensional shear ($\hat{\Omega}$)** This parameter is the ratio of the planetary rotation timescale to the forcing timescale, which is the inverse of the background baroclinic shear, $\Omega^{-1}$:

$$\hat{\Omega} = \frac{2(\gamma L_d^2)^{-1}}{\Omega^{-1}} = \frac{\text{Rotation Time}}{\text{Forcing Time}}. \tag{14}$$

$\hat{\Omega}$ measures the strength of the background shear, which provides the kinetic energy for the growth of vortices and jets via conversion of potential energy. A large value of $\hat{\Omega}$ indicates strong shear that can readily overcome the stabilizing effect of the planetary PV gradient and the dissipation due to damping, leading to vigorous baroclinic instability and vortex formation.

Together, $\hat{\mu}^{-1}$ and $\hat{\Omega}$ define the dynamical regime of the model. The competition between forcing ($\hat{\Omega}$) and relaxation ($\hat{\mu}^{-1}$) determines the resulting polar patterns and vortex intensities. The nondimensional governing equations are:

$$\frac{\partial \hat{q}_i}{\partial \hat{t}} + J(\hat{\Psi}_i + \hat{\psi}_i,\, \hat{q}_i + \hat{Q}_i + \hat{f}) = -\hat{\mu}\hat{q}_i + \hat{\nu}\hat{\nabla}^4\hat{q}_i, \tag{15a}$$

$$\hat{q}_i = \hat{\nabla}^2\hat{\psi}_i + \frac{\hat{\psi}_{3-i} - \hat{\psi}_i}{2\alpha_i}, \tag{15b}$$

$$\hat{\Psi}_i = (-1)^{i+1}\alpha_{3-i}\hat{\Omega}\hat{r}^2, \tag{15c}$$

$$\hat{Q}_i = (-1)^{i+1}4\alpha_{3-i}\hat{\Omega} + \frac{(-1)^i\hat{\Omega}\hat{r}^2}{2\alpha_i}, \tag{15d}$$

$$\hat{f} = \frac{2f_0}{\gamma L_d^2} - \frac{1}{2}\hat{r}^2. \tag{15e}$$

Major variables are listed in Table 1. Henceforth, we omit the circumflex $\hat{(\cdot)}$ on nondimensional variables in Eq. 15 for notational simplicity, unless stated otherwise.

| Symbol | Description | Defining Equation or Units |
|---|---|---|
| | **Dimensional Variables** | |
| $r, \varphi$ | Radial and azimuthal coordinates | m, rad |
| $R$ | Domain radius | m |
| $a$ | Planetary radius | m |
| $\Omega_p$ | Planetary rotation rate | rad $s^{-1}$ |
| $f$ | Coriolis parameter | $s^{-1}$ |
| $f_0$ | Coriolis parameter at the pole | $2\Omega_p$ |
| $\gamma$ | Planetary vorticity gradient at the pole | $2\Omega_p/a^2$ |
| $H_i$ | Mean thickness of layer $i$ | m |
| $\Psi_i$ | Background streamfunction in layer $i$ | $m^2$ $s^{-1}$ |
| $\psi_i$ | Perturbation streamfunction in layer $i$ | $m^2$ $s^{-1}$ |
| $Q_i$ | Background PV in layer $i$ | $s^{-1}$ |
| $q_i$ | Perturbation PV in layer $i$ | $s^{-1}$ |
| $\Omega$ | Background vertical shear magnitude | $s^{-1}$ |
| $L_d$ | Rossby radius of deformation | $\sqrt{g'(H_1+H_2)}/f_0$ |
| $\mu$ | Rayleigh drag coefficient (relaxation rate) | $s^{-1}$ |
| $\nu$ | Hyperviscosity coefficient | $m^4$ $s^{-1}$ |
| $V$ | Characteristic barotropic eddy velocity | m $s^{-1}$ |
| $L_{Rh}$ | Rhines scale | m |
| $\epsilon$ | Energy injection/dissipation rate | $m^2$ $s^{-3}$ |
| | **Nondimensional Parameters** | |
| $\hat{\Omega}$ | Nondimensional forcing (background shear) | $2\Omega/(\gamma L_d^2)$ |
| $\hat{\mu}$ | Nondimensional relaxation rate | $2\mu/(\gamma L_d^2)$ |
| $\hat{\mu}^{-1}$ | Nondimensional relaxation timescale | $(\gamma L_d^2)/(2\mu)$ |
| $\alpha_i$ | Fractional thickness of layer $i$ | $H_i/(H_1+H_2)$ |
| $m$ | Azimuthal (zonal) wavenumber | integer |
| $k$ | Radial wavenumber | - |
| $c$ | Complex phase speed | - |
| $\sigma$ | Growth rate of unstable modes | $m \cdot \mathrm{Im}(c)$ |

Table 1: List of major variables and parameters used in this study. The variables in Eq. 15 are nondimensional; for notational simplicity, the circumflex $\hat{(\cdot)}$ is omitted from these variables in later sections.

# 3 Linear Stability Analysis

We perform a linear stability analysis to determine the conditions under which the background flow is subject to baroclinic instability. This analysis reveals whether infinitesimal perturbations to the background state will grow or decay, with growing modes indicating an instability that can lead to the formation of coherent vortices.

## 3.1 Linearized equations and normal modes

We linearize the governing QGPV equation (Eq. 15) around the background state by assuming that the perturbation streamfunction $\psi_i$ and PV anomaly $q_i$ are small. This process yields a linearized equation for the PV anomaly (neglecting the numerical viscosity):

$$\frac{\partial q_i}{\partial t} + J(\Psi_i, q_i) + J(\psi_i, Q_i + f) + \mu q_i = 0. \tag{16}$$

Expressed in terms of the streamfunction anomaly, this system can be written in matrix form as:

$$\begin{aligned}(\partial_t + \mu) \begin{bmatrix} \nabla^2 - \frac{1}{2\alpha_1} & \frac{1}{2\alpha_1} \\ \frac{1}{2\alpha_2} & \nabla^2 - \frac{1}{2\alpha_2} \end{bmatrix} \begin{bmatrix} \psi_1 \\ \psi_2 \end{bmatrix} + \frac{\partial}{\partial \varphi} \begin{bmatrix} 2\alpha_2\Omega & 0 \\ 0 & -2\alpha_1\Omega \end{bmatrix} \begin{bmatrix} \nabla^2 - \frac{1}{2\alpha_1} & \frac{1}{2\alpha_1} \\ \frac{1}{2\alpha_2} & \nabla^2 - \frac{1}{2\alpha_2} \end{bmatrix} \begin{bmatrix} \psi_1 \\ \psi_2 \end{bmatrix} \\ + \frac{\partial}{\partial \varphi} \begin{bmatrix} \frac{\Omega}{\alpha_1} + 1 & 0 \\ 0 & -\frac{\Omega}{\alpha_2} + 1 \end{bmatrix} \begin{bmatrix} \psi_1 \\ \psi_2 \end{bmatrix} = 0.\end{aligned} \tag{17}$$

We seek normal mode solutions to this linear system of the form:

$$\psi_i(r, \varphi, t) = \mathrm{Re}\left\{ A_i J_m(kr) e^{im(\varphi - ct)} \right\}, \tag{18}$$

where $J_m(kr)$ is the Bessel function of the first kind of order $m$, representing the radial structure. Here, $m$ is the integer zonal (azimuthal) wavenumber, $k$ is the radial wavenumber determined by the boundary condition $J_m(kR) = 0$, and $c$ is the complex phase speed. The real part of $c$ is the wave's angular propagation speed, while its imaginary part, $c_i = \mathrm{Im}(c)$, determines the mode's stability. A mode is unstable if $c_i > 0$, and its exponential growth rate is given by $\sigma = mc_i$.

## 3.2 The dispersion relation and growth rate

Substituting the normal mode solution into the linearized system (Eq. 17) yields a 2x2 algebraic eigenvalue problem for the perturbation $\psi_i$:

$$\begin{bmatrix} \left(k^2 + \frac{1}{2\alpha_1}\right)\left(c - 2\alpha_2\Omega + i\,\frac{\mu}{m}\right) + \frac{\Omega}{\alpha_1} + 1 & -\frac{c}{2\alpha_1} + \frac{\alpha_2}{\alpha_1}\Omega - i\,\frac{\mu}{2\alpha_1 m} \\ -\frac{c}{2\alpha_2} - \frac{\alpha_1}{\alpha_2}\Omega - i\,\frac{\mu}{2\alpha_2 m} & \left(k^2 + \frac{1}{2\alpha_2}\right)\left(c + 2\alpha_1\Omega + i\,\frac{\mu}{m}\right) - \frac{\Omega}{\alpha_2} + 1 \end{bmatrix} \begin{bmatrix} \psi_1 \\ \psi_2 \end{bmatrix} = 0. \tag{19}$$

For a non-trivial solution, the determinant of this matrix must be zero. This condition produces the dispersion relation, a polynomial equation for the complex phase speed $c$.

For the simplified case of two layers with equal thickness ($\alpha_1 = \alpha_2 = 0.5$), the dispersion relation reduces to a quadratic equation for $c$:

$$\underbrace{(k^4 + 2k^2)}_{a_1} c^2 + \underbrace{\left[2(k^2+1) + i\,\frac{2\mu}{m}(k^4 + 2k^2)\right]}_{a_2} c + \underbrace{\left[1 - \frac{\mu^2}{m^2}(k^4 + 2k^2) - \Omega^2(k^4 - 2k^2) + i\,\frac{2\mu}{m}(k^2+1)\right]}_{a_3} = 0. \tag{20}$$

The solutions are given by the quadratic formula:

$$c = \frac{-a_2 \pm \sqrt{\Delta}}{2a_1}, \quad \text{where} \quad \Delta = a_2^2 - 4a_1a_3 = 4 + 4\Omega^2(k^8 - 4k^4). \tag{21}$$

$\Delta$ is a real value for all $\mu$. The growth rate for any unstable mode is calculated numerically as $\sigma = m \cdot \mathrm{Im}(c)$. As shown in Fig. 4, for a given set of parameters, instability occurs over a finite range of zonal wavenumbers $m$. The planetary PV gradient ($\gamma$) stabilizes long waves, creating a longwave cutoff, while the decoupling of the layers at small scales creates the shortwave cutoff. The presence of drag ($\mu > 0$) consistently reduces the growth rate for all unstable modes and can completely stabilize the flow if it is sufficiently strong (Fig. 4b).

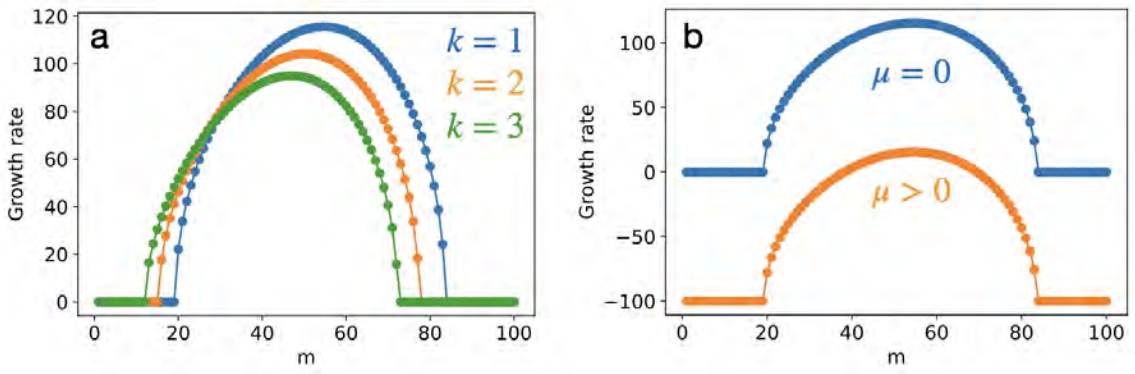


Figure 4: Linear Growth Rate Analysis. (a) Growth rate $\sigma$ versus azimuthal wavenumber $m$ for three radial wavenumbers $k$ ($\Omega = 3.5$, $\mu = 1 \times 10^{-2}$). Increasing $k$ shifts the band of unstable modes toward longer wavelengths (smaller $m$). (b) The stabilizing effect of damping ($\Omega = 3.5$). The undamped case ($\mu = 0$, blue) exhibits a range of unstable modes, while a sufficiently large damping coefficient ($\mu = 1 \times 10^2$, orange) stabilizes the system, making the growth rate negative for most $m$.

### 3.3 Necessary condition for instability

An instability occurs if at least one mode has a positive growth rate ($\sigma > 0$, which requires $c_i > 0$). To simplify the analysis, we first consider the undamped case ($\mu = 0$), where the

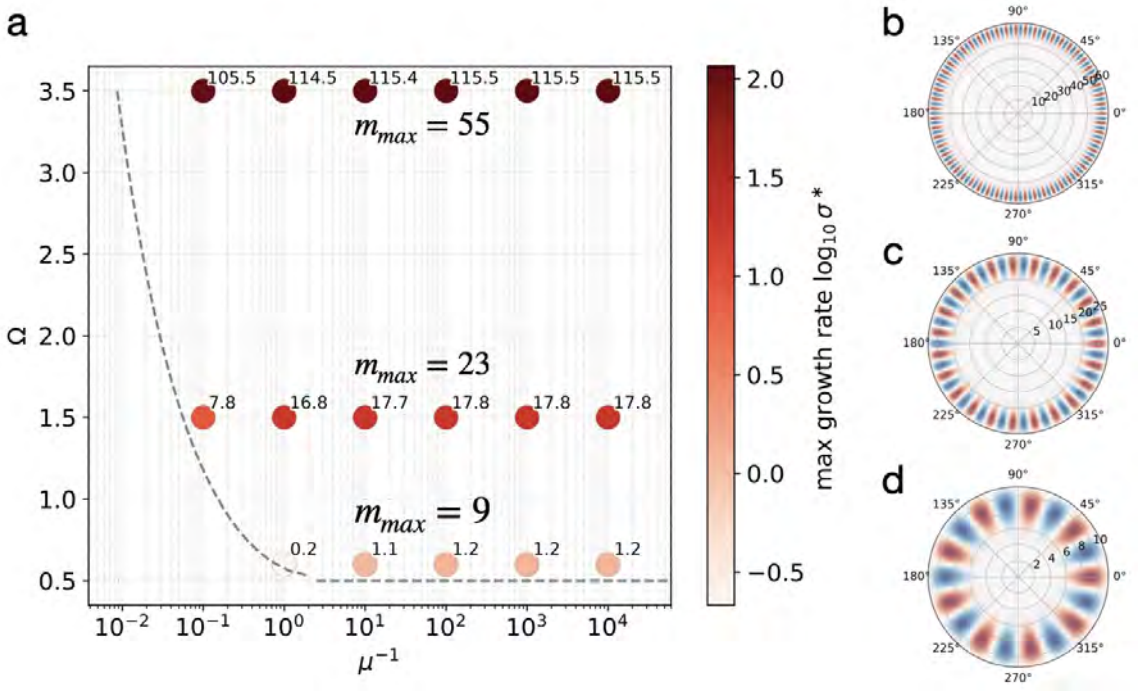


Figure 5: Linear Instability in the nondimensional Parameter Space. (a) The maximum growth rate $\sigma^*$ (color scale shown in $\log_{10}$, with numeric values in natural units near circles) and the corresponding most unstable wavenumber $m_{\max}$ across the parameter space of forcing $\Omega$ and inverse damping $\mu^{-1}$. The dashed gray line shows the boundary calculated by Eq. 24, above which baroclinic instability occurs. Stronger forcing (larger $\Omega$) increases both the growth rate and the most unstable wavenumber. Damping ($\mu$) reduces the growth rate but has no effect on $m_{\max}$. (b-d) Eigenfunctions for the upper-layer PV anomaly of the most unstable modes for $\Omega = 0.6$ ($m_{\max} = 55$), $\Omega = 1.5$ ($m_{\max} = 23$), and $\Omega = 3.5$ ($m_{\max} = 9$). Red and blue indicate positive and negative anomalies, respectively. The lower layer (not shown) has a similar structure but is phase-shifted, leading to a vertical tilt.

coefficients $a_2$ and $a_3$ are real. In this limit, an instability exists only if the discriminant $\Delta$ is negative. For $\mu = 0$, the necessary condition for instability is $\Delta < 0$, which becomes:

$$\Omega^2(k^8 - 4k^4) + 1 < 0, \tag{22}$$

Eq. 22 requires that $k^4$ cannot be too small (a longwave cutoff for instability) and $k^4 < 4$ (a shortwave cutoff for instability). This condition also defines a critical forcing strength, $\Omega_c$, below which the flow is stable for all wavenumbers. The minimum value of $\Omega$ that permits instability is found by maximizing the term $(4k^4 - k^8)$, which yields:

$$\Omega_c = \min_k \left( \frac{1}{4k^4 - k^8} \right)^{1/2} = 0.5 \quad (\text{at } k^4 = 2). \tag{23}$$

This is the minimum nondimensional forcing required to generate baroclinic instability in the frictionless limit.

When damping is included ($\mu > 0$), it reduces the growth rate of all modes and can fully stabilize the flow. The instability condition becomes more complex, requiring $\mathrm{Im}(\sqrt{\Delta}) > \mathrm{Im}(a_2)$. This leads to a critical damping value, $\mu_c$, above which all modes are stable:

$$\mu_c = \max_{m,k} \left\{ \frac{\left[\Omega^2(4k^4 - k^8) - 1\right]^{1/2} m}{k^4 + 2k^2} \right\}. \tag{24}$$

The stability analysis results are summarized in the nondimensional parameter space spanned by the nondimensional forcing strength ($\Omega$) associated with the background vertical wind shear and the inverse nondimensional relaxation rate ($\mu^{-1}$). Figure 5a maps the maximum growth rate $\sigma^*$ and the most unstable zonal wavenumber $m_{\max}$ across this space.

The analysis reveals that the forcing parameter $\Omega$ is the primary determinant of the flow's characteristics. Stronger forcing (larger $\Omega$) leads to both a larger maximum growth rate and a larger most unstable wavenumber $m_{\max}$. The relaxation parameter $\mu$ primarily controls the magnitude of the growth rate, with weaker damping (larger $\mu^{-1}$) permitting faster-growing instabilities, but it does not alter the wavenumber of the most unstable mode.

Although larger $\Omega$ values select for larger $m_{\max}$, this does not imply that stronger shear favors smaller vortices. This is because the domain radius $R$ in our model is proportional to $\Omega$ (Eq. 12), so the physical wavelength of the most unstable mode remains relatively consistent. The eigenfunctions corresponding to these modes (Fig. 5b-d) illustrate the spatial structure of the initial perturbations, providing a template for the pattern of vortices that emerges from the linear phase of the instability.

# 4 Nonlinear Numerical Simulations

## 4.1 Model setup

To investigate the nonlinear evolution of the system beyond the predictions of linear theory, we conduct a series of numerical simulations using the open-source Dedalus framework [6]. The simulations solve the nondimensional QGPV equations (Eq. 15) within a disk domain. The equations are discretized using a spectral method, with Fourier modes in

the azimuthal direction ($\varphi$) and Chebyshev polynomials in the radial direction ($r$). For the results presented, the numerical grid employs $N_\varphi = 800$ azimuthal modes and $N_r = 240$ radial modes, corresponding to 1200 azimuthal and 360 radial grid points based on a dealiasing factor of 3/2. We employ a third-order, four-stage Runge-Kutta scheme (RK443) for time integration, with an adaptive time step $\Delta t$ determined by a Courant-Friedrichs-Lewy (CFL) condition to ensure numerical stability. Small-scale dissipation is handled by a linear drag (Rayleigh friction, $\mu$) and a hyperviscosity term ($-\nu\nabla^4 q_i$) that removes enstrophy at the grid scale. In Dedalus, linear terms are placed on the left-hand side of the equation and treated implicitly (except for $J(\Psi_i, q_i)$), whereas nonlinear terms are placed on the right-hand side and treated explicitly.

We perform a suite of numerical experiments by systematically varying the two key nondimensional parameters: the relaxation, $\mu^{-1}$, and the background shear, $\Omega$. The relaxation timescale is varied over six orders of magnitude, $\mu^{-1} \in [10^{-1}, 10^5]$, while the shear is explored for three representative values, $\Omega \in \{0.6, 1.5, 3.5\}$. We do not explore $\Omega > 3.5$, as the required computational resolution becomes prohibitive; for such strong shear, the Rossby deformation radius becomes too small relative to the domain size to be adequately resolved. All simulations were performed on the *Svante* High Performance Computing cluster at MIT.

## 4.2 Simulation results

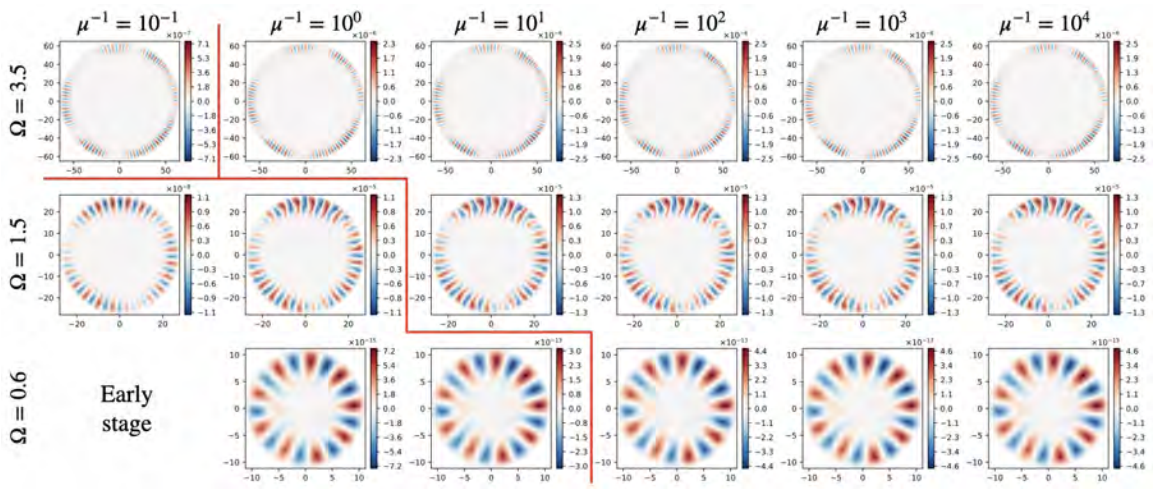


Figure 6: Snapshots of the barotropic PV anomaly, $(q_1+q_2)/2$, in the early stage of nonlinear simulations. The parameter space is defined by the nondimensional background shear, $\Omega$ (rows), and the nondimensional relaxation time, $\mu^{-1}$ (columns). Most simulations are in the linear phase, with structures similar to the eigenmodes in Fig. 5. Red and blue indicate positive (cyclonic) and negative (anticyclonic) PV, respectively. The x- and y-axes in each panel represent nondimensional radius (nondimensionalized by $L_d/\sqrt{2}$). The red lines separate three distinct dynamical regimes shown in Fig. 8.

The temporal evolution of the simulations reveals three distinct phases, illustrated with

snapshots of the barotropic PV anomaly, $(q_1 + q_2)/2$, in Figures 6-8. Initially, the system undergoes an early, linear growth stage (Fig. 6). During this phase, small-amplitude anomalies develop into wave-like structures whose dominant wavenumber ($m$) corresponds to the fastest-growing eigenmode predicted by linear theory (Fig. 5). As the waves amplify, the system enters an intermediate, nonlinear stage (Fig. 7), where the waves break and roll up into coherent eddies. These eddies then migrate meridionally due to the $\beta$ effect: cyclonic (positive) vortices drift poleward, and anticyclonic (negative) vortices drift equatorward. Finally, the system settles into a statistically steady state (Fig. 8), which organizes into one of three distinct dynamical regimes: a weakly nonlinear regime, a vortex regime, or a jet regime.

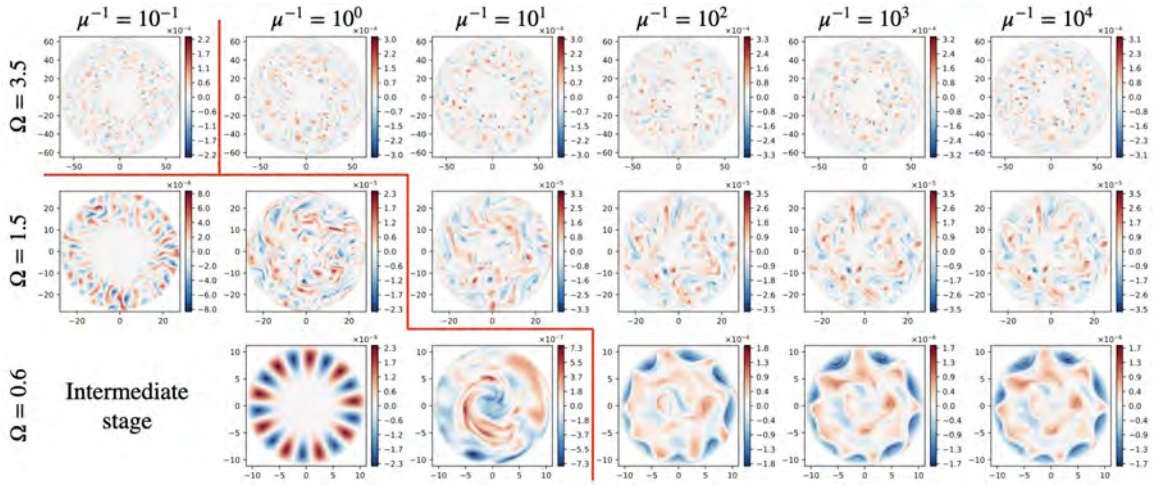


Figure 7: Same as Fig. 6, but for snapshots in the intermediate stage. This phase is characterized by baroclinic eddies migrating poleward (except simulations in the lower left), which homogenizes the background PV gradient.

### 4.2.1 I: Weakly nonlinear regime

At short relaxation times ($\mu^{-1} \lesssim 10^0$), corresponding to strong damping and rapid restoration toward the background state, the system resides in a weakly nonlinear regime. Here, strong drag dissipates energy so efficiently that the initial baroclinic instabilities are prevented from growing to large amplitudes. The resulting flow (e.g., Fig. 8, $\Omega = 1.5, \mu^{-1} = 10^{-1}$) is characterized by weak, wave-like structures whose patterns closely resemble the eigenfunctions of the most unstable modes predicted by linear stability analysis (Fig. 5). In this state, nonlinear effects act to weaken the mean shear and potential vorticity gradients, thereby halting the linear growth and maintaining a steady balance between energy input and dissipation. Consequently, meridional mixing is inefficient, and the background PV gradient is barely modified (Fig. 9a). At the regime boundary (e.g., $\Omega = 1.5$, $\mu^{-1} = 10^0$ and $\Omega = 0.6$, $\mu^{-1} = 10^1$ ), nonlinear effects start to take over.

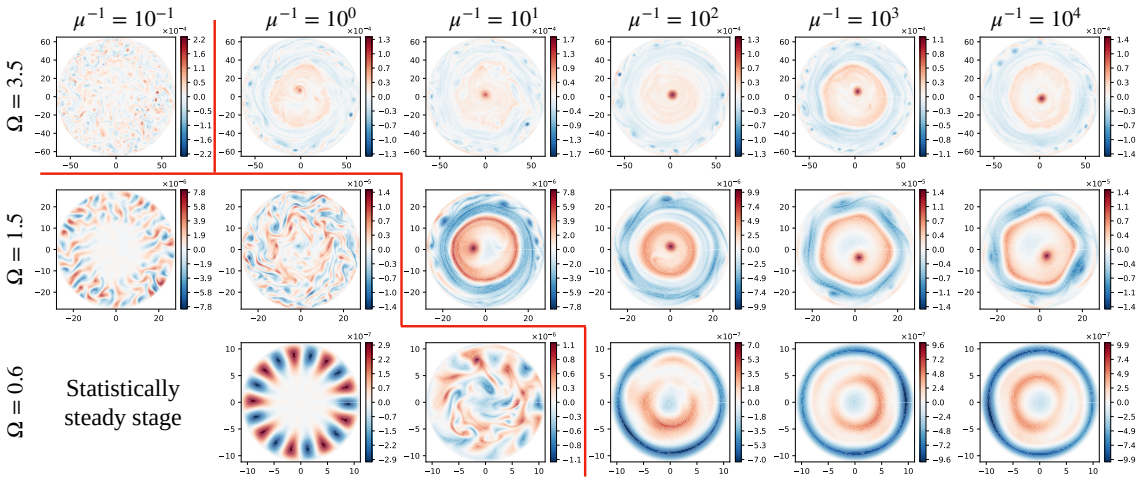


Figure 8: Snapshots of the barotropic PV anomaly, $(q_1 + q_2)/2$, in the statistically steady stage. Three distinct dynamical regimes emerge: a **weakly nonlinear regime** at strong relaxation (small $\mu^{-1}$, lower-left), a **vortex regime** at intermediate relaxation (middle panels), and a **jet regime** at weak relaxation (large $\mu^{-1}$, right panels).

#### 4.2.2 II: Vortex regime

At sufficiently strong shear (e.g., $\Omega = 3.5$) and slow relaxation, the system transitions into a vortex-dominated regime. In this state, linearly unstable modes grow to finite amplitude, allowing nonlinear interactions to become significant. The waves break and roll up into a field of coherent, isolated vortices (Fig. 8, $\Omega = 3.5$, $\mu^{-1} = 10^{-1}$). These vortices vigorously mix the potential vorticity, flattening the background PV gradient that sustains them (Fig. 9b). To further examine this regime, we conducted additional experiments varying $\mu^{-1}$ from $1 \times 10^{-1}$ to $8 \times 10^{-1}$. As shown in Fig. 10, increasing the relaxation time (i.e., weakening the damping) promotes vortex merger and drives a gradual transition toward a jet-dominated state. A distinct central polar vortex and surrounding jet become increasingly prominent as $\mu^{-1}$ increases, culminating in a fully organized jet–vortex structure for $\mu^{-1} = 1$.

#### 4.2.3 III: Jet regime

For cases with long relaxation times (large $\mu^{-1} \gtrsim 10^{1}$), the system transitions into a jet-dominated regime (Fig. 8). In this state, the extended lifetime of individual vortices allows inverse energy cascades to develop [3, 16], whereby smaller eddies merge and organize into a large-scale, zonally symmetric flow. The structure of the final equilibrium, however, depends strongly on the background shear $\Omega$. At low shear ($\Omega = 0.6$), the system organizes into broad circumpolar zonal jets without forming a coherent polar vortex, resulting in a stable westerly current dominating the barotropic flow. In contrast, for moderate to strong shear ($\Omega \geq 1.5$), the inverse cascade leads to the emergence of a strong, persistent cyclonic vortex centered near the pole and surrounded by a prominent jet. Interestingly, the surrounding jet appears sharper and more coherent at $\Omega = 1.5$ than at $\Omega = 3.5$, where

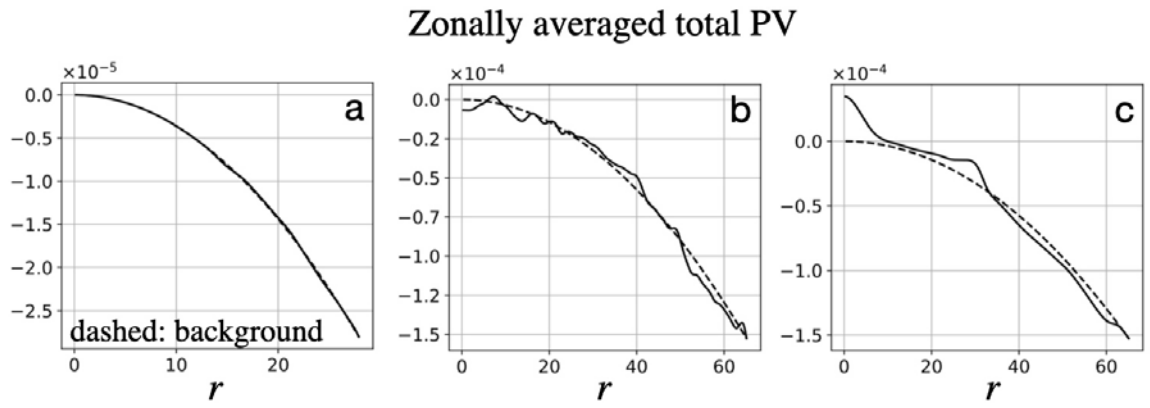


Figure 9: Zonally averaged total potential vorticity (PV) profiles for the three distinct dynamical regimes at one time step in the statistically steady stage. The total barotropic PV is defined as $\langle (q_1 + q_2)/2 \rangle_\varphi - r^2/2$. The dashed line in each panel shows the background PV profile, while the solid line shows the zonally averaged total PV from the simulation at one time step. (a) In the **weakly nonlinear regime**, the PV profile closely follows the background state. (b) In the **vortex regime**, the PV gradient is flattened within $r = 20$, a signature of efficient mixing by coherent vortices. (c) In the **jet regime**, the profile develops a "staircase" structure, with well-mixed regions separated by a sharp step at $r \approx 30$ corresponding to a zonal jet that acts as mixing barriers. The strong positive PV

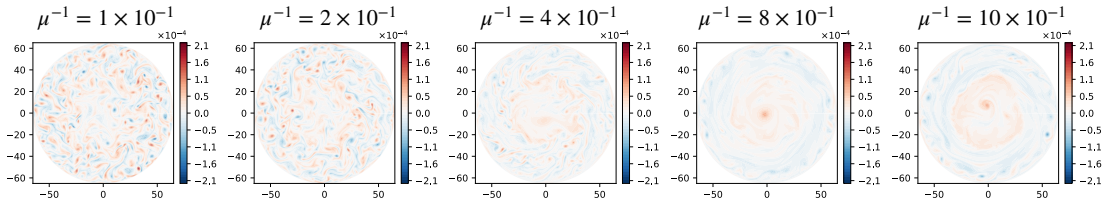


Figure 10: Transition from the vortex regime to the jet regime, shown in terms of snapshots of the PV field, as the relaxation time $\mu^{-1}$ increases for a fixed shear of $\Omega = 3.5$. At strong drag ($\mu^{-1} = 0.1$, left), the flow is a disorganized field of vortices. As drag weakens (moving right), vortices merge, and a central polar vortex begins to emerge ($\mu^{-1} = 0.4$). By $\mu^{-1} = 1.0$ (right), the system has fully transitioned into an organized state dominated by a strong, central cyclonic vortex encircled by a jet.

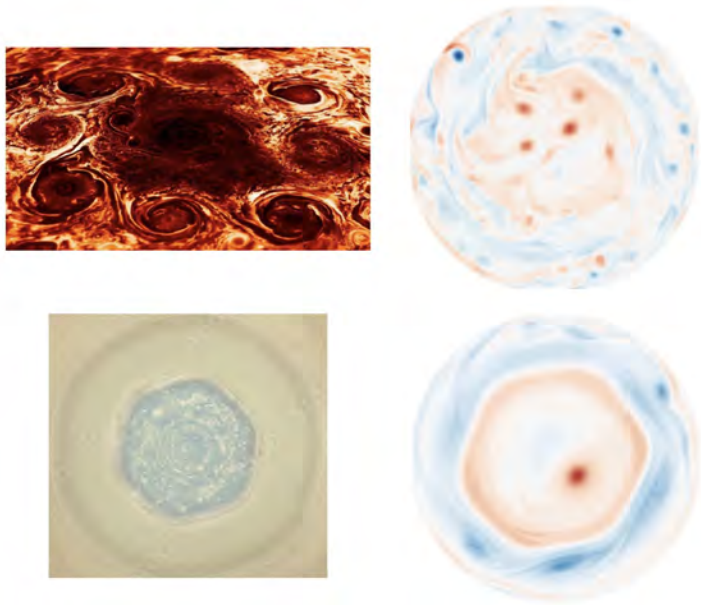

Figure 11: Comparison of simulation results with observations of Jupiter and Saturn [21, 22]. (Top) A snapshot of a simulation, visualized in terms of PV, in the jet regime ($\Omega = 3.5, \mu^{-1} = 10^0$, right) qualitatively reproduces the multi-vortex structure observed at Jupiter's north pole by Juno (left). (Bottom) A simulation at very weak damping ($\Omega = 1.5, \mu^{-1} = 10^4$, right) successfully generates a stable polygonal jet analogous to Saturn's hexagonal jet stream observed by Cassini (left).

enhanced baroclinicity weakens its structure.

During the simulation at $\Omega = 3.5$ and $\mu^{-1} = 10^0$, a set of parameters within Jupiter's range, a short-lived pattern reminiscent of Jupiter's polar "crystal" structure emerges (Fig. 11). A particularly striking behavior occurs for $\Omega = 1.5$ under very weak damping ($\mu^{-1} \in [10^3, 10^4]$), where the jet surrounding the polar vortex develops a stable polygonal pattern—appearing as a pentagon or hexagon (Figs. 8 and 11). In these cases, the central vortex is frequently displaced from the geometric center of the domain. Such polygonal jets are famously observed at Saturn's poles [4] and have been reproduced in both laboratory experiments and numerical models [2]. They are generally attributed to instabilities and standing Rossby wave patterns that form along sharp PV gradients within the jet. The mechanisms controlling the number of vertices, maintaining their stability, and producing off-center vortices remain open questions.

### 4.3 Energetics of the baroclinic system

To understand the energy balance that sustains the vortices and jets in the nonlinear regimes, we analyze the system's energetics. The evolution of the total energy density, $E = \frac{1}{2}\langle \alpha_1 |\nabla\psi_1|^2 + \alpha_2 |\nabla\psi_2|^2 + L_d^{-2}(\psi_1 - \psi_2)^2 \rangle$, which is the sum of the kinetic and available potential energy, is derived by multiplying the QGPV equation (Eq. 9) by $-\alpha_i \psi_i$ and integrating over the domain. In a statistically steady state, the injection of energy from the background shear must balance the dissipation by drag. The energy evolution equation is given by:

$$(\partial_t - 2\mu)E = \epsilon = \sum_i \alpha_i U_i \overline{v_i' q_i'} = 2\alpha_1\alpha_2 \Omega r (\overline{v_1' q_1'} - \overline{v_2' q_2'}) \tag{25a}$$

$$\approx 2\alpha_1\alpha_2 \Omega r K_e \partial_r (\overline{q_2} + Q_2 - \overline{q_1} - Q_1) \tag{25b}$$

$$\approx 2\alpha_1\alpha_2 \Omega r K_e \partial_r (Q_2 - Q_1) \tag{25c}$$

$$= 4(\Omega^2 / L_d^2) r^2 (V L_{Rh}) \tag{25d}$$

where $K_e$ is the eddy diffusivity and $V$ represents the root-mean-square barotropic eddy velocity. The energy injection rate, $\epsilon$, which balances the dissipation ($2\mu E$) in a statistically steady state, is derived from the work done by the background flow ($U_i = \partial\Psi_i/\partial r$) on the eddies. The exact expression for this energy conversion is given in Eq. (25a), where the injection is written in terms of the zonally-averaged radial eddy flux of potential vorticity ($\overline{v_i' q_i'}$).

To simplify this expression, we parameterize the eddy PV flux using a mixing-length argument, assuming the flux is a downgradient diffusion process: $\overline{v_i' q_i'} \approx -K_e \partial_r (\overline{q_i} + Q_i)$. Here, $K_e$ is an effective eddy diffusivity. Substituting this into the energy balance yields Eq. (25b), which relates the energy injection to the gradient of the total mean PV. We assume that the mean induced PV gradients ($\overline{q_i}$) are small and largely cancel each other out compared to the imposed background PV gradient. This allows us to approximate the expression by retaining only the background PV gradient term, as shown in Eq. (25c). Finally, following the scaling theory of [13], the eddy diffusivity is proportional to the characteristic eddy velocity and the mixing length, which in this case is the Rhines scale,

$L_{Rh}$. So, we set $K_e \sim V L_{Rh}$. Substituting the explicit form of the background PV gradient $(Q_2 - Q_1)$ and this scaling for $K_e$ leads to the final expression for the energy injection rate (Eq. (25d)). This result provides a crucial link between the external parameters of the system ($\Omega$, $L_d$) and the emergent velocity scale ($V$) of the resulting turbulence. The physical pathway for energy is governed by the principles of two-dimensional turbulence. Baroclinic instability injects energy at a characteristic scale, typically the Rossby deformation radius, $L_d$. This energy then cascades to larger scales (smaller wavenumbers) via an inverse energy cascade, leading to the vortex mergers and jet formation observed in our simulations (Fig. 8). This process continues until the cascade is arrested at a larger scale, the Rhines scale $L_{Rh} \approx (V/\gamma)^{1/3}$, where the eddy turnover time becomes comparable to the period of planetary Rossby waves. At this scale, the turbulent eddies are sheared apart into zonal jets, and the energy is ultimately dissipated by the Rayleigh drag [30].

By equating the energy injection rate with the cascade rate at the arrest scale ($\epsilon \sim V^3/L_{Rh}$), one can derive scaling laws for the characteristic eddy velocity ($V$) and the energy level of the system. This balance yields the following predictions for the characteristic barotropic velocity and energy injection rate:

$$V \sim \Omega^3 L_d^{-3} \gamma^{-2} \tag{26a}$$

$$\epsilon \sim \Omega^8 L_d^8 \gamma^{-5} \tag{26b}$$

Therefore, $L_{Rh} = \Omega/(L_d\gamma)$. We test these theoretical predictions against our suite of numerical simulations using the scaling relations above. Figure 12 plots the numerically-diagnosed, time-averaged barotropic velocity ($V_{bt}$) and energy dissipation rate ($\epsilon$) against their corresponding theoretical scaling laws, averaged over the last several hundred time steps in the steady stage. In these plots, the size of the circles is proportional to the forcing strength, $\Omega$, while the color represents the drag coefficient, $\mu$, with lighter shades for smaller $\mu$ (weaker drag) and darker shades for larger $\mu$ (stronger drag). The data from all simulations collapse well around the best-fit lines, confirming that the Held-Larichev scaling theory provides a decent description of the system's energetics over the $\gamma$-plane as well, despite the theory is designed for the mid-latitude $\beta$-plane. As expected, a larger forcing/shear ($\Omega$) consistently leads to a more turbulent state, characterized by a stronger final eddy velocity and a larger energy injection rate. Interestingly, the behavior of both $V$ and $\epsilon$ with respect to the relaxation, $\mu$, is non-monotonic. This arises from the dual role of the parameter $\mu$: it represents both energy dissipation (Rayleigh friction) and the restoration of the background state. Increasing $\mu$ enhances the drag, which tends to reduce the final eddy velocity. However, a larger $\mu$ also restores the background PV gradient more rapidly, preventing the eddies from generating a strong mean flow that would otherwise weaken the background shear and suppress baroclinic conversion. Depending on the regime, one of these competing effects can dominate, leading to the observed non-monotonic relationship between the drag and the overall energy level of the system.

## 5 Discussion and Conclusion

In this study, we developed and analyzed a two-layer quasi-geostrophic model on a $\gamma$-plane to investigate whether baroclinic instability can serve as a primary driver for the diverse

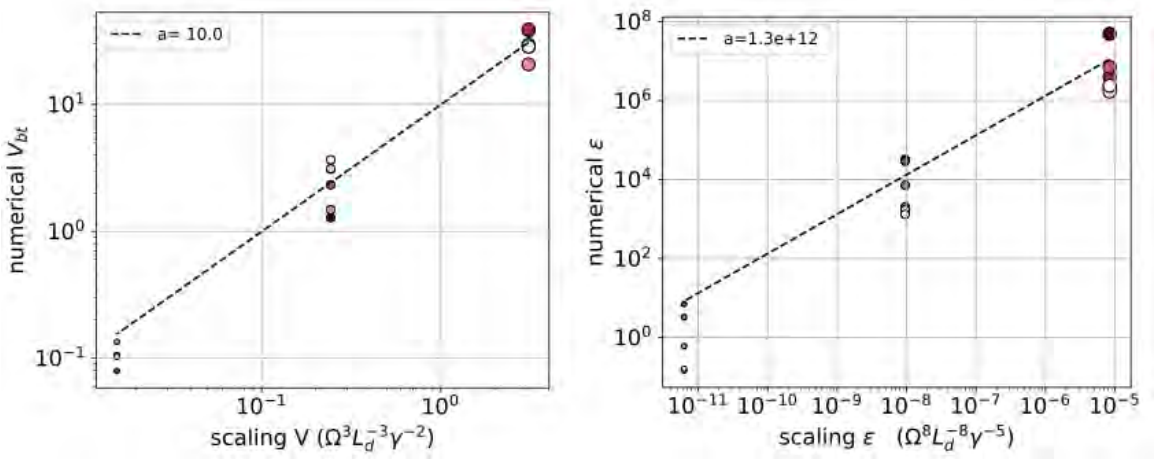


Figure 12: Numerical verification of the scaling theory for the baroclinic system. Left: The diagnosed barotropic eddy velocity ($V_{bt}$) from simulations versus the theoretical scaling, $V \sim \Omega^3 L_d^{-3}\gamma^{-2}$. Right: The diagnosed energy dissipation rate ($\epsilon$) versus the theoretical scaling, $\epsilon \sim \Omega^8 L_d^8 \gamma^{-5}$. The size of the circles represents the forcing strength $\Omega$, and the color indicates the drag coefficient $\mu$ (lighter for small $\mu$, darker for large $\mu$). The data points cluster around the dashed best-fit lines, confirming the validity of the scaling theory. The legends show the proportionality constant (slope) for a line passing through the origin, indicating a strong linear relationship between the simulation results and the theoretical scaling.

polar vortex structures observed on giant planets.

Our linear stability analysis confirmed that the fundamental properties of baroclinic instability on a polar $\gamma$-plane are consistent with the classic theory developed for the mid-latitude $\beta$-plane. We derived the dispersion relation and demonstrated the existence of both shortwave and longwave cutoffs for instability, with the growth rate and the most unstable mode being primarily controlled by the background shear, $\Omega$. This linear framework provided crucial predictions for the initial scales of eddy formation in our nonlinear simulations.

The core of our findings comes from the nonlinear simulations performed with the Dedalus framework. By systematically varying the nondimensional shear ($\Omega$) and relaxation ($\mu^{-1}$), we identified three distinct dynamical regimes:

1. A **weakly nonlinear regime** at short relaxation times, where the flow is dominated by small-amplitude wave-like structures resembling the most unstable linear modes.

2. A **vortex regime** at stronger shear and short relaxation times, characterized by a field of many coherent vortices actively mixing potential vorticity.

3. A **jet regime** at long relaxation, where an inverse energy cascade leads to the self-organization of the flow into large-scale zonal jets and stable, coherent polar vortices.

Interestingly, some of our simulation results seem to resemble the observed fluid patterns over the polar regions of Jupiter and Saturn. A transient stage in the jet regime at high shear ($\Omega = 3.5, \mu^{-1} = 10^0$) qualitatively reproduces the multi-vortex "crystal-like" structure observed by Juno at Jupiter's pole, although it is not stable in that simulation. Meanwhile, the jet regime at lower shear and very weak damping ($\Omega = 1.5, \mu^{-1} = 10^4$) successfully generates a stable, polygonal jet stream encircling a central cyclone, providing a strong analog to Saturn's famous hexagonal vortex.

Furthermore, our analysis of the system's energetics showed that the simulations adhere to the scaling laws predicted by the classic theory of geostrophic turbulence over $\beta$ plane [13]. The decent collapse of our simulation data with the theoretical predictions for eddy velocity and energy injection rate validates that the underlying dynamics are governed by an inverse energy cascade arrested at the Rhines scale.

In conclusion, our results seem to suggest that baroclinic instability is potentially capable of driving the range of polar dynamics observed on giant planets. The competition between shear-driven turbulence and dissipation naturally leads to the emergence of distinct, self-organized states that bear a striking resemblance to both Jupiter's and Saturn's poles.

For future work, we plan to relax some of the idealizations in the current model. A key next step is to explore the effect of unequal layer depths ($H_1 \neq H_2$). This modification will allow for a more realistic representation of the vertical structure of the atmospheres, particularly on Jupiter, where a relatively shallow weather layer is thought to exist. Investigating how differential layer depths modulate the instability and the subsequent nonlinear evolution will be crucial for refining the mapping between our model parameters and the specific conditions on each planet.

## Acknowledgements

I would like to express my sincere gratitude to my advisors, Wanying Kang, Glenn Flierl, Chang Liu, Adrian van Kan, and Keaton Burns, for their patient guidance and insightful discussions throughout this project. I am especially grateful to Wanying and Glenn for their tremendous support. As this was my first time working on geophysical fluid dynamics on other planets, it has been a fun and surprising summer. I am amazed at how much I have learned. I owe a special thanks to Keaton Burns for his invaluable help with Dedalus; he is truly a hero. I also thank Pascale Garaud and David Goluskin for organizing this wonderful summer school, and my fellow students for their companionship and support.

## References

[1] A. Adriani, A. Mura, G. Orton, and et al., *Clusters of cyclones encircling Jupiter's poles*, Nature, 555 (2018), pp. 216–219.

[2] A. C. B. Aguiar, P. L. Read, R. D. Wordsworth, T. Salter, and Y. H. Yamazaki, *A laboratory model of Saturn's North Polar Hexagon*, Icarus, 206 (2010), pp. 755–763.

[3] A. Alexakis and L. Biferale, *Cascades and transitions in turbulent flows*, Physics Reports, 767 (2018), pp. 1–101.

[4] K. H. Baines, T. W. Momary, L. N. Fletcher, A. P. Showman, M. Roos-Serote, R. H. Brown, B. J. Buratti, R. N. Clark, and P. D. Nicholson, *Saturn's north polar cyclone and hexagon at depth revealed by Cassini/VIMS*, Planetary and Space Science, 57 (2009), pp. 1671–1681.

[5] S. R. Brueshaber, K. M. Sayanagi, and T. E. Dowling, *Dynamical regimes of giant planet polar vortices*, Icarus, 323 (2019), pp. 46–61.

[6] K. J. Burns, G. M. Vasil, J. S. Oishi, D. Lecoanet, and B. P. Brown, *Dedalus: A flexible framework for spectral simulations*, Physical Review Research, 2 (2020), p. 023068.

[7] T. Cai, *Examination of vorticity and divergence on a rotating turbulent convection model of Jupiter's polar vortices*, Journal of Geophysical Research: Planets, 129 (2024), p. e2023JE008281.

[8] T. Cai, K. L. Chan, and H. G. Mayr, *Deep, closely-packed, long-lived cyclones on Jupiter's poles*, The Planetary Science Journal, 2 (2021), p. 81.

[9] A. Carruthers, S. Thomson, and W. Seviour, *The role of vortex shielding on polar crystal formation & vortex dynamics on Jupiter*, in EGU General Assembly 2023, Vienna, Austria, 2023. EGU23-14801.

[10] S. Chen, A. P. Ingersoll, and C. Li, *Vortex crystals at Jupiter's poles: emergence controlled by initial small-scale turbulence*, Icarus, 429 (2025), p. 116438.

[11] B. F. Farrell and P. J. Ioannou, *Formation of jets by baroclinic turbulence*, Journal of the Atmospheric Sciences, 65 (2008), pp. 3353–3375.

[12] B. Gallet and R. Ferrari, *The vortex gas scaling regime of baroclinic turbulence*, Proceedings of the National Academy of Sciences, 117 (2020), pp. 4491–4497.

[13] I. M. Held and V. D. Larichev, *A scaling theory for horizontally homogeneous, baroclinically unstable flow on a $\beta$-plane*, Journal of the Atmospheric Sciences, 53 (1996), pp. 946–952.

[14] A. P. Ingersoll, S. P. Ewald, F. Tosi, et al., *Vorticity and divergence at scales down to 200-km within and around the polar cyclones of Jupiter*, Nature Astronomy, 6 (2022), pp. 1280–1286.

[15] Y. Kaspi and G. R. Flierl, *Formation of jets by baroclinic instability on gas planet atmospheres*, Journal of the Atmospheric Sciences, 64 (2007), pp. 3177–3194.

[16] R. H. Kraichnan, *Inertial ranges in two-dimensional turbulence*, Physics of Fluids, 10 (1967), pp. 1417–1423.

[17] C. Li, A. P. Ingersoll, A. P. Klipfel, and H. Brettle, *Modeling the stability of polygonal patterns of vortices at the poles of Jupiter as revealed by the Juno spacecraft*, Proceedings of the National Academy of Sciences, 117 (2020), pp. 24082–24087.

[18] L. Li, K. H. Baines, M. A. Smith, R. A. West, S. Pérez-Hoyos, H. J. Trammell, A. A. Simon-Miller, B. J. Conrath, P. J. Gierasch, G. S. Orton, C. A. Nixon, G. Filacchione, P. M. Fry, and T. W. Momary, *Emitted power of Jupiter based on Cassini CIRS and VIMS observations*, Journal of Geophysical Research, 117 (2012).

[19] L. Li, X. Jiang, R. A. West, and et al., *Less absorbed solar energy and more internal heat for Jupiter*, Nature Communications, 9 (2018), p. 3709.

[20] J. Liu and T. Schneider, *Mechanisms of jet formation on the giant planets*, Journal of the Atmospheric Sciences, 67 (2010), pp. 3652–3672.

[21] National Aeronautics and Space Administration and NASA, *Cassini mission*. `https://science.nasa.gov/mission/cassini/about-the-mission/`.

[22] ——, *Juno mission*. `https://science.nasa.gov/mission/juno/`.

[23] M. E. O'Neill, K. A. Emanuel, and G. R. Flierl, *Polar vortex formation in giant planet atmospheres due to moist convection*, Nature Geoscience, 8 (2015), pp. 523–526.

[24] ——, *Weak jets and strong cyclones: shallow-water modeling of giant planet polar caps*, Journal of the Atmospheric Sciences, 73 (2016), pp. 1841–1855.

[25] P. Read, D. Kennedy, N. Lewis, H. Scolan, F. Tabataba-Vakili, Y. Wang, S. Wright, and R. Young, *Baroclinic and barotropic instabilities in planetary atmospheres: energetics, equilibration and adjustment*, Nonlinear Processes in Geophysics, 27 (2020), pp. 147–173.

[26] R. K. Scott, *Polar accumulation of cyclonic vorticity*, Geophysical and Astrophysical Fluid Dynamics, 105 (2010), pp. 409–420.

[27] R. K. Scott and L. M. Polvani, *Forced-dissipative shallow-water turbulence on the sphere and the atmospheric circulation of the giant planets*, Journal of the Atmospheric Sciences, 64 (2007), pp. 3158–3176.

[28] J. Shi and W. Kang, *Polar vortex dynamics on gas giants: insights from 2D energy cascades*. Under revision, 2025.

[29] L. Siegelman, W. R. Young, and A. P. Ingersoll, *Polar vortex crystals: emergence and structure*, Proceedings of the National Academy of Sciences, 119 (2022), p. e2120486119.

[30] G. K. Vallis, *Atmospheric and oceanic fluid dynamics: fundamentals and large-scale circulation*, Cambridge University Press, 2017.

| REPORT DOCUMENTATION PAGE | 1. Report No. WHOI-2025-13 | 2. | 3. Recipient's Accession No. |
|---|---|---|---|
| 4. Title and Subtitle<br>2025 Program of Study: Instabilities and Bifurcations in GFD | | | 5. Report Date<br>December 2025<br>6. |
| 7. Author(s)<br>Pascale Garaud and David Goluskin | | | 8. Performing Organization Rept. No.<br>10. Project/Task/Work Unit No. |
| 9. Performing Organization Name and Address<br>Woods Hole Oceanographic Institution | | | 11. Contract(C) or Grant(G) No.<br>(C)<br>(G) OCE-1829864 |
| 12. Sponsoring Organization Name and Address<br>National Science Foundation Program Manager Dr. Baris M. Uz 15 Eisenhower Avenue Alexandria, VA 22314 | | | 13. Type of Report & Period Covered<br>Technical Report<br>14. |

15. Supplementary Notes

This report should be cited as: Woods Hole Oceanographic Institution Technical Report, WHOI-2025-13 https://doi.org/10.1575/1912/72576

16. Abstract (Limit: 200 words)

The theme of the Geophysical Fluid Dynamics Program for summer 2025 was Instabilities and Bifurcations in GFD. The first week of principal lectures were delivered by Joseph Pedlosky (WHOI), focusing on the baroclinic instability and other linear and nonlinear instabilities in a geophysical context. The second week of principal lectures were delivered by Laurette Tuckerman (ESPCI Paris), who taught the mathematical underpinnings needed to understand instabilities and bifurcations in fluid systems. These proceedings contain notes on the ten principal lectures, produced by student fellows together with the lecturers. They also contain reports by the student fellows on their summer research projects. Detailed notes are not included for the summer's many other stimulating activities, which included near-daily research seminars, a tutorial on geophysical models by Glenn Flierl, a tutorial on the Dedalus code by Keaton Burns, a presentation by the summer's co-directors on how to give good talks, and an example of a very good talk: the Sears Public Lecture by Jennifer MacKinnon (UC San Diego) entitled "Fresh, Salty or Spicy: How Layering of Different Types of Water Controls Heat, Hurricanes and Habitats in the Gulf of Mexico."

17. Document Analysis

a. Descriptors

Geophysical fluid dynamics,
Baroclinic Instabilities in Fluid Systems,
Bifurcations in Fluid Systems

b. Identifiers/ Open-Ended Terms

c. COSATI Field/ Group

| 18. Availability Statement | 19. Security Class (This Report) | 21. No. of Pages |
|---|---|---|
| Approved for public release, distribution unlimited | | 406 |
| | 20. Security Class (This Page) | 22. Price |